

**THE ELASTIC AND INELASTIC BEHAVIOR OF WOVEN GRAPHITE
FABRIC REINFORCED POLYIMIDE COMPOSITES**

**Kevin H. Searles
B.S., Mechanical Engineering Technology
Oregon Institute of Technology
Klamath Falls, Oregon, 1993**

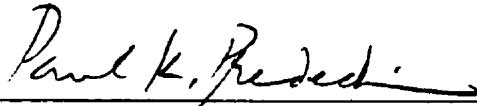
**A thesis submitted to the faculty of the
Oregon Graduate Institute of Science and Technology
in partial fulfillment of the
requirements for the degree
Doctor of Philosophy
in
Materials Science and Engineering**

September, 2000

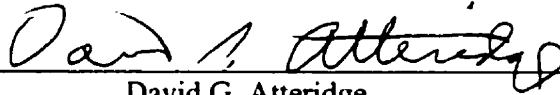
The thesis "The Elastic and Inelastic Behavior of Woven Graphite Fabric Reinforced Polyimide Composites" by Kevin H. Searles has been examined and approved by the following Examination Committee:



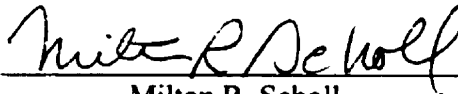
Maciej S. Kumosa, Thesis Research Advisor
Center for Advanced Materials & Structures
Professor, Dept. of Engineering
University of Denver, Denver, CO 80208



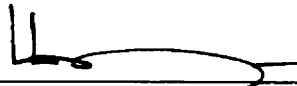
Paul K. Predecki
Center for Advanced Materials & Structures
Professor, Dept. of Engineering
University of Denver, Denver, CO 80208



David G. Atteridge
Professor
Dept. of Mechanical Engineering
Portland State University, Portland, OR 97207



Milton R. Scholl
Associate Professor
Dept. of Materials Science and Engineering
Oregon Graduate Institute of Science and Technology
Beaverton, OR 97006



Lemmy L. Meekisho
Associate Professor
Dept. of Mechanical Engineering
Portland State University, Portland, OR 97207

DEDICATION

To

**My mother Marcia, my wife Kezia and
my daughters Derica and Tristin ...**

ACKNOWLEDGMENTS

I must begin by expressing my deepest gratitude toward my thesis advisor Dr. Maciej Kumosa. His long-distance support, funding and numerous ideas were critical to the accomplishment of this work. The many discussions held with him on the theoretical and applied sciences of composite materials have certainly broadened my understanding and appreciation of the subjects. I sincerely appreciate his support of my endeavor as well as the hospitality of his family during my many research visits to Colorado.

To the members of my thesis committee, Drs. Paul K. Predecki, David G. Atteridge, Milton R. Scholl, Lemmy L. Meekisho and James D. Harvey, I express my sincere appreciation for critical reviews of this document and the thought invoking discussions on many aspects of the science of materials. Dr. Lemmy Meekisho, thank you for the support of and teachings on finite element analysis using ANSYS. Upon reading, you can imagine the influence of those teachings on this work.

To my colleague Greg Odegard, friend Lucas Kumosa, faculty and staff of Oregon Graduate Institute of Science and Technology and the University of Denver and fellow students, I appreciate the ideas, support, warmth and company. To my mother Marcia, my wife Kezia and my daughters Derica and Tristin, I could not have completed this work without your love and support.

This work was supported by the Air Force Office of Scientific Research (AFOSR) under contracts F49620-96-1-0314 and F49620-95-1-0250 inclusive from April, 1995 to July, 1999. This work was performed in close collaboration with Mr. M. Castelli of the NASA Glenn Research Center and Mr. R. Cairo of Pratt & Whitney. The composite materials investigated in this work were supplied by both organizations. Additional support also came from the Department of Materials Science and Engineering, Oregon Graduate Institute of Science and Technology and the Center for Advanced Materials and Structures, University of Denver.

TABLE OF CONTENTS

DEDICATION	iii
ACKNOWLEDGMENTS	iv
List of Tables	ix
List of Figures	xi
Nomenclature	xxi
ABSTRACT	xxvii
SECTION 1. INTRODUCTION	1
1.1. General Textile Categories	3
1.1.1. 2-D Quasi-Laminar Composite Systems	3
1.2. Ideal Textile Geometries	4
1.2.1. Woven 8HS Geometry	4
1.3. Graphite Polyimides	5
1.3.1. Polypyromellitimide Morphology	7
1.3.2. Commercial Types	8
1.4. WGFRR Composite Behavior	8
SECTION 2. BACKGROUND	17
2.1. Linear Elastic Behavior of a Solid	19
2.1.1. Force and Stress	20
2.1.1.1. Equations of Equilibrium	21
2.1.2. Displacement and Strain	23
2.1.2.1. Equations of Compatibility	25
2.1.3. Material Properties: Hooke's Law	26
2.2. Mechanics of a Composite Lamina	28
2.2.1. Unidirectional Composite Lamina	28
2.2.1.1. General Constitutive Relations	28
2.2.1.2. Simplified Constitutive Relations	31

2.2.2. Woven Fabric Lamina	34
2.2.2.1. One-Dimensional Characterization	36
2.2.2.2. Two-Dimensional Characterization	38
2.2.2.3. Three-Dimensional Characterization	40
2.3. Mechanics of a Composite Laminate	42
2.3.1. Classical Lamination Theory	42
2.3.2. Laminate Constitutive Relations	45
2.3.2.1. Considerations for Thick Laminates	45
2.3.2.2. Considerations for Temperature	46
2.4. Failure Behavior in Composite Laminates	48
2.4.1. Modes of Crack Propagation	49
2.4.2. Failure Classifications	50
2.4.3. Numerical Schemes	56
SECTION 3. MICRO- AND MESOSCALE ELASTIC BEHAVIOR	67
3.1. Prediction of Elastic Constants	67
3.1.1. Examination of Lamina Geometry	68
3.1.1.1. Woven Tow Cross-Section	68
3.1.1.2. Woven Tow Centerline	70
3.1.1.3. Woven Tow Surfaces	71
3.1.2. Micromechanics Approach	71
3.1.2.1. Evaluation of Woven Tow Properties	72
3.1.2.2. Composite Cylinder Assemblage	73
3.1.2.3. Strain Energy Equivalence	77
3.1.3. Mesomechanics Approach	82
3.1.3.1. Evaluation of Woven Lamina Properties	82
3.1.3.2. Compliance Transformation	84
3.1.3.3. Application of Classical Lamination Theory	86
3.1.3.4. Numerical Strain Energy Method	88

3.2. Fundamental Stress Distributions	90
3.2.1. Finite Element Model	93
3.2.1.1. Geometry and Materials	94
3.2.1.2. Boundary Conditions	95
3.2.2. Stress Modeling	96
3.2.2.1. Kriging Interpolation	97
3.2.2.2. Punctual Kriging	98
3.3. Results and Discussion	99
SECTION 4. MACROSCALE ELASTIC AND INELASTIC BEHAVIOR	160
4.1. Shear and Biaxial Properties	160
4.1.1. The Experimental Tests	161
4.1.1.1. Materials	168
4.1.1.2. Specimen Designs	169
4.1.1.3. Apparatus	172
4.1.2. Apparent Elastic Constants	176
4.1.2.1. Stress and Strain	176
4.1.3. Apparent Failure Stresses	178
4.1.3.1. Comparisons at Elevated Temperatures	180
4.2. Modeling of Shear and Biaxial Tests	180
4.2.1. Structural Nonlinearities	181
4.2.1.1. Geometric	182
4.2.1.2. Boundary Contact	185
4.2.2. Load Eccentricities	188
4.2.2.1. Numerical Models	191
4.2.2.2. Properties and Boundary Conditions	192
4.3. Nonlinear Material Behavior in Shear	193
4.3.1. Anisotropic Plasticity	195
4.3.2. Damage and Failure	199

4.3.2.1. Progressive Damage Criterion	200
4.3.2.2. Damage Reconstruction	202
4.4. Results and Discussion	205
SECTION 5. CONCLUSIONS	291
SECTION 6. SUGGESTIONS FOR FUTURE WORK	298
References	301
APPENDIX A	310
A.1. Fortran 77 Code: Prediction of Elastic Constants	310
A.1.1. Sample Input Data	329
A.2. Fortran 77 Code: Methods of Hashin, Halpin-Tsai and Chamis	337
A.2.1. The Method of Hashin	337
A.2.2. The Method of Halpin-Tsai	342
A.2.3. The Method of Chamis	344
APPENDIX B	348
B.1. ANSYS User Files - 8HS Woven Lamina	348
B.1.1. ¼ Symmetry 3-D Square Array RVE	348
B.1.2. 8HS Woven 3-D IVE	352
APPENDIX C	372
C.1. ANSYS User Files - Validation of Shear and Biaxial Tests	372
C.1.1. 2-D Biaxial Iosipescu Model (geometric, boundary contact)	373
C.1.2. 3-D Biaxial Iosipescu Model (load eccentricities)	383
C.1.3. 3-D Biaxial Iosipescu Model (plasticity, damage)	393
APPENDIX D	404
D.1. Mechanical Design - Modified Loading Blocks	404
Biographical Note	409

List of Tables

1.1.	Material properties for selected aerospace alloys and polymer matrix composites	12
3.1.	Reported constituent elastic properties for various graphite and carbon-based, anisotropic fibers and polyimide-type matrices	111
3.2.	Micromechanics results for 8HS woven tow elastic properties based on CCA theory for composite systems identified from constituent properties in Table 3.1	112
3.3.	Non-zero extension, extension-bending coupling and bending compliance constants predicted by the present micro-to-mesoscale analytical mechanics model for an 8HS woven fabric lamina and equivalent cross-ply laminate	113
3.4.	Elastic properties predicted by the present micro-to-mesoscale analytical mechanics model for various 16-layered composite systems considered	114
3.5.	Apparent elastic properties obtained by off-axis tensile and biaxial Iosipescu shear experiments (c.f. Section 4)	115
3.6.	Metrics for the fiber, tow, lamina and composite plaque obtained from SEM micrographs and C-SCAN data	115
3.7.	SMM and FE results for elastic properties of the F-b ^(H) and F-c ^(H) systems evaluated at tow and laminate fiber volume fractions	116
3.8.	Maximum and minimum normalized stresses extrapolated to irregularly spaced grids within cutting planes	117
4.1.	Nominal dimensions for specimens used in the experimental program. For specification of variable callout, Figure 4.6 serves as the reference	229
4.2.	Description of ANSYS 5.3 capabilities for solving problems involving geometric nonlinearities. (c.f. [79])	230

4.3.	Material properties assumed in the 3-D analyses of load eccentricities imposed on the biaxial and modified biaxial Iosipescu specimens	230
4.4.	Imposed boundary conditions on blocks for eccentric loading of the biaxial Iosipescu specimen in three dimensions	231
4.5.	Imposed boundary conditions on blocks for eccentric loading of the modified biaxial Iosipescu specimen in three dimensions	232
4.6.	Material properties, yield stresses and tangent moduli assumed for the 3-D anisotropic plasticity analysis based on Hill's orthotropic yield function and the variations of tension and compression	233
4.7.	Apparent elastic properties obtained by off-axis tensile and biaxial Iosipescu shear experiments (verification in Section 3)	234
4.8.	Apparent stresses for graphite-polyimide Iosipescu specimens established at the onset of damage (O.O.D.), the onset of failure (O.O.F.) and catastrophic failure (C.F.)	234
4.9.	Apparent stresses for graphite-polyimide Iosipescu specimens established at the onset of failure (O.O.F.) and catastrophic failure (C.F.) as a function of temperature	235
4.10.	Linear elastic and nonlinear solutions to internal stresses at the center of the biaxial and modified biaxial Iosipescu models	236
4.11.	Comparison of the shear loads at the onset of failure and the maximum shear loads for the short and long block configurations	237
4.12.	(a) Calculated global loads and moments from reactions at the loading blocks of the biaxial model	238
	(b) Calculated global loads and moments from reactions at the loading blocks of the modified biaxial model	239

List of Figures

1.1.	Textile forms identified by NASA's technology program ACT	13
1.2.	8HS woven fabric geometries: (a) repeat unit cell, and (b) reduction to a simplified repeat element	14-15
1.3.	Chemical structure of Polypyromellitimide (PMR15)	16
2.1.	Surface components of normal and shear stresses	58
2.2.	Stress components acting on an elemental cube	58
2.3.	Complete force description on an elemental cube	59
2.4.	Deformation of elemental cube	59
2.5.	Element in-plane shear strains	60
2.6.	Local deformation of elemental cube	60
2.7.	Continuous fiber unidirectional composite lamina	61
2.8.	Continuous fiber unidirectional composite lamina with fibers oriented at an angle λ from the reference axis	61
2.9.	Derivation of one-dimensional crimp or fiber undulation model	62
2.10.	Definition of 2-D shape functions for X-Z slice	62
2.11.	Definition of 2-D shape functions for Y-Z slice	63
2.12.	Laminate subjected to in-plane force and moment resultants	63
2.13.	Crack propagation modes: (a) tensile, (b) shearing, and (c) tearing	64
2.14.	Damage mechanisms in aligned fiber composites subjected to on-axis loading conditions: (a) transverse matrix cracking, (b) fiber breakage, and (c) interfacial shear failure	65
2.15.	Evolution of fiber damage in aligned fiber composites: (a) fiber break with interfacial debonding, (b) fiber break expanding matrix crack, (c) matrix crack with fiber bridging, and (d) compilation of a, b, and c	66
3.1.	Evaluation of the tow cross-section geometry from a SEM micrograph of the 8HS woven composite plaque	118

3.2.	(a) Tow cross-section with thresholding applied to determine the perimeter, and (b) binary representation of the tow calibrated to the centroid for digitization	119
3.3.	(a) Evaluation of the woven tow undulation from a SEM micrograph of the 8HS woven composite plaque, and (b) binary representation of the undulation calibrated to the mutually orthogonal tow centroid for digitization	120
3.4.	Rendition of the upper surfaces of the 8HS representative element derived from cubic spline interpolation and m^{th} -order polynomial approximations	121
3.5.	Evaluation of the woven tow V_f from image analysis of a SEM micrograph with applied thresholding	122
3.6.	$\frac{1}{4}$ symmetry 3-D FE model assumed for the analysis of tow longitudinal elastic properties	123
3.7.	3-D FE model assumed for the analysis of tow longitudinal and transverse shear elastic properties	123
3.8.	4^{th} -order polynomial fits to upper and lower woven tow cross-section perimeters halved about the respective tow centroid.	124
3.9.	4^{th} -order polynomial fit to the woven tow undulation centerline with respect to the centroid of the mutually orthogonal tows	125
3.10.	Definition of the off-axis angle of undulation for evaluation of average transformed reduced compliance relative to the principal material coordinates	126
3.11.	Evolution of the idealized volume element (IVE) FE model from the representative volume element (RVE)	127
3.12.	3-D FE model assumed for the analysis of 8HS woven fabric composite elastic properties	128

3.13.	(a) Finite element discretization of 8HS woven IVE into 4757 elements and 9474 nodes using 10-node tetrahedral elements, and (b) coordinate system used to identify imposed boundary constraints	129
3.14.	Orientation of CP1-3 within the volume element and transition of cross-sectional tow geometries from CP1-3	130
3.15.	Comparison between the FE analysis and micromechanics solutions for the woven tow longitudinal tensile modulus E_{11} over the range of V_f from 0 to 1	131
3.16.	Comparison between the FE analysis and micromechanics solutions for the woven tow transverse tensile modulus E_{22} over the range of V_f from 0 to 1	132
3.17.	Comparison between the FE analysis and micromechanics solutions for the woven tow longitudinal shear modulus G_{12} over the range of V_f from 0 to 1	133
3.18.	Comparison between the FE analysis and micromechanics solutions for the woven tow longitudinal Poisson's ratio ν_{12} over the range of V_f from 0 to 1	134
3.19.	Comparison between the FE analysis and micromechanics solutions for the woven tow transverse Poisson's ratio ν_{23} over the range of V_f from 0 to 1	135
3.20.	Variation in 8HS woven fabric lamina extensional compliances over the range of local angles of undulation from 0° to 16° as predicted by the current model	136
3.21.	Variation in 8HS woven fabric lamina extension-bending coupling compliances over the range of local angles of undulation from 0° to 16° as predicted by the current model	137
3.22.	E_x/E_y - G_{xy} chart mapping the off-axis elastic behavior for several composite systems considered against experimental data (c.f. Section 4)	138

3.23.	ν_{xy} - G_{xy} chart mapping the off-axis elastic behavior for several composite systems considered against experimental data (c.f. Section 4)	139
3.24.	ν_{xy} - E_x/E_y chart mapping the off-axis elastic behavior for several composite systems considered against experimental data (c.f. Section 4)	140
3.25.	Sample 490 point data set for normalized uniaxial tensile stress within CP1 (tension)	141
3.26.	(a) Uniaxial tensile stress distribution within CP1 under applied uniaxial tension	142
	(b) Uniaxial transverse normal stress distribution within CP1 under applied uniaxial tension	143
3.27.	(a) Uniaxial tensile stress distribution within CP2 under applied uniaxial tension	144
	(b) Uniaxial transverse normal stress distribution within CP2 under applied uniaxial tension	145
3.28.	(a) Uniaxial tensile stress distribution within CP3 under applied uniaxial tension	146
	(b) Uniaxial transverse normal stress distribution within CP3 under applied uniaxial tension	147
3.29.	(a) Uniaxial compressive stress distribution within CP1 under applied uniaxial compression	148
	(b) Uniaxial transverse normal stress distribution within CP1 under applied uniaxial compression	149
3.30.	(a) Uniaxial compressive stress distribution within CP2 under applied uniaxial compression	150
	(b) Uniaxial transverse normal stress distribution within CP2 under applied uniaxial compression	151
3.31.	(a) Uniaxial compressive stress distribution within CP3 under applied uniaxial compression	152

(b) Uniaxial transverse normal stress distribution within CP3 under applied uniaxial compression	153
3.32. (a) In-plane shear stress distribution within CP1 under applied in-plane shear	154
(b) Uniaxial transverse normal stress distribution within CP1 under applied in-plane shear	155
3.33. (a) In-plane shear stress distribution within CP2 under applied in-plane shear	156
(b) Uniaxial transverse normal stress distribution within CP2 under applied in-plane shear	157
3.34. (a) In-plane shear stress distribution within CP3 under applied in-plane shear	158
(b) Uniaxial transverse normal stress distribution within CP3 under applied in-plane shear	159
4.1. Force, shear and moment diagrams for the Iosipescu shear test method	240
4.2. Biaxial fixture based on the Iosipescu shear test method	241
4.3. Environmental chamber for shear testing at elevated temperatures	241
4.4. Ply-level shear-tension ($-\alpha$) and shear-compression ($+\alpha$) biaxial stress states in a composite Iosipescu specimen	242
4.5. Representation for evaluating ply-level elastic behavior in the off-axis tensile composite specimens (c.f. Section 4)	243
4.6. Specimen designs for experimental program (a) biaxial Iosipescu, (b) modified biaxial Iosipescu, and (c) standard tension/off-axis tension. (Refer to Table 4.1 for dimensional callouts.)	244
4.7. Room temperature experimental apparatus based on the Dillon tensile test pilot at the University of Denver. Tests conducted at OGIST's MSE fracture and failure laboratory replaced the Dillon with the Instron DTS Model 1230-20 excluding the environmental chamber	245

4.8.	Shear strain distributions along the notch root axis in Iosipescu specimens with (a) 0° fiber orientation and (b) 90° fiber orientation. With small gages, the shear strain measured in (a) appears to be higher than in (b). (After Ifju 1991.) ⁷³	246
4.9.	Elevated temperature experimental apparatus based on the MTS Model 880 Dynamic Material Test System at the University of Denver's Physics Department. The test platform employed hydraulic grips with smooth and serrated wedge inserts for mechanical testing without or with acoustic emission sampling	247
4.10.	Placement of R.I. Model 4184 strip heaters	248
4.11.	Placement of Model B1025 broadband AE transducers	248
4.12.	(a) Two-dimensional finite element model of the biaxial Iosipescu specimen with 6235 nodes, 2608 8-node quadrilateral and 6-node triangular isoparametric elements (PLANE82) and 210 contact pseudo-elements (CONTAC48)	249
	(b) Two-dimensional finite element model of the modified biaxial Iosipescu specimen with 5973 nodes, 6454 8-node quadrilateral and 6-node triangular isoparametric elements (PLANE82) and 1174 contact pseudo-elements (CONTAC48)	249
4.13.	Load cases under consideration in the eccentric loading of biaxial and modified biaxial graphite-PMR15 Iosipescu specimens: (a) CASE A - shear loading, (b) CASE B - shear and asymmetric loading, (c) CASE C - shear and anti-symmetric loading, (d) CASE D - shear and lateral bending, and (e) CASE E - shear and lateral rotation	250-252
4.14.	(a) Three-dimensional finite element model of the biaxial Iosipescu specimen with 4106 nodes, 604 8-node layered structural solid elements (SOLID46), 64 8-node structural solid elements (SOLID45) and 4400 contact pseudo-elements (CONTAC49)	253

	(b) Three-dimensional finite element model of the modified biaxial Iosipescu specimen with 4426 nodes, 604 8-node layered structural solid elements (SOLID46), 192 8-node structural solid elements (SOLID45) and 13056 contact pseudo-elements (CONTAC49)	253
4.15.	Orientation of cutting planes for removing damage sample	254
4.16.	Removed sample showing locations of imaging targets	254
4.17.	Comparison of shear stress-strain data for the stacked rosette gage and Iosipescu shear gage obtained from the first graphite-PMR15 plaque	255
4.18.	(a) Five-step shear loading/unloading tests to determine the linear elastic regime of the first graphite-PMR15 plaque using the biaxial Iosipescu fixture and shear gages (2-side average)	256
	(b) Re-scaled five-step shear loading/unloading scheme to illustrate delineation of the linear elastic regime and onset of damage based on deviation from least-squares fit line	257
4.19.	(a) Superimposed shear stress-displacement and shear stress-strain curves for graphite-PMR15 Iosipescu specimens from the first and third plaques	258
	(b) Superimposed shear stress-displacement and shear stress-strain curves for graphite-PMR15 Iosipescu specimens from the first and fourth plaques	259
4.20.	(a) Stress-displacement curves for standard and off-axis tensile tests from graphite-PMR15 specimens belonging to the third plaque ($\beta = 0^\circ, 15^\circ, 30^\circ$ and 45°)	260
	(b) Stress-strain curves for standard and off-axis tensile tests from graphite-PMR15 specimens belonging to the third plaque ($\beta = 0^\circ, 15^\circ, 30^\circ$ and 45°) ..	261
4.21.	Superimposed shear stress-displacement and shear stress-strain curves for graphite-PMR15 specimens from the first plaque tested at $\alpha = 0^\circ, +30^\circ$ and -30°	262

4.22.	Comparative shear stress-displacement curves for Iosipescu specimens from the graphite-PMR15 and graphite-Avimid R composite plaques	263
4.23.	Shear stress-displacement curves for graphite-PMR15 specimens (plaque #2) at various temperatures	264
4.24.	Shear stress-displacement curves for graphite-Avimid R specimens (warp-aligned) at various temperatures	265
4.25.	Shear stress-displacement curves for graphite-Avimid R specimens (0°/90°) at various temperatures	266
4.26.	Representation of strain-shear stress relationships as a function of temperature for graphite-PMR15 Iosipescu specimens from plaque #2	267
4.27.	(a) Trends in the average shear stresses at the onset of failure	268
	(b) Trends in the average shear stresses at their maximums	268
4.28.	Shear and normal stress distributions along the notch root axis of the biaxial Iosipescu model	269
4.29.	Biaxial stress ratios from the biaxial Iosipescu model for various loading angles	270
4.30.	Shear stress distributions along the notch root axis of the biaxial Iosipescu model for ($\mu = 0.3$)	271
4.31.	Shear and normal stress distributions along the notch root axis of the modified biaxial Iosipescu model	272
4.32.	Biaxial stress ratios from the modified biaxial Iosipescu model for various loading angles	273
4.33.	Shear stress distributions along the notch root axis of the modified biaxial Iosipescu model for ($\mu = 0.3$)	274
4.34.	Integrated surface strains and lateral displacements of each load angle and eccentric case considered for the biaxial Iosipescu analyses	275
4.35.	Integrated surface strains and lateral displacements of each load angle and eccentric case considered for the modified biaxial Iosipescu analyses	276

4.36.	Plastic strain contours from biaxial Iosipescu analysis at an applied shear stress of 19.6 MPa (2.8 ksi), (a) γ_{xy}^{pl} , and (b) ε_{zz}^{pl}	277
4.37.	Plastic strain contours from biaxial Iosipescu analysis at an applied shear stress of 25.8 MPa (3.7 ksi), (a) γ_{xy}^{pl} , and (b) ε_{zz}^{pl}	278
4.38.	Plastic strain contours from biaxial Iosipescu analysis at an applied shear stress of 31.9 MPa (4.6 ksi), (a) γ_{xy}^{pl} , and (b) ε_{zz}^{pl}	279
4.39.	Plastic strain contours from biaxial Iosipescu analysis at an applied shear stress of 61.4 MPa (8.9 ksi), (a) γ_{xy}^{pl} , and (b) ε_{zz}^{pl}	280
4.40.	Plastic strain contours from biaxial Iosipescu analysis at an applied shear stress of 90.7 MPa (13.2 ksi), (a) γ_{xy}^{pl} , and (b) ε_{zz}^{pl}	281
4.41.	Progression of failure along notch root of Iosipescu specimens subjected to applied shear stresses of (a) 23.1 MPa (3.4 ksi), (b) 46.1 MPa (6.7 ksi) and (c) 69.2 MPa (10.1 ksi)	282
4.42.	Progression of failure along notch root of Iosipescu specimens subjected to applied shear stresses of (a) 92.3 MPa (13.4 ksi), (b) 111.5 MPa (16.2 ksi) and (c) 111.5 MPa (16.2 ksi) at higher magnification	283
4.43.	Onset of failure (a) and catastrophic failure (b) with out-of-plane deformation (bulging) along the notch root of Iosipescu specimens subjected to shear at a loading angle $\alpha = 0^\circ$	284
4.44.	Two-dimensional damage serial reconstruction of shear tested (a) notch and (b) center sample targets	285
4.45.	Two-dimensional damage serial reconstruction of untested (a) notch and (b) center sample targets	286
4.46.	Sample center and notch target damage fractions from tested and untested Iosipescu specimens	287
4.47.	Prediction of the progression of damage in woven fabric composite biaxial Iosipescu specimens at shear strains γ_{xy} of (a) 0.38%, (b) 0.75%, and (c) 1.13%	288

4.48.	Prediction of the progression of damage in woven fabric composite biaxial Iosipescu specimens at shear strains γ_{xy} of (d) 1.50%, (e) 1.88%, and (f) 2.25%	289
4.49.	Influence of structural nonlinearities, anisotropic plasticity and progressive damage on the shear stress-strain response of the biaxial Iosipescu model as compared to experiments (plaque #4)	290

Nomenclature

x, y, z	Axes of the structural coordinate system
$1, 2, 3$	Axes of the principal material coordinate system
F_n, F_t	Resolved normal and tangential forces
A	Cross-sectional area
$F_x, F_y, F_z, M_x, M_y, M_z$	Forces and moments in the structural coordinate system
$\sigma_x, \sigma_y, \sigma_z, \tau_{xy}, \tau_{xz}, \tau_{yz}$	Stresses in the structural coordinate system
$\epsilon_x, \epsilon_y, \epsilon_z, \gamma_{xy}, \gamma_{xz}, \gamma_{yz}$	Strains in the structural coordinate system
$\sigma_{ij} (i,j = 1,2,3)$	Stresses in the principal material coordinate system
$\epsilon_{ij} (i,j = 1,2,3)$	Strains in the principal material coordinate system
f_x, f_y, f_z	Body forces due to gravity
u, v, w	Unit displacements in the structural coordinate directions
$E_x, E_y, E_z, G_{xy}, G_{xz}, G_{yz}, \nu_{xy}, \nu_{xz}, \nu_{yz}$	Structural or engineering elastic properties
$C_{ij} (i,j = 1,2,6)$	Components of the stiffness matrix
$S_{ij} (i,j = 1,2,6)$	Components of the compliance matrix
$Q_{ij} (i,j = 1,2,6)$	Components of the reduced stiffness matrix or matrix of mathematical moduli
$\bar{Q}_{ij}(\lambda) (i,j = 1,2,6)$	Components of the transformed reduced stiffness matrix for fibers aligned at an angle λ to the principal axis
$\bar{S}_{ij}(\lambda) (i,j = 1,2,6)$	Components of the local reduced and average compliance matrix for fibers aligned at an angle λ
$A_{ij}, B_{ij}, D_{ij} (i,j = 1,2,6)$	Components of the extension, coupling and bending stiffness matrices
n_c	Number of woven tow exchanges

$h_1(x), h_2(x), h_1(y), h_2(y), a_1, a_u,$	Parameters as defined in Figures 2.9, 2.10 and 2.11
$a_v, a_w, g_w, u_i, \zeta, \zeta_w, h, h_t, h_{fill},$	
$h_{warp}, b_i, a_i, g_i, \zeta_i, u_w, g_f$	
V	Volume
$Q_{ij}^M, Q_{ij}^W, Q_{ij}^F (i,j = 1,2,6)$	Components of the reduced stiffness matrices for the constituent matrix, warp and fill tows
$a_{ij}, b_{ij}, d_{ij} (i,j = 1,2,6)$	Components of the extension, coupling and bending compliance matrices
Ψ_{warp}, Ψ_{fill}	Period of woven tow undulation per Eq. 2.45
ξ_{warp}, ξ_{fill}	Functions for tow centerlines per Eq. 2.46
k^{th}	Ply designation within a stacked laminate
N_x, N_y, N_{xy}	Ply-level forces
M_x, M_y, M_{xy}	Ply-level moments
ϵ_o, κ_o	Mid-plane strain and curvature
$[Q_x, Q_y]$	Thickness shear force resultants as per Eq. 2.53
T_g	Glass transition temperature
M_w	Molecular weight
T	Temperature
α_{ij}	Linear coefficients of thermal expansion
a	Woven tow width
V_f, V_m	Fiber and matrix volume fractions
\bar{x}, \bar{z}	Coordinates of woven tow centroid
$p_j(x)$	Natural-ended cubic spline representation
r	Half-fiber diameter
R	Half-fiber center-to-center spacing

k^*, G^*	Transverse bulk modulus and transverse shear modulus
U^*	Strain energy stored in a heterogeneous RVE
W^*	External work done on a heterogeneous RVE
$\delta_x, \delta_y, \delta_z$	Prescribed displacements
P_x, P_y, P_z	Resultant surface reactions
$u_{ij} (i,j = 1,2,3)$	Boundary displacements
$n_{ij} (i,j = 1,2,3)$	Outwardly unit normal vectors of the surface S
ϕ_r, ϕ_w	Maximum off-axis angles of warp and fill tow undulation
[K]	Total stiffness matrix
{u}	Nodal degree of freedom vector
{F ⁿ }, {F ^e }	Applied nodal load and element load vectors
Q(x _i , y _j)	Unknown point to be estimated by interpolation
w _n	Weighting given to the n th known point
D _{ij}	Distances from known points P _i to known points P _j
w, t, h	Width, thickness and distance between notches of Iosipescu specimens
P ₁ , P ₂	Load components derived from force and moment considerations
c, l	Moment arm lengths for inner and outer load components
α, β	Angles relative to global load axes for Iosipescu and off-axis tensile tests
$\epsilon_{-45}, \epsilon_{+45}$	Normal strains oriented at $\pm 45^\circ$ to principal plane
$\bar{\epsilon}_{-45}^*$	Strain averaged over the nominal gage grid area
[B _n], [B _v], [T _n]	Co-rotational algorithm, small strain-displacement relationship and rigid body rotation

$[R], [I], [U]$	Rotation, identity and right stretch or shape change matrices
$[F^{int}]$	Element restoring force
u^A, u^B	Nodal displacements on opposing contact and target surfaces A and B
$n, g_n(\xi, n)$	Surface normal and separation function
F_n, F_s, F_c	Normal force, sliding force and critical friction resistance
μ	Coefficient of static friction
f_n, λ_{i-1}	Contact penalty function and Lagrange multiplier at iteration (i + 1)
K_n, g_Δ, ω	Input contact stiffness, contact gap and compatibility tolerance (user)
$\{N_s\}, \{N_n\}$	Interpolation vectors of some local s-n coordinate system relative to a contacting plane
σ_{ij}^y	Material yield parameter
F, G, H, L, M, N	Orthotropic material parameters given in terms of the yield stresses
X, Y, Z	Tensile or compressive yield stresses
R, S, T	Shear yield stresses
$f(\sigma_{ij})$	Yield criterion
[N]	Matrix describing yield stress variation with orientation
$\{M\}$	Strength differential vector
$\epsilon^{el}, \epsilon^{pl}, \epsilon^t$	Elastic, plastic and trial components of strain
\hat{U}_{ij}, U_{ij}^c	Volume equivalent linear elastic strain energy density and critical strain energy density
$f_g(\gamma_{xy})$	Damage growth function

Abbreviations

1-D, 2-D, 3-D	One-dimensional, two-dimensional, three-dimensional
UD	Unidirectional composite
ACT	Advanced Composite Technology
HS	Harness-satin
RTM	Resin transfer molding
RFI	Resin film infusion
PMC	Polymer matrix composite
TOS	Thermal oxidative stability
PMR15	Polymerization of monomer reactants, formulated molecular weight 1500
MDA	Methylene-dianiline
WGFRP	Woven graphite fiber (fabric) reinforced polyimide
CCA	Composite cylinder assemblage
SP, PS	Series-parallel and parallel-series
CLT	Classical lamination theory
CTE	Coefficient of thermal expansion
CDS	Characteristic damage state
SENB	Single-edge notched beam
FE, FEA	Finite element, finite element analysis
DCB	Double cantilever beam
MMB	Mixed-mode bending
ENF	End-notch flexure
IVE	Idealized volume element
SEM	Scanning electron microscopy

GSCS	Generalized self-consistent scheme
RVE	Representative volume element
DOF	Degree of freedom
CP	Cutting plane
SMC	Sheet moulding compound
ASTM	American Society for Testing and Materials
PEEK	Polyetheretherketon
Ti-SiC	Titanium-silicon carbide
MTS	Material Test System
AE	Acoustic emission
A/D	Analog-to-digital

ABSTRACT

THE ELASTIC AND INELASTIC BEHAVIOR OF WOVEN GRAPHITE FABRIC REINFORCED POLYIMIDE COMPOSITES

Kevin H. Searles, Ph.D.

Oregon Graduate Institute of Science and Technology, 2000

Supervising Professor: Maciej S. Kumosa

In many aerospace and conventional engineering applications, load-bearing composite structures are designed with the intent of being subjected to uniaxial stresses that are predominantly tensile or compressive. However, it is likely that biaxial and possibly triaxial states of stress will exist throughout the in-service life of the structure or component. The existing paradigm suggests that unidirectional tape materials are superior under uniaxial conditions since the vast majority of fibers lie in-plane and can be aligned to the loading axis. This may be true, but not without detriment to impact performance, interlaminar strength, strain to failure and complexity of part geometry. In circumstances where a sufficient balance of these properties is required, composites based on woven fabric reinforcements become attractive choices.

In this thesis, the micro- and mesoscale elastic behavior of composites based on 8HS woven graphite fabric architectures and polyimide matrices is studied analytically and numerically. An analytical model is proposed to predict the composite elastic constants and is verified using numerical strain energy methods of equivalence. The model shows good agreement with the experiments and numerical strain energy equivalence. Lamina stresses generated numerically from in-plane shear loading show substantial shear and transverse normal stress concentrations in the transverse undulated tow which potentially leads to intralaminar damage.

The macroscale inelastic behavior of the same composites is also studied experimentally and numerically. On an experimental basis, the biaxial and modified biaxial Iosipescu test methods are employed to study the weaker-mode shear and biaxial failure properties at room and elevated temperatures. On a numerical basis, the macroscale inelastic shear behavior of the composites is studied. Structural nonlinearities and material nonlinearities are identified and resolved. In terms of specimen-to-fixture interactions, load eccentricities, geometric (large strains and rotations) nonlinearities and boundary contact (friction) nonlinearities are explored. In terms of material nonlinearities, anisotropic plasticity and progressive damage are explored. A progressive damage criterion is proposed which accounts for the elastic strain energy densities in three directions. Of the types of nonlinearities studied, the nonlinear shear stress-strain behavior of the composites is principally from progressive intralaminar damage. Structural nonlinearities and elastoplastic deformation appear to be inconsequential.

INTRODUCTION

There has been a growing interest, particularly in the last ten years, to use composite materials in structural component applications primarily within the military and aerospace sectors. Although these sectors drive the greatest use of composites on a percent weight basis, focus is shifting towards expanding use in commercial applications where higher strength-to-weight ratios, damage tolerance and near net-shapability are important considerations. Of the numerous classes of composite material systems employed for use in structural applications ranging from aircraft and space structures to automotive and biomedical applications, unidirectional (UD) composite systems have received the most treatment. However, UD composites are limited in applications requiring orthogonal reinforcement, increased intra- and interlaminar shear strength, better impact resistance and near net-shapability over complex geometries. Orthogonal woven fabric or textile composites overcome some of the aforementioned limitations found in UD composites. Woven fabric structural composite systems for engineering structures draw on many traditional fabric forms and processes. In general, the systems employed for aerospace structural applications are those fabrics that most effectively translate stiff, strong yarns into stiff, strong composites [1].

A woven fabric composite has an internal structure that may be defined across several scales. If we begin at the molecular scale, structural details of both the polymer matrix and fibers profoundly affect stiffness and strength. A preferred choice in aerospace materials, the carbon fibers owe their strength and axial stiffness to the oriented graphitic sheets of preferentially arranged carbon atoms. The polymer matrix properties are determined by the degree of crosslinking, packing density, backbone chemistry, i.e. aromaticity and chain

morphology. Stepping up to the next scale, several orders of fibers in the neighborhood of 10^3 - 10^4 are arranged into yarn bundles (tows). These tows behave as highly anisotropic entities with high strength and stiffness properties preferential to the long axis. Although the tows are oriented in the same general direction, there arises some statistical variation in stresses and strains from tow to tow due to randomness. Therefore, at the scale of roughly 10^{-3} m (10^2 mils), we can average out the heterogeneous structures at the previous scale and consider composite elastic properties as approximately uniform. Finally, the engineering structure itself, possibly at this scale, may no longer be distinctly separate from its composite constituents and in fabricating the woven fabric composite we may simultaneously be fabricating the engineering structure.

The unique structures of fabric composites do also bring with them potential problems in mechanical testing and evaluations. The majority of current test methods were developed for unidirectional composite structures, random short-fiber composite structures and simple woven systems. Due to microstructural differences in the laminated composite architectures, there is inherent uncertainty as to whether the apparent elastic properties measured for fabrics, using current test methodologies, are indeed accurate representations of material behavior. This uncertainty becomes even greater when the composite is evaluated to determine response throughout a stress quadrant since the majority of in-service composite loading conditions will likely be biaxial to some degree. Therefore, to design against the weakest mode or modes of failure, we must clearly understand the failure mechanisms and behavior.

It is now well established, in large part by NASA's Advanced Composite Technology (ACT) program defined in 1990, that the fiber architecture plays a large role in governing the mechanical response of woven fabric reinforced composite materials [1]. Tow interlacing results in inhomogeneous local displacement fields not found in unidirectional tape systems. Since loading methods and specimen dimensions developed for tape composite systems may not be applicable to fabric composites, it becomes necessary to understand composite material behavior, not only at the macroscale where loading conditions are delineated, but

also at the meso- and microscales where crack nucleation, damage zone development and catastrophic failure are initiated. Relationships need to be established that consolidate these structural scales and bridge any discrepancies found between the behaviors exhibited by test specimens and their considerably larger structural counterparts.

1.1. General Textile Categories

There are many groups of woven fabric forms that have been identified and developed. However, the most important groups that serve as aerospace structural candidates have been identified, partially investigated by the ACT program and grouped as shown in Figure 1.1. Basically, the primary groupings (weaves, braids, etc...) are categorized according to the machines and processes used to create them. The dimensionality divisions determine whether the fiber preform, minus the matrix, can transport loads continuously in two or three linearly independent directions. Considerable effort has been dedicated and is continuing in regard to understanding the mechanical behavior of the two-dimensional woven forms, particularly the plain and satin weaves vis-à-vis two-dimensional (2-D) quasilaminar systems.

1.1.1. 2-D Quasilaminar Composite Systems

Most woven fabric reinforced composites designed for sheet and skin applications fall into the category of a 2-D quasilaminar system. If the application demands high in-plane strength and stiffness, the majority of the fibers must lie in-plane with few dedicated for through-thickness reinforcement. Any dedication of fibers for thickness reinforcement would be detrimental to the in-plane properties. Woven fabric composites that behave in most ways like laminates are referred to as “quasilaminar” [1]. In addition, these composites may also exhibit degrees of varying quasi-isotropy implying minor variation in off-axis properties within the given lamina plane.

1.2. Ideal Textile Geometries

Woven fabric composites are formed by the process of interlacing two individual fiber bundles or tows perpendicular to one another and impregnating with a matrix to form a layer. Each layer is stacked in some desired orientation and cured to form a laminate. The crosswise tows are referred to as fill or weft tows and the lengthwise weaver tows are referred to as warp tows. The pattern of interlacing warp tows with weft tows is fundamental in defining and classifying a two-dimensional weave. In referring to a 2-D weave pattern, it is useful to describe the type of pattern by the number of weft tows interlaced ($n_i - 1$) within a given repeating unit or cell [2]. Thus, a plain weave ($n_i = 2$) interlaces every other weft tow, a twill weave ($n_i = 3$) interlaces after every second weft tow, a four-harness satin (4HS, $n_i = 4$) after every third, a 5HS ($n_i = 5$) after every fourth and an 8HS ($n_i = 8$) after every seventh weft tow. There are several advantages associated with the tow interlacing such as increased intra- and interlaminar shear strength, impact resistance and near net-shape part production. The tradeoff with these benefits is the loss of in-plane strength and stiffness, which depends on the number of fibers aligned within the plane of interest. Obviously, when micro- and mesoscale geometric features and processing parameters contribute to the overall mechanical behavior of woven fabric composites, reasonable models are needed that account for this variation to provide sound design data.

1.2.1. Woven 8HS Geometry

As previously mentioned, there are several 2-D weave architectures for woven fabric composites. The simplest of patterns, the plain weave pattern, characterized by a one-over/one-under interlacing, reduces the composite stiffness and strength due to the frequent exchanges of tow positions from top to bottom. There are other patterns that reduce the number of exchanges and increase the length of the straight segments referred to as the "float". Of particular interest within the aerospace structural design community are the satin

weave architectures, especially the eight-harness satin or 8HS woven architecture. Since exchanges are minimal and the float is longer, the composite affords the opportunity to be formed into complex shapes (drape) while still providing a certain degree of mutually orthogonal reinforcement.

A geometric feature unique to satin architectures is that of lamina asymmetry. There are predominantly warp tows on one side of the lamina while the other side is predominantly weft tows. The tow bends and interlace locations are also asymmetric, leading to coupling between extension and bending as well as coupling between extension and in-plane shear, i.e. $B_{ij}, D_{ij} \neq 0$. Laminate symmetry and quasi-isotropic laminate behavior may be ascertained depending on the number of laminae considered and desired orientation during the layup sequence.

Most textile processes produce patterns that are periodic in nature. That is, the patterns of interlaced tows or yarns repeat in one or two directions. The geometry and periodicity of a textile is conveniently described in terms of unit cells. What is unique in this definition is that the stress and strain distribution in a periodic textile composite is also periodic, provided the external loading conditions are uniform. When the external loads are not uniform, periodicity in the stress and strain distributions no longer exists. The term unit cell, borrowed from crystallography, defines the requirement that the complete textile pattern can be constructed from spatially translated copies of the unit cell without rotating or reflecting. The unit cell representation for an 8HS woven fabric lamina is shown in Figure 1.2(a). Examination of the 8HS unit cell reveals that even further simplification is possible, leading to the smaller repeat unit sub-cell shown in Figure 1.2(b).

1.3. Graphite Polyimides

High temperature polymers and polymer matrix composites are finding increased use in the aerospace and electronics industries. At present time, polymer matrix composites account for about 4% by weight of commercial aircraft and about 10% of military aircraft. Current

predictions are that, within the next decade, up to 65% of new commercial and military aircraft could be polymer composites [3].

Graphite polyimides are advanced thermosetting polymer composites that have become highly relevant in the realm of elevated temperature applications. These composites have extremely good specific properties and are stable to temperatures as high as 360 °C (680 °F). Epoxy based, fiber reinforced polymer matrix composites have already achieved widespread acceptance as engineering materials for structural applications. These composites possess a high specific strength, stiffness and endurance to fatigue. The room temperature specific strengths of structural epoxies are higher than aluminum, titanium alloys and some super alloys. Epoxy matrices make attractive choices for resin transfer molding (RTM) and resin film infusion (RFI) processes because there is an extensive amount of data available and epoxies also meet the requirement of having a low viscosity for complete wetting and preform permeability. Notwithstanding, the current status suggests the need for matrix replacements which retain comparable or better wetting characteristics for RTM and RFI processes, exhibit favorable interlaminar properties and achieve much higher thermal oxidative stability for use not only in aerostructures, but also aeropulsion systems.

The bulk of the aerospace industry uses graphite fiber reinforced epoxy composites. The upper service temperature of these materials is limited to about 150 °C (300 °F). In many applications however, temperatures greater than 200 °C (390 °F) are commonplace. The strength of graphite epoxies would begin to diminish far below this temperature. Hence, there is a growing demand for other polymer matrix composites (PMC's) with much higher upper service temperatures. Some of the more common applications for advanced composites might include aeropulsion system components such as turbine engine compressor casings, bearings, exhaust thruster rings, reversers and external surfaces for supersonic aircraft and missiles. In such applications, upper service temperatures could approach 425 °C (800 °F). Materials used in these environments must possess a good balance of mechanical properties over a wide temperature range, withstand fluctuations in temperature and experience a low percentage of weight loss, even after long term exposure (60,000 hrs) at or near upper service

temperatures. To maintain mechanical properties, the polymer glass transition temperature T_g must be at least 25 °C (77 °F) higher than its intended use temperature.

In most cases, there are essential considerations for using PMC's in the previously mentioned applications. One of the foremost considerations would be the significant reduction of weight while another would be increased specific strength properties. PMC's exhibit greater than three-fold higher specific strengths compared with titanium and other traditional aerospace materials due to much lower densities and similar apparent strength values. Table 1.1 shows a comparison of the densities and specific strengths for a variety of popular aerospace materials.

1.3.1. Polypyromellitimide Morphology

It has become a requirement in the realm of emerging sciences and technologies that processable polymers are endowed with superior thermal oxidative stability (TOS) and mechanical properties, particularly at elevated temperatures. Accordingly, the structural feature common to these polymers is an aromatic backbone associated with rigidity, resonance stabilization and high bond dissociation energies. Since the polymer degradation mechanism is principally oxidative in nature, heterocyclic units may be added to increase the char yield at higher temperatures. Polypyromellitimides, or commonly polyimides such as PMR15 (see Figure 1.3), are among the best candidates for processable and thermally stable matrix resins, although processing by methods such as vacuum bag autoclaving are more expensive than injection molding or RTM.

Generally, high temperature polyimide derivatives evolve from a two-step addition and condensation chemistry. Oligomers are formed via a condensation polymerization and endcapped with reactive groups which undergo an addition polymerization at a higher temperature. Usually, condensation reactions cure with the evolution of composite blister and void forming by-products, however the use of reactive endcaps limits molecular weight. In the case of PMR15, the formulated molecular weight is nominally 1500 f.m.w. and the

stoichiometric ratio of the reactants is 2.0 moles of monomethylester of 5-norbornene-2, 3-dicarboxylic acid to 2.09 moles of dimethylester of 3, 3', 4, 4'-benzophenonetetracarboxylic acid [3, 4]. The final preparation of a neat resin involves a partial imidization of reactants with solvent evaporation occurring at 121 °C (250 °F).

1.3.2. Commercial Types

Polyimides are available commercially with the trade names PMR15, PMR-II-50, VCAP-75, Avimid R, AMB-21, CSPI and LaRC™ RP 46. The PMR polyimide class was formulated at the NASA Glenn Research Center and PMR15 is currently the polyimide that has been put to maximum commercial use. However, there is ongoing research at NASA to find a suitable replacement for PMR15 due to the high levels of carcinogenic toxicity associated with 4,4'-methylene dianiline (MDA). Meanwhile, it remains to be seen how other commercially available replacement polyimides compare to the performance of conventional PMR15.

Most advanced polyimide composite systems are manufactured from prepregs in the form of fabrics or tapes, pre-impregnated with the PMR monomer resin. The prepregs are subsequently cut and set to the required shapes prior to cure by compression or autoclave molding using a vacuum bag system. The plies are subjected to specific temperature-pressure cure cycles and the resulting structural laminate is ultrasonically C-scanned for percent void.

1.4. WGFRP Composite Behavior

For successful application of woven graphite fiber, reinforced polyimide (WGFRP) composites, it is essential to develop a reliable database of material properties and a thorough understanding of damage and failure behavior, particularly at elevated temperatures. Microcracking and other lifelong fatigue problems must be understood and solved to meet the extreme operating conditions of advanced aerospace systems. To maintain the structural

integrity of WGFPR laminates and to ensure that their mechanical properties remain within design specifications, the composite systems are restricted to operate within a limited temperature range. At low temperatures, differential strains induced by thermal coefficient mismatches may be of sufficient amplitude to result in matrix cracking and interfacial debonding in the absence of any external load. The temperature at which microcracking occurs depends on the composite system layup, constituent thermal properties, residual stresses induced by resin shrinkage and the thermal history. At elevated temperatures, the composite displays extensive nonlinear behavior under transverse tension, transverse compression and shear as a result of matrix softening. Moreover, in the assessment of suitability for engineering applications involving long term static and dynamic loadings, information is required regarding the stability of the composite in resisting damage initiation at high strain rates and at temperatures approaching in-service conditions.

A major limitation of many PMC systems is the inability of these materials to resist intralaminar and interlaminar damage initiation and propagation under multiaxial monotonic and cyclic loading conditions. Specific to this dissertation research effort, the performance of 8HS woven fabric reinforced, graphite polyimide composites subjected to both biaxial (shear dominated) mechanical loads and thermal loads is evaluated using standardized experimental test methods, novel analytical approaches and numerical simulations. The ability to predict the elastic properties and fully understand damage and ultimate failure mechanisms in PMC's subjected to mixed-mode loading conditions is important for further composite materials research and development. Some of the important requirements for adequate predictions are reliable constituent property data, judicious application of existing theories and reasonable micromechanics, mesomechanics and macromechanics models.

In this thesis, Section 2 provides a survey of the framework for existing theories on the linear elastic behavior of homogeneous and composite materials, explicitly describing analytical and numerical schemes previously adopted for n-dimensional analyses of woven fabric composites. In Section 3, emphasis is placed on the micro- to mesomechanics and approach established by the author for evaluating the elastic behavior of woven 8HS

composite laminates. Woven tow (micromechanics) elastic properties are determined by the Composite Cylinder Assemblage (CCA) method and validated by finite element analyses according to strain energy equivalence. The 8HS woven fabric lamina (mesomechanics) elastic properties are determined by a unique and simplified mechanics approach combined with Classical Lamination Theory. Validation is performed in a manner similar to that of the woven tows. A detailed thickness lamina stress analysis is also conducted for the following fundamental load cases: uniaxial tension, uniaxial compression and in-plane shear. Stresses are modeled by uniquely employing a punctual kriging interpolation algorithm.

Section 4 is dedicated to a macromechanics evaluation and experimental assessment of apparent room temperature properties and elevated temperature properties [to 315 °C (600 °F)]. Details are given regarding the In-Plane Biaxial and Modified Biaxial test methods employed, the test coupon design and experimental apparatus. In addition, various considerations of the Iosipescu tests, including geometric nonlinearities (large displacements and rotations), boundary contact nonlinearities (friction) and load eccentricities (torsion and out-of-plane bending) are explored. Within the framework of nonlinear material behavior, an area and volume visualization method is presented to characterize the composite nonlinear shear behavior associated with the onset of internal damage (i.e., transverse matrix cracking) prior to interlaminar failure. A qualitative comparison is pursued between experimentally observed nonlinear behavior and finite element analyses which independently model anisotropic plasticity and progressive damage (element death). The main conclusions drawn from this investigation are listed in Section 5 and Section 6 looks at possible suggestions for future work in regard to the study of WGFRP composite materials.

In Appendix A, the FORTRAN 77 compiler code is presented in accordance with the simplified mechanics approach from Section 3. Appendices B and C present the ANSYS user input files developed for this investigation as follows: 3-D woven tow property prediction, 3-D 8HS woven fabric lamina property prediction and stress analysis, 2-D biaxial and modified biaxial Iosipescu shear tests (geometric and boundary contact nonlinearities), 3-D Iosipescu shear test (load eccentricities) and 3-D Iosipescu shear test (plasticity and

progressive damage). Finally, Appendix D details the mechanical drawings for the redesigned loading blocks (modified biaxial Iosipescu fixture) used to evaluate the effect of load point placement on the failure process in Iosipescu specimens.

Table 1.1. Material properties for selected aerospace alloys and polymer matrix composites.³

Material	Density g/cm³ (lb/in³)	Youngs Modulus GPa	Strength MPa (ksi)	Specific Strength cm (10⁴) (in (10³))	Upper Use Temperature (°C)
(Ti-6Al-4V)	4.43 (0.16)	114	1100 (160)	248 (1000)	371
(6061-T6)	2.71 (0.098)	69	310 (45)	114 (459)	177
Low Alloy Steel	7.85 (0.283)	207	2050 (297)	261 (1050)	800
Carbon-Epoxy	1.62 (0.058)				
Longitudinal	----	220	1400 (203)	864	140
Transverse	----	7	38 (5.52)	(3500)	
Graphite-PMR15	1.65 (0.060)				
Longitudinal	----	220	1400 (203)	848	288
Transverse	----	8	51 (7.40)	(3380)	
Graphite-Avimid N	1.71 (0.062)				
Longitudinal	----	220	1400 (203)	819	316
Transverse	----	9	7.59 (1.1)	(3270)	

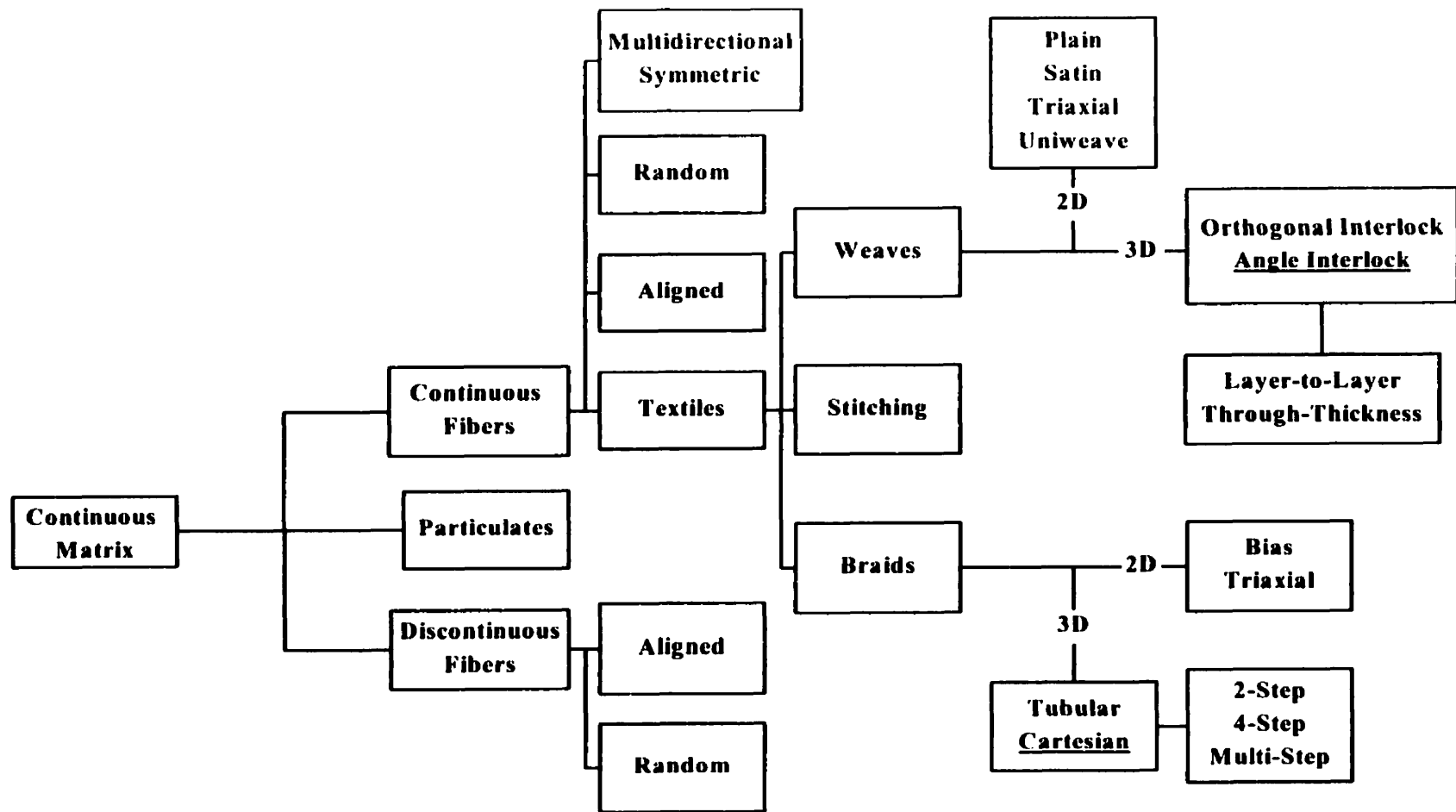


Figure 1.1. Textile forms identified by NASA's technology program ACT.¹

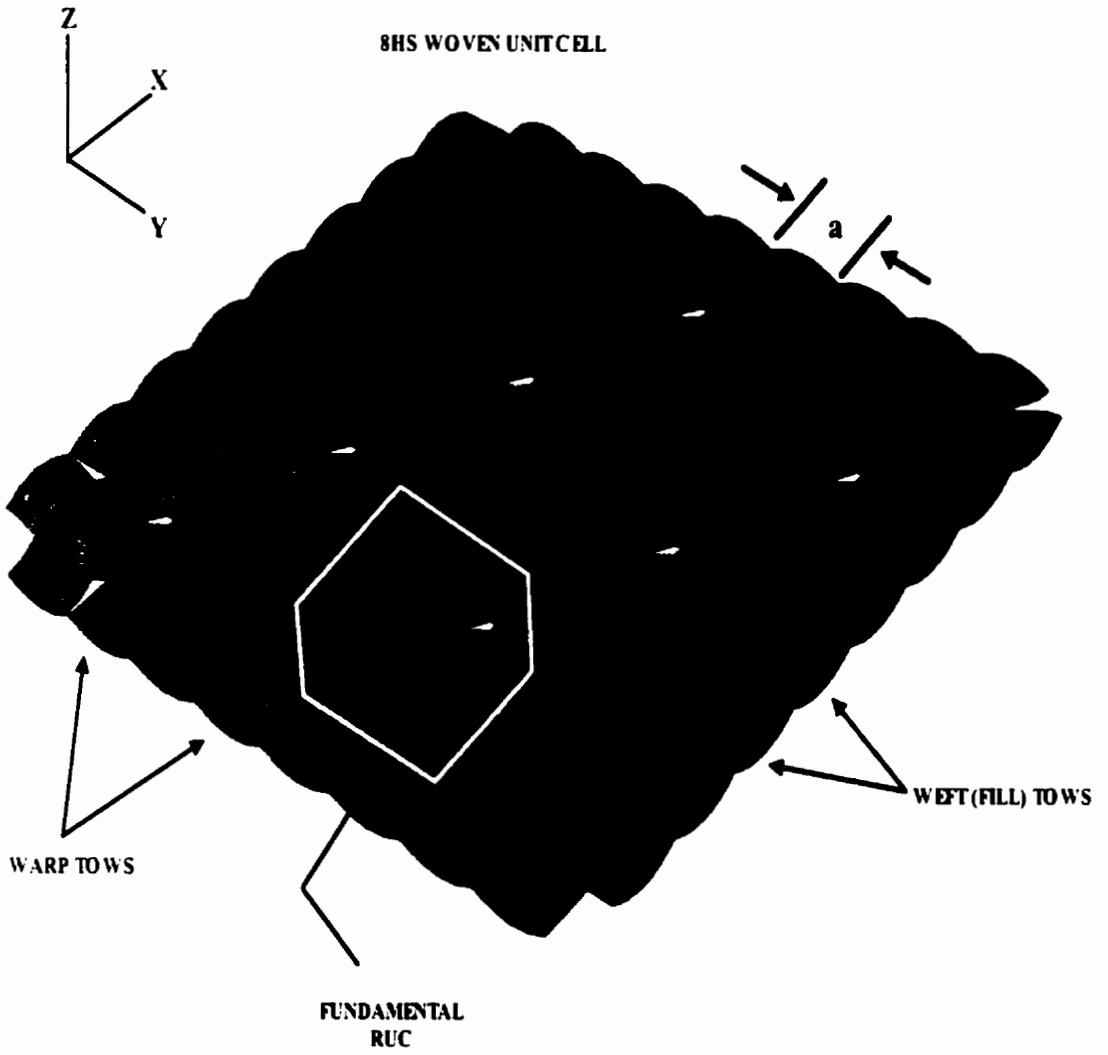
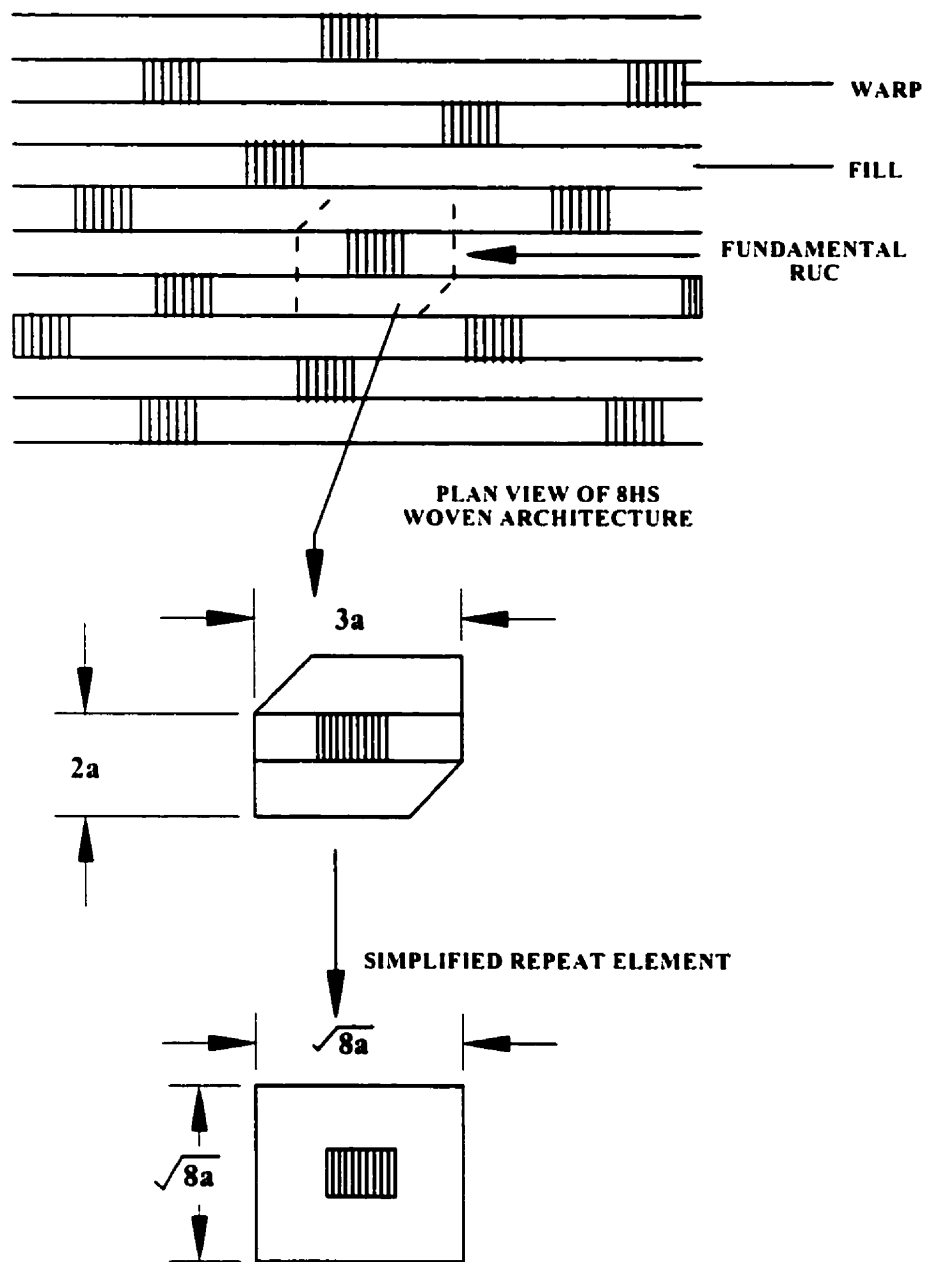


Figure 1.2. 8HS woven fabric geometries: (a) repeat unit cell (RUC).



(b)

Figure 1.2. 8HS woven fabric geometries: (b) reduction to a simplified repeat element.²

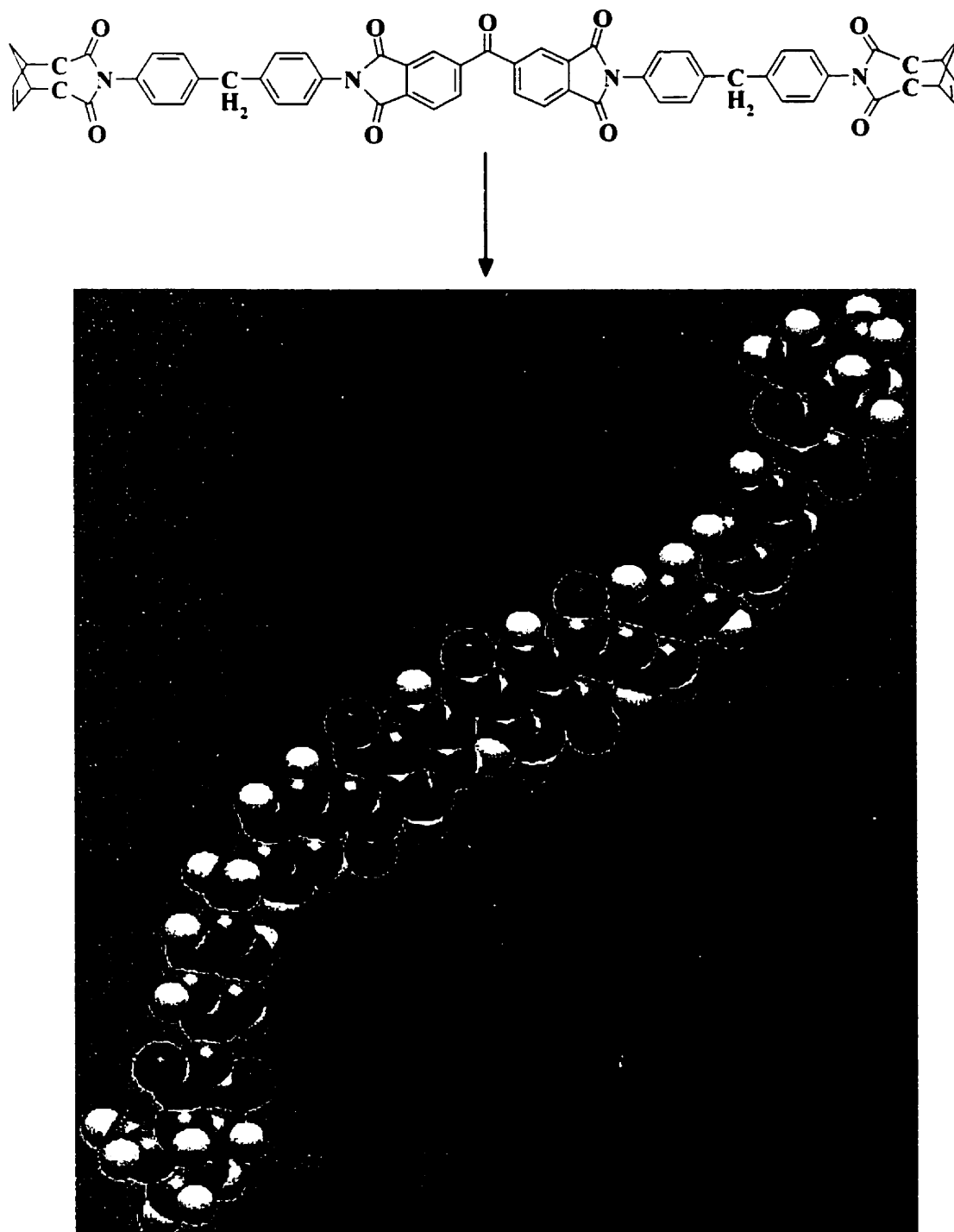


Figure 1.3. Chemical structure of Polypyromellitimide (PMR15).⁴

BACKGROUND

Prior to initiating a research effort such as this forthcoming investigation on the behavior of 8HS WGFRP composite materials, it is essential to perform an extensive search on all past and present literature. This enables the investigator to explore unresolved issues without duplicating previous efforts. The exhaustive search on available and reliable literature specific to the performance and failure of the aforementioned materials has revealed that little information exists related to shear dominated, biaxial behavior and failure characteristics. Regardless of this fact, judicious application of universally accepted theory for other composite systems is also pertinent for woven fabric composites.

Fundamental to the mathematical treatment of all polymer matrix composite materials is a thorough understanding of the concepts of stress, strain and, in general, the linear elastic behavior of a solid body. Within the framework of classical elastic theory, the linear elastic behavior of a solid body can be described by mathematical models from which the internal displacements and forces are found in terms of the spatial coordinates. The classical formulation of the theory of elasticity is a consequence of three cardinal assumptions [5]:

- internal stresses are at a state of equilibrium,
- displacements are continuous and compatible deformation exists,
- stress-strain relations are governed by Hooke's law.

In the beginning of this section, the sets of equations are presented that form the backbone for mathematically describing the behavior of a general, three-dimensional body at rest. For the purposes of derivation, certain restrictions are placed on the material properties and nature of body deformation. The concept of stress is defined and relationships are shown in

terms of the stress components, body forces and applied loads. Strain is also defined, at this point, in terms of displacements and the resulting strain-displacement relations constitute an essential element of the theory of elasticity. Based on the intensive¹ quantities stress and strain, linearly elastic material behavior is shown to obey Hooke's law which connects six local (point) strains to six local stresses and states that [5]

- stress and strain are linearly related and response is instantaneous,
- application of force or displacement produces stress,
- normal stresses (strains) result only in normal strains (stresses),
- shearing stresses (strains) result only in shearing strains (stresses), and
- only two independent material constants exist in linear elasticity.

Following the formulation for linear elastic behavior of a solid body, linear elastic behavior of polymer matrix composites is considered. Unlike the analysis of bulk solids which are assumed to be homogeneous and isotropic, the analysis of PMC's may account for heterogeneity and anisotropy. That is, the properties at a point in the composite body will probably not be the same in every direction, nor will they be independent of body position. Fundamental to this treatment is the knowledge of the elastic behavior of a UD composite lamina. The relation between stress and strain, referred to as the constitutive relation (a generalization of Hooke's law), is first presented for the comprehensive three-dimensional case. Insight is given as to the physical interpretation of the behavior of a non-isotropic body, followed by reduction to a simplified two-dimensional analysis based on an underlying assumption of plane stress or plane strain behavior. Existing mathematical models are also presented for the interpretation of behavior in woven fabric laminae, given the established foundation for UD laminae from which to build.

Subsequent to the discussion of theory governing lamina behavior, the constitutive relations for a composite laminate composed of bonded laminae are outlined. Accordingly,

¹ An intensive quantity suggests local association to a point and stress and strain are limiting ratios of infinitesimals.

analysis of laminate elastic properties are based on adopting the classical approach of Kirchhoff thin plate theory, i.e. classical lamination theory given within the bounds of the following assumptions [6]:

- laminae are perfectly bonded to each other, i.e. no slip occurs,
- the interfacial bonds are infinitely thin, and
- lamina thickness varies minimally, and
- the laminate has the characteristics of a thin sheet.

As with the outline for mathematical treatment of composite laminae, the general three-dimensional laminate case is demonstrated, followed by simplifications. Finally, failure behavior in composite laminates is identified inclusive of universally accepted modes of crack propagation and types of failure. In contrast to isotropic and homogeneous materials which typically exhibit self-similar crack growth processes, fiber composites will often contain cracks that do not propagate along their original orientations because of micro-heterogeneity. In isotropic materials, the direction of crack growth is dictated by the principal loading condition. As an example, uniaxial tension produces a uniaxial state of stress on the plane of a crack. However, the plane of fracture in aligned composite materials is determined by both the loading and fiber directions. In two-dimensional composite architectures such as a woven fabric composite, multiple planes of fracture can be envisaged leading to the concept of damage zones. Accumulation of damage and formation of local zones will also be touched upon in this section.

2.1. Linear Elastic Behavior of a Solid

As was previously mentioned, the formulation of the theory of elasticity requires adherence to the principles of stress equilibrium, displacement continuity and stress-strain relations which are a material property. When boundary conditions are stated in terms of geometric constraints and applied body loads, three sets of equations completely define the linear elastic behavior of a body. They are the equilibrium equations, strain-displacement equations and

stress-strain equations. What follows is the concise identification of each set beginning with those equations of equilibrium.

2.1.1. Force and Stress

Newton's first law requires that rigid, solid body equilibrium is a result of balanced forces and moments that prevent the body from translating or moving along a path and rotating. That is $\Sigma F_x = 0$, $\Sigma F_y = 0$, $\Sigma F_z = 0$ and $\Sigma M_x = 0$, $\Sigma M_y = 0$, $\Sigma M_z = 0$ with reference to the rectangular Cartesian coordinate system. Since the entire body is in equilibrium, then so to is any part within the body. With that in mind, it is typical to distinguish between two distinct types of forces, external and internal forces. A body can be subjected to different types of external loads, but they are classified as either a surface load with units of force per unit area or a body force with units of force per unit volume. Surface loads occur when one body comes into direct contact with another body while body loads occur when one body exerts a force on another body exempt of any physical contact. Internal surface forces occur on unseen internal surfaces and are stresses if considered as force per unit area. The stress and stress components on an internal surface, as shown in Figure 2.1, are given by

$$\sigma = \lim_{\Delta A \rightarrow 0} \frac{\Delta F_n}{\Delta A}, \quad \tau = \lim_{\Delta A \rightarrow 0} \frac{\Delta F_t}{\Delta A} \quad (2.1)$$

where $\Delta F_{n,t}$ are the resolved normal and tangential surface force components acting on an element ΔA of the area A while σ and τ represent the normal and tangential (shearing) components of stress.

The concept illustrated by Figure 2.1 can be extended to a more general case of a complete stress state, at a point, in rectangular Cartesian coordinates. By considering a rectangular element of finite size in order to show the surfaces on which stresses may act, it is reasonable that three normal stresses and six shearing stresses (three if symmetry is accounted for) define the complete state of stress shown in Figure 2.2.

2.1.1.1. Equations of Equilibrium

These stresses (positive for convention) are related to each other according to the equilibrium equations. In reference to Figure 2.3, a Taylor's series expansion yields [7]

$$\begin{aligned}\sigma_x(x+dx, y, z) &= \sigma_x(x, y, z) + \frac{\partial \sigma_x}{\partial x} dx \\ \tau_{xy}(x+dx, y, z) &= \tau_{xy}(x, y, z) + \frac{\partial \tau_{xy}}{\partial x} dx \\ \tau_{xz}(x+dx, y, z) &= \tau_{xz}(x, y, z) + \frac{\partial \tau_{xz}}{\partial x} dx\end{aligned}\quad (2.2)$$

which presents the stresses on one face of the elemental cube in terms of those stresses on the opposite face (for clarity, stresses on two pairs of faces are not shown). For force equilibrium in the x-direction and moment equilibrium about the z-direction, the stresses must be converted to forces by multiplication of the corresponding areas. Thus, along the positive x-direction, the concise force summation due to [7] is given as

$$\begin{aligned}\left(\sigma_x + \frac{\partial \sigma_x}{\partial x} dx\right) dy dz - \sigma_x dy dz + \left(\tau_{xy} + \frac{\partial \tau_{xy}}{\partial y} dy\right) dx dz - \tau_{xz} dx dz \\ + \left(\tau_{xz} + \frac{\partial \tau_{xz}}{\partial z} dz\right) dx dy - \tau_{xz} dx dy + f_x dx dy dz = 0\end{aligned}\quad (2.3)$$

where \mathbf{f}_x or $\rho \mathbf{g}_x$ is the force due to gravity and the only body force under consideration. Similarly, in considering moment equilibrium about the z-axis passing through the center of the element, there are no body moments present, thus concise moment summation follows

$$\begin{aligned}\left(\tau_{xy} + \frac{\partial \tau_{xy}}{\partial x} dx\right) dy dz \frac{dx}{2} + \tau_{xy} dy dz \frac{dx}{2} - \left(\tau_{yx} + \frac{\partial \tau_{yx}}{\partial y} dy\right) dz dx \frac{dy}{2} \\ - \tau_{yx} dz dx \frac{dy}{2} = 0\end{aligned}\quad (2.4)$$

Upon further simplification of Eq. 2.3, the x-direction force equilibrium relationship is given:

$$\frac{\partial \sigma_x}{\partial x} + \frac{\partial \tau_{xy}}{\partial y} + \frac{\partial \tau_{xz}}{\partial z} + f_x = 0 \quad (2.5)$$

By repeating the same exercise for the other directions and converting stresses to forces by multiplication of corresponding areas, the remaining two force equilibrium equations are

$$\begin{aligned} \frac{\partial \tau_{yx}}{\partial x} + \frac{\partial \sigma_y}{\partial y} + \frac{\partial \tau_{yz}}{\partial z} + f_y &= 0 \\ \frac{\partial \tau_{zx}}{\partial x} + \frac{\partial \tau_{zy}}{\partial y} + \frac{\partial \sigma_z}{\partial z} + f_z &= 0 \end{aligned} \quad (2.6)$$

Likewise, the simplification of the moment summation about the z-axis (Eq. 2.4) in which the limit as $dx \rightarrow 0$ and $dy \rightarrow 0$, and cancellation of the common factor ($dx \, dy \, dz$) gives

$$\begin{aligned} \tau_{xy} + \frac{\partial \tau_{xy}}{\partial x} \frac{dx}{2} - \tau_{yx} - \frac{\partial \tau_{yx}}{\partial y} \frac{dy}{2} &= 0 \\ \downarrow \\ \tau_{xy} &= \tau_{yx} \end{aligned} \quad (2.7)$$

The additional equations determined from moments about the other axes are $\tau_{yz} = \tau_{zy}, \tau_{zx} = \tau_{xz}$ and expressing the force and moment equilibrium equations in matrix notation are given by

$$-\begin{bmatrix} f_x \\ f_y \\ f_z \end{bmatrix} = \begin{bmatrix} \frac{\partial}{\partial x} & 0 & 0 & \frac{\partial}{\partial y} & 0 & \frac{\partial}{\partial z} \\ 0 & \frac{\partial}{\partial y} & 0 & \frac{\partial}{\partial x} & \frac{\partial}{\partial z} & 0 \\ 0 & 0 & \frac{\partial}{\partial z} & 0 & \frac{\partial}{\partial y} & \frac{\partial}{\partial x} \end{bmatrix} \begin{bmatrix} \sigma_x \\ \sigma_y \\ \sigma_z \\ \tau_{xy} \\ \tau_{yz} \\ \tau_{zx} \end{bmatrix} \quad (2.8)$$

Based on the derivation resulting in Eq. 2.8, the six equations couple the nine stresses and it is assumed that each stress is uniform across the face of the element in Figure 2.3. Also, the stress state at a point, given by a specific orientation, will uniquely determine the stress

state at the same point with respect to any arbitrary orientation within the same coordinate system according to the rules of stress transformation readily available in the literature.

2.1.2. Displacement and Strain

The displacements of a point within a solid body can be determined by measuring the translation of that point, subsequent to solid body loading, in the x, y and z-directions relative to the location in a specific coordinate system when the body is not experiencing a load. Rigid body displacement refers to the condition when all points within a body move by the same amount, while deformation is an indication of relative displacement occurring between two or more points within a body. In reference to Figure 2.4, the displacements in the coordinate directions are denoted by u , v and w , respectively. Consider two points in an undeformed elemental cube denoted by 1 and 2. If point 1 is expressed in terms of x, y and z-coordinates, then the position of 2, with respect to 1, is located at $x + dx$, $y + dy$, and $z + dz$. In examining the relative motion between these two points, a line is connected between them with the distance given by $dt^2 = dx^2 + dy^2 + dz^2$. In the strained state, the distance of the line between the relative points 1' and 2' is defined as $d't'^2 = d'x'^2 + d'y'^2 + d'z'^2$. The coordinate displacements u , v and w of (1) are differentiable functions given by $u = x' - x$, $v = y' - y$ and $w = z' - z$. Solution to the line distance in the strained state by substitution may be expressed as $d't'^2 = dx^2 + dy^2 + dz^2 + 2dudx + 2dvdy + 2dwdz + du^2 + dv^2 + dw^2$. Therefore, the relative distance between the strained and unstrained states is given by [7]

$$ds'^2 - ds^2 = 2(du dx + dv dy + dw dz) + du^2 + dv^2 + dw^2 \quad (2.9)$$

Following the rules governing differentiation of partials

$$\begin{aligned} du &= \frac{\partial u}{\partial x} dx + \frac{\partial u}{\partial y} dy + \frac{\partial u}{\partial z} dz \\ dv &= \frac{\partial v}{\partial x} dx + \frac{\partial v}{\partial y} dy + \frac{\partial v}{\partial z} dz \end{aligned} \quad (2.10)$$

$$dw = \frac{\partial w}{\partial x} dx + \frac{\partial w}{\partial y} dy + \frac{\partial w}{\partial z} dz$$

Eq. 2.9 can be rewritten as Eq. 2.11 where the strains are partials in terms of displacements as shown by Eq. 2.12

$$\Delta ds^2 = 2\varepsilon_x dx^2 + 2\varepsilon_y dy^2 + 2\varepsilon_z dz^2 + 2\gamma_{xy} dx dy + 2\gamma_{yz} dy dz + 2\gamma_{zx} dz dx \quad (2.11)$$

$$\begin{aligned} \varepsilon_x &= \frac{\partial u}{\partial x} + \frac{1}{2} \left(\left(\frac{\partial u}{\partial x} \right)^2 + \left(\frac{\partial v}{\partial x} \right)^2 + \left(\frac{\partial w}{\partial x} \right)^2 \right) \\ \varepsilon_y &= \frac{\partial v}{\partial y} + \frac{1}{2} \left(\left(\frac{\partial u}{\partial y} \right)^2 + \left(\frac{\partial v}{\partial y} \right)^2 + \left(\frac{\partial w}{\partial y} \right)^2 \right) \\ \varepsilon_z &= \frac{\partial w}{\partial z} + \frac{1}{2} \left(\left(\frac{\partial u}{\partial z} \right)^2 + \left(\frac{\partial v}{\partial z} \right)^2 + \left(\frac{\partial w}{\partial z} \right)^2 \right) \end{aligned} \quad (2.12)$$

$$\begin{aligned} \gamma_{xy} &= \frac{\partial v}{\partial x} + \frac{\partial u}{\partial y} + \frac{\partial u}{\partial x} \frac{\partial u}{\partial y} + \frac{\partial v}{\partial x} \frac{\partial v}{\partial y} + \frac{\partial w}{\partial x} \frac{\partial w}{\partial y} \\ \gamma_{yz} &= \frac{\partial w}{\partial y} + \frac{\partial v}{\partial z} + \frac{\partial u}{\partial y} \frac{\partial u}{\partial z} + \frac{\partial v}{\partial y} \frac{\partial v}{\partial z} + \frac{\partial w}{\partial y} \frac{\partial w}{\partial z} \\ \gamma_{zx} &= \frac{\partial u}{\partial z} + \frac{\partial w}{\partial x} + \frac{\partial u}{\partial z} \frac{\partial u}{\partial x} + \frac{\partial v}{\partial z} \frac{\partial v}{\partial x} + \frac{\partial w}{\partial z} \frac{\partial w}{\partial x} \end{aligned}$$

If it is assumed that the deflections are small compared to the characteristic solid body dimensions, then it is reasonable to ignore the squares and products of the first partial displacement derivatives in Eq. 2.12. By dropping the higher-order terms, the simplification leads to the recognizable linear strain-displacement relationships given by the following:

$\varepsilon_x = \frac{\partial u}{\partial x}$, $\varepsilon_y = \frac{\partial v}{\partial y}$, $\varepsilon_z = \frac{\partial w}{\partial z}$, $\gamma_{xy} = \frac{\partial v}{\partial x} + \frac{\partial u}{\partial y}$, $\gamma_{yz} = \frac{\partial w}{\partial y} + \frac{\partial v}{\partial z}$, $\gamma_{zx} = \frac{\partial u}{\partial z} + \frac{\partial w}{\partial x}$ where ε and γ are the normal and shear strain components. Consistent with matrix notation, the linear strain-displacement equations can be rewritten as [7]

$$\begin{bmatrix} \varepsilon_x \\ \varepsilon_y \\ \varepsilon_z \\ \gamma_{xy} \\ \gamma_{yz} \\ \gamma_{zx} \end{bmatrix} = \begin{bmatrix} \frac{\partial}{\partial x} & 0 & 0 \\ 0 & \frac{\partial}{\partial y} & 0 \\ 0 & 0 & \frac{\partial}{\partial z} \\ \frac{\partial}{\partial y} & \frac{\partial}{\partial x} & 0 \\ 0 & \frac{\partial}{\partial z} & \frac{\partial}{\partial y} \\ \frac{\partial}{\partial z} & 0 & \frac{\partial}{\partial x} \end{bmatrix} \begin{bmatrix} u \\ v \\ w \end{bmatrix} \quad (2.13)$$

2.1.2.1. Equations of Compatibility

Shearing strains have a physical interpretation as changes in the angular orientation of a body [7]. In other words, a shearing strain can be defined as the reduction in what was originally a right angle for the case of a two-dimensional element. In reference to Figure 2.5, an undeformed element is defined by ABCD. Subsequent to shear deformation, the element edges AC and AD have rotated to their new positions denoted by lines A'C' and A'D' through the angles γ_1 and γ_2 . According to small angle approximations, the derivatives of the displacements forming the angles are equivalent to the sines of the angles, so the shearing strain γ_{xy} may be defined by

$$\gamma_1 + \gamma_2 = \frac{\partial u}{\partial y} + \frac{\partial v}{\partial x} = \gamma_{xy} \quad (2.14)$$

For the three-dimensional case, a similar explanation exists for defining the shear strains γ_{yx} and γ_{zx} . If the displacements are eliminated from the strain-displacement equations, the compatibility equations can be defined. As an example, the following operations and substitutions are performed for the strain component γ_{xy} given by Eq. 2.15 [7]:

$$\begin{aligned}
\frac{\partial^2}{\partial x \partial y} (\gamma_{xy}) &= \frac{\partial^2}{\partial x \partial y} \left(\frac{\partial u}{\partial y} \right) + \frac{\partial^2}{\partial x \partial y} \left(\frac{\partial v}{\partial x} \right) = \frac{\partial^2}{\partial y^2} \left(\frac{\partial u}{\partial x} \right) + \frac{\partial^2}{\partial x^2} \left(\frac{\partial v}{\partial y} \right) \\
&= \frac{\partial^2}{\partial y^2} (\epsilon_x) + \frac{\partial^2}{\partial x^2} (\epsilon_y)
\end{aligned} \tag{2.15}$$

By similar substitutions, the remaining equations of compatibility can be found from the strain-displacement relationships and are given by

$$\begin{aligned}
\frac{\partial^2}{\partial y \partial z} (\gamma_{yz}) &= \frac{\partial^2}{\partial z^2} (\epsilon_y) + \frac{\partial^2}{\partial y^2} (\epsilon_z) \\
\frac{\partial^2}{\partial z \partial x} (\gamma_{zx}) &= \frac{\partial^2}{\partial x^2} (\epsilon_z) + \frac{\partial^2}{\partial z^2} (\epsilon_x) \\
2 \frac{\partial^2}{\partial y \partial z} (\epsilon_x) &= \frac{\partial}{\partial x} \left(-\frac{\partial}{\partial x} (\gamma_{yz}) + \frac{\partial}{\partial y} (\gamma_{zx}) + \frac{\partial}{\partial z} (\gamma_{xy}) \right) \\
2 \frac{\partial^2}{\partial z \partial x} (\epsilon_y) &= \frac{\partial}{\partial y} \left(\frac{\partial}{\partial x} (\gamma_{yz}) - \frac{\partial}{\partial y} (\gamma_{zx}) + \frac{\partial}{\partial z} (\gamma_{xy}) \right) \\
2 \frac{\partial^2}{\partial x \partial y} (\epsilon_z) &= \frac{\partial}{\partial z} \left(-\frac{\partial}{\partial x} (\gamma_{yz}) + \frac{\partial}{\partial y} (\gamma_{zx}) - \frac{\partial}{\partial z} (\gamma_{xy}) \right)
\end{aligned} \tag{2.16}$$

These equations (Eqs. 2.15 and 2.16) represent the physical fact that a solid body remains intact after deformation, i.e. neighboring points within the body are in a mappable, one-to-one relationship.

2.1.3. Material Properties and Hooke's Law

The equilibrium, linear strain displacement and compatibility relations are independent of, and thus, say nothing about the material or materials of a solid body. They are applicable to any continuous, solid body experiencing small displacements. The relationships between stress and strain, dependent on material characteristics, are the stress-strain equations. The equations which connect the six stresses at a point to the six strains at a point are referred to

as Hooke's law. Hooke's law describes the linear elastic behavior of a solid and, essentially, the law is reemphasized by the following [5]:

- stress and strain are linearly related,
- application of either force or displacement can produce stress,
- stress-strain response is instantaneous,
- normal stresses directly refer to normal strains,
- shear stresses directly refer to shear strains, and
- there are two independent material constants in linear elasticity for homogeneity and isotropy.

The local deformation of a linear elastic, homogeneous and isotropic elemental cube due to axial stress is shown in Figure 2.6. If three normal stresses are applied simultaneously and no angular distortion is present, then superposition of individual stress results gives $\varepsilon_x = \frac{1}{E}[\sigma_x - \nu(\sigma_y + \sigma_z)]$, $\varepsilon_y = \frac{1}{E}[\sigma_y - \nu(\sigma_z + \sigma_x)]$, $\varepsilon_z = \frac{1}{E}[\sigma_z - \nu(\sigma_x + \sigma_y)]$, where E and ν are Young's modulus and Poisson's ratio, respectively. If purely shear stresses are applied to the cube to produce angular distortions, this can be expressed in terms of the shear modulus G as $\gamma_{xy} = \frac{\tau_{xy}}{G}$, $\gamma_{yz} = \frac{\tau_{yz}}{G}$, $\gamma_{zx} = \frac{\tau_{zx}}{G}$. Again, in remaining consistent with matrix notation, these six equations which define Hooke's law and relate stress to strain are rewritten as

$$\begin{bmatrix} \sigma_x \\ \sigma_y \\ \sigma_z \\ \tau_{xy} \\ \tau_{yz} \\ \tau_{zx} \end{bmatrix} = \begin{bmatrix} \lambda + 2G & \lambda & \lambda & 0 & 0 & 0 \\ \lambda & \lambda + 2G & \lambda & 0 & 0 & 0 \\ \lambda & \lambda & \lambda + 2G & 0 & 0 & 0 \\ 0 & 0 & 0 & G & 0 & 0 \\ 0 & 0 & 0 & 0 & G & 0 \\ 0 & 0 & 0 & 0 & 0 & G \end{bmatrix} \begin{bmatrix} \varepsilon_x \\ \varepsilon_y \\ \varepsilon_z \\ \gamma_{xy} \\ \gamma_{yz} \\ \gamma_{zx} \end{bmatrix} \quad (2.17)$$

where

$$\lambda = \frac{\nu E}{(1 + \nu)(1 - 2\nu)} \quad (2.18)$$

2.2. Mechanics of a Composite Lamina

In the previous section, the governing equations of classical elastic theory for a homogeneous, isotropic solid body were described. According to Hooke's law, it was established that only two independent elastic material constants were necessary to specify the constitutive relations. The relations that exist among the five possible constants are defined accordingly as $G = \frac{E}{2(1+\nu)}$, $K = \frac{E}{3(1-2\nu)}$, $k = \frac{E}{2(1-\nu-2\nu^2)}$, where E is Young's modulus, G is the shear modulus, ν is Poisson's ratio, K is the bulk modulus and k is the plane strain bulk modulus. For a generally anisotropic material, where the material properties vary with direction, twenty-one independent constants are needed to describe elastic stress-strain behavior.

2.2.1. Unidirectional Composite Lamina

A UD composite lamina having continuous and straight fibers in a matrix, as illustrated by Figure 2.7, can be considered a homogeneous and orthotropic (three mutually perpendicular planes of symmetry) continuum where the consideration of homogeneity is valid if the scale in question is considerably larger than the inter-fiber spacing. Further, the lamina can also be treated as transversely isotropic in the x_2 and x_3 material coordinate directions (see Figure 2.7) if it is assumed that the fibers are randomly distributed having circular cross-sections. With this, the number of independent elastic material constants necessary to describe the elastic behavior of a UD lamina reduces from twenty-one to five. Of the five constants, four can be experimentally determined from a series of static off-axis tensile tests.

2.2.1.1. General Constitutive Relations

Hooke's law can be generalized using a contracted form of tensor notation and expressed concisely by the following equation [6]:

$$\sigma_i = \sum_{j=1}^6 C_{ij} \varepsilon_j \quad (2.19)$$

where $i, j = 1, \dots, 6$, σ_i are the components of stress, C_{ij} is the stiffness matrix and ε_j are the components of strain. Since the stiffness constants are symmetrical, i.e. $C_{ij} = C_{ji}$ the expanded form of Eq. 2.19 is given in matrix notation by

$$\begin{bmatrix} \sigma_1 \\ \sigma_2 \\ \sigma_3 \\ \tau_{23} \\ \tau_{31} \\ \tau_{12} \end{bmatrix} = \begin{bmatrix} C_{11} & C_{12} & C_{13} & C_{14} & C_{15} & C_{16} \\ & C_{22} & C_{23} & C_{24} & C_{25} & C_{26} \\ & & C_{33} & C_{34} & C_{35} & C_{36} \\ & & & C_{44} & C_{45} & C_{46} \\ & & & & C_{55} & C_{56} \\ & & & & & C_{66} \end{bmatrix} \begin{bmatrix} \varepsilon_1 \\ \varepsilon_2 \\ \varepsilon_3 \\ \gamma_{23} \\ \gamma_{31} \\ \gamma_{12} \end{bmatrix} \quad (2.20)$$

(SYM)

From the matrix notation denoting the generalized constitutive relation in Eq. 2.20, further manipulation gives an explicit definition for the six equations that relate stress to strain as

$$\begin{aligned} \sigma_1 &= C_{11}\varepsilon_1 + C_{12}\varepsilon_2 + C_{13}\varepsilon_3 + C_{14}\gamma_{23} + C_{15}\gamma_{31} + C_{16}\gamma_{12} \\ \sigma_2 &= C_{12}\varepsilon_1 + C_{22}\varepsilon_2 + C_{23}\varepsilon_3 + C_{24}\gamma_{23} + C_{25}\gamma_{31} + C_{26}\gamma_{12} \\ \sigma_3 &= C_{13}\varepsilon_1 + C_{23}\varepsilon_2 + C_{33}\varepsilon_3 + C_{34}\gamma_{23} + C_{35}\gamma_{31} + C_{36}\gamma_{12} \\ \tau_{23} &= C_{14}\varepsilon_1 + C_{24}\varepsilon_2 + C_{34}\varepsilon_3 + C_{44}\gamma_{23} + C_{45}\gamma_{31} + C_{46}\gamma_{12} \\ \tau_{31} &= C_{15}\varepsilon_1 + C_{25}\varepsilon_2 + C_{35}\varepsilon_3 + C_{45}\gamma_{23} + C_{55}\gamma_{31} + C_{56}\gamma_{12} \\ \tau_{12} &= C_{16}\varepsilon_1 + C_{26}\varepsilon_2 + C_{36}\varepsilon_3 + C_{46}\gamma_{23} + C_{56}\gamma_{31} + C_{66}\gamma_{12} \end{aligned} \quad (2.21)$$

There is also a set of inverted relations which correspond to those defined by Eqs. 2.19 to 2.21 and connect strain to stress in terms of the compliance matrix S_{ij} . The inverted set is [6]

$$\varepsilon_i = \sum_{j=1}^6 S_{ij} \sigma_j, \quad \begin{bmatrix} \varepsilon_1 \\ \varepsilon_2 \\ \varepsilon_3 \\ \gamma_{23} \\ \gamma_{31} \\ \gamma_{12} \end{bmatrix} = \begin{bmatrix} S_{11} & S_{12} & S_{13} & S_{14} & S_{15} & S_{16} \\ & S_{22} & S_{23} & S_{24} & S_{25} & S_{26} \\ & & S_{33} & S_{34} & S_{35} & S_{36} \\ & & & S_{44} & S_{45} & S_{46} \\ & & & & S_{55} & S_{56} \\ & & & & & S_{66} \end{bmatrix} \begin{bmatrix} \sigma_1 \\ \sigma_2 \\ \sigma_3 \\ \tau_{23} \\ \tau_{31} \\ \tau_{12} \end{bmatrix} \quad (2.22)$$

(SYM)

Likewise, the six equations that relate strain to stress are

$$\begin{aligned}
 \varepsilon_1 &= S_{11}\sigma_1 + S_{12}\sigma_2 + S_{13}\sigma_3 + S_{14}\tau_{23} + S_{15}\tau_{31} + S_{16}\tau_{12} \\
 \varepsilon_2 &= S_{12}\sigma_1 + S_{22}\sigma_2 + S_{23}\sigma_3 + S_{24}\tau_{23} + S_{25}\tau_{31} + S_{26}\tau_{12} \\
 \varepsilon_3 &= S_{13}\sigma_1 + S_{23}\sigma_2 + S_{33}\sigma_3 + S_{34}\tau_{23} + S_{35}\tau_{31} + S_{36}\tau_{12} \\
 \gamma_{23} &= S_{14}\sigma_1 + S_{24}\sigma_2 + S_{34}\sigma_3 + S_{44}\tau_{23} + S_{45}\tau_{31} + S_{46}\tau_{12} \\
 \gamma_{31} &= S_{15}\sigma_1 + S_{25}\sigma_2 + S_{35}\sigma_3 + S_{45}\tau_{23} + S_{55}\tau_{31} + S_{56}\tau_{12} \\
 \gamma_{12} &= S_{16}\sigma_1 + S_{26}\sigma_2 + S_{36}\sigma_3 + S_{46}\tau_{23} + S_{56}\tau_{31} + S_{66}\tau_{12}
 \end{aligned} \tag{2.23}$$

For a UD lamina that exhibits orthotropic symmetry and transverse isotropy in the $x_2 - x_3$ material principal coordinate plane (refer to Figure 2.7), the following constitutive relations, in terms of components of the stiffness matrix, hold [2]:

$$\begin{bmatrix} \sigma_1 \\ \sigma_2 \\ \sigma_3 \\ \sigma_{23} \\ \sigma_{13} \\ \sigma_{12} \end{bmatrix} = \begin{bmatrix} C_{11} & C_{12} & C_{13} & 0 & 0 & 0 \\ C_{12} & C_{22} & C_{23} & 0 & 0 & 0 \\ C_{13} & C_{23} & C_{33} & 0 & 0 & 0 \\ 0 & 0 & 0 & C_{44} & 0 & 0 \\ 0 & 0 & 0 & 0 & C_{55} & 0 \\ 0 & 0 & 0 & 0 & 0 & C_{66} \end{bmatrix} \begin{bmatrix} \varepsilon_1 \\ \varepsilon_2 \\ \varepsilon_3 \\ 2\varepsilon_{23} \\ 2\varepsilon_{13} \\ 2\varepsilon_{12} \end{bmatrix} \tag{2.24}$$

where the C_{ij} components, defined in terms of the engineering elastic constants, are

$$\begin{aligned}
 C_{11} &= \frac{E_{11}(1 - \nu_{23}^2)}{1 - 2\nu_{12}\nu_{21} - \nu_{23}^2 - 2\nu_{12}\nu_{21}\nu_{23}} \\
 C_{22} = C_{33} &= \frac{E_{22}(1 - \nu_{12}\nu_{21})}{1 - 2\nu_{12}\nu_{21} - \nu_{23}^2 - 2\nu_{12}\nu_{21}\nu_{23}} \\
 C_{44} &= G_{23} \\
 C_{55} = C_{66} &= G_{12} \\
 C_{12} = C_{13} &= \frac{(\nu_{21} + \nu_{21}\nu_{23})E_{11}}{1 - 2\nu_{12}\nu_{21} - \nu_{23}^2 - 2\nu_{12}\nu_{21}\nu_{23}} = \frac{(\nu_{12} + \nu_{12}\nu_{23})E_{22}}{1 - 2\nu_{12}\nu_{21} - \nu_{23}^2 - 2\nu_{12}\nu_{21}\nu_{23}} \\
 C_{23} &= \frac{(\nu_{23} + \nu_{12}\nu_{21})E_{22}}{1 - 2\nu_{12}\nu_{21} - \nu_{23}^2 - 2\nu_{12}\nu_{21}\nu_{23}}
 \end{aligned} \tag{2.25}$$

As with the generalized form of constitutive relations for a UD composite lamina, Eq. 2.24 may also be inverted for the case of an orthotropic lamina leading to strain-stress relations in terms of the compliance matrix:

$$\begin{bmatrix} \varepsilon_1 \\ \varepsilon_2 \\ \varepsilon_3 \\ 2\varepsilon_{23} \\ 2\varepsilon_{13} \\ 2\varepsilon_{12} \end{bmatrix} = \begin{bmatrix} S_{11} & S_{12} & S_{13} & 0 & 0 & 0 \\ S_{12} & S_{22} & S_{23} & 0 & 0 & 0 \\ S_{13} & S_{23} & S_{33} & 0 & 0 & 0 \\ 0 & 0 & 0 & S_{44} & 0 & 0 \\ 0 & 0 & 0 & 0 & S_{55} & 0 \\ 0 & 0 & 0 & 0 & 0 & S_{66} \end{bmatrix} \begin{bmatrix} \sigma_1 \\ \sigma_2 \\ \sigma_3 \\ \sigma_{23} \\ \sigma_{13} \\ \sigma_{12} \end{bmatrix} \quad (2.26)$$

2.2.1.2. Simplified Constitutive Relations

It is evident from Figure 2.7 that the constitutive relations for a composite lamina can be simplified if the dimension in the x_3 (thickness) direction is considered to be sufficiently smaller than both of the in-plane dimensions. This consideration reduces the problem to two-dimensions, either of the plane stress or plane strain form. Clearly, the implication is that the nonzero stresses are arbitrarily restricted to in-plane, hence the nonzero quantities are not functions of x_3 ($\sigma_3 = \tau_{23} = \tau_{31} = 0$). For this, the stress-strain relation for a UD lamina given in terms of the matrix of mathematical moduli becomes

$$\begin{bmatrix} \sigma_1 \\ \sigma_2 \\ \sigma_6 \end{bmatrix} = \begin{bmatrix} Q_{11} & Q_{12} & 0 \\ Q_{12} & Q_{22} & 0 \\ 0 & 0 & Q_{66} \end{bmatrix} \begin{bmatrix} \varepsilon_1 \\ \varepsilon_2 \\ \varepsilon_6 \end{bmatrix} \quad (2.27)$$

where Q_{11} , Q_{22} , Q_{12} and Q_{66} are identified as the reduced stiffnesses. The equation above suggests that no coupling exists between tensile and shear strains [6], i.e. orthotropic composite materials exhibit no shearing strains when applied loads act coincident to the principal material directions. The Q_{ij} components of the reduced stiffness matrix from Eq. 2.27 are given in terms of the engineering constants as

$$\begin{aligned}
Q_{11} &= C_{11} = \frac{E_{11}}{1 - \nu_{12}\nu_{21}} \\
Q_{22} &= C_{22} = \frac{E_{22}}{1 - \nu_{12}\nu_{21}} \\
Q_{66} &= \frac{1}{2}(C_{11} - C_{12}) = G_{12} \\
Q_{12} &= C_{12} = \frac{\nu_{12}E_{22}}{1 - \nu_{12}\nu_{21}} = \frac{\nu_{21}E_{11}}{1 - \nu_{12}\nu_{21}}
\end{aligned} \tag{2.28}$$

The reciprocal of Eq. 2.27, the strain-stress relation, is given by

$$\begin{bmatrix} \varepsilon_1 \\ \varepsilon_2 \\ \varepsilon_6 \end{bmatrix} = \begin{bmatrix} S_{11} & S_{12} & 0 \\ S_{12} & S_{22} & 0 \\ 0 & 0 & S_{66} \end{bmatrix} \begin{bmatrix} \sigma_1 \\ \sigma_2 \\ \sigma_6 \end{bmatrix} \tag{2.29}$$

When the direction of applied load does not coincide with a principal material direction, then coupling between tensile and shear strains exists. Consider the sufficiently thin, UD lamina with fibers oriented at an angle λ to the principal coordinate axis shown in Figure 2.8. From classical theory of elasticity, the stress-strain relation becomes [6]

$$\begin{bmatrix} \sigma_x \\ \sigma_y \\ \tau_{xy} \end{bmatrix} = \begin{bmatrix} \bar{Q}_{11} & \bar{Q}_{12} & \bar{Q}_{16} \\ \bar{Q}_{12} & \bar{Q}_{22} & \bar{Q}_{26} \\ \bar{Q}_{16} & \bar{Q}_{26} & \bar{Q}_{66} \end{bmatrix} \begin{bmatrix} \varepsilon_x \\ \varepsilon_y \\ \gamma_{xy} \end{bmatrix} \tag{2.30}$$

where the \bar{Q}_{ij} components of the matrix are referred to as the transformed and reduced stiffness components. In terms of the reduced stiffness matrix components and λ , the transformed and reduced stiffness components have the following values:

$$\begin{aligned}
\bar{Q}_{11} &= Q_{11} \cos^4 \lambda + 2(Q_{12} + 2Q_{66}) \sin^2 \lambda \cos^2 \lambda + Q_{22} \sin^4 \lambda \\
\bar{Q}_{22} &= Q_{11} \sin^4 \lambda + 2(Q_{12} + 2Q_{66}) \sin^2 \lambda \cos^2 \lambda + Q_{22} \cos^4 \lambda \\
\bar{Q}_{66} &= (Q_{11} + Q_{22} - 2Q_{12} - 2Q_{66}) \sin^2 \lambda \cos^2 \lambda + Q_{66} (\sin^4 \lambda + \cos^4 \lambda)
\end{aligned} \tag{2.31}$$

$$\begin{aligned}
\bar{Q}_{12} &= (Q_{11} + Q_{22} - 4Q_{66})\sin^2 \lambda \cos^2 \lambda + Q_{12}(\sin^4 \lambda + \cos^4 \lambda) \\
\bar{Q}_{16} &= (Q_{11} - Q_{12} - 2Q_{66})\sin \lambda \cos^3 \lambda + (Q_{12} - Q_{22} + 2Q_{66})\sin^3 \lambda \cos \lambda \\
\bar{Q}_{26} &= (Q_{11} - Q_{12} - 2Q_{66})\sin^3 \lambda \cos \lambda + (Q_{12} - Q_{22} + 2Q_{66})\sin \lambda \cos^3 \lambda
\end{aligned}$$

As before, inverting Eq. 2.30 leads to the familiar strain-stress relation given by

$$\begin{bmatrix} \varepsilon_x \\ \varepsilon_y \\ \gamma_{xy} \end{bmatrix} = \begin{bmatrix} \bar{S}_{11} & \bar{S}_{12} & \bar{S}_{16} \\ \bar{S}_{12} & \bar{S}_{22} & \bar{S}_{26} \\ \bar{S}_{16} & \bar{S}_{26} & \bar{S}_{66} \end{bmatrix} \begin{bmatrix} \sigma_x \\ \sigma_y \\ \tau_{xy} \end{bmatrix} \quad (2.32)$$

Relationships similar to Eq. 2.31 are possible for the components of the transformed compliance matrix in terms of the compliances and the off-axis angle λ . They are given by

$$\begin{aligned}
\bar{S}_{11} &= S_{11} \cos^4 \lambda + (2S_{12} + S_{66})\sin^2 \lambda \cos^2 \lambda + S_{22} \sin^4 \lambda \\
\bar{S}_{22} &= S_{11} \sin^4 \lambda + (2S_{12} + S_{66})\sin^2 \lambda \cos^2 \lambda + S_{22} \cos^4 \lambda \\
\bar{S}_{66} &= 2(2S_{11} + 2S_{22} - 4S_{12} - S_{66})\sin^2 \lambda \cos^2 \lambda + S_{66}(\sin^4 \lambda + \cos^4 \lambda) \\
\bar{S}_{12} &= (S_{11} + S_{22} - S_{66})\sin^2 \lambda \cos^2 \lambda + S_{12}(\sin^4 \lambda + \cos^4 \lambda) \\
\bar{S}_{16} &= (2S_{11} - 2S_{12} - S_{66})\sin \lambda \cos^3 \lambda - (2S_{22} - 2S_{12} - S_{66})\sin^3 \lambda \cos \lambda \\
\bar{S}_{26} &= (2S_{11} - 2S_{12} - S_{66})\sin^3 \lambda \cos \lambda - (2S_{22} - 2S_{12} - S_{66})\sin \lambda \cos^3 \lambda
\end{aligned} \quad (2.33)$$

Finally, if the local elastic properties are known with respect to the material coordinate system, the engineering elastic constants can be determined for the Cartesian coordinate system. Combination of Eq. 2.33 with the relations for compliances, in terms of engineering elastic constants, results in the following:

$$\begin{aligned}
E_x &= \left[\frac{1}{E_1} \cos^4 \lambda + \left(\frac{1}{G_{12}} - \frac{2\nu_{12}}{E_1} \right) \sin^2 \lambda \cos^2 \lambda + \frac{1}{E_2} \sin^4 \lambda \right]^{-1} \\
E_y &= \left[\frac{1}{E_1} \sin^4 \lambda + \left(\frac{1}{G_{12}} - \frac{2\nu_{12}}{E_1} \right) \sin^2 \lambda \cos^2 \lambda + \frac{1}{E_2} \cos^4 \lambda \right]^{-1}
\end{aligned} \quad (2.34)$$

$$G_{xy} = \left[2 \left(\frac{2}{E_1} + \frac{2}{E_2} + \frac{4\nu_{12}}{E_1} - \frac{1}{G_{12}} \right) \sin^2 \lambda \cos^2 \lambda + \frac{1}{G_{12}} (\sin^4 \lambda + \cos^4 \lambda) \right]^{-1}$$

$$\nu_{xy} = E_x \left[\frac{\nu_{12}}{E_1} (\sin^4 \lambda + \cos^4 \lambda) - \left(\frac{1}{E_1} + \frac{1}{E_2} - \frac{1}{G_{12}} \right) \sin^2 \lambda \cos^2 \lambda \right]$$

2.2.2. Woven Fabric Lamina

The analytical and numerical treatments adopted for evaluating the performance of textile structural, reinforcing composite materials are not as well established compared to UD composite reinforcing materials. One reason the level of understanding has not reached the maturity that it has for UD composites is purely due to composite material and processing design evolution. Primarily though, a precise understanding of textile structural composite, elastic and nonlinear behavior is tied directly to the level of complexity. Behavior of these composite architectures is dictated by a greater number of geometric and processing parameters vis-à-vis UD composite architectures. Parameters such as fabric lamina structure (weave style, tow density, fabric count, tow crimp, warp/fill tow characteristics) and fabric laminate structure (lamina sequence, lamina orientation, asymmetry, balance) greatly influence the composite behavior under multiaxial loading, in-service conditions. Under such conditions, these parameters may result in coupled interactions, thus complicating the nature of the problem. Therefore, it is necessary to either account for as many parameters as possible, or make reasonable assumptions/simplifications when developing analytical and numerical techniques to analyze woven fabric composite behavior. What follows is an account of analytical models found in the literature for analysis of woven fabric composite laminae.

Several analytical methodologies have been proposed to predict the linear elastic and nonlinear behavior of woven fabric composites, particularly for two-dimensional orthogonal plain weave architectures [2,8-14]. Ishikawa and Chou [2,8-9] have developed three models,

viz. the mosaic model, the crimp or fiber undulation model and the bridging model. The one-dimensional mosaic model idealized the fabric structure as an assemblage of asymmetric pieces of cross-ply laminates by omitting tow continuity and interlacing. Stiffness constants were evaluated based on the assumption of either isostrain (parallel) or isostress (series) conditions. Variation in stress and strain near the interlaced regions was neglected and the model provided reasonable upper and lower bounded solutions to in-plane stiffness constants. The one-dimensional crimp or fiber undulation model extended the series mosaic model to include tow continuity and undulation, but only in the direction of applied load. The undulated tow was also treated as a single fiber, hence tow cross-sectional shape was excluded. This model was particularly well-suited for fabrics with a minimal number of fill tows per warp tow exchange (n_p), such as defined by a plain weave. The stiffness constants predicted by this model were lower than those predicted by the series mosaic model because transformed and reduced stiffness was evaluated as a function of the local off-axis angle in the filling direction. For satin weave architectures, the two-dimensional bridging model was proposed and this model was essentially a combination of the series and parallel models, again with continuity and undulation considered only in the direction of applied load. For this model, it was postulated that the regions immediately surrounding either end of the interlaced region acted as load bridges and regions immediately adjacent had the same average mid-plane strain and curvature. Comparisons made with experimental results for satin weave composites showed good agreement.

Naik *et al.* [11-13] developed a two-dimensional model to account for fiber continuity and undulation in both the warp and fill tow directions. The model idealized tow geometry with equations of periodic functions that constrained a tow to conform to the mutually orthogonal tow. For plain weaves with a closed architecture, i.e. adjacent tows in contact, the resemblance was a good match, however asymmetry resulted in open weaves if the gap was not taken into account. Woven fabric lamina, in-plane elastic constants were determined by homogenization of through-thickness properties (from lamina slices cut off-axis or on-axis) and assembling slices in a series-parallel (SP) or parallel-series (PS) fashion.

The upper bounded prediction of elastic moduli from the 2-D PS model was less than the parallel mosaic model and greater than the series mosaic model, while the lower bounded prediction from the 2-D SP model was less than the series mosaic model.

To more accurately represent both the open and closed plain weave geometries, Walsh and Ochoa [14] developed a revised set of three-dimensional shape equations. Their model did not constrain the tows to conform, thus the representation of the lamina by successive cross-sections was symmetric and correct for open weaves. However, the model did assume periodic functions and lenticular (idealized) cross-sectional tow shapes exhibiting two-axis symmetry. The mathematical moduli were homogenized with respect to the global coordinates by through-thickness integration and in-plane average elastic properties were found by simultaneous solutions to homogenization processes along the fill and warp directions. Comparisons to experimentally determined apparent properties for S-RIM plain weave composites showed quite good agreement.

2.2.2.1. One-Dimensional Characterization

The one-dimensional fiber crimp model considers continuity and undulation in the filling direction with a cross-sectional slice at $x = 0$ described by the shape functions due to Ishikawa and Chou (refer to Figure 2.9). The periodic function given to describe the sectional shapes of the warp yarns and filling yarns are, respectively

$$h_2(y) = \begin{pmatrix} \frac{h_t}{2} & \leftarrow & (0 \leq y \leq a_0) \\ \left[1 - \sin \left\{ \left(y - \frac{a}{2} \right) \frac{\pi}{a_u} \right\} \right] \frac{h_t}{4} & \leftarrow & \left(a_0 \leq y \leq \frac{a}{2} \right) \\ - \left[1 + \sin \left\{ \left(y - \frac{a}{2} \right) \frac{\pi}{a_u} \right\} \right] \frac{h_t}{4} & \leftarrow & \left(\frac{a}{2} \leq y \leq a_2 \right) \\ -\frac{h_t}{2} & \leftarrow & \left(a_2 \leq y \leq \frac{n_g a}{2} \right) \end{pmatrix} \quad (2.35)$$

$$h_1(y) = \begin{pmatrix} 0 & \leftarrow (0 \leq y \leq a_0) \\ \left[1 + \sin \left\{ \left(y - \frac{a}{2} \right) \frac{\pi}{a_u} \right\} \right] \frac{h_t}{4} & \leftarrow (a_0 \leq y \leq a_2) \\ \frac{h_t}{2} & \leftarrow \left(a_2 \leq y \leq \frac{n_g a}{2} \right) \end{pmatrix}$$

The extension, extension-bending coupling and bending stiffness matrices, that is \mathbf{A}_{ij} , \mathbf{B}_{ij} , and \mathbf{D}_{ij} , are evaluated by assuming that classical lamination theory is applicable to infinitesimal slices of d_y along the y -axis. This being the case, the extension stiffness matrix, as an example, is found by integrating the in-plane mathematical moduli for each constituent through-thickness. Over the range of $0 \leq y \leq \frac{a}{2}$, the summation of the average moduli with respect to the local off-axis angle ζ gives A_{ij} according to the following equation from [2]:

$$A_{ij}(y) = \int_{\frac{-h}{2}}^{\frac{h_1(y)-h_t}{2}} Q_{ij}^M dz + \int_{\frac{h_1(y)-h_t}{2}}^{\frac{h_1(y)}{2}} Q_{ij}^F(\zeta) dz + \int_{\frac{h_1(y)}{2}}^{\frac{h_2(y)}{2}} Q_{ij}^W dz + \int_{\frac{h_2(y)}{2}}^{\frac{h}{2}} Q_{ij}^M dz \quad (2.36)$$

where the superscripts M, F and W denote the matrix, fill and warp constituents. The local off-axis angle is given by $\zeta(y) = \arctan\left(\frac{d}{dy} h_1(y)\right)$. The fill tow matrix of local mathematical moduli is expressed in terms of the undulation angle in the filling direction and the constituent tow elastic properties as

$$Q_{ij}^F(\zeta) = \begin{bmatrix} \frac{E_{xx}^F(\zeta)}{D_v} & \frac{E_{xx}^F(\zeta) \nu_{yx}^F}{D_v} & 0 \\ \frac{E_{xx}^F(\zeta) \nu_{yx}^F}{D_v} & \frac{E_{xx}^F(\zeta)}{D_v} & 0 \\ 0 & 0 & G_{xy}^F(\zeta) \end{bmatrix} \quad (i, j = 1, 2, 6) \quad (2.37)$$

where the following relationship holds:

$$D_v = \frac{1 - (\nu_{yx}^F(\zeta))^2 E_{xx}^F(\zeta)}{E_{yy}^F(\zeta)} \quad (2.38)$$

Expressions in the manner of Eq. 2.36 can also be written for the extension-bending coupling and bending stiffnesses over all regions. The expressions for the A_{ij} , B_{ij} , D_{ij} stiffnesses can be expanded in terms of lamina thickness and explicitly stated for $0 \leq y \leq \frac{a}{2}$ as

$$\begin{aligned} A_{ij}(y) &= Q_{ij}^M \left[h_1(y) - h_2(y) + h - \frac{h_t}{2} \right] + Q_{ij}^F(\zeta) \frac{h_t}{2} + Q_{ij}^W [h_2(y) - h_1(y)] \\ B_{ij}(y) &= \frac{1}{2} Q_{ij}^F(\zeta) \left[h_1(y) - \frac{h_t}{4} \right] h_t + \frac{1}{4} Q_{ij}^W [h_2(y) - h_1(y)] h_t \\ D_{ij}(y) &= \frac{1}{3} Q_{ij}^M \left\{ \left[h_1(y) - \frac{h_t}{2} \right]^3 - h_2^3(y) + \frac{h^4}{4} \right\} \\ &\quad + \frac{1}{3} Q_{ij}^F(\zeta) \left[\frac{h_t^3}{8} - \frac{3h_t^2 h_1(y)}{4} + \frac{3h_t h_1^2(y)}{2} \right] + \frac{1}{3} Q_{ij}^W [h_2^3(y) - h_1^3(y)] \end{aligned} \quad (2.39)$$

2.2.2.2. Two-Dimensional Characterization

The 2-D series-parallel (SP) and parallel-series models (PS) consider fiber continuity and undulation in both directions. Referring to the weave cross-sections (X-Z, Y-Z) shown in Figures 2.10 and 2.11, the regions a_1 to a_5 and b_1 to b_5 are given by Naik *et al.* [11-13] as

$$\begin{aligned} a_1 &= \frac{1}{2} (a_{warp} - u_{fill}), \quad a_2 = \frac{1}{2} a_{warp}; \quad a_3 = \frac{1}{2} (a_{warp} + g_{warp}) \\ a_4 &= \frac{1}{2} (a_{warp}) + g_{warp}; \quad a_5 = \frac{1}{2} (a_{warp} + u_{fill}) + g_{warp} \\ b_1 &= \frac{1}{2} (a_{fill} - u_{warp}), \quad b_2 = \frac{1}{2} a_{fill}; \quad b_3 = \frac{1}{2} (a_{fill} + g_{fill}) \\ b_4 &= \frac{1}{2} (a_{fill}) + g_{fill}; \quad b_5 = \frac{1}{2} (a_{fill} + u_{warp}) + g_{fill} \end{aligned} \quad (2.40)$$

The two-dimensional shape equations are determined by taking through-thickness slices of a plain weave unit cell across the warp tow (Y-axis @ $y = 0$) and across the fill tow (X-axis @ $x = 0$). The shape equations are written to idealize the geometry of the on-axis fill tow or off-axis warp tow according to periodic functions in terms of the bounds described by regions in Eq. 2.40. The functions constrain the geometry of the on-axis tow to follow the off-axis tow, which is suitable for closed-gap architectures. These functions due to [11] are given by

$$\begin{aligned}
 hx_2(x) &= \left(\begin{array}{l} \frac{h_{fill} + h_{warp}}{2} \quad 0 \leq x \leq a_1 \\ \left[\frac{h_{fill} + h_{warp}}{2} - hx_1(a_2) \right] \cos \left\{ \frac{\pi(x - a_1)}{u_{warp}} \right\} + hx_1(a_2) \quad a_1 \leq x \leq a_2 \\ - \left[\frac{h_{fill} + h_{warp}}{2} - hx_1(a_2) \right] \cos \left\{ \frac{\pi(x - a_5)}{u_{warp}} \right\} + hx_1(a_2) \quad a_4 \leq x \leq a_5 \\ - \frac{h_{fill} + h_{warp}}{2} \quad a_5 \leq x \leq (a_f + g_f) \end{array} \right) \quad (2.41) \\
 hx_1(x) &= \left(\begin{array}{l} \frac{h_{warp} - h_{fill}}{2} \quad 0 \leq x \leq a_1 \\ \left[1 + \sin \left\{ \frac{\pi(x - a_3)}{u_{warp} + g_{fill}} \right\} \right] \frac{h_{fill}}{2} + \frac{h_{warp} - h_{fill}}{2} \quad a_1 \leq x \leq a_5 \\ \frac{h_{warp} + h_{fill}}{2} \quad a_5 \leq x \leq (a_f + g_f) \end{array} \right)
 \end{aligned}$$

Since the geometry of mutually orthogonal tows of the plain weave are constrained to conform as given by Eq. 2.41, it is expected that the local off-axis angle of undulation for the warp tow is identical to the derivative of the fill tow undulation. With this, the local off-axis angle of undulation for the warp tow is given by

$$\zeta_w(y) = \tan^{-1} \left\{ - \frac{h_{fill}}{2} \left(\frac{\pi}{u_{warp}} \right) \sin \left[\frac{\pi(y - b_1)}{u_{warp}} \right] \right\} \quad b_1 \leq y \leq b_2 \quad (2.42)$$

$$\zeta_w(y) = \tan^{-1} \left\{ -\frac{h_{fill}}{2} \left(\frac{\pi}{u_{warp}} \right) \sin \left[\frac{\pi \left(\frac{u_{warp}}{2} \right)}{u_{warp}} \right] \right\} \quad b_2 \leq y \leq b_3$$

The extension, extension-bending coupling and bending stiffnesses are evaluated from the mathematical moduli for each constituent of the infinitesimal (dx or dy) slices, identical to the procedure outlined for one-dimensional characterization. The SP approach then adopts a two-step assembly scheme to determine the elastic constants of the plain weave, fabric lamina. First, all infinitesimal through-thickness slices along the applied loading direction (on-axis) are assembled assuming the stresses are the same in each slice, thus an isostress condition. Second, all cross-sections on-axis are assembled assuming an isostrain (same strain) condition. Accordingly, the average in-plane compliances on-axis are found from [11]

$$\bar{a}_{ij}^f(y), \bar{b}_{ij}^f(y), \bar{d}_{ij}^f(y) = (a_{warp} + g_{warp})^{-1} \int_0^{a_{warp} + g_{warp}} a_{ij}(x, y), b_{ij}(x, y), d_{ij}(x, y) dx \quad (2.43)$$

The average, in-plane stiffness constants are found by integrating the inverted average compliances from Eq. 2.43 with an isostrain condition according to

$$\bar{A}_{ij}^{fw}, \bar{B}_{ij}^{fw}, \bar{D}_{ij}^{fw} = (a_{fill} + g_{fill})^{-1} \int_0^{a_{fill} + g_{fill}} \bar{A}_{ij}^f(y), \bar{B}_{ij}^f(y), \bar{D}_{ij}^f(y) dy \quad (2.44)$$

Alternatively, the PS approach merely reverses the order of integration in the SP scheme to determine the elastic constants.

2.2.2.3. Three-Dimensional Characterization

The main difference in the approach due to [14] is in defining the shape equations based on periodic functions that describe the tow centerline and tow perimeter explicitly, thus

avoiding constrained tow geometries and asymmetry in open-gap plain weave architectures. Here, the gap defined by observations of micrographs from S-RIM composite cross-sections is accounted for in terms of the period of undulation given by an idealization of the mutual tow:

$$\begin{aligned}\psi_{fill} &= 2(a_{warp} + g_{warp}) \\ \psi_{warp} &= 2(a_{fill} + g_{fill})\end{aligned}\quad (2.45)$$

Since the period ψ of each tow undulation is independently defined in terms of the off-axis tow width a and gap g , the local off-axis angle of undulation for the warp tow is not identical to the derivative of the fill tow, hence the orthogonal tow geometries are not constrained to conform. In arriving at the shape equations that describe the upper and lower warp or fill tows independently of each other, the tow centerlines are modeled according to the prescribed height of the off-axis tow. The cosine functions describing the centerlines ξ_{fill} and ξ_{warp} are given by

$$\begin{aligned}\xi_{fill} &= -\left(\frac{h_{warp}}{2}\right) \cos\left[\frac{2\pi(x - a_1)}{\psi_{fill}}\right] \\ \xi_{warp} &= \left(\frac{h_{fill}}{2}\right) \cos\left[\frac{2\pi(y - b_1)}{\psi_{warp}}\right]\end{aligned}\quad (2.46)$$

A comparable set of cosine functions, referenced from the centerlines, describe the orthogonal tow cross-sectional perimeters bounded by the regions 0 to $(a_{warp} + g_{warp})$ and 0 to $(a_{fill} + g_{fill})$. A process similar to that described for two-dimensional characterization is adopted for evaluating the elastic constants once the shape functions and local off-axis undulation angles have been established. As noted by Walsh, this method does not inadvertently force larger local angles of undulation for open architectures where increasingly smaller undulation angles are expected due to the presence of a gap between adjacent tows. In other words, an open weave architecture is not prescribed to follow the same geometry as a closed weave architecture. Because of this, a more accurate estimation

of the off-axis stiffness leads to greater accuracy in predicting the remaining in-plane elastic constants for the plain weave laminae.

2.3. Mechanics of a Composite Laminate

In this section, the methods used for evaluating the elastic properties of laminates from the properties and orientation of individual laminae are outlined. Reasonable evaluations of composite laminate elastic and thermoelastic properties are important in the design composite plates and components since it is essential that laminate response to external loads and conditions can be predicted [6]. The most established theory for analysis of laminates takes the form of the Kirchhoff hypothesis for thin plates or classical linear thin plate theory. Following the adaptation of this theory for analysis of composite laminates, commonly referred to as classical lamination theory (CLT), the subsequent four assumptions are made: [2,5]

- Upon application of a load to a plate with a through-thickness, lineal element normal to the plane of the plate, the element undergoes at most a translation and rotation with respect to the initial coordinate system, but remains normal to the plate.
- The plate resists in-plane and lateral loads only by in-plane action, bending and transverse shear stress, not by through-thickness, block-like tension or compression.
- There is a neutral plane, on which extensional strains may not be zero but bending strains are zero in all directions.
- The laminate midplane is analogous to the neutral plane of the plate.

2.3.1. Classical Lamination Theory

According to the foregoing assumptions for adaptation of the Kirchhoff hypothesis for thin plates, the strain components can be derived from the midplane strains and curvatures. The midplane strains are expressed as $\varepsilon'_{xx} = \frac{\partial u'}{\partial x}$, $\varepsilon'_{yy} = \frac{\partial v'}{\partial y}$, $\gamma'_{xy} = \frac{\partial u'}{\partial y} + \frac{\partial v'}{\partial x}$ where u' and v' are

expressed in terms of the x and y coordinate directions. The midplane curvatures are expressed as $\kappa_{xx} = -\frac{\partial^2 w}{\partial x^2}$, $\kappa_{yy} = -\frac{\partial^2 w}{\partial y^2}$, $\kappa_{xy} = -\frac{\partial^2 w}{\partial x \partial y}$ and are related to the z -coordinate direction. Here, κ_{xy} refers to the curvature of twist about the plane of the plate. The strain components are expressed in matrix form as [5]

$$\begin{Bmatrix} \varepsilon_x \\ \varepsilon_y \\ \gamma_{xy} \end{Bmatrix} = \begin{Bmatrix} \varepsilon_{x,0} \\ \varepsilon_{y,0} \\ \gamma_{xy,0} \end{Bmatrix} + z \begin{Bmatrix} -\frac{\partial^2 w}{\partial x^2} \\ -\frac{\partial^2 w}{\partial y^2} \\ -2\frac{\partial^2 w}{\partial x \partial y} \end{Bmatrix}, \quad \{\varepsilon\} = \{\varepsilon\}_0 + z\{\kappa\}_0 \quad (2.47)$$

The equation above implies that the strains vary linearly with z meaning that through-thickness sections remain plane and normal after deformation relative to the original coordinate system with its origin at the midplane. If the strains vary linearly, then lamina (ply) stresses must vary in proportion to lamina stiffnesses. In terms of the laminate, the ply stress components are given by

$$\begin{aligned} \{\sigma\}_k &= [Q_{xy}]_k \{\varepsilon\}_k \\ &= [Q_{xy}]_k \{\varepsilon\}_0 + z_k [Q_{xy}]_k \{\kappa\}_0 \end{aligned} \quad (2.48)$$

where the subscript k denotes the contribution from the k^{th} ply within the composite laminate. According to the plate shown in Figure 2.12, the forces and moments have a lineal distribution. In reference to the stress components for the k^{th} ply in Eq. 2.48, force and moment equilibrium are considered.

The forces and moments that are responsible for producing in-plane ply stresses are denoted by N_x , N_y , N_{xy} , M_x , M_y and M_{xy} where the N 's are the ply-level forces and the M 's are the ply-level moments. For force equilibrium, the integrated, through-thickness laminate stress must be equivalent to the corresponding force that produces it. The total force, determined from contributions of all plies within the laminate, can be expressed by the following [2]:

$$\begin{aligned}
\begin{Bmatrix} N_x \\ N_y \\ N_{xy} \end{Bmatrix} &= \sum_{k=1}^n \int_{h_{k-1}}^{h_k} (\sigma_{x,k}, \sigma_{y,k}, \tau_{xy,k}) dz \\
\{N\} &= \left[\sum_{k=1}^n [Q_{xy}]_k \int_{h_{k-1}}^{h_k} dz \right] \{\varepsilon\}_0 + \left[\sum_{k=1}^n [Q_{xy}]_k \int_{h_{k-1}}^{h_k} z dz \right] \{\kappa\}_0 \\
&= \left[\sum_{k=1}^n (h_k - h_{k-1}) [Q_{xy}]_k \right] \{\varepsilon\}_0 + \left[\sum_{k=1}^n \frac{1}{2} (h_k^2 - h_{k-1}^2) [Q_{xy}]_k \right] \{\kappa\}_0 \\
&= [A] \{\varepsilon\}_0 + [B] \{\kappa\}_0
\end{aligned} \tag{2.49}$$

Likewise, the total moment determined from contributions of all plies within the composite laminate can be expressed as [2]

$$\begin{aligned}
\begin{Bmatrix} M_x \\ M_y \\ M_{xy} \end{Bmatrix} &= \sum_{k=1}^n \int_{h_{k-1}}^{h_k} (\sigma_{x,k}, \sigma_{y,k}, \tau_{xy,k}) z dz \\
\{M\} &= \left[\sum_{k=1}^n [Q_{xy}]_k \int_{h_{k-1}}^{h_k} z dz \right] \{\varepsilon\}_0 + \left[\sum_{k=1}^n [Q_{xy}]_k \int_{h_{k-1}}^{h_k} z^2 dz \right] \{\kappa\}_0 \\
&= \left[\sum_{k=1}^n \frac{1}{2} (h_k^2 - h_{k-1}^2) [Q_{xy}]_k \right] \{\varepsilon\}_0 + \left[\sum_{k=1}^n \frac{1}{3} (h_k^3 - h_{k-1}^3) [Q_{xy}]_k \right] \{\kappa\}_0 \\
&= [B] \{\varepsilon\}_0 + [D] \{\kappa\}_0
\end{aligned} \tag{2.50}$$

The peculiar mechanical behavior of composite laminates can be discerned by examining Eqs. 2.49 and 2.50. Equation 2.49 implies that changes in curvature (bending strains), stretching and squeezing are brought about by the tensile forces and compressive forces given by $\{N\}$. Also, Eq. 2.50 implies that the moments given by $\{M\}$, in addition to changes in curvature, can produce squeezing and stretching strains.

2.3.2. Laminate Constitutive Relations

From the previous force and moment equilibrium analysis, the constitutive relations for laminated composites can be expressed in a condensed form as follows:

$$\begin{Bmatrix} N \\ M \end{Bmatrix} = \begin{bmatrix} A & B \\ B & D \end{bmatrix} \begin{Bmatrix} \varepsilon_0 \\ \kappa_0 \end{Bmatrix} \quad (2.51)$$

where the **A**, **B** and **D** matrices are the extension, extension-bending coupling and bending stiffnesses, respectively. Upon expansion of Eq. 2.51, the solution to the stiffnesses can be written in terms of summations of transformed and reduced stiffnesses (from Eq. 2.30) belonging to individual laminae having h_k^{th} thicknesses

$$\begin{aligned} [A] &= \sum_{k=1}^n (h_k - h_{k-1}) [Q_{xy}]_k \\ [B] &= \sum_{k=1}^n \frac{1}{2} (h_k^2 - h_{k-1}^2) [Q_{xy}]_k \\ [D] &= \sum_{k=1}^n \frac{1}{3} (h_k^3 - h_{k-1}^3) [Q_{xy}]_k \end{aligned} \quad (2.52)$$

2.3.2.1. Considerations for Thick Laminates

When the thickness dimension of the laminate compared to the in-plane dimensions is such that the laminate cannot any longer be considered sufficiently thin, other considerations must be given to through-thickness behavior which forces departure from classical plate theory. Transverse shear deformation present in anisotropic materials having high ratios of Young's moduli to interlaminar shear moduli can be approximately accounted for in thin plate theory by allowing the transverse shear strains to be non-zero. These strains can be related, by appropriate constitutive relations, to the thickness shear force resultants Q_x and Q_y (see Figure 2.12) defined in Eq. 2.54 [2]:

$$[Q_x, Q_y] = \int [\sigma_{xz}, \sigma_{yz}] dz \quad (2.53)$$

The existence of transverse shear deformation results in new expressions for the curvatures in terms of the rotations of the midplane normals ω_x and ω_y about the y and x axes. It is important to note that the new curvatures are not equivalent to the curvatures established in the classical theory of thin plates. Based on a generalized form of the stiffness matrix \bar{C}_{ij} and Eq. 2.51 written in terms of the new curvatures, the shear force resultants can be stated as [2]

$$\begin{aligned} \begin{Bmatrix} Q_y \\ Q_x \end{Bmatrix} &= a_k \begin{Bmatrix} A_{44} & A_{45} \\ A_{45} & A_{55} \end{Bmatrix} \begin{Bmatrix} \frac{\partial w^\circ}{\partial y} + \omega_y \\ \frac{\partial w^\circ}{\partial x} + \omega_x \end{Bmatrix} \\ A_{ij} &= \int \bar{C}_{ij} dz \quad (i, j = 1, 2, 4, 5, 6) \\ \{B_{ij}, D_{ij}\} &= \int \bar{C}_{ij}(z, z^2) dz \quad (i, j = 1, 2, 6) \end{aligned} \quad (2.54)$$

The constant a_k , as described in [2], is found by a match of the exact elasticity solution to an approximate solution which satisfies vanishing, thick-plate surface transverse shear stresses. Further, solution to the thick plate analysis is found by substitution of the above equations into the motion equation and determining the unknowns based on the total energy of the system. This procedure and its solutions are further explained in other works as cited specifically by Chou [2].

2.3.2.2. Considerations for Temperature

Another factor to consider when evaluating the behavior of polymer matrix composites exposed to extreme conditions is the effect of temperature. Deformations in composite laminates can occur from both externally applied mechanical loads and thermal loads arising from temperature changes. Since polymers undergo dimensional and elastic property changes

related to characteristic thermophysical properties, it can be expected that composites having constituent polymer matrices will behave similarly. Thermophysical properties such as thermal diffusivity serve as useful metrics for evaluating how quickly composite materials will respond to changes in thermal environments. Owing to the uniqueness of materials such as UD composites, the aligned fibers are insensitive to these changes, so susceptibility is governed mainly by the polymer matrix. That is, transverse and shear properties are most likely to be affected.

The process of manufacturing composites from advanced thermosetting matrices such as epoxies and polyimides involves polymerization of liquid monomers. The degree of polymerization and crosslinking influences the mechanical behavior and is dependent on parameters such as temperature and pressure. Polymer characteristics such as molecular weight (M_w) and glass transition temperature (T_g) are important considerations in end-use applications involving structural reinforcement and hostile environments. These characteristics tend to be greatly influenced by the degree of crosslinking that takes place during the thermosetting process as illustrated by time-temperature-transformation diagrams [15]. At a temperature above T_g and log time below vitrification, the majority of crosslinking occurs. At this temperature, the polymer matrix is still viscous enough to be considered "stress-free". In the later stages of cure and post-cure, microstresses within a composite arise due to resin shrinkage and differential thermal contraction between the fibers and matrix. The level of these stresses depends on the shrinkage characteristics of the matrix and differences between fiber and matrix coefficients of thermal expansion (α). When the composite is exposed to elevated temperature environments, changes in residual stress levels particularly influence shear and transverse failure processes and properties.

Changes in stresses due to thermal loads are considered self-equilibrating and dilatational when the entire composite laminate is considered [2]. In general, laminate properties along the fiber directions are a lot less sensitive to the effects of temperature in comparison to shear properties and properties transverse to the fiber directions. Classical lamination theory can be modified to account for the non-mechanical strains due to thermally

and hygroscopically induced deformations. For brevity, the macroscopically homogeneous, composite constitutive relation given by Eq. 2.20 is modified to account for temperature effects here as follows:

$$\begin{bmatrix} \sigma_1 \\ \sigma_2 \\ \sigma_3 \\ \tau_{23} \\ \tau_{31} \\ \tau_{12} \end{bmatrix} = \begin{bmatrix} C_{11} & C_{12} & C_{13} & C_{14} & C_{15} & C_{16} \\ & C_{22} & C_{23} & C_{24} & C_{25} & C_{26} \\ & & C_{33} & C_{34} & C_{35} & C_{36} \\ & & & C_{44} & C_{45} & C_{46} \\ & & & & C_{55} & C_{56} \\ & & & & & C_{66} \end{bmatrix} \left\{ \begin{bmatrix} \varepsilon_1 \\ \varepsilon_2 \\ \varepsilon_3 \\ \gamma_{23} \\ \gamma_{31} \\ \gamma_{12} \end{bmatrix} - \begin{bmatrix} \alpha_1 \\ \alpha_2 \\ \alpha_3 \\ \alpha_{23} \\ \alpha_{31} \\ \alpha_{12} \end{bmatrix} \Delta T \right\} \quad (2.55)$$

(SYM)

where the products $\alpha_{ij}\Delta T$ indicate the strains due to a thermal load, α_{ij} are the linear coefficients of thermal expansion (CTE) and ΔT is a uniform change in temperature from the reference temperature where residual microstresses are non-existent. For the purposes of lamina scale analysis, Eq. 2.55 is reduced to the following constitutive relation (Eq. 2.30):

$$\begin{bmatrix} \sigma_x \\ \sigma_y \\ \tau_{xy} \end{bmatrix} = \begin{bmatrix} \bar{Q}_{11} & \bar{Q}_{12} & \bar{Q}_{16} \\ \bar{Q}_{12} & \bar{Q}_{22} & \bar{Q}_{26} \\ \bar{Q}_{16} & \bar{Q}_{26} & \bar{Q}_{66} \end{bmatrix} \left\{ \begin{bmatrix} \varepsilon_x \\ \varepsilon_y \\ \gamma_{xy} \end{bmatrix} - \begin{bmatrix} \alpha_x \\ \alpha_y \\ \alpha_{xy} \end{bmatrix} \Delta T \right\} \quad (2.56)$$

If the principal material coordinate in the fiber direction differs from the reference coordinate axis by some angle λ , then the CTE's given in Eq. 2.56 are arrived at through tensor transformations defined by $\alpha_x = \alpha_{11}\cos^2\lambda + \alpha_{22}\sin^2\lambda$, $\alpha_y = \alpha_{22}\cos^2\lambda + \alpha_{11}\sin^2\lambda$ and $\alpha_{xy} = (\alpha_{11} - \alpha_{22})\sin\lambda\cos\lambda$. Analogies to Eqs. 2.49 and 2.50 can be made by considering the CTE's and temperature changes as a function of laminate thickness and time as detailed in [2].

2.4. Failure Behavior of Composite Laminates

In most structural component applications where advanced composites are desired for their strength-to-weight, dimensional stability and performance tailoring characteristics, it is not

uncommon for these materials to experience biaxial or even triaxial loads. From the design and application perspectives, it is necessary to accurately characterize the linear elastic and nonlinear behaviors under mixed-mode loadings capable of producing damage and catastrophic failure. Ultimately, the ability to predict bounds for mechanical properties, determine residual load carrying capacities and understand damage mechanisms in fiber reinforced composites subjected to weaker-mode (shear dominated), biaxial loading conditions are important for furthering development. In this section, the most commonly characterized modes of crack propagation and types of failure in PMC's are understood.

2.4.1. Modes of Crack Propagation

Mechanisms of crack formation and crack propagation in continuous fiber composites are governed by the microstructure and the state of stress in the immediate vicinity of the crack front. Continuous fiber composites exhibit micro-heterogeneity and contain intrinsic micro-imperfections such as voids, debonds at the fiber-matrix interface and matrix cracks. In contrast to homogeneous and isotropic materials which exhibit a self-similar crack growth behavior, crack orientation and growth in composites is dominated by the principal loading condition and local heterogeneity in front of the propagating crack. In isotropic materials, there are three fundamental modes or types of loadings that a crack can experience as illustrated in Figure 2.13. In reference to planes that define mating crack faces, mode I (opening or tensile) has a tendency to open a crack due to an applied, principal load normal to the crack plane. Mode II (shearing) has a tendency to slide one crack face relative to the other in a parallel direction. Mode III (anti-plane shearing or tearing) has a tendency to slide one crack face relative to the other in a normal, out-of-plane direction. It is not uncommon for a cracked body to experience combinations of two or three modes simultaneously (referred to as a mixed-mode problem). The plane of fracture in aligned composite materials is determined by both the mode of applied loading and the fiber directions. In two-dimensional composite architectures such as a woven fabric composite, multiple planes of

fracture can be envisaged leading to the concept of damage zones. What follows is a description of the various types of failure observed in composite laminates due to the presence of single and mixed-mode loadings under static (monotonic) and dynamic (low cycle fatigue) conditions.

2.4.2. Failure Classifications

In laminated composite materials, classification of failure becomes a question of scale and is typified by the mode or modes of loading. To help classify types and modes of failure, it is useful to define two scales, the lamina scale (mesoscale) and the laminate scale (macroscale). At the macroscale, there are three main classifications to characterize types of prevalent failure. Each classification is dependent upon the location of cracking within the laminate and the plane or planes on which cracking occurs. In continuous fiber composites, intralaminar failure refers to a dominant mode where the majority of cracks are localized to the matrix or fiber-matrix interface of individual laminae and growth is transverse (x_3) to the material principal direction for the aligned fibers. Interlaminar failure refers to a dominant mode where the majority of cracks lie in a plane between adjacent laminae and growth is in-plane along the interface (x_1 or x_2). This type of failure is often the result of some combination of mode I, mode II and mode III fracture processes. Translaminar failure refers to a dominant mode where intralaminar cracking progresses across more than one lamina and fiber separation often results. Ultimately, laminate failure as a whole is highly dependent on the properties of individual laminae and their summed interactions. The concepts of equal load sharing (load transfer), edge effects and ply constraints may play a significant role.

At the mesoscale, individual laminae can fail in different modes depending on the external loading conditions. It is essential to understand the failure mechanisms in order to predict lamina strength in terms of constituent fiber and matrix strengths [6]. It is often assumed that the distribution of strength within all continuous fibers in an aligned fiber lamina is the same. Although unrealistic, this assumption is adopted for meso- and

macroscale predictions in order to ease the computational efforts in predicting behavior. Realistically, the strength of continuous fibers are a variable distribution as are the sizes and numbers of inherent flaws or crack nucleation sites. By adopting the more realistic assumption, an adequate explanation can be given to account for the micromechanisms associated with crack nucleation and growth under monotonic and cyclic on-axis or off-axis loading conditions.

After Talreja [16], mechanical or (and) thermomechanical loads which induce a set of irreversible physical or chemical processes that lead to permanent changes within the microstructure of a material may be referred to as "damage". Damage in PMC's takes the form of a collective set of randomly oriented and shaped matrix cracks, fiber breaks and interface debonds. The singular formation of damage is more readily apparent in such processes as low-cycle fatigue compared to static processes which result in rapid accumulation to catastrophic failure. Damage in and of itself can be separated into two phases, a saturation state followed by secondary cracking and large delaminations. The state of saturation or characteristic damage state (CDS) defines multiple occurrences of matrix cracks that eventually saturate. In the second phase, secondary cracks and delaminations localize at some preferential location of primary cracking to form zones of damage development. Final failure leading to a marked decrease in load carrying capacity may stem from either fiber fracture or severe interactions of multiple cracks. Prediction of lamina response to the first damage phase requires either singular determination of stresses around individual crack tips or a homogenization approach that smears the effects of multiple cracks into a locally homogeneous field. Prediction of response to the second phase is much more difficult, since families of cracks may emerge having similar effects, but each family acting differently on the failure process.

Aligned fiber lamina damage mechanisms under on-axis tensile loading conditions can be divided into three distinct categories as shown in Figure 2.14 [16]. Preliminarily, transverse cracking within the matrix usually originates from two possible scenarios. The first scenario assumes that the matrix is free of voids, debonds or any other inherent flaws.

From a near-atomic viewpoint, separation within a polymer matrix material occurs when enough work is applied to separate polymer chains held by secondary van der Waals forces. This is referred to as chain scission [17]. Also a question of scale, the formation of separation resulting from chain scission depends on whether local heterogeneity exists between polymer molecules and chains. A crystalline polymer exhibits a certain degree of symmetry, therefore molecular stresses should be more evenly distributed compared to those in amorphous polymers. The second scenario assumes that the matrix is not devoid of flaws, i.e. voids, impurities, debonds. Formation of flaws may be linked to the first scenario if formed from localized phenomena such as shear yielding or crazing which leads to 100% straining and cavitation [17]. Usually, transverse matrix cracks nucleate from flaws introduced during the manufacturing process. These flaws serve as stress concentrations and magnify stress locally so global stress exceeds the material cohesive strength.

As shown in Figure 2.14(a), lamina strains may be of a sufficiently low magnitude to confine cracks to the matrix only (dispersed failure). Straining above the characteristic dispersive failure can cause crack growth to occur until the fiber-matrix interface is reached. When the crack-tip stress exceeds the fiber-break stress, separation occurs as shown in Figure 2.14(b). Once the crack grows to a length sufficient for crack-tip shear stresses to exceed interfacial strength, propagation continues along the interface (see Figure 2.14(c)) eventually leading to fiber pull-out. A detailed evolution of fiber break processes expanded from Figure 2.14(b) is illustrated in Figures 2.15(a-d). Subsequent to a fiber break, tensile stresses near the void edges are magnified causing transverse crack progression to an adjacent fiber. If adjacent fibers are stronger than the failed fiber, only successive matrix cracking may occur. This may lead to fiber bridging where a portion of the load previously supported by the matrix is redistributed to the intact fibers. It is likely that lamina damage development under on-axis tensile loading conditions exists as combinations of damage depicted in Figure 2.15(d).

When a continuous, aligned fiber lamina is subjected to off-axis tensile loading conditions, the predominant mode of failure is dependent upon the angle of the loading axis

relative to the fiber axis. Three simple fracture modes are plausible: longitudinal tensile fracture, transverse tensile fracture and intralaminar shear fracture [6]. At small angles between the loading and fiber axes, damage and failure mechanisms are dictated as previously described. As the angle increases, damage accumulation is by both mode I and mode II conditions, i.e. mixed-mode. In this regime, there are interactions between tensile stresses and shear stresses that lead to transverse tensile and intralaminar shear cracks within a given plane. As the loading axis becomes normal to the fiber axis, crack growth progresses by mode I (opening displacements) and transverse fiber debonding occurs.

For two-dimensional woven fabric composite laminae, evolution of damage leading to catastrophic failure is influenced by loading conditions, fiber count (tow densities), tow geometry, weave architecture (tow waviness) and lamina fiber volume fraction. For laminates, overall fiber volume fraction and layup sequence (constraining and asymmetry) must also be considered. Several accounts [2, 18-24] have been made for characterization of the failure processes in plain and 8HS woven composite materials, primarily for simple uniaxial tensile and compressive loading conditions. Ishikawa and Chou utilized their fiber crimp and bridging models to study the nonlinear "knee" stress-strain behavior in woven fabric composites. For plain weave composites, they found that the knee phenomenon was attributed to successive failures of transverse tows (warp tows) such that the stress-strain curve became linear again after the lowest strain in the failed region reached the transverse breaking strain ϵ_2 . For satin weave composites, it was determined that the knee stress was higher than in plain weave composites for a given knee strain due to the presence of bridging zones for load transfer.

Naik *et al.* [18] analyzed the uniaxial and off-axis tensile failure behavior in plain weave fabric composites with and without a central hole. It was found that failure in on-axis tensile specimens was essentially linear and catastrophic while severity of nonlinear behavior in off-axis specimens was a function of the angle between the loading and tow axes. The strength in the notched woven composites was higher than in the un-notched composites due to more significant tow reorientation. Subsequent to matrix failure, it was observed that the

woven tows in the off-axis composites gradually reoriented towards the plane of principal stress. This phenomenon of reorientation was manifested by periodic rising and falling in the stress-strain curve and higher loading at failure as well. The presence of a hole or notch permitted reorientation to occur faster, thus raising the failure strength of the notched woven fabric composites.

Farouk and Langrana [19] investigated the mode I fracture process (translaminar) in plain weave graphite-PMR15 using single-edge, notched beam (SENB) specimens and acoustic emission. They characterized the mode I fracture process according to the following stages:

- elastic deformation with few acoustic events and a linear relationship of load with displacement,
- pseudo-plastic deformation showing acoustic events due to matrix cracking and fiber pull-out with a monotonic, but nonlinear load increase, and
- failure showing a marked increase in acoustic events that characterize fiber breakage followed by rapid crack propagation.

It was concluded that the mode I fracture process in the woven graphite-PMR15 SENB specimens exemplified behavior typical of brittle matrix composites, viz. matrix cracking followed by fiber pull-out and fiber breakage.

A detailed experimental and computational investigation was carried out by Mirzadeh and Reifsnider [20] to evaluate tow strain distributions in 8HS Celion (C3000) woven graphite-PMR15 composites subjected to uniaxial compression (filling direction). Two-dimensional finite element simulations of adjacent tows were compared with strains obtained from an experimental photomechanics (Moire interferometry) study. In comparing the photomechanics results with the finite element analysis (FEA) results, they found that FEA revealed the presence of a bending moment at the center of undulation and near the adjacent warp tow, but photomechanics did not show a moment. Strains determined by the two methods, for the most part, showed good correlation and it was concluded that periodicity of the undulations reflected periodicity and complexity of the strains. Grape and Gupta [21]

also analyzed the failure behavior of 8HS carbon/polyimide-based and carbon-carbon composite laminates under uniaxial compression as well as a more convoluted loading condition, biaxial compression. Their findings indicated that the polyimide-based composites which were void-free compared to the carbon-based composites (a result of carbonization steps) suffered less out-of-plane deformation in compression. This suppressed failure by shear fault and kink band formation as observed for the carbon-based composites. Principal failure in the polyimide-based composites was interlaminar in nature and aligned with the primary axis of loading. The tolerance of far greater strain in compression as exhibited by the polyimide-based composites was attributed to better interlaminar fracture toughness. It was concluded that both families of 8HS woven composites fail when the critical compressive failure strain is reached in the direction of the tows.

Naik [22] developed a general purpose, micromechanics analysis technique implemented in a user-program TEXCAD to predict thermomechanical properties, damage initiation and progression in plain weave and two-dimensional triaxial braided composites. Parametric studies were also performed to investigate the effects of tow geometry, spacing, undulation angle, braid angle and overall fiber volume fraction on tensile, compressive and shear strength properties. For the plain weave architecture, it was found that an increased angle of undulation lowered tensile and compressive strength due to an increase in the rate of damage accumulation. Damage accumulation in the tows and nonlinear response of the matrix was also found to be detrimental to performance in shear.

Gyekenyesi *et al.* [23] conducted an experimental investigation to study the elevated temperature [255 °C (491 °F)], static tensile and fatigue behaviors of 8HS woven graphite-AMB21 composites with the emphasis on new testing techniques. For the static tests, it was noted that linear stress-strain behavior was observed up to 90% of the ultimate load, while nonlinearity near or at failure was attributed to tow failure and matrix cracking. They also concluded that elevated temperature had no effect on the tensile modulus and strength properties. In terms of isothermal fatigue, strain ratcheting behavior was observed at the beginning and ending of fatigue life and outside of this behavior, a general trend of increased

stiffness was observed for an increasing number of fatigue cycles. This was associated with the periodic straightening and kinking of on-axis tows resulting in lock up.

Alif *et al.* [24] investigated the mode I, mode II and mixed-mode interlaminar fracture processes in SHS woven carbon-epoxy composites using double cantilever beam (DCB), end-notched flexure (ENF) and mixed-mode bending (MMB) experimental tests. They identified transverse tow debonds as the mechanism primarily responsible for fracture and noted that the fracture toughness-crack length curve showed and increased resistance to propagation due to an unwieldy growth path around the interface of the transverse (fill) tow. "Stick-slip" behavior was observed in the nonlinear regime of the load-displacement curve as a result of the growth resistance and the energy consumed to debond fill tows was estimated at 50.0 J/m^2 (3.4 ft-lbs/ft^2).

2.4.3. Numerical Schemes

Several numerical models have also been proposed to predict the elastic properties and overall mechanical behavior of plain weave fabric composites. Zhang and Harding [25] developed a model based on the finite element method for micromechanics analyses and principle of strain energy equivalence. Although the plain weave fabric lamina was modeled considering undulation in one direction, it was suggested that a two-dimensional case should be considered. A more representative case of the actual plain weave unit cell was developed by Blackketter *et al.* [26] The tow cross-sectional aspect ratio which was obtained from photomicrographs, was included in the finite element model and the observed fiber volume fraction was obtained by iteration. Tows were assumed to conform perfectly to each other, resulting in a mathematically continuous model. An incremental iterative finite element algorithm was developed to analyze tensile loading responses, shear loading responses and estimate some of the effects of damage through stiffness reduction schemes.

Extensive work on 2-D and 3-D finite element analyses of plain weave fabric composites has been done by Whitcomb *et al.* [27-29] A new 2-D finite macro element was

developed and evaluated to account for element spatial variation of material properties. Detailed stress analyses of plain weave fabric composites were also performed using a global/local finite element method. It was found that surface stress distributions differed from internal stress distributions and failure behavior was influenced by a geometric feature defined as the tow waviness ratio. Effective elastic moduli were also found to be sensitive to the tow waviness ratio and increasing tow waviness in plain weave composites, subjected to uniaxial tensile loads, resulted in initial failure due to high transverse normal stress. In this case, the particular failure mode was 0° fiber tow separation. When the tow waviness decreased, the initial failure mode was 0° fiber tow fracture from high longitudinal stress. The deformation behavior also tended towards that of cross-ply laminates.

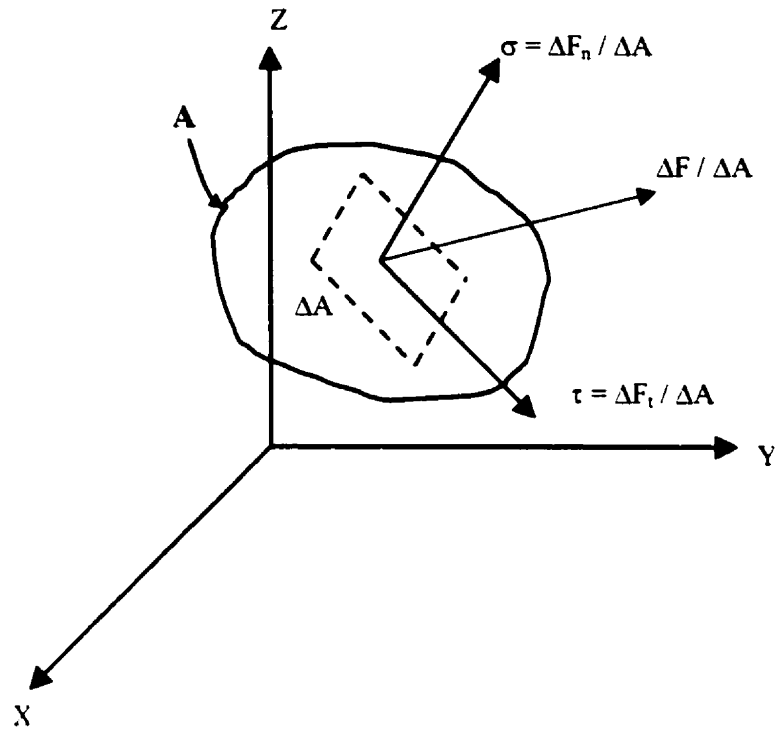


Figure 2.1. Surface components of normal and shear stresses.

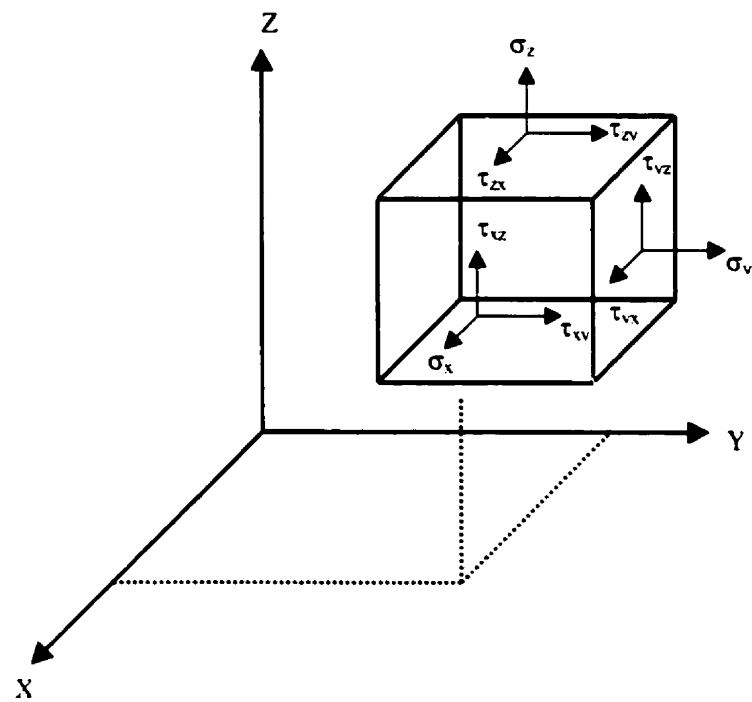


Figure 2.2. Stress components acting on an elemental cube.

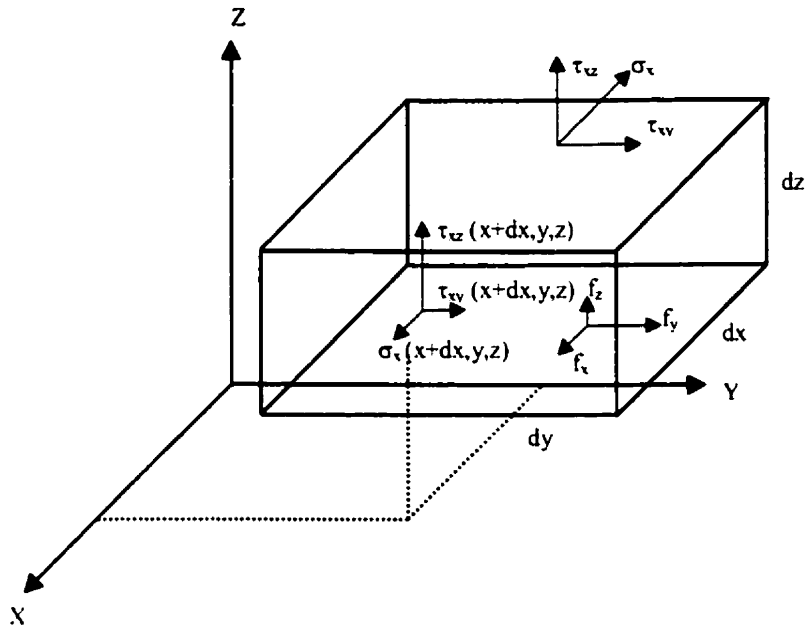


Figure 2.3. Complete force description on elemental cube. (After Easley 1989.)⁷

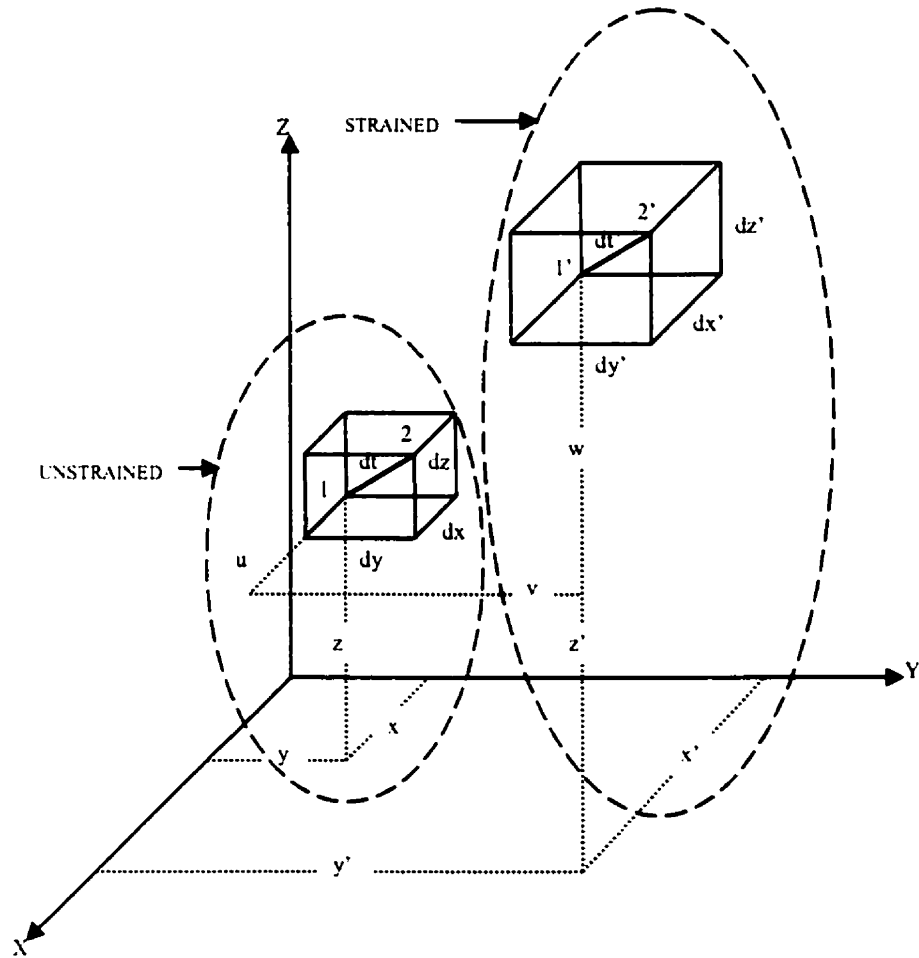


Figure 2.4. Deformation of elemental cube. (After Easley 1989.)⁷

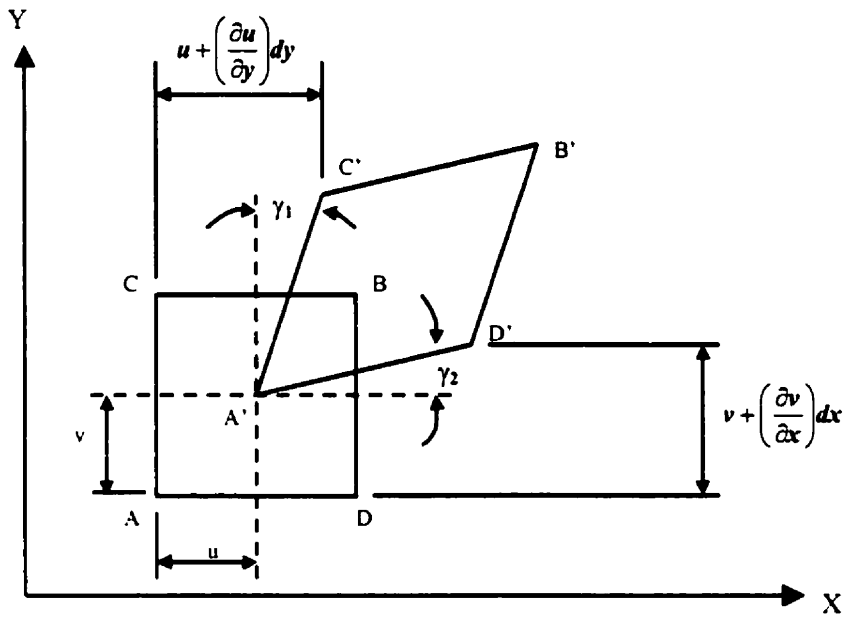


Figure 2.5. Element in-plane shear strains. (After Easley 1989.)⁷

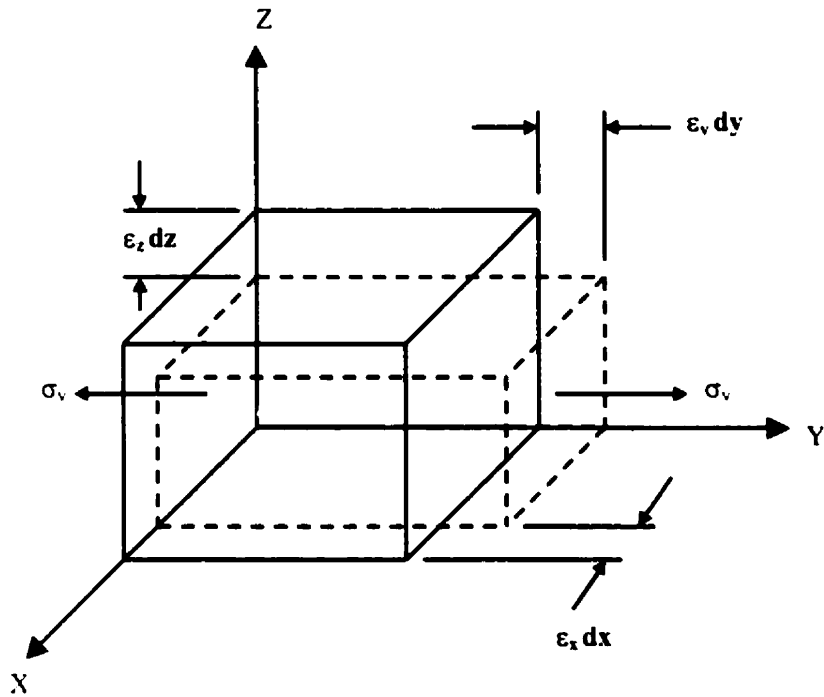


Figure 2.6. Local deformation of elemental cube. (After Easley 1989.)⁷

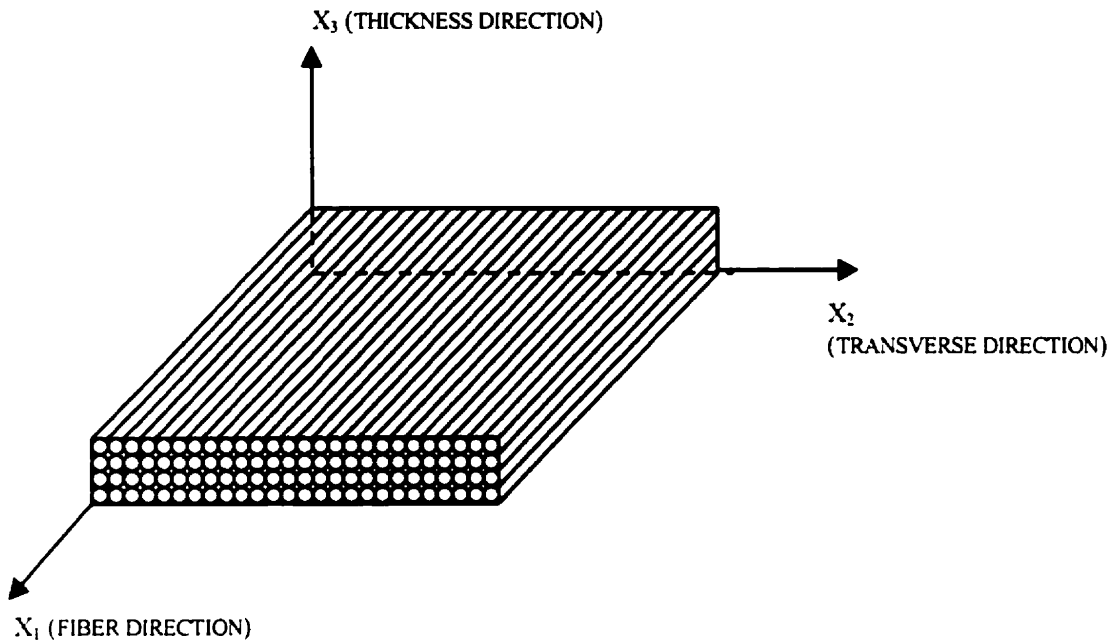


Figure 2.7. Continuous fiber unidirectional composite lamina. (After Chou 1992.)²

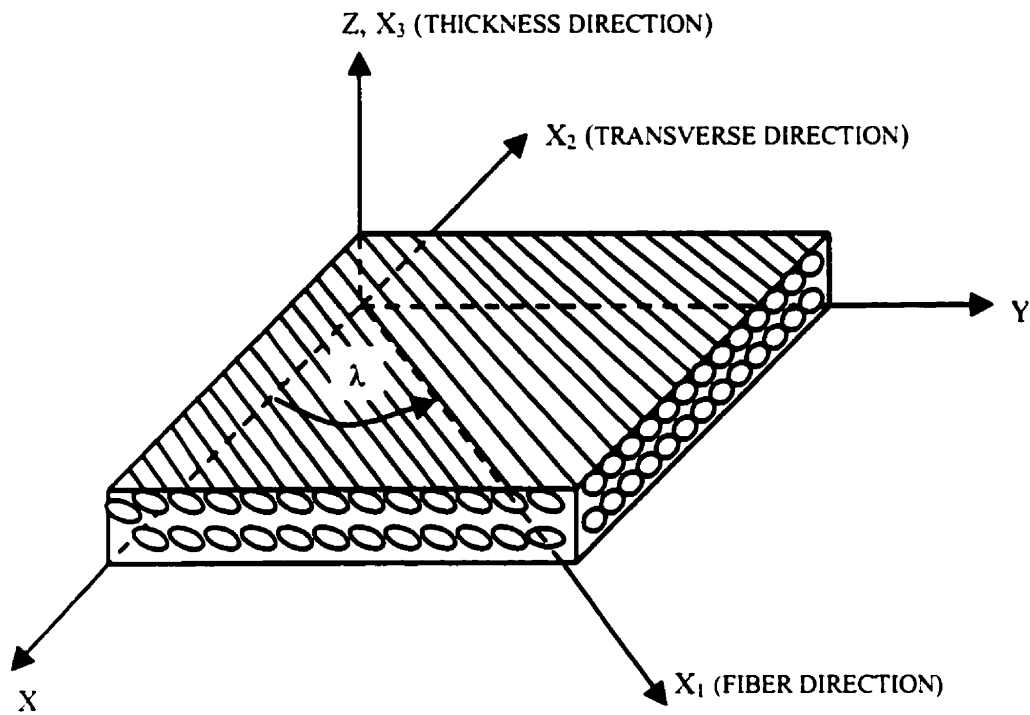


Figure 2.8. Continuous fiber unidirectional composite lamina with fibers oriented at an angle λ from the reference axis. (After Chou 1992.)²

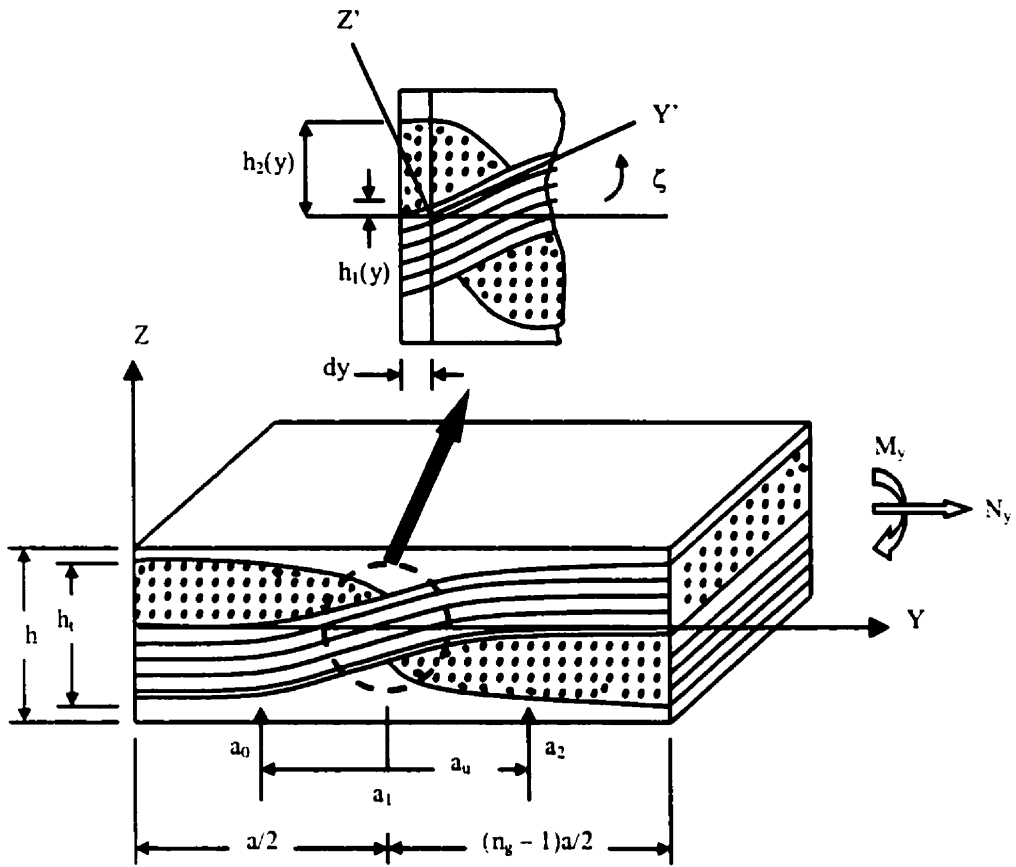


Figure 2.9. Derivation of one-dimensional crimp or fiber undulation model. (After Chou 1992.)²

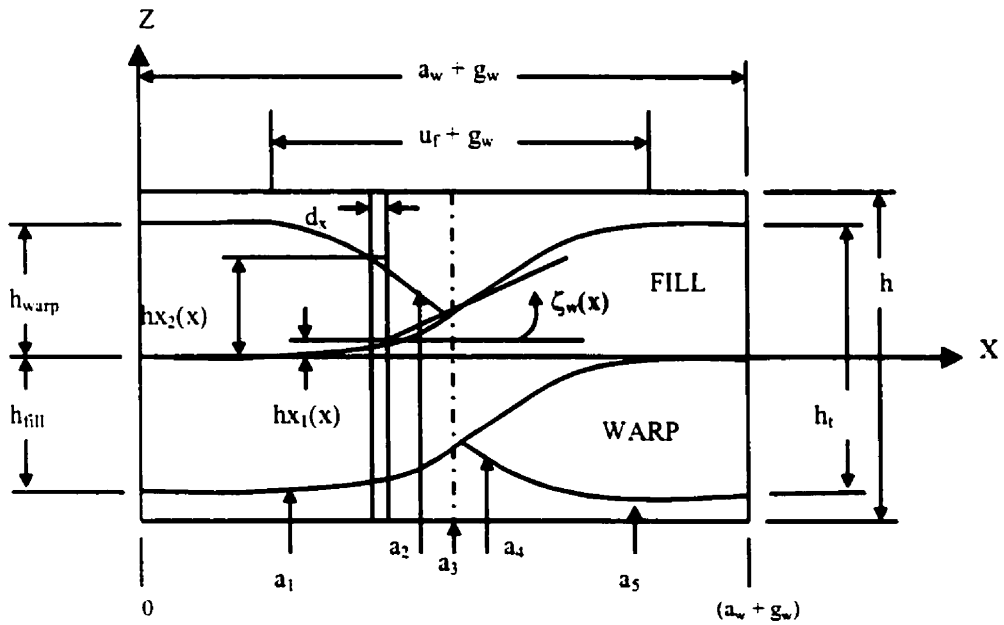


Figure 2.10. Definition of 2-D shape functions for X-Z slice. (After Naik *et al.* 1992.)¹¹

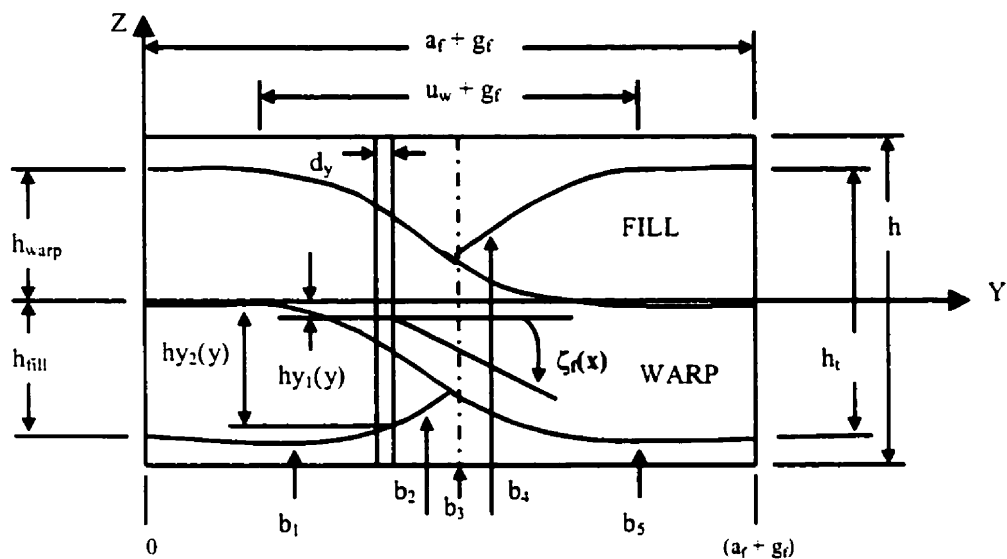


Figure 2.11. Definition of 2-D shape functions for Y-Z slice.
(After Naik *et al.* 1992.)¹¹

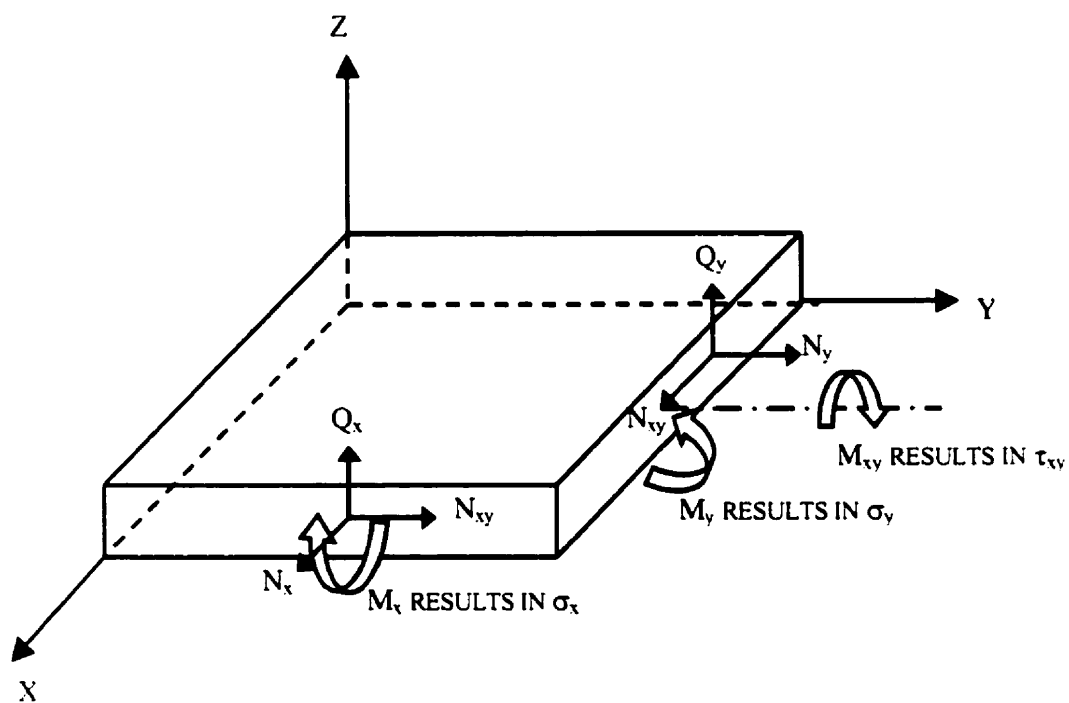


Figure 2.12. Laminate subjected to in-plane force and moment resultants.
(After Krishnamachari 1992.)⁵

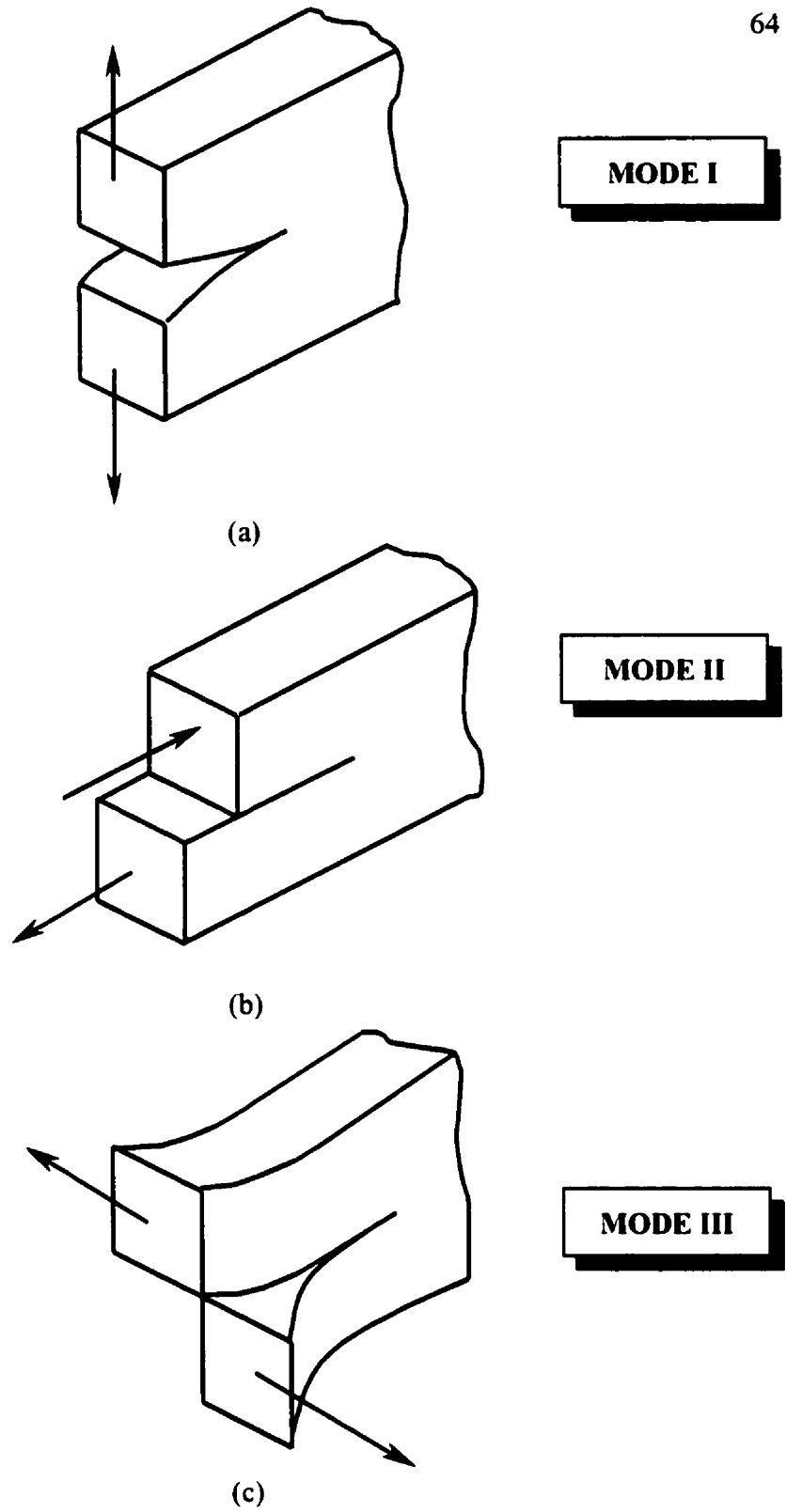


Figure 2.13. Crack propagation modes: (a) tensile, (b) shearing, and (c) tearing.

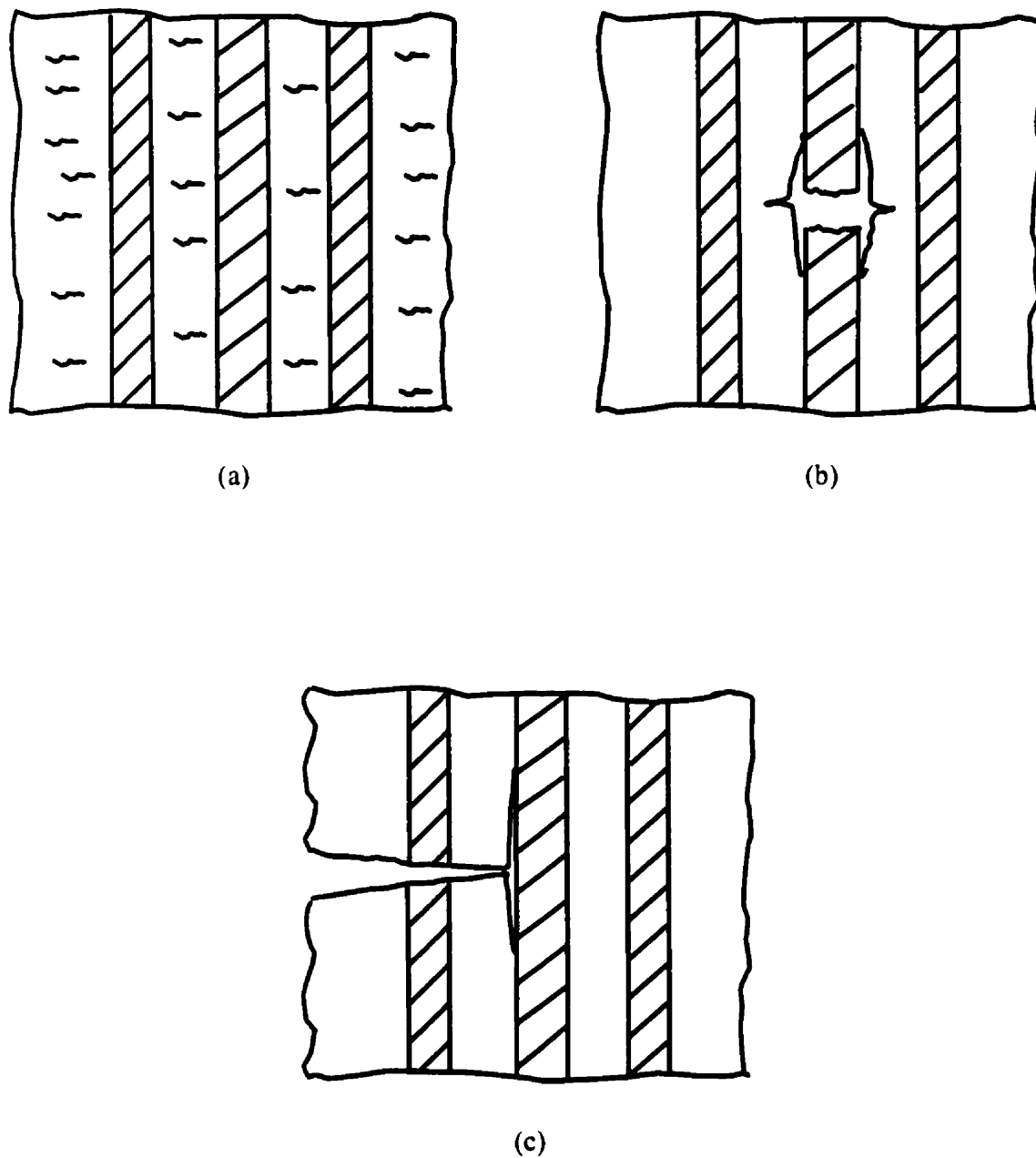


Figure 2.14. Damage mechanisms in aligned fiber composites subjected to on-axis loading conditions: (a) transverse matrix cracking, (b) fiber breakage, and (c) interfacial shear failure. (After Talreja 1987.)¹⁶

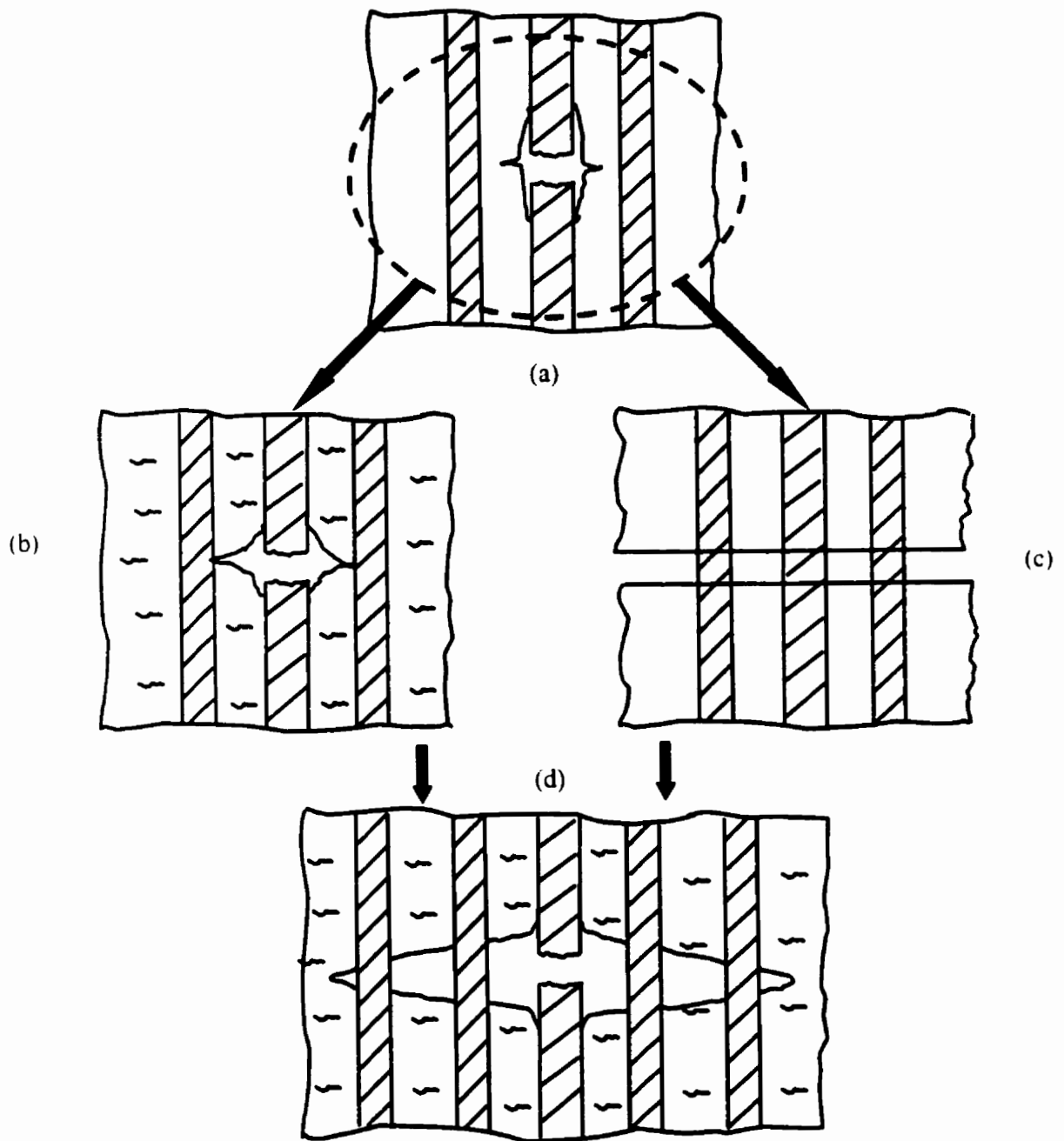


Figure 2.15. Evolution of fiber damage in aligned fiber composites: (a) fiber break with interfacial debonding, (b) fiber break expanding matrix crack, (c) matrix crack with fiber bridging, and (d) compilation of a, b, and c. (After Talreja 1987.)¹⁶

MICRO- AND MESOSCALE ELASTIC BEHAVIOR

3.1. Prediction of Elastic Constants

Based on the comprehensive review of theories presented in the literature and just summarized for the elastic analyses of woven fabric composites, it becomes readily apparent that more effort has been spent on understanding the behavior of composite architectures based on the plain weave vis-à-vis architectures based on the satin weave. With the exception of models proposed by Chou *et al.*, little work has explicitly been outlined for 8HS woven fabric composites. Rather, it has been stated in the various other works that the theories developed for plain weaves could be extended to satin weaves provided modifications were made to include the straight portion of the tows adjacent to the interlaced region. To the author's knowledge, no formal analytical analysis has been presented exclusively for an arbitrary and random 8HS weave pattern and verified both by experimental and finite element methods. In light of this, the intentions of the current research presented herein are twofold: 1) development of a simplified two-dimensional micro-to-mesomechanics model suitable for estimating the elastic constants in 8-harness satin woven fabric composites, based on random tow cross-sectional shapes and tow arrangements lacking contiguity; 2) assessment of the model validity by comparing the estimations to those obtained from 3-D finite element based, strain energy analyses and mechanical testing. The simplified mechanics model presented here assumes that the woven 8HS fabric lamina may be treated as a two-layered laminate if the micromechanics analysis is carried out using the woven fabric tow average V_f . The finite element model presented for verification purposes represents an idealized volume element (IVE) from a fabric unit cell where the IVE V_f is

reached through an iterative process.

In the course of analyzing the composite lamina behavior, it is commonplace to choose a modified square boundary of equivalent area to the hexagonal boundary for simplicity of calculation. By adopting the notation of Chou [2], the equivalent sub-cell major dimensions are given as:

hexagonal dimensions: $(3a) \times (3a)$ simplified dimensions: $(\sqrt{8}a) \times (\sqrt{8}a)$

where a is the width of the warp or weft tow. In addition to boundary generalizations, calculations are often reduced by assuming tow cross-sections of the following shapes: rectangular, perfectly elliptical and lenticular, i.e. shaped like a biconvex lens. The strain energy analyses presented in this research assume the model geometry within the larger repeat unit, but the simplified mechanics approach does not idealize the tow cross-sectional shape as lenticular and symmetric. The model geometry is employed using the simplified dimensions only to facilitate ease in application of suitable prescribed displacement boundary conditions.

3.1.1. Examination of Lamina Geometry

3.1.1.1. Woven Tow Cross-Section

Evaluation of woven composite lamina and laminate stiffness requires an accurate description of the woven tow geometry, including both the woven tow cross-section and tow centerline. Rather than assuming an idealized geometry described in terms of complimentary functions that force contiguity between the warp and fill tows, the particular shape of the 8HS woven tow cross-section observed in SEM micrographs (Figure 3.1) may be described by specific rational B-splines and polynomial functions where $z = f(x \text{ or } y)$, depending on the tow considered. If a given threshold level is applied to the micrograph of the lamina

cross-section, a binary image can be rendered that separates the tows from the matrix sufficiently to allow for boundary digitizing². As shown successively in Figures 3.2(a) and 3.2(b), this technique permits an accurate tow rendition and recording of coordinate pairs ($[x, z]$ or $[y, z]$) of points selected around the perimeter of the tow. The mathematical representation of the particular shape of a reproduced tow cross-section retains somewhat better accuracy if the perimeter is halved about an imaginary axis through the geometric center or centroid as given by

$$\bar{x} = \frac{\int x dA}{\int_A dA} \quad \bar{z} = \frac{\int z dA}{\int_A dA} \quad (3.1)$$

where \bar{x} represents the x-coordinate of the warp tow centroid and the numerators are formulations of the "first moment" of the area element dA about the z and the x axes, respectively. The relationship is similar for locating the fill tow centroid.

Once the coordinate pairs are established for the upper and lower half of the tow cross-section (with respect to the centroid), the points can be joined using a piecewise polynomial interpolation method such as spline interpolation. The simplest continuous polynomial approximation would be by piecewise linear functions. However, corners would exist that are not representative of the actual tow cross-sectional shape. More practical, natural-ended, cubic splines $p(x)$ are adopted to join the points along the perimeter and are given by cubic polynomials of the following form:

$$p_j(x) = a_{j0} + a_{j1}(x - x_j) + a_{j2}(x - x_j)^2 + a_{j3}(x - x_j)^3 \quad (3.2)$$

² Thresholding implements an algorithm to select all regions of pixels having similar contrasts and applies the same color level to these regions, either black or white in the case of a binary threshold. Levels of threshold are determined by locations on a histogram range from 0-255.

Cubic splines on an interval $\mathbf{a} \leq \mathbf{x} \leq \mathbf{b}$ corresponding to the space between two points or nodes have, by definition, continuous first and second derivative everywhere in that interval. The cubic polynomial coefficients are determined using Taylor's formula in the following manner to obtain

$$\begin{aligned}
 a_{j0} &= p(x_j) = f_j \\
 a_{j1} &= p'_j(x_j) = k_j \\
 a_{j2} &= \frac{1}{2} p''_j(x_j) = \frac{3}{h^2} (f_{j+1} - f_j) - \frac{1}{h} (k_{j+1} + 2k_j) \\
 a_{j3} &= \frac{1}{6} p'''_j(x_j) = \frac{2}{h^3} (f_j - f_{j+1}) + \frac{1}{h^2} (k_{j+1} + k_j)
 \end{aligned} \tag{3.3}$$

The strain energy minimization by using splines to fit curves through points is proportionate to the square of the second derivative of the spline. Curve fits chosen by natural splines result in a linear graph of the interval endpoints because natural splines are functions that result in the integral tending towards zero as follows:

$$\int_a^b p''(x)^2 dx \rightarrow 0 \tag{3.4}$$

3.1.1.2. Woven Tow Centerline

The geometric description of the warp or fill tow centerline is approached in the same manner as the description of the tow cross-section. An appropriate threshold level is applied to an SEM micrograph of the lamina or laminate edge (see Figure 3.3(a)), rendering a binary outline of the woven tow path as it passes over or under a mutually orthogonal tow (fill). To arrive at coordinate pairs for points representing the tow centerline, the path thickness represented by Figure 3.3(b) must be divided evenly along the path with respect to an imaginary axis through the geometric center of the orthogonal tow. By advancing in increments along the path and determining the new centroid at each increment, the difference between z-coordinates of the upper and lower digitized points (path perimeter) yields a new

point that coincides with the centroid. Necessarily, the tow centerline and geometric center of the tow should be identical. Piecewise polynomial approximations for natural-ended splines that satisfy Eq. 3.4, as previously described, are also used to connect the centerline points in a continual fashion.

3.1.1.3. Woven Tow Surfaces

Once the particular geometry of the woven tow cross-sections and centerlines is known, upper and lower tow surfaces may be accurately described by two-dimensional approximations in terms of $z = f(x, y)$. Additionally, rendition of tow volumes is possible by extruding either the warp or fill tow cross-section along the path defined by its mutually orthogonal centerline. At this stage, it is also possible to delineate the adjacency of neighboring tows in both closed and open weave architectures and characterize the requisite lamina and laminate volume fractions. Figure 3.4 displays such an arrangement of upper fill tow surfaces created from two-dimensional piecewise approximations with the local off-axis angle of undulation given as ζ and in-plane dimensions defined according to reduction of the 8HS woven unit cell. The simplest case of describing the lamina geometry assumes that the lower fill tow surfaces are reflections of the upper fill tow surfaces along the z-axis, and the resulting set of fill tow volumes is a reflection of the mutual warp tow volumes rotated 90° about an imaginary z-axis (through the interlace). Although it is certainly plausible that variations in tow cross-sections arise from the manufacturing process, inaccuracies in lamina stiffness calculations are trivial compared with those stemming from discrepancies in constituent properties and volume fractions.

3.1.2. Micromechanics Approach

A suitable laminate analysis for carbon fiber based, woven fabric composites distinctly emerges from three structural scales due to inherent differences between constituent material

properties and lamina architectures. At the micromechanics scale, it is beneficial to analyze the interactions between individual fibers, fiber bundles and the surrounding matrix. Composite Cylinder Assemblage (CCA) theory is usually employed and affords simple, closed-form solutions to predict effective elastic properties at this scale by treating the constituent phases as transversely isotropic. At the mesomechanics scale, the complex lamina geometry is either simplified to facilitate the ease of computations or the geometry is represented by periodic shapes and trigonometric functions. Judicious use of classical lamination theory is applicable at the mesoscale to homogenize through-thickness properties and arrive at Cartesian planar stiffness constants in terms of thickness cross-sections, i.e. mathematical moduli - Q_{ij} 's. Average laminae compliances or stiffnesses are found, depending on the order of integration, by assuming isostress and isostrain conditions during the assembly of infinitesimal thickness slices. Prediction of macroscale laminate elastic properties involves application of classical lamination theory an additional time to homogenize mesoscale lamina properties in terms of the total composite laminate thickness. The macroscale elastic behavior of the laminate is dependent on the ply arrangement and the values obtained at this scale can equally be compared to the apparent experimental elastic properties.

3.1.2.1. Evaluation of Woven Tow Properties

A woven fabric lamina may be considered as a "composite within a composite" with the bundled tows, surrounded by a matrix, forming the first composite material and the woven lamina, surrounded by a matrix, forming the second composite material. The least complicated approach to take in evaluating the elastic properties of the 8HS woven fabric tow is to treat individual tows as unidirectional composites composed of continuous arrays of fibers and surrounding matrix. In practice, the fiber-to-fiber "lattice" spacings and diameters are highly irregular, so it does not make much sense to evaluate fiber volume fraction based on the argument of maximum 2-D circle packing density (analogous to the

Kepler Conjecture) with regular tessellations of the form

$$V_f^{hexagonal} = \frac{\pi}{2\sqrt{3}} \left(\frac{r}{R} \right)^2$$

$$V_f^{square} = \frac{\pi}{4} \left(\frac{r}{R} \right)^2$$
(3.5)

where R is half the center-to-center spacing of fibers and r is half the fiber diameter. Instead, it is more practical to evaluate fiber volume fraction based on observations and measurements of scanning electron micrographs taken from actual laminate cross-sections. Analyses of SEM images taken from several cross-sections lead to measured binary ratios (normalization of the number of white pixels to the total image area in pixels) in the range of 0.71/1.00 to 0.74/1.00 as shown in Figure 3.5 for the composites considered here. The measured binary ratios or area fractions can be considered to be an equivalent representation of the measured tow volume fractions if the phases are assumed to be infinitely long and continuous and if variations in tow-to-tow cross-sections are considered negligible. Once the ranges of measured volume fractions of fibers and constituent material properties are determined, CCA theory can be applied successfully to calculate the equivalent elastic properties, in the principal material directions, of the unidirectional composite laminae (warp and fill tows). Subsequently, classical lamination theory may also be applied to evaluate lamina and laminate properties.

3.1.2.2. Composite Cylinder Assemblage

The CCA model due to Hashin and Rosen [30-32] gives closed-form, analytical expressions for the effective elastic constants of a UD lamina where the transversely isotropic (assumed) fiber and matrix are modeled as concentric cylinders. The longitudinal Young's modulus E_{11} of the UD composite lamina is given by

$$E_{11} = E_{11}^f V_f + E_{11}^m V_m + \frac{4V_f V_m (v_{12}^f - v_{12}^m)^2}{\frac{V_m}{k_f} + \frac{V_f}{k_m} + \frac{1}{G_{23}^m}} \quad (3.6)$$

where the sub- and superscripts **f** and **m** denote material properties of the constituent fiber and matrix phases, respectively. The subscript 1 refers to the longitudinal fiber direction and the subscripts 2 and 3 refer to the directions transverse to the fiber. The matrix volume fraction is $V_m = (1 - V_f)$. The transverse Young's modulus E_{22} is a bounded solution and the bounds are given by

$$E_{22}^{UB} = \frac{4k_t^* G_t^{*UB}}{k_t^* + G_t^{*UB} \left(1 + \frac{4k_t^* v_{12}^2}{E_{11}} \right)} \quad (3.7)$$

$$E_{22}^{LB} = \frac{4k_t^* G_t^{*LB}}{k_t^* + G_t^{*LB} \left(1 + \frac{4k_t^* v_{12}^2}{E_{11}} \right)}$$

where the superscripts UB and LB are the upper and lower bounds of the solution to the transverse Young's modulus. Both the upper bounded and lower bounded solutions for E_{22} are dependent on the transverse bulk modulus k_t^* of the UD lamina and a bounded solution for the transverse shear modulus G_t^* , as well:

$$k_t^* = \frac{k_m (1 - V_f) (k_f + G_{23}^m) + k_f V_f (k_m + G_{23}^m)}{(1 - V_f) (k_f + G_{23}^m) + V_f (k_m + G_{23}^m)} \quad (3.8)$$

Although a more accurate Generalized Self Consistent Scheme (GSCS) for G_t^* has been developed based on equivalent, homogeneous composite properties (single fiber surrounded by an equivalent composite instead of constituent matrix material), the upper and lower bound solutions for G_t^* are adopted for the sake of maintaining consistency. The bounded

solutions are carried through the complete analysis in its entirety for woven tow properties. The concise forms for the upper and lower bounds are given as

$$G_t^{*UB} = G_{23}^m \left(1 + \frac{V_f(1 + \beta_m)}{\left(\frac{\gamma + \beta_m}{\gamma - 1}\right) - V_f \left(1 + \frac{3V_m^2 \beta_m^2}{V_f^3 \alpha + 1}\right)} \right) \quad (3.9)$$

$$G_t^{*LB} = G_{23}^m + \frac{V_f}{\frac{1}{G_{23}^f - G_{23}^m} + \frac{V_m(k_m + 2G_{23}^m)}{2G_{23}^m(k_m + G_{23}^m)}}$$

The bounds given by Eq. 3.9 are acceptable solutions when the fiber transverse shear modulus is larger than the transverse shear modulus of the matrix and the fiber bulk modulus is larger than the matrix bulk modulus, that is when $G_{23}^f > G_{23}^m$ and $k_f > k_m$. If the opposite conditions exist, then the upper and lower bounds for the transverse shear modulus of the UD lamina are given by

$$G_t^{*LB} = G_{23}^m \left(1 + \frac{V_f(1 + \beta_m)}{\left(\frac{\gamma + \beta_m}{\gamma - 1}\right) - V_f \left(1 + \frac{3V_m^2 \beta_m^2}{V_f^3 \alpha + 1}\right)} \right) \quad (3.10)$$

$$G_t^{*UB} = G_{23}^m + \frac{V_f}{\frac{1}{G_{23}^f - G_{23}^m} + \frac{V_m(k_m + 2G_{23}^m)}{2G_{23}^m(k_m + G_{23}^m)}}$$

In either case, the following relationships, given in terms of the constituent fiber or matrix elastic properties, hold for the fiber and matrix transverse bulk moduli with the fiber transverse bulk modulus defined as

$$k_f = \left(\frac{4}{E_{22}^f} - \frac{4\nu_{12}^{f2}}{E_{11}^f} - \frac{1}{G_{23}^f} \right)^{-1} \quad (3.11)$$

and the matrix transverse bulk modulus defined as

$$k_m = \left(\frac{4}{E_{22}^m} - \frac{4\nu_{12}^{m2}}{E_{11}^m} - \frac{1}{G_{23}^m} \right)^{-1} \quad (3.12)$$

while relationships between the fiber and matrix transverse bulk and shear moduli are given as the following:

$$\beta_f = \frac{k_f}{k_f + 2G_{23}^f}, \quad \beta_m = \frac{k_m}{k_m + 2G_{23}^m} \quad (3.13)$$

$$\alpha = \frac{\beta_m - \gamma\beta_f}{1 + \gamma\beta_f}, \quad \gamma = \frac{G_{23}^f}{G_{23}^m} \quad (3.14)$$

The remaining in-plane elastic properties, the longitudinal shear modulus G_{12} and longitudinal Poisson's ratio ν_{12} of the UD composite lamina, can be expressed accordingly:

$$G_{12} = G_{12}^m \left(\frac{V_m G_{12}^m + G_{12}^f (1 + V_f)}{G_{12}^m (1 + V_f) + V_m (G_{12}^f)} \right) \quad (3.15)$$

$$\nu_{12} = \nu_{12}^f V_f + \nu_{12}^m V_m + \frac{V_f V_m (\nu_{12}^f - \nu_{12}^m) \left(\frac{1}{k_m} - \frac{1}{k_f} \right)}{\frac{V_m}{k_f} + \frac{V_f}{k_m} + \frac{1}{G_{23}^m}} \quad (3.16)$$

If the transverse Poisson's ratio ν_{23} of the UD composite is desired, then a bounded solution can be given in terms of the upper or lower derivations of the transverse shear modulus according to the expression

$$\nu_{23} = \frac{E_{22}}{2G_1^*} - 1 \quad (3.17)$$

3.1.2.3. Strain Energy Equivalence

Accurate application of numerical methods to validate the elastic properties determined from the CCA model involves the analysis of a representative volume element (RVE). The RVE is modeled based on a periodic fiber packing sequence and although the ideal square or hexagonal packing model given by Eq. 3.5 is chosen for simplicity, the numerical fiber volume fraction is made equivalent, by iteration, to the actual fiber volume fraction determined from SEM cross-sections. From a numerical standpoint, it is important that the RVE accurately represents periodicity and the accompanying periodic boundary conditions. Without such accuracy, the RVE elastic constants predicted will not be representative of the composite. If the proper choices are made for a periodic geometry and boundary conditions, the stress and strain states should also be periodic even though they are not necessarily uniform as in homogenous materials. By assuming strain energy equivalence, it can be shown (see Sun and Vaidya, cf. [33]) that subjecting the periodic RVE to appropriate surface tractions or displacements that would produce uniform stresses in a homogenous medium is valid here. Macro-stress and strain, based on classical lamination theory pertaining to average moduli of homogenous media, are derived via an average of the stress and strain tensor over the RVE volume as follows where the averages are given as

$$\begin{aligned} \sigma_{ij}^{ave} &= \frac{1}{V} \int_V \sigma_{ij}(x, y, z) dV \\ \varepsilon_{ij}^{ave} &= \frac{1}{V} \int_V \varepsilon_{ij}(x, y, z) dV \end{aligned} \quad (3.18)$$

According to strain energy equivalence criteria, the strain energy \mathbf{U}' is stored in the heterogeneous RVE with a potential equivalent to external work \mathbf{W}' done by a force acting

on the volume. It can be assumed that the difference in this strain energy and that of the homogeneous volume (U) yields the following relationship:

$$U' - U = \frac{1}{2} \int_V \frac{\partial}{\partial x_j} [\sigma_{ij} (u_i - u_i^{ave})] dV \quad (3.19)$$

where u_i represent boundary displacements. If the volume is discretized in such a manner that produces a large number of elements and nodes, the use of Eq. 3.19 becomes somewhat unwieldy to manage. In the place of the volume integral, the divergence theorem of Gauss can be applied to convert the volume integral into a surface integral by

in general :

$$\begin{aligned} \iiint_T \text{div } \mathbf{F} \, dV &= \iint_S \mathbf{F} \cdot \mathbf{n} \, dA \\ \iiint_T \left(\frac{\partial F_1}{\partial x} + \frac{\partial F_2}{\partial y} + \frac{\partial F_3}{\partial z} \right) dx \, dy \, dz &= \iint_S (F_1 \cos \alpha + F_2 \cos \beta + F_3 \cos \gamma) \, dA \end{aligned} \quad (3.20)$$

where T is a closed and bounded region in space whose boundary is a piecewise smooth surface S . If $\mathbf{F}(x, y, z)$ is a vector function that is continuous and has continuous first partials in the T domain, then \mathbf{n} is the outwardly normal unit vector of S . Therefore, Eq. 3.19 becomes

$$U' - U = \frac{1}{2} \int_S \sigma_{ij} (u_i - u_i^{ave}) n_j \, dS \quad (3.21)$$

Similarly, Gaussian divergence theorem may also be applied to the volume integral given in Eq. 3.18 to yield a relationship for tensorial strain in terms of a surface integral as given by the following equation:

$$\varepsilon_{ij} = \frac{1}{2V} \int_S (u_i n_j + u_j n_i) \, dS \quad (3.22)$$

where V is the RVE volume, S is the boundary RVE surface, u_i is the i^{th} component of displacement and n_j is the j^{th} component of the outwardly normal unit vector. From Eq. 3.22, displacements can be prescribed on the boundary surface and tractions can be determined from resulting surface reactions to prescribed displacements. In all cases, it is assumed that the Cartesian and principal material coordinate systems are coincident.

Uniaxial Tensile Case (E_{xx}) - For the case of axial loading, a quarter-symmetry RVE can be modeled to determine the longitudinal tensile elastic modulus. The following boundary conditions are imposed (with node matching) on the finite element model shown in Figure 3.6:

$$\delta_x(0, y, z) = 0$$

$$\delta_x(0.5a, y, z) = \text{constant}$$

Clearly, Eq. 3.22 reduces to the more apparent definition of strain as given by

$$\varepsilon_{xx}^{ave} = \frac{1}{V} \int_S u_x n_x dS = \frac{\delta_x}{0.5a} \quad (3.23)$$

The average stress in the RVE can be determined by equating the external work to the strain energy stored within the RVE and solving [33]:

$$\frac{1}{2} P_x \delta_x = \frac{1}{2} \sigma_{xx}^{ave} \varepsilon_{xx}^{ave} V \quad (3.24)$$

therefore

$$\sigma_{xx}^{ave} = \frac{P_x}{(0.5b)(0.5c)} \quad (3.25)$$

Finally, the longitudinal tensile modulus and Poisson's ratio are obtained as follows, assuming a prescribed displacement (δ_x) of unity. This is based on the premise that $\mathbf{a} = \mathbf{b}$ and P_x is the resultant surface reaction derived from the prescribed boundary conditions

$$E_{xx} = \frac{P_x}{(0.5c)} \quad \text{and} \quad v_{xy} = -\left(\frac{\delta_y}{\delta_x}\right) \quad (3.26)$$

Transverse Tensile Cases ($E_{yy} = E_{zz}$) - Similarly, the transverse tensile elastic moduli E_{yy} and E_{zz} can be calculated, based on the above derivations, and by assuming that the following boundary conditions again apply to the finite element model shown in Figure 3.6:

$$\begin{aligned} \delta_y(x, 0, z) &= 0 \\ \delta_y(x, 0.5b, z) &= \text{constant} \\ E_{yy} &= \frac{P_y}{(0.5a)} \quad \text{and} \quad v_{yz} = -\left(\frac{\delta_z}{\delta_y}\right) \end{aligned} \quad (3.27)$$

$$\begin{aligned} \delta_z(x, y, 0) &= 0 \\ \delta_z(x, y, 0.5c) &= \text{constant} \\ E_{zz} &= \frac{P_z}{(0.5b)} \quad \text{and} \quad v_{zx} = -\left(\frac{\delta_x}{\delta_z}\right) \end{aligned} \quad (3.28)$$

Longitudinal Shear Case (G_{xy}) - The case of longitudinal shear loading requires more specific boundary conditions imposed on a full representation of the square array, i.e. no planes of symmetry are assumed. Since this type of loading is independent of the long axis (axis parallel to the fiber), boundary conditions must be such that both the Y-Z planes at $x = 0$ and $x = 1.0a$ displace identically to each other. Ideally, this also implies that nodes on opposing faces share the same planar locations. To satisfy this requirement, the following boundary conditions are applied to the finite element model in Figure 3.7:

$$\begin{aligned} \delta_x(x, 0, z) &= \delta_y(x, 0, z) = \delta_z(x, 0, z) = 0 \\ \delta_x(x, 1.0b, z) &= \text{constant} \\ \delta_y(x, 1.0b, z) &= 0 \end{aligned}$$

To assure that both Y-Z planar surfaces at $x = 0$ and $x = 1.0a$ displace by an identical amount

at every point on each surface, the additional prescribed boundary conditions are

$$\delta_x(0, y, z) = \delta_x(1.0a, y, z)$$

$$\delta_y(0, y, z) = \delta_y(1.0a, y, z)$$

$$\delta_z(0, y, z) = \delta_z(1.0a, y, z)$$

As in the previous cases of deriving the axial and transverse tensile elastic constants, a similar solution for the longitudinal shear modulus is adopted from Sun and Vaidya and shown as well. Again, application of Gaussian divergence theorem to the RVE yields the following relationship for average equivalent shear strain γ_{xy} :

$$\gamma_{xy}^{ave} = \frac{2}{V} \int_V \varepsilon_{xy} dV = \frac{1}{V} \int_S (u_x n_y + u_y n_x) dS \quad (3.29)$$

Accordingly, by equating the external work to the strain energy stored within the RVE [33] and reducing Eq. 3.29 according to prescribed boundary conditions, a relationship is obtained for the longitudinal shear modulus in terms of the equivalent force. Based on the premise that $\mathbf{a} = \mathbf{b}$ and \mathbf{P}_{xy} is the resultant surface reaction derived from the prescribed boundary conditions

$$\begin{aligned} \gamma_{xy}^{ave} &= \frac{\delta_{xy}}{(0.5b)(0.5b)} \quad \text{and} \quad \frac{1}{2} P_{xy} \delta_{xy} = \frac{1}{2} \sigma_{xy}^{ave} \gamma_{xy}^{ave} V \\ \sigma_{xy} &= \frac{P_{xy}}{2(0.5a)(0.5c)} \end{aligned} \quad (3.30)$$

therefore, based on the premise that $\mathbf{a} = \mathbf{b}$ and \mathbf{P}_{xy} is the resultant surface reaction derived from the prescribed boundary conditions, the longitudinal shear modulus is given by

$$G_{xy} = \frac{P_{xy}}{(0.5c)} \quad (3.31)$$

This analysis can also be employed for the case of transverse shear (G_{yz}) similarly. An

alternate set of boundary conditions are imposed to deform the RVE (Figure 3.7) in a manner such that it forms an unrestricted parallelepiped about the fiber axis

$$\begin{aligned} \delta_x(x, y, 0) &= \delta_x(x, y, 1.0c) = \delta_x(x, 0, z) = \delta_x(x, 1.0b, z) = 0 \\ - [\delta_y(x, y, 0)] &= \delta_y(x, y, 1.0c) = \text{constant} \\ - [\delta_z(x, 0, z)] &= \delta_z(x, 1.0b, z) = \text{constant} \end{aligned}$$

3.1.3. Mesomechanics Approach

At the mesoscale, classical lamination theory is considered applicable for evaluating the equivalent elastic properties of the woven fabric lamina. Several mathematical models [8-14, 34-35] have previously been proposed to account for the woven fabric geometry in evaluating elastic properties, particularly for the plain open and closed weave architectures. For satin weaves specifically, Ishikawa and Chou proposed the bridging model which was necessarily a combination of their series and parallel models. The 2-D bridging model treats the non-interlacing tows surrounding the interlaced region as an assemblage of cross-ply laminates that act as load bridges. Tow undulation is considered only in the loading direction while the cross-sectional geometry and orthogonal undulation are not considered. In this research, a simplified 2-D model is proposed for the 8HS woven architecture that accounts for actual undulation of mutually orthogonal tows and actual tow cross-sections, including random variation.

3.1.3.1. Evaluation of Woven Lamina Properties

The basic premise of the simplified 2-D model considers the 8HS woven fabric lamina as a laminate having two layers and a V_f equivalent to that of the woven fabric tows. From the digitized reproduction of the tow centerlines and tow cross-sections by cubic spline interpolation, m^{th} -order polynomials are fitted according to the method of least-squares approximation. As an example, consider a straight line $z = a + bx$ or $z = c + dy$ (consistent

with the previously established coordinate system) fitted through the given points $(x_1, z_1), \dots, (x_n, z_n)$ or $(y_1, z_1), \dots, (y_n, z_n)$ so that the sum of the squares of the distances of those points from the straight line is a minimum, where the distance is measured from the z -direction. The point ordinate $a + bx_j$ or $c + dy_j$ corresponds to an abscissa x_j or y_j . Therefore, the distance from (x_j, z_j) and (y_j, z_j) is $|z_j - a - bx_j|$ and $|z_j - c - dy_j|$, respectively. In general, a polynomial of degree m is given by

$$p(x) = b_0 + b_1x + \dots + b_mx^m \quad ; \quad m \leq n-1 \quad (3.32)$$

and the sum of the squares of the distances q takes the form given by

$$q = \sum_{j=1}^n (z_j - p(x_j))^2 \quad (3.33)$$

$$\frac{\partial q}{\partial b_0} = 0, \quad \dots, \quad \frac{\partial q}{\partial b_m} = 0$$

where q depends on $(m + 1)$ parameters b_0, \dots, b_m and there are $(m + 1)$ conditions or minimums which give a system of $(m + 1)$ normal equations. Upon extending the example for the case of a second-order least-squares polynomial approximation with a quadratic polynomial of the following form:

$$p(x) = b_0 + b_1x + b_2x^2 \quad (3.34)$$

where the normal equations (summation from 1 to n implied) are given by

$$\begin{aligned} b_0n + b_1 \sum x_j + b_2 \sum x_j^2 &= \sum z_j \\ b_0 \sum x_j + b_1 \sum x_j^2 + b_2 \sum x_j^3 &= \sum x_j z_j \\ b_0 \sum x_j^2 + b_1 \sum x_j^3 + b_2 \sum x_j^4 &= \sum x_j^2 z_j \end{aligned} \quad (3.35)$$

This system is symmetric and solution to the unknowns b_0, b_1 and b_2 is accomplished by one of the more commonly used numerical methods such as Gauss elimination, Gauss-Seidel

iteration or LU-factorization. A modified method of Gauss elimination with LU-factorization is employed to solve the system of normal equations for the unknowns in m^{th} -order polynomial fits of the upper and lower tow cross-sectional perimeters and tow centerline as illustrated by Figures 3.8 and 3.9. The success criterion used for determining the appropriate polynomial order of fit is a coefficient of determination $R^2 \geq 0.95$.

3.1.3.2. Compliance Transformation

The equivalent elastic properties of the warp and fill laminae can be determined by evaluating the average reduced compliance for the local off-axis angle of undulation. The local off-axis angle of undulation for the warp and fill tows is given by

$$\begin{aligned}\zeta_w(x) &= \tan^{-1} \frac{\partial}{\partial x} [z = p(x)] \\ \zeta_f(y) &= \tan^{-1} \frac{\partial}{\partial y} [z = p(y)]\end{aligned}\tag{3.36}$$

where ζ is the local off-axis angle as represented in Figure 3.4 and z is given in terms of x or y and is equivalent to the least-squares polynomial approximation for either the warp or fill tow centerlines (defined by Eq. 3.32 for a m^{th} -order polynomial). The particular off-axis angle reduces the effective elastic constants with respect to the Cartesian (global) coordinate directions. Solution to derivatives in (3.36) are the slopes of secant lines that approximate lines tangent to any segment of the least-squares polynomials. Unlike numerical integration which is a smoothing process, differentiation is much less accurate since the derivative is the limit of the difference quotient. The forward difference quotient tends to underestimate the derivative and the backward difference quotient tends to overestimate the derivative. The symmetric difference quotient provides the best approximation to the slope of the tangent

$$\frac{dz}{dx} = \lim_{\Delta x \rightarrow 0} \left[\frac{p(x + \Delta x) - p(x - \Delta x)}{2\Delta x} \right]\tag{3.37}$$

From Hooke's law, the constitutive relations of a UD lamina which relate strain to stress in terms of the compliance matrix S_{ij} can be expressed in the generalized form with contracted notation

$$\varepsilon_i = \sum_{j=1}^6 S_{ij} \sigma_j \quad (3.38)$$

where $i, j = 1, \dots, 6$ in reference to the material principal coordinate system $x_1 - x_2 - x_3$. For a UD lamina with fibers oriented at an angle ζ with respect to the Cartesian reference axis (see Figure 3.10), the generalized form of the constitutive relations in terms of the transformed reduced compliance matrix \bar{S}_{ij} can be expressed as

$$\begin{bmatrix} \varepsilon_x \\ \varepsilon_y \\ \gamma_{xy} \end{bmatrix} = \begin{bmatrix} \bar{S}_{11} & \bar{S}_{12} & \bar{S}_{16} \\ \bar{S}_{12} & \bar{S}_{22} & \bar{S}_{26} \\ \bar{S}_{16} & \bar{S}_{26} & \bar{S}_{66} \end{bmatrix} \begin{bmatrix} \sigma_x \\ \sigma_y \\ \tau_{xy} \end{bmatrix} \quad (3.39)$$

In this case, the transformed reduced compliance constants \bar{S}_{ij} where $i, j = 1, \dots, 6$ can be written for the transversely isotropic warp or fill tows as follows (after [36]):

$$\begin{aligned} S_{11}(\zeta) &= \frac{\cos^4(\zeta)}{E_{11}} + \left(\frac{1}{G_{12}} - \frac{2\nu_{12}}{E_{11}} \right) \cos^2(\zeta) \sin^2(\zeta) + \frac{\sin^4(\zeta)}{E_{22}} \\ S_{22}(\zeta) &= \frac{1}{E_{22}} \\ S_{66}(\zeta) &= \frac{\cos^2(\zeta)}{G_{12}} + \frac{\sin^2(\zeta)}{G_{23}} \\ S_{12}(\zeta) &= \frac{\nu_{21} \cos^2(\zeta)}{E_{22}} + \frac{\nu_{23} \sin^2(\zeta)}{E_{22}} \\ \nu_{21} &= \frac{E_{22}}{E_{11}} \nu_{12} \end{aligned} \quad (3.40a-e)$$

The effective elastic properties for the equivalent warp and fill laminae are determined by inverting the averaged, local transformed compliance. The average compliance is the mean

integral value of the local compliance given as

$$\bar{S}_{ij}^{ave} = \frac{1}{\phi} \int_0^{\phi} \bar{S}_{ij}(\zeta) d\zeta \quad (3.41)$$

where the limit of integration ϕ is defined as the maximum off-axis angle of warp or fill tow undulation. The maximum off-axis angle may be stated as

$$\begin{aligned} \phi_w &= \max \left[\tan^{-1} \frac{\partial}{\partial x} [z = p(x)] \right] \\ \phi_f &= \max \left[\tan^{-1} \frac{\partial}{\partial y} [z = p(y)] \right] \end{aligned} \quad (3.42)$$

and determined for the warp or fill tow centerline by utilizing techniques to sort the local off-axis angles into ascending order by numerical methods such as straight insertion, quicksort and Shell's method.

3.1.3.3. Application of Classical Lamination Theory

The elastic properties of the woven fabric lamina can be evaluated using classical lamination theory (CLT). Knowing the effective elastic properties of the warp and fill laminae, the lamina can typically be treated as a three-layered laminate and evaluated at the V_f of that specific lamina. It is also proposed that the lamina can be treated as a two-layered laminate and evaluated at a V_f equivalent to an average value for the woven warp and fill tows. Under the assumptions of the Kirchhoff conjecture for thin plates, the constitutive relations in condensed form are given as [2]

$$\begin{Bmatrix} N \\ M \end{Bmatrix} = \begin{bmatrix} A & B \\ B & D \end{bmatrix} \begin{Bmatrix} \epsilon_0 \\ \kappa_0 \end{Bmatrix} \quad (3.43)$$

where N and M are membrane stress and moment resultants, respectively. The strain and

curvature of the laminate midplane are ϵ_0 and κ_0 . The [A], [B] and [D] (extensional, extensional-bending coupling, bending) stiffness matrices are evaluated accordingly by

$$\begin{aligned}
 [A_{ij}, B_{ij}, D_{ij}] &= \sum_{k=1}^n \int_{h_{k-1}}^{h_k} (1, z, z^2) [\bar{Q}_{ij}]_k dz \quad (i, j = 1, 2, 6) \\
 [A_{ij}] &= \sum_{k=1}^n (h_k - h_{k-1}) [\bar{Q}_{ij}]_k \\
 [B_{ij}] &= \sum_{k=1}^n \frac{1}{2} (h_k^2 - h_{k-1}^2) [\bar{Q}_{ij}]_k \\
 [D_{ij}] &= \sum_{k=1}^n \frac{1}{3} (h_k^3 - h_{k-1}^3) [\bar{Q}_{ij}]_k
 \end{aligned} \tag{3.44a-c}$$

where $[\bar{Q}_{ij}]_k$ are the reduced mathematical moduli of the laminate k^{th} -layer corresponding to the lamina defined by a thickness $(h_k - h_{k-1})$. On the basis of assuming that the equivalent two-layered laminate is composed of UD laminae with transformed tows (fibers) in the x and y directions, the non-vanishing stiffness constants are given as

$$\begin{aligned}
 A_{11} = A_{22} &= \frac{(E_{11} + E_{22})h}{2D_v} & D_{11} = D_{22} &= \frac{(E_{11} + E_{22})h^3}{24D_v} \\
 A_{12} &= \frac{\nu_{12}E_{22}h}{D_v} & D_{12} &= \frac{\nu_{12}E_{22}h^3}{12D_v} \\
 A_{66} &= G_{12}h & D_{66} &= \frac{G_{12}h^3}{12} \\
 B_{11} = -B_{22} &= \frac{(E_{11} - E_{22})h^2}{8D_v}
 \end{aligned} \tag{3.45a-g}$$

where the following relationship does apply:

$$D_v = 1 - \nu_{12}\nu_{21} \tag{3.46}$$

In Eqs. 3.45(a-g), E_{11} and E_{22} are the Young's moduli, G_{12} is the in-plane shear modulus and

ν_{12} is the Poisson's ratio determined from inversion of the averaged compliance given by Eq. 3.41. In reference to the geometrical midplane of the two-layered laminate, the total laminate thickness h is determined by evaluating the average warp and fill tow thicknesses h_w and h_r . The average tow thicknesses can be determined by analysis of the least-squares polynomial approximations $p(x, y)$ to the perimeter of the tow cross-sections. Given a maximum tow width of a , the mean value of thickness $\pm \frac{h}{2}$, in reference to the midplane, is found by

$$h_w = \int_0^a p(x) dx = p(x^*) (a - 0)$$

$$\frac{1}{a - 0} \int_0^a p(x) dx = p(x^*) \quad (3.47)$$

Assuming the polynomials were approximations to points defining the upper and lower perimeter about the geometric center of the respective tow (Eq. 3.5), then the thickness represents the sum of mean values evaluated by Eq. 3.47.

3.1.3.4. Numerical Strain Energy Method

With reference to the numerical strain energy approach adopted for verification of the micromechanics solution, a similar numerical analysis can also be employed to verify the results obtained from the simplified 2-D mesomechanics model. The 8HS woven fabric lamina repeat volume element is simplified to an idealized volume (IVE) having planar dimensions as suggested by Ishikawa and Chou [2]. Under presumptions similar to those for the treatment of thin homogeneous plates, the top and bottom lamina surfaces are left free of tractions, i.e. a single ply analysis. Lamina elastic constants are evaluated by prescribing linearly independent displacements suitable for the requisite state of deformation. As with the numerical verification of woven tow properties, a direct frontal or wavefront solver is used in the finite element analysis to compute macrostress components obtained from averaging forces on IVE faces in the directions of interest. As an example, the macrostress

component σ_{xx} in the Cartesian coordinate system can be obtained by

$$\sigma_{xx} = \frac{1}{(\sqrt{8} a)(h_t)} \sum_n F_R^{(n)}(x_1 = x = \sqrt{2} a, x_2 = y, x_3 = z) \quad (3.48)$$

where $F_R^{(n)}$ is the nodal reaction at the n^{th} node on the face normal (at $x_1 = \sqrt{2}a$) and summation occurs over all nodes on that face. It is worthwhile to note that use of Eq. 3.48 in the manner presented is equivalent from a numerical perspective to the use of Eq. 3.18. Evolution of the IVE from the RVE is shown in Figure 3.11 where the lamina thickness (h) given above is influenced by the exact V_f determined from an iterative process.

In general, the equations for solving static and linear finite element analyses are of one of the following forms [37]:

$$\begin{aligned} [K]\{u\} &= \{F\} \\ [K]\{u\} &= \{F^a\} + \{F^r\} \end{aligned} \quad (3.49)$$

where $[K]$ represents the total stiffness matrix, $\{u\}$ is the nodal degree of freedom (DOF) vector and $\{F\}$ is decomposed into the applied load vector $\{F^a\}$ and the nodal reaction load vector $\{F^r\}$. The total applied load vector is the sum of the applied nodal load vector $\{F^n\}$ and total of all element load vector effects $\{F^e\}$. Nodal DOF values on every node can be obtained if boundary conditions are sufficient to guarantee a unique solution to Eq. 3.49. The nodal reaction load, i.e. the $\sum F_R^{(n)}$ in Eq. 3.48 is considered for all pertinent DOF's where only the loads at imposed DOF are output can be written as

$$\{F^R\} = [K]\{u\} - \{F^n\} - \{F^e\} \quad (3.50)$$

Displacement boundary conditions are imposed on the lateral faces of the IVE in a manner that would produce uniform strains in an equivalent homogeneous medium. For instance, a uniform strain state in the warp direction (ϵ_{xx} in reference to the model shown in Figure 3.12) implies that the following boundary conditions are applicable

$$\begin{array}{ll}
(\delta_x(0, y, z) - \delta_x(\sqrt{8a}, y, z) = \text{const.}) & (\delta_x(x, 0, z) - \delta_x(x, \sqrt{8a}, z) = 0) \\
(\delta_y(0, y, z) - \delta_y(\sqrt{8a}, y, z) = 0) & (\delta_y(x, 0, z) - \delta_y(x, \sqrt{8a}, z) = 0) \\
(\delta_z(0, y, z) - \delta_z(\sqrt{8a}, y, z) = 0) & (\delta_z(x, 0, z) - \delta_z(x, \sqrt{8a}, z) = 0)
\end{array}$$

For the remaining planar states of deformation, the non-zero boundary conditions are

$$\begin{array}{ll}
\epsilon_{yy} & (\delta_y(x, 0, z) - \delta_y(x, \sqrt{8a}, z) = \text{const.}) \\
\gamma_{xy} & (\delta_x(x, 0, z) - \delta_x(x, \sqrt{8a}, z) = \text{const.}) \quad (\delta_y(0, y, z) - \delta_y(\sqrt{8a}, y, z) = \text{const.})
\end{array}$$

3.2. Fundamental Stress Distributions

Woven fabric composites offer the potential of providing increased intra- and interlaminar strength and damage tolerance in comparison to traditional composites. Two-dimensional orthogonal woven fabric composites, such as those based on the plain and satin harness weaves, provide better bi-directional stability and balanced properties than their unidirectional (UD) counterparts. They also offer higher packing densities in relation to thickness and they exhibit greater resistance to impact loads. However, the in-plane elastic properties are usually lower since the interlaced regions exist out-of-plane and these regions contribute to the inefficient translation of elastic properties from the fibers to the fabric.

The process of manufacturing woven preregs from numerous bundles, containing several thousand fibers, involves repeated handling of the fibers. Repeated handling of the fibers and bundles may lower the statistical bundle strength and promote potential sites for crack nucleation. The interlaced regions often act as concentrations for stress while the regions adjacent to the interlacings often act as bridges for the transfer of load depending on the loading condition. A periodic network of these interlaced and bridging regions might provide a certain path for crack growth or provide a means to blunt it. Usually, this periodicity leaves a characteristic damage state (CDS) which is defined by the accumulation of damage zones.

Damage zones made up of intralaminar, interlaminar and translaminar cracking are much more complicated to predict and characterize when compared to the more predictable failures found in aligned fiber composites. Unlike the behavior of aligned fiber composites, woven fabric composite behavior tends to be more three-dimensional in nature. Although accurate predictions of strengths and modes of failure are nearly impossible in these materials without considering micromechanics and material nonlinearities, a practical starting point is the analysis of lamina stress distributions. Since the behavior of woven fabric composites tends to be suggested spatially rather than in-plane, it only makes sense that lamina stress distributions should be analyzed spatially to evaluate bundle (tow)-matrix interactions.

The amount of three-dimensional work done to evaluate the stress-strain behavior in woven fabric composites has been very limited in comparison to 2-D and quasi 3-D studies. From the standpoint of finite element analysis, the woven fabric architecture is quite cumbersome to model in 3-D. The boundary conditions which accurately represent the periodic displacements of a repeat unit cell (RUC) within a stacked laminate are not fully understood. Additionally, an infinite number of perturbations are possible with respect to the waviness of tows, lenticular shapes of tow cross-sections and arrangement of laminae within a stacked laminate. Until recently, the sheer computing horsepower needed for even the simplest of 3-D analyses was not widely available and software was not robust enough to handle the more complex modeling tasks involving Boolean operations. Considering the number of nodes and elements required for an accurate description of a single lamina, let alone a woven laminate which considers any of the possible perturbations, it is no wonder that the depth of studies in 3-D stress analysis of woven fabric composites has been limited.

Woven fabric composites may be viewed as distinctly separate on three geometric scales, the microscale (constituent fibers and matrix), mesoscale (woven laminae) and macroscale (woven laminate). It is far too complicated to model details of the microscale since numerous and discrete heterogeneities are present. At this scale, it makes more sense to homogenize behavior and treat the woven tows as transitional, i.e. UD composite

materials. At the mesoscale, it is much more feasible to include details of the geometry in modeling the behavior of woven composites. This type of work on mesoscale modeling of behavior in woven composites, particularly the plain weave architecture, has been performed largely by Whitcomb *et al.* [27-29], Blackketter *et al.* [26], Ishikawa and Chou [2,8-9], Foye [38] and Marrey *et al.* [39].

In *Refs 27-29*, a 2-D finite macroelement was developed which accounted for element spatial variation of material properties. Two-dimensional stress analyses of plain weave fabric composites were performed using a global-to-local finite element method. The macroelement was also extended to the 3-D case which utilized submodeling or substructuring (global-to-local) techniques. It was found that surface stress distributions differed from internal distributions and failure behavior was influenced by the degree of tow waviness. Increases in tow waviness showed little influence on effective properties, but affected initial failure in uniaxial tension due to higher transverse normal stress. Stress analyses for the 3-D model considered the effects of stacked boundaries, but were resolved into 2-D contour plots along single cutting planes only for the case of uniaxial tension.

A more representative case of the actual plain weave unit cell was modeled, in *Ref 26*, using details obtained from photomicrographs. The observed tow aspect ratio was included in the model and the correct fiber volume fraction was obtained by iteration. An incremental iterative finite element algorithm was employed to analyze tensile and shear stress-strain behavior and estimate the effects of progressive damage by stiffness reduction. Analysis of stress distributions within the plain weave unit cell was not included. *Refs 2,8-9* considered idealized cross-sections in establishing their one-dimensional (1-D) and quasi 2-D mosaic, fiber bridging and undulation models. The models were simple and effective for predicting thermoelastic properties of plain and satin weave composites, but detailed analyses of stress distributions were not possible since internal boundaries were not representative.

A finite element scheme was developed (*Ref 38*) using replacement elements to model the unit cell with inhomogeneities which predicted overall cell elastic properties

reasonably well. In *Ref39*, the thermoelastic properties of plain and five-harness satin (5HS) woven composites were evaluated by considering the woven unit cells within a continuum and as explicit plates of finite thickness. The continuum model considered the unit cells as rectangular parallelepiped geometries having periodic boundary conditions to maintain continuity of stresses across cell boundaries. The homogeneous plate model was a direct analysis which modeled strains and curvatures independently to arrive at thermoelastic properties.

The objective of this study was to determine the stress distributions in a 3-D 8HS woven fabric volume element along multiple cutting planes for the cases of uniaxial tension, compression and in-plane shear. These stress distributions within each plane were represented by surfaces derived from grids of sparse, irregularly spaced data which was smoothed using kriging interpolation. To the author's knowledge, a detailed analysis of stress variation through-thickness, by surface interpolation, has not been performed for any woven composites. The advantage of such a method is that stresses, from interaction of the interlaced region with the bridging regions, are suggested spatially rather than in-plane.

3.2.1. Finite Element Model

The linear elastic, finite element model proposed for this study was introduced in the aforementioned section. Initially, the goal was to model the woven cell as it appeared in micrographs of laminate cross-sections. The exact shapes of the woven tow centerline and cross-section obtained from digitized scanning electron microscopy (SEM) micrographs were included in modeling the geometry of the 8HS volume element. These random and irregular shapes were later discarded due to failed Boolean operations and mesh discretizations lacking continuity. However, the cross-sectional aspect ratio, averaged from several woven tows, was retained along with the lamina volume fraction measured using image analysis. Difficulties encountered in establishing the correct matrix volume fraction were similar to the problems reported by others in the literature [26,29]. Details of the model geometry,

material properties and boundary conditions assumed for the analysis of a single lamina subjected to fundamental loading conditions are discussed below.

3.2.1.1. Geometry and Materials

Due to errors in meshing the real shapes of the woven tows and centerlines, an idealized volume element (IVE) was employed. The basic 8HS woven IVE is shown in Figure 3.13(a) with the matrix removed for clarity. The IVE from a RUC consists of three warp tows running in the x-direction and three fill tows running in the y-direction. The center warp tow interlaces the center fill tow by running over the top of it and under the adjacent fill tows. Similarly, the center fill tow runs over the tops of the adjacent warp tows. All of the pockets bounded by neighboring tows are filled with matrix material. The hexagonal boundary of the IVE was reduced to a square boundary [2,8-9] to simplify the imposed boundary conditions.

The major area of the IVE is given by $\sqrt{8a}$ where a is the average width of a woven tow. In this work, the average width was 1393.6 μm (54.9 mils) with an average lenticular aspect ratio of 8.3:1. The overall lamina thickness h depends on the volume fraction of matrix within the lamina. For a certain volume fraction, the heights of the lateral faces are adjusted incrementally until the difference between the IVE volume and tow volumes converges on the matrix volume fraction. A matrix volume fraction of 0.36, as an example, required h to be 341 μm (13.4 mils). The IVE was meshed with ten-node tetrahedral elements which have three degrees of freedom and exhibit quadratic displacement behavior. The mesh shown in Figure 3.13(a) was limited to 4757 elements and 9474 nodes. The material properties were arbitrarily selected from the composite systems studied and compared in Section 3.1. Although that work was generally based on woven graphite fibers embedded in a PMR15 matrix, the range for reported constituent properties was found to be quite large. It was decided that the constituent material properties having the lowest values would be used, those of composite system A-a. They are

Fibers - C3000:

$$E_{11} = 234.5 \text{ GPa (34.0 Msi)} \quad E_{22} = 13.8 \text{ GPa (2.0 Msi)} \quad E_{33} = 13.8 \text{ GPa (2.0 Msi)}$$

$$\begin{array}{lll}
 G_{12} = 11.4 \text{ GPa (1.7 Msi)} & G_{13} = 4.8 \text{ GPa (0.7 Msi)} & G_{23} = 4.8 \text{ GPa (0.7 Msi)} \\
 \nu_{12} = 0.20 & \nu_{13} = 0.25 & \nu_{23} = 0.25
 \end{array}$$

Matrix - PMR15:

$$E_{11} = 3.3 \text{ GPa (0.48 Msi)} \quad G_{12} = 1.2 \text{ GPa (0.17 Msi)} \quad \nu_{12} = 0.36$$

Tows - UD C3000 - PMR15:

$$\begin{array}{lll}
 E_{11} = 169.8 \text{ GPa (24.6 Msi)} & E_{22} = 9.2 \text{ GPa (1.3 Msi)} & E_{33} = 9.2 \text{ GPa (1.3 Msi)} \\
 G_{12} = 4.6 \text{ GPa (0.67 Msi)} & G_{13} = 3.1 \text{ GPa (0.45 Msi)} & G_{23} = 3.1 \text{ GPa (0.45 Msi)} \\
 \nu_{12} = 0.24 & \nu_{13} = 0.37 & \nu_{23} = 0.37
 \end{array}$$

3.2.1.2. Boundary Conditions

The coordinate system adopted for the application of prescribed boundary conditions is shown in Figure 3.13(b). It was assumed that this model is not part of a continuum in the z -direction, but a single lamina having a finite thickness. The top and bottom lamina surfaces parallel to the x - y plane are free of tractions and opposing lateral faces are still assumed to be bounded by neighboring volume elements, therefore imposed constraints on these faces needed to be periodic. Referring to Figure 3.13(b), the constraints imposed for nominal tensile loading along the y -direction parallel to the fill tows are

$$\begin{array}{ll}
 \delta_y(x, \sqrt{8}a, z) = 0 & \delta_y(x, 0, z) = -\delta_{\text{applied}} \\
 \delta_x\left(\frac{-\sqrt{8}a}{2}, y, z\right) = 0 & \delta_x\left(\frac{\sqrt{8}a}{2}, y, z\right) = k
 \end{array} \quad (3.51)$$

where the variable k refers to a constant which is an unknown displacement due to Poisson contraction. For nominal compressive loading along the y -direction, the imposed constraints were identical to those given by Eq. 3.51, except the sign is reversed on the applied

displacement δ .

The constraints imposed for in-plane shear loading assumed that the sheared faces remained straight after deformation and the nodes on opposing faces normal to the direction of shear displaced by identical amounts. These constraints are

$$\begin{aligned}
 \delta_y \left(\frac{-\sqrt{8a}}{2}, y, z \right) &= 0 & \delta_y \left(\frac{\sqrt{8a}}{2}, y, z \right) &= -\delta_{\text{applied}} \\
 \delta_x \left(\frac{-\sqrt{8a}}{2}, y, z \right) &= 0 & \delta_x \left(\frac{\sqrt{8a}}{2}, y, z \right) &= 0 \\
 \delta_{x,y} \left(x, \sqrt{8a}, z \right) &= \delta_{x,y} \left(x, 0, z \right)
 \end{aligned} \tag{3.52}$$

3.2.2. Stress Modeling

The main focus of this work was to determine stress distributions through the thickness of an 8HS IVE in terms of the imposed constraints described in the previous section. Evaluation of the stress distributions along multiple planes served to explain the interactions between the interlaced region and the adjacent bridging regions. Although cumbersome, the most straightforward method to extract stress surfaces from the solution of a finite element model is by using a number of sweeping lines. The sweeping lines are particular lines in which the stresses of interest are known or can be extrapolated from nearby nodes. By moving the line(s) through the model thickness, a cutting plane can be generated. Whether the plane becomes a regularly spaced or irregularly spaced grid depends on the number of stress values extrapolated along a line and the number of increments through the thickness. If they are equal, the grid is regularly spaced. Herein, the number of tetrahedral finite elements that spanned the volume permitted a total of forty-nine extrapolated stress values along a sweep line. The line was incremented in the z-direction ten times, resulting in an irregularly spaced grid made up of 490 points per cutting plane. The details of the orientations of cutting planes (CP1-CP3), with respect to the warp and fill tows, are illustrated in Figure 3.14. Changes in

cross-sectional tow geometries are also delineated as the CP transitions from 1 to 3. Symmetry was exploited and the CP's only needed to span half-way across the volume and lie within a quarter-quadrant.

3.2.2.1. Kriging Interpolation

Computational constraints can place limits on the number of stress values extracted from the finite element solution. The disadvantage in producing a stress surface from a sparse data set is that information may be lost or misrepresented. One method which can be employed to statistically "fill" the sparse data set is kriging interpolation [40-41]. This method of interpolation predicts unknown values from data observed at known locations. The basic premise of the kriging algorithm is to estimate a certain unknown point with the weighted sum of known points in terms of minimizing the error in spatial distribution of the predicted values. Consider a set of N known points \mathbf{P} where each point P_i is expressed in terms of its coordinates (x_i, y_i) and a stress (Z_i) . The unknown point Q_{ij} may be estimated by calculating the weighted sum of \mathbf{P}

$$Q(x_i, y_j) = \sum_1^n w_n Z_n \quad (3.53)$$

where w_n is the weighting given to the n^{th} known point. Individual weightings can be assigned to all unknown points which constitute the target surface of points N . The key of the algorithm involves the appropriate selection of weights for each estimation based on error variance. Rather than using covariance to calculate each weight set or vector w_{ij} , a variogram \mathbf{V} is constructed

$$\mathbf{V} = \begin{bmatrix} D_{11} & D_{12} & \cdots & D_{1N} \\ D_{21} & D_{22} & \cdots & D_{2N} \\ \cdots & \cdots & \cdots & \cdots \\ D_{N1} & D_{N2} & \cdots & D_{NN} \end{bmatrix} \quad (3.54)$$

where the elements D_{ij} are the distances from known points P_i to known points P_j . The weight vector w_{ij} can then be calculated by $w_{ij} = d_{ij} V^{-1}$ where d_{ij} are the distances from the unknown points to each known point. Once the weights are known, the unknown points can be calculated in terms of the known points.

3.2.2.2. Punctual Kriging

The specific form of kriging interpolation used to generate stress surfaces from the sparse data sets is punctual kriging. Also referred to as ordinary kriging, it is the simplest variety of kriging. With punctual kriging, the estimation and error of estimation depend on the chosen weights. The optimal weights which produce unbiased estimates and have the smallest variance are obtained by solving a set of simultaneous equations. Consider three known stress values P_1 , P_2 and P_3 used to estimate the n^{th} unknown stress value Q . Three weights w_1 , w_2 and w_3 are required to make an estimate of the unknown stress value. The punctual kriging algorithm begins with the three simultaneous equations

$$\begin{aligned} w_1 \gamma(a_{11}) + w_2 \gamma(a_{12}) + w_3 \gamma(a_{13}) &= \gamma(a_{1n}) \\ w_1 \gamma(a_{21}) + w_2 \gamma(a_{22}) + w_3 \gamma(a_{23}) &= \gamma(a_{2n}) \\ w_1 \gamma(a_{31}) + w_2 \gamma(a_{32}) + w_3 \gamma(a_{33}) &= \gamma(a_{3n}) \end{aligned} \quad (3.55)$$

where $\gamma(a_{ij})$ represents the semivariance between points i and j having the distance of a between them. The values of the semivariances are taken from either a known or estimated semivariogram and an unbiased solution is ensured with a fourth equation. This fourth equation is given by

$$w_1 + w_2 + w_3 = 1 \quad (3.56)$$

To assure that the minimum possible error in estimation is obtained, a Lagrange multiplier λ is introduced. The complete set of equations can be represented in matrix form according to the following

$$\begin{bmatrix} \gamma(a_{11}) & \gamma(a_{12}) & \gamma(a_{13}) & 1 \\ \gamma(a_{21}) & \gamma(a_{22}) & \gamma(a_{23}) & 1 \\ \gamma(a_{31}) & \gamma(a_{32}) & \gamma(a_{33}) & 1 \\ 1 & 1 & 1 & 0 \end{bmatrix} \begin{bmatrix} w_1 \\ w_2 \\ w_3 \\ \lambda \end{bmatrix} = \begin{bmatrix} \gamma(a_{1n}) \\ \gamma(a_{2n}) \\ \gamma(a_{3n}) \\ 1 \end{bmatrix} \quad (3.57)$$

Once the weights [w] are known, the estimation (Q) and variance (s^2) of the estimation can be made from

$$\begin{aligned} Q &= w_1 P_1 + w_2 P_2 + w_3 P_3 \\ s^2 &= w_1 \gamma(a_{1n}) + w_2 \gamma(a_{2n}) + w_3 \gamma(a_{3n}) + \lambda \end{aligned} \quad (3.58)$$

The variance of estimation represents the real scatter of all estimates about the true value. The biggest advantage with punctual kriging as well as other kriging varieties is that estimations have minimum error associated with them and the error is always quantified. A more detailed explanation discussing the salient issues of the punctual kriging method and other kriging methods can be found in *Refs* 40-41.

3.3. Results and Discussion

Prediction of Elastic Constants - The ranges of constituent properties for the graphite or carbon fibers and polyimide matrices considered in this investigation are presented in Table 3.1. With reference to this table, all subsequent results presented are in terms of a particular composite system. As an example, system F-c^(H) refers to a composite possessing the upper limit of reported values for T650-35 (3k) fiber properties combined with the upper values for PMR15 matrix properties. The F-b^(H) and F-c systems are used here extensively for comparison as they are more representative of an average of constituent properties for the composite materials tested in the experimental program. It is seen from Table 3.1 that the reported range for fiber-based properties varies significantly, particularly in the transverse directions. Graphite and carbon-based fibers exhibit highly anisotropic behavior so this is not

entirely unexpected, particularly considering the difficulty in obtaining or estimating these values.

On the basis of CCA theory, Table 3.2 presents the results for several composite systems having various combinations of constituent properties. Upper and lower bounds for the transverse tensile and shear elastic properties are shown in accordance with the bounded CCA prediction. The {H} represents an upper bound where the transverse shear modulus of the fiber is much greater than the matrix shear modulus, while the lower bound {L} represents the opposite. As expected, the greatest difference between the upper and lower bounds occurs with the greatest range between fiber transverse and matrix shear moduli exhibited by system B-b. The F-c^(H) system appears to maintain the best balance of longitudinal and transverse properties. Clearly, Table 3.2 also shows that intralaminar and transverse shear behaviors are influenced more by the elastic properties of the matrix than of the fibers. CCA theory provides a simple closed-form expression for the equivalent composite shear modulus in terms of the matrix shear modulus and rule-of-mixtures ratio. Therefore, a nominal increase of 12% in fiber shear properties results in a 5% increase of equivalent shear properties while the same increase in matrix shear properties adds an additional 5 or 6%.

Linear elastic finite element results for the micromechanics analysis of woven tow properties from the example composite system F-b^(H), as a function of V_f , are provided in Figures 3.15-3.19. For the periodic geometry of a quarter-symmetry square array RVE, fiber diameter was held constant at 7.37 μm (0.29 mils) and requisite volume fractions of surrounding matrix were achieved by numerical iteration. The apparent elastic moduli were determined using two approaches: 1) averaged stress – applied strain (dividing the equivalent force from summed nodal reactions by the normal area), and 2) strain energy principles (equating the external work to internal strain energy). Comparisons of the present results were made with the analytical micromechanics solutions of Hashin and Rosen (CCA) [30-32], Halpin-Tsai [42] and Chamis [43]. For the longitudinal tensile modulus E_{11} , agreement between the numerical and closed-form solutions is excellent as shown in Figure 3.15.

Although the practical range of V_f approximately varies from 0.3 to a theoretical maximum of 0.8, the entire range from absolute matrix to absolute fiber is shown for the purpose of comparison. It is evident from Figure 3.16 that the numerical solution for the transverse tensile modulus E_{22} tends to converge on the lower CCA bound near a V_f of 0.45 and the upper CCA bound near 0.65. Beyond this, the current model predicts slightly larger values for E_{22} compared with the closed-form solutions. Within the useful range, the numerical solution for the intralaminar shear modulus G_{12} predicts values near the model presented by Chamis for highly anisotropic materials such as carbon-based fibers. As seen from Figure 3.17, the FE model suggests an average approximation that falls within the bounds provided by the analytical micromechanics solutions as the V_f approaches 0.65. At a V_f between 0.7 and 0.8, the FE model suggests an upper bound approximation to the shear modulus.

The results for the longitudinal Poisson's ratio ν_{12} and transverse Poisson's ratio ν_{23} are presented in Figures 3.18 and 3.19. The analytical approaches essentially predict a linear reduction in ν_{12} with increasing V_f , the exception being a minor inflection in the CCA solution near 0.4. The FE model transitions from an underestimate to an overestimate in the range of 0.4 to 0.5. The reasons for such a trend are twofold: first of all, a somewhat linear declination in the longitudinal Poisson's ratio with increasing V_f is expected due to a reduction in the amount of transverse straining possible from contraction. This depends not only on the degree of anisotropy of the fiber, but also on the fiber volume fraction, constituent Poisson's ratios and constituent plain strain bulk moduli. Here, the difference in magnitudes of relative transverse straining occurring in the fiber and matrix for a given applied longitudinal strain govern the slope of the line over the range of V_f considered. Secondly, the transition in ν_{12} between 0.4 and 0.6 as seen in Figure 3.18 seems to be highly dependent on the FE discretization procedure. The quarter-symmetry RVE, constructed for the longitudinal and transverse tensile load cases, used 159 ten-node isoparametric tetrahedral elements (354 nodes) while the full RVE, constructed for the longitudinal and transverse shear loading cases, used 1049 ten-node isoparametric tetrahedral elements (1768 nodes). Further mesh refinement, particularly in the thickness direction, tended to result in

both Poisson's ratios converging on the solution predicted by the theories. For ν_{12} , the trending line became more linear and any inflection was less evident. Changes in the solution for ν_{23} shown in Figure 3.19 subsequent to further through-thickness mesh refinement were similar. Under the auspices for calculating the transverse Poisson's ratio according to the relationship $\nu_{23} = (E_{22}/2G_{23})-1$, the trend in behavior with increasing V_f appears to be a consequence of the larger or smaller difference in increasing transverse tensile stiffness of the equivalent composite relative to transverse shear about the fiber axis. Given this, the magnitude of change in stiffness behavior in transverse tension and shear seems equivalent within the ranges of 0 to 0.4 V_f and 0.6 to 0.8 V_f .

Based on the same requisite volume fractions as considered in the tow analysis, Table 3.3 compares the non-zero extension, extending-bending coupling and bending compliance solutions for 8HS woven laminae having the same T650-35 fiber properties, but different polyimide matrix properties. These values are compared with a baseline solution for a lamina having no undulations, essentially a UD cross-ply. If differences in non-zero terms are compared for each lamina, it is clearly suggested that variation in properties of the matrix influence the diagonal {66} and off-diagonal {12} terms to a greater extent. Upon closer scrutiny, it is found that these terms diminish by some 20-30% when matrix elastic properties are augmented by approximately 40%, implying enhanced stiffnesses. The present model also suggests an inverse behavior when comparisons are made between both lamina architectures. That is, a significant increase occurs in diagonal extension and bending {11} terms when local off-axis undulation angles ranging from 10-12.3° (using quick-sort and Shell's methods) are considered as observed for the 8HS architectures in this investigation. Contrarily, the extension-bending coupling terms reduce to 18% of their baseline value while very little finite change is evident for the diagonal {66} terms. Variations in extension and extension-bending coupling compliances with local angle of undulation are shown in Figures 3.20 and 3.21. The ranges indicated are for a woven lamina with a system of type F-b^(H) having a measured tow V_f of 0.72. Two important indices are evident from these range charts: 1) constituent elastic properties, and 2) angle of undulation. It appears that the present

model would predict maximum extension $\{A_{11,22}\}$ terms and minimum extension-bending coupling $\{B_{11,-22}\}$ terms near an undulation angle of 16° . This seems reasonable for the case of a plain weave architecture ($n_i = 2$) depending on the size of the gap between adjacent tows.

The macroscale laminate solutions for several of the composite systems are provided in Table 3.4 on the basis of results from the mesoscale predictions carried over from CCA (see Table 3.2). The composite laminate elastic properties are based on a 16-layer laminate having a total thickness of 5.00 mm (0.20 in), representative of the composite plaques tested in tension, off-axis tension and shear. In comparing the macroscale results with the range of apparent elastic properties determined experimentally (c.f. Section 4) and given in Table 3.5, it can be seen that the model tends towards underestimating the mean of E_{11} and E_{22} by 7.5% and ν_{12} by 14%, while overestimating the mean of G_{12} by 21% for the F-c^(H) system. Additionally, the gap would increase by 15% for E_{11} and E_{22} of the F-b^(H) system, but G_{12} would be underestimated by 7%. This suggests that either the actual matrix properties lie in between the \underline{b} and \underline{c} constituent system properties or the simplified model predicts average diagonal $[A_{ij}]^{-1}$ terms greater than what is to be expected. However, considering the range in measured apparent composite elastic properties, the model seems to provide reasonable bounded approximations.

Structure-performance maps for evaluating the composite off-axis elastic behavior, in terms of constituent system properties, are shown in Figures 3.22-3.24. In total, the off-axis performance of six systems was determined, five in the type A, B, C, F systems and the composites from the experimental program. Relationships between the longitudinal and transverse tensile moduli, intralaminar shear modulus and longitudinal Poisson's ratio were established over off-axis angles (β) ranging from 0° to 45° according to the familiar transformation expressions. For the range of angles considered, agreement between the various systems and the experiments seems to be quite good. Presumably, the remaining angles in the second-half of the quadrant should result in identical curves since reinforcement is mutually orthogonal. In this work, it was initially assumed that this was the case and subsequently verified through experimentation. In instances where curves did not match

would tend to indicate the extent of unbalanced properties, i.e. more orthotropic than quasi-isotropic ($0/90^\circ$ vs. warp-aligned). The usefulness of the structure-performance maps lies in the ability to tailor the architecture and constituent properties to suit a desired off-axis elastic behavior with some degree of certainty. From these maps, knowledge of the complete range of in-plane elastic response is only a matter of measuring a particular elastic constant for a given system once the relationships are firmly established.

The relevant metrics presented in Table 3.6 for the 8HS woven composite architectures considered were determined by image analysis of SEM micrographs and C-SCAN data. This information was passed into the simplified mesoscale model as well as the woven tow and lamina FE models. From this table, an average fiber diameter of $7.37\ \mu\text{m}$ (0.29 mils) was used in the micromechanics FE models as previously described. These solutions to the woven tow elastic properties were passed into the mesomechanics IVE model having a major tow width of $1393.60\ \mu\text{m}$ (54.87 mils). The resulting tow aspect ratio of 8.3:1 and corresponding volume fraction of matrix were correctly established by numerical iteration. Analytical and numerical elastic analyses of the F-b^(H) and F-c^(H) composite systems evaluated at the equivalent tow and laminate V_f were compared to the experimentally obtained properties. The results from these comparisons are presented in Table 3.7.

The composite elastic properties obtained from the present analytical approach are in agreement with the composite elastic properties obtained from the finite element analyses for both systems and fiber volume fractions under consideration. Additionally, when compared with the apparent elastic properties presented in Table 3.5, the results in Table 3.7 tend to reiterate the notion that the actual range of constituent properties for the composite materials tested lies somewhere in between those assumed for F-b^(H) and F-c^(H). It is also suggested that assuming the tow V_f in the simplified, two-layer lamina model serves as a much better lower bound approximation to experimentally determined elastic properties than assuming the laminate V_f when considering the F-b^(H) system. Mostly, the predicted and experimental elastic properties tend to converge on the F-c^(H) system with the exception of

the intralaminar shear modulus, which is slightly overestimated.

Stress Distributions - Two issues will be addressed below. First, the stress distributions in the 8HS woven IVE will be presented for the three fundamental loading conditions and cutting planes. The variants in stress surfaces will be discussed in the manner of possible interactions between the interlaced and bridging regions. Second, potential failure modes will be discussed by comparing the normalized stress magnitudes to the assumed strengths of the constituent materials.

For determining the variants in stress distributions within each CP, the 10 x 49 irregularly spaced grids were constructed from the assembly of sweep lines, each of which represented 10 points of stress extrapolated from nearby nodes. An example of these points for the uniaxial tensile stress state within CP1, due to applied tension, is shown in Figure 3.25. Each irregularly spaced grid was correlated to a much finer, regularly spaced grid of 50 x 50 using a neighborhood search radius of 2 and a smoothing factor of 0.5. Stresses under consideration were uniaxial tensile, compressive, in-plane shear and transverse normal stresses. The values extrapolated to a sweep line at a given z-increment were normalized to the average applied stress calculated from summed nodal reactions ($F_y^{R\{n\}}$) and given by the following:

$$\bar{\sigma}_y = \left| \frac{1}{(\sqrt{8} a)(h)} \sum_n F_y^{R\{n\}}(x = \pm x, y = 0, z = \pm z) \right| \quad (3.59)$$

where a is the average tow width, h is the average lamina thickness and the superscript $\{n\}$ refers to individual nodes.

Table 3.8 lists the minimum and maximum normalized stresses from each CP in terms of the loading condition. It can be seen that both applied tensile and compressive loads result in the highest normalized uniaxial tensile and compressive stresses (σ_y) within CP3. Furthermore, the greatest transverse normal stress (σ_z) range occurs within CP2. In shear, it appears that the magnitudes of concentrated, in-plane shear stress (σ_{xy}) are similarly

distributed between all three cutting planes. Shear loading also exhibits the greatest normalized range of transverse tension within CP2 compared to the other cutting planes that are subjected to either tension or compression. This tends to support the results described in other work (c.f. Section 4) where the author reports transverse tension as responsible for the out-of-plane deformation (bulging) observed in Iosipescu shear and off-axis tensile specimens.

The uniaxial tensile and transverse normal stress distributions resulting from an applied tensile load are presented in Figures 3.26-3.28 for CP1-3, respectively. Using the cross-section of CP1 from Figure 3.14 as a guide, it can be seen in Figure 3.26(a) that the maximum and minimum tensile stress peaks lie between $0.50 (1/\sqrt{2} \cdot a)$ and $0.75 (3\sqrt{2}/4 \cdot a)$. Also, these peaks are nearly anti-symmetric with respect to the fill tow centerline. An analysis of local displacements and moment summations performed in this study suggests that straightening of the fill tow is constrained at its boundary with the interlaced region by mutually orthogonal warp tows on either side. The coupling between extension and bending tends towards bending which appears to place the fill tow in tension and the sections above and below (bounded by the warp tows) in compression.

In Figure 3.26(b), the transverse normal stress peaks at $\pm 3\%$ of the applied stress and is essentially constant across the cutting plane at the location within the tows where the off-axis angle is a maximum at $0.707 (2\sqrt{2}/3 \cdot a)$. Here, relative local displacements indicate that fill tow straightening pushes the interlaced warp tow out-of-plane (+z), but the warp tow is being constrained by adjacent, straight warp tows. The straight warp tows counteract this (+z) movement leading to the adjacent, straight fill tows being pushed slightly in the (-z) direction. In comparison to the plain weave analysis [c.f. 29], it seems that the presence of normal stresses due to tension are lessened by the bridging regions, smaller angle of undulation and absence of a neighboring ply constraint.

Figures 3.27(a) and 3.27(b) show the uniaxial tensile and transverse normal stress distributions from an applied tensile load for CP2. The predicted tensile stress exceeds the applied stress in two regions, between $y = 0$ to 0.25 and $y = 0.6$ to 0.75 where the maximum

off-axis angle of warp tow undulation occurs at $x = +(\sqrt{2/3} \cdot a)$. The depths at which both peaks occur (between 0 to -0.2) are coincident with both the outer edge of the straight, transverse warp tow and boundary between the straight and interlaced, transverse warp tows. This indicates that the gradual reduction in the aspect ratio of the tow cross-section to an acute angle results in magnification of the tensile stress. The effect of coupling on the transverse normal stress within the interlaced warp tow is greater than in CP1, although it can still be considered negligible at a maximum in compression of 8%. The difference between the tensile and compressive peaks is a result of the difference in relative out-of-plane movement of the undulated warp tow as compared to the straight warp tow.

Figures 3.28(a) and 3.28(b) show the uniaxial tensile and transverse normal stress distributions from an applied tensile load for CP3. As within CP2, the stress peaks are similarly located and coincident with the outer edge and inner boundary of the transverse warp tows. However, the stress concentration at $x = +(2\sqrt{2/3} \cdot a)$ is magnified by a factor of four compared to the stress concentration at $x = +(\sqrt{2/3} \cdot a)$ since the greatest tensile stress is realized within the bridging region. Figure 6(b) shows that there is some compressive transverse stress on the bottom of the center warp tow near the boundary of the interlaced fill tow as a result of fill tow stretching and movement of the warp tow.

The uniaxial compressive and transverse normal stress distributions resulting from an applied compressive load are presented in Figures 3.29-3.31 for CP1-3, respectively. The greatest distinction between the stress distributions for applied tension and applied compression is the resulting state of stress. That is, the magnitudes of the stresses are exactly the same for each cutting plane, but the signs of the stresses are opposite. If the behavior of the tows within the planes is exactly opposite in uniaxial compression in comparison to uniaxial tension, then the reasoning should be opposite also. For example, consider the uniaxial compressive and transverse normal stress distributions for CP1 as presented in Figures 3.29(a) and 3.29(b), respectively. In compression, the center fill tow is prone to bending and possibly kinking. The coupling places the fill tow in compression and the sections above and below (bounded by the warp tows) in tension. The transverse normal

stress distribution is exactly opposite in this case because the center fill tow itself moves out-of-plane (-z) which also pushes the bridging tows slightly out-of-plane. For CP2 [Figures 3.30(a) and 3.30(b)] and CP3 [Figures 3.31(a) and 3.31(b)], the magnification effects of the transverse warp tow edges are similar to the case of applied tension.

Figures 3.32-3.34 show the in-plane shear stress and transverse normal stress distributions for CP1-3 as a result of an applied, in-plane shear load. Clearly, the magnitudes of the peak in-plane shear stresses are similar for all three cutting planes. Also, the transverse normal stress concentration is much greater within CP2 than for any plane under the uniaxial loading conditions. It can be seen in Figure 3.32(a) that the maximum shear stress in CP1 is 2.3 times greater than the applied stress and occurs in the region of $y = (2\sqrt{2}/3*a)$, where the center warp tow bounds the center fill tow on the concave side of undulation. The shear stress gradually increases from the point where the tow path transitions off-axis and reaches a maximum with attainment of the maximum, local off-axis angle of undulation. In Figure 3.32(b), transverse tension within CP1 appears constant at 3% except for the upper surface and mid-plane at $y = 0$ where it decreases.

In Figure 3.33(a), the maximum shear stress concentration in the undulated warp tow is 2.4 times greater than the applied stress where the off-axis angle of undulation is a maximum. The peak tends to follow the path where the edge of the undulated section of the fill tow interlaces with the center warp tow. The maximum normal stress within CP2, as seen in Figure 3.33(b) is 65% of the applied stress with nearly a 100% range. For CP3, Figure 3.34(a) shows the maximum to be 1.8 times greater and increasing as the center section of the undulated warp tow is reached. In comparison to CP2, the normal stress range is the next largest at 33% as shown in Figure 3.34(b). The summed moments and relative, local displacements suggest that coupling between shear and bending is greater within the bridging region, i.e. CP3. Shearing of the transverse warp tows is constrained by the undulated fill tow and shearing of the longitudinal fill tows is constrained by the undulated warp tow. This "locking" causes a rotation about the z-axis which pushes the center warp tow out-of-plane (+z) within the region of CP2 at $y = (2\sqrt{2}/3*a)$.

Failure Considerations - The results for the stress distributions in the 8HS woven fabric composite, given in the previous section, cannot be used with absolute certainty to predict failure initiation. There are several reasons for this: first of all, matrix plasticity was not considered in this analysis. It is not clear to what degree plastic flow occurs in the resin rich pockets even though neat PMR-type resins typically exhibit elastic-brittle behavior in tension and shear. Secondly, the lenticularly shaped tows were assumed to have edges with acute angles. Clearly, there must be significant stress magnifications from the presence of sharp corners. However, it is believed that trends in distributions should be similar, but the magnitudes of the peaks might change, particularly for applied tension and compression within CP2-3. Lastly, structural nonlinearities (e.g. tow rotation and friction) were not considered in this analysis. Ideally, the interlaced tows should be allowed to slide over each other upon failure of the boundaries and resin pockets. For the case of in-plane shear, this would result in stress redistribution and residual stiffness.

From the computational viewpoint, including both structural and material nonlinearities in the analysis of an IVE having adequate mesh density becomes too memory and storage intensive. Also, modeling of woven tow edges having radii presents two additional problems. A much finer mesh is required near the edges to maintain the radii and Boolean modeling operations usually fail when intersections of corners are not distinctly sharp. If the limitations of the model presented here are accepted, a course approximation of failure initiation for each of the loading conditions could be given.

Based on work by the author (c.f. Section 4), the tows can be treated as UD composite materials having the following normal and shear failure stresses: $X_{11}^{\text{tow}} = \pm 900$ MPa (130.1 ksi), $X_{22}^{\text{tow}} = X_{33}^{\text{tow}} = +40/-180$ MPa (+5.8/-26.1 ksi), $X_{12}^{\text{tow}} = 60$ MPa (8.7 ksi) and $X_{11}^{\text{matrix}} = 75$ MPa (10.9 ksi). For simplicity, it is assumed that the interphase failure stress is the same as the matrix and the matrix fails in tension under shear loading conditions. If the normalized stress distributions presented in the previous section are compared with the normalized failure stresses, then failure initiation can be approximated. For the cases of tensile and compressive loading, the applied stress is 29.0 MPa (4.2 ksi) relative to a

prescribed displacement δ of 5.0 μm (0.2 mils). For the case of in-plane shear loading, the applied stress is 2.7 MPa (0.4 ksi) at a prescribed displacement of 5.0 μm (0.2 mils). Based on the assumed failure stresses, an applied tensile load in the fill direction should cause the undulated warp tow to fail in transverse tension near $x = +(2\sqrt{2/3})\cdot a$. In this region, both the in-plane $\{\sigma_y\}$ and normal transverse stresses exceed $X_{22,33}$ of the warp tow. For compression, only the normal transverse stress exceeds X_{33} of the warp tow.

For the applied shear stress of 2.7 MPa (0.4 ksi), the shear failure stress X_{12}^{tow} is not exceeded in any one of the regions. However, in-plane shear $\{12\}$ and normal $\{33\}$ tensile failures may still be extrapolated at higher applied stresses since the model is linear elastic. For an applied shear stress of 25.0 MPa (3.6 ksi), the undulated warp tow fails in shear at its edge $y = (2\sqrt{2/3}\cdot a)$ from $x = 0$ to $+(\sqrt{2}\cdot a)$. Normal tensile stress $\{33\}$ in this region is 41% of the tow failure stress. Possibly, tensile matrix failure at the tow boundaries occurs prior to failure of the transverse warp tow in shear. If this is the case, then the undulated warp tow would be forced further out-of-plane increasing the normal tensile stress. Normal tensile failure could initiate due to an applied shear stress not much greater than what is required for in-plane shear failure. From experiments, this has been observed on several occasions for the 8HS woven fabric composites tested off-axis and in shear. It is also worth noting that the onset of intralaminar damage (discussed in the subsequent section) of these composites, using the Iosipescu shear test, was found to be approximately 25.0-35.0 MPa (3.6-5.1 ksi).

Table 3.1. Reported constituent elastic properties for various graphite and carbon-based, anisotropic fibers and polyimide-type matrices.

System	Ref	Fibers	E_{11} GPa (Msi)	E_{22} GPa (Msi)	G_{12} GPa (Msi)	G_{23} GPa (Msi)	ν_{12}	ν_{23}
A	20	C3000	234.5 (34.0)	13.8 (2.0)	11.4 (1.7)	4.8 (0.7)	.20	.25
B	24	IM7*	276.0 (40.0)	56.0 (8.1)	28.0 (4.1)	16.7 (2.4)	.25	----
C	33	AS4	235.0 (34.1)	14.0 (2.0)	28.0 (4.1)	----	.20	.25
D	11	T-300	230.0 (33.4)	40.0 (5.8)	24.0 (3.5)	14.3 (2.1)	.26	----
E	26	AS4	221.0 (32.1)	13.8 (2.0)	13.8 (2.0)	5.5 (0.8)	.20	.25
F	†	T650-35 (3k) ^a	243.4 ^(L) 258.6 ^(H) (37.5)	40.0 (5.8)	25.0 (3.6)	14.0 (2.0)	.20 .26	.25

System	Ref	Matrix ^b	E_{11} GPa (Msi)	G_{12} GPa (Msi)
a	20	PMR15	3.3 (0.48)	1.2 (0.17)
b	†		3.24 (0.46)	1.2 (0.17)
c	††		4.0 ^(L) 4.5 ^(H) (0.65)	1.5 1.7 (0.25)
d	†††	Avimid R	3.6 (0.5)	1.4 (0.2)

* Constituent property maxima.

^aLow density.

^bIsotropic.

^cNASA LeRC and Amoco Corp.

^{††}ASM Engineered Materials Handbook, Vol. 1: Composites.

^{†††}DuPont-AMS.

Table 3.2. Micromechanics results for 8HS woven tow elastic properties based on CCA theory for composite systems identified from constituent properties in Table 3.1.

Micromechanics Analysis of Woven Tows									
Composite System[†]	E₁₁ GPa (Msi)	E₂₂ {H} GPa (Msi)	E₂₂ {L} GPa (Msi)	G₁₂ GPa (Msi)	ν₁₂	G₂₃ {H} GPa (Msi)	G₂₃ {L} GPa (Msi)	G₃₃ {H} GPa (Msi)	G₃₃ {L} GPa (Msi)
A-a	169.8 (24.6)	9.2 (1.3)	8.8 (1.3)	4.6 (0.67)	0.24	3.1 (0.45)	2.9 (0.42)	3.1 (0.45)	2.9 (0.42)
B-b	199.6 (28.9)	16.6 (2.4)	14.2 (2.1)	5.9 (0.86)	0.28	5.8 (0.84)	4.7 (0.68)	5.8 (0.84)	4.7 (0.68)
C-c ⁽¹⁾	170.4 (24.7)	10.1 (1.5)	9.7 (1.4)	7.0 (1.0)	0.25	3.7 (0.54)	3.5 (0.51)	3.7 (0.54)	3.5 (0.51)
D-d	166.6 (24.2)	16.0 (2.3)	14.3 (2.1)	6.4 (0.93)	0.29	5.8 (0.84)	4.9 (0.71)	5.8 (0.84)	4.9 (0.71)
E-a	160.1 (23.2)	9.1 (1.3)	8.6 (1.2)	4.9 (0.71)	0.24	3.4 (0.49)	3.1 (0.45)	3.4 (0.49)	3.1 (0.45)
F-c ⁽¹⁾	176.4 (25.6)	17.3 (2.5)	15.4 (2.2)	6.8 (0.99)	0.24	6.1 (0.88)	5.2 (0.75)	6.1 (0.88)	5.2 (0.75)
F-c ⁽¹⁾	187.5 (27.2)	18.4 (2.7)	16.6 (2.4)	7.4 (1.1)	0.29	6.5 (0.94)	5.6 (0.81)	6.5 (0.94)	5.6 (0.81)
F-d ⁽¹⁾	187.2 (27.2)	16.2 (2.3)	14.5 (2.1)	6.5 (0.94)	0.29	5.8 (0.84)	4.9 (0.71)	5.8 (0.84)	4.9 (0.71)

[†]Denotes fiber and matrix constituents.

Note: Properties indicated by {H} or {L} represent bounds, i.e. $G_{23}^I \geq G^m$ or $G_{23}^I \leq G^m$.

Composite system (F-b)⁽¹⁾ assumed for mesomechanics and macromechanics analyses.

Table 3.3. Non-zero extension, extension-bending coupling and bending compliance constants predicted by the present micro-to-mesoscale analytical mechanics model for an 8HS woven fabric lamina and equivalent cross-ply composite.

Composite Lamina (8HS-weave)	$[A_{11}, A_{22}]^{-1} \{H\}$ $\times 10^{-4}$	$[A_{66}]^{-1} \{H\}$ $\times 10^{-3}$	$[A_{12}]^{-1} \{H\}$ $\times 10^{-3}$	$[B_{11}, -B_{22}]^{-1} \{H\}$ $\times 10^{-5}$	$[D_{11}, D_{22}]^{-1} \{H\}$ $\times 10^{-8}$	$[D_{66}]^{-1} \{H\}$ $\times 10^{-6}$	$[D_{12}]^{-1} \{H\}$ $\times 10^{-6}$
F-b ^(H)	0.594	0.653	0.940	0.117	0.997	0.110	0.158
F-c ^(H)	0.526	0.504	0.775	0.106	0.883	0.085	0.127
F-d ^(H)	0.562	0.581	0.862	0.112	0.944	0.098	0.145
Composite Laminate* (Cross-ply)	$[A_{11}, A_{22}]^{-1} \{H\}$ $\times 10^{-4}$	$[A_{66}]^{-1} \{H\}$ $\times 10^{-3}$	$[A_{12}]^{-1} \{H\}$ $\times 10^{-3}$	$[B_{11}, -B_{22}]^{-1} \{H\}$ $\times 10^{-5}$	$[D_{11}, D_{22}]^{-1} \{H\}$ $\times 10^{-8}$	$[D_{66}]^{-1} \{H\}$ $\times 10^{-6}$	$[D_{12}]^{-1} \{H\}$ $\times 10^{-6}$
F-b ^(H)	0.367	0.652	0.854	0.650	0.617	0.109	0.143
F-c ^(H)	0.360	0.502	0.701	0.660	0.605	0.084	0.118
F-d ^(H)	0.365	0.579	0.788	0.650	0.613	0.097	0.132

*Comparison made equivalent considering the 8HS as a "2-ply" laminate.

*Cross-ply interpreted as a 1st order polynomial fit.

Note: Units are consistently SI with $[A B D]^{-1}$ in terms of $(\text{MPa} \cdot \text{mm})^{-1}$.

{H} indicates upper-bounded elastic constants.

Table 3.4. Elastic properties predicted by the present micro-to-mesoscale analytical mechanics model for various 16-layered composite systems considered.

Properties of Woven 8 HS N-Layered Laminate (from Mesomechanics Analysis)										
Composite System [†]	E_{11} {H} GPa (Msi)	E_{11} {L} GPa (Msi)	E_{22} {H} GPa (Msi)	E_{22} {L} GPa (Msi)	E_{22} {L} GPa (Msi)	G_{12} {H} GPa (Msi)	G_{12} {L} GPa (Msi)	G_{12} {L} GPa (Msi)	ν_{12} {H}	ν_{12} {L}
A-a	51.7 (7.49)	51.4 (7.45)	51.7 (7.49)	51.4 (7.45)	51.4 (7.45)	4.5 (0.65)	4.4 (0.64)	4.4 (0.64)	.047	.042
B-b	66.7 (9.67)	65.1 (9.44)	66.7 (9.67)	65.1 (9.44)	65.1 (9.44)	5.9 (0.86)	5.8 (0.84)	5.8 (0.84)	.065	.050
C-c ⁽¹⁾	61.6 (8.93)	61.3 (8.89)	61.6 (8.93)	61.3 (8.89)	61.3 (8.89)	6.8 (0.99)	6.8 (0.99)	6.8 (0.99)	.044	.041
D-d	62.6 (9.08)	61.4 (8.91)	62.6 (9.08)	61.4 (8.91)	61.4 (8.91)	6.4 (0.93)	6.3 (0.91)	6.3 (0.91)	.068	.057
E-a	51.5 (7.47)	51.2 (7.43)	51.5 (7.47)	51.2 (7.43)	51.2 (7.43)	4.8 (0.70)	4.8 (0.70)	4.8 (0.70)	.042	.038
F-c ⁽¹⁾	66.3 (9.62)	65.1 (9.44)	66.3 (9.62)	65.1 (9.44)	65.1 (9.44)	6.8 (0.99)	6.7 (0.97)	6.7 (0.97)	.063	.052
F-c ⁽¹⁾	71.5 (10.37)	70.3 (10.19)	71.5 (10.37)	70.3 (10.19)	70.3 (10.19)	7.4 (1.07)	7.4 (1.07)	7.4 (1.07)	.070	.060
F-d ⁽¹⁾	66.8 (9.69)	65.6 (9.51)	66.8 (9.69)	65.6 (9.51)	65.6 (9.51)	6.4 (0.93)	6.4 (0.93)	6.4 (0.93)	.065	.054

[†]Denotes fiber and matrix constituents.

Note: Properties indicated by {H} or {L} represent bounds, i.e. $G_{21}^f \gg G^m$ or $G_{21}^f \ll G^m$.

N-layered laminate assumed with $N = 16$, thickness of 5.0 mm and $V_f = 0.72$ (tow equivalent).

Table 3.5. Apparent elastic properties obtained by off-axis tensile and biaxial Iosipescu shear experiments (c.f. Section 4).

Experimental Test	Apparent Elastic Properties			
	E_{11} GPa (Msi)	E_{22} GPa (Msi)	G_{12} GPa (Msi)	ν_{12}
On-Axis / Off-Axis Tension	76.9 ± 6.2 ($11.1 \pm .9$)	76.9 ± 6.2 ($11.1 \pm .9$)	6.0 ± 0.5 ($.9 \pm .07$)	$.08 \pm .03$
Biaxial Iosipescu Shear			6.5 ± 1.0 ($.9 \pm .15$)	

Table 3.6. Metrics for the fiber, tow, lamina and composite plaque obtained from SEM micrographs and C-SCAN data.

Metric	Geometric Scale			
	Fiber μm (mils)	Tow μm (mils)	Lamina μm (mils)	Plaque mm (in)
Diameter	7.37 (0.29)	----	----	----
Major Width	----	1393.60 (54.87)	4180.80 (164.60)	304.80 (12.00)
Major Thickness	----	167.70 (6.60)	301.25-392.00 (11.86-15.43)	3.92-5.50 (0.15-0.22)
V_f	----	0.71-0.74	0.68-0.72	0.58-0.62

Table 3.7. SMM and FE results for elastic properties of the F-b^(H) and F-c^(H) evaluated at tow and laminate fiber volume fractions.

V_f	System	Model	E_{11} GPa (Msi)	E_{22} GPa (Msi)	G_{12} GPa (Msi)	ν_{12}
0.72	F-b ^(H)	SMM	62.70 (9.09)	62.70 (9.09)	5.70 (0.83)	0.06
	F-b ^(H)	FE	63.90 (9.27)	63.90 (9.27)	5.00 (0.73)	0.13
	F-c ^(H)	SMM	71.00 (10.30)	71.00 (10.30)	7.40 (1.07)	0.07
	F-c ^(H)	FE	73.60 (10.67)	73.60 (10.67)	6.90 (1.00)	0.14
0.62	F-b ^(H)	SMM	50.60 (7.34)	50.60 (7.34)	4.30 (0.62)	0.06
	F-b ^(H)	FE	54.70 (7.93)	54.70 (7.93)	3.70 (0.54)	0.13
	F-c ^(H)	SMM	58.50 (8.48)	58.50 (8.48)	5.70 (0.83)	0.06
	F-c ^(H)	FE	63.50 (9.21)	63.50 (9.21)	5.10 (0.74)	0.14

Note: SMM refers to the present analytical simplified mechanics model.
FE refers to the equivalent force and strain energy finite element models.

Table 3.8. Maximum and minimum normalized stresses extrapolated to irregularly spaced grids within cutting planes.

Load Case	Stress Normalized	CP	Samples	Min	Max	Range
Tension	$\frac{\sigma}{\sigma_y}$	1	490	-0.42	0.77	1.19
		2	490	-0.21	1.39	1.60
		3	490	-0.04	5.42	5.46
	$\frac{\sigma_{ i}}{\sigma_y}$	1	490	-0.03	0.03	0.06
		2	490	-0.08	0.04	0.12
		3	490	-0.07	0.02	0.09
Compression	$\frac{\sigma}{\sigma_y}$	1	490	-0.77	0.42	1.19
		2	490	-1.39	0.21	1.60
		3	490	-5.42	0.04	5.46
	$\frac{\sigma_{ i}}{\sigma_y}$	1	490	-0.03	0.03	0.06
		2	490	-0.04	0.08	0.12
		3	490	-0.02	0.07	0.09
In-plane Shear	$\frac{\sigma_{ x}}{\sigma_y}$	1	490	-0.11	2.33	2.44
		2	490	-0.11	2.40	2.51
		3	490	-0.15	1.79	1.93
	$\frac{\sigma_{ i}}{\sigma_y}$	1	490	-0.11	0.06	0.16
		2	490	-0.30	0.65	0.95
		3	490	-0.20	0.13	0.33

Note: The macrostresses $\bar{\sigma}_{ij}$ are evaluated by summation of nodal reaction forces from prescribed displacements on lateral faces. Prescribed displacements are arbitrarily set at 5.0 μm (0.20 mils).

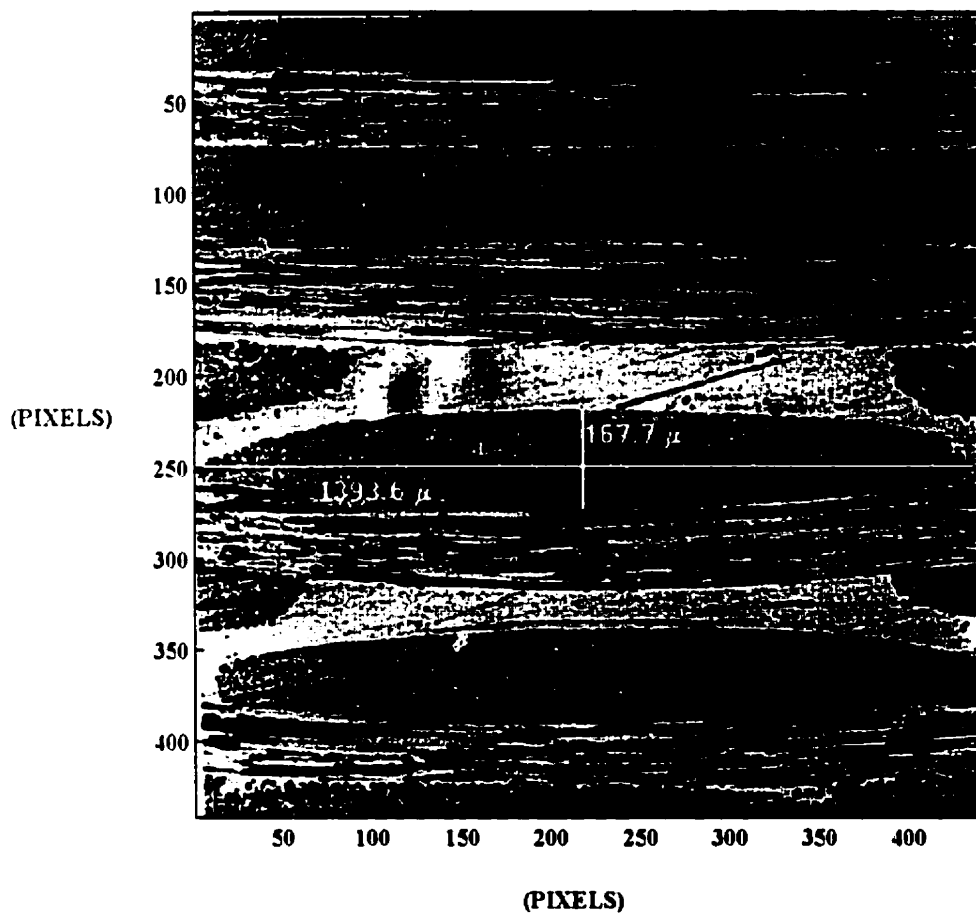
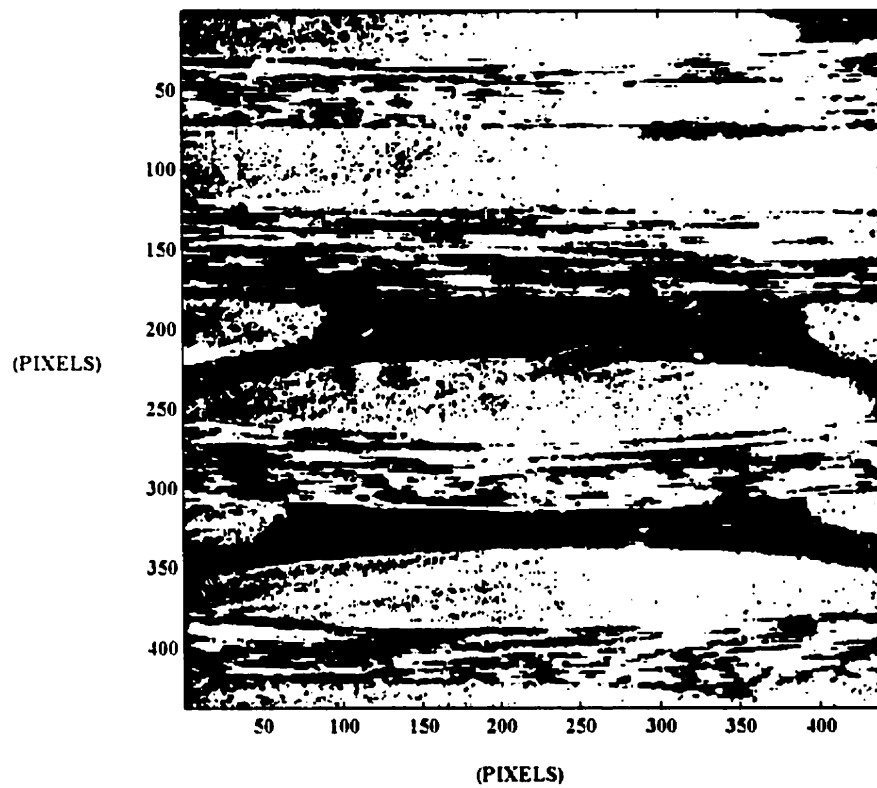
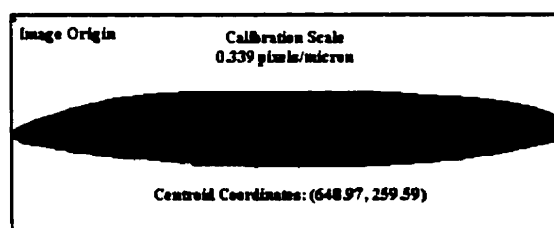


Figure 3.1. Evaluation of the tow cross-section geometry from a SEM micrograph of the 8HS woven composite plaque.

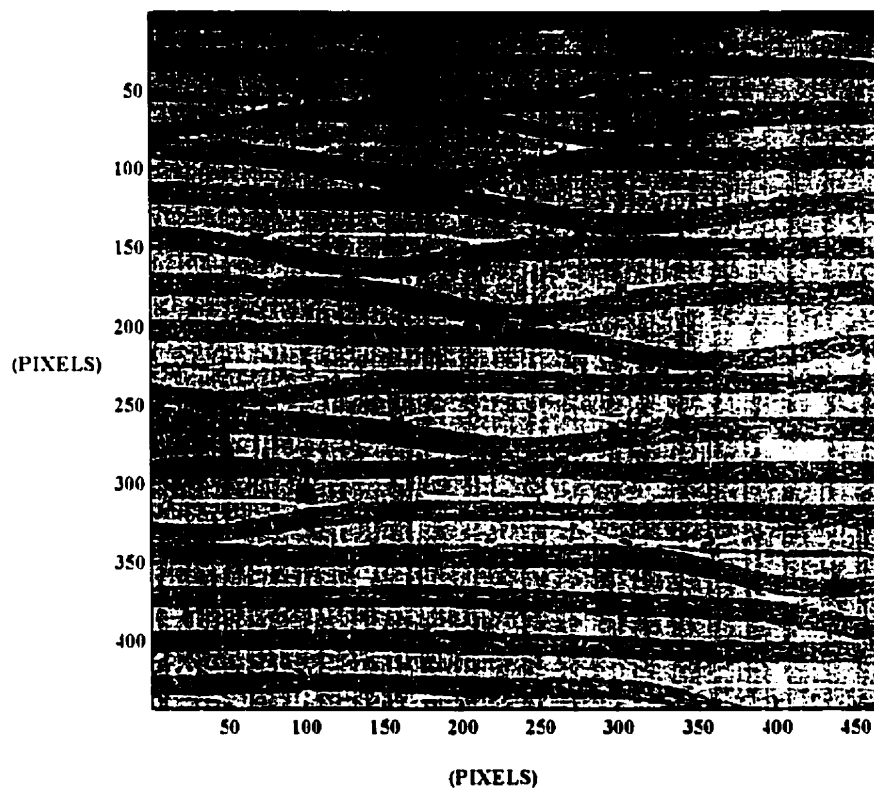


(a)

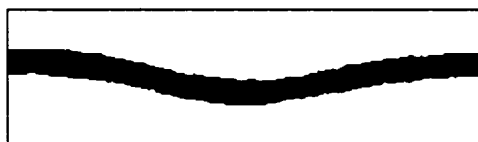


(b)

Figure 3.2. (a) Tow cross-section with thresholding applied to determine the perimeter, and (b) binary representation of the tow calibrated to the centroid for digitization.



(a)



(b)

Figure 3.3. (a) Evaluation of the woven tow undulation from a SEM micrograph of the 8HS woven composite plaque, and (b) binary representation of the undulation calibrated to the mutually orthogonal tow centroid for digitization.

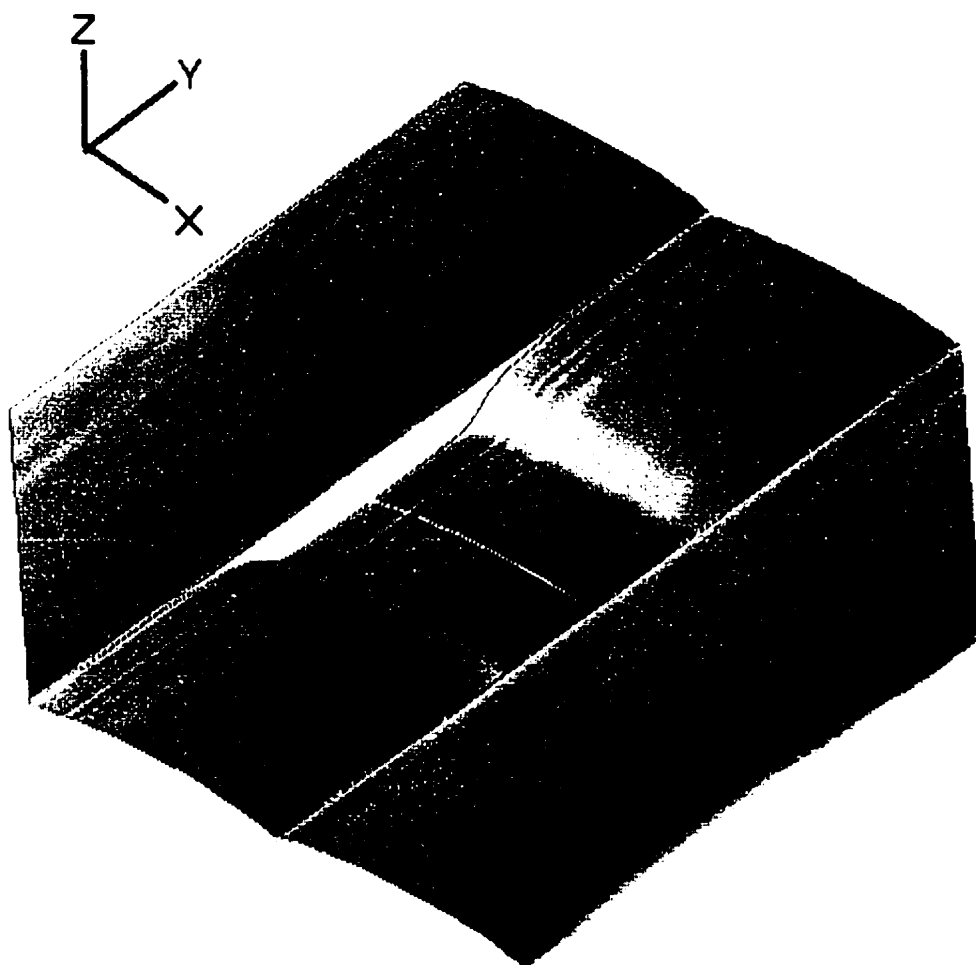


Figure 3.4. Rendition of the upper surfaces of the 8HS representative element derived from cubic spline interpolation and m^{th} -order polynomial approximations.

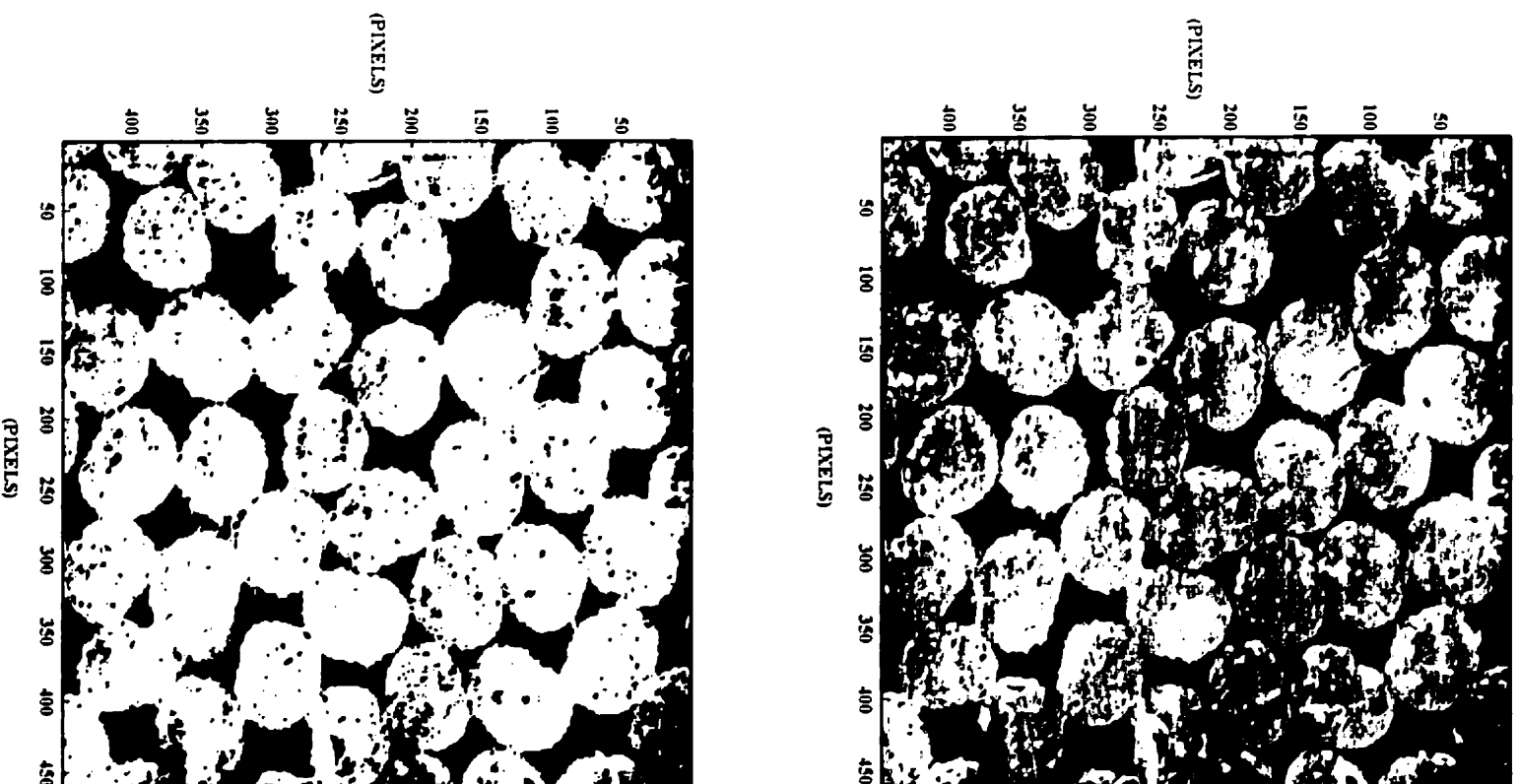


Figure 3.5. Evaluation of the woven tow V_f from image analysis of a SEM micrograph with applied thresholding.

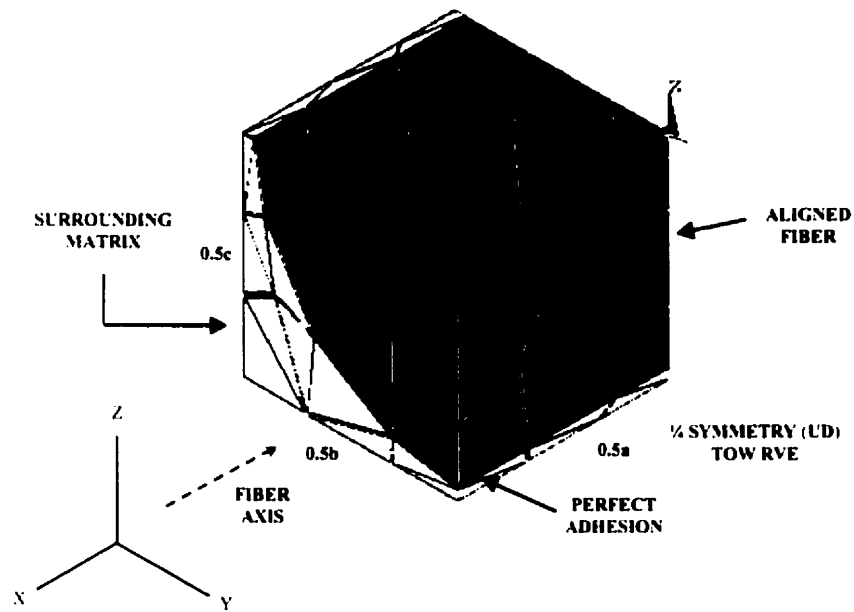


Figure 3.6. $1/4$ symmetry 3-D FE model assumed for the analysis of tow longitudinal elastic properties.

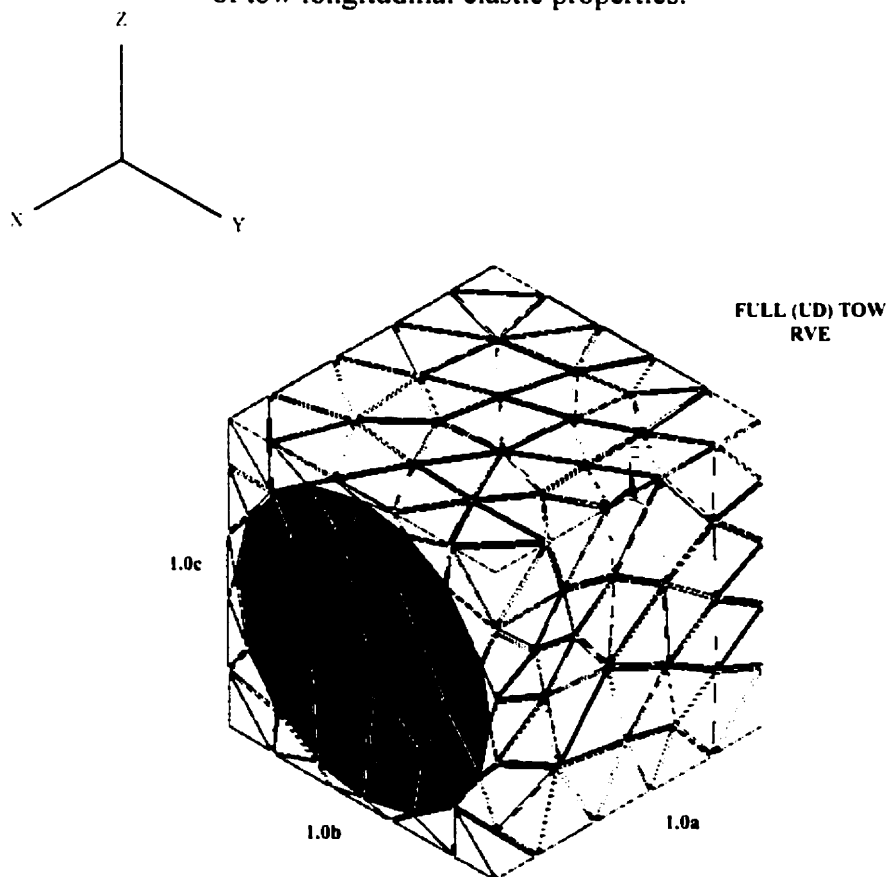
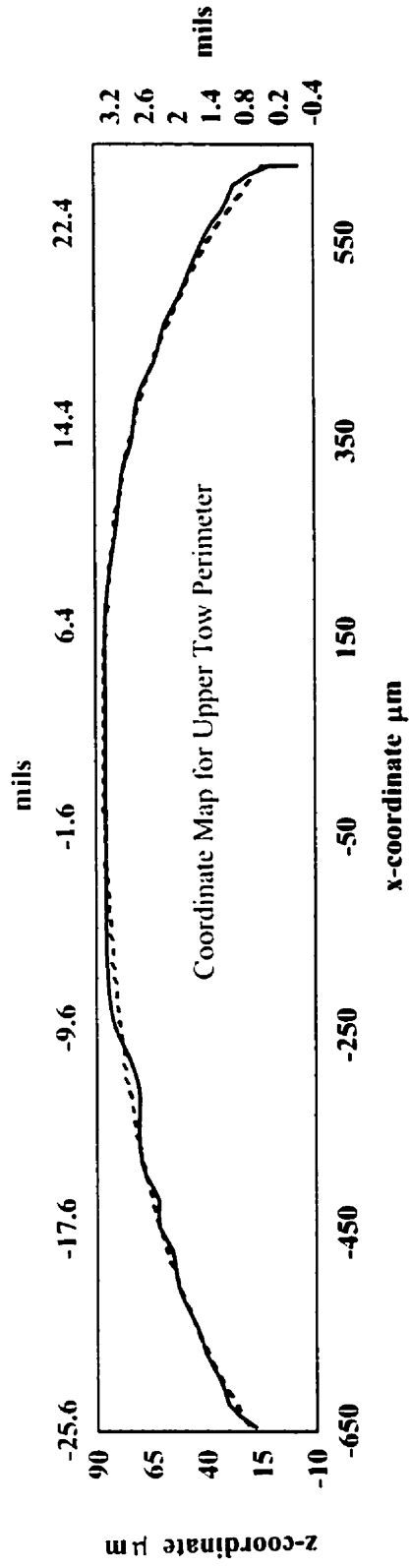


Figure 3.7. 3-D FE model assumed for the analysis of tow longitudinal and transverse shear elastic properties.



Upper Polynomial

$$y = -2E-10x^4 - 5E-08x^3 - 8E-05x^2 + 0.0109x + 86.37$$

$$R^2 = 0.987$$

Lower Polynomial

$$y = 5E-10x^4 - 4E-08x^3 + 1E-06x^2 + 0.0046x - 86.693$$

$$R^2 = 0.9866$$

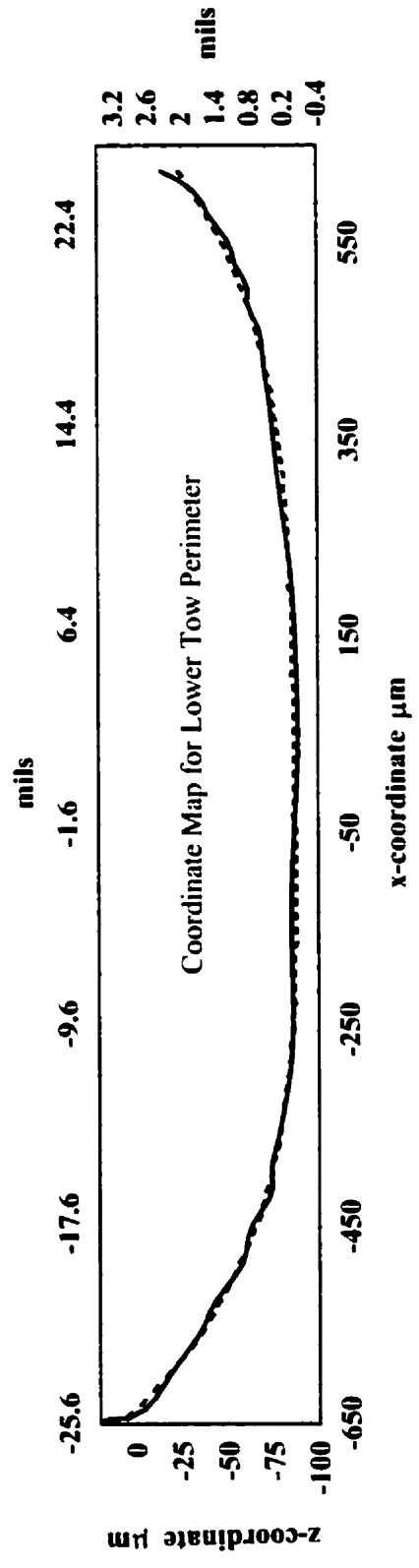
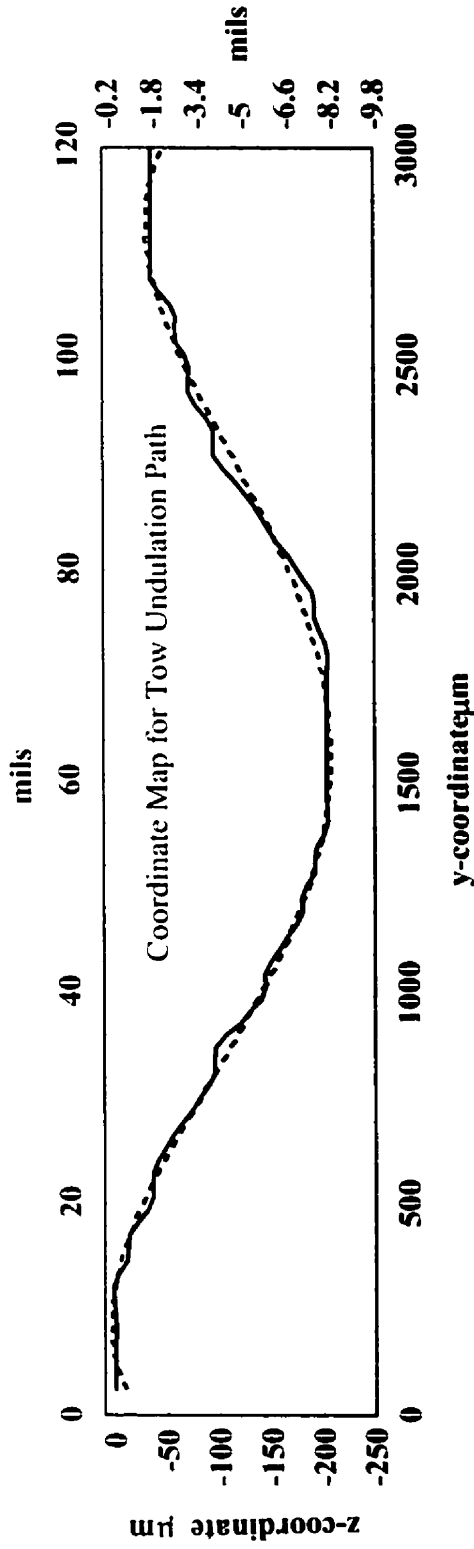


Figure 3.8. 4th-order polynomial fits to upper and lower woven tow cross-section perimeters halved about the respective tow centroid.



Tow Undulation Path Polynomial

$$y = -6.6E-11x^4 + 4.1E-07x^3 - 7.2E-04x^2 + 2.7E-01x - 24.2$$

$$R^2 = 0.9929$$

Figure 3.9. 4th-order polynomial fit to the woven tow undulation centerline with respect to the centroid of the mutually orthogonal tows.

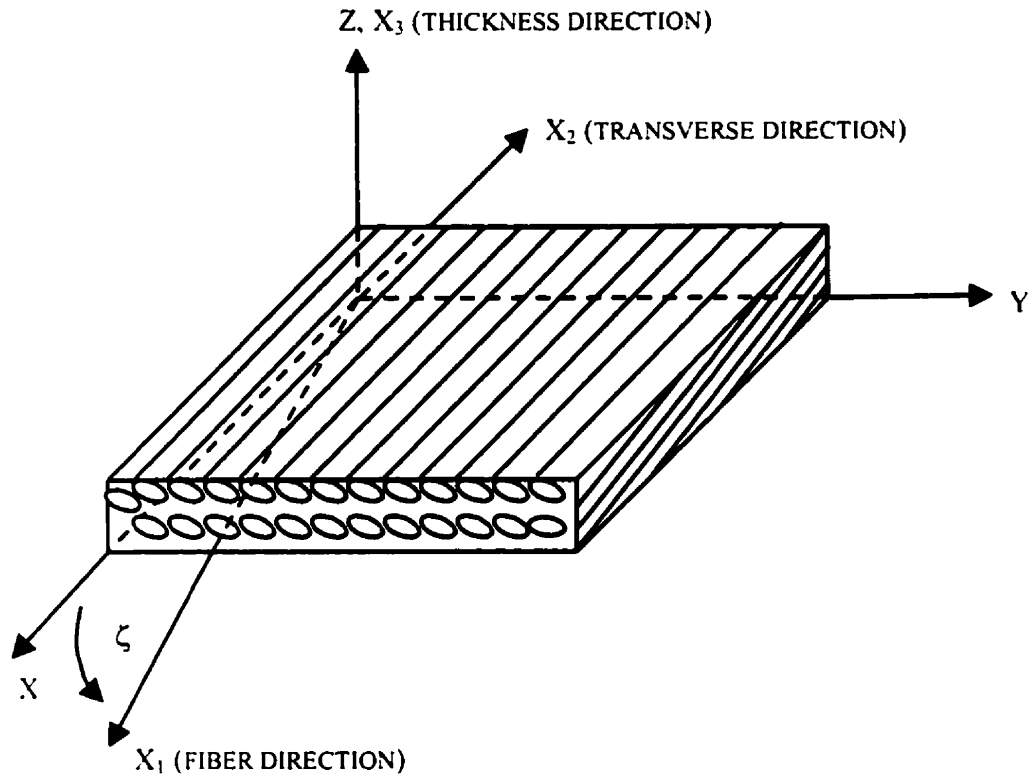


Figure 3.10. Definition of the off-axis angle of undulation for evaluation of average transformed reduced compliance relative to the principal material coordinates.

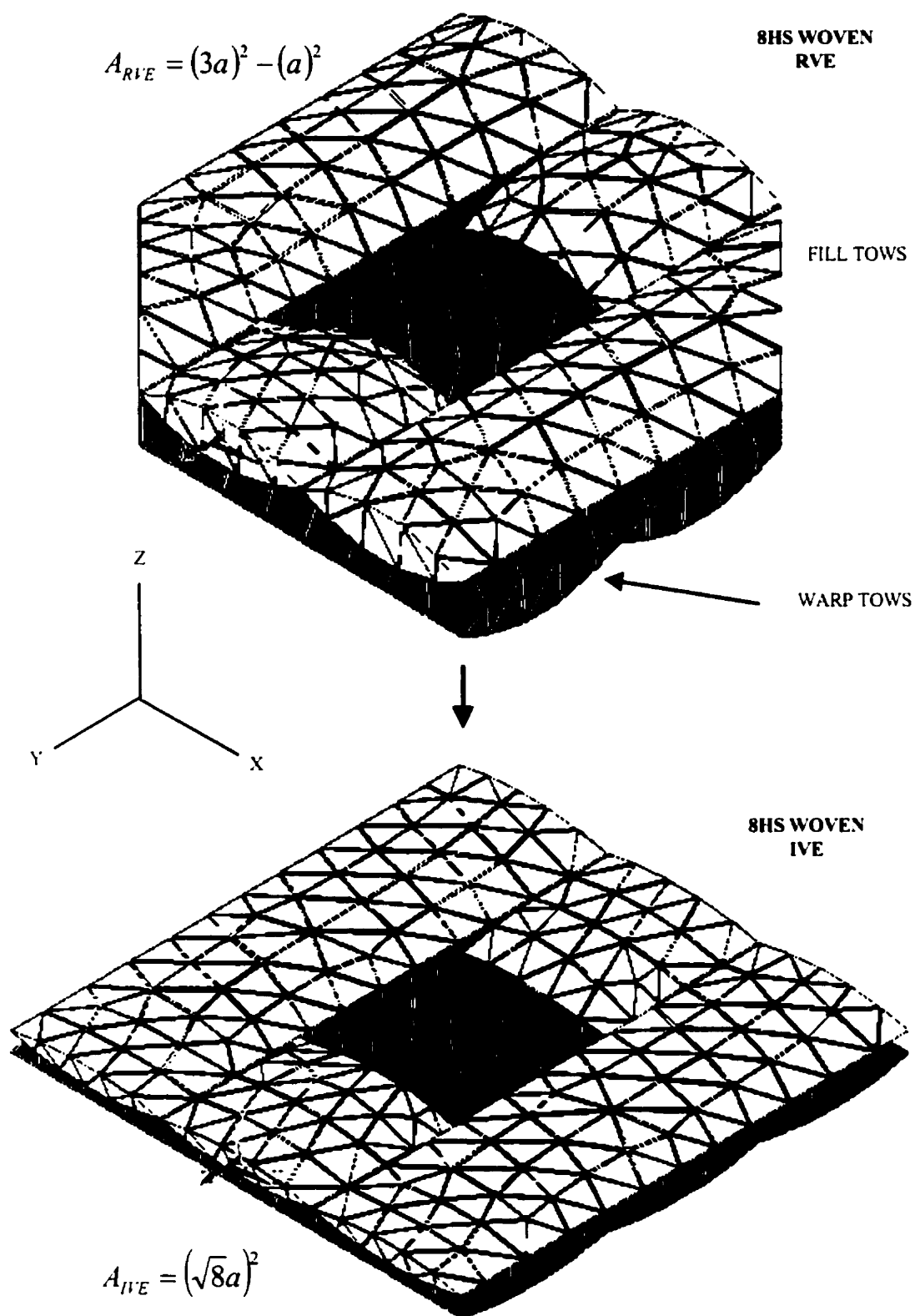


Figure 3.11. Evolution of the idealized volume element (IVE) FE model from the representative volume element (RVE).

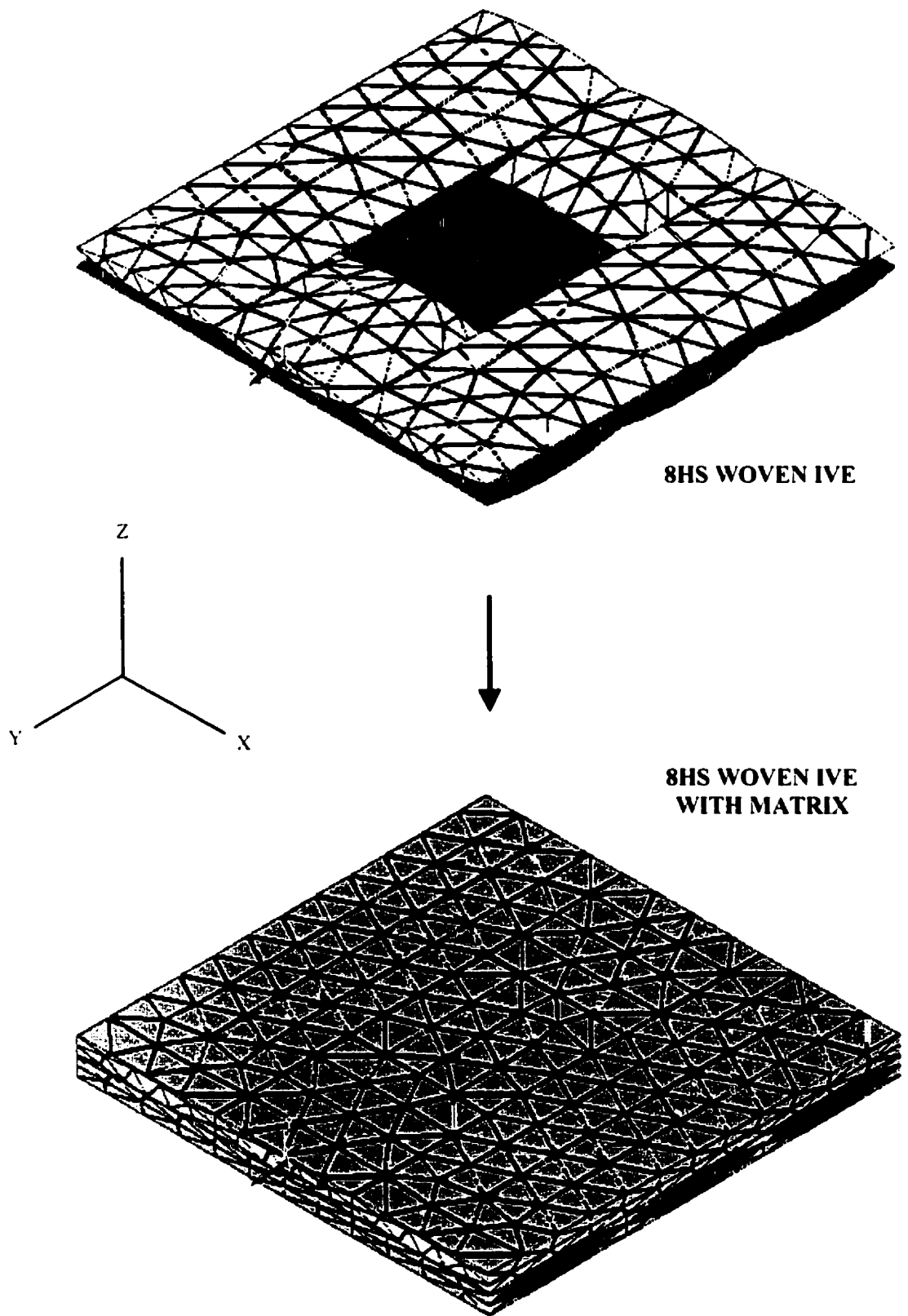
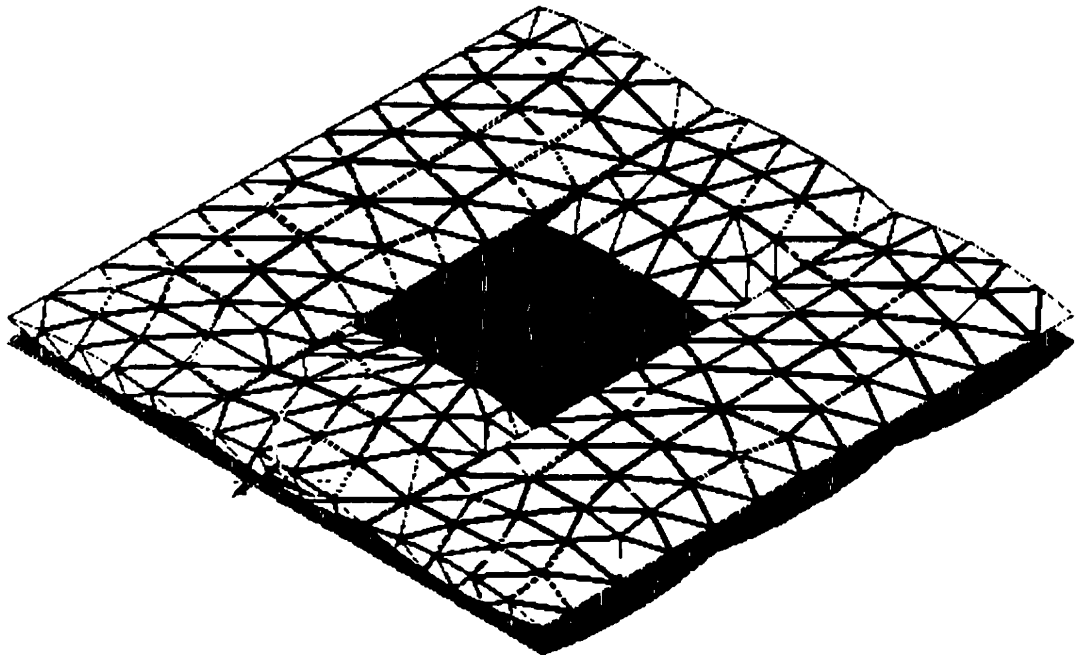
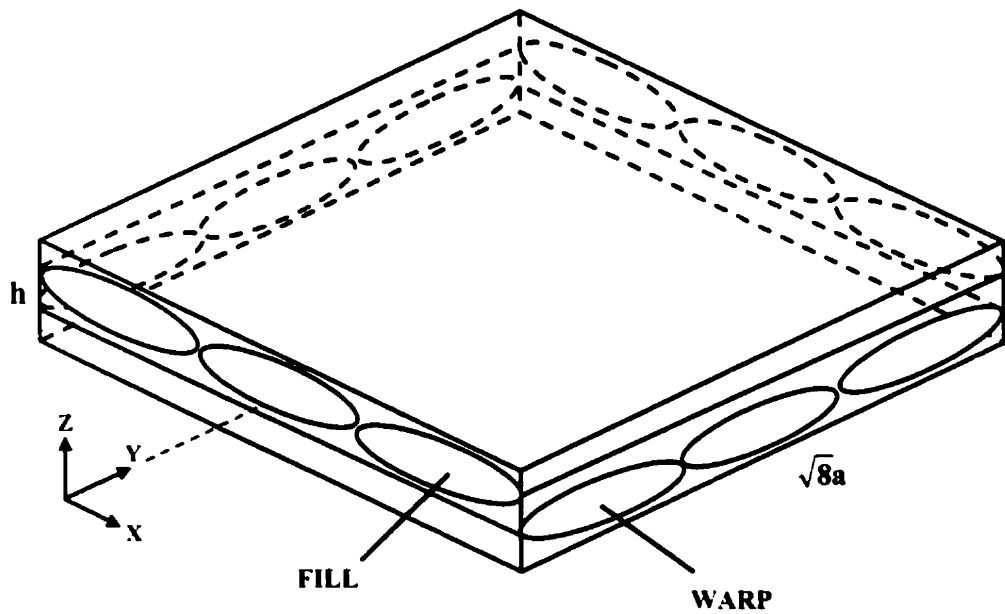


Figure 3.12. 3-D FE model assumed for the analysis of 8HS woven fabric composite elastic properties.



(a)



(b)

Figure 3.13. (a) Finite element discretization of 8HS woven IVE into 4757 elements and 9474 nodes using 10-node tetrahedral elements, and (b) coordinate system used to identify imposed boundary constraints.

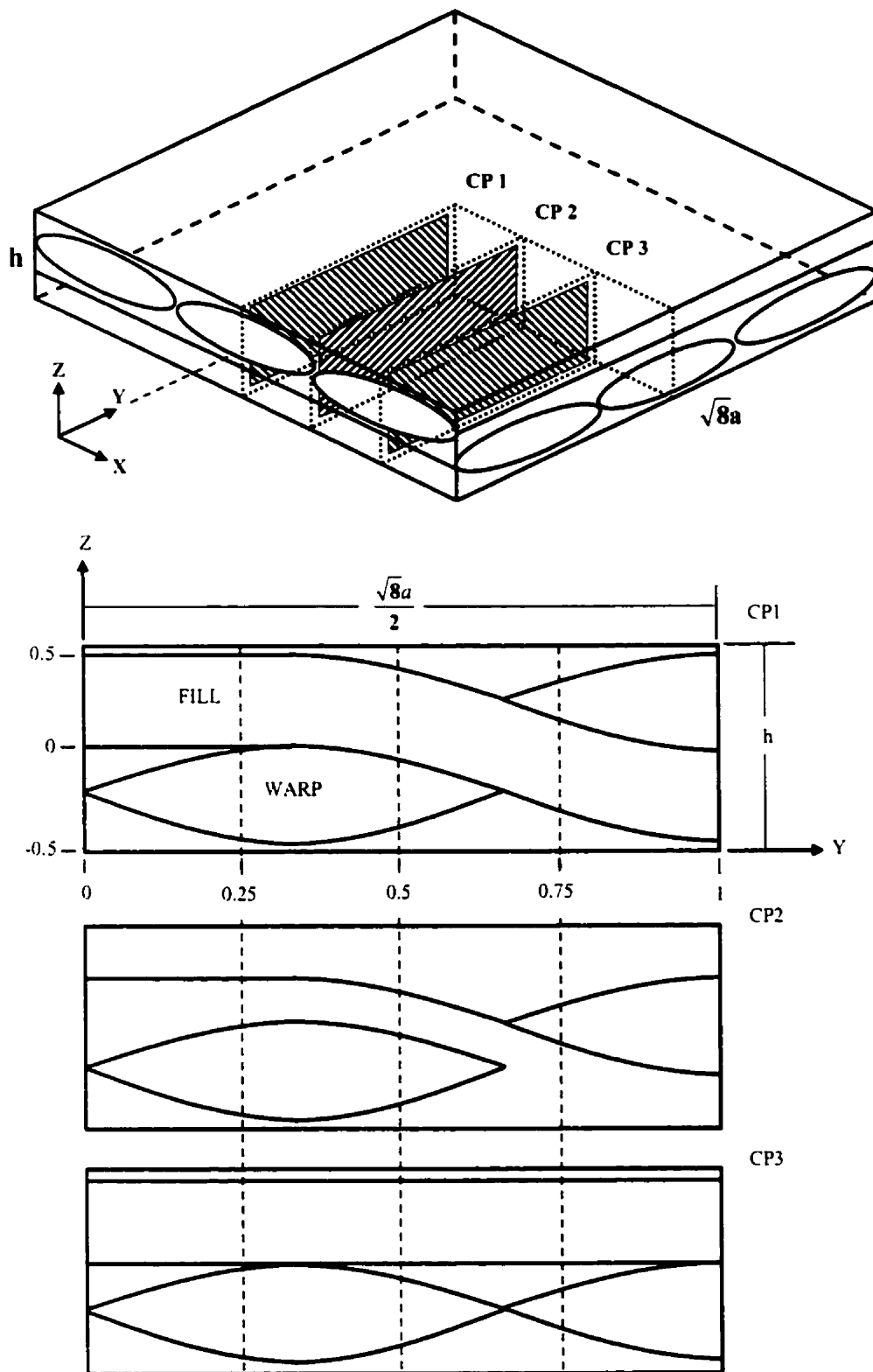


Figure 3.14. Orientation of CP1-3 within the volume element and transition of cross-sectional tow geometries from CP1-3.

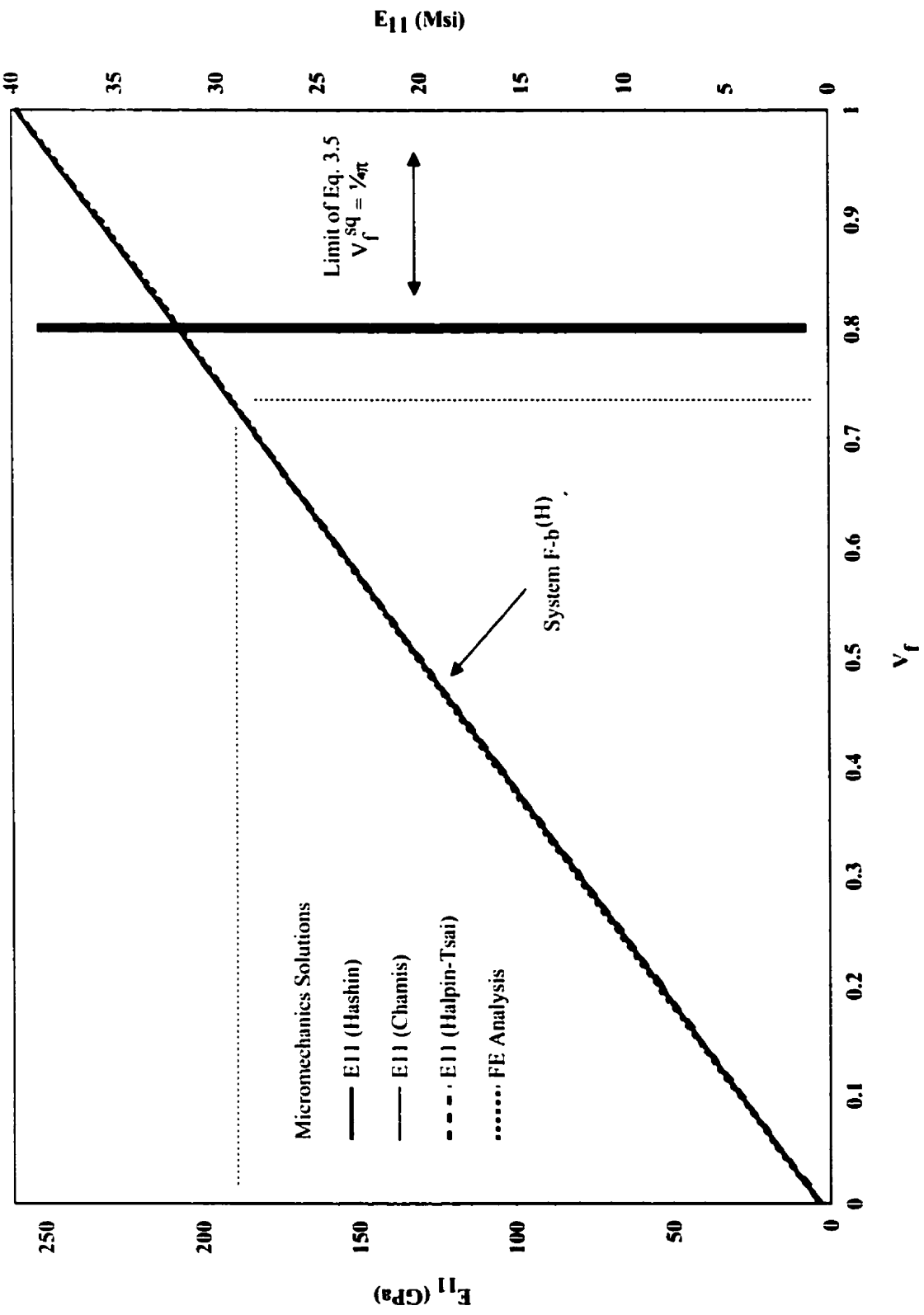


Figure 3.15. Comparison between the FE analysis and micromechanics solutions for the woven tow longitudinal tensile modulus E_{11} over the range of V_f from 0 to 1.

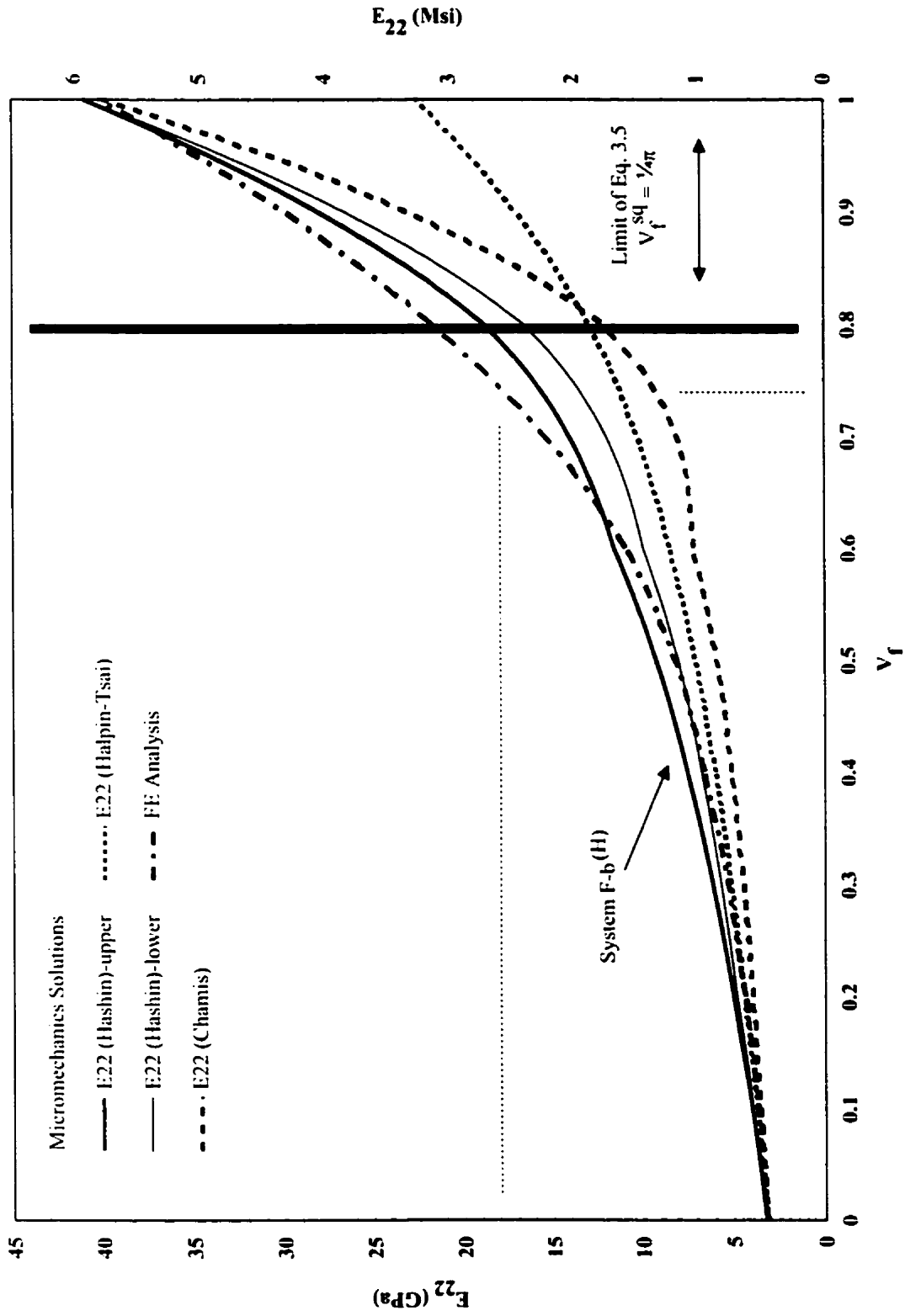


Figure 3.16. Comparison between the FE analysis and micromechanics solutions for the woven tow transverse tensile modulus E_{22} over the range of V_f from 0 to 1.

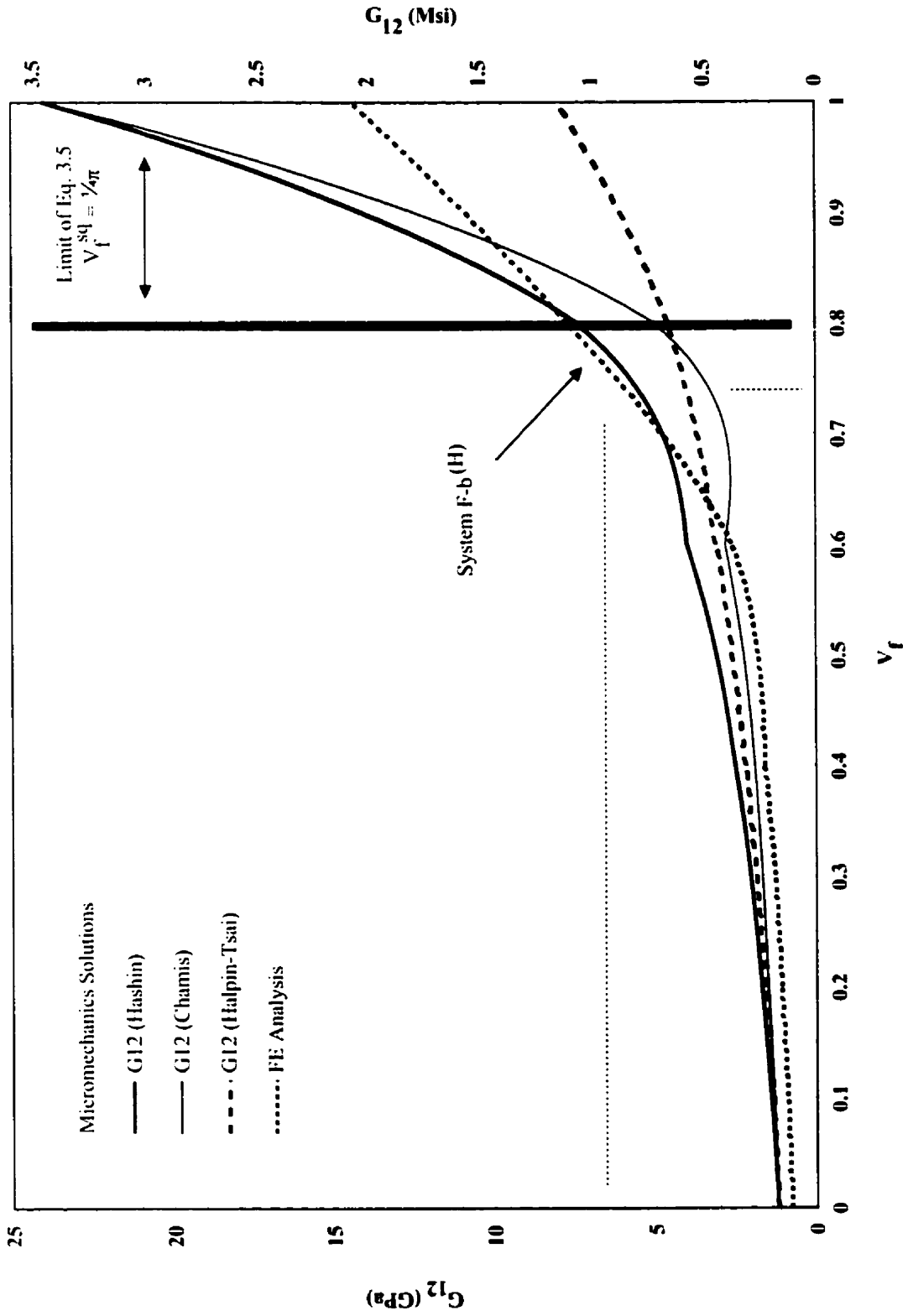


Figure 3.17. Comparison between the FE analysis and micromechanics solutions for the woven tow longitudinal shear modulus G_{12} over the range of V_f from 0 to 1.

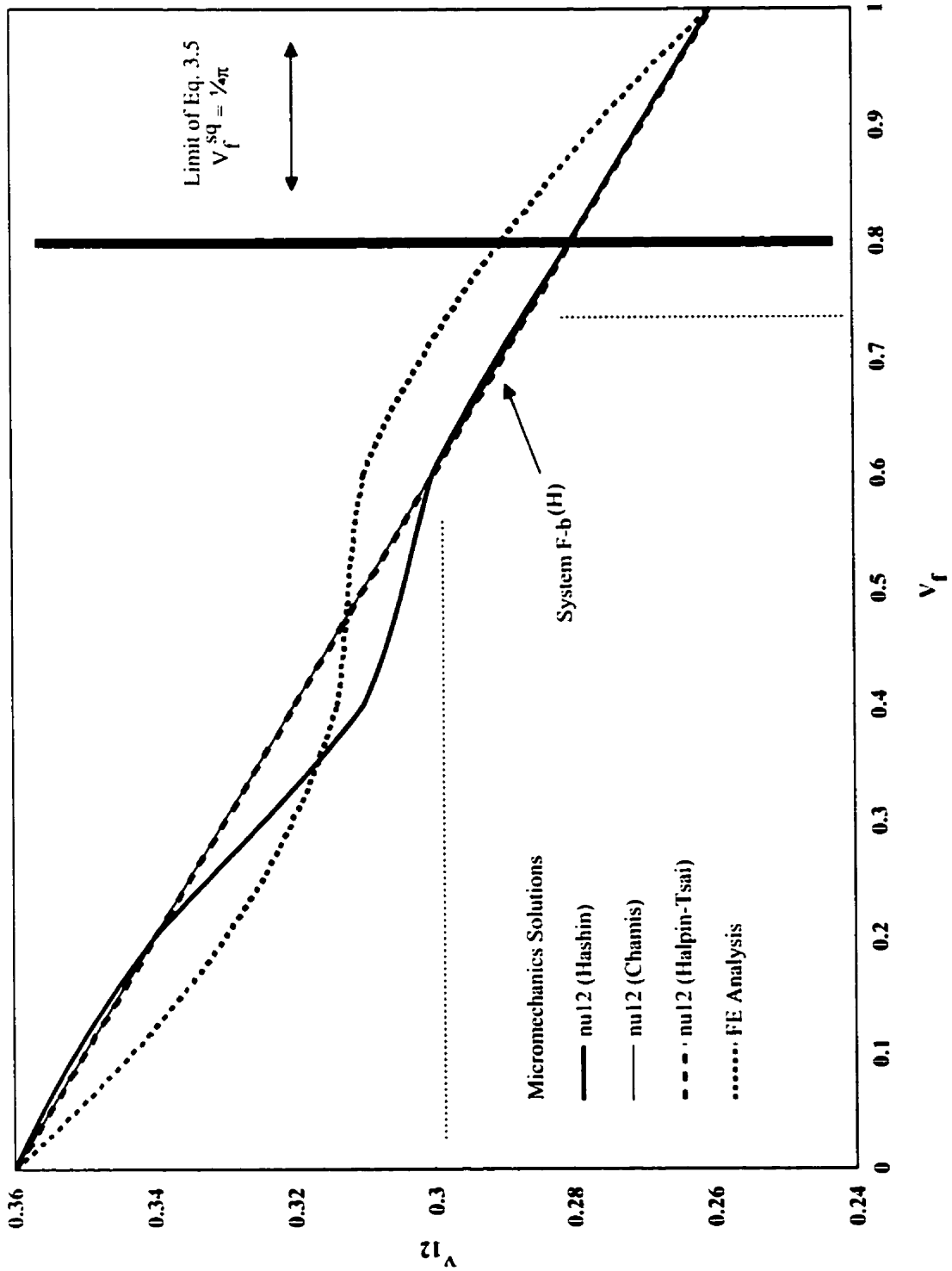


Figure 3.18. Comparison between the FE analysis and micromechanics solutions for the woven tow longitudinal Poisson's ratio ν_{12} over the range of V_f from 0 to 1.

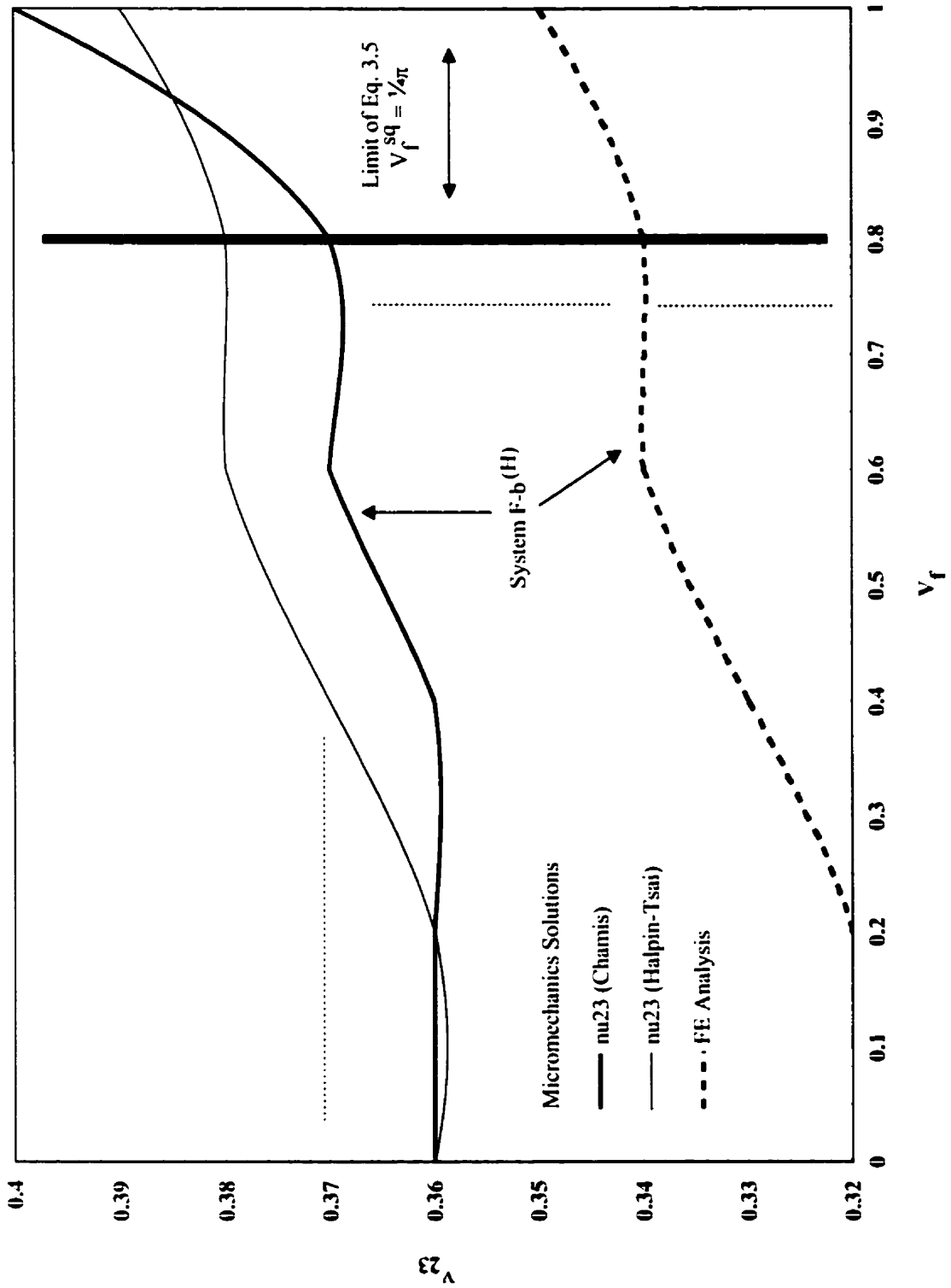


Figure 3.19. Comparison between the FE analysis and micromechanics solutions for the woven tow transverse Poisson's ratio ν_{23} over the range of V_f from 0 to 1.

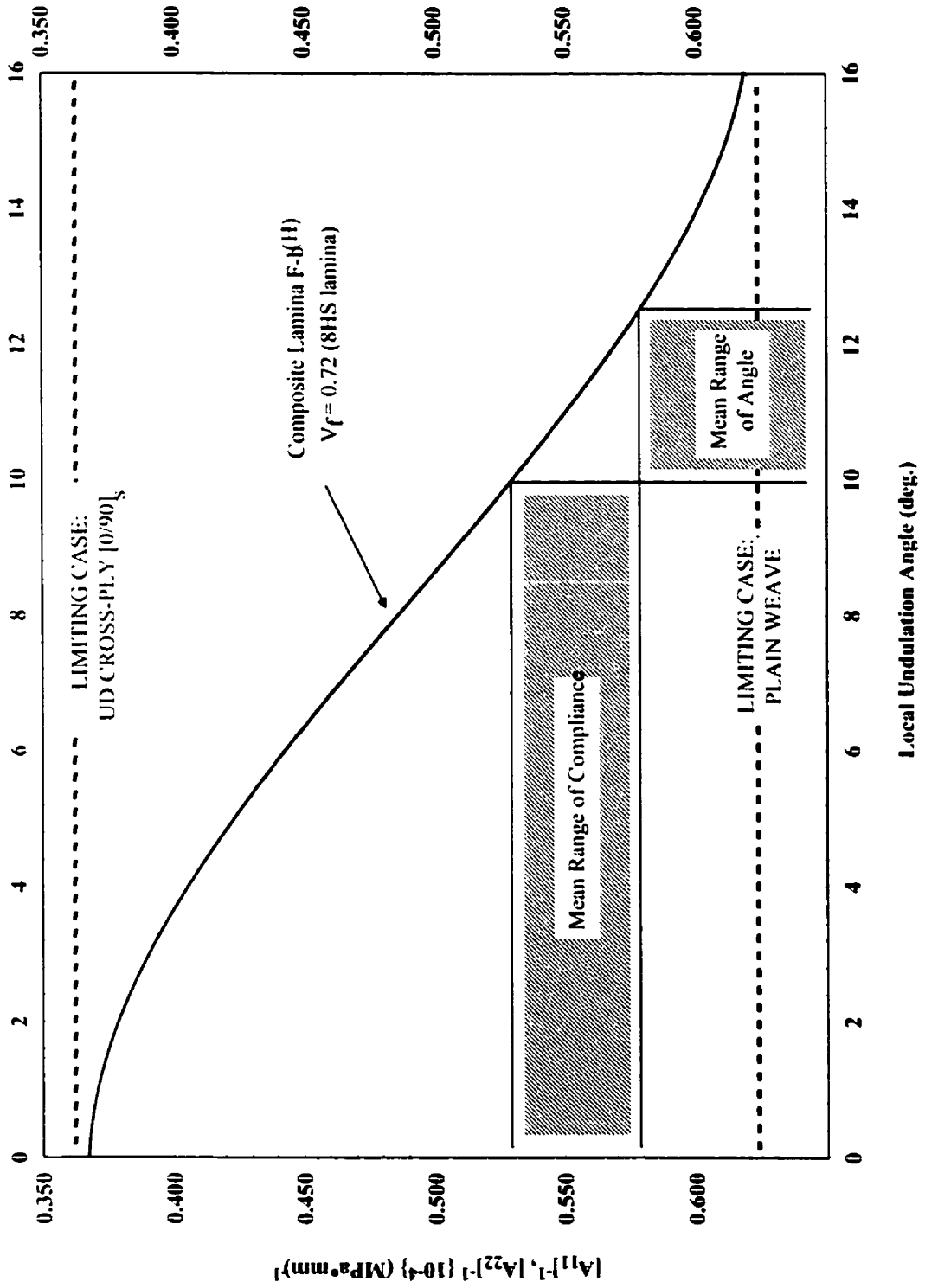


Figure 3.20. Variation in 8HS woven fabric lamina extensional compliances over the range of local angles of undulation from 0° to 16° as predicted by the current model.

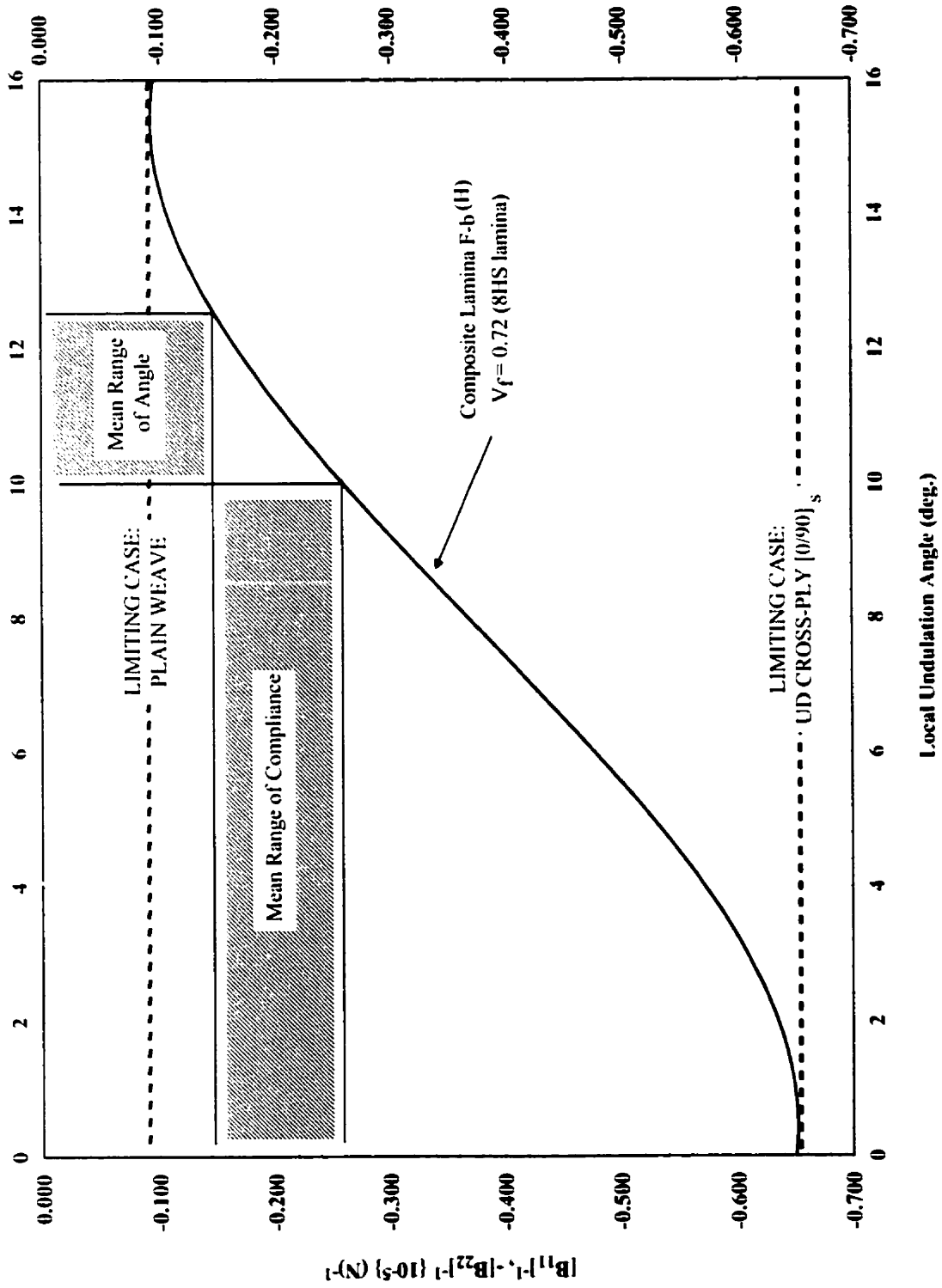


Figure 3.21. Variation in 8HS woven fabric lamina extension-bending coupling compliances over the range of local angles of undulation from 0° to 16° as predicted by the current model.

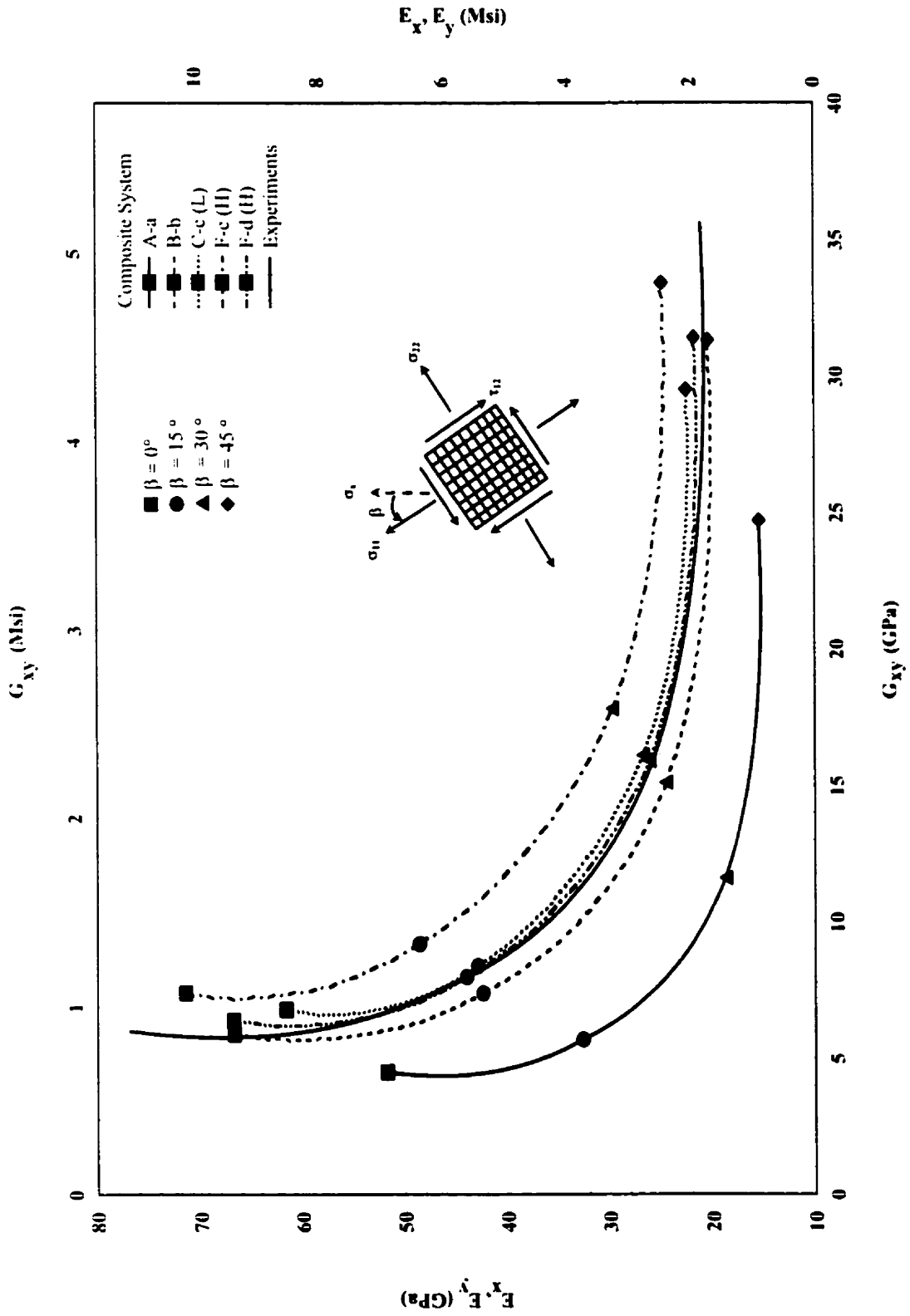


Figure 3.22. E_x/E_y - G_{xy} chart mapping the off-axis elastic behavior for several composite systems considered against experimental data (c.f. Section 4).

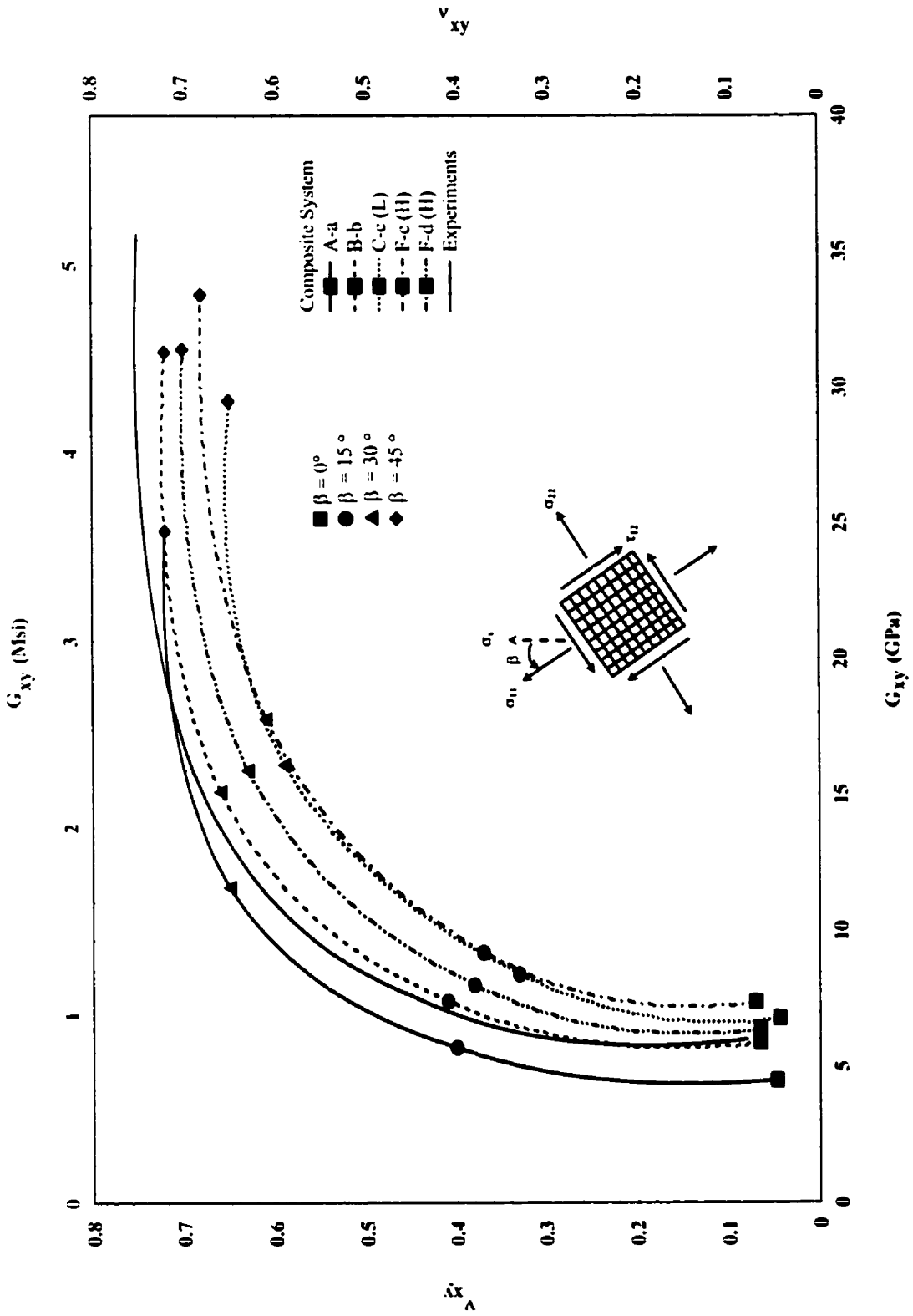


Figure 3.23. ν_{xy} - G_{xy} chart mapping the off-axis elastic behavior for several composite systems considered against experimental data (c.f. Section 4).

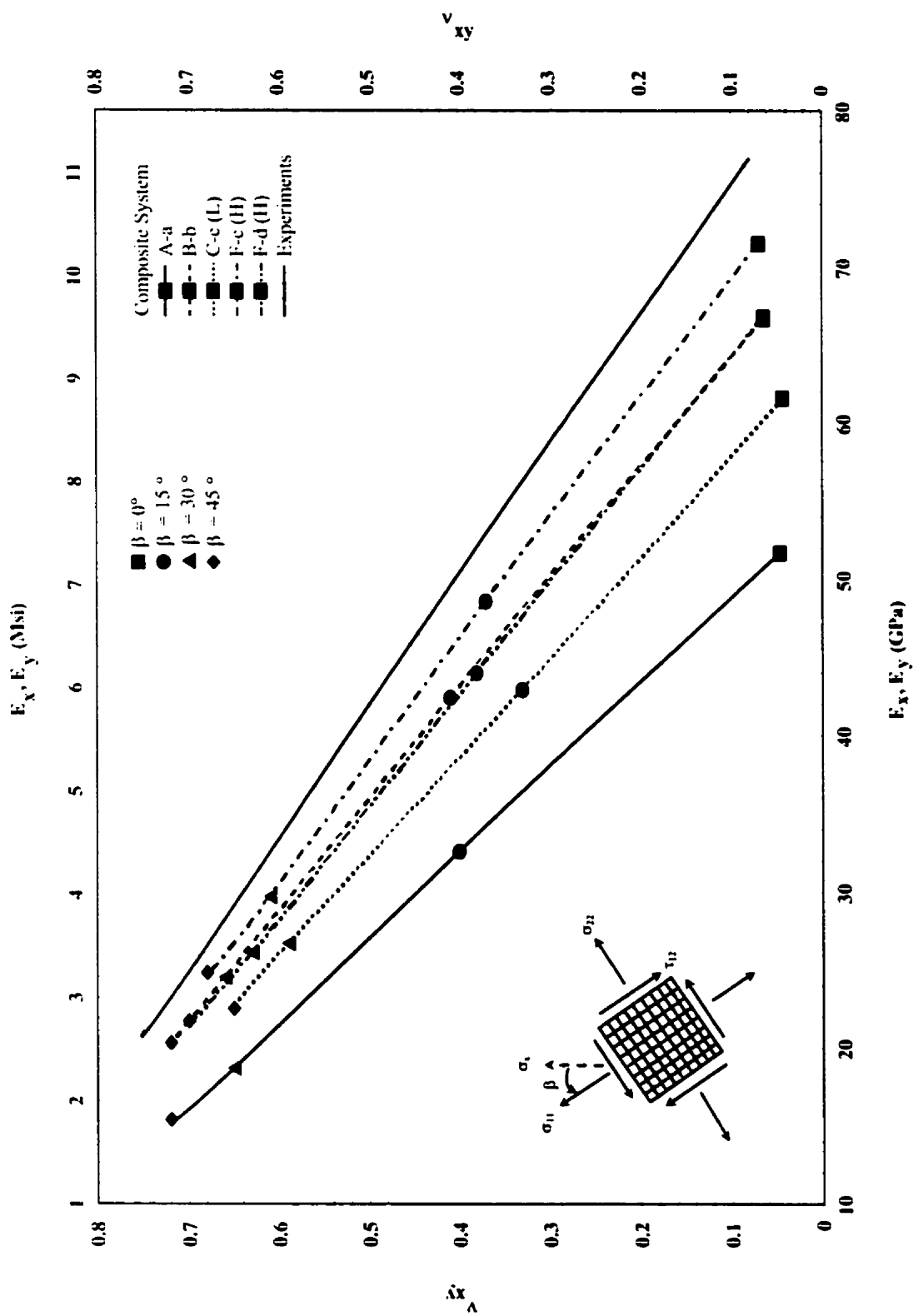


Figure 3.24. ν_{xy} - E_x - E_y chart mapping the off-axis elastic behavior for several composite systems considered against experimental data (c.f. Section 4).

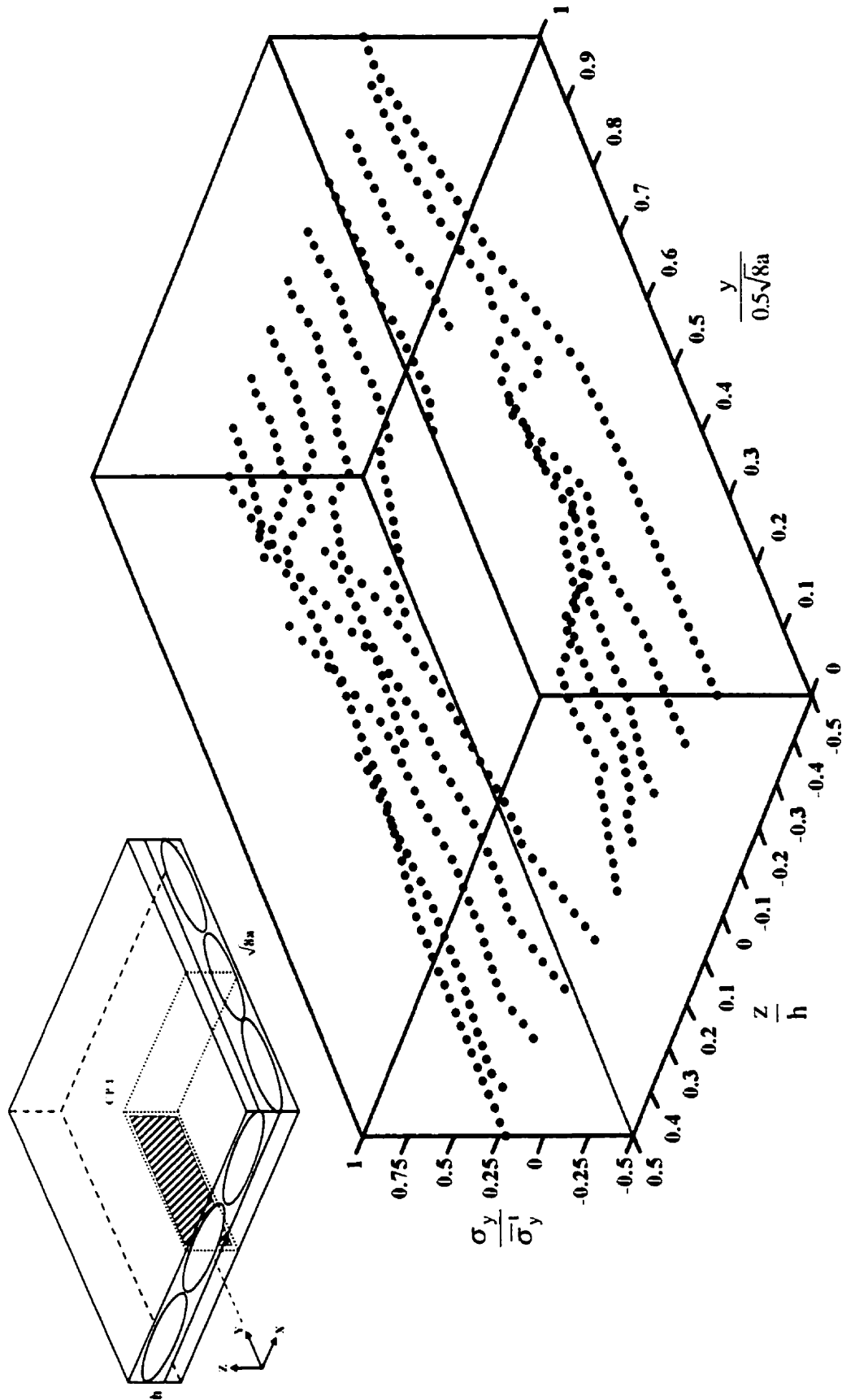


Figure 3.25. Sample 490 point data set for normalized uniaxial tensile stress within CPI (tension).

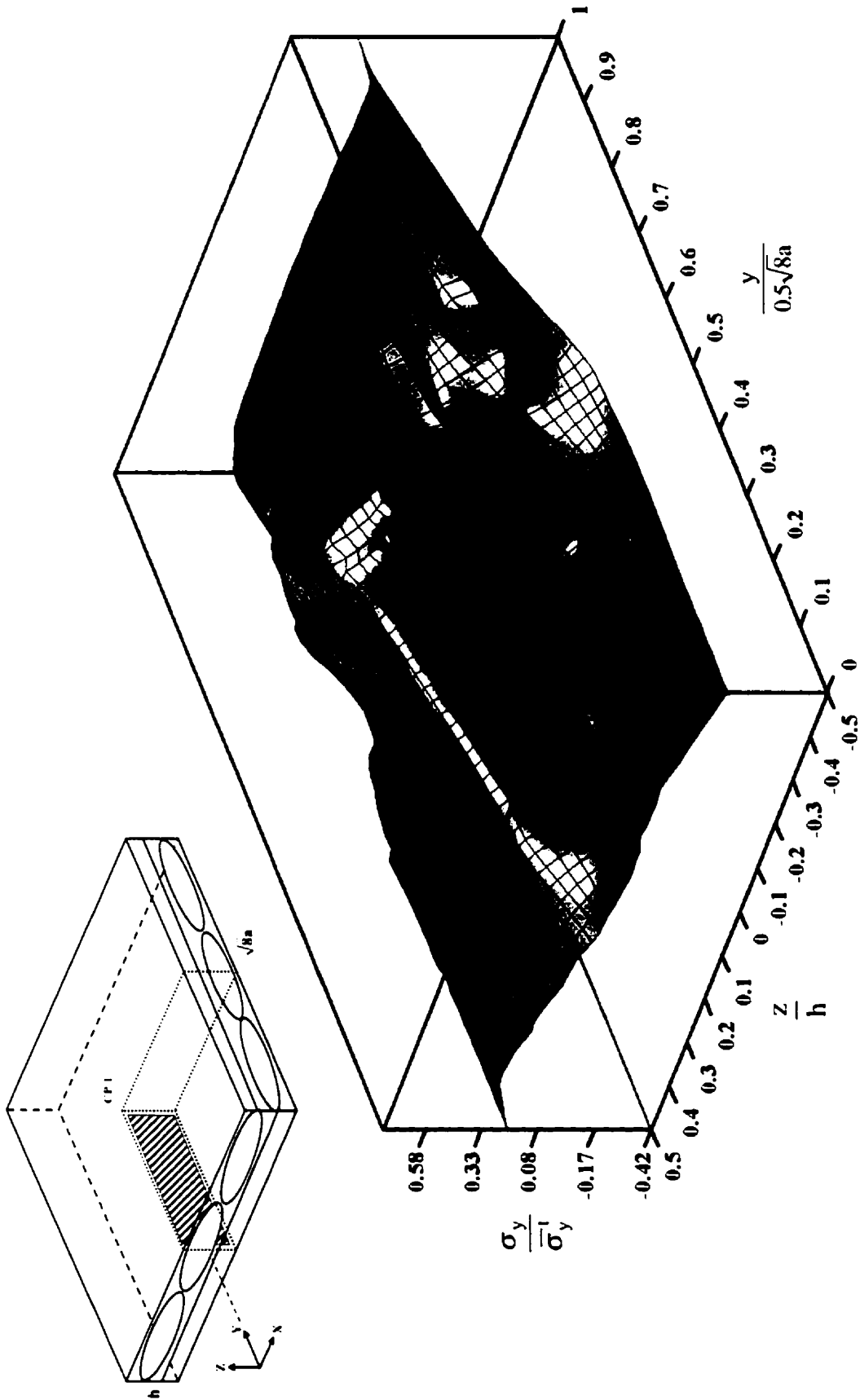


Figure 3.26(a). Uniaxial tensile stress distribution within CPI under applied uniaxial tension.

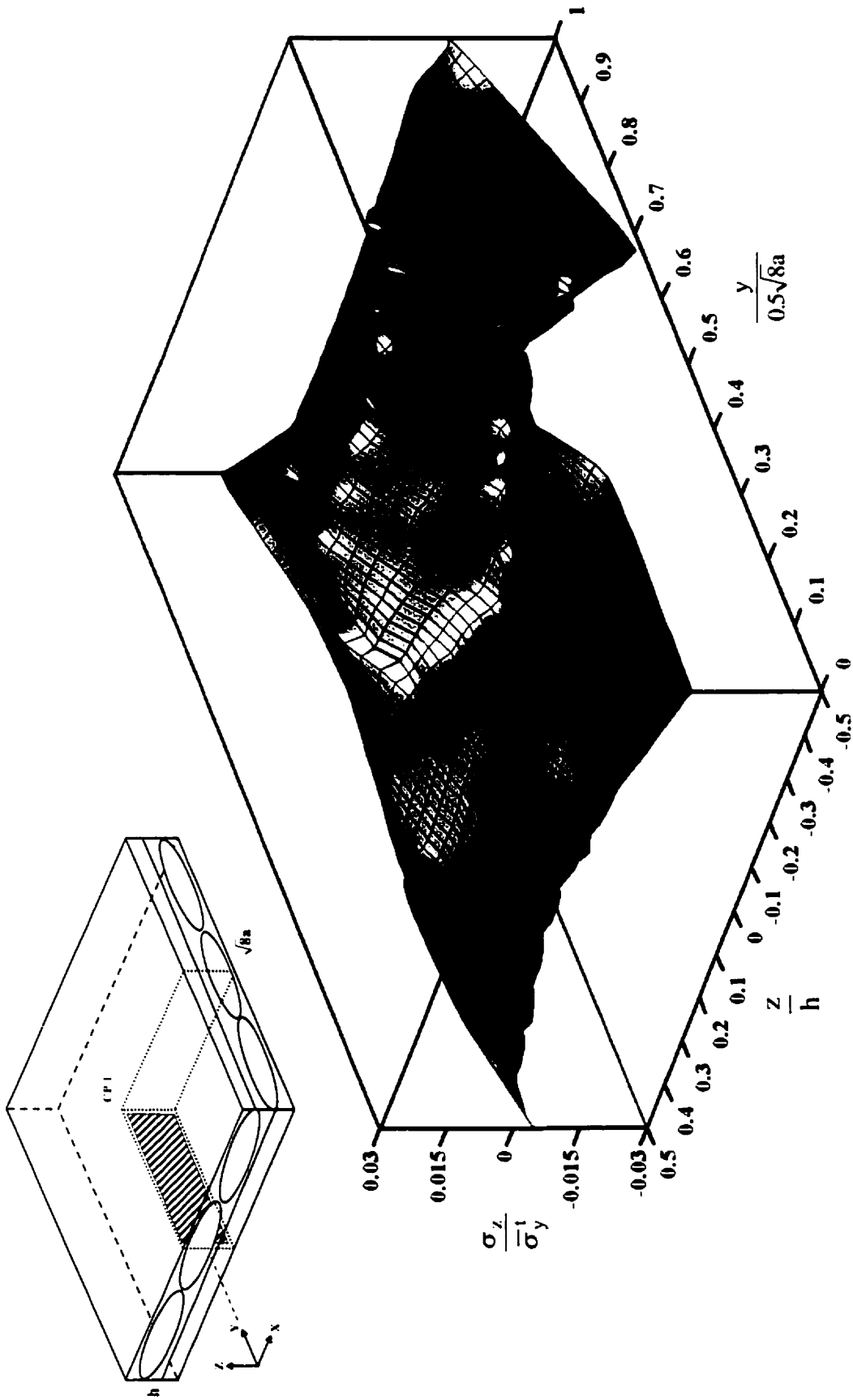


Figure 3.26(b). Uniaxial transverse normal stress distribution within CP1 under applied uniaxial tension.

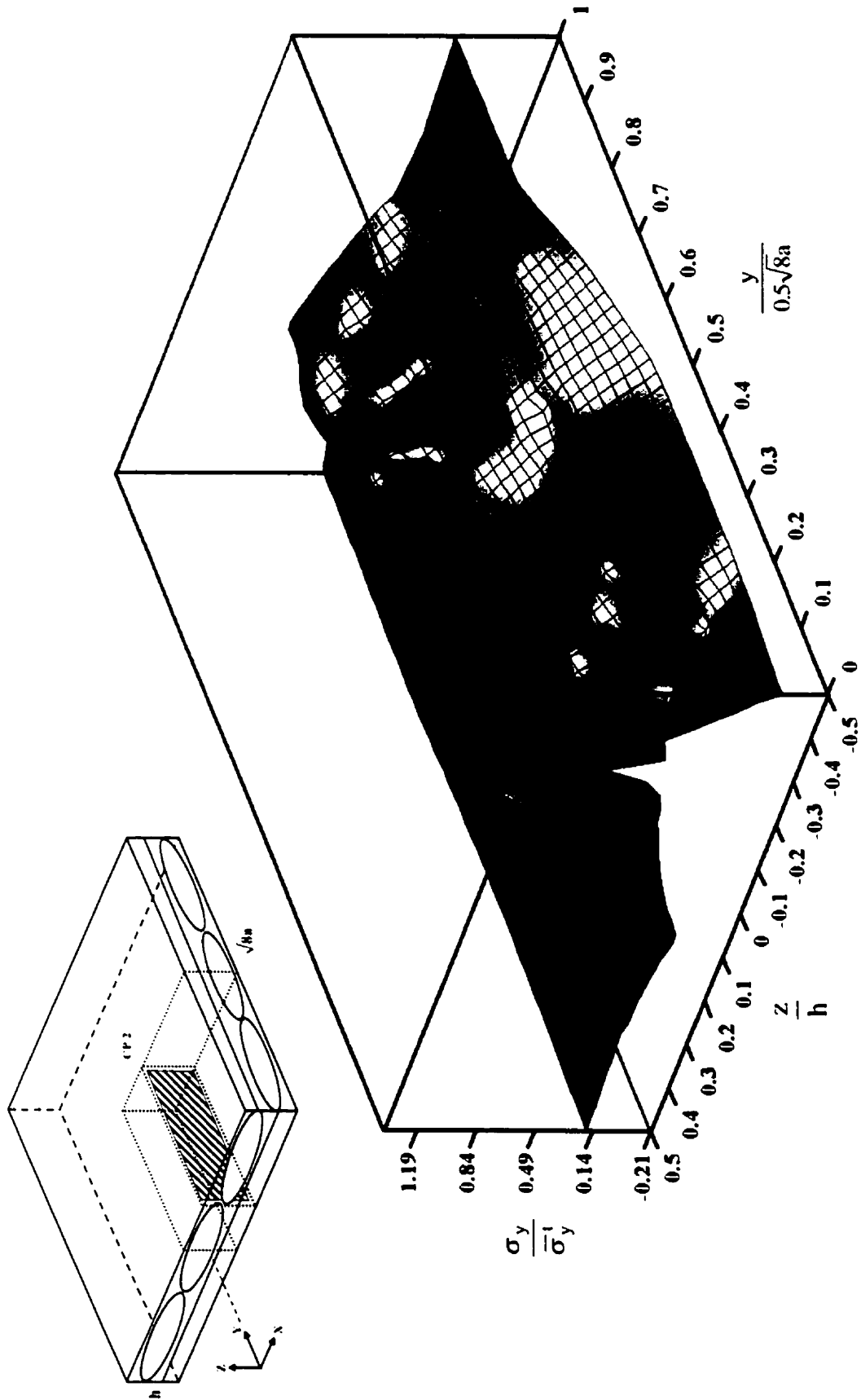


Figure 3.27(a). Uniaxial tensile stress distribution within CP2 under applied uniaxial tension.

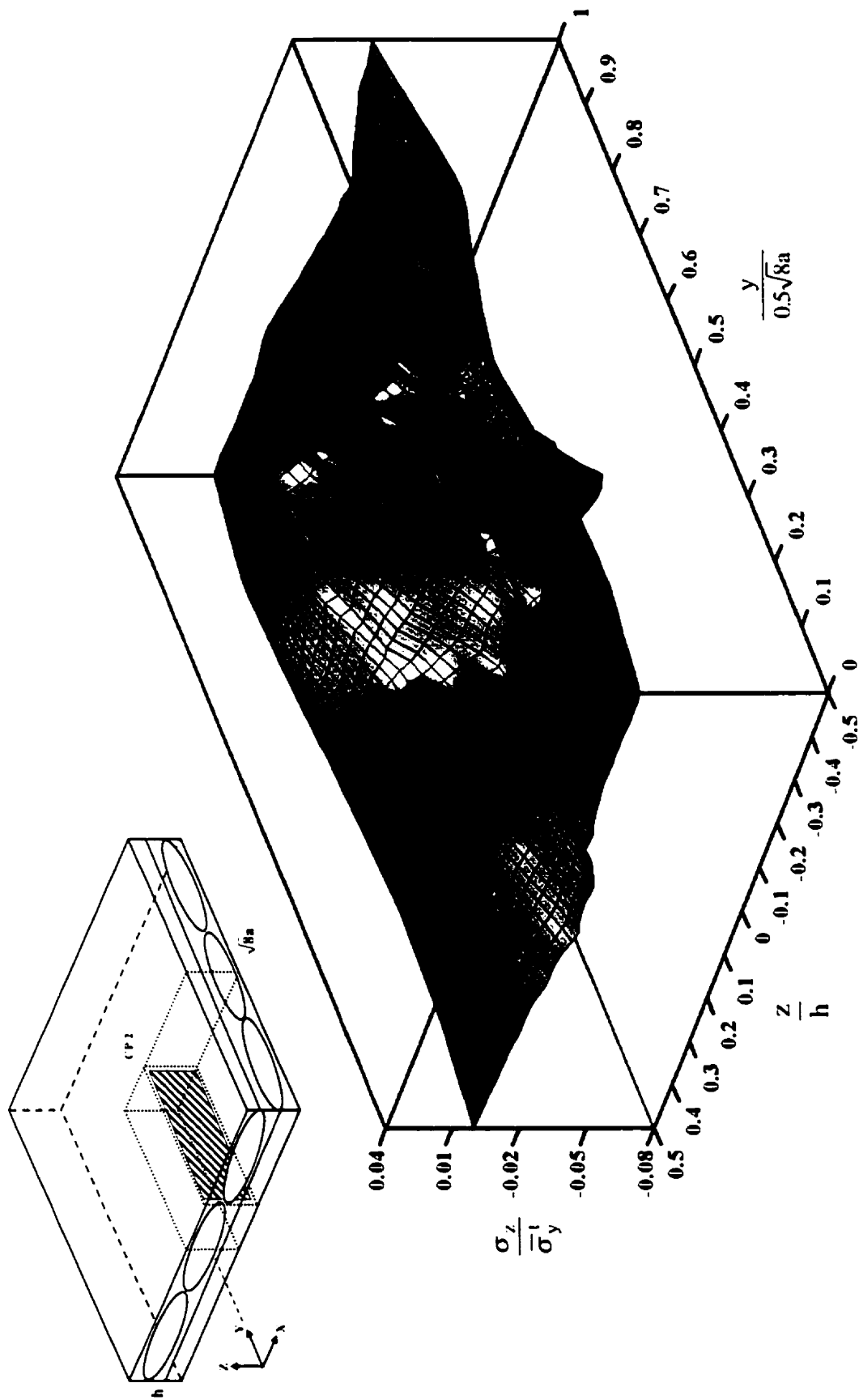


Figure 3.27(b). Uniaxial transverse normal stress distribution within CP2 under applied uniaxial tension.

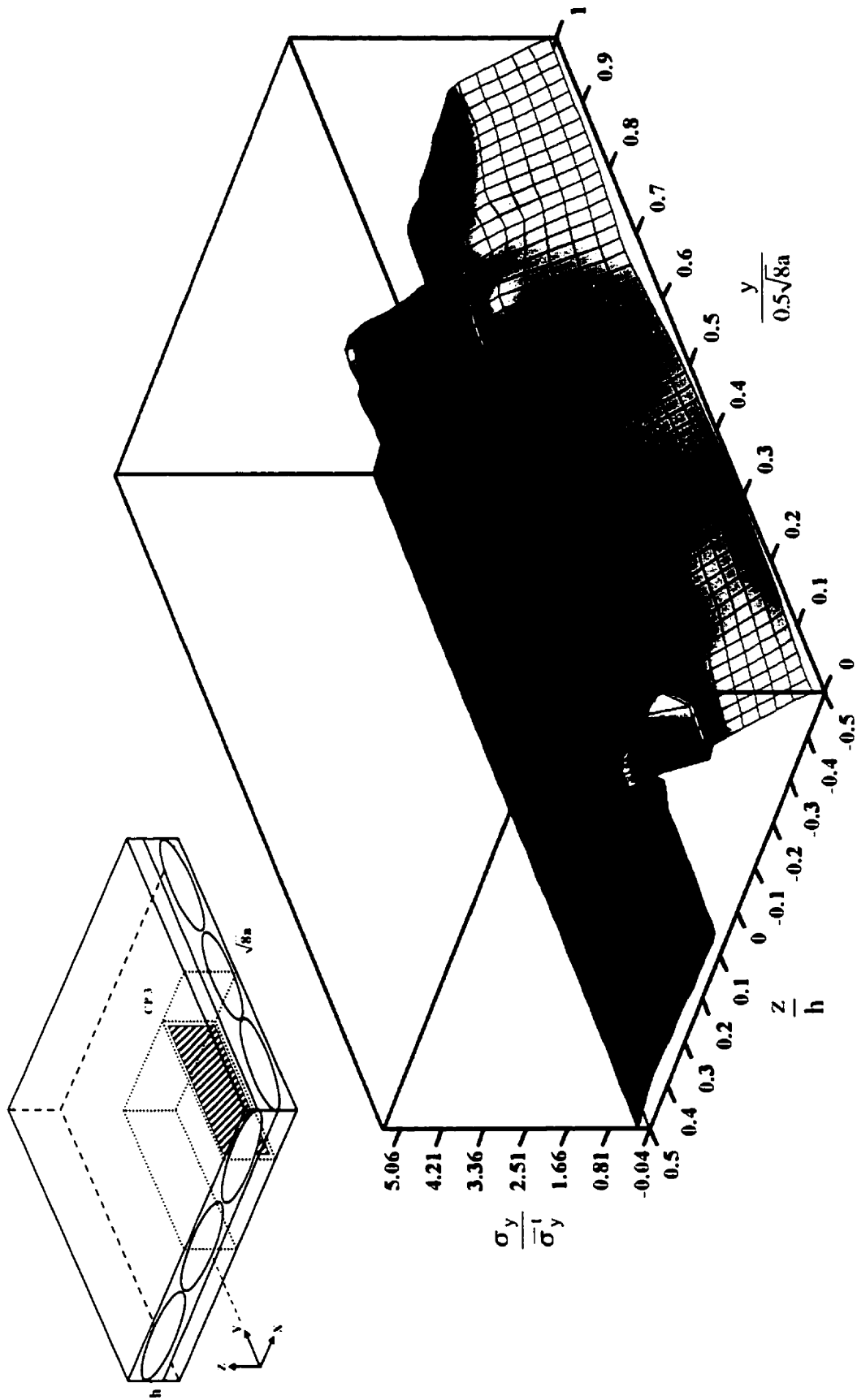


Figure 3.28(a). Uniaxial tensile stress distribution within CP3 under applied uniaxial tension.

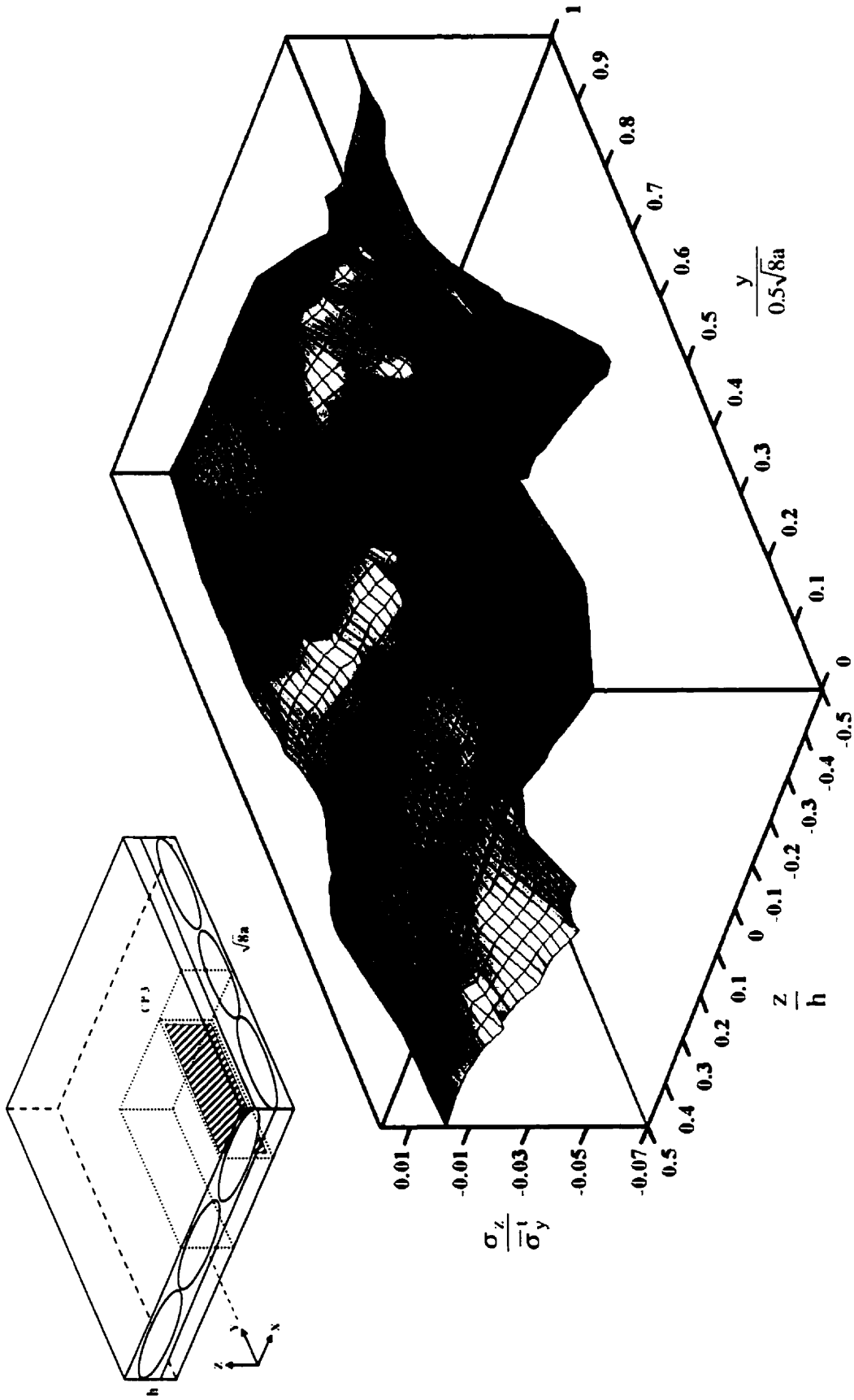


Figure 3.28(b). Uniaxial transverse normal stress distribution within CP3 under applied uniaxial tension.

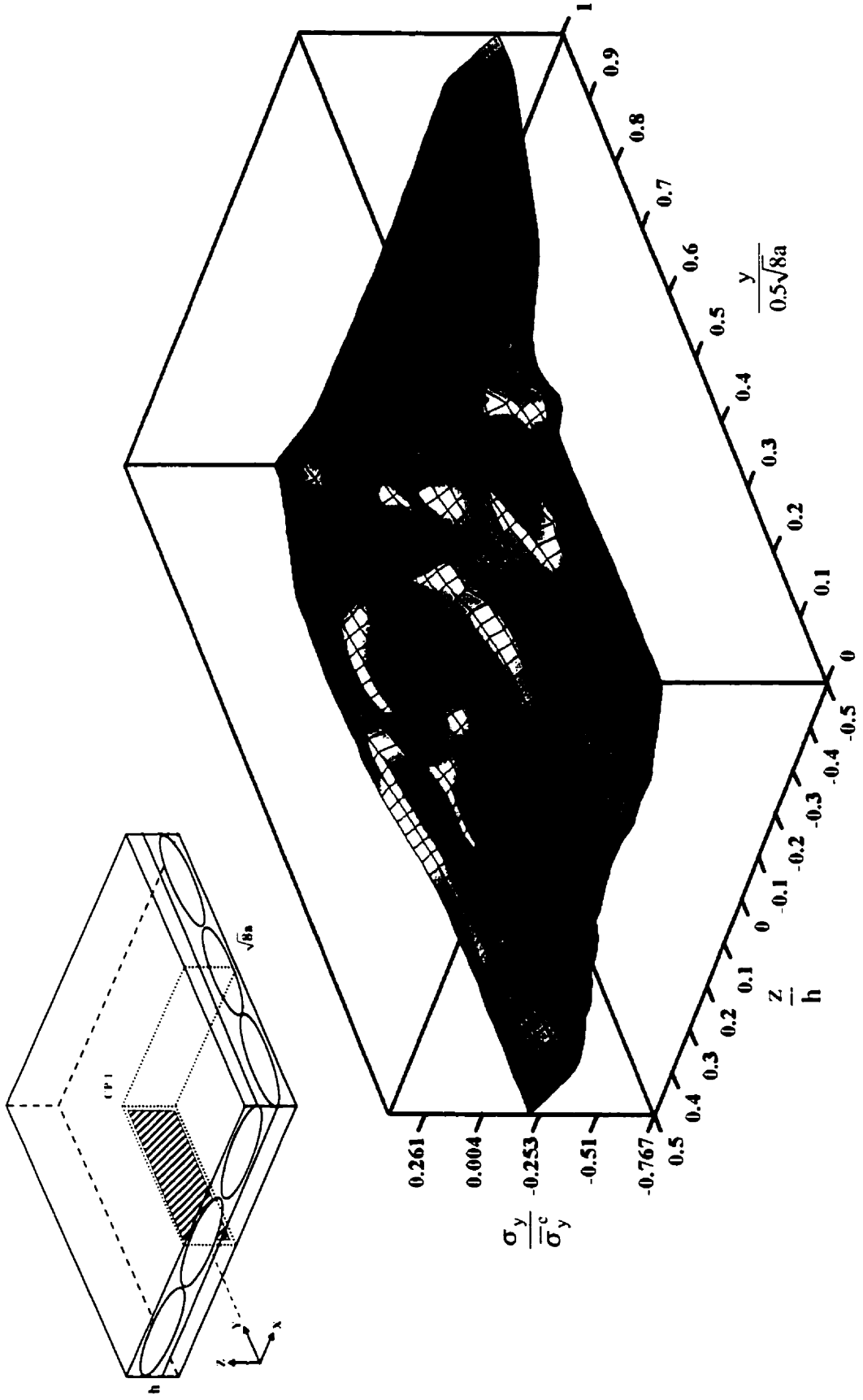


Figure 3.29(a). Uniaxial compressive stress distribution within CP1 under applied uniaxial compression.

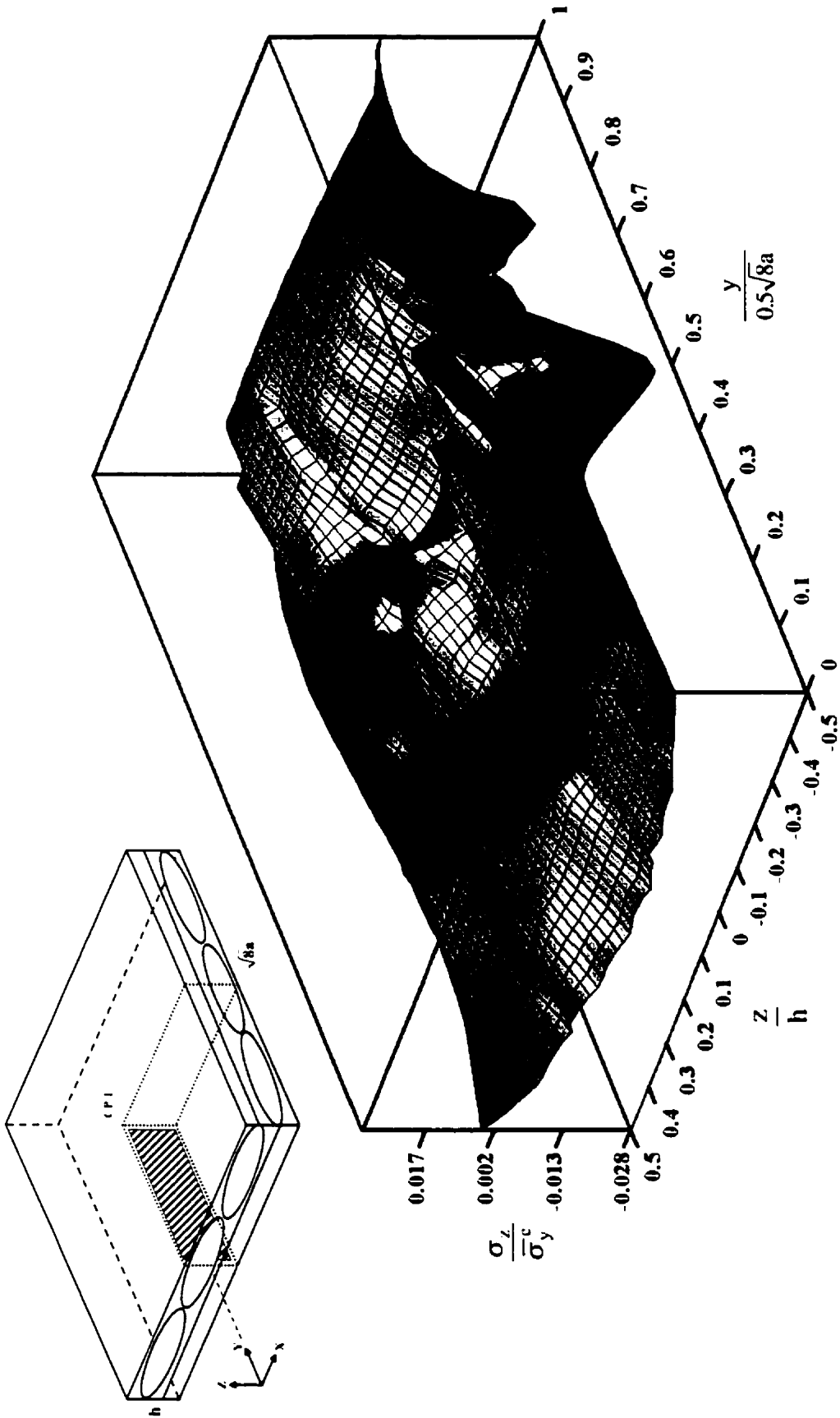


Figure 3.29(b). Uniaxial transverse normal stress distribution within CP1 under applied uniaxial compression.

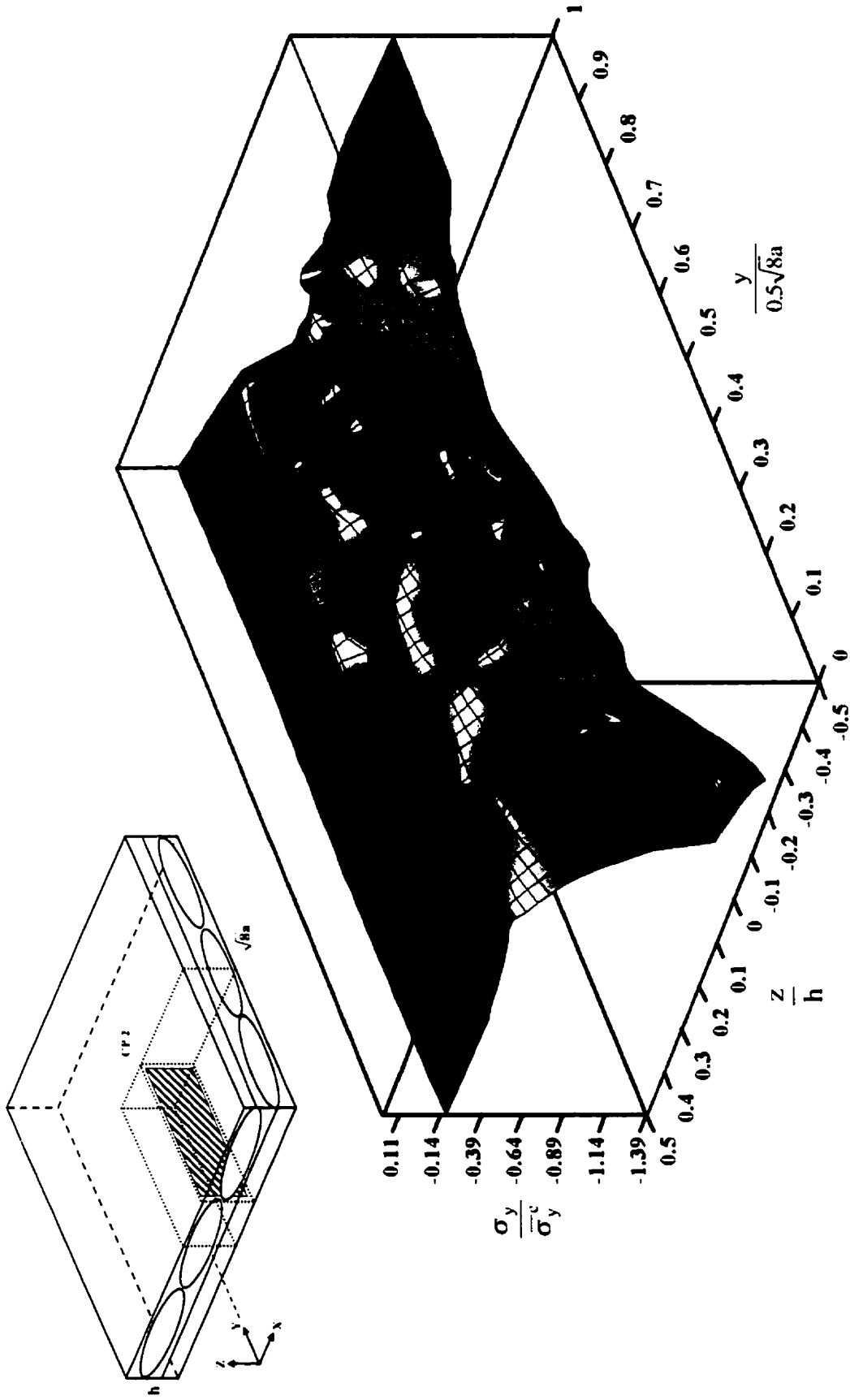


Figure 3.30(a). Uniaxial compressive stress distribution within CP2 under applied uniaxial compression.

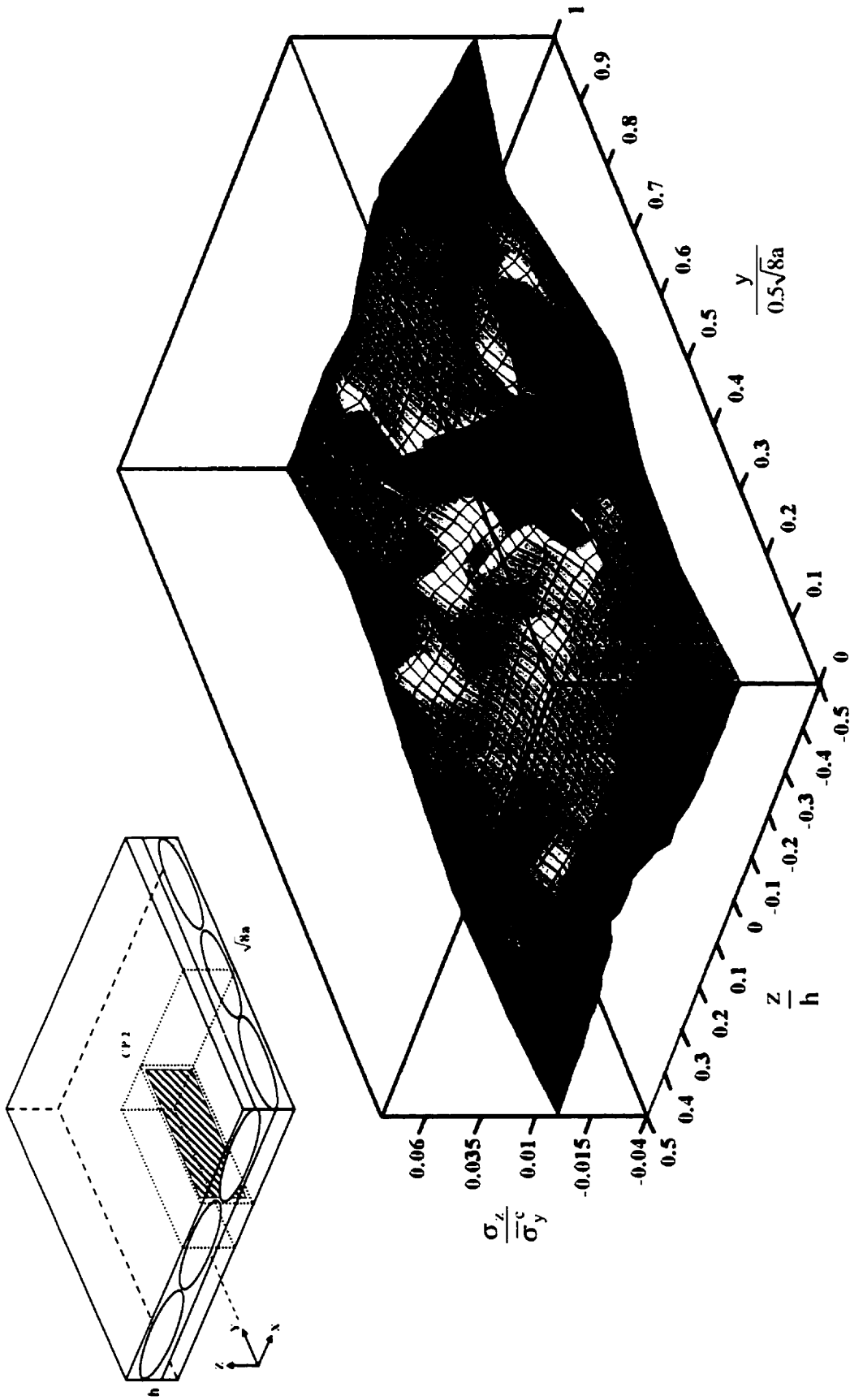


Figure 3.30(b). Uniaxial transverse normal stress distribution within CP2 under applied uniaxial compression.

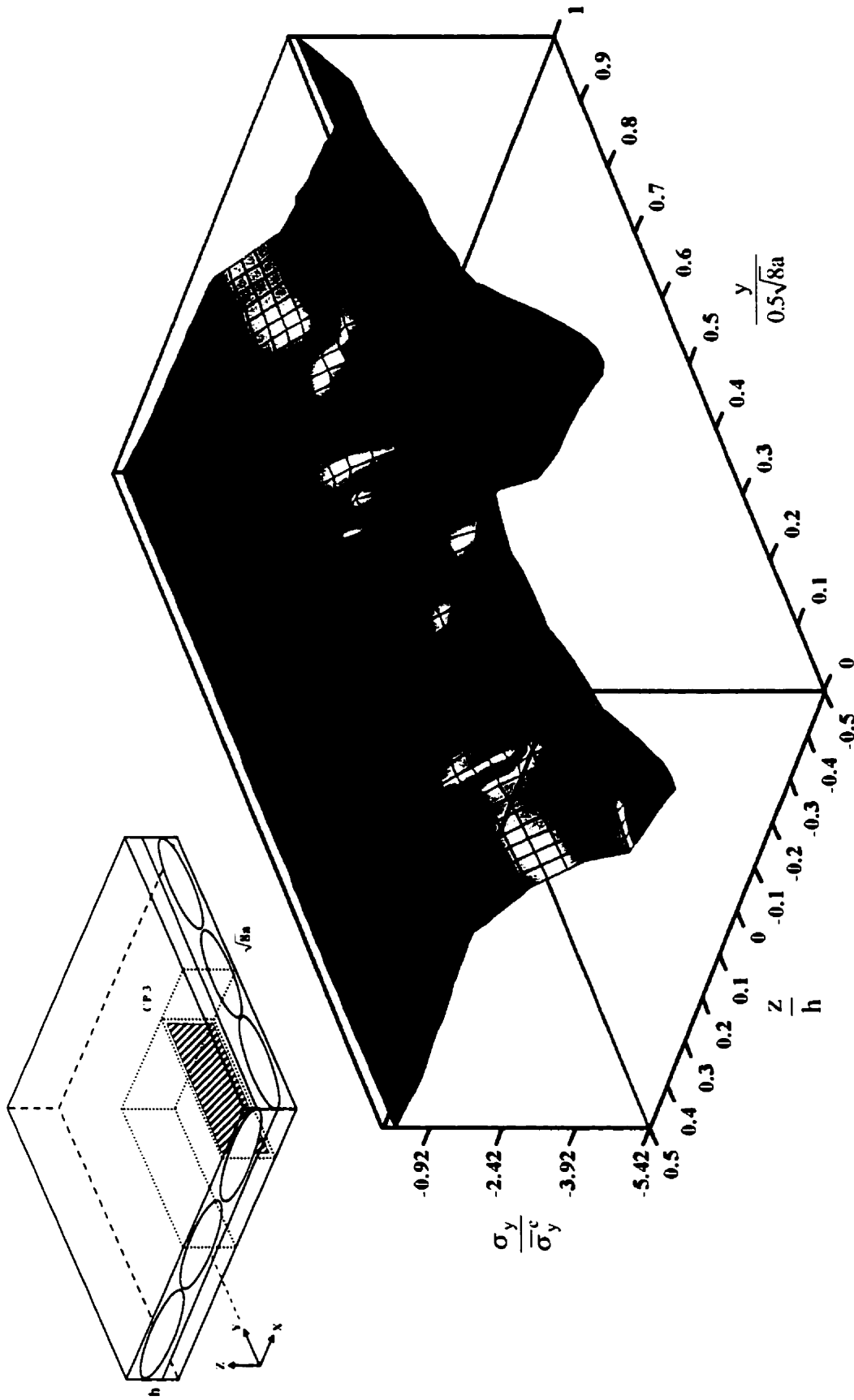


Figure 3.31(a). Uniaxial compressive stress distribution within CP3 under applied uniaxial compression.

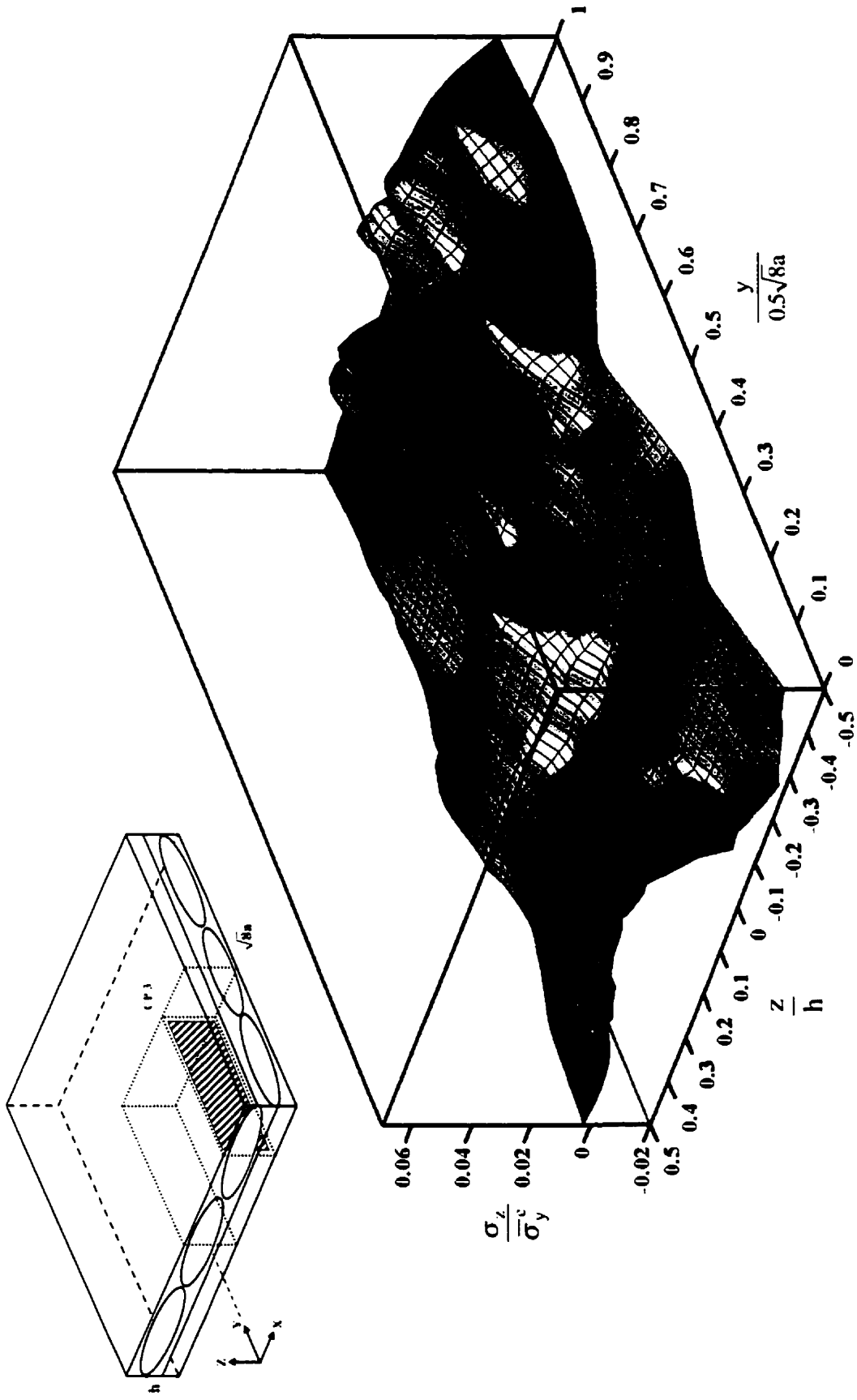


Figure 3.31(b). Uniaxial transverse normal stress distribution within CP3 under applied uniaxial compression.

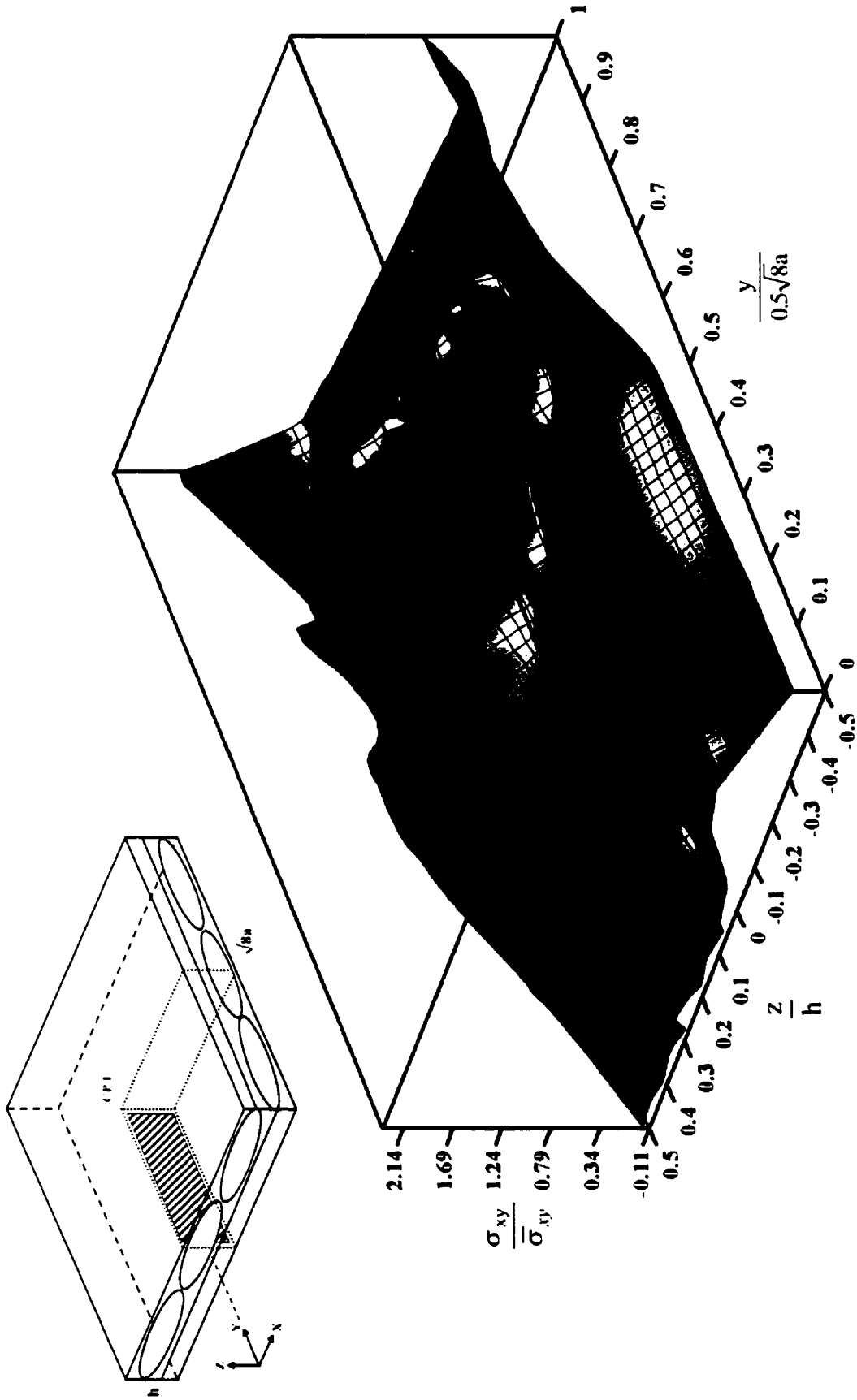


Figure 3.32(a). In-plane shear stress distribution within CP1 under applied in-plane shear.

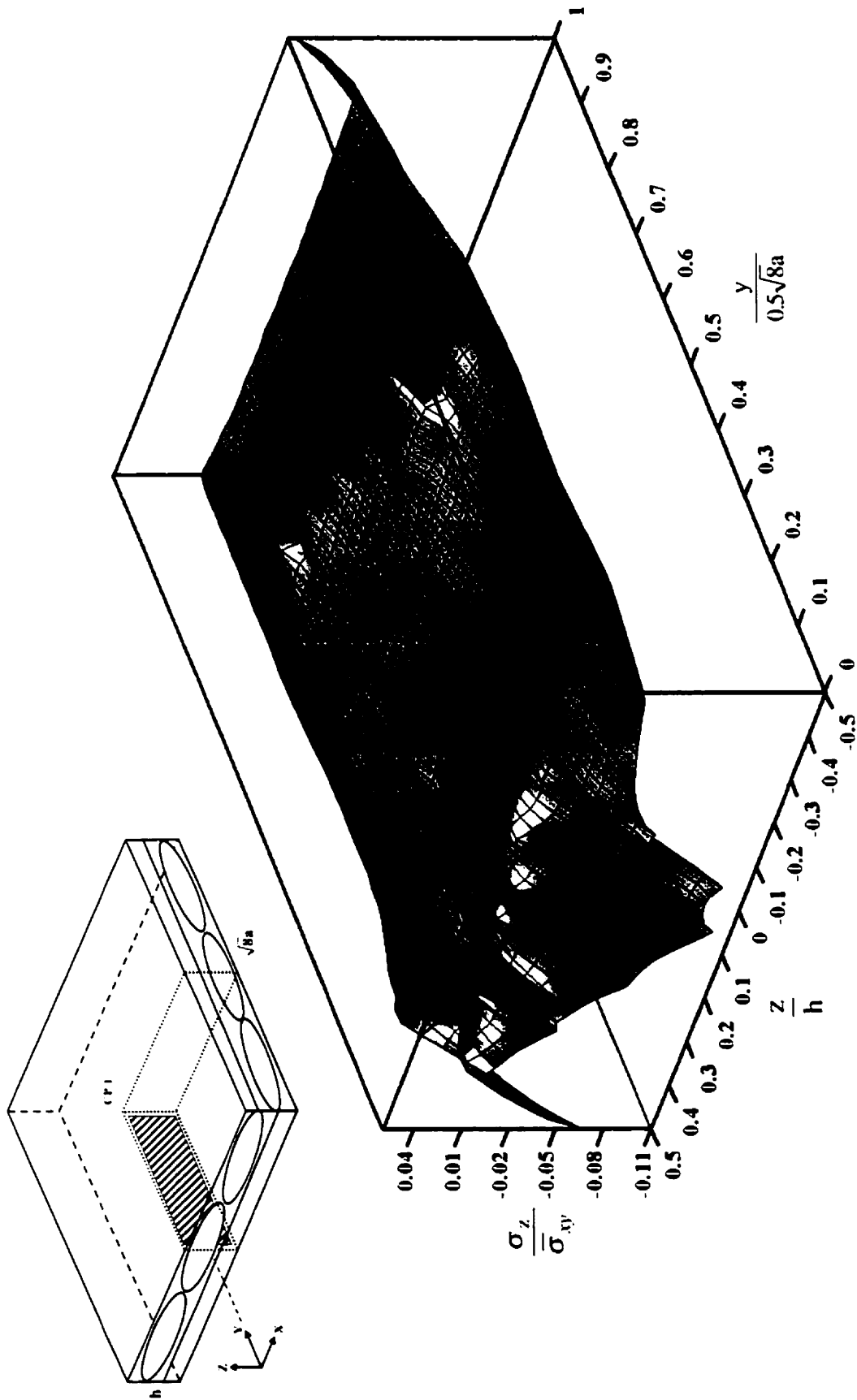


Figure 3.32(b). Uniaxial transverse normal stress distribution within CP1 under applied in-plane shear.

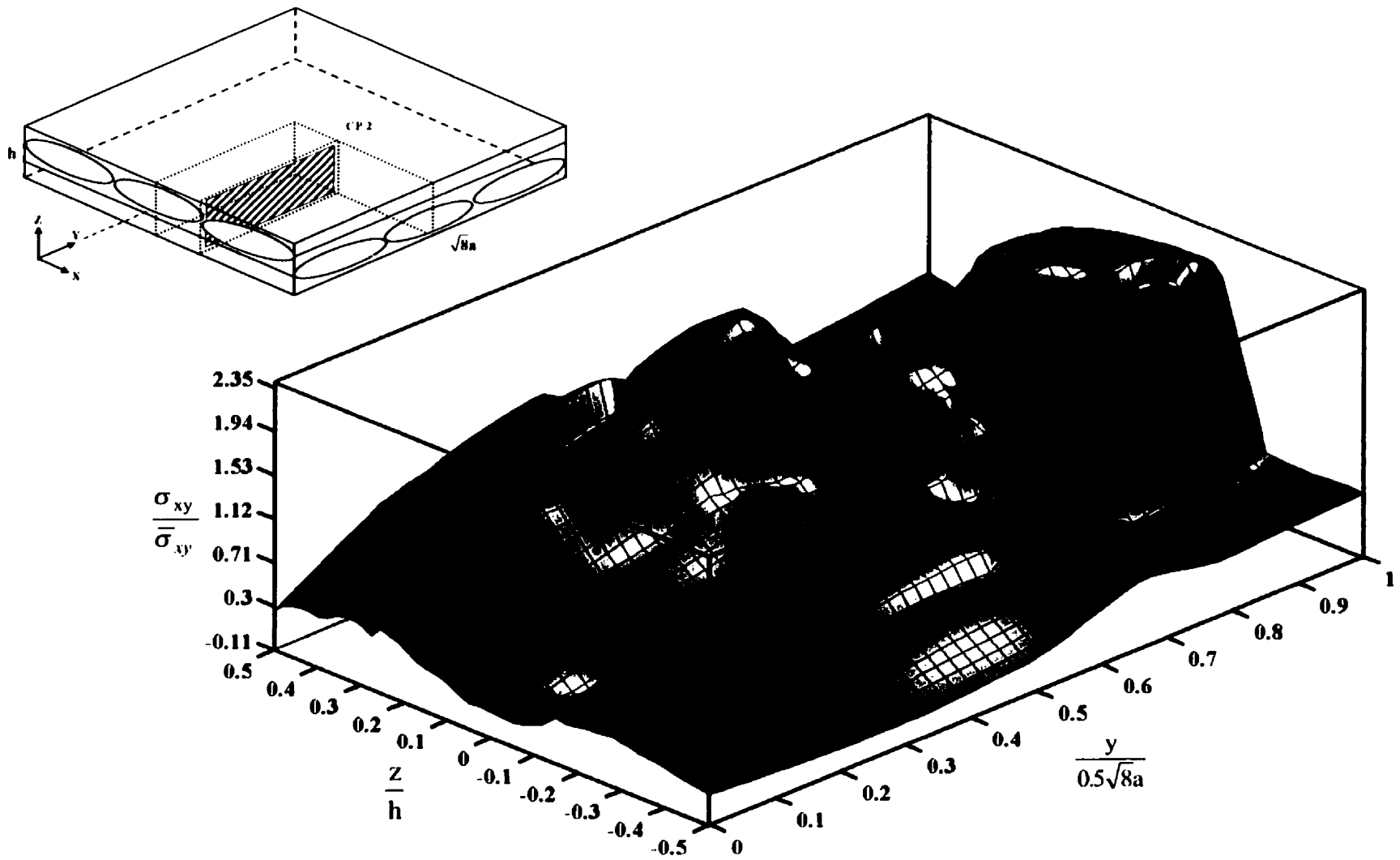


Figure 3.33(a). In-plane shear stress distribution within CP2 under applied in-plane shear.

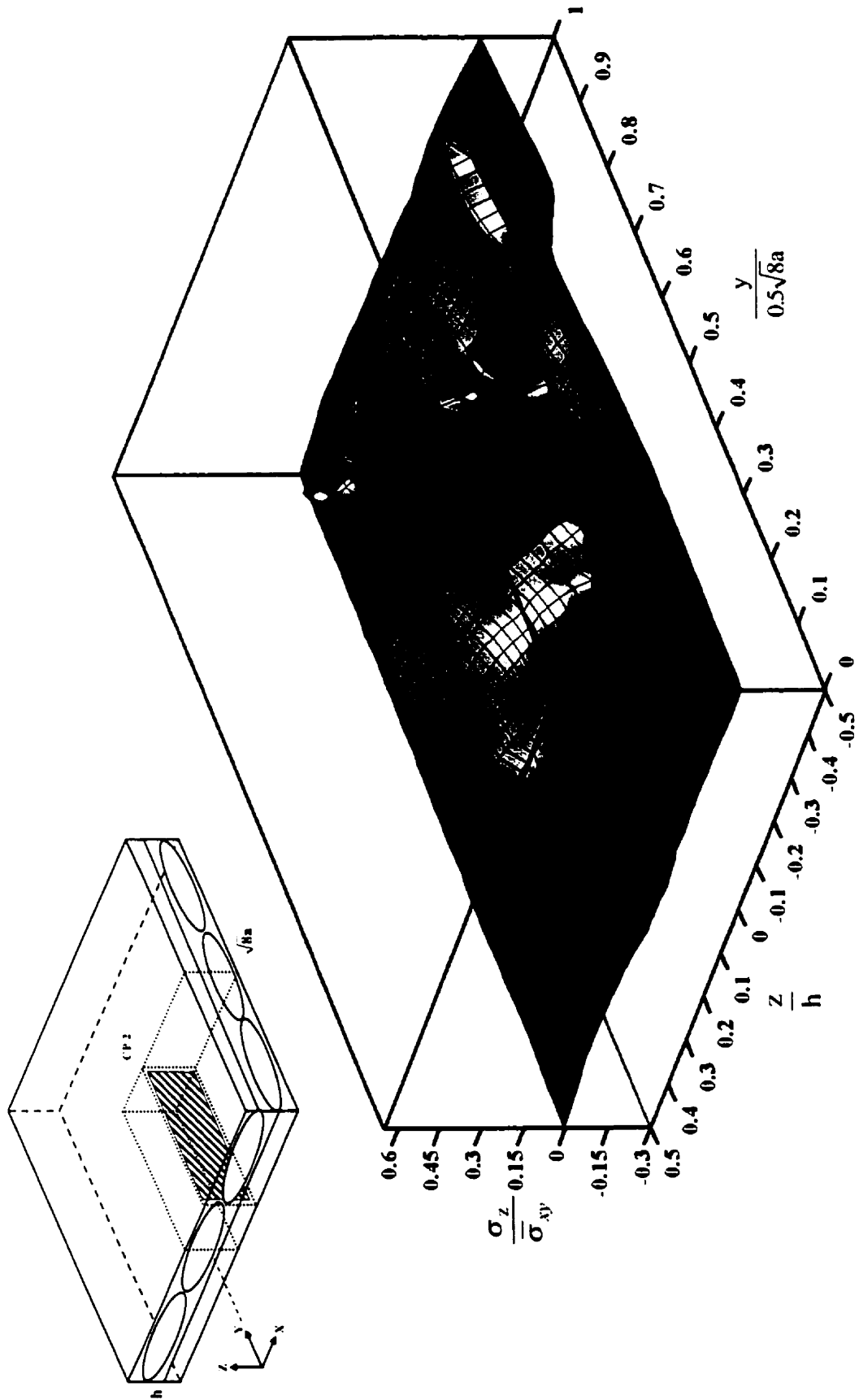


Figure 3.33(b). Uniaxial transverse normal stress distribution within CP2 under applied in-plane shear.

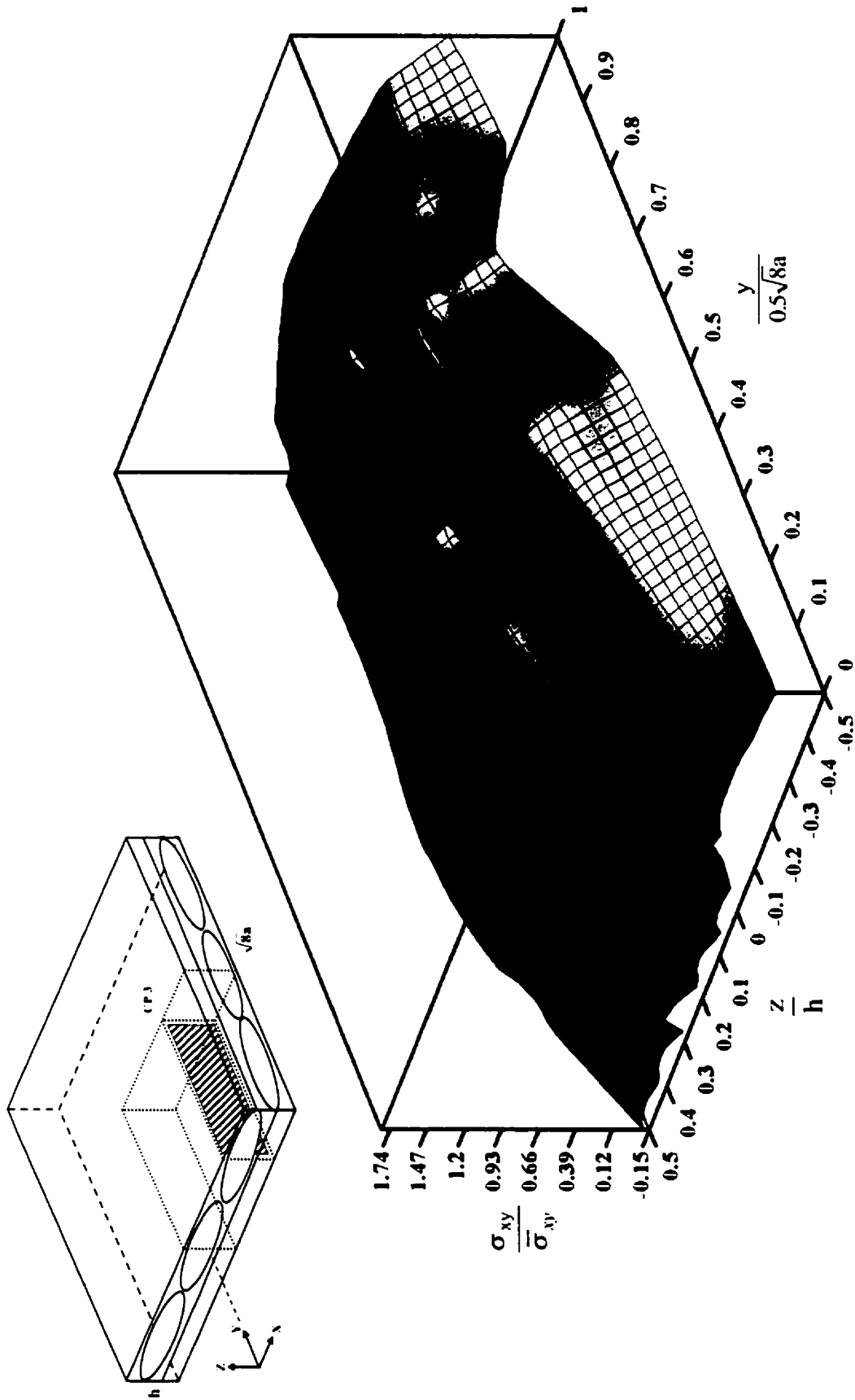


Figure 3.34(a). In-plane shear stress distribution within CP3 under applied in-plane shear.

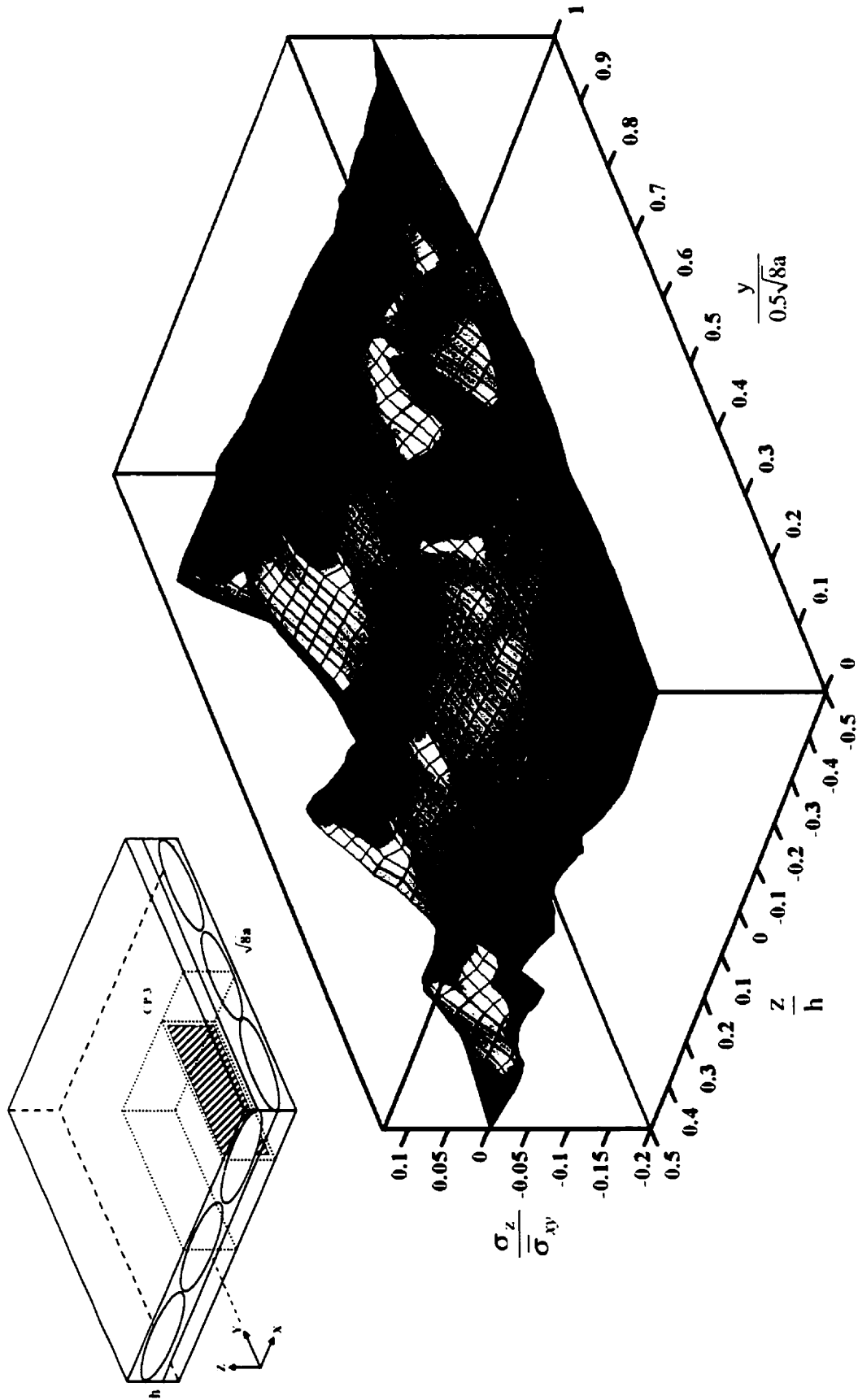


Figure 3.34(b). Uniaxial transverse normal stress distribution within CP3 under applied in-plane shear.

MACROSCALE ELASTIC AND INELASTIC BEHAVIOR

In many aerospace and conventional engineering applications, load bearing composite structures and components are designed with the intent of being subjected to uniaxial stresses that are predominantly tensile or compressive. In this way, the principal reinforcing direction of the fibers may be aligned during the manufacturing process, i.e. tailored to offer greater stiffness and potentially minimize strength knockdown in the direction of interest. However, throughout the in-service life of the structure or component it is likely that biaxial and possibly triaxial states of stress will exist. If of sufficient magnitudes exceeding some critical stress, these multiaxial states may induce damage which greatly reduces the loading carrying capabilities of the structure and may potentially lead to catastrophic failure. It is here where the tradeoffs are made when tailoring the performance of composite structures to suit a particular expectation. The existing paradigm suggests that UD tape materials are superior under uniaxial conditions since the vast majority of the fibers lie in-plane and can be aligned to the loading axis. This may be true, but not without detriment to impact performance, interlaminar strength, strain-to-failure and complexity of part geometries.

4.1. Shear and Biaxial Properties

In circumstances where sufficiently high in-plane orthogonal stiffnesses are required along with higher strain-to-failure and impact resistance, composites based on woven fabrics such as the 8HS architecture become an attractive choice. This is particularly true if the end use is a component having a greater level of geometric detail. As suggested in Section 1.0, the behavior of components having geometric detail at the scale of roughly 10^{-3} m (10^2 mils) may be synonymous with behavior of the woven composite structures themselves. Therefore, it

is extremely important to be able to accurately determine the elastic and strength properties while at the same time characterizing the principal types of failure that occur within the various locations of stress space. The majority of experimental testing standards developed for evaluating these properties and characteristics were done so on the basis of UD composite materials. Consequently, the databases and levels of understanding that exist for woven composites are not as prevalent as those that exist for their UD counterparts. There seems to be some level of agreement though that the ASTM-type tests established for UD tape materials are suitable for the simpler 2-D woven laminates that behave in a manner similar to conventional laminates, i.e. quasi-laminar.

Of the ASTM standardized tests available for evaluating the uniaxial tensile, off-axis tensile and intralaminar shear behaviors of conventional laminates, two seem to show the most promise in terms of associated facility and material costs, namely ASTM D 3039-76 (cf. [44]) and ASTM D 5379-93 (cf. [45]). The later of these, based primarily on the early works of Iosipescu and Arcan, serves as the author's experimental basis for shear characterization of 8HS woven fabric composites. Notwithstanding, a modified version of this test is adopted for evaluating the biaxial shear properties of 8HS woven fabric composites exposed to both room temperature and elevated temperature environments. As part of the process for assessing whether the modified fixture produces reasonable results for these composites, the off-axis tensile test is also used: 1) to check results from the biaxial shear tests, and 2) to aide in understanding the complex stress states that may result from the biaxial shear test given that these complexities are already well-publicized for other composite materials in reference to the standard intralaminar shear test.

4.1.1. The Experimental Tests

In 1967, N. Iosipescu proposed a method to determine the shear properties of metals that was relatively simple to conduct and employed small, easily fabricated specimens [46]. The basis for the Iosipescu test was classical beam theory which formalizes the existence of pure shear

relative to a cross-section of a beam loaded in such a manner to produce a zero bending moment. This manner of loading, in terms of the force, shear and moment diagrams, is illustrated in Figure 4.1. From beam theory, the shear stress distribution along the throat where the zero moment exists is parabolic. Iosipescu postulated that the inclusion of 90° opposing v-notches at this location would produce a uniform shear distribution instead of the parabolic distribution. His argument was that the isostatics of the stress-free surfaces at ± 45° resulted in coincidence of the plane of principal stress, thus the principal stresses would be zero at the notch root. Hence, there should be no existence of normal stresses or shear stress concentrations at either notch root. However, a plethora of experimental and numerical studies have proved his original argument to be incorrect.

The original test used cylindrical test specimens with a 90° v-notch cut completely around the circumference of the specimen mid-section. This specimen transforms the parabolic shear distribution into a distribution that is constant between the notches. Failure by shear is also more easily promoted due to the reduced cross-section. For this test, the average shear stress is obtained by dividing the cross-sectional area between the notch roots into the applied load **P**

$$\bar{\tau}_{xy} = \frac{P}{A} = \frac{P}{(w)(t)} \quad (4.1)$$

where **w** is the distance between opposing notch roots and **t** is the “as received” thickness of the specimen. Adams and Walrath [47-49] suggested that the Iosipescu shear test method was suitable for determining material in-plane and through-thickness shear properties of unidirectional composites and sheet moulding compounds (SMC’s) by using flat, rectangular specimens with notches machined at the mid-length. With the efforts of Adams, Walrath and Slepetz *et al.* [50], the Iosipescu specimen geometry and loading scheme have been certified through extensive investigations and finite element analyses. Additionally, more comprehensive investigations by Adams and Walrath [51], which included analyzing the

stress distributions in the Iosipescu specimen as a function of geometry and orthotropy ratio (E_{11}/E_{22}), resulted in a redesigned specimen and fixture.

The Wyoming test, in accordance with ASTM D 5379-93 uses a coupon with opposing v-notches and generates a predominant state of shear stress in the gage section from counteracting moments produced by two force couples. Shear strain is measured at the center of the notch root axis by two strain gages oriented at $\pm 45^\circ$ to the longitudinal axis of the specimen (likewise, the same orientation to the notch root axis). For highly orthotropic materials, it has been demonstrated that the shear stress distribution around the notch root is weakly dependent on notch depth and strongly dependent on notch angle and radius. It has also been demonstrated by Barnes *et al.* [52] that the apparent shear moduli of UD 0° and 90° glass-polyester Iosipescu specimens is nearly the same, though the apparent intralaminar shear strength was strongly dependent on fiber orientation.

Comparative studies have been made between isotropic and orthotropic specimens to determine the questionable influences of geometry, loading configuration and fiber direction on stress distributions and to understand why the shear stress field is not uniform as originally speculated by Iosipescu. Kumosa *et al.* [53-54] compared the numerically generated von Mises stress contours from force-couple and prescribed displacement boundary conditions to isochromatic fringe patterns observed during shear tests. They found that the force-couple boundary conditions originally proposed by Iosipescu provided a closer match to the observed fringe patterns than did the displacement boundary conditions proposed by Adams and Walrath. Several researchers have also employed moiré interferometry techniques and isochromatics as tools to evaluate the state of stress in Iosipescu specimens. Displacement fields and fringe patterns have been compared with finite element results to evaluate loading configurations, boundary conditions and experimental errors. Ifju [55-56] opted for a more compact version of the specimen with u-shaped notches and a larger throat. Combined with interferometry and a newly proposed shear gage [57] which measures an average of the shear strain field from the top to bottom notch, the

compact specimen was shown to produce measurable shear strains having less scatter compared with the now traditional test.

As a result of lengthy studies conducted by Broughton and Kumosa [53-54, 58], a new in-plane biaxial shear test fixture was designed. Based upon the aforementioned Iosipescu shear test and the Arcan in-plane stress method [59], the biaxial test fixture allows rotation of the externally applied load in reference to the specimen notch root axis and is capable of measuring mixed-mode failure and fracture properties of isotropic and composite materials. It has successfully been used for measuring room temperature, mixed-mode failure properties of UD carbon-epoxy, glass-polymer, carbon-PEEK, Ti-SiC and Teak wood [60-62]. It has also been employed in the current research program for characterizing the elastic and biaxial shear failure properties of 8HS woven graphite fabric and UD graphite-polyimide (PMR15 and Avimid R) composites at room and elevated temperatures approaching 315 °C (600 °F). Lastly, the biaxial fixture in conjunction with a newly modified version have been used to establish the influences of geometric, boundary contact and material nonlinearities on observable nonlinear shear stress-strain behaviors [63-68].

Based on the biaxial Iosipescu test fixture shown in Figure 4.2, the components of load applied to the individual blocks, as a function of the externally applied compressive load P at some angle α to P_0 , can be derived using moment and force balance considerations. Referring to Figure 4.4, consider the following expressions for load components as a function of loading angle:

$$P_1 = \frac{P}{\left[1 - \left\{ \frac{2c - h' \tan(\alpha)}{l + h' \tan(\alpha)} \right\} \right]}, \quad P_2 = \frac{P}{\left[\left\{ \frac{l + h' \tan(\alpha)}{2c - h' \tan(\alpha)} \right\} - 1 \right]} \quad (4.2)$$

where P is the externally applied load and the angle α is taken as positive when the specimen is rotated counter-clockwise and negative when rotated clockwise. Thus, the test specimen is loaded in shear-tension for negative loading angles ($-\alpha$) and in shear-compression for positive loading angles ($+\alpha$). Consequently, for any calculations involving the load

components, the signs are carried. From Figure 4.4, it becomes obvious that the expressions given by Eq. 4.2 are admissible only for values of α in the range $\alpha_{cr}^- \leq \alpha \leq \alpha_{cr}^+$ where the critical load angles are given by

$$\alpha_{cr}^+ = \tan^{-1}\left(\frac{2c}{h'}\right), \quad \alpha_{cr}^- = \tan^{-1}\left(-\frac{\frac{l}{2} - c}{h'}\right) \quad (4.3)$$

According to the approach outline here, it has been suggested that the composite biaxial strength properties may be obtained as originally proposed by Arcan [59]. It follows then that Eq. 4.1 would be modified to account for the loading angle:

$$\bar{\tau}_{xy} = \frac{P_a}{A} = \frac{P_a}{(w)(l)} [\cos(\alpha)] \quad (4.4)$$

From an experimental viewpoint, the apparent in-plane shear modulus G_{xy} and shear strength X_{xy} can be evaluated by measuring the applied load, cross-section and shear strain between opposing v-notches. According to global coordinates (X, Y, Z) rather than the principal material coordinates (x_1, x_2, x_3), the apparent in-plane shear modulus is then defined:

$$G_{xy} = \frac{\int \tau_{xy} dy}{\int \gamma_{xy} dy} \quad (4.5)$$

where the integrated shear stress τ_{xy} is the far-field load divided by the cross-sectional area between the notches, γ_{xy} is the shear strain and the integrations are line integrals having limits equivalent to the notch root axis. The shear strain cannot be measured directly with strain gages, however, according to the previous theory normal strains oriented at $\pm 45^\circ$ are a measurable representation of shear strain given a pure shear state. The normal strains can be represented in terms of the strains in the specimen coordinate directions by

$$\begin{aligned}\varepsilon_{+45} &= \varepsilon_x \cos^2(45^\circ) + \varepsilon_y \sin^2(45^\circ) + \gamma_{xy} \sin(45^\circ)\cos(45^\circ) \\ \varepsilon_{-45} &= \varepsilon_x \cos^2(-45^\circ) + \varepsilon_y \sin^2(-45^\circ) + \gamma_{xy} \sin(-45^\circ)\cos(-45^\circ)\end{aligned}\quad (4.6)$$

Subtracting the strain in the positive direction from the strain in the negative direction defines the shear strain in terms of the measured gage strains, e.g.

$$\gamma_{xy} = \varepsilon_{+45} - \varepsilon_{-45} \quad (4.7)$$

It can also be reasoned that the average strain measured by a gage having a nominal grid area $A \times B$ can be defined as follows:

$$\bar{\varepsilon}_{45}^* = \frac{1}{AB} \int_{-A/2}^{A/2} \int_{-B/2}^{B/2} \varepsilon_{45}^* ds^* dt^* \quad (4.8)$$

where ds^* and dt^* are in reference to the axial and transverse gage dimensions A and B , respectively. It is recommended to monitor strains on both faces of the specimen to minimize erroneous shear modulus measurements as a result of specimen twisting and lateral instability. The apparent modulus then is calculated from the average of readings obtained from both gages.

Since efficient characterization of intralaminar shear properties has long been a subject of controversy because of the difficulty in producing a state of pure shear in practical laboratory test specimens, the off-axis tensile test was also used to check results obtained from the biaxial Iosipescu tests. The tensile test on UD composites having fibers oriented at some angle to the loading axis has been successfully employed for a number of years by researchers to obtain composite elastic properties, apparent failure stresses and verify material symmetry assumptions of a particular composite system. This test is as equally attractive in its simplicity as the Iosipescu test is to conduct, however it does have disadvantages. The biggest disadvantage associated with the off-axis tensile test is that the configuration can introduce errors in the measured elastic ply-level material parameters due

to an effect of end-constraint [69]. Under a uniformly applied axial stress, the ends of the specimen attempt to rotate from shear-extensional coupling. The amount of rotation is influenced by the angle of fiber orientation, specimen geometry, material anisotropy and end constraint. If the ends of the specimen are firmly gripped, rotation cannot take place and a highly inhomogeneous state of deformation takes place in the specimen. This may lead to erroneous measurements of composite material properties and premature failure outside of the specimen gage section near the grips.

For characterizing the behavior of UD composites, the most popular off-axis configurations have been the 10° and $\pm 45^\circ$ tests. In 1977, Chamis *et al.* [70] proposed that the 10° off-axis tensile test should be considered as a standard for intralaminar testing of UD composite materials based on the theoretical and experimental results from their investigation. Some of their arguments for selecting this test over other practices were: (1) the use of a familiar procedure (ASTM D 3039-74), (2) specimens can be cut from the same composite plaque used for evaluating longitudinal and transverse properties, (3) specimens are free of lamination residual stresses in contrast to $\pm 45^\circ$ specimens, and (4) the intralaminar shear strain approaches its maximum when the angle between the fibers and direction of applied load is 10° . The specific disadvantages cited in reference to this configuration aside from care in preparing and aligning the specimen and gages were: (1) three strains needed to be measured at a point, and (2) both stresses and strains required transformation.

By adopting the off-axis tensile test for woven fabric composites, the ply-level stresses in specimens with tows oriented at an angle β to the principal loading axis can be determined from established transformation equations which are derivable from force-equilibrium considerations. With reference to Figure 4.5, the stresses are given by

$$\begin{aligned}\sigma_{11}^f &= \sigma_x \cos^2 \beta \\ \sigma_{22}^f &= \sigma_x \sin^2 \beta \\ \tau_{12}^f &= \sigma_x \sin \beta \cos \beta\end{aligned}\tag{4.9}$$

where β refers to the angle between the tows and applied stress (σ_x) along the long axis of the specimen and the superscript f refers to the principal fiber coordinate at the ply-level. The ply-level strains in the off-axis specimens can be determined using strain gages with three elements individually oriented at 0° , 45° and 90° . On the basis of the shearing strain interpreted from the gages as $\gamma_{xy} = (-\varepsilon_x + 2\varepsilon_{45} - \varepsilon_y)$, the strains in the material coordinate system, in terms of the gage strains and off-axis angle, are given by

$$\begin{aligned}\varepsilon_{11}^f &= \varepsilon_x \cos^2 \beta + \varepsilon_y \sin^2 \beta + \left((-\varepsilon_x + 2\varepsilon_{45} - \varepsilon_y) \sin \beta \cos \beta \right) \\ \varepsilon_{22}^f &= \varepsilon_x \sin^2 \beta + \varepsilon_y \cos^2 \beta - \left((-\varepsilon_x + 2\varepsilon_{45} - \varepsilon_y) \sin \beta \cos \beta \right) \\ \gamma_{12}^f &= (-\varepsilon_x + \varepsilon_y) \sin 2\beta + \left((-\varepsilon_x + 2\varepsilon_{45} - \varepsilon_y) \cos 2\beta \right)\end{aligned}\quad (4.10)$$

4.1.1.1. Materials

In this research, three different composite systems, based on woven graphite fabric, reinforced polyimides were mechanically tested. Four composite plaques impregnated with a PMR15 matrix were provided by the NASA Glenn Research Center and two composite plaques impregnated with an Avimid R (dianhydride-diamine monomers) matrix were provided by Pratt & Whitney. The PMR type composites were reinforced with a sized T650-35/3k 8HS cloth from Amoco Performance Products Inc., and the stacking sequence was $[0^\circ]_{16S}$ with floating undulations. The dimensions of the cut prepreps used for assembling the PMR laminates were 304.8 mm x 304.8 mm (12.0 in x 12.0 in) with total laminate thicknesses of 4.82 mm (0.19 in), 5.15 mm (0.20 in), 5.50 mm (0.22 in) and 5.38 mm (0.21 in) for plaques one through four, respectively.

The Avimid R type composites were also reinforced with a sized T650-35/3k 8HS cloth from Amoco Performance Products Inc. The stacking sequence for the first laminate was $[0^\circ]_{10S}$ with floating undulations and the sequence for the second laminate was $[0^\circ/90^\circ]_{10S}$. The cut prepreg dimensions used for assembling the Avimid R laminates were

identical to the PMR laminates, but total laminate thicknesses were 3.92 mm (0.15 in) for both plaques one and two.

All composite systems followed a simulated autoclave curing cycle according to General Electric specifications. Subsequent to layup, the prepreg would be placed into a preform mold for approximately one hour at 200 °C (392 °F) allowing for partial imidization and dimensional stability (B-staging). Next, the stack would be moved to a matched mold and cured under a specific pressure-temperature-time profile. A typical profile might have proceeded as follows (data arbitrarily chosen due to sensitivity of information): ramp from room temperature to 200 °C (392 °F) at 2.8 °C (5 °F)/min and hold for 60 minutes; apply 14.2 atmospheres (200 psi) pressure at the end of sixty minutes, ramping pressure at 1.4 atmospheres (20 psi)/min and simultaneously ramping temperature at 1.7 °C (3 °F)/min until curing temperature, say 350 °C (662 °F) is attained; hold final temperature and pressure for two hours and then reverse ramp rates until room temperature and atmospheric pressure are attained. Primary and possibly secondary post-cure cycles were used to raise both the T_g and thermo-oxidative stability of the composite systems.

The number of post-cure treatments required was dependent on the desired thermomechanical properties. Fiber volume fraction, void content and density were commonly evaluated using acid digestion techniques and ultrasonic C-scans (ASTM D 2734 and ASTM D 3171). All composite plaques C-scanned and used for mechanical testing showed exceptional density and uniformity with only varying attenuation near the edges indicating possible defects. Any material showing attenuation was further inspected with a microscope prior to being used and if questionable, it was immediately discarded.

4.1.1.2. Specimen Designs

The Iosipescu specimen dimensions called out by the standard require specimen sizing in reference to the Wyoming-type test fixture. For that standard fixture, the nominal specimen dimensions are given by a length of 76.0 mm (3.0 in), width of 20.0 mm (0.75 in), notch root

axis length of 12.0 mm (0.45 in), notch radius of 1.3 mm (0.05 in), notch depth of 4.0 mm (0.15 in) and an included notch angle of 90° . The specimen design employed in this work for the biaxial Iosipescu fixture is shown in Figure 4.6(a) using Table 4.1 as a reference. The two most significant changes between the standard specimen geometry and the geometry shown in Figure 4.6(a) are the nominal lengthening to 80.0 mm (3.15 in) and sharpening of the notch radius to 0.45 mm (0.018 in). The biaxial fixture uses shorter loading blocks with reaction centers between the outer loading blocks and inner loading blocks placed further apart. Lengthening of the specimen is required to maintain anti-symmetric loading and balanced moments across the entire span of the specimen. A criticism towards this type of design has been made by several researchers in regard to the close proximity of inner load points with respect to the notch. They argue that larger transverse compressive stresses are present which are likely to “spill” into the gage section of the Iosipescu specimen and have detrimental effects on both the shear stress distribution and failure process. To dispute their arguments and ascertain the influences that placement of load centers has on the shear stresses and failure process, a new loading block design was mated to the biaxial fixture (see Appendix D). These blocks distribute the load at contacting regions on the specimen in the same manner as the standard suggests. The specimen design for this configuration termed the modified biaxial fixture is shown in Figure 4.6(b) using Table 4.1 as a reference also.

In regard to sharpening of the notch radius, previous work (cf. 51-54, 58, 60-62) showed that the effects of singular stresses at the notch tip and their contribution to a reduction in apparent shear strength tended to be insignificant when the notch radius was greater than 0.35 mm (0.0137 in). In addition, several trial shear tests were performed using 8HS woven fabric composites to calibrate the test equipment and it was observed that failure of these specimens was not classically UD orthotropic, i.e. cracks did not seem to nucleate at the roots of the notches and propagate away from the roots resulting in distinctive load drops. Rather, the entire gage section appeared to manifest as one large (almost symmetric) zone of damage which seemed to be self-contained within the throat between the notches. In light of these facts, the decision was made to leave the grinding wheel “as-is” with an

included radius of 0.45 mm (0.018 in) instead of taking the risk and possibly damaging the wheel by redressing it to produce a larger notch radius.

The biaxial and modified biaxial Iosipescu shear test specimens were machined from the first two PMR and Avimid R type plaques, resulting in seventy-two graphite-polyimide specimens and seventy-two graphite-Avimid R specimens. The last two PMR plaques were reserved for off-axis tension tests, although sixteen shear test specimens were machined from the remaining material of both plaques. Each specimen blank was cut with a diamond-tipped blade and included a 2.0 mm (0.078 in) allowable tolerance on all sides for more precise machining operations. Each blank was then surfaced ground to final dimensions and the notches were ground to the desired depth using a grinding wheel dressed in the form of a v-notch having a 90° included angle. Special precautions were taken during the critical step of machining the notches and all operations were performed under a copious flow of water. Post-machining requirements included immediate specimen drying to reduce moisture absorption by the matrix and examination of all surfaces with an optical microscope. In all instances where visible damage from machining was noticed, the specimens were discarded (or used as a trial). Notch radii of all specimens were held consistently at 0.45 mm (0.018 in).

The tensile and off-axis tensile specimens were machined to final dimensions (see Figure 4.6(c) and Table 4.1) called out by the standard using a surface milling machine instead of a surface grinder. Post-machining requirements also included drying to prevent moisture absorption and optical examination of all surfaces. Aluminum tabs were epoxied to the specimen ends to prevent crushing within the hydraulic grips and the ends were pinned with steel pins to prevent slipping under predicted loads high enough to cause failure. The aluminum tabs were tapered by 15° at the ends opposite the grips to relieve stress concentrations and avoid premature failure near the grips. A composite oblique end-tab configuration, which has shown a great deal of promise in eliminating the effects associated with end-constraints [71] in UD composite materials, was not used on the woven fabric composite specimens. The reasoning was that although ply-level extensional-shear coupling would be present, the rotation at the specimen ends would be somewhat lessened compared

to UD composite materials because of orthogonal reinforcement within each ply and symmetric stacking within the laminate.

4.1.1.3. Apparatus

The shear and biaxial shear experimental tests at room temperature were predominantly carried out on an Instron platform within the fracture and fatigue laboratory at Oregon Graduate Institute of Science & Technology's Materials Science Department. Due to the lack of facilities for elevated temperature shear testing of composite materials, the second phase of experiments was moved to the Advanced Materials and Structures laboratory at the University of Denver. The available platforms included an apparatus based on a Dillon tensile tester which was piloted for shear testing during the course of this research and an MTS platform which was adapted for elevated temperatures during the initial stages of off-axis testing and final stage of shear testing.

The room temperature experiments, depicted schematically in Figure 4.7, were performed on a closed-loop, servo-hydraulic Instron Dynamic Test System (Model 1230-20) with a 88.96 kN (20.0 kips) load capacity. All mechanical tests performed at room temperature were displacement controlled and monotonic compressive loads were applied at a constant crosshead displacement rate of 0.5 mm/min (0.0197 in/min). Strain measurements were obtained by three different series of gage configurations for the purpose of comparing apparent elastic properties. The smaller configuration was the Micro Measurements WA-06-060WR-120 45° rectangular, three-element stacked rosette. The legs could be oriented at -45°/90°/+45° in half-bridge configuration to evaluate shear strain directly using Eq. 4.7 or the legs could be oriented at 0°/45°/90° and the shear strain be resolved from the component strains. This series of gage is fully encapsulated constantan and temperature self-compensating with an active grid area of 2.31 mm² (0.0036 in²). The larger configurations were the Micro Measurements A2A-06-C085C-500 ±45°, stacked Iosipescu

shear gage and the Micro Measurements N2A-06-C032B-500/SP61 $\pm 45^\circ$, side-by-side Iosipescu shear gage. These gages were also used in a half-bridge configuration to evaluate shear strain directly from Eq. 4.7 without influence of normal strains. These series of gages provide polyimide encapsulation and temperature self-compensation with active grid areas of 24.41 mm² (0.038 in²) and 9.50 mm² (0.015 in²).

The main reason behind the use of the larger shear gages was to eliminate erroneous measurements of the apparent shear modulus associated with the smaller, centrally located rosettes. It is widely understood now that the use of small gages to measure the average shear strain may produce as much as 30% error in shear modulus values depending upon the specimen geometry, material orientation, loading condition and orthotropy ratio [57,72-73]. A classic example of this can be demonstrated when measuring the shear moduli of 0° UD and 90° UD carbon-epoxy Iosipescu specimens using the same type of small strain gages. Beam theory predicts that both values should be the same, however what actually occurs can be seen by Figure 4.8. Since a small gage only measures average strain locally at the specimen center, it can be expected that differences may be large when the strain distributions are vastly different. In the past, correction factors have been assigned to account for these errors due to orientation and orthotropy ratio, but these factors aren't necessary when the shear gage is used. Strain integration along the entire notch root axis provides much more agreeable results between the two material systems.

It has also been suggested in the literature that the lack of consistency in strain measurements from specimen-to-specimen and in particular, from the + leg to the - leg, might be due to specimen twist and out-of-plane bending, although these types of explicit eccentricities had not previously been investigated. As compensation for these possible effects on shear strain measurements, gages were placed on both sides of each Iosipescu specimen and the average strain taken from both gages was used to calculate the shear modulus. It was expected that the back-to-back strain gage configuration would provide the best repeatability among the specimens.

The elevated temperature experiments, depicted schematically in Figure 4.9, were performed on the basis of two configurations. The initial groundwork for understanding composite behavior at elevated temperatures was based on an open-loop, mechanically driven Dillon tensile test platform having a 44.48 kN (10.0 kips) load capacity. For this platform, a forced-convection environmental chamber (refer to Figure 4.3) was custom built to fit between the stationary crosshead and load screw. For shear and biaxial testing, a custom fixture was also designed to fit within the chamber and compress the biaxial Iosipescu fixture when tension was applied at a constant crosshead displacement rate of 0.5 mm/min (0.0197 in/min). Strain measurements were obtained using the smaller configuration Micro Measurements WK-06-060WR-120 45°, rectangular three-element stacked rosette designated for wide range temperature applications. This series of gage is fully encapsulated K-alloy with high endurance leadwires and temperature self-compensating with an active grid area of 2.31 mm² (0.0036 in²). The temperature range of this gage, which is the widest available for standard configurations, is -269 °C to 400 °C (-452 °F to 750 °F) pending short-term exposure. At test temperatures above 260 °C (500 °F), conventional tin alloy soft solders melt and strain gage leadwires oxidize. To overcome this, a silver solder paste was used to attach fiberglass encased leadwires to the strain gages. For testing at 315.6 °C (600 °F), a temperature-cured epoxy coating (M-Bond GA-61) was also employed to protect the gage contacts against oxidation.

Preliminary testing of the PMR15 (second plaque) and Avimid R (plaques one and two) based composites using the Dillon platform proved to be very cumbersome and time consuming. Since the biaxial shear test fixture was completely enclosed within the insulated chamber, access to the specimen or fixture for minor adjustments in specimen position was nearly impossible. Additionally, the fiberglass encased leadwires were so stiff that proper routing through the bottom of the chamber to avoid grounding on the biaxial fixture became a problem and often resulted in the leadwire contacts being pulled from the specimen surface. Aside from the twenty-four hour cure time required for the adhesive used to attach the strain gages, one to two hours was required for curing the protective epoxy coating as well as six

to twelve hours to allow for heating and cooling of both the environmental chamber and test fixture. Optimistically, static testing of five specimens required fourteen to twenty days to account for many of the various issues which arose throughout the process, in particular, avoidance of noxious fumes.

Based on the problems associated with using the Dillon tester, the choice was made to move to a different test apparatus and redesign the experimental setup to permit shear and tensile testing at room and elevated temperatures. The MTS Model 880 Dynamic Material Test System was chosen and is a closed-loop, servo-hydraulic mechanical test system with a 222.4 kN (50 kips) load capacity. All elevated temperature tests performed using this system were displacement controlled and monotonic compressive and tensile loads were applied at constant crosshead displacement rates of 0.5 mm/min (0.0297 in/min). The hydraulically actuated grips were fitted with smooth faced wedges for acoustic emission purposes and serrated wedges were added for standard tension testing. The assembly of components for acquiring test data from this experimental setup as illustrated in Figure 4.9 served several purposes. As in the previous cases, the Measurements Group 2120A strain signal conditioner and 2000 A/D converter were used to acquire data from the strain gages and the Type K thermocouples. For heating specimens, the chamber was replaced by two Research Inc. 4184 infrared strip heaters, a Model 60906 SCR (SC rectifier) to supply power to the heaters and a Omega CN4400 for closed-loop temperature control. Placement of the infrared strip heaters with respect to the MTS grips is shown in Figure 4.10. The main benefits of the strip heaters over the chamber were focusing of the heat source, rapid heating and cooling to the ambient which was much larger than the heat sink.

Acoustic emission monitoring capabilities were also integrated into the setup to evaluate the amplitudes of acoustic events and rate of events as functions of applied displacement and fiber angle relative to the axis of tensile loading. Time-of-flight characteristics could be measured using two Digital Wave Model B1025 transducers (Figure 4.11) in which the signals were amplified with Digital Wave AE broadband pre-amps. The amplified signals were conditioned by passing through high and low-pass filtering prior to

being acquired using Digital Wave parametrics and counter/timer hardware. With this arrangement, single event characteristics could be studied at any point in time during the test in addition to the accumulation of events which spanned the entire test.

4.1.2. Apparent Elastic Constants

4.1.2.1. Stress and Strain

A study of the literature pertaining to measurement of composite elastic constants suggests that more than one proposed method exists for correctly interpreting stress-strain data when evaluating apparent composite properties. According to ASTM D 5379, the shear chord modulus of elasticity is calculated as the slope of the shear stress-shear strain line as defined by two points lying within the linear regime. Although the test procedure is fairly straightforward, the manner in which the departure from linear elastic behavior (i.e. transition or yield) is determined is somewhat ambiguous. Depending on the test conditions and behavior of the composite, this departure could be elastic-brittle, elastic-perfect plastic, bilinear elastoplastic or multilinear elastoplastic in nature and hence, increasingly more subtle. In composites which undergo significant plastic deformation prior to damage development, the separation between strain recorded at the deviation from linearity and strain calculated at the transition becomes greater which may lead to a false sense of where the yield point actually occurs. For this reason, the transition point was not considered within this study to determine the first 50% of the linear elastic regime where the shear modulus was calculated.

The method adopted for data reduction in determining the extensional and shear elastic properties is similar to the method proposed in *Ref. 74*. Unlike highly orthotropic composite materials which might require stress and strain correction factors to account for the lack of uniformity across the gage section, correction factors were not calculated for the 8HS woven fabric composites. It was assumed that these composites behaved as quasi-

isotropic laminates, provided they were symmetrically oriented. Preliminary load-unload tests at increasingly higher loads were used to indicate the range of strains within the linear regimes and roughly establish where the first 50% occurred. These tests provided an indication of the limiting strain at the point when the unloading slope began to change. These tests also showed that slight nonlinear behavior was present at the beginning of the load history for both types of tests even though a small preload was used to "seat" the fixtures. For the shear tests, it seemed that additional sliding and load repartitioning occurred until the contacting surfaces became perfectly mated at which time the shear response became linear. For the tensile tests, the initial nonlinear response was directly associated with seating of the serrated wedge inserts into the grips. In both test cases, these initial responses were ignored in estimating the 50% region of the linear elastic regimes. Least-squares straight lines were fitted to the experimental data and the point where the fitted lines began to deviate from the experimental curve marked the endpoint for the linear regime. Once the endpoint was established, the slope of the line was calculated using the first half of the line. If deviation from the least-squares fit was not clearly evident, then the slope was calculated within the first 20-25% of the maximum load capacity.

Preliminary comparisons of shear strain readings from gages placed on the front and back of each Iosipescu specimen caused some concern. Not only were the readings significantly different between gages, but the readings were also different between the +leg and -leg, each oriented at $\pm 45^\circ$ to the notch root axis. The concern was that these differences would not provide accurate and repeatable shear modulus measurements. A possible explanation of these differences was given by Adams *et al.* [75] in their comprehensive experimental strain analysis of the Iosipescu shear test specimen. They concluded that the difference in strain measurements observed between the +leg and the -leg of a two-element rosette was not a result of strain gage misalignment in terms of rotation about the center of the specimen gage section. This difference was, however, a function of the degree of orthotropy exhibited by the material. Materials which had greater orthotropy ratios showed greater differences between the strains measured at $\pm 45^\circ$. This behavior was also duplicated

by the author using UD carbon-epoxy and isotropic titanium-aluminide Iosipescu specimens. Apparently, materials with low transverse stiffness result in higher normal strain ϵ_y in the gage section of Iosipescu specimens and the higher longitudinal strain ϵ_x is a result of Poisson effects induced by compression from the inner loading blocks. The net outcome is that the presence of these strains does not affect the shear modulus calculations (c.f. Eqs. 4.5-4.7) because a shift of the Mohr's circle representation of the strain state shows that the tensile and compressive strains at 45° change in magnitudes by the same amount, i.e. the compressive strain increases while the tensile strain decreases.

Apart from the explanation given for the difference in shear strains from each leg, it has been suggested by others for UD composite materials that the difference between shear strain calculated from the front and back gages is due to specimen twisting from an applied torsion about the long axis. In the preliminary stages of this study, twisting of the 8HS woven fabric composites was also noticed, however as will be discussed later, torsion was not the cause of unequal gage readings. Rather, the difference arose from lateral bending which proved to be unavoidable in the Iosipescu test because the nature of specimen loading is always anti-symmetric.

4.1.3. Apparent Failure Stresses

One of the primary concerns in the design of composite components is knowledge of the composite strengths. In order to accurately predict composite failure and assign factors of safety or design allowables, designers must employ reasonable failure criteria. The inputs to these failure criteria are usually in terms relating the measured ultimate strengths to the applied stresses. So it becomes necessary then to be able to correctly evaluate the composite strength properties. The problem lies in attempting to clarify what is meant in defining the material tensile strength or shear strength for example. Not only does this clarification become a question of semantics, but we are finding that it is also test dependent which contradicts the notion of strength being intrinsic. Although the semantics are somewhat

ambiguous as set forth in the standards for tensile and in-plane shear testing, in the strictest sense, the term "strength" should imply the stress reached at failure when failure is governed solely by a homogeneous and uniform stress field, whether it is pure shear or pure tension. This is where the controversy emerges: few, if any, of the available experimental tests for composite materials can produce a pure and uniform stress state.

For two of the most popular tests used to determine composite strength properties of UD composites, examples of this problem have been made completely obvious by *Refs. 76-77*. From the arguments given by those authors, it might make more sense to view the composite apparent tensile and in-plane shear strengths as the resistances of the material to macroscopic shear and tensile loading as produced by the given experimental test. This explanation, then, tends to fall in-line with the comments made in *Ref. 77* and is the viewpoint adopted for evaluating strength properties of composites based on woven fabric reinforcements.

The process of evaluating the composite shear strength properties has proved to be a very wide-open and debatable issue, therefore it was decided to characterize the woven fabric composite shear and biaxial "strengths" on the basis of three types of exhibited behavior. After all, the issue of apparent strength has been a debatable one so the concept of how failure is strictly defined must be arguable also. For the shear and biaxial Iosipescu specimens tested at room temperature, the shear stresses were determined at the onset of nonlinearity, as established in the previous section, and the shear stresses were also determined at the onset of failure and at the maximum loading capacity. The onset of failure was chosen to coincide with the inflection point on each stress-displacement curve. The likelihood of strain gage debonding was high at large strains and both the load (stress)-displacement and stress-strain results were necessary to determine failure stresses. For the shear Iosipescu specimens tested at elevated temperatures, the failure stresses were considered only at the onset of failure and the maximum loading capacity on the stress-displacement curves. Above 204.4 °C (400 °F), behavior would likely be very nonlinear and reasonable comparisons of elastic limits might be questionable.

4.1.3.1. Comparisons at Elevated Temperatures

In addition to knowledge of composite failure behavior at room temperature, much remains to be learned about the mechanical behavior of composites exposed to thermomechanical loads. Structural composite architectures based on cost effective and easily processed polyimides, such as PMR15, have often been employed in turbofan engine components. Previous studies have addressed the elevated temperature performance of composites based on PMR15 under thermal, static tensile and fatigue loading conditions, but no work has addressed the quasi-static shear and biaxial performance as a function of temperature. Considering that PMR15 polyimide resin is not environmentally friendly to process, a suitable replacement resin (non MDA) cannot be suggested until all aspects of PMR-based composite behavior are fully realized. In this study, the elevated temperature experiments were performed to evaluate the influence of matrix composition and ply orientation on shear deformation and shear failure behavior. Iosipescu specimens from the second graphite-PMR15 plaque $[0^\circ]_{16S}$ were compared to specimens from the graphite-Avimid R plaques $[0^\circ]_{10S}$ and $[0^\circ/90^\circ]_{10S}$. The degradation of stiffness and strength properties was explored together with the effects of viscoplastic behavior. Due to the difficulties associated with quasi-static shear and biaxial testing at elevated temperatures, the results were too limited to suggest statistical significance. However, these initial studies were fundamentally necessary to support any future efforts in life prediction of the polyimide composites exposed to harsh environments.

4.2. Modeling of Shear and Biaxial Tests

From the preliminary shear and biaxial test results obtained during the equipment calibration phase at room temperature, it was noticed that the stress-displacement curves were mostly linear or bilinear, but the shear stress-strain curves were highly nonlinear. It also appeared that the slopes of both responses were dependent on the biaxial loading conditions. Clearly,

a complete understanding of the elastic and inelastic behavior required knowledge of the damage and failure processes in conjunction with the fixture-to-specimen interactions. In assessing the woven fabric composite response to shear and biaxial deformation, certain structural and material nonlinearities were identified. The structural nonlinearities were boundary contact (friction) and large strains/rotations (geometric), while the material nonlinearities were elastoplastic deformation and progressive damage. The challenge was to determine which of these nonlinearities was the most characteristic of the shear and biaxial load histories.

4.2.1. Structural Nonlinearities

In practice, the in-plane shear response of most composite materials is exhibited by severe nonlinearity. The nonlinearity is usually attributed to plastic deformation of the matrix. However, it is certainly possible that this response could be partly composed of geometric nonlinearities, i.e. large rotations and displacements as well as boundary contact nonlinearities such as sliding between the specimen contacting surfaces and the fixture loading blocks. These effects could be especially well-pronounced in the Iosipescu specimens subjected to large displacements. Since the woven fabric composites investigated in this research fail at large displacements, especially under biaxial loading conditions, these nonlinear effects must be evaluated numerically. The influence of these effects on the stresses and failure process needs to be established.

Ho *et al.* [78] previously had investigated the effect of structural and material nonlinearities on the stress distributions in UD graphite-epoxy Iosipescu specimens subjected to relatively small displacements. They concluded that nonlinearities cannot be ignored when evaluating the stress distributions in 0° and 90° specimens, however their approach was questionable. In analyzing the nonlinear response of Iosipescu specimens, two conditions are never known *a priori*, namely the nonlinear constitutive equations and friction between the specimen contacting surfaces and fixture loading blocks. In their analysis, the friction

coefficient and constitutive relationships were modified iteratively until a good match was obtained between the numerical and experimental results. This is not strictly correct because a match can almost always be obtained between both sets of results. Ideally, the numerical results should depend only on the unknown coefficient of friction and not on modifications to the nonlinear material behavior.

Attempts were made herein to establish the effects of specimen sliding and geometric nonlinearity (due to the change in specimen geometry) on the global mechanical response and internal stresses of the Iosipescu specimens. The finite element computations were performed assuming that the specimens were loaded in both the biaxial and modified biaxial fixtures. Large displacements [$\delta \geq 3$ mm (0.1 in)] were prescribed and the boundary contact condition allowed Coulomb friction (sticking-sliding) with a coefficient range of 0.1 to 0.8. Both 2-D finite element models shown in Figures 4.12(a) and (b) employed contact point-to-surface pseudo-elements from the ANSYS element library (CONTAC48) which were placed at the interfaces between the loading blocks and the specimens. The models maintained a thickness of unity and were constrained at the specimen center against vertical and horizontal displacements ($\delta_x, \delta_y = 0$). The loading blocks on the right side were prescribed displacements of $\delta_y = -0.5\delta$ whereas the loading blocks on the opposite side of the specimen were prescribed positive displacements of the same magnitude. Thus, the total prescribed displacement acting on the specimens was equal to δ . Using these boundary conditions, the effect of specimen rotation with structural nonlinearities was also studied by resolving the prescribed displacements into component displacements of $\delta_x(\sin \alpha)$ and $\delta_y(\cos \alpha)$.

4.2.1.1. Geometric

Geometric nonlinearities refer to the nonlinear behaviors associated with a structure as it deflects. Since the stiffness $[K]$ is a function of the displacement $\{u\}$, shape change prescribed by large deflections causes the stiffness to change. In their investigation of geometric nonlinearities in the Iosipescu test, Ho *et al.* stated that the specimen distortion in

0° and 90° UD composites did not influence the shear response because of the overestimation of distortion angles due to fiber rotation. An important aspect here was to determine whether or not this rotational behavior, when coupled with contact analysis, was influential on the stress field distribution in woven fabric composites.

When 2-D eight-node isoparametric finite elements are employed in a nonlinear analysis, the ANSYS program can account for four types of geometric nonlinearities: large deflection, large strain, stress stiffening and spin softening (see Table 4.2) [79]. The large deflection procedure is used when rotations are large and the stress induced mechanical strains are small. According to related theory, the approach adopted to solve large deflection problems incorporates a co-rotational algorithm of the form

$$[B_n] = [B_v][T_n] \quad (4.11)$$

where $[B_v]$ represents the usual small strain-displacement relationship in the original coordinate system and $[T_n]$ relates the orthogonally transformed element coordinates to the original coordinates, the difference indicating the amount of rigid body rotation. In contrast, the large strain procedure assumes mechanically induced strains are of a finite nature and that there is an associated volume change in the material. The volume change can be described in terms of the deformation gradient where $[I]$ is the identity matrix and the deformation gradient $[F]$ defines the difference between position vectors for the deformed and undeformed positions of a deformed body:

$$\frac{dV}{dV_o} = \det[F] \quad (4.12)$$

where

$$[F] = [I] + \frac{\partial \{u\}}{\partial \{X\}} \quad (4.13)$$

Based on the right polar decomposition theorem, the deformation gradient can be separated into rotation and shape change according to

$$[F] = [R][U] \quad (4.14)$$

where $[R]$ is the rotation matrix ($[R]^T[R] = [I]$) and $[U]$ is the right stretch or shape change matrix. This theorem specifies that material lines will remain orthogonal even though they will not after a shearing type of deformation.. Either of these conditions may be augmented through implementation of stress stiffening which couples the in-plane and transverse displacements, generating an additional stiffness matrix. Stress stiffening tends to reduce oscillations in convergences associated with problems posing a high degree of structural nonlinearity such as exhibited in large displacement and element rotation problems. The reduction in convergence oscillations directly reflects upon the reduction in total problem solution times.

Direct implementation of the co-rotational algorithm involves [79] determining the updated element transformation matrix $[T_n]$, extracting the deformational displacement $\{u_n^d\}$ from the total element displacement $\{u_n\}$ for computing both the stresses and restoring force $\{F_c^{nr}\}$ and updating the node rotations from the rotational increments $\{\Delta u\}$. From Eq. 4.11, the elemental tangent stiffness matrix takes the form

$$[K] = \int_V [T_n]^T [B_v]^T [D] [B_v] [T_n] dV \quad (4.15)$$

and the element restoring force is

$$[F^{nr}] = \int_V [T_n]^T [B_v]^T [D] \{\varepsilon_n^{el}\} dV \quad (4.16)$$

The elastic strain is computed by $[B_v]\{u_n^d\}$ and the element deformational displacement is responsible for straining.

4.2.1.2. Boundary Contact

Friction is a complex phenomenon and is a function of the surface roughness, temperature, materials in contact and relative velocities. The contact problem involving mutual boundaries and friction is highly nonlinear, not only because of the varying conditions, but because of the friction itself. According to Chen and Yeh [80], contact or collision between component surfaces cannot allow for penetration and the contact tractions are always compressive. Mathematically, Xiaoyu [81] has presented the relationship for bodies (A and B) that cannot penetrate into each other:

$$(\mathbf{u}^B - \mathbf{u}^A) \cdot \mathbf{n} + g_n \geq 0 \quad (4.17)$$

where \mathbf{u}^A and \mathbf{u}^B are the displacements of a pair of opposing surface nodes and $\mathbf{n} = \mathbf{n}^B = -\mathbf{n}^A$, where the \mathbf{n} 's are the surface normals and g_n is the separation function given by

$$g_n(\xi, \eta) = \zeta^B(\xi, \eta) - \zeta^A(\xi, \eta) \quad (4.18)$$

The coordinates (ξ, η, ζ) are in reference to some defined local coordinate system and ζ^A or ζ^B is the local shape of body A or body B. Coulomb's law states that the sliding force F_s , transmitted between two bodies cannot exceed a fraction of the normal force F_n . That is

$$|F_s| \leq -\mu F_n = F_c \quad (4.19)$$

where F_c is the critical friction resistance and μ is the coefficient of friction. Beyond F_c ,

relative sliding between the bodies will start to occur. As sliding occurs, tangential forces arise between opposing contact and target surfaces. Contact kinematics is concerned with the precise tracking of the nodes and surfaces to define clear and unambiguous contact conditions, e.g. to delineate between an open or closed contact situation. How this task is accomplished depends on the numerical algorithm employed to manipulate both the tangential forces (sliding) and normal forces (sticking and penetration). Depending on the solution method, rules for contact compatibility must be met.

The ANSYS finite element analysis code [79, 82-83] permits the user to specify two methods for enforcing contact compatibility, the penalty method or a combined penalty plus Lagrange multiplier method. To conduct a contact finite element analysis as in the case of modeling boundary contact between the Iosipescu fixture loading blocks and specimen, a stiffness relationship must be established between the areas of contact. This can be accomplished via an imaginary spring placed between the mating areas when contact occurs. Under the penalty method, compatibility is enforced by means of a contact stiffness as

$$f_n = \begin{cases} K_n \cdot g_\Delta & g_\Delta \leq 0 \\ 0 & g_\Delta > 0 \end{cases} \quad (4.20)$$

where K_n is the input contact stiffness and g_Δ is the contact gap. For the combined penalty plus Lagrange multiplier method, a Lagrange multiplier component of force is computed locally and iteratively. This component can be expressed as

$$f_n = \min(0, K_n, g + \lambda_{i+1})$$

$$\lambda_{i+1} = \begin{cases} \lambda_i + \alpha(K_n \cdot g_\Delta) & |g_\Delta| \geq \omega \\ \lambda_i & |g_\Delta| < \omega \\ \alpha < 1 \end{cases} \quad (4.21)$$

where λ_{i+1} is the Lagrange multiplier force at iteration (i+1) and ω is a user defined compatibility tolerance. In any case, the contact stiffness has to be selected so it is large

enough to keep the penetration acceptably small, but small enough to ensure that convergence or ill-conditioning is not caused. Since user input values for the normal and tangential forces are not known *a priori*, suitable approximations must be made through iterations and trial-and-error. A reasonable starting point for estimating contact stiffness and tangential force for gross solids can be assumed as

$$K_n = f \cdot E \cdot h, \quad K_t = 0.01K_n \quad (4.22)$$

where f is a factor between 0.01 and 100, E is the elastic modulus of the more pliable contacting material and h is a measure of the characteristic contact length. It should be noted that these estimates may or may not constrain the model from over-penetration of mutual surfaces. The proper choice will depend on the compliance ratio of the contacting material to the target material. If the ratio is extremely high and (or) the displacement is large, gap criteria may not be met.

In implementing the elastic Coulomb friction model which allows both sticking and sliding conditions, the tangent stiffness matrix, formed by the outer product of interpolation vectors, is of the form

$$[K] = \begin{cases} K_n \{N_n\} \{N_n\}^T + K_s \{N_s\} \{N_s\}^T & \dots \textit{sticking} \\ K_n \{N_n\} \{N_n\}^T & \dots \textit{sliding} \\ [0] & \dots \textit{open} \end{cases} \quad (4.23)$$

where the interpolation vectors $\{N_s\}$ and $\{N_n\}$ are given in terms of a local s-n coordinate system relative to the contacting plane as

$$\begin{aligned} \{N_s\} &= \begin{bmatrix} -\frac{1}{2}(1-s^*) & 0 & -\frac{1}{2}(1+s^*) & 0 & 1 & 0 \end{bmatrix}^T \\ \{N_n\} &= \begin{bmatrix} 0 & -\frac{1}{2}(1-s^*) & 0 & -\frac{1}{2}(1+s^*) & 0 & 1 \end{bmatrix}^T \end{aligned} \quad (4.24)$$

where s^* is dimensionless and ranges from -1.0 to +1.0. Initially, contact is treated as elastic sticking and the goal is to determine the penetration g and the contact point s^* regardless of frictional forces. Subsequent to initial contact, friction develops according to

$$f_s = \begin{cases} K_t u_s^e < F f_s & \dots \textit{sticking} \\ f_s & \dots \textit{sliding} \end{cases} \quad (4.25)$$

4.2.2. Load Eccentricities

Over the last fifteen years, a number of researchers have contributed significantly to identifying and understanding many of the idiosyncrasies associated with the testing of composite materials using the Iosipescu shear test. The popularity of this test for shear characterization of composite materials is, in large part, due to three factors. The test specimen geometry is simple and relatively easy to produce, the material and associated facility costs can be made low compared with more advanced test schemes and the test is reasonably easy to conduct, or so things appear. The reality is that interactions between the Iosipescu shear test fixture and specimen can be complex and often lead to a combined state of stress which lacks uniformity, contrary to what was originally theorized [46].

The existence of vast amounts of data for numerous composite materials supports the idea that degrees of interaction are made highly dependent on geometry, material anisotropy and material orientation, further lending credibility to the problems associated with completely understanding the test. As an example, an improperly designed test can eccentrically load a specimen and produce unwanted characteristics like erroneous shear modulus measurements and failures at loads below the actual apparent shear strength. To this end, a great deal of time has been spent by many to understand these problems and interpret which behavior is truly representative of the test. Likewise, time has been invested in attempts to optimize the design of the specimen, fixture and testing apparatus with a fair amount of documented success [48-49,51-52,54,58,63,66,84-89].

According to beam theory which serves as the basis for the Iosipescu test, an anti-symmetrically loaded beam absent of any bending moment produces a pure shear stress distribution that is classically parabolic along the gage section where the bending moment is zero. When opposing notches, each having a 90° included angle, are located on either side of the gage section a more uniform shear stress distribution results. However, if this load condition changes from being anti-symmetric to some other condition, questions arise as to the states of stress and strain produced within the gage section and on the specimen surface. Besides the requirement of load anti-symmetry, other factors such as specimen width and load point effects can influence the outcome of the Iosipescu test.

Traditionally, the load configuration has been explained as either a point load or an evenly distributed load, but finite element analyses and certain experiments have shown that neither assumption is correct. In fact, the shapes of the distributions at the regions of fixture contact tend to depend on characteristics of the deformation process and the manner in which the load is repartitioned. The principle of St. Venant has also been adopted in many cases (including the author's own work) to rule out the possibility that compression induced by the inner contact regions near the notches does not spill into the gage section and affect the failure process. More than likely, it is not discernible on the specimen macroscale whether this is, in fact, a realistic assumption. From a practical standpoint then, the Iosipescu shear test should be viewed as a complex balance between a compression test which induces Euler buckling, a bending test and a pure shear test with the shear component being the most prevalent. This balance can and has been shown to be swayed by test fixture design, thin test specimens, material anisotropy, notch geometry, contact surface heterogeneity and nonlinearities to name a few.

Odom *et al.* [87] focused on three concerns specific to the test using the Wyoming fixture, namely interactions at the fixture-specimen interfaces, specimen twisting and fixture misalignment. They found that the modified Wyoming fixture does not anti-symmetrically load the specimen as suggested by the differences in the distribution of strain measurements from gages placed on the specimen beneath the regions of fixture contact. They also concluded that compliance mismatch between fixture halves was not the reason for specimen twisting and the

often reported large differences in strain measurements between the front and back surfaces of the specimen. With a lateral moment applied to the fixture, it was shown that these differences did not appear to be a function of increasing moment. Lastly, it was shown that fixture misalignment seemed to be largely responsible for erroneous shear modulus measurements. On unidirectional carbon-epoxy, they reported a 21% error in measurement for 2.72° misalignment. In a later experiment involving a new Wyoming fixture design with improved bearing fits, it was concluded that observed twisting and strain mismatch was attributable to lateral instability of the specimen, although this was never proved [89].

In their whole-field strain analysis, Xing *et al.* [85] employed moiré interferometry and finite element analysis to evaluate the experimental errors associated with the effects of specimen twist, bending moment and the loading points for woven graphite-epoxy composites. Twisting was simulated by forcing non-simultaneous contact of the load points through the use of small diameter wire placed between one side of the specimen and fixture. Moiré interferometry results indicated a 50% increase in shear strain from the addition of a torsional load component for the same load as applied in the ideal case. Pierron *et al.* [74,78] identified poorly profiled contacting surfaces as responsible for differences observed between strain measurements on the front and back faces of Iosipescu specimens. A surface profilometer was used to measure deflections on the contacting surfaces and it was found that poorly profiled 0° UD composite specimens presented less scatter in strain measurements than similarly profiled $0^\circ/90^\circ$ cross-ply composite specimens. They reasoned that the surface hardness in the cross-ply specimens (due to the 90° reinforcing fibers) was higher than in the UD specimens. This prevented load repartitioning and led to specimen twist from the additional torsion.

In this numerical study, the goal was to explicitly impose four types of eccentric loads to the Iosipescu specimen, in combination with shear, and identify which mode resulted in the largest difference in surface strains. It needed to be established what effect (if any) eccentric loads had on the stress-strain distributions between alternating layers of ply and matrix. Additionally, it was necessary to establish the influence of load point spacing on the generation of additional moments which could bias the measurement of elastic properties.

Of the nearly infinite number of load perturbations possible, five modes were identified (including the case of shear) for comparison as shown in Figures 4.13(a-e). Case (A) is the condition of shear where there are no resultant moments M_x and M_y . Case (B) is the condition of shear + asymmetric torsion where, ideally, torsion is imposed to one-half of the specimen and the resultant moment M_x exists, but is less than Case (C). For Case (C) which is shear + anti-symmetric torsion, opposing torsion is imposed to both sides of the specimen and the resultant moment M_x is the largest of all cases. Case (D) is the condition of shear + lateral bending where the top and bottom surfaces of the specimen bend towards each other about the long axis rather than twist in opposite directions. Lastly, Case (E) is the condition of shear + lateral rotation where poorly profiled contacting surfaces slide on the fixture loading blocks in such a manner that the specimen becomes unstable along one edge.

4.2.2.1. Numerical Models

Two 3-D numerical models were proposed for this study and are shown in Figure 4.14. The finite element model of the biaxial Iosipescu specimen, shown in Figure 4.14(a), consists of eight-node, layered structural elements (SOLID46) from the ANSYS element library [90]. The ply and matrix layer thicknesses were selected based on a sixteen ply, quasi-isotropic graphite-PMR15 composite having a nominal thickness of 5.0 mm (0.2 in). The total number of layers within a single SOLID46 element through-thickness were thirty-one. Measurements of actual ply thicknesses of 289.0 μm (11.4 mils) suggested a matrix interface thickness of 25.0 μm (0.98 mils). Considering that interface thicknesses ranging from 10-100 μm (0.39-3.9 mils) were reported by the NASA Glenn Research Center³ for similar composites, the thicknesses chosen for each layer in these numerical models seemed reasonable. The finite element model of the modified biaxial Iosipescu specimen (see Figure 4.14(b)) shared identical element/layer properties and both models permitted geometric nonlinearities and

³ Data provided by Mr. Mike Castelli of the NASA Glenn Research Center.

boundary contact (CONTAC49) at the specimen-to-fixture interfaces. From the previous 2-D studies, the coefficient of friction between the blocks and specimen contacting surfaces was chosen as 0.3.

4.2.2.2. Properties and Boundary Conditions

The analytical model presented in Section 3 along with the results from the early phases of experimental testing and 2-D finite element analyses provided the basis for the material properties assumed in this study. These properties are presented in Table 4.3. The boundary conditions imposed were done so in a manner representing what might be plausible if a specimen was carelessly placed in the test fixture or if the mating contact surface profiles were mismatched. For each load case, the loading blocks were moved relative to the specimen centerline (x-axis in Figure 4.13) in ways which would produce the desired eccentricity. Assume that the coordinate system is located at the specimen center, in reference to Figure 4.13, and has the same orientation as shown. The boundary conditions imposed with respect to each eccentric load case are presented in Tables 4.4 and 4.5 for the biaxial and modified biaxial models, respectively. The x, y and z-coordinate displacements in these tables are normalized to the locations of the centers of force distribution ($[\pm c$ or $\pm l$, $\pm h/2 + a$, $\pm t/2 + \text{constant}]$ as given in Table 4.1). For this study, the constant in $\pm z$ was arbitrarily chosen as 3. This implies that the moments about the x-axis were induced from displacements offset by three times the specimen half-width to produce the desired eccentricity.

Shear, shear-compression and shear-tension stress states were numerically generated in the specimen gage section to determine the influence of biaxial stresses on the load eccentricities and calculated surface strains. The prescribed displacements for the shear-compression and eccentric shear-compression loading conditions were resolved into the component displacements in x and y such that $\delta_x' = \delta_x(\sin \alpha)$ and $\delta_y' = \delta_y(\cos \alpha)$, where $\alpha = +30^\circ$ was counter-clockwise from the vertical load axis. Similarly, the prescribed

displacements for the shear-tension and eccentric shear-tension loading conditions were resolved into component displacements where $\alpha = -30^\circ$ was clockwise from the vertical load axis. For all cases, the assumed global displacement δ was arbitrarily set at 0.05 mm (2.0×10^{-3} in) and each half of the specimen was prescribed $\pm 0.5\delta$.

The resultant global loads P and residual moments M_i (where $i \dots x,y,z$) were calculated from the summed reactions F_y at the loading blocks due to prescribed displacements. The resultant loads were calculated on each side of the specimen relative to its centerline by adding the reaction at the inner loading block to the reaction at the outer loading block. The residual moments were also calculated on each side of the specimen by summing the block reactions F_i (where $i \dots x,y,z$) at the inner and outer loading blocks about the specimen center.

4.3. Nonlinear Material Behaviors in Shear

The in-plane shear response of most composites is highly nonlinear as suggested in Section 4.2.1. Results for 8HS woven fabric composites based on polyimide matrices tend to support this statement even though data from neat resin tests implies elastic-brittle behavior. Although structural nonlinearities might contribute to some degree, the severity of the observed nonlinear shear behavior clearly suggests that material nonlinearities must play an important part. In order to evaluate the significance and type of nonlinear material behaviors, the author has proposed a set of numerical analyses which decompose these nonlinearities into those responses which are macroscale, elastoplastic or plastic along with those responses which indicate macroscale, progressive damage.

The problem of evaluating composite material nonlinearities at the macroscale can really be viewed as either one of two cases. In the first case, a solution to the nonlinear material problem may be derived on the basis of forcing experimental data to collapse on a particular mathematical relationship which best fits the behavior and is in-line with plasticity theory. In the second case, a solution may be reached by applying generalized functions of

plasticity theory on the basis of assuming that the material behaves accordingly and provides reasonable agreement to experimental data. Several researchers have successfully implemented models to predict the elastic-plastic response of UD polymer matrix composites [68,91-94]. However, determining the nonlinear mechanical response of woven fabric composites using experimental uniaxial and (or) biaxial tests has been limited [18,20-21,95]. Of the few published attempts to apply a macroscopic continuum approach to determine the plastic behavior of woven fabric composites, Vaziri *et al.* [96] suggested a model which requires knowledge of the axial and shear yield strengths. These yield strengths can be difficult to obtain experimentally for most composite materials and their model only provided a bilinear approximation of plastic properties. Naik [22] suggested an empirical relationship between shear stress and shear strain, however this type of approach cannot be generalized to various fiber architectures, e.g. UD composites, 2-D woven fabric composites or 3-D woven fabric composites.

More recently, Odegard *et al.* [68] proposed a inelastic constitutive relation for woven fabric composites based on a power law-type of behavior. This approach followed the first case described above for deriving nonlinear material behavior in that experimental data from a series of off-axis tensile tests was collapsed into an effective stress-strain curve. The only limit to this approach was that the ANSYS finite element code did not readily permit describing nonlinear material using a power law relationship. A work-around was implemented in which the power law curve was approximated with a series of progressive bilinear numerical approximations. The results for shear deformation at small strains were in good agreement with the experimental results for 8HS woven fabric composites tested using the modified biaxial Iosipescu fixture.

This work focused on the second case described above for deriving nonlinear material behavior. A generalized yield function for 3-D anisotropic plasticity was applied to numerically evaluate the nonlinear material behavior of biaxial Iosipescu specimens tested under shear dominated, biaxial loading conditions. The finite element model adopted the same geometry as the model used to study load eccentricities. However, the element type was

changed because the layered SOLID46 elements do not permit plastic material behavior, nor do they permit element death which is focused on in Section 4.3.2 for progressive damage analysis. The finite element model consists of 7391 nodes and 1044 twenty-node isoparametric, structural brick elements (SOLID95) from the ANSYS element library [97]. The model also consists of 5232 CONTACT49 pseudo-elements, again with an assumed friction coefficient of 0.3 chosen from the results of the 2-D finite element analyses. The composite elastic properties, yield stresses and tangent moduli are given in Table 4.6.

4.3.1. Anisotropic Plasticity

Plasticity theory provides a mathematical framework to characterize the elastoplastic response of materials. For rate and time independent plasticity, three ingredients are a necessity to the theory, namely the yield criterion, the flow rule and the hardening rule. Plastic strains are assumed to develop instantaneously and irreversible straining is indicated at a certain level of stress. That is, a material develops plastic strains when an equivalent stress is equal to some defined material yield parameter σ_{ij}^y such that

$$f(\{\sigma_{ij}^e\}) = \sigma_{ij}^y \quad (4.26)$$

If the yield parameter or criterion is not exceeded at a current stress level, then stresses will develop according to linear elastic constitutive relations. For orthotropic solids, Hill [98] proposed a quadratic yield function in terms of stresses to reflect differences in strengths due to anisotropy. This quadratic yield function is of the form

$$\begin{aligned} f(\sigma_{ij}) = & \frac{F}{2}(\sigma_{22} - \sigma_{33})^2 + \frac{G}{2}(\sigma_{33} - \sigma_{11})^2 \\ & + \frac{H}{2}(\sigma_{11} - \sigma_{22})^2 + L(\sigma_{23})^2 + M(\sigma_{31})^2 + N(\sigma_{12})^2 = 1 \end{aligned} \quad (4.27)$$

where the subscripts 1, 2 and 3 refer to the principal directions of a generally orthotropic material and F, G, H and L, M, N are parameters that characterize the current state of anisotropy. The first three orthotropic material parameters **F**, **G** and **H** are defined in terms of the tensile yield stresses (X, Y, Z), in the principal directions, to be

$$\begin{aligned} G + H &= (X^2)^{-1}, & 2F &= (Y^2)^{-1} + (Z^2)^{-1} - (X^2)^{-1} \\ H + F &= (Y^2)^{-1}, & 2G &= (Z^2)^{-1} + (X^2)^{-1} - (Y^2)^{-1} \\ F + G &= (Z^2)^{-1}, & 2H &= (X^2)^{-1} + (Y^2)^{-1} - (Z^2)^{-1} \end{aligned} \quad (4.28)$$

where only one of the F, G or H parameters can be negative and the yield stresses differ considerably. Together with two similar inequalities, $F \geq G$ only if $X \geq Y$. The last three orthotropic material parameters **L**, **M** and **N** are defined in terms of the shear yield stresses (R, S, T), with respect to the principal directions, to be

$$2L = (R^2)^{-1}, \quad 2M = (S^2)^{-1}, \quad 2N = (T^2)^{-1} \quad (4.29)$$

The theory adopted here for plasticity in woven fabric composites extends Hill's theory for orthotropic solids to account for a difference in yield strength in tension and compression. With ANSYS [99], the associative flow rule is assumed and plastic strains occur normal to the yield surface which is a distorted circular cylinder initially shifted in stress space. Work hardening is also assumed which suggests that the surface expands in size while remaining centered about its initial centerline. The yield criterion in Eq. 4.26 is then redefined to be

$$3f(\sigma_{ij}) = \{\sigma_{ij}\}^T [N] \{\sigma_{ij}\} - \{\sigma_{ij}\}^T \{M\} - k = 0 \quad (4.30)$$

where **[N]** describes the variation of the yield stress with orientation and takes the form of

$$N = \begin{bmatrix} N_{11} & N_{12} & N_{13} & 0 & 0 & 0 \\ N_{12} & N_{22} & N_{23} & 0 & 0 & 0 \\ N_{13} & N_{23} & N_{33} & 0 & 0 & 0 \\ 0 & 0 & 0 & N_{44} & 0 & 0 \\ 0 & 0 & 0 & 0 & N_{55} & 0 \\ 0 & 0 & 0 & 0 & 0 & N_{66} \end{bmatrix} \quad (4.31)$$

$\{M\}$ is a strength differential vector that accounts for the differences in yield strength between tension and compression and \mathbf{k} is the material yield parameter.

Plastic strains are incremented according to the associative flow rule given by the relationship

$$\{d\varepsilon_{ij}^{pl}\} = d\lambda \left\{ \frac{\partial f(\sigma_{ij})}{\partial \sigma_{ij}} \right\} \quad (4.32)$$

where $d\lambda$ is a Lagrangian multiplier which determines the amount of plastic straining. It is evident that the size of the plastic increment is related to the current stress state, the total strain increment and the form of the yield and potential surfaces. Since the current stress state is reduced by plastic straining to satisfy the yield criterion, the criterion must represent a closed surface. From this, the independence of the uniaxial strengths are restricted through satisfying three conditions. The first condition, the consistency equation must be met because plastic incompressibility is assumed. This equation is given by

$$\frac{X^+ - X^-}{(X^+)(X^-)} + \frac{Y^+ - Y^-}{(Y^+)(Y^-)} + \frac{Z^+ - Z^-}{(Z^+)(Z^-)} = 0 \quad (4.33)$$

where X, Y and Z are the uniaxial strengths and the superscripts + and – indicate tension and compression, respectively. The second condition is that the yield strengths must also define a closed, elliptical yield surface by meeting the equation

$$N_{11}^2 + N_{22}^2 + N_{33}^2 - 2(N_{11}N_{22} + N_{22}N_{33} + N_{11}N_{33}) < 0 \quad (4.34)$$

where the individual terms of the **[N]** matrix can be evaluated by

$$N_{jj} = \frac{k}{(\sigma_j^+)(\sigma_j^-)}, \quad j = 1 \text{ to } 6 \quad (4.35)$$

and σ_j^{\pm} are the tensile and compressive yield strengths in (x, y, z, xy, xz, yz). Assuming that $N_{11} = 1$, the material yield parameter can be determined by $k = (\sigma_x^+)(\sigma_x^-)$. The third condition is that the elliptical yield surface must be satisfied through an equivalent plastic strain level of 20% since work hardening requires the yield strengths to change with increased plastic straining.

Numerical implementation of plastic straining employs a Euler backward scheme to enforce the consistency equation which ensures that updated parameters lie on the closed yield surface. Based on a trial strain, a trial stress is used to evaluate the equivalent stress. If the yield stress is not exceeded, no plastic strain increment is necessary. However, if the yield stress is exceeded, then the Lagrangian multiplier is determined using a local Newton-Raphson iteration procedure and the plastic strain increment is calculated from Eq. 4.32. The current plastic strain is updated from the previous step (if it exists) and the elastic strains are given by

$$\{\boldsymbol{\varepsilon}^{el}\} = \{\boldsymbol{\varepsilon}^t\} - \{d\boldsymbol{\varepsilon}^{pl}\} \quad (4.36)$$

where $\boldsymbol{\varepsilon}^t$ refers to the trial strains and $d\boldsymbol{\varepsilon}^{pl}$ are the plastic strain increments. Knowing the elastic strain components, the stress components are readily available according to the relationship $\{d\boldsymbol{\sigma}\} = [\mathbf{D}] \{d\boldsymbol{\varepsilon}^{pl}\}$ where **[D]** is the strain-displacement matrix.

4.3.2. Damage and Failure

Several damage and failure criteria have been proposed to predict the initiation of damage and strengths of composite materials. These criteria are usually either stress or strain based and may be categorized as explicit or empirical. The maximum stress and maximum strain criteria are explicit. That is, failure is assumed to occur when singular stresses or strains exceed their critical values in any one of the principal material directions. Unlike the explicit failure criteria, empirical failure models adopt some form of a quadratic or higher-order polynomial which best approximates the failure surface. The polynomials also typically include one or more interaction terms that can be difficult to experimentally obtain. The best-known of these criteria which can be quadratic in stress or strain space are the Tsai-Hill, Tsai-Wu and Hashin criteria [100-102]. These criteria maintain some interactions in terms and essentially have extended the von Mises yield criterion to account for the orthotropic behavior exhibited by many composite materials. The main disadvantages of the first two criteria is that they cannot predict failure modes well and they tend to underestimate failure stresses under certain biaxial conditions. The advantage of the Hashin criterion is that fiber failure in tension or compression is indicated as well as matrix failure in tension or compression.

From the standpoint of including one or more of the above failure criteria in a progressive damage scheme using finite element analysis, implementation can prove to be complicated. Often, what was done in the past was to incorporate the appropriate criterion to indicate either a fiber-based failure or a matrix-based failure and reduce stiffnesses at “failed” element integration points in the direction of failure. With this approach, it intuitively made sense to permit a near-zero stiffness in the failed directions upon satisfying the criterion while permitting residual stiffness in the other directions. The stiffness reduction scheme often adopted for UD and plain woven composites in these instances was similar to the scheme proposed by Blacketter *et al.* [26]. That is, the reduction multiplier was biased towards the failure mode and total element failure occurred after 65-70% of the points failed.

For many finite element codes, implementing such a continuous or “progressive” reduction scheme through the entire load history is not as problematic as with other codes. In ANSYS, making changes to material stiffness on a element integration point basis is less straightforward than making material stiffness changes to suggest damage on the basis of total element failure. However, it doesn’t make much sense intuitively to employ any of the previous failure theories as criteria to fail elements altogether. With this approach (element death scenario), a damage criterion which accounts for both stress and strain over a given volume seems to be more appropriate.

4.3.2.1. Progressive Damage Criterion

The failure criterion proposed by the author for use in predicting the progression of damage in 8HS woven fabric composites, subjected to shear and biaxial loads, is based on the total of the average strain energy density to critical strain energy density ratios

$$\frac{\bar{U}_{11}}{U_{11}^c} + \frac{\bar{U}_{22}}{U_{22}^c} + \frac{\bar{U}_{33}}{U_{33}^c} + \frac{\bar{U}_{12}}{U_{12}^c} + \frac{\bar{U}_{23}}{U_{23}^c} + \frac{\bar{U}_{13}}{U_{13}^c} \geq 1 \quad (4.37)$$

where the \bar{U}_{ij} are the volume equivalent, linear elastic strain energy densities and the U_{ij}^c are the critical strain energy densities determined from experimental stress-strain curves. The volume average elastic strain energy densities are given by

$$\bar{U}_{ij} = \frac{1}{2} \bar{\sigma}_{ij} \bar{\varepsilon}_{ij} \quad (4.38)$$

where the average stresses and strains are derived by averaging the respective tensors over each of the finite element volumes (V) as

$$\bar{\sigma}_{ij} = \frac{1}{V} \int_V \sigma_{ij}(x, y, z) dV, \quad \bar{\varepsilon}_{ij} = \frac{1}{V} \int_V \varepsilon_{ij}(x, y, z) dV \quad (4.39)$$

Combining Eqs. 4.37, 4.38 and 4.39 yields

$$\begin{aligned} & \frac{\int_V \sigma_{11} dV \int_V \varepsilon_{11} dV}{V^2 \sigma_{11}^c \varepsilon_{11}^c} + \frac{\int_V \sigma_{22} dV \int_V \varepsilon_{22} dV}{V^2 \sigma_{22}^c \varepsilon_{22}^c} + \frac{\int_V \sigma_{33} dV \int_V \varepsilon_{33} dV}{V^2 \sigma_{33}^c \varepsilon_{33}^c} \\ & + \frac{\int_V \sigma_{12} dV \int_V \varepsilon_{12} dV}{V^2 \sigma_{12}^c \varepsilon_{12}^c} + \frac{\int_V \sigma_{23} dV \int_V \varepsilon_{23} dV}{V^2 \sigma_{23}^c \varepsilon_{23}^c} + \frac{\int_V \sigma_{13} dV \int_V \varepsilon_{13} dV}{V^2 \sigma_{13}^c \varepsilon_{13}^c} \geq 1 \end{aligned} \quad (4.40)$$

This equation implies that failure occurs when the sum of various combinations of the six ratios of instantaneous strain energy densities to critical strain energy densities becomes equivalent to one. It further suggests that the material is generally orthotropic and each of the principal strain energy densities are independent of each another. In this study, Eq. 4.40 was implemented in a ANSYS progressive damage routine using the full Newton-Raphson incremental iterative method.

At each load step, every element within the 3-D model of the biaxial Iosipescu specimen was checked to see if the failure criterion was satisfied. If failure was calculated, the element was “killed” by reducing its stiffness to a value well below that of unity (0.50). A very small value was necessary to maintain some discrete stiffness and avoid convergence difficulties. Although the element physically remained within the model, there was no contribution on calculating the load vector. At each new load step, additional elements which met the criterion were failed and the tangent stiffness matrix was recomputed. When equilibrium was established between the internal (using the updated tangent stiffness matrix) and external load vectors, the analysis was advanced to the next load step. The failed elements were stored in each load step in reference to the critical strain energy density that was exceeded. The motivation behind storing the failed elements was: 1) to identify which components of Eq. 4.40 were the most representative, and 2) to see if some order of qualitative comparison existed with the damage reconstructed from the composite Iosipescu specimens using the procedure outlined in following the section.

4.3.2.2. Damage Reconstruction

For 0° UD composite specimens (fibers oriented parallel to the long axis of the Iosipescu specimen), failure under all loading conditions, either shear or biaxial, occurs as a result of axial splits initiated at the roots of the notches [54,58, 60-62]. These form parallel to the fibers and propagate on one side of the notch tip away from the innermost loading point. The split formation is always manifested by two successive drops on the stress-displacement curve. Unidirectional composite specimens having 90° fibers (oriented parallel to the notch root axis) always fail catastrophically. For all loading angles, cracks originate at the notch root and propagate in an unstable manner parallel to the fibers.

The failure process in both 0° and 90° UD Iosipescu specimens can be easily determined since the failure is through-thickness and the cracks are visible on the specimen surface. For the woven fabric composites, the failure process is much more complex and can vary through the thickness. In this case, the failure characteristics cannot be determined by examining only the specimen surface, therefore a detailed analysis of through-thickness damage is required.

In order to thoroughly evaluate the damage zone development and failure modes most prevalent in the graphite-PMR15 Iosipescu specimens subjected to shear dominated, biaxial loading conditions, specimen dissection and serial image reconstruction are required. Typical methods used to image composite material damage rely on SEM backscattering, texture mapping, stereo pair imaging, grid generation and solid modeling. The proposed method combines certain aspects of these typical methods and yields potentially more useful information regarding the initiation and development of damage in the specimens through-thickness.

Following a shear test, the central section of the tested Iosipescu specimen was removed along predefined cutting planes (see Figure 4.15) using a Buehler Isomet low speed saw. All cuts were made with a diamond-tipped, circular blade immersed in a special cutting fluid to permit smoother “cut” surfaces and keep the blade cool. Once the central specimen

section was removed, the surface of the sample was saturated with Gatan G-60 quartz-crystalline epoxy and pressurized at 310.3 kPa (45.0 psi) for twenty-four hours to “drive” the epoxy into the fracture surfaces. The main reasons for using the Gatan G-60 were its low viscosity, temperature curing requirements and capabilities for making sub- μ adhesive joints.

After twenty-four hours of pressurization and curing, the sample was placed in a 6.4 cm (2.5 in) diameter mold and hard-mounted using sample preparation epoxy. The hard-mount allowed for safe handling during the hand polishing process using lapping disks and it allowed for secure placement within the SEM. A sample jig was also designed which was capable of moving the sample by a specific value in the z-direction. This was necessary to consistently maintain the same working distance within the SEM after each polish operation. The hard-mounted sample was initially polished just enough to remove the top layer of epoxy and expose the sample surface. This was designated as the z-axis reference surface and tagged index-00. Two sets of three image registration holes were located around the boundaries of the regions of interest (ROI). One of the sets of image registration holes was located at the section center while the other set was located near the top of the notch as shown in Figure 4.16.

After exposing index-00, the surface was sputtered with 150 Å (5.9×10^{-4} mils) of Au-Pd deposit from a Technics Hummer II, dc sputtering system. This was done to prevent localized charging and poor image sampling during the image capturing process. Images were captured using the Zeiss Model 960 analytical SEM in backscatter mode. The working distance was fixed at 16.0 mm (0.63 in), the beam current was 20 kV and the maximum magnification set by the screen capture board was 45x. After imaging index-00, a $350 \mu\text{m} \pm 25 \mu\text{m}$ ($13.8 \text{ mils} \pm 0.98 \text{ mils}$) thickness was polished away to expose index-01 which was again saturated with epoxy. The image capturing and sample polishing processes were repeated until the midline of the composite laminate was reached, at which point the processes were stopped. It was assumed that the damage would be symmetric about the midline since the out-of-plane deformation observed in the Iosipescu specimens, tested in shear, appeared to be nearly symmetric. These processes were also repeated on an untested

specimen to evaluate whether or not polishing caused additional damage.

From the image captures, 2-D “damage maps” were created using the public domain program NIH Image. The program was developed at the U.S. National Institutes of Health and is freely available via the internet at <http://rsb.info.nih.gov/nih-image/>. All indexes were treated separately for both the center target and the notch target. A low-pass smoothing filter was applied in conjunction with a 3x3 median (rank) filter and the image threshold was manually adjusted. The combination of both filters and manual thresholding helped to establish where the edges of damage were relative to the undamaged composite material. The filters smoothed out image noise (artifacts) and thresholding separated darker contrast from lighter contrast. For this analysis, 3x3 smoothing kernels were of the form

$$\begin{bmatrix} 1 & 1 & 1 \\ 1 & 1 & 1 \\ 1 & 1 & 1 \end{bmatrix} \quad \text{or} \quad \begin{bmatrix} 1 & 1 & 1 \\ 1 & 4 & 1 \\ 1 & 1 & 1 \end{bmatrix} \quad (4.41)$$

and were assumed to remove noise from 1-D or 2-D signals while preserving the image information content. According to Bovik *et al.* [103], the 2-D rank filter may be defined as

$$\hat{X}_{ij} = \text{median} \left\{ X_{i',j'} : (i', j') \in W(i, j) \right\} \quad (4.42)$$

where $W(i, j)$ reflects centering of the filter window at image coordinates (i, j) . Basically, each pixel within a 3x3 neighborhood was replaced with a median value or, all nine pixels were sorted and the center was replaced with a median from the neighborhood.

Once the process of edge detection was finished, the maps were stacked in order and averaged, resulting in 2-D image composites. At this point, a partial quantitative analysis was done to determine the area fractions of damage as a function of the depth from the sample surface. Objects were analyzed using the public domain program UTHSCSA Image Tool 1.25. The program was developed at the University of Texas Health Sciences Center at San Antonio and is freely available from the internet by anonymous FTP at maxrad6.uthscsa.edu.

Important characteristics in the analysis were the number of objects per index, the area of each object, the mean area size and standard deviation.

4.4. Results and Discussion

Apparent Elastic Constants - Two sizes (three types) of strain gages were used to establish the effect of gage size on the error in shear modulus calculations as reported by *Refs 55,57*. The legs of the smaller and centrally located rosette were oriented at $-45^{\circ}/90^{\circ}/+45^{\circ}$ in a half-bridge configuration to evaluate shear strain and the legs of the larger shear gages (either side-by-side or stacked) were oriented at $\pm 45^{\circ}$. In both instances, shear strain was directly calculated from the measured normal strains using Eq. 4.7 and the shear modulus was calculated from the average of shear strains on the front and back faces of each specimen. An example of gage size effect on the measured strains from PMR15-type Iosipescu specimens is shown in Figure 4.17. It can be seen that there is minimal effect of gage size on measured normal strains at $\pm 45^{\circ}$ for an applied shear stress at or below 20.0 MPa (2.9 ksi). Specifically, the difference in average shear strain between both gage sizes is less than 5.0%. This suggests two possibilities: 1) the shear stress and strain distributions along the notch root axes of 8HS woven fabric composite Iosipescu specimens are fairly uniform, or 2) local surface shear stress and strain heterogeneity occurs on a scale smaller than the size of the rosette gage [2.3 mm^2 ($3.6 \times 10^{-3} \text{ in}^2$)].

Since the average shear strains calculated using either size of gage were nearly equivalent for the PMR15 and Avimid R composite systems, the following results for shear modulus, as reported in Table 4.7, were independent of the specified type of gage. The shear modulus for each composite system was calculated using the slope of the shear stress-strain curve within the first 20% of the linear elastic regime. The ending point of the linear regime was identified according to the method described in Section 4.1.2.1. That is, the ending point on a shear stress-strain curve was that point common to the deviation of several progressive reloading curves from a least-squares fit line as shown in Figure 4.18. A scaled

representation of the departure from a least-squares fit line is shown in Figure 4.18(b) for five typical graphite-PMR15 (first plaque) reloading curves. In that instance, the curves clearly deviate from the least-squares fit at a shear stress of 23.0 MPa (3.3 ksi) and corresponding shear strain of 0.3%. This implies that the shear modulus, i.e. the slope taken within the first 20% of the line length, equates to 7.5 GPa (1.09 Msi) for that particular example. It can also be seen in Figure 4.18(b) that the shear stress-strain response is bilinear from 0.3% to 0.6% strain with a 17.0% reduction in the elastic modulus. This reduction, the tangent shear modulus, is attributed to the onset of intralaminar damage.

Figures 4.19(a) and 4.19(b) compare superimposed shear stress-displacement shear stress-strain curves of Iosipescu specimens from the third and fourth PMR15-type plaques with a specimen from the first PMR15-type plaque. These curves represent specimens tested using the biaxial Iosipescu fixture at $\alpha = 0^\circ$. The effect of variations in laminate fiber volume fraction and manufacturing process are readily apparent. The thicker plaques do not seem to demonstrate as substantial of a reduction in applied shear stress when compared to the thinner plaque. For a given level of stress, there is also considerably more straining in the plaques having a lower volume fraction of fibers. This seems to suggest that added matrix material takes up the additional stress and prolongs a catastrophic type of failure in exchange for progressive intralaminar damage. The prolonged progression of intralaminar damage may explain the bilinear response seen in the stress-displacement curves for the thicker plaques.

From the series of standard and off-axis tensile tests, typical examples of stress-displacement and stress-strain responses for the third PMR15 plaque can be seen in Figures 4.20(a) and 4.20(b) ($\beta = 0^\circ, 15^\circ, 30^\circ, 45^\circ$). As the angle between the woven tows and principal loading axis increases, the severity of nonlinearity increases similar to that exhibited by the shear stress-strain curves for the Iosipescu specimens. Unlike the shear stress-displacement and shear stress-strain curves which are vastly different, the off-axis tensile stress-displacement and stress-strain curves are similar. With the exception of the off-axis test at $\beta = 15^\circ$, the relationship between displacement and strain remains essentially

constant. This is not the case with the shear tests which require both types of curves to fully understand the mechanical response.

It can be seen in Figure 4.20(b) that the tensile response at $\beta = 0^\circ$ is linear elastic. Although it is not shown in this figure, the entire response could be characterized as elastic-brittle which was the case for nearly all of the specimens tested on-axis in tension. In using the first 20% of the curve to calculate the tensile modulus, a value of 75.0 GPa (10.9 Msi) was arrived at for this particular example. The range of values for the tensile modulus as determined from all tensile specimens tested on-axis is reported in Table 4.7. Differences between the tensile modulus calculated along the warp tows {11} and along the fill tows {22} were negligible, so the fabrics were considered to be primarily balanced. For the purpose of verifying the shear modulus values obtained using the Iosipescu method, the range for the shear modulus obtained using the off-axis tests is also reported. For off-axis data, the shear modulus was calculated using the familiar equations of transformation (c.f. Eqs. 4.9 and 4.10). On average, the shear modulus obtained using the biaxial Iosipescu shear test was 7.7% higher than the shear modulus obtained using off-axis tensile test. In off-axis tension, the distribution of strain within the gage section of the tensile specimen tended to be more uniform than the distribution of strain within the gage section of the biaxial Iosipescu specimen, i.e. less parabolic. Therefore, the integrated strain was slightly higher which resulted in a lower shear modulus for a given level of applied stress.

Apparent Biaxial Failure Properties - At room temperature, the graphite-PMR15 specimens machined from the same composite plaque possessed quite repeatable loading and failure characteristics when subjected to shear ($\alpha = 0^\circ$), shear-tension ($-45^\circ < \alpha < 0^\circ$) or shear-compression ($+45^\circ > \alpha > 0^\circ$) loading conditions. However, comparisons made between these biaxial loading conditions revealed obvious differences in the characteristics. For example, the stress-displacement and stress-strain curves in Figure 4.21 show the responses of specimens from the first plaque tested at loading angles of 0° , $+30^\circ$, and -30° . The stress-displacement responses are quite linear and similar at a lower applied stress, but the responses to biaxial loading conditions become much more evident at a higher applied stress.

Clearly, the slopes of both curves for each angle are the greatest in shear followed by shear-compression and shear-tension. Moreover, sudden drops in the applied stress are apparent upon reaching the maximum load carrying capacity of the specimens.

In all shear test cases, a general trend towards stress stability was observed after the maximum load carrying capacity was reached. The shear-compression test cases also showed some stress stability, but it was more of a gradual declination rather than a plateau beginning at a crosshead displacement of 7.0 mm (0.28 in). The exceptions to this observed stress stabilization were the shear-tension test cases associated with the larger displacements. Here, the responses led to a significant secondary and, at times, a tertiary rise following a drop in applied stress. It is believed that these additional rises and falls in stress were a result of the transfer of load to intact tows and realignment of the intact tows towards the principal loading axis. Since the composite tensile failure stresses are twice the composites compressive failure stresses [21], it is more likely that the tows could withstand additional stress in tension upon realigning.

The biaxial responses of the graphite-PMR15 specimens machined from the second plaque were similar to the biaxial responses of specimens from the first plaque for a low to intermediate applied stress. However, the stress-displacement curves did not show the presence of a sudden drop in stress after reaching a maximum. Rather, the applied stress gradually decreased with no distinct point of inflection on the curves as illustrated in Figure 4.22. The graphite-Avimid R systems were dependent on the biaxial loading conditions as well, but the stress-displacement curves were entirely different (see Fig. 4.22). In all cases, a "knee" phenomenon characteristic of propagating multiple transverse matrix cracks was observed instead of the sudden drop associated with delaminations and the onset of failure.

The range of apparent shear and biaxial failure stresses of the composites were determined at three key stages in the load history, defined in this investigation as the onset of damage (transverse matrix cracking), the onset of failure (delamination) and catastrophic failure (maximum load capacity). The values at each of these key stages were evaluated by superimposing plots of the stress-displacement and stress-strain curves on the same ordinate

plot unit-scale. The stress at the onset of damage is the point where the stress-strain response begins to deviate from linearity as outlined in Section 4.1.2.1. The stress at the onset of failure is the point where the stress-displacement response deviates from linearity. The stress at catastrophic failure is the point on the stress-displacement curve that is synonymous with the maximum applied stress. For determining the point at the onset of failure, one parallel line was drawn over the linear regime and a second line was drawn tangent to the inflection point. A third vertical line was placed at the intersection of the first two lines and the onset of failure was that point formed at the intersection of the vertical line with the stress-displacement curve. It is believed that the onset of failure, as defined by this method, represents significant damage development on the 8HS woven fabric composites.

For the bulk of PMR15-type specimens machined from the first plaque, the interpreted values for the onset of failure and catastrophic failure were nearly identical. However, the stress-displacement curves for the specimens from the second plaque displayed onsets of failure at values below catastrophic failure. For the Avimid R-type Iosipescu specimens, the onset was considered to be the same point as the knee. The shear and biaxial failure stresses of the composites were evaluated from the average stress in the specimen gage section and calculated, at this point, using Eq. 4.4. The ranges of failure stresses calculated for the three defined stages of progressive failure are given in Table 4.8. The data presented in this table was obtained from room temperature tests utilizing the biaxial Iosipescu fixture with short loading blocks.

The data in Table 4.8 shows that the shear and biaxial stresses of the PMR15-type specimens, established from the applied stresses at the onset of failure, are generally higher than the shear and biaxial stresses of the Avimid R-type specimens. The data also shows that there is little difference between the stresses for the PMR15-type specimens from the first and second plaques. The effect of a tensile dominated loading angle on the failure stress seems to be negligible, however the effect of a compressive dominated loading angle indicates that compression plays a role in reducing the apparent stress at the onset of failure. The Avimid R composite systems show this trend as well, but there is more scatter in the

experimental results.

Elevated temperature Iosipescu shear testing ($\alpha = 0^\circ$) of the PMR15-type composite specimens, machined from the second plaque, was performed using the experimental setup shown in Figure 4.9. Elevated temperature tests were not performed using the first plaque due to an insufficient number of remaining specimens. Elevated temperature shear tests were also performed using the Avimid R warp-aligned and $0^\circ/90^\circ$ composites and all of these experiments utilized the biaxial Iosipescu fixture with short loading blocks. The effect of different loading block geometries on the elevated temperature failure stresses was not examined, again due to an insufficient number of composite specimens.

The shear stress-displacement curves at various temperatures are shown in Figure 4.23 for the PMR15 specimens and in Figures 4.24 and 4.25 for the Avimid R warp-aligned and $0^\circ/90^\circ$ specimens, respectively. It can be seen that the stress-displacement curves for both Avimid R composite architectures show similarities as a function of temperature. However, these curves are quite different in comparison to the shear stress-displacement curves for PMR15. It can also be seen that the shear stresses at the onset of failure and the maximum shear stresses for all three composite systems are influenced by temperature. As for the stresses at the onset of damage, they were not established because a distinct inflection point on the shear stress-strain curves was undefined. The reason for this was that the stiffness decreased much more rapidly than the apparent failure stresses did with increasing temperatures. In studying typical representations of the gage strain-shear stress curves (see Figure 4.26) for tests at 24.4°C (76.0°F), 204.4°C (400.0°C) and 260.0°C (500°F), the severity of stiffness reductions are obvious. If the maximum shear stresses from the PMR15 composite at these temperatures [120.8 MPa (17.5 ksi), 104.7 MPa (15.2 ksi), 97.2 MPa (14.1 ksi)] are compared with the shear moduli [6.0 GPa (0.87 Msi), 3.0 GPa (0.44 Msi), 2.8 GPa (0.41 Msi)], it is evident that the reduction in strength properties is much smaller than the reduction in stiffness properties.

Certainly, the influence of temperature on the apparent strength properties of Avimid R is greater than for PMR15. The data presented in Table 4.9 and Figures 4.27(a) and (b)

emphasize this fact more clearly. The data in these figures represents the average of three specimens at each indicated temperature. As far as the stresses at the onset of failure are concerned, a larger reduction was observed for the Avimid R composites above 200 °C (392 °F) in comparison to the reduction observed for the PMR15 composites. At maximum load capacities, this trend was still the same even though the Avimid R tended to perform 20.0% better at room temperature. As suggested by Figures 4.27(a) and 4.27(b), the room temperature, interlaminar fracture toughness of Avimid R is superior to PMR15. However, the shear stability of the PMR15 matrix is superior to that of the Avimid R matrix at temperatures in excess of 250 °C (482 °F).

Structural Nonlinearities - The structural nonlinearities associated with the biaxial and modified biaxial Iosipescu shear tests are geometric and boundary contact nonlinearities. These two types of structural nonlinearities encompass the effects associated with large material rotations and friction between two surfaces in direct contact as defined in Sections 4.2.1.1 and 4.2.1.2. For both biaxial shear test methods, five cases of friction were considered. More than one case was considered to determine the influence of sliding on the stress distributions along the notch root axis of the woven fabric composite Iosipescu specimen. The coefficients of static friction (μ) assumed for the first through fifth cases were 0.1, 0.3, 0.5, 0.8 and ∞ (linear elastic), respectively. Unlike the study performed by Ho *et al.* [78], the purpose here was not to assume that the friction coefficient was known *a priori*. Rather, the purpose was to vary the coefficient over a likely range and determine which coefficient had the greatest definitive impact on the stresses (if any) and biaxial ratios as a function of the applied loading angle.

The normal and shear stress distributions along the notch root axis of a woven graphite fabric Iosipescu specimen (biaxial) are presented in Figure 4.28 for the five cases of sticking-sliding contact. The stresses are normalized to the applied shear stress for a shear strain of 0.6%. The applied shear stress was determined by summing nodal reactions at the loading blocks. The position along the notch root axis is given in reference to the origin at the specimen center. It can be seen in Figure 4.28 that the influence of sliding on the

distribution of shear stress at the specimen center is negligible while slightly influential near opposing notches. The influence of sliding on the normal stresses, however, is not negligible. As the contact conditions progress from sliding to sticking, the tensile and compressive stresses increase by factors of 3.7 and 1.6, respectively. When the specimen is compressed and sheared, it shortens. If specimen shortening is not resisted by friction, the tensile stress decreases. Since the fiber reinforcement is orthogonal, some counteraction also occurs from the Poisson effect due to compression.

The increasing trend with the sliding condition is similar for both normal stresses although the growth in σ_x from 0.5 to 0.8 is considerably less than the growth in σ_y from 0.5 to 0.8. Also, the shapes of the normal compressive stress distributions are similar for each condition of contact, but the shapes of the transverse tensile stress distributions change for each condition of contact. The tensile stress distributions become increasing more parabolic as the friction coefficient increases. This indicates greater bending on the inclined notch faces as contact progresses from sliding to sticking. The severity of bending also tends to grow as loading progresses since the resistance of friction must increase with the normal force to maintain the same coefficient.

The biaxial ratios of the normal stresses to the applied shear stress are presented in Figure 4.29 for the biaxial Iosipescu specimen. The variation of the biaxial ratios with the applied loading angle is presented for each case of friction. Firstly, it can be seen that stress state is always biaxial regardless of the loading angle. Secondly, each group of biaxial ratios converges within the domain of the loading angle α between 6° and 12° shear-tension. In this domain, the tensile stress at the specimen center is only 2.0-5.0% of the shear stress, however the compressive stress at the specimen center is nearly 30.0%. For all fixed friction coefficients other than 0.1, the biaxiality trends point to changing sticking-contact sliding conditions. These changes suggest that load repartitioning between 30° shear-tension and 20° shear-compression causes greater sticking in comparison to sliding. Also, the transition from transverse tensile stress ($+\sigma_x$) to transverse compressive stress ($-\sigma_x$) is not centered about the 0° loading angle. This further implies that sliding is more difficult in shear-compression

compared to shear-tension. The reason for this is because the loading block surfaces penetrate further into the composite material surfaces under shear-compression loading conditions.

In Figure 4.30, the distribution of shear stress along the notch root axis of the biaxial Iosipescu specimen is shown for each loading angle considered and only for the contact condition $\mu = 0.3$. Clearly, the distributions under shear-tension or shear-compression loading conditions are not evenly spaced on either side of $\alpha = 0^\circ$. Under shear-tension loading conditions, the reduction in shear stress becomes more significant between -15° and -30° . In addition, the parabolic distribution along the notch root axis tends to flatten in comparison to the distribution at $+40^\circ$. Again, these results reiterate the influence greater surface penetration by the loading blocks under shear-compression loading conditions. If the trends in the distributions of shear strain along the notch root axis of biaxial Iosipescu specimens are similar to the shear stress distributions, a substantial amount of error in the calculation of the shear modulus can be envisaged. This could especially be the circumstance when small and centrally located gages were used in conjunction with Eq. 4.5.

The normal and shear stress distributions along the notch root axis of a woven graphite fabric Iosipescu specimen (modified biaxial) are presented in Figure 4.31 for the five cases of sticking-sliding contact. The stresses are normalized to the applied shear stress for a shear strain of 0.6%. The applied shear stress was determined in the same manner as for the biaxial Iosipescu specimen. It can be seen in Figure 4.31 that the influence of sliding on the distribution of shear stress at the specimen center is also negligible with the same influence near the opposing notches. The influence of sliding on the normal stresses is much less in comparison to the influence of the loading blocks on the normal stresses. The most noticeable effects produced by the modified biaxial configuration and varying contact conditions are much flatter stress distributions and normal stresses which nearly coincide with each other. Also, the growth of the transverse tensile stress with an increasing friction coefficient is less compared to the biaxial configuration. For instance, the tensile stress

increases by a factor of 1.5 from $\mu = 0.1 - \infty$ compared with 3.6 for the biaxial configuration. The increase in the normal compressive stress component from a factor of 1.6 to 2.8 coincides with the longer blocks having an increased surface area of contact.

The biaxial ratios of the normal stresses to the applied shear stress are presented in Figure 4.32 for the modified biaxial Iosipescu specimen. The variation of the biaxial ratios with the applied loading angle is presented for each case of friction. The most notable difference between these biaxial ratios and the ratios for the short block configuration is that the stress state is not always biaxial. What is most interesting is that a state of pure shear seems to occur within the range of α between 15° and 20° shear-tension. In this regime, there is little to no occurrence of the normal stresses acting at the specimen center. Moreover, the tensile and compressive biaxial ratios are almost juxtaposed for each contact condition and the domain is smaller. Obviously, these characteristics are tied fully to the loading block configuration which induces a compression field further away from the notch root axis.

In Figure 4.33, the distribution of shear stress along the notch root axis of the modified biaxial Iosipescu specimen is shown for each loading angle considered and only for the contact condition $\mu = 0.3$. Similar to the biaxial Iosipescu specimen, the biaxial shear stress distributions are not evenly spaced on either side of $\alpha = 0^\circ$. It can also be seen that the shear stress at the center for 15° shear-compression drops below the shear stress at 0° due to load repartitioning and an immediate change from sticking to sliding. In comparison to the shear stress distributions for the biaxial load case, a large reduction in the shear stress also occurs for the modified biaxial case from 15° to 30° shear-tension. Furthermore, the trend in the parabolic shape of the distributions is the same but the distributions are even flatter than those associated with the biaxial case.

In Table 4.10, the internal stresses are shown for the two finite element models loaded in shear with 1.0 mm (0.04 in), 2.0 mm (0.08 in) and 3.0 mm (0.12) prescribed displacements and a coefficient of static friction $\mu = 0.3$. The shear stresses are calculated in the same manner as the previous examples. Again, the nonlinear effects, geometric and

boundary contact nonlinearities, have marginal influence on internal shear stresses and greater influence on normal stresses for both models. There is good agreement between the shear stresses determined at the specimen center and from nodal summation. It can be seen that the growth of compression along the notch root axis σ_y in the biaxial model is high, almost 50% of the shear stress. The growth of compression in the modified biaxial model having longer loading blocks is smaller in comparison. In this case, the compression grows to about 10% of the shear stress. This is not surprising since the long blocks, in accordance with the ASTM standard, were designed to reduce the compression by moving the centers of force distribution away from the notch root axis.

It can be expected that the stresses in the Iosipescu specimen will change if the specimen is rotated either towards shear-tension or shear-compression. It is clearly evident that the loading angle affects the mechanical response of the specimen in a manner similar to what is observed experimentally as shown in Figure 4.21. What is more important is the fact that the stresses at the center of the biaxial Iosipescu specimen are always biaxial and large compressive stresses are always present, despite the angle of applied load. Examination of the stresses at the center of a modified biaxial Iosipescu specimen, as a function of the loading angle, reveals that the normal compressive stress can be entirely eliminated if the specimen is loaded at an angle between 15-20° shear-tension. Within this range, the shear stress field in the gage section is nearly pure with only a small tensile stress component. This small of a tensile stress component cannot affect the process of failure considerably in the woven fabric composites.

Effects of Loading Points - The biaxial fixture employs short loading blocks. It has previously been shown that large compressive stresses develop in the specimen gage section for blocks of this geometry. It could be speculated that the in-plane compression along the notch root axes of the fabric composite specimens might affect the failure load and mode of failure. In the previous section, it was shown that the compression may be entirely eliminated by employing a modified loading block geometry and by rotating the specimens toward shear-tension.

Since the admixture of the old and newly designed blocks (refer to Appendix D) permits different combinations of in-plane biaxial shear and compressive stress fields to be generated, their effects on the failure processes in PMR15 and Avimid R composites can be studied. If the compression generated by the shorter loading block configuration was influential in promoting the failure process in the composites, both the applied loads at the onset of failure and the applied maximum loads should increase with application of the longer blocks. As seen in Table 4.11, this speculation is clearly contradicted. Table 4.11 shows that there are significant differences between the failure loads for the thinner and thicker PMR15 specimens tested in the fixture using the shorter loading blocks. These differences most likely are due to improved interlaminar strength resulting from variation in the matrix volume fraction. However, if the failure loads are compared for specimens taken from the same plaque, the change due to block configuration is insignificant.

The same statement can be made in regard to Avimid R samples tested under the same conditions. For these materials (warp-aligned), the average load at the onset of failure (knee) was 4.56 kN (1.03 kips) when the short loading blocks were used while the average maximum load was 6.45 kN (1.45 kips). If these loads are compared with the loads for the same specimen tested in shear using the longer blocks [4.89 kN (1.10 kips) and 6.56 kN (1.47 kips)], it can immediately be concluded that the effect of the normal compression on the failure loads is negligible. This same behavior was also observed for the 0°/90° specimens tested in shear using the two different loading block geometries. In this case, the average loads at the knee and the average maximum loads for the short blocks were 4.55 kN (1.02 kips) and 6.75 kN (1.52 kips) whereas the same average loads for the specimens tested using the longer blocks were 4.89 kN (1.10 kips) and 6.56 kN (1.47 kips), respectively.

Effects of Load Eccentricities - The resultant moments and global loads are shown in Tables 4.12(a) and 4.12(b) for the five eccentric cases (including in-plane biaxial loads), two different loading block geometries and biaxial loading conditions (applied shear, shear-tension and shear-compression). It can be seen that the effect of eccentric loads on the

resultant moments and reactions is quite substantial. Significant differences can also be observed for the effect of the eccentric loads on the moments and reactions from the biaxial (short blocks) and modified biaxial (long blocks) loading block configurations. For the same applied displacements, type of eccentricity and biaxial loading condition, the resultant forces and moments from the short blocks are much higher. The forces and moments are also noticeably affected by the biaxial loading conditions, especially for the short block configuration. The highest resultant forces occur for in-plane shear-compression loading without eccentricities present (Case (A), shear-compression) followed by the cases of pure shear and shear-tension. Most importantly, for all biaxial loading conditions and both block geometries in Cases (A) and (E), there are no resultant axial M_x , bending M_y and shear M_z moments on either side of the specimen. For Cases (B), (C) and (D), the resultant moments M_x , M_y and M_z are very high with the highest M_x and M_y for Case (C) and the highest M_z for Case (B).

Since large axial, bending and shear moments are present if the specimens are modeled with eccentric loads (Cases (B), (C) and (D)), large differences should be observed in the shear strain calculations on the front and back surfaces. The axial, bending and shear moments must generate out-of-plane deformations of the Iosipescu specimens either for the case of shear or for shear dominated biaxial loading conditions. Figures 4.34 and 4.35 show the integrated shear strains on the front and back surfaces for the five load cases and two block geometries considered with shear, shear-tension and shear-compression loads. If the specimens are loaded in-plane in pure shear, shear-compression and shear-tension without eccentric loading, i.e. Case (A), no difference is observed for the shear strains on the front and back specimen surfaces. This is true for both loading block geometries.

Rotation of the specimen changes the magnitude of integrated shear strains. For the same applied displacement, the magnitudes of shear strains are higher for the short loading blocks. For Cases (B), (C) and (D), the differences between the front and back shear strains are noticeable with the difference being the largest for Case (C). This implies that the twisting of the specimen will result in the largest difference between the front to back shear

strain measurements. However, this difference is not caused by the axial moment M_x . The bending moment M_y is the largest in Case (C) and is generated in addition to M_x when the specimen is permitted to twist. Therefore, the bending moment must generate large out-of-plane bending deformation which causes increased front to back shear strain difference. The bending moment M_y arises from the anti-symmetric action of the loading blocks on the specimen and cannot be avoided. For Case (C), this action is more severe than for the other cases. However, the severity is somewhat lessened through the use of the longer blocks.

The magnitudes of the out-of-plane displacements δ_z are also shown in Figures 4.34 and 4.35 for the eccentric load cases, three shear dominated biaxial loading conditions and two block geometries. In the case of in-plane biaxial loads (without eccentricities), the out-of-plane displacements are the highest when the specimens are loaded in shear-compression (Poisson effect). The magnitude of these displacements increases substantially when eccentric loads are present, particularly for Case (C). Twisting of the specimens generates not only M_x , but also increasingly higher M_y which forces the specimen surfaces out-of-plane in a curved manner. This curvature becomes more pronounced when boundary contact (friction) is considered at the interfaces between the loading blocks and specimens.

In addition to the evaluation of shear strains on the front and back specimen surfaces, the strain and stress gradients through the thicknesses of the layered Iosipescu specimens were also considered. The magnitude of shear stress in each of the composite layers is significantly higher than magnitude of shear stress in each of the polyimide matrix layers. The largest shear stress gradients occur in Case (C) for both loading block configurations, however the effect of eccentric loads on the gradients appears to be weaker for the long block configuration. Shear strain gradients are also present for all eccentric load cases except Case (A) and Case (E). Similar to the stress gradients, the long block configuration also weakens the effect of eccentric loads on the strain gradients.

It can be observed from the data presented in Figures 4.34 and 4.35 that the eccentric loads are responsible for the difference in shear strains measured for a variety of Iosipescu specimens subjected either to shear, shear-tension or shear-compression. Since the eccentric

loads also affect the stress distributions through the specimen thickness, it can be expected that they should affect the failure process. Even if loading block geometries similar to the longer blocks (modified biaxial) are employed, eccentric loads will substantially influence the measurements of shear strain and determination of apparent shear strength. If specimen twisting is allowed, large axial M_x and bending M_y moments will be generated which create large shear stress and strain gradients through the specimen thickness. The magnitudes of the moments and gradients will not only depend on the amount of torsion, but also on the composite architecture studied using either the shear or biaxial Iosipescu tests.

The presence of eccentric loads will also affect the failure analysis of composites using the Iosipescu test, but their influence on the failure process will strongly depend on the nonlinear material behavior. Iosipescu specimens must be modeled considering the effect of eccentric loads in conjunction with boundary contact, geometric and material nonlinearities. The material nonlinearities, which could be due to plasticity and(or) damage, might either increase or decrease the effect of eccentric loads on the failure process.

Plastic Deformation - The theory which was adopted to model the elastoplastic deformation in the woven fabric composite biaxial Iosipescu specimens extended Hill's theory for orthotropic solids. Hill's theory proposed a quadratic yield function in terms of stresses to reflect the differences in strength due to anisotropy. The extension to his theory accounts for strength differences in tension and compression as well. The main drawback in implementing the extended theory to account for the plastic deformation in the woven fabric composites is quasi-isotropy. That is, the requirements for consistency and a closed, elliptical yield surface are ill-suited for quasi-isotropic behavior. These requirements, per the definitions given in Section 4.3.1, are well-suited for highly anisotropic behavior.

For consistency coincident with a closed and elliptical yield surface at 20% plastic straining, the compressive strength requirements in the $\{11\}$ and $\{22\}$ directions needed to be 40% higher than the values reported in [21]. Also, the tensile strength requirement for $\{33\}$ needed to be marginally higher than the value assumed according to 0° UD graphite-polyimide data. Initially, this caused some concern as a potential for generating

underestimates of {11} and {22} plastic straining. However, a review of the numerical data over the applied shear load history revealed that the parameters most responsible for satisfying the yield function were not in terms of $-\sigma_{11}$ or $-\sigma_{22}$. The yield function was principally satisfied in terms of σ_{12} and $+\sigma_{33}$ to a lesser extent. Since the tensile strength in {33} was overestimated, the {zz} plastic zones represented by the plastic strain contours in Figure 4.36(b) through Figure 4.40(b) are slightly underestimated.

The in-plane shear (γ_{xy}^{pl}) and transverse tensile (ϵ_{zz}^{pl}) plastic strain contours for an applied shear stress of 19.6 MPa (2.8 ksi) are shown in Figure 4.36. In Figure 4.36(a), it can be seen that plastic shear deformation initially occurs beneath the inner corners of the inner opposed loading blocks. Simultaneously, transverse tensile plastic zones begin to form in the same regions as shown in Figure 4.36(b). The formation of these zones at the indicated locations seems reasonable for a shear stress of 19.6 MPa (2.8 ksi), since a minute amount of crushing is actually observed within the same regions of the composite specimens for an applied shear stress of approximately 25.0 MPa (3.6 ksi). Moreover, the shapes of the depressions observed on the specimen contacting surfaces beneath the loading blocks suggest deformation (crushing process) which could be associated with transverse tensile plastic strains.

For an applied shear stress of 25.8 MPa (3.7 ksi), the plastic in-plane shear strain and transverse tensile strain contours are shown in Figures 4.37(a) and (b), respectively. Plastic shear deformation occurs at the opposing notches and merges with the zones formed beneath the inner loading blocks. Immediately, the plastic shear deformation at each notch progresses toward the center of the biaxial model along the notch root axis as shown in Figure 4.37(a). In Figure 4.37(b), it can be noticed that transverse tensile plastic straining progresses by a small amount along the inclined notch faces adjacent to the inner blocks. This is due to an increase in bending along the inclined face coupled with shear along the notch root axis. The in-plane shear (γ_{xy}^{pl}) and transverse tensile (ϵ_{zz}^{pl}) plastic strain contours for an applied shear stress of 31.9 MPa (4.6 ksi) are shown in Figure 4.38. As shown in Figure 4.38(a), growth of the plastic shear zone advances in size and magnitude according to the sequence described

above while growth of the plastic transverse tensile zones advance to the notches [Figure 4.38(b)].

At an applied shear stress of 61.4 MPa (8.9 ksi), the size of the in-plane shear [Figure 4.39(a)] and transverse tensile [Figure 4.39(b)] plastic strain zones are considerable in comparison to the size of the zones at 48% lower applied stress. Within the gage section of the biaxial Iosipescu model, plastic shear straining has increased by a full-order of magnitude as seen in Figure 4.39(a). In Figure 4.39(b), transverse tensile plastic straining has increased by a half-order of magnitude and the zones at the opposing notches have merged into the center of the gage section. At this level of stress, it is conceivable, judging from the shape and magnitude of the plastic transverse tensile strain contours, that coupling between shear within in the gage section and bending along the notch faces has been fully realized.

For an applied shear stress of 90.7 MPa (13.2 ksi), the shear and bending coupling within the notch regions causes transverse compressive plastic straining at the juxtaposed face of each notch. This effect can be seen in Figure 4.40(b). Assuming that interlaminar cracks are present within the gage section of the specimen at this stress level, the state of strain in Figure 4.40(b) implies that subsequent crack nucleation and growth are anti-symmetric. That is, the positive transverse strain on the upper right and lower left inclined notch faces generates crack opening displacements while the negative transverse strain on the upper left and lower right inclined notch faces generates crack closing displacements. In comparison, the change in the state of plastic shear strain [see Figure 4.40(a)] at 90.7 MPa (13.2 ksi) is minimal and practically implies uniformity of plastic distortion within the gage section.

Damage Morphology - The deformation and failure processes in the graphite-PMR15 Iosipescu specimens were vastly different compared to the graphite-Avimid R specimens. Moreover, the deformation and failure processes seemed to depend highly on plaque thickness, matrix properties and ply configuration, e.g. warp-aligned versus 0°/90°. As far as both PMR-type composite systems are concerned, the macrofailure process starts with some evidence of intralaminar and translaminar cracking which eventually leads to the

formation of principally large delaminations within the specimen gage section. These delaminations are especially large in the case of specimens machined from the first plaque. Eventually, one or more of the interlaminar cracks propagates catastrophically. This results in a rapid drop in applied load and permanent, out-of-plane deformation (bulging) on both specimen faces. For the thicker plaques (second, third and fourth), the formation of interlaminar cracks and large delaminations is constrained due to, perhaps, higher interlaminar fracture toughness properties. In these cases, the rapid drops in applied load were not observed.

The sequence of events leading to in-plane kinking, bulging (see Figure 4.43) and transverse kinking as a specimen is loaded is shown in Figures 4.41-4.42. It can be seen in Figure 4.43(a) that damage along the notch roots has progressed to the stage when interlaminar cracks have manifested between all plies with substantial evidence of intra- and translaminar cracking. At the stage of catastrophic failure as shown in Figure 4.43(b), out-of-plane deformation and transverse kinking are severe. These effects are more pronounced under shear-compression loading conditions because larger in-plane compressive stresses are generated within the gage section (refer to the biaxial ratios in Figs. 4.29 and 4.32). Since the compressive stresses are larger, opening displacements will occur at the tips of interlaminar cracks, thereby making the interlaminar failure process easier. This might explain why the maximum applied load (stress) for specimens tested in shear-compression decreases continually subsequent to reaching a maximum stress. For specimens tested under shear-tension loading conditions, it would be expected that the interlaminar failure process is more difficult since closing displacements are created.

The macrofailure process that determines failure in the Avimid R-type composite systems is the formation of principally intralaminar cracks along the notch root axis. The second mechanism is the ensuing formation of interlaminar cracks. These interlaminar cracks begin to form at the time when the "knee" becomes noticeable on the stress-displacement curve. Since this composite system appears to have good interlaminar fracture properties, e.g. $G_{IC}^{Avimid R} = 1.0 \text{ kJ/m}^2$ (68.6 ft-lbs/ft²) and $G_{IC}^{PMR 15} = 0.3 \text{ kJ/m}^2$ (20.6 ft-lbs/ft²), the

interlaminar failure process is not as severe as for the PMR 15-type system and it always occurs at a higher applied stress. Therefore, it is expected the less out-of-plane deformation would be exhibited which was the case in this investigation.

The morphology of the damage zones within the gage sections of the Iosipescu specimens tested at elevated temperatures seems to be similar to the specimen damage morphology at room temperature. That is, the same form of permanent deformation was observed and associated with interlaminar cracking. However, it is difficult to assess, at this stage, whether the cracking was more or less severe in the elevated temperature specimens compared to the room temperature specimens.

2-D Damage Reconstruction - Figures 4.44 and 4.45 present 2-D damage maps for a shear tested graphite-PMR15 Iosipescu specimen from the second plaque. The shaded areas shown in these maps represent damage generated at the specimen center [Fig. 4.44(b)] and an area very close to the notch root [Fig. 4.44(a)]. Each 2-D damage map denotes an approximate area on the specimen of 9.0 mm^2 ($1.4 \times 10^{-2} \text{ in}^2$) which is 9.5% of the square area of a repeat unit cell. Below each pixel-by-pixel averaged composite damage map, a profile plot is presented showing the relative pixel contrast intensities, by average gray values, as a function of the image width. The profile plot illustrates where the majority of cracking is distributed across each map and gives an indication of crack size compared to the image width. From these maps, the location and magnitude of local damage in the sample areas can be estimated.

Following the shear test, an observation of the Iosipescu specimen surface indicated that the woven tows were reoriented from their initial orientations. In fact, all of the woven fabric specimens tested in shear and off-axis showed this characteristic. Prior to the test, the tows were orthogonal with the long axis and notch root axis of the specimen. Due to the large shear stresses generated during the shear test, tow rotation took place within the gage section and the final tow orientation was 45° from the notch root axis. From this, it is not unreasonable to assume that the diagonal shaded areas on both maps could represent a combination of intralaminar failure at the tow matrix interfaces and failure at the tow undulations.

Very little cracking is evident in the longitudinal direction, i.e. parallel to the long axis of the specimen. The vertical cracking, indicated by the much larger areas on the left sides of the maps, seems to represent the interlaminar failure process. It is possible that one or several of the vertical cracks could be associated with the CDS (onset of failure) and maximum load capacities shown on the stress-strain and stress-displacement curves (see Fig. 4.19). From these damage map results and the results presented for the analysis of lamina stress distributions in Section 3.3, it might prove worthwhile to speculate on a reasonable sequence of events related to understanding the failure processes in shear.

First of all, the shearing process probably causes the matrix rich pockets and tow boundaries to fail in tension which permits easier rotation of the tows. Secondly, the CDS is defined when enough intralaminar damage progressively develops to the point where the bridging regions can no longer transfer load and the interlaced regions fail. Almost simultaneously, the ends of the specimen move toward the specimen centerline and the tows kink as a result of shear and compression. Finally, at some critical point in the loading history, interlaminar cracks develop and propagate under transverse normal tension. The increased normal tension in combination with progressive interlaminar cracking permits the specimen to bulge out-of-plane from its centerline which forces the tows to transversely kink as shown in Figure 4.43(b). If the fracture toughness G_{IC} of the interfaces between layers is low, some portion of the interlaminar cracks can propagate catastrophically within the specimen causing a noticeable drop in the applied load.

Since it can be argued that the damage shown in the maps could be artifacts and(or) induced during the sample surface polishing steps, an untested specimen was also subjected to the same procedure. Figures 4.45(a) and 4.45(b) represent the untested center and notch target maps prepared using the techniques described in Section 4.3.2.2. The differences between tested and untested center target maps are obvious as are the differences between tested and untested notch target maps. The shaded regions on the maps belonging to the untested sample likely represent the voids trapped during the process of manufacturing the composite plaques. Significant damage caused by the polishing process is not readily

obvious from the center and notch target maps.

An important observation can be made when comparing the maps presented in Figs. 4.44(a) and 4.44(b). Clearly, the amount of damage generated at the center of the Iosipescu specimen is much higher than the damage generated close to the notch root. It seems as if the specimen developed large shear stresses at its center in the absence of high stress concentrations at the roots of the notches. If this is true, then the woven fabric composite materials offer an advantage in shear testing over UD composite materials by avoiding the questionable influences of stress concentrations on the failure process. However, for this fact to be of merit, the reconstructed damage must be quantifiable in some fashion that enables comparisons to be made.

Damage area fractions represent the ratio of crack-inclusive areas to the total area. In this study, all images that were captured for reconstruction retained a 230,400 sq. pixel area, i.e. a 480 x 480 resolution. Figure 4.46 shows the measured difference in damage between the center and notch targets by relating the area fraction of damage to the distance from the specimen surface. It can be seen that damage accumulated near the upper notch is less significant compared to the specimen center. The area fraction for the notch target area ranges from 3% to just over 4% while the area fraction for the center target area progresses from 8% to 12.5%. It seems as if the shear initiated catastrophic failure (load reduction) may originate near the centerline of the specimen and propagate outwards in two directions, through-thickness and along the length. From Figure 4.46, it is evident that the polishing operation does not alter the state of the material since the area fractions range from 0.3% to 0.68% for both targets. Also, these values are nearly identical to the measurements reported from C-SCAN data following the post-cure of the composite plaques.

Another important observation can be made by comparing these 2-D damage results with the plastic strain contours shown in Figures 4.36-4.40. If it is believed that plastic strains could give some indications of the onset of damage and initiation of failure in these composites, then the 2-D damage maps contradict the 3-D plasticity analysis for shear. The plasticity contours suggested that plastic shear straining originated under the loading blocks

and propagated rapidly to the notches prior to advancing towards the specimen center. This would mean that the measured damage at the notch roots of the Iosipescu specimen should be at least equivalent to, if not greater than the measured damage at the specimen center. Since this is clearly not the case, one or more of the following facts must be true: (1) the proposed method of 2-D damage reconstruction does not adequately capture the majority of damage within the composite, (2) the composite does not behave in shear according to the proposed plasticity model, or (3) the assumption that plastic straining might suggest yield and initiation of failure is a bad assumption for these composite materials.

Predicting Progressive Damage - As presented in Section 4.3.2.1, a novel failure criterion was proposed to model the macroscale progressive damage in woven fabric composite Iosipescu specimens. The criterion is based on the summation of the ratios of average strain energy densities to critical strain energy densities determined from experimental stress-strain curves. The failure criterion, defined by Eq. 4.40, implies that failure occurs when the sum of the six ratios becomes equivalent to or exceeds unity.

For this study, every element within the numerical model of the biaxial Iosipescu specimen was checked at the end of each load step to see if the failure criterion was satisfied (refer to Appendix C.1.3 for the example ANSYS input file). When failure was detected, the element was “killed” by simply reducing its total stiffness to 50% of its initial value. This percent reduction in stiffness was selected on the basis of the difference between the experimentally observed shear stress prior to catastrophic failure and the shear stress observed upon stability after failure. The criterion and stiffness reduction scheme were established in terms of the total element distortion rather than distortion in one or more principal directions. This meant that any residual stiffnesses were not preferential to the direction(s) where failure went undetected. The advantage of this progressive damage scheme was the ease in which it could be implemented using ANSYS. The disadvantage of this progressive damage scheme was a lack of sense for the direction in which damage progressed, wherefore, it was suitable for merely a macroscale study.

The elements within the gage section of the biaxial Iosipescu model that were

predicted by the criterion to fail are shown in Figures 4.47 and 4.48 for numerically integrated shear strains (along the notch root axis) ranging from 0.38% to 2.25%. The measured volumes of recalled elements which were damaged are also presented. It can be seen in Figure 4.47 that damage due to applied shear ($\alpha = 0^\circ$) is first predicted along the notch faces and is oriented anti-symmetrically with respect to the notch root axis. According to the model, this first occurrence happens at a calculated shear strain of 0.38%, nearly synonymous with the point predicted by the analysis considering anisotropic plasticity singularly. It can also be seen that the most substantial increase in the progression of damage occurs between 0.38% and 0.75% shear strain. In terms of the calculated volume of damage, there is a greater than full-order of magnitude increase from 29.1 mm³ (0.2×10^{-2} in³) to 365.3 mm³ (2.2×10^{-2} in³). However, between shear strains of 1.50%, 1.88% and 2.25% (Figure 4.48), the growth of damage diminishes to approximately 10% with a maximum predicted damage volume of 1105.9 mm³ (6.7×10^{-2} in³).

In Figure 4.49, the shear stress-strain curves, considering structural nonlinearities, anisotropic plasticity and anisotropic plasticity coupled with progressive damage, are compared to typical experimental shear stress-strain curves obtained from biaxial Iosipescu specimens belonging to the fourth composite plaque. Clearly, the results from the progressive damage analysis are in the best agreement with the experimental data. In fact, the agreement is quite good. Moreover, the damage model has predicted the onset of damage at 25.0 MPa (3.6 ksi). Comparing with a typical experimental value of 23.0 MPa (3.3 ksi) for the onset of damage [c.f. Figure 4.18(b)], yields a difference of less than 10%. This means that the nonlinear shear stress-strain behavior is almost entirely attributed to the progression of damage and has very little to do with plastic deformation or structural nonlinearities. It also implies that any numerical analysis of the Iosipescu test, for the purpose of predicting macroscale shear stress-strain behavior and strength properties, must include structural and material nonlinearities. A linear elastic approach, often adopted in the past by researchers, would lead to a substantial discrepancy.

In comparing the volumes of damage generated numerically with the fractions

produced from the serial reconstruction technique presented in Section 4.3.2.2, it is apparent that an acceptable and practical quantitative correlation is not possible. Due to computational constraints, the biaxial Iosipescu model was generated to have a single-element thickness. Even though the physical damage in the gage sections of the woven fabric composite specimens seems to be constant through-thickness, the reconstruction technique tends to capture more micro- and mesoscale information. Intuitively, it does not make sense to attempt some quantitative comparison of damage acquired by two different methods at two different scales. From a qualitative viewpoint however, the shape of the cumulative physical damage zone within the gage section of the specimen does compare very well with the numerically generated damage zone. Without knowledge of a practical correlation though, it is merely a coincidence that the maximum numerical damage fraction of 14.1% [total model volume of 7840.4 mm³ (0.5 in³)] is similar to the reconstructed fraction of 12.5% (Figure 4.46).

The progression of macroscale damage in the woven 8HS fabric composite, due to an applied in-plane shear stress, was found numerically to follow a sigmoidal growth function of percent shear strain as given by

$$f_g(\gamma_{xy}) = \frac{-18.52}{1 + e^{\frac{(\gamma_{xy}(\%) - 1.05)}{0.51}}} + 16.02 \quad (4.43)$$

where $f_g(\gamma_{xy})$ is the damage growth function in terms of the total (elastic+plastic) shear strain and γ_{xy} is the total percent shear strain. The function given by Eq. 4.43 yielded a coefficient of determination r^2 of 0.9996. This damage function still requires testing for uniqueness against physical damage data. A supplemental technique for serial reconstruction of transverse sections has been pursued, but problems still exist in regard to the accuracy of stacked image registration. Once a solution to this problem has been found, three-dimensional damage fractions can be measured and tested against Eq. 4.43. A reasonable and unique fit may confirm both the reconstruction method and progressive damage scheme.

Table 4.1. Nominal dimensions for specimens used in the experimental program. For specification of variable callout, Figure 4.6 serves as the reference.

Specimen Type	Variable Dimension Callout - mm (in)										
	(L)	(l)	(h')	(t)	(a)	(b)	(b')	(c)	(w)	(r)	(θ)
Biaxial Iosipesu	80.0 (3.15)	35.0 (1.38)	20.0 (0.79)	as received	2.5 (0.09)	10.0 (0.39)	----	9.0 (0.35)	12.0 (0.47)	0.45 (0.017)	90°
Modified Biaxial Iosipesu	76.2 (3.0)	25.4 (1.0)	19.1 (0.75)	as received	2.5 (0.09)	34.9 (1.37)	25.4 (1.0)	20.65 (0.81)	12.0 (0.47)	0.45 (0.017)	90°
Standard Tension	228.6 (9.0)	----	25.4 (1.0)	as received	25.4 (1.0)	38.1 (1.5)	----	----	----	----	15°
Off-Axis Tension	228.6 (9.0)	----	25.4 (1.0)	as received	25.4 (1.0)	38.1 (1.5)	----	----	----	----	15°

Table 4.2. Description of ANSYS 5.3 capabilities for solving problems involving geometric nonlinearities. (c.f. [79])

Geometric Nonlinearity	Strains	Rotations	Shape Changes
Large Strain	YES (assumed finite)	YES (may be large)	YES
Large Deflection	YES (assumed small)	YES (large)	NO (only rigid body)
Stress Stiffening	YES (assumed small)	YES (assumed small) 1 st -order approximation	----
Spin Softening	YES (assumed small)	YES (assumed small) radial mass motion and subject to angular velocity	----

Table 4.3. Material properties assumed in the 3-D analyses of load eccentricities imposed on the biaxial and modified biaxial Iosipescu specimens.

Material	Material Properties - GPa (Msi)[†]								
	E₁₁	E₂₂	E₃₃	G₁₂	G₁₃	G₂₃	v₁₂	v₁₃	v₂₃
Composite	70.0 (10.2)	70.0 (10.2)	11.3 (1.6)	7.0 (1.0)	4.9 (0.7)	5.1 (0.72)	0.10	0.25	0.27
Matrix	4.0 (0.58)	4.0 (0.58)	4.0 (0.58)	1.5 (0.2)	1.5 (0.2)	1.5 (0.2)	0.35	0.35	0.35
Block	400.0 (58.0)	400.0 (58.0)	400.0 (58.0)	153.8 (22.3)	153.8 (22.3)	153.8 (22.3)	0.30	0.30	0.30

[†]Assigned to specified layers (31 total) within SOLID46 elements.

Table 4.4. Imposed boundary conditions on blocks for eccentric loading of the biaxial Iosipescu specimen in three dimensions.

Load Case	Imposed Boundary Conditions			
	Right-Side (Inner)	Right-Side (Outer)	Left-Side (Inner)	Left-Side (Outer)
A	$\delta_x(0.225x, y, 0) = 0$	$\delta_x(0.875x, -y, 0) = 0$	$\delta_x(-0.225x, -y, 0) = 0$	$\delta_x(-0.875x, y, 0) = 0$
	$\delta_y(0.225x, y, 0) = -0.5\delta$	$\delta_y(0.875x, -y, 0) = -0.5\delta$	$\delta_y(-0.225x, -y, 0) = 0.5\delta$	$\delta_y(-0.875x, y, 0) = 0.5\delta$
	$\delta_z(0.225x, y, 0) = 0$	$\delta_z(0.875x, -y, 0) = 0$	$\delta_z(-0.225x, -y, 0) = 0$	$\delta_z(-0.875x, y, 0) = 0$
B	$\delta_x(0.225x, y, 3.0z) = 0$	$\delta_x(0.875x, -y, -3.0z) = 0$	$\delta_x(-0.225x, -y, 0) = 0$	$\delta_x(-0.875x, y, 0) = 0$
	$\delta_y(0.225x, y, 3.0z) = -0.5\delta$	$\delta_y(0.875x, -y, -3.0z) = -0.5\delta$	$\delta_y(-0.225x, -y, 0) = 0.5\delta$	$\delta_y(-0.875x, y, 0) = 0.5\delta$
	$\delta_z(0.225x, y, 3.0z) = 0$	$\delta_z(0.875x, -y, -3.0z) = 0$	$\delta_z(-0.225x, -y, 0) = 0$	$\delta_z(-0.875x, y, 0) = 0$
C	$\delta_x(0.225x, y, 3.0z) = 0$	$\delta_x(0.875x, -y, -3.0z) = 0$	$\delta_x(-0.225x, -y, 3.0z) = 0$	$\delta_x(-0.875x, y, -3.0z) = 0$
	$\delta_y(0.225x, y, 3.0z) = -0.5\delta$	$\delta_y(0.875x, -y, -3.0z) = -0.5\delta$	$\delta_y(-0.225x, -y, 3.0z) = 0.5\delta$	$\delta_y(-0.875x, y, -3.0z) = 0.5\delta$
	$\delta_z(0.225x, y, 3.0z) = 0$	$\delta_z(0.875x, -y, -3.0z) = 0$	$\delta_z(-0.225x, -y, 3.0z) = 0$	$\delta_z(-0.875x, y, -3.0z) = 0$
D	$\delta_x(0.225x, y, 3.0z) = 0$	$\delta_x(0.875x, -y, 3.0z) = 0$	$\delta_x(-0.225x, -y, 3.0z) = 0$	$\delta_x(-0.875x, y, 3.0z) = 0$
	$\delta_y(0.225x, y, 3.0z) = -0.5\delta$	$\delta_y(0.875x, -y, 3.0z) = -0.5\delta$	$\delta_y(-0.225x, -y, 3.0z) = 0.5\delta$	$\delta_y(-0.875x, y, 3.0z) = 0.5\delta$
	$\delta_z(0.225x, y, 3.0z) = 0$	$\delta_z(0.875x, -y, 3.0z) = 0$	$\delta_z(-0.225x, -y, 3.0z) = 0$	$\delta_z(-0.875x, y, 3.0z) = 0$
E	$\delta_x(0.225x, y, 3.0z) = 0$	$\delta_x(0.875x, -y, -3.0z) = 0$	$\delta_x(-0.225x, -y, -3.0z) = 0$	$\delta_x(-0.875x, y, 3.0z) = 0$
	$\delta_y(0.225x, y, 3.0z) = -0.5\delta$	$\delta_y(0.875x, -y, -3.0z) = -0.5\delta$	$\delta_y(-0.225x, -y, -3.0z) = 0.5\delta$	$\delta_y(-0.875x, y, 3.0z) = 0.5\delta$
	$\delta_z(0.225x, y, 3.0z) = 0$	$\delta_z(0.875x, -y, -3.0z) = 0$	$\delta_z(-0.225x, -y, -3.0z) = 0$	$\delta_z(-0.875x, y, 3.0z) = 0$

Table 4.5. Imposed boundary conditions on blocks for eccentric loading of the modified biaxial Iosipescu specimen in three dimensions.

Load Case	Imposed Boundary Conditions			
	Right-Side (Inner)	Right-Side (Outer)	Left-Side (Inner)	Left-Side (Outer)
A	$\delta_x(0.542x, y, 0) = 0$	$\delta_x(0.667x, -y, 0) = 0$	$\delta_x(-0.542x, -y, 0) = 0$	$\delta_x(-0.667x, y, 0) = 0$
	$\delta_y(0.542x, y, 0) = -0.5\delta$	$\delta_y(0.667x, -y, 0) = -0.5\delta$	$\delta_y(-0.542x, -y, 0) = 0.5\delta$	$\delta_y(-0.667x, y, 0) = 0.5\delta$
	$\delta_z(0.542x, y, 0) = 0$	$\delta_z(0.667x, -y, 0) = 0$	$\delta_z(-0.542x, -y, 0) = 0$	$\delta_z(-0.667x, y, 0) = 0$
B	$\delta_x(0.542x, y, 3.0z) = 0$	$\delta_x(0.667x, -y, -3.0z) = 0$	$\delta_x(-0.542x, -y, 0) = 0$	$\delta_x(-0.667x, y, 0) = 0$
	$\delta_y(0.542x, y, 3.0z) = -0.5\delta$	$\delta_y(0.667x, -y, -3.0z) = -0.5\delta$	$\delta_y(-0.542x, -y, 0) = 0.5\delta$	$\delta_y(-0.667x, y, 0) = 0.5\delta$
	$\delta_z(0.542x, y, 3.0z) = 0$	$\delta_z(0.667x, -y, -3.0z) = 0$	$\delta_z(-0.542x, -y, 0) = 0$	$\delta_z(-0.667x, y, 0) = 0$
C	$\delta_x(0.542x, y, 3.0z) = 0$	$\delta_x(0.667x, -y, -3.0z) = 0$	$\delta_x(-0.542x, -y, 3.0z) = 0$	$\delta_x(-0.667x, y, -3.0z) = 0$
	$\delta_y(0.542x, y, 3.0z) = -0.5\delta$	$\delta_y(0.667x, -y, -3.0z) = -0.5\delta$	$\delta_y(-0.542x, -y, 3.0z) = 0.5\delta$	$\delta_y(-0.667x, y, -3.0z) = 0.5\delta$
	$\delta_z(0.542x, y, 3.0z) = 0$	$\delta_z(0.667x, -y, -3.0z) = 0$	$\delta_z(-0.542x, -y, 3.0z) = 0$	$\delta_z(-0.667x, y, -3.0z) = 0$
D	$\delta_x(0.542x, y, 3.0z) = 0$	$\delta_x(0.667x, -y, 3.0z) = 0$	$\delta_x(-0.542x, -y, 3.0z) = 0$	$\delta_x(-0.667x, y, 3.0z) = 0$
	$\delta_y(0.542x, y, 3.0z) = -0.5\delta$	$\delta_y(0.667x, -y, 3.0z) = -0.5\delta$	$\delta_y(-0.542x, -y, 3.0z) = 0.5\delta$	$\delta_y(-0.667x, y, 3.0z) = 0.5\delta$
	$\delta_z(0.542x, y, 3.0z) = 0$	$\delta_z(0.667x, -y, 3.0z) = 0$	$\delta_z(-0.542x, -y, 3.0z) = 0$	$\delta_z(-0.667x, y, 3.0z) = 0$
E	$\delta_x(0.542x, y, 3.0z) = 0$	$\delta_x(0.667x, -y, -3.0z) = 0$	$\delta_x(-0.542x, -y, -3.0z) = 0$	$\delta_x(-0.667x, y, 3.0z) = 0$
	$\delta_y(0.542x, y, 3.0z) = -0.5\delta$	$\delta_y(0.667x, -y, -3.0z) = -0.5\delta$	$\delta_y(-0.542x, -y, -3.0z) = 0.5\delta$	$\delta_y(-0.667x, y, 3.0z) = 0.5\delta$
	$\delta_z(0.542x, y, 3.0z) = 0$	$\delta_z(0.667x, -y, -3.0z) = 0$	$\delta_z(-0.542x, -y, -3.0z) = 0$	$\delta_z(-0.667x, y, 3.0z) = 0$

Table 4.6. Material properties, yield stresses and tangent moduli assumed for the 3-D anisotropic plasticity analysis based on Hill's orthotropic yield function and the variations of tension and compression.

Material	Material Properties - GPa (Msi) [*]								
	E_{11}	E_{22}	E_{33}	G_{12}	G_{13}	G_{23}	ν_{12}	ν_{13}	ν_{23}
Composite	70.0 (10.2)	70.0 (10.2)	11.3 (1.6)	7.0 (1.0)	4.9 (0.7)	5.1 (0.72)	0.10	0.25	0.27
Matrix	4.0 (0.58)	4.0 (0.58)	4.0 (0.58)	1.5 (0.2)	1.5 (0.2)	1.5 (0.2)	0.35	0.35	0.35
Block	400.0 (58.0)	400.0 (58.0)	400.0 (58.0)	153.8 (22.3)	153.8 (22.3)	153.8 (22.3)	0.30	0.30	0.30
Yield Stresses - MPa (ksi) ^{**}									
	X^+	X^-	Y^+	Y^-	Z^+	Z^-	R	S	T
Composite	990.0 (144)	990.0 (144)	990.0 (144)	990.0 (144)	497.0 (72.1)	497.0 (72.1)	95.0 (13.8)	53.0 (7.7)	53.0 (7.7)
Tangent Moduli - Multiplier ^{***}									
	$E'_{t,11}$	$E'_{c,11}$	$E'_{t,22}$	$E'_{c,22}$	$E'_{t,33}$	$E'_{c,33}$	G'_{12}	G'_{13}	G'_{23}
Composite	0.01	0.01	0.01	0.01	.0064	.0064	0.0	0.0	0.0

^{*}Assigned to SOLID95 structural brick elements.

^{**}Based on iterations which satisfy consistency (Eq. 4.33) and a closed elliptical yield surface (Eq. 4.34).

^{***}Assumes nearly linear elastic normal behavior and elastic, perfect plastic shear behavior.

Table 4.7. Apparent elastic properties obtained by off-axis tensile and biaxial Iosipescu shear experiments (verification in Section 3).

Experimental Test	Apparent Elastic Properties			
	E_{11} GPa (Msi)	E_{22} GPa (Msi)	G_{12} GPa (Msi)	ν_{12}
On-Axis / Off-Axis Tension	76.9 ± 6.2 ($11.1 \pm .9$)	76.9 ± 6.2 ($11.1 \pm .9$)	6.0 ± 0.5 ($.9 \pm .07$)	$.08 \pm .03$
Biaxial Iosipescu Shear			6.5 ± 1.0 ($.9 \pm .15$)	

Table 4.8. Apparent stresses for graphite-polyimide Iosipescu specimens established at the onset of damage (O.O.D.), the onset of failure (O.O.F.) and catastrophic failure (C.F.).

α	Average Apparent Stresses								
	O.O.D. MPa (ksi)			O.O.F. MPa (ksi)			C.F. MPa (ksi)		
	PMR	AVR1	AVR2	PMR	AVR1	AVR2	PMR	AVR1	AVR2
-40°	29.0 (4.2)	25.5 (3.7)	27.8 (4.0)	105.8 (15.3)	82.0 (11.9)	85.0 (12.3)	106.3 (15.4)	122.3 (17.7)	138.0 (20.0)
-30°	29.8 (4.3)	26.2 (3.8)	29.6 (4.3)	111.2 (16.1)	87.7 (12.7)	87.6 (12.7)	111.2 (16.1)	128.7 (18.7)	137.2 (19.9)
-20°	-----	-----	-----	106.0 (15.4)	94.8 (13.7)	94.8 (13.7)	109.1 (15.8)	133.9 (19.4)	137.2 (19.9)
0°	31.0 (4.5)	26.2 (3.8)	29.6 (4.3)	110.2 (15.9)	102.6 (14.9)	100.1 (14.5)	113.7 (16.5)	137.5 (19.9)	147.3 (21.4)
20°	-----	-----	-----	107.8 (15.6)	88.2 (12.8)	92.5 (13.4)	108.0 (15.7)	116.5 (16.9)	122.0 (17.7)
30°	29.2 (4.2)	25.1 (3.6)	28.0 (4.0)	107.0 (15.5)	84.4 (12.2)	85.6 (12.4)	107.0 (15.5)	111.0 (16.1)	117.0 (16.9)
40°	28.8 (4.1)	24.4 (3.5)	27.0 (3.9)	100.4 (14.6)	78.0 (11.3)	78.0 (11.3)	100.4 (14.6)	99.0 (14.4)	109.0 (15.8)

Table 4.9. Apparent stresses for graphite-polyimide Iosipescu specimens established at the onset of failure (O.O.F.) and catastrophic failure (C.F.) as a function of temperature.

System	Temperature °C (°F)	Average Apparent Stresses	
		O.O.F. MPa (ksi)	C.F. MPa (ksi)
PMR15	24.4 (76.0)	110.2 (15.9)	113.7 (16.5)
	204.4 (400.0)	87.6 (12.7)	104.7 (15.2)
	260.0 (500.0)	73.2 (10.6)	97.2 (14.1)
	287.8 (550.0)	64.4 (9.3)	89.1 (12.9)
	315.6 (600.0)	53.1 (7.7)	72.0 (10.4)
Avimid R_1	24.4 (76.0)	102.6 (14.9)	137.5 (19.9)
	204.4 (400.0)	77.4 (11.2)	113.5 (16.5)
	232.2 (450.0)	68.0 (9.9)	107.6 (15.6)
	260.0 (500.0)	54.4 (7.9)	94.6 (13.7)
	315.6 (600.0)	23.1 (3.4)	36.1 (5.2)
Avimid R_2	24.4 (76.0)	100.1 (14.5)	147.3 (21.4)
	204.4 (400.0)	74.5 (10.8)	118.2 (17.1)
	232.2 (450.0)	70.9 (10.3)	117.0 (17.0)
	260.0 (500.0)	50.8 (7.4)	108.7 (15.8)
	315.6 (600.0)	27.2 (3.9)	46.1 (6.7)

Note: Avimid R_1 denotes the warp-aligned composite system and Avimid R_2 denotes the 0°/90° composite system.

Table 4.10. Linear elastic and nonlinear solutions to internal stresses at the center of the biaxial and modified biaxial Iosipescu models.

Model	Nonlinear Solution [†]					Linear Elastic Solution ^{††}			
	δ - mm (in)	σ_x - MPa (ksi)	σ_y - MPa (ksi)	τ_{xy} - MPa (ksi)	P/A - MPa (ksi)	σ_x - MPa (ksi)	σ_y - MPa (ksi)	τ_{xy} - MPa (ksi)	P/A - MPa (ksi)
Biaxial	1.0 (0.04)	-14.5 (-2.1)	-183.1 (-26.6)	-500.5 (-72.6)	-526.3 (-76.3)	5.7 (0.8)	-147.2 (-21.3)	-530.8 (-77.0)	-557.7 (-80.9)
	2.0 (0.08)	25.5 (3.7)	-430.0 (-62.4)	-1019.4 (-147.9)	-1073.4 (-155.7)	11.4 (1.7)	-294.4 (-42.7)	-1061.6 (-154.0)	-1115.5 (-161.8)
	3.0 (0.12)	116.3 (16.9)	-726.7 (-105.4)	-1537.3 (-223.0)	-1619.4 (-234.9)	17.2 (2.5)	-441.6 (-64.0)	-1592.4 (-231.0)	-1673.1 (-242.7)
Modified Biaxial	1.0 (0.04)	-22.9 (-3.3)	-183.1 (-26.6)	-323.7 (-46.9)	-307.9 (-44.7)	7.9 (1.1)	-27.9 (-4.1)	-365.5 (-53.0)	-353.1 (-51.2)
	2.0 (0.08)	-25.3 (-3.7)	-72.4 (-10.5)	-648.9 (-94.1)	-614.0 (-89.1)	15.7 (2.3)	-55.8 (-8.1)	-731.0 (-106.0)	-706.2 (-102.4)
	3.0 (0.12)	-16.6 (-2.4)	-104.6 (-15.2)	-969.2 (-140.6)	-910.7 (-132.1)	23.6 (3.4)	-83.7 (-12.1)	-1096.5 (-159.0)	-1059.3 (-153.6)

[†] Solution obtained assuming boundary contact and geometric nonlinearities with a friction coefficient of 0.3.

^{††} Solution obtained assuming perfect contact with infinite friction.

Table 4.11. Comparison of the shear loads at the onset of failure and the maximum shear loads for the short and long block configurations.

PMR15 (plaque #1)		PMR15 (plaque #2)		PMR15 (plaque #2)	
Failure Onset Load - kN (kips)	Maximum Load - kN (kips)	Failure Onset Load - kN (kips)	Maximum Load - kN (kips)	Failure Onset Load - kN (kips)	Maximum Load - kN (kips)
5.83 (1.31)	5.83 (1.31)	6.95 (1.56)	7.39 (1.66)	6.50 (1.46)	7.23 (1.63)
5.56 (1.25)	5.56 (1.25)	6.82 (1.53)	7.54 (1.70)	7.17 (1.61)	7.90 (1.78)
6.18 (1.39)	6.00 (1.35)	-----	-----	-----	-----
6.29 (1.41)	6.29 (1.41)	-----	-----	-----	-----
Average	5.96 (1.34)	6.89 (1.55)	7.46 (1.68)	6.84 (1.54)	7.56 (1.70)
	Short Blocks	Short Blocks	Short Blocks	Long Blocks	Long Blocks

Table 4.12(a). Calculated global loads and moments from reactions at the loading blocks of the biaxial model.

Biaxial Model (short blocks)	Left Side of Specimen				Right Side of Specimen			
	P*	M _x **	M _y **	M _z **	P*	M _x **	M _y **	M _z **
CASE (A):								
shear ($\alpha = 0^\circ$)	-1511.2	0	0	-6.92	1511.2	0	0	-6.92
shear-compression ($\alpha = +30^\circ$)	-1567.2	0	0	-6.71	1567.2	0	0	-6.71
shear-tension ($\alpha = -30^\circ$)	-1397.5	0	0	-7.11	1397.5	0	0	-7.11
CASE (B):								
shear + asymmetric torsion ($\alpha = 0^\circ$)	-1206.6	426.6	-218.9	-938.0	1206.6	-437.5	218.9	959.6
shear + asymmetric torsion ($\alpha = +30^\circ$)	-1230.8	434.5	-252.5	-880.7	1230.8	-432.0	251.1	873.0
shear + asymmetric torsion ($\alpha = -30^\circ$)	-1234.1	317.8	-107.0	-548.9	1234.1	-316.0	106.5	538.4
CASE (C):								
shear + anti-symmetric torsion ($\alpha = 0^\circ$)	-969.2	739.5	-511.8	-2.23	969.2	-739.5	511.8	-2.23
shear + anti-symmetric torsion ($\alpha = +30^\circ$)	-996.8	742.0	-576.4	-1.99	996.8	-742.0	576.4	-1.99
shear + anti-symmetric torsion ($\alpha = -30^\circ$)	-1089.9	558.0	-282.8	-3.63	1089.9	-558.0	282.8	-3.63
CASE (D):								
shear + lateral bending ($\alpha = 0^\circ$)	-982.4	690.3	-400.1	-2.38	982.4	-690.3	400.1	-2.38
shear + lateral bending ($\alpha = +30^\circ$)	-1001.6	708.6	-442.5	-1.99	1001.6	-708.6	442.5	-1.99
shear + lateral bending ($\alpha = -30^\circ$)	-1096.4	528.0	-175.4	-0.88	1096.4	-528.0	175.4	-0.88
CASE (E):								
shear + lateral rotation ($\alpha = 0^\circ$)	-981.8	1.92	-0.89	-2.84	981.8	1.92	-0.89	-2.84
shear + lateral rotation ($\alpha = +30^\circ$)	-999.3	1.78	-0.96	-2.48	999.3	1.78	-0.96	-2.48
shear + lateral rotation ($\alpha = -30^\circ$)	-1108.7	1.42	-0.37	-4.15	1108.7	1.42	-0.37	-4.15

Note: * SI units of force are in (N). To convert to FPS units of (lbs_f), multiply by 0.22.

** SI units of moments are in (N*mm). To convert to FPS units of (lbs_f*in), multiply by 8.85 x 10⁻³.

Table 4.12(b). Calculated global loads and moments from reactions at the loading blocks of the modified biaxial model.

Modified Biaxial Model (long blocks)	Left Side of Specimen				Right Side of Specimen			
	P*	M _x **	M _y **	M _z **	P*	M _x **	M _y **	M _z **
CASE (A):								
shear ($\alpha = 0^\circ$)	-880.5	0	0	-1.12	880.5	0	0	-1.12
shear-compression ($\alpha = +30^\circ$)	-913.8	0	0	-0.07	913.8	0	0	-0.07
shear-tension ($\alpha = -30^\circ$)	-796.0	0	0	-1.97	796.0	0	0	-1.97
CASE (B):								
shear + asymmetric torsion ($\alpha = 0^\circ$)	-783.0	150.8	-144.7	-480.9	783.0	-150.4	144.3	479.3
shear + asymmetric torsion ($\alpha = +30^\circ$)	-799.6	164.6	-136.2	-474.9	799.6	-164.4	135.8	474.7
shear + asymmetric torsion ($\alpha = -30^\circ$)	-728.6	170.1	-81.9	-371.2	728.6	-169.8	81.7	368.2
CASE (C):								
shear + anti-symmetric torsion ($\alpha = 0^\circ$)	-696.2	284.3	-323.8	-0.47	696.2	-284.3	323.8	-0.47
shear + anti-symmetric torsion ($\alpha = +30^\circ$)	-710.0	292.7	-342.8	0.04	710.0	-292.7	342.8	0.04
shear + anti-symmetric torsion ($\alpha = -30^\circ$)	-661.1	310.8	-211.7	-1.03	661.1	-310.8	211.7	-1.03
CASE (D):								
shear + lateral bending ($\alpha = 0^\circ$)	-704.3	244.4	-226.4	-0.53	704.3	-244.4	226.4	-0.53
shear + lateral bending ($\alpha = +30^\circ$)	-714.4	265.7	-253.5	0.12	714.4	-265.7	253.5	0.12
shear + lateral bending ($\alpha = -30^\circ$)	-665.3	275.3	-108.1	-1.07	665.3	-275.3	108.1	-1.07
CASE (E):								
shear + lateral rotation ($\alpha = 0^\circ$)	-703.7	0.26	-0.28	-0.65	703.7	0.26	-0.28	-0.65
shear + lateral rotation ($\alpha = +30^\circ$)	-711.5	0.13	-0.29	-0.11	711.5	0.13	-0.29	-0.11
shear + lateral rotation ($\alpha = -30^\circ$)	-667.5	0.26	-0.22	-1.19	667.5	0.26	-0.22	-1.19

Note: * SI units of force are in (N). To convert to FPS units of (lbs_f), multiply by 0.22.

** SI units of moments are in (N*mm). To convert to FPS units of (lbs_f*in), multiply by 8.85×10^{-3} .

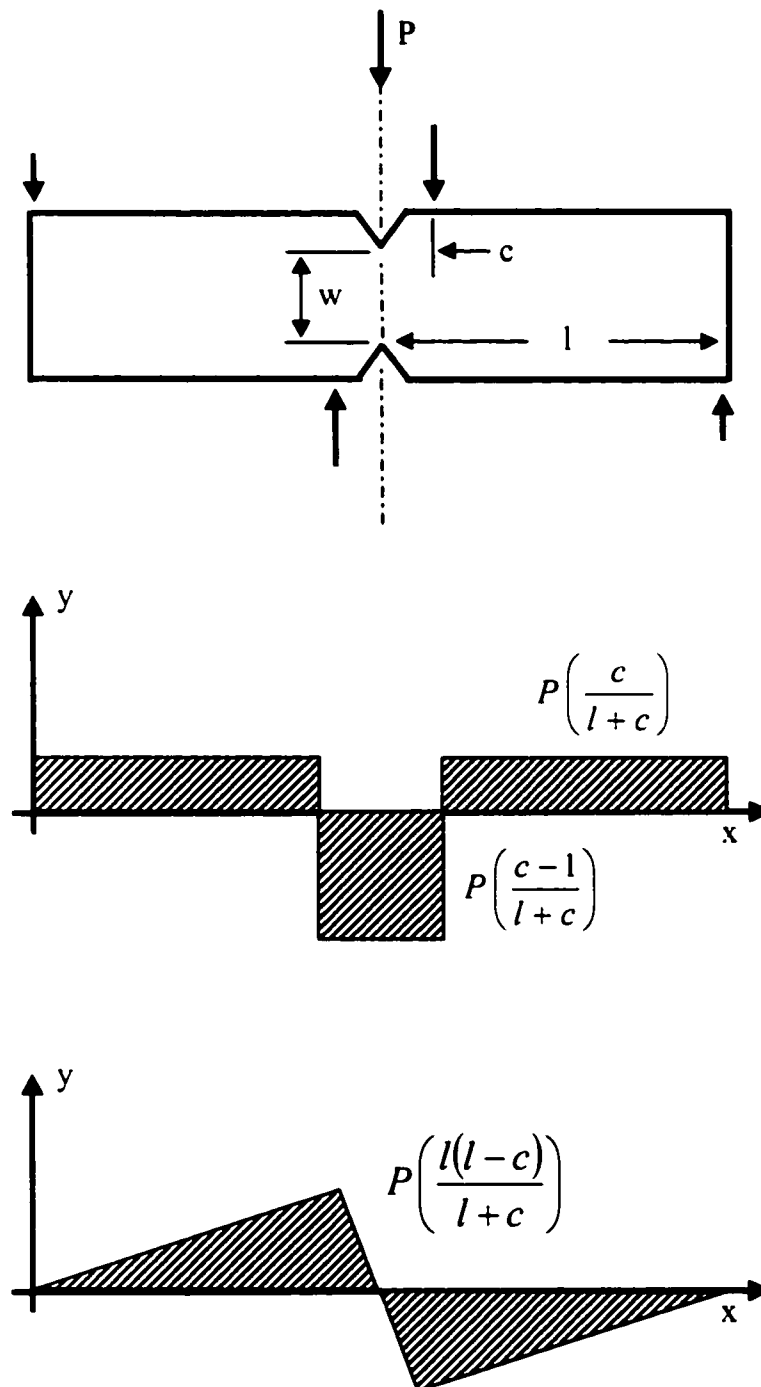


Figure 4.1. Force, shear and moment diagrams for the Iosipescu shear test method.

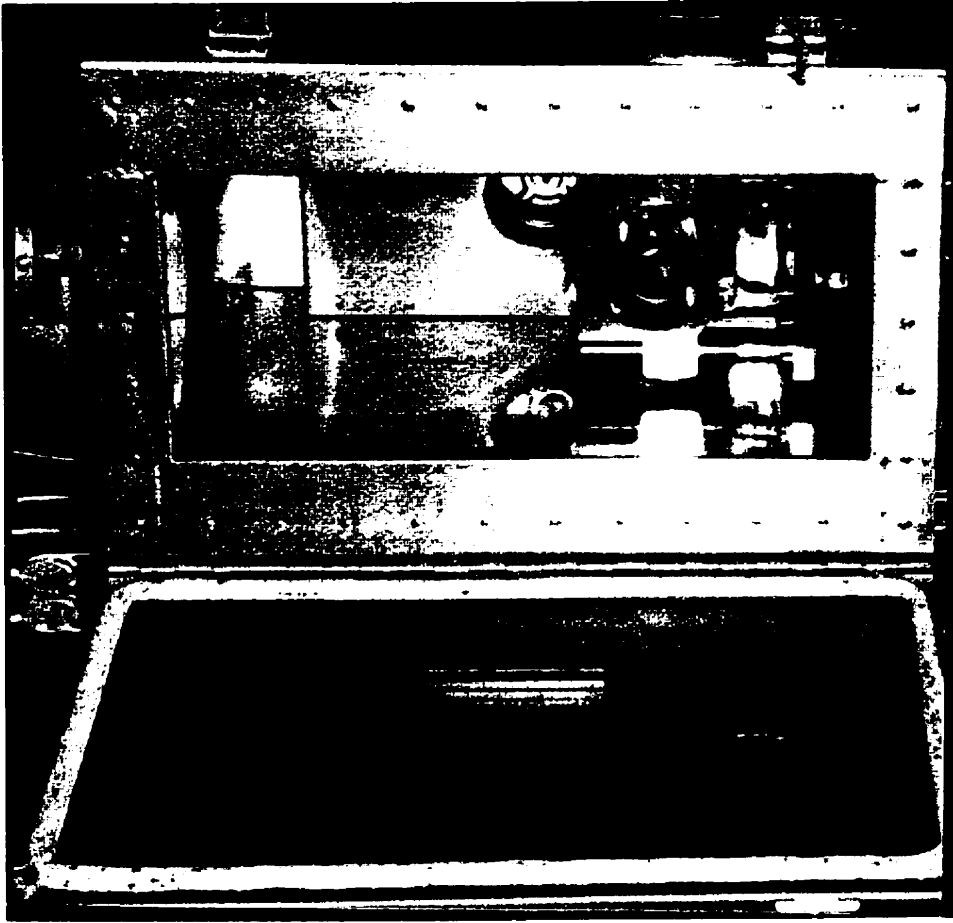


Figure 4.3. Environmental chamber for shear testing at elevated temperatures.

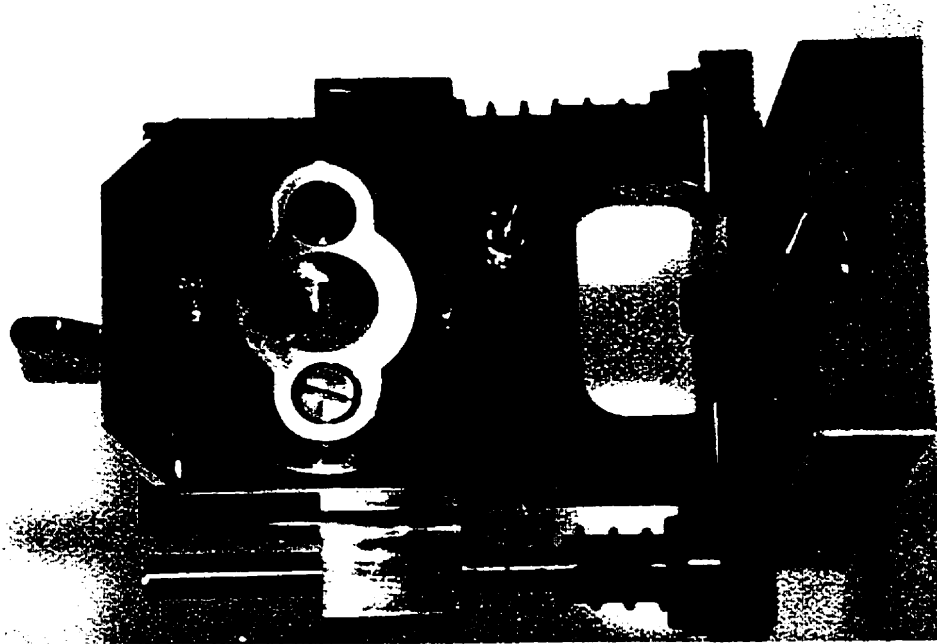


Figure 4.2. Biaxial fixture based on the Iosipescu shear test method.

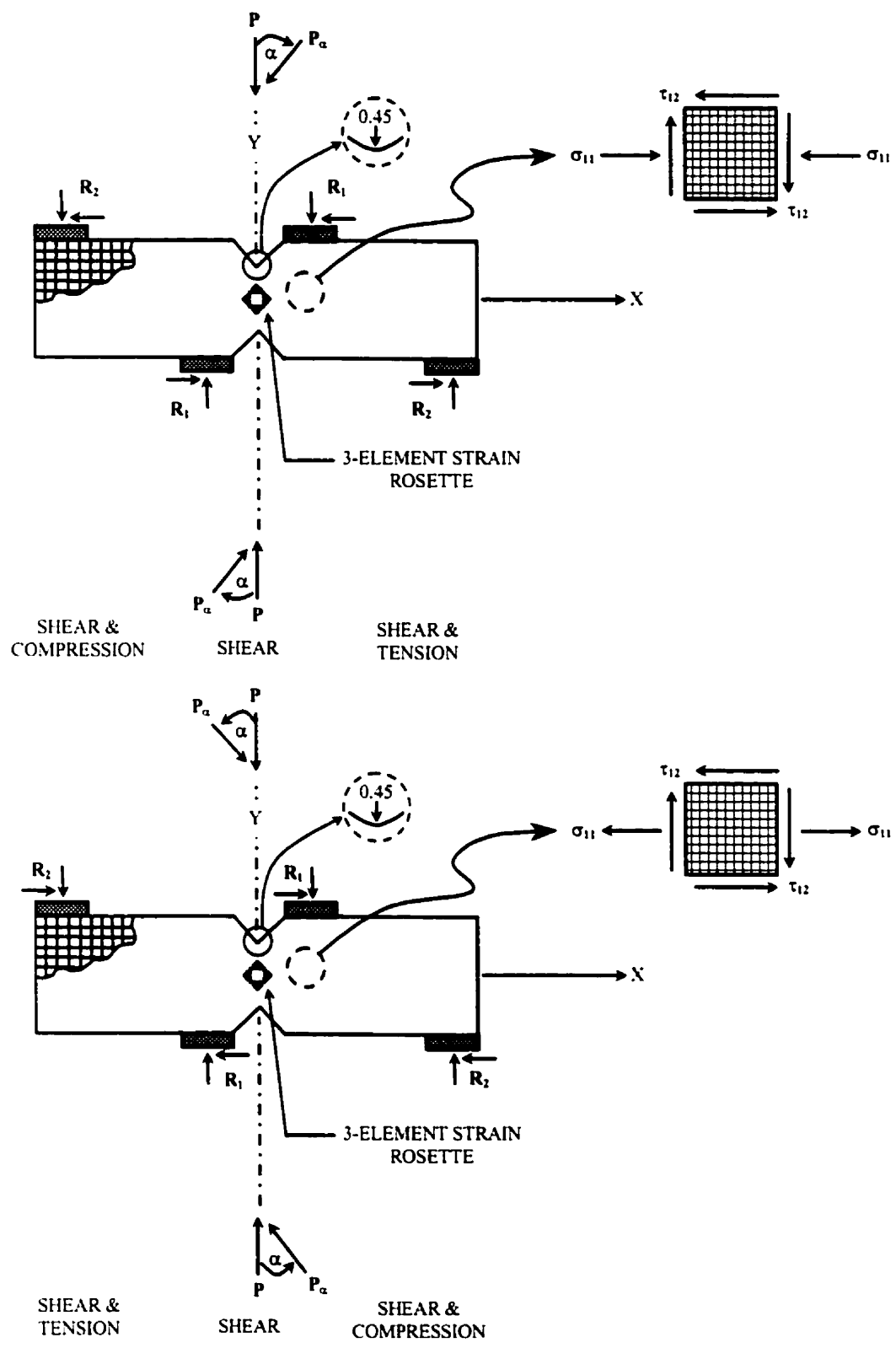


Figure 4.4. Ply-level shear-tension ($-\alpha$) and shear-compression ($+\alpha$) biaxial stress states in a composite Iosipescu specimen.

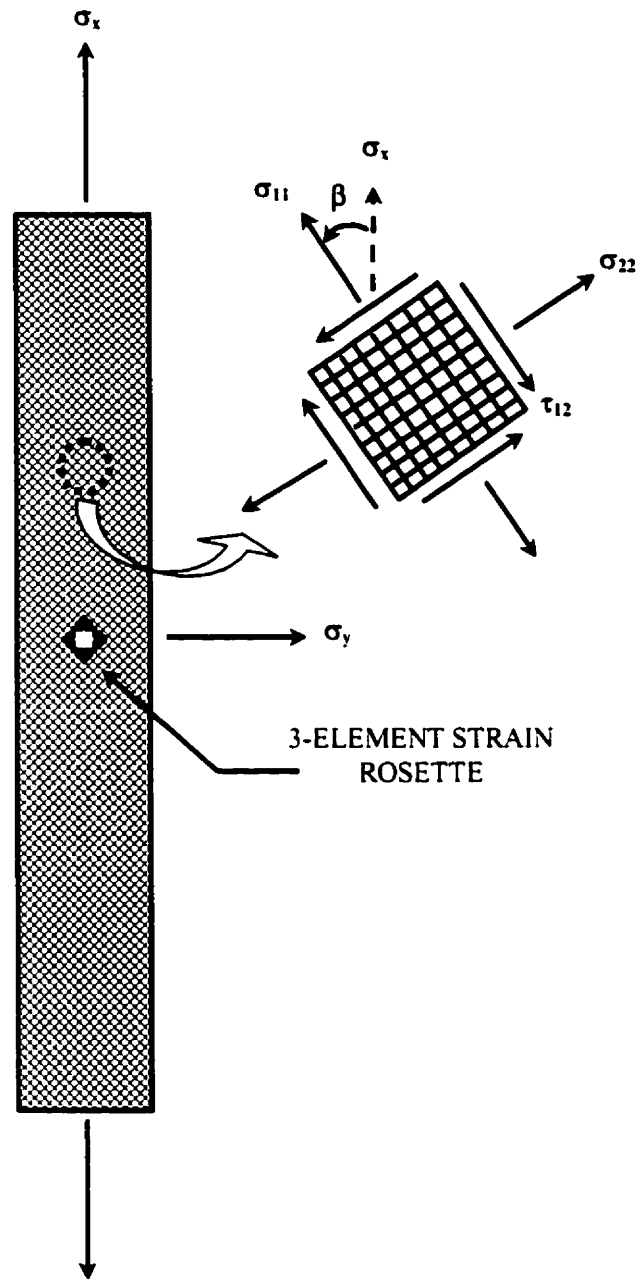


Figure 4.5. Representation for evaluating ply-level elastic behavior in the off-axis tensile composite specimens (c.f. Section 4).

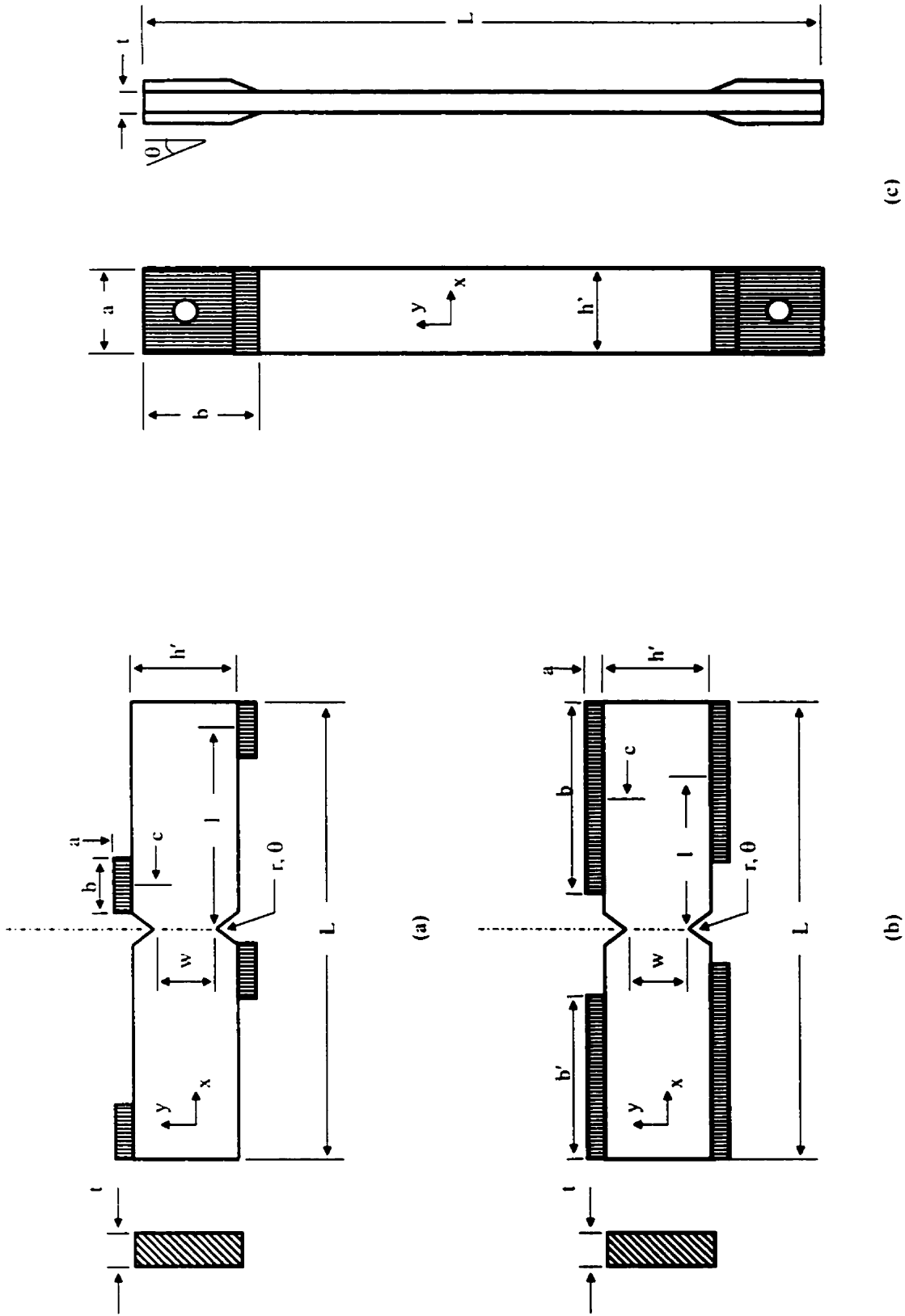


Figure 4.6. Specimen designs for experimental program (a) biaxial Iosipescu, (b) modified biaxial Iosipescu, and (c) standard tension/off-axis tension. (Refer to Table 4.1 for dimensional callouts.)

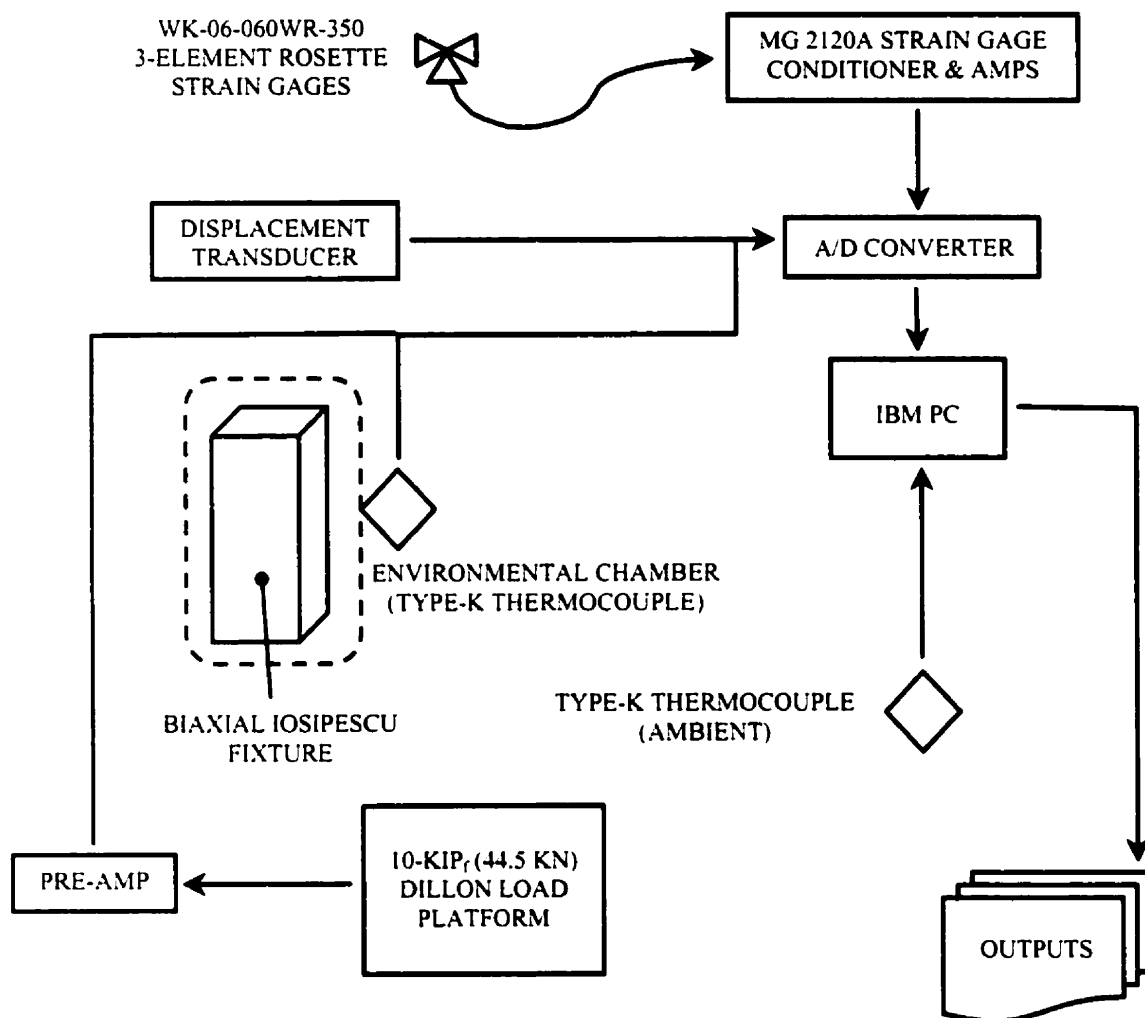
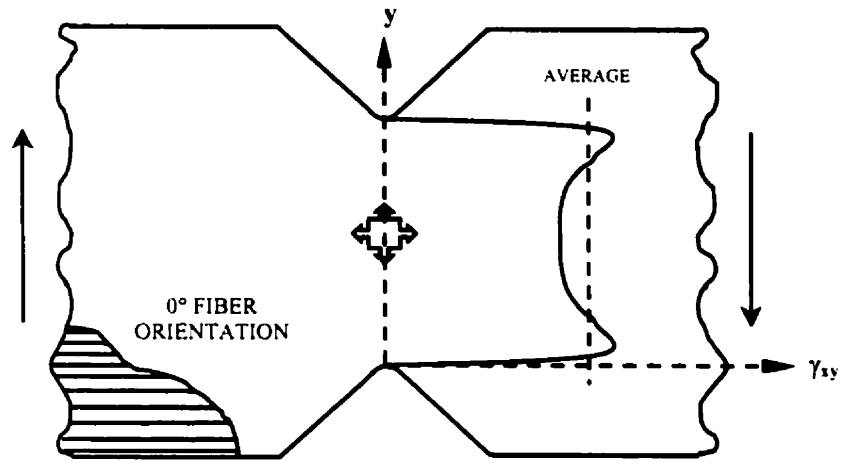
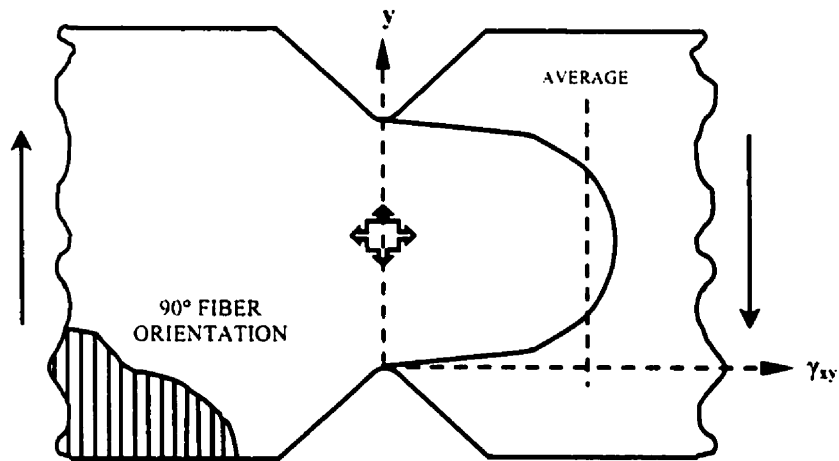


Figure 4.7. Room temperature experimental apparatus based on the Dillon tensile test pilot at the University of Denver. Tests conducted at OGIST's MSE fracture and failure laboratory replaced the Dillon with the Instron DTS Model 1230-20 excluding the environmental chamber.



(a)



(b)

Figure 4.8. Shear strain distributions along the notch root axis in Iosipescu specimens with (a) 0° fiber orientation and (b) 90° fiber orientation. With small gages, the shear strain measured in (a) appears to be higher than in (b). (After Ifju 1991.)⁷³

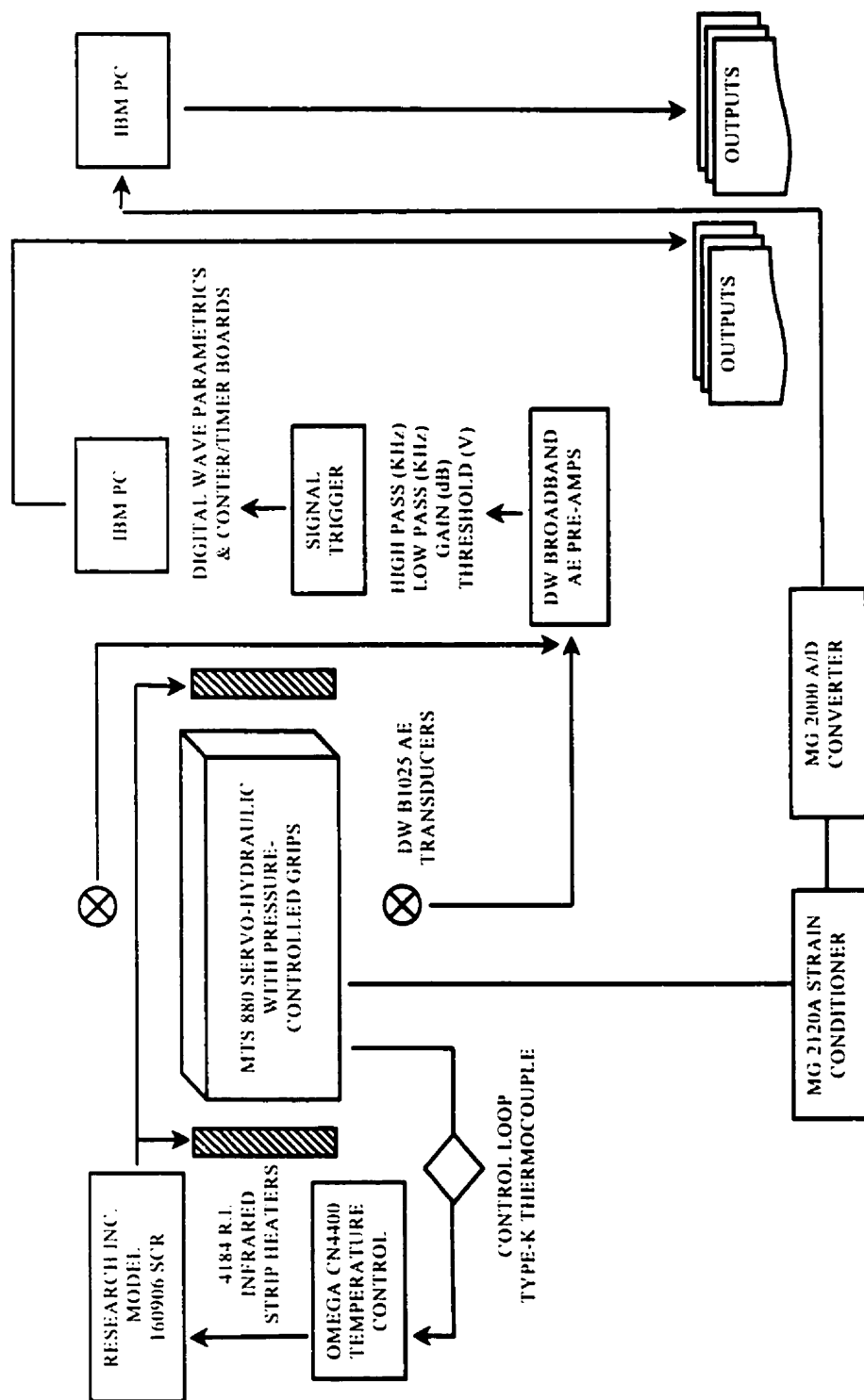


Figure 4.9. Elevated temperature experimental apparatus based on the MTS Model 880 Dynamic Material Test System at the University of Denver's Physics Department. The test platform employed hydraulic grips with smooth and serrated wedge inserts for mechanical testing without or with acoustic emission sampling.

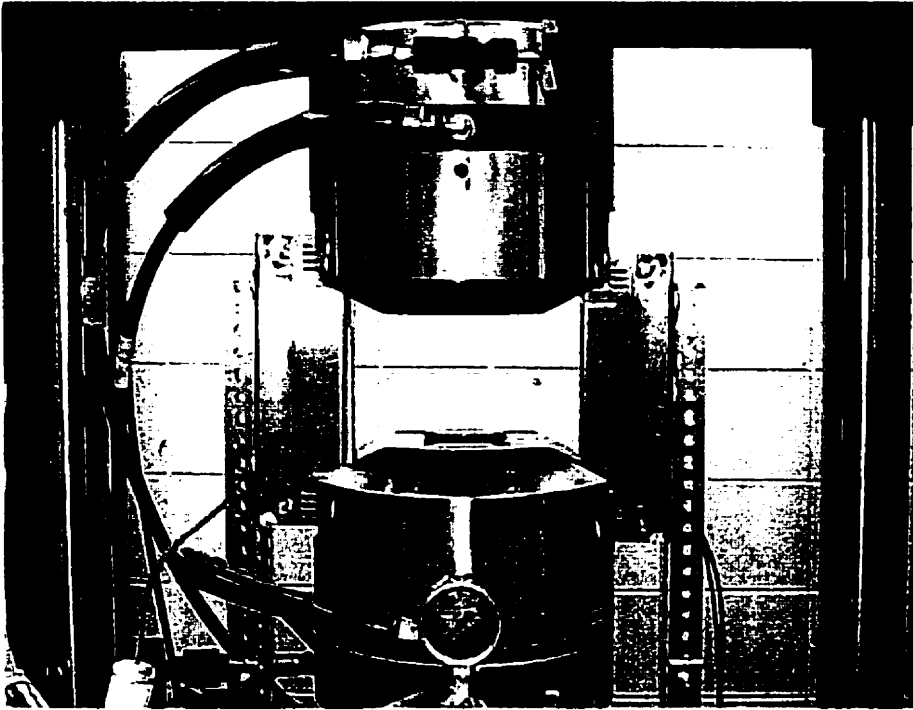


Figure 4.10. Placement of R.I. Model 4184 strip heaters.

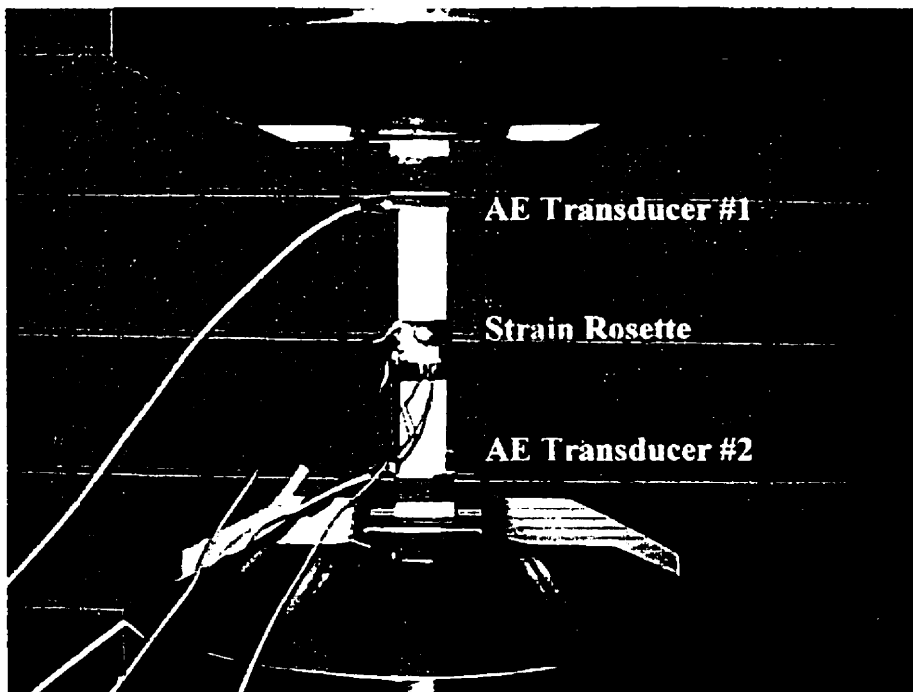


Figure 4.11. Placement of Model B1025 broadband AE transducers.

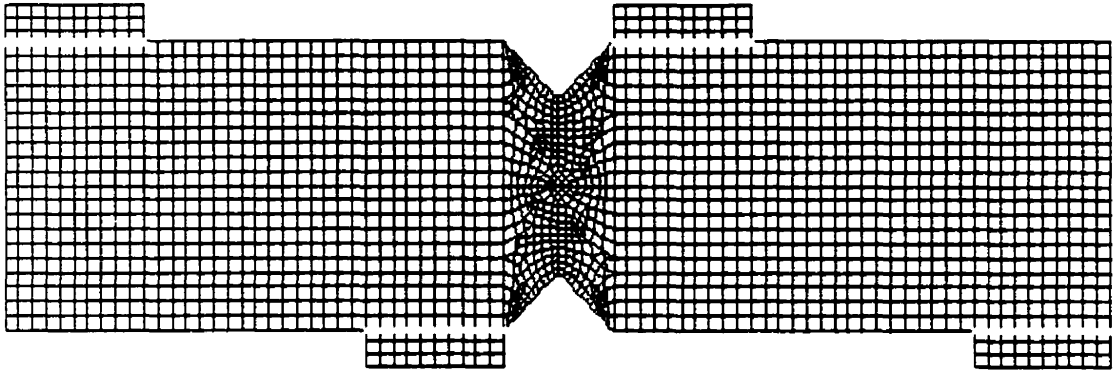


Figure 4.12(a). Two-dimensional finite element model of the biaxial Iosipescu specimen with 6235 nodes, 2608 8-node quadrilateral and 6-node triangular isoparametric elements (PLANE82) and 210 contact pseudo-elements (CONTAC48).

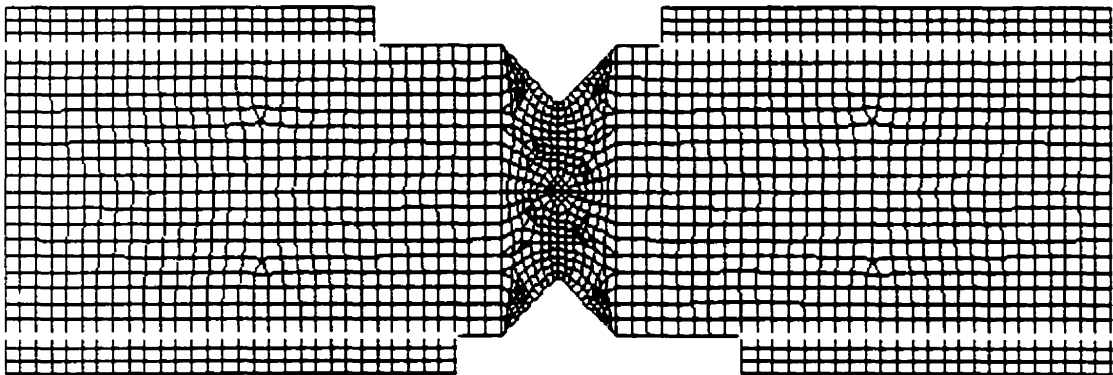
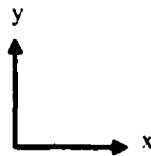


Figure 4.12(b). Two-dimensional finite element model of the modified biaxial Iosipescu specimen with 5973 nodes, 6454 8-node quadrilateral and 6-node triangular isoparametric elements (PLANE82) and 1174 contact pseudo-elements (CONTAC48).

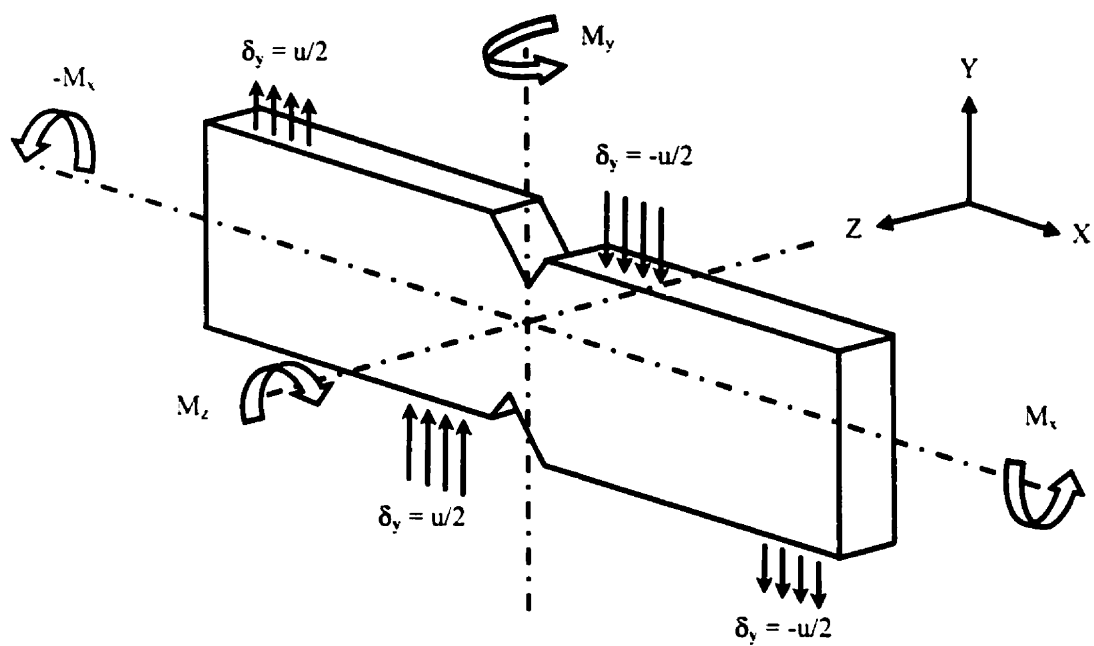


Figure 4.13(a). CASE A

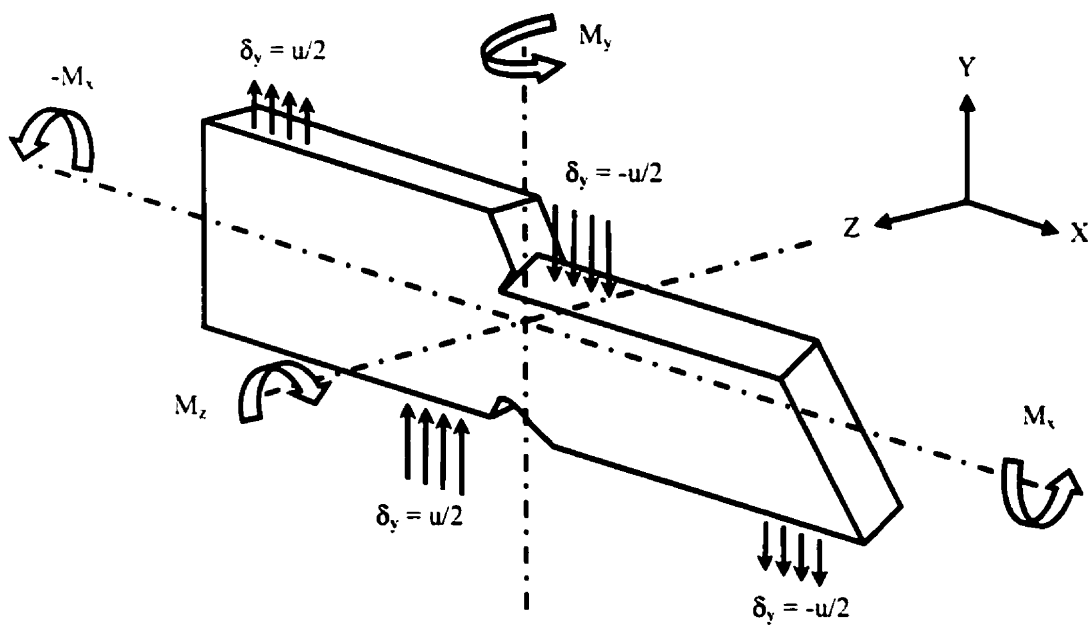


Figure 4.13(b). CASE B

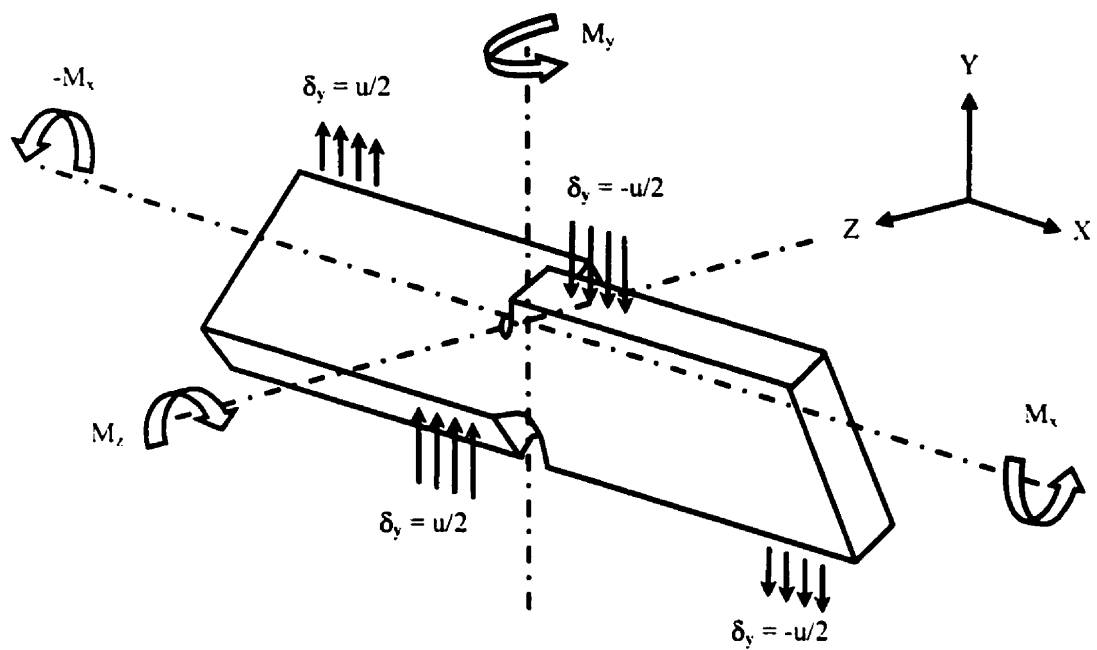


Figure 4.13(c). CASE C

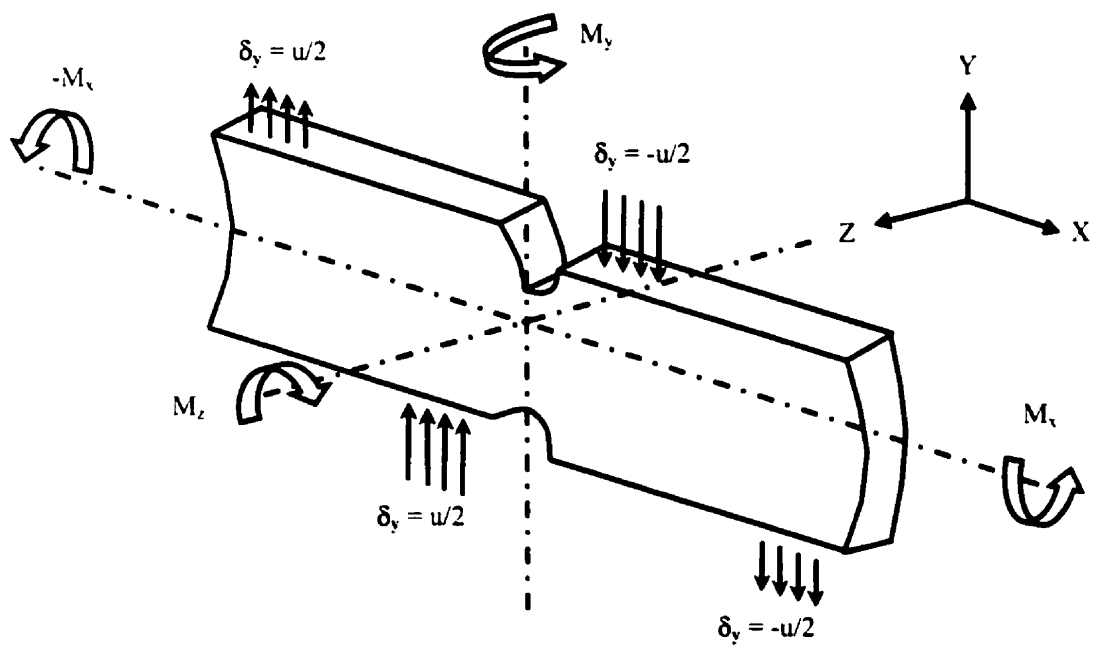


Figure 4.13(d). CASE D

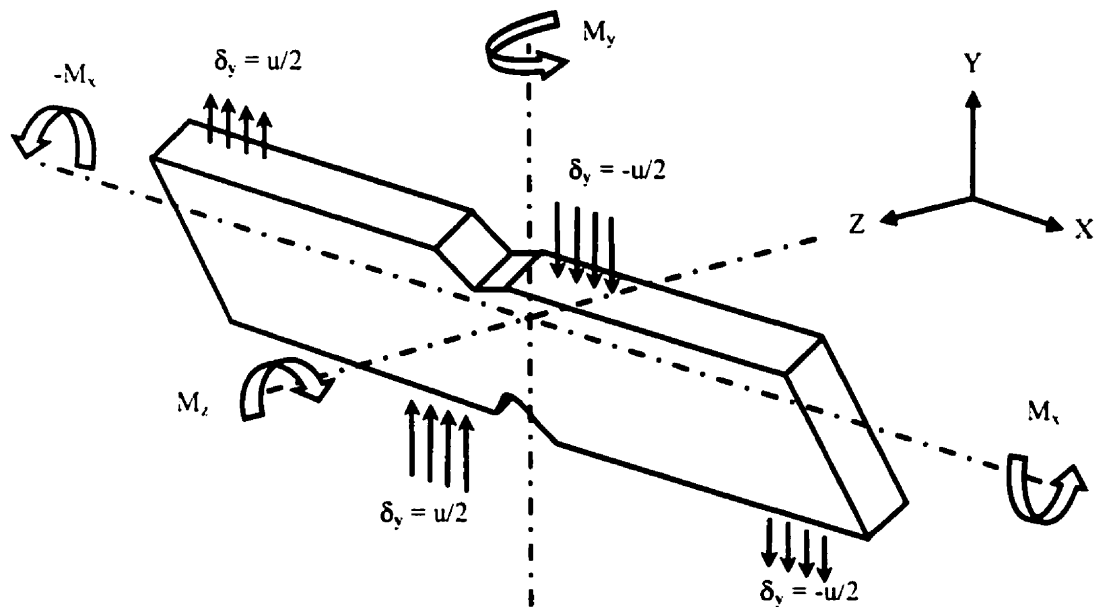


Figure 4.13(e). CASE E

Figure 4.13. Load cases under consideration in the eccentric loading of biaxial and modified biaxial graphite-PMR15 Iosipescu specimens: (a) CASE A - shear loading, (b) CASE B - shear and asymmetric loading, (c) CASE C - shear and anti-symmetric loading, (d) CASE D - shear and lateral bending, and (e) CASE E - shear and lateral rotation.

Figure 4.14(a). Three-dimensional finite element model of the biaxial Iosipescu specimen with 4106 nodes, 604 8-node layered structural solid elements (SOLID46), 64 8-node structural solid elements (SOLID45) and 4400 contact pseudo-elements (CONTACT49).

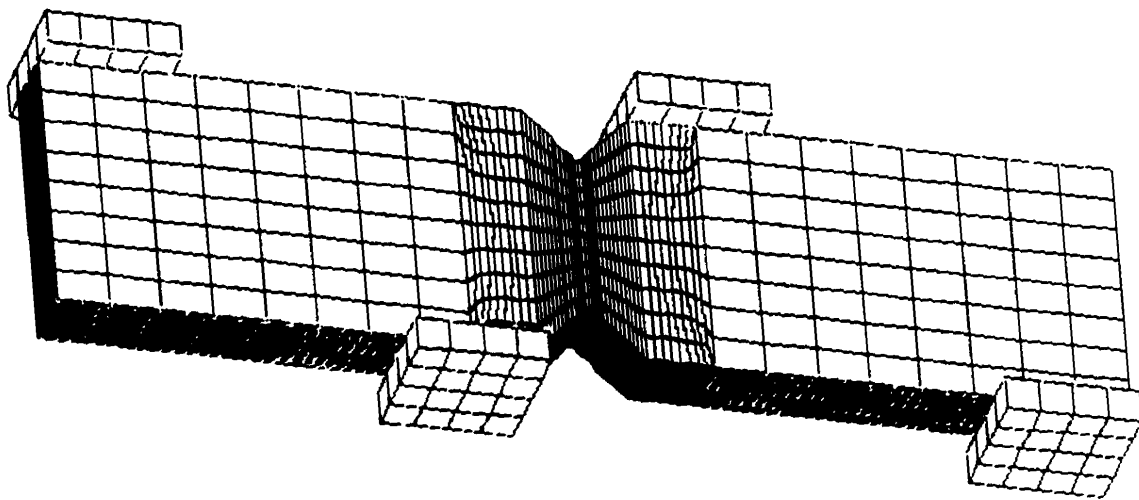
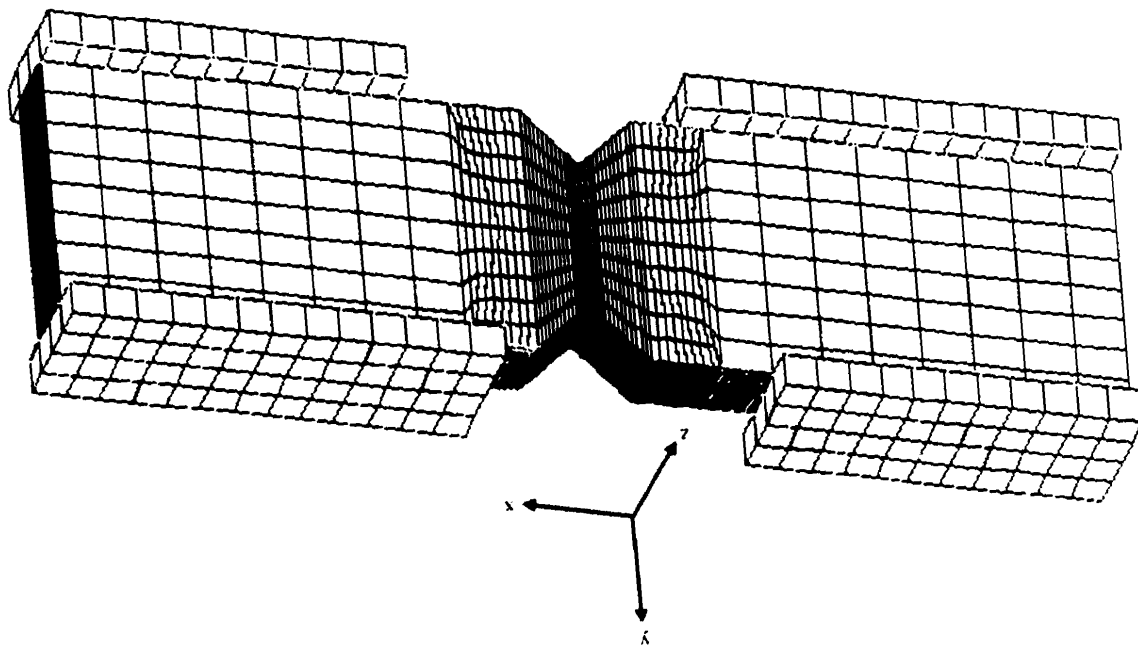


Figure 4.14(b). Three-dimensional finite element model of the modified biaxial Iosipescu specimen with 4426 nodes, 604 8-node layered structural solid elements (SOLID46), 192 8-node structural solid elements (SOLID45) and 13056 contact pseudo-elements (CONTACT49).



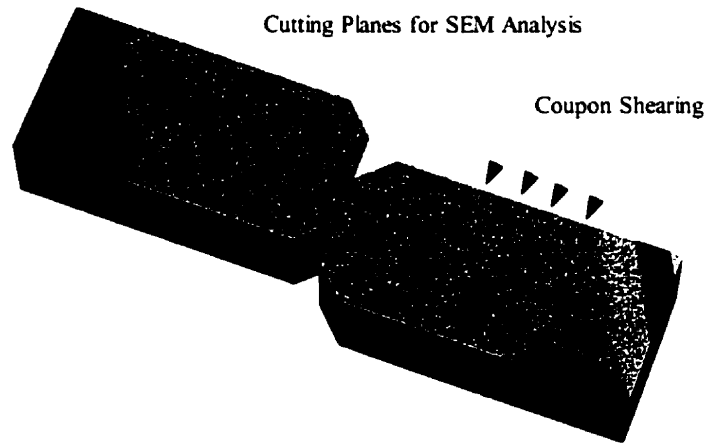


Figure 4.15. Orientation of cutting planes for removing damage sample.

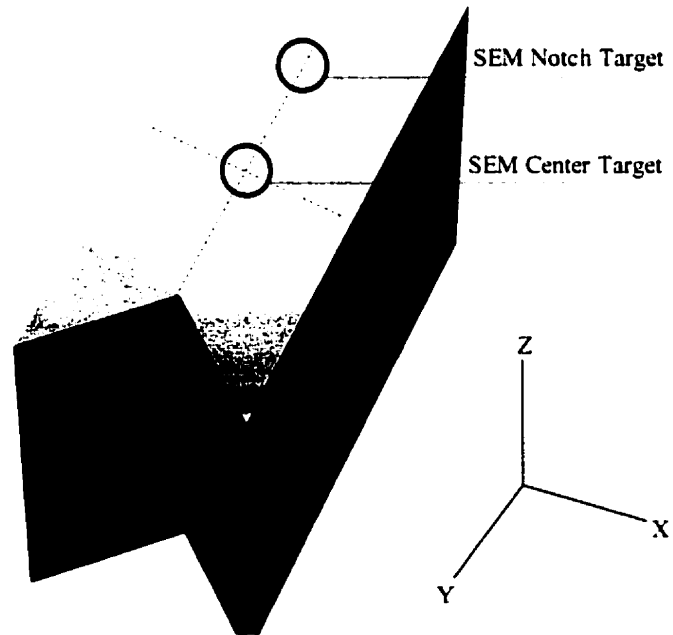


Figure 4.16. Removed sample showing locations of imaging targets.

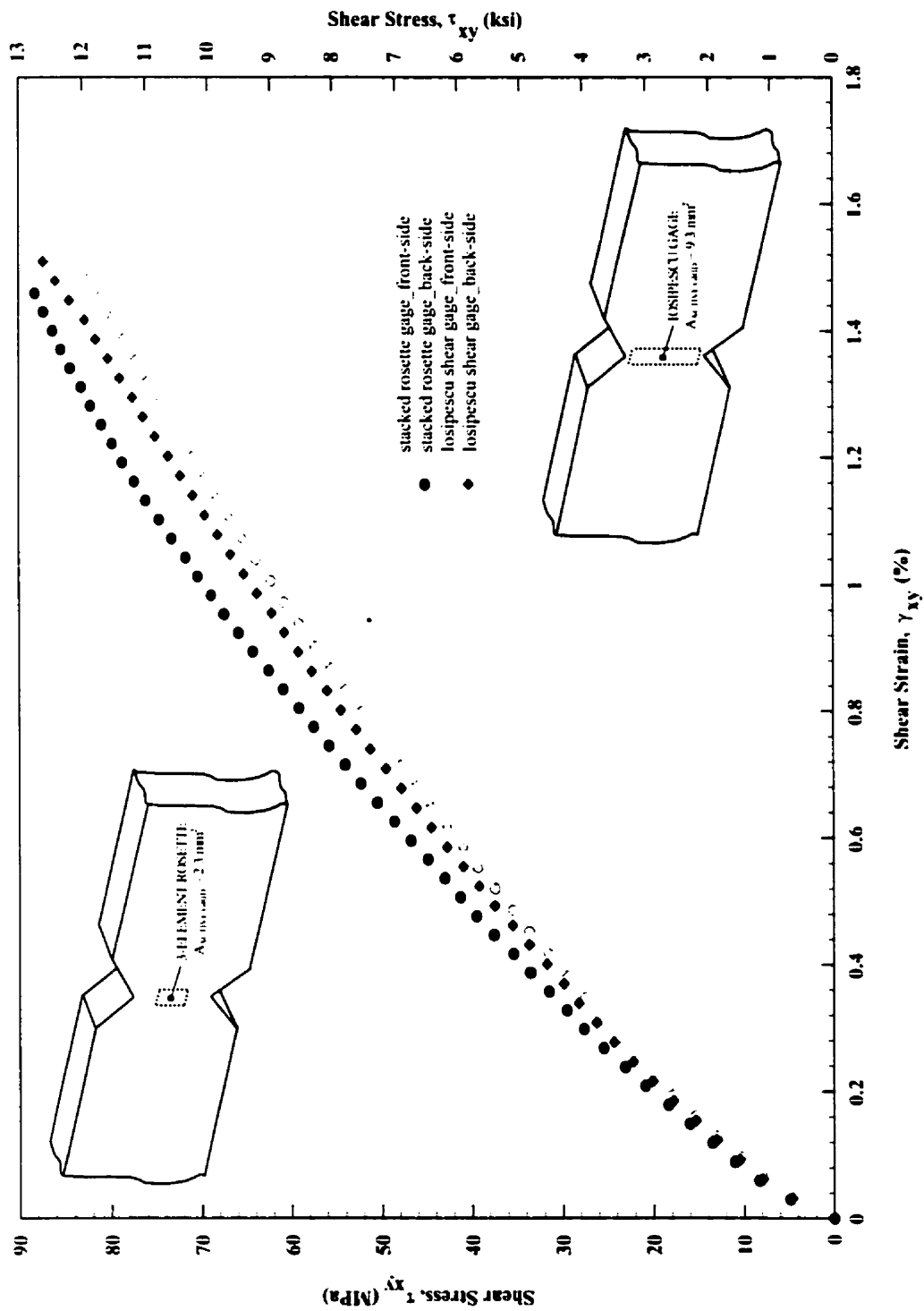


Figure 4.17. Comparison of shear stress-strain data for the stacked rosette gage and Iosipescu shear gage obtained from the first graphite-PMR15 plaque.

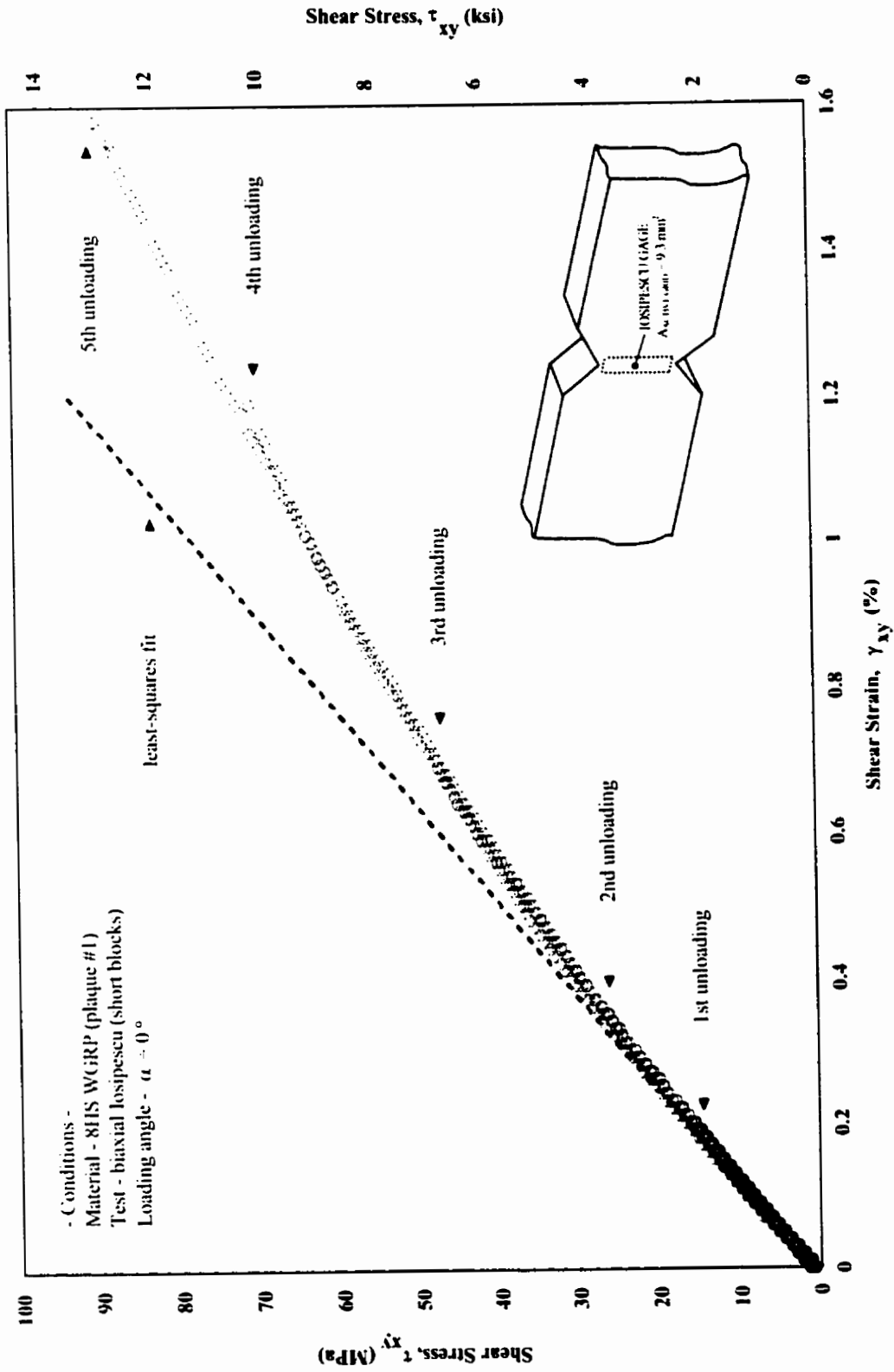


Figure 4.18(a). Five-step shear loading/unloading tests to determine the linear elastic regime of the first graphite-PMR15 plaque using the biaxial Iosipescu fixture and shear gages (2-side average).

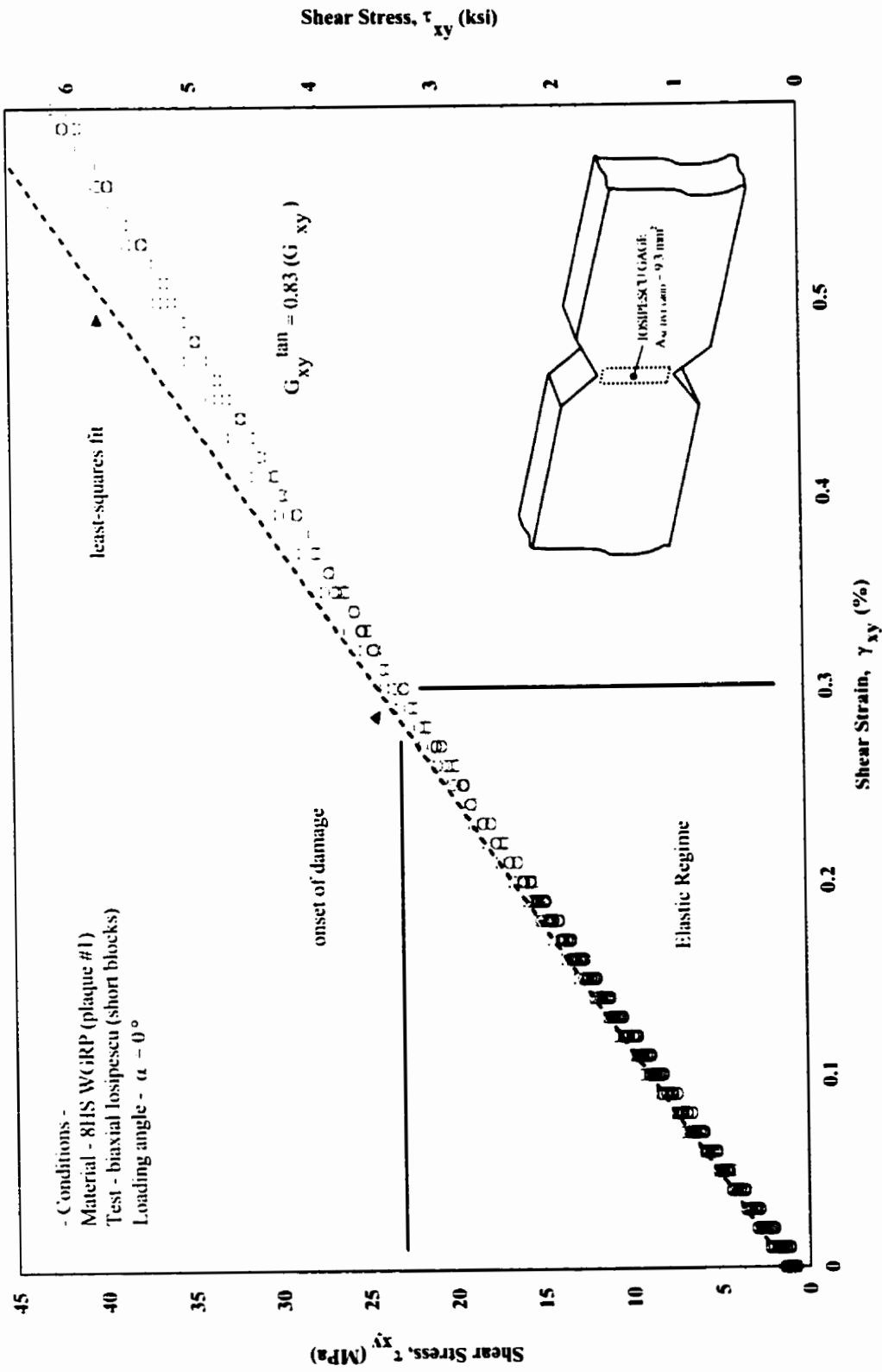


Figure 4.18(b). Re-scaled five-step shear loading/unloading scheme to illustrate delineation of the linear elastic regime and onset of damage based on deviation from least-squares fit line.

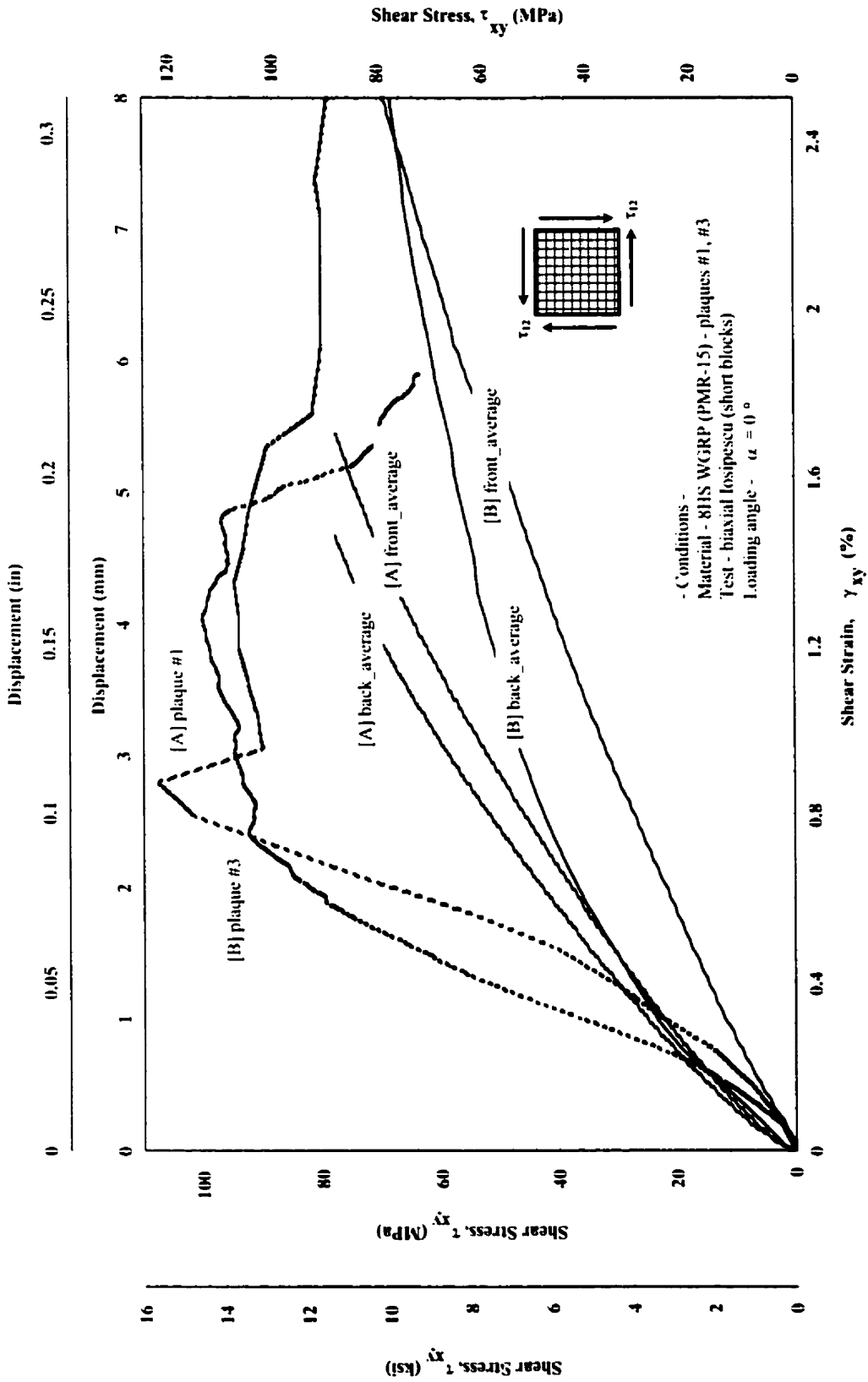


Figure 4.19(a). Superimposed shear stress-displacement and shear stress-strain curves for graphite-PMR15 Iosipescu specimens from the first and third plaques.

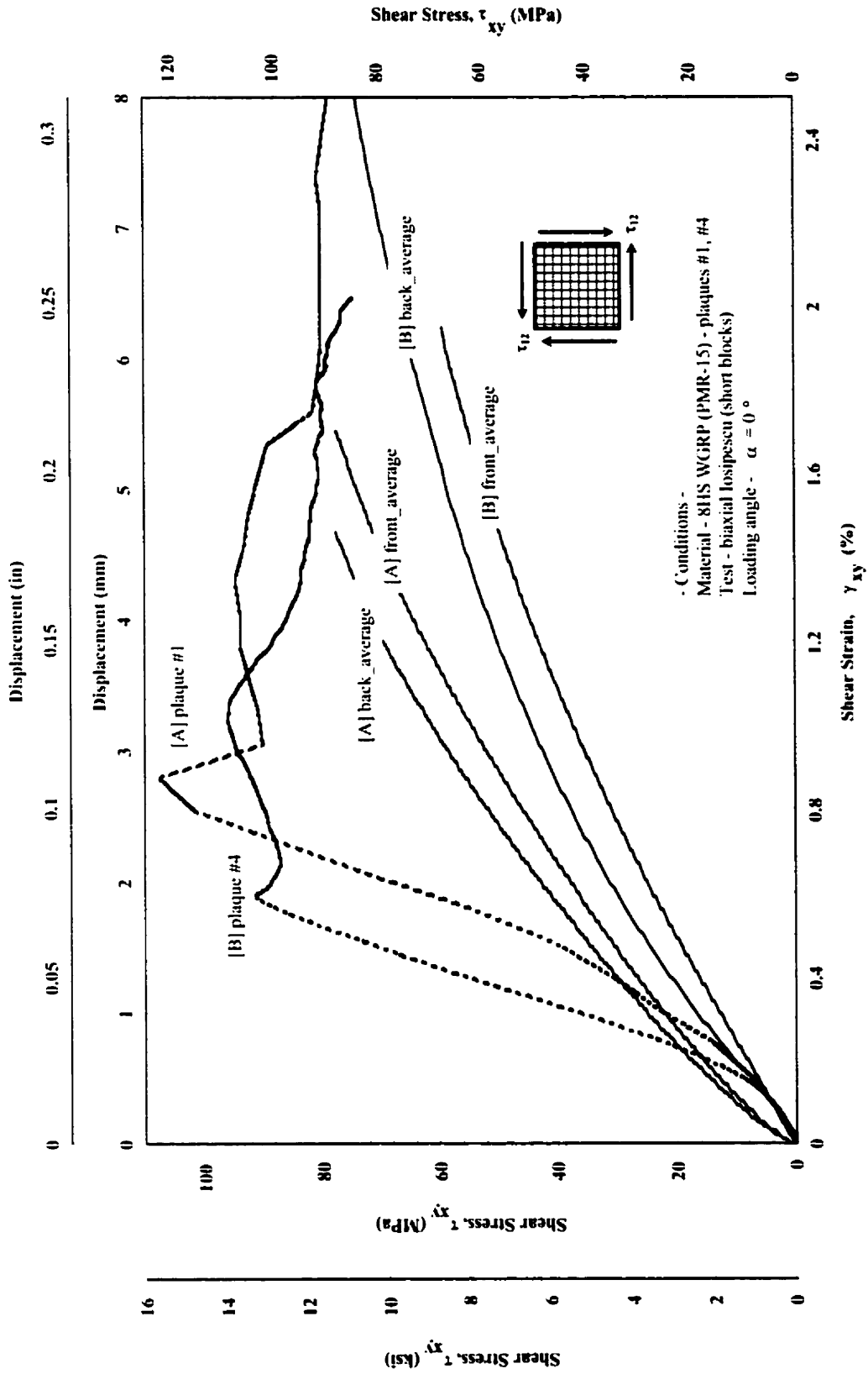


Figure 4.19(b). Superimposed shear stress-displacement and shear stress-strain curves for graphite-PMR15 losipescu specimens from the first and fourth plaques.

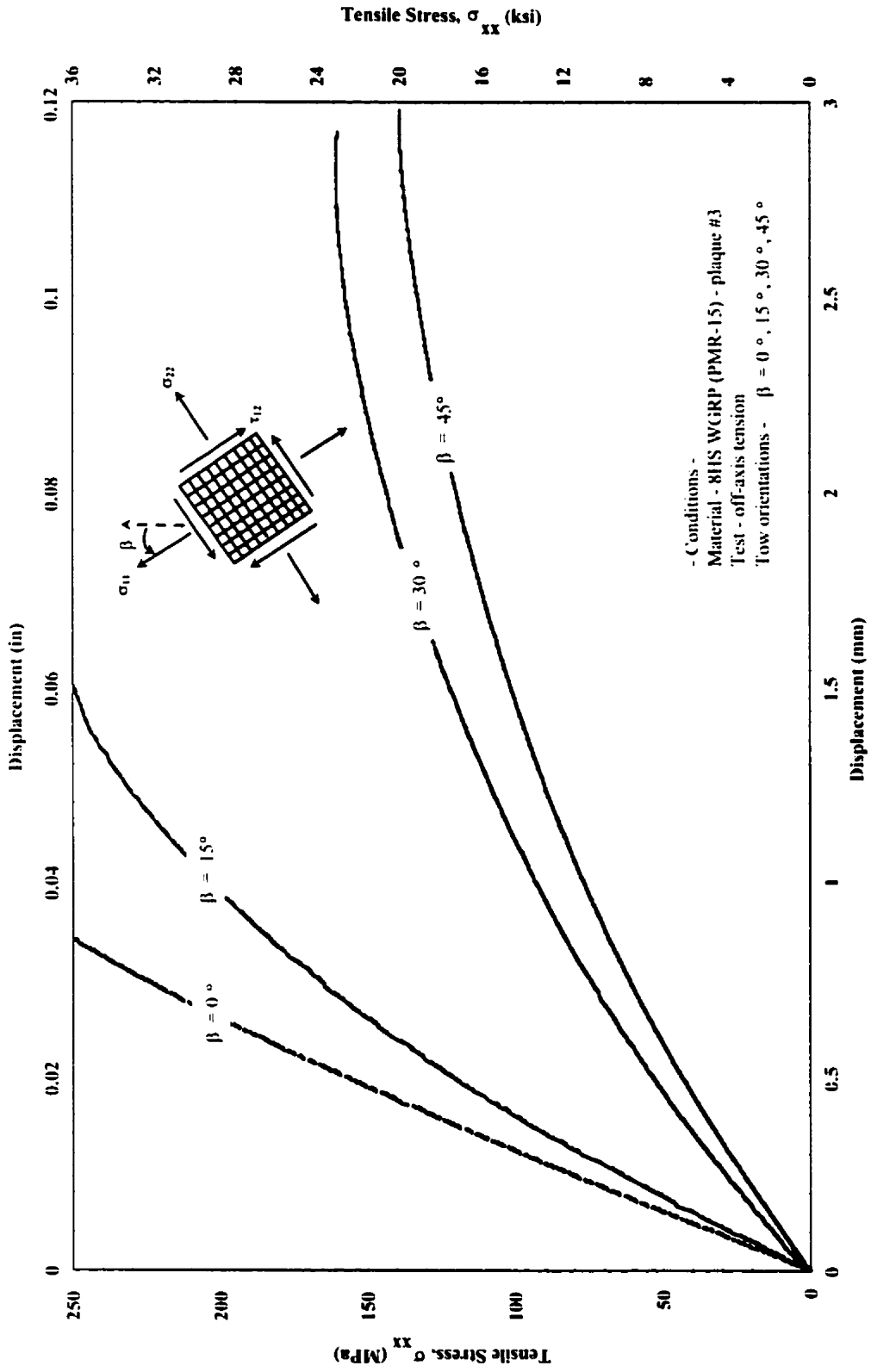


Figure 4.20(a). Stress-displacement curves for standard and off-axis tensile tests from graphite-PMR15 specimens belonging to the third plaque ($\beta = 0^\circ, 15^\circ, 30^\circ$ and 45°).

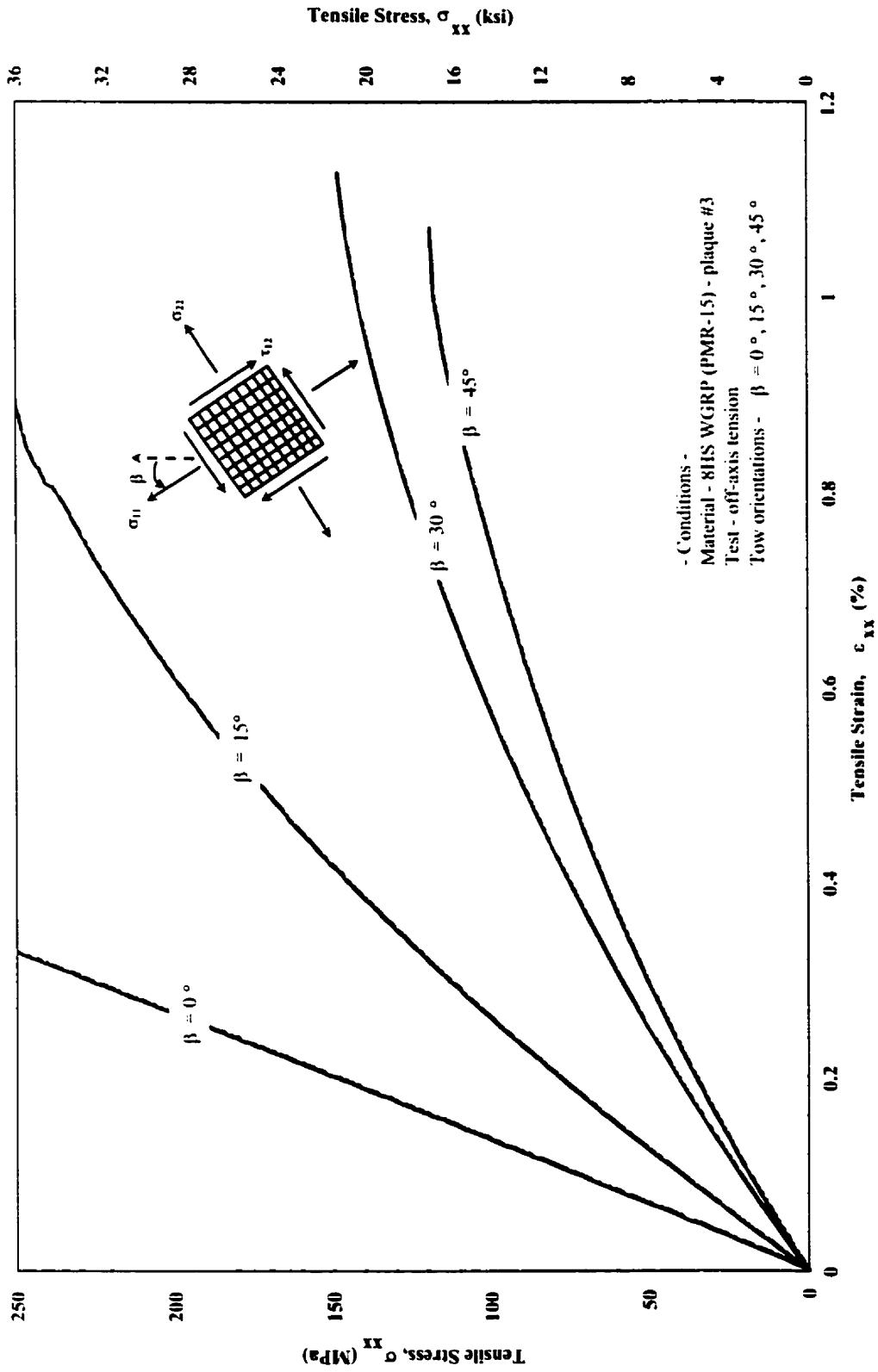


Figure 4.20(b). Stress-strain curves for standard and off-axis tensile tests from graphite-PMR15 specimens belonging to the third plaque ($\beta = 0^\circ, 15^\circ, 30^\circ$ and 45°).

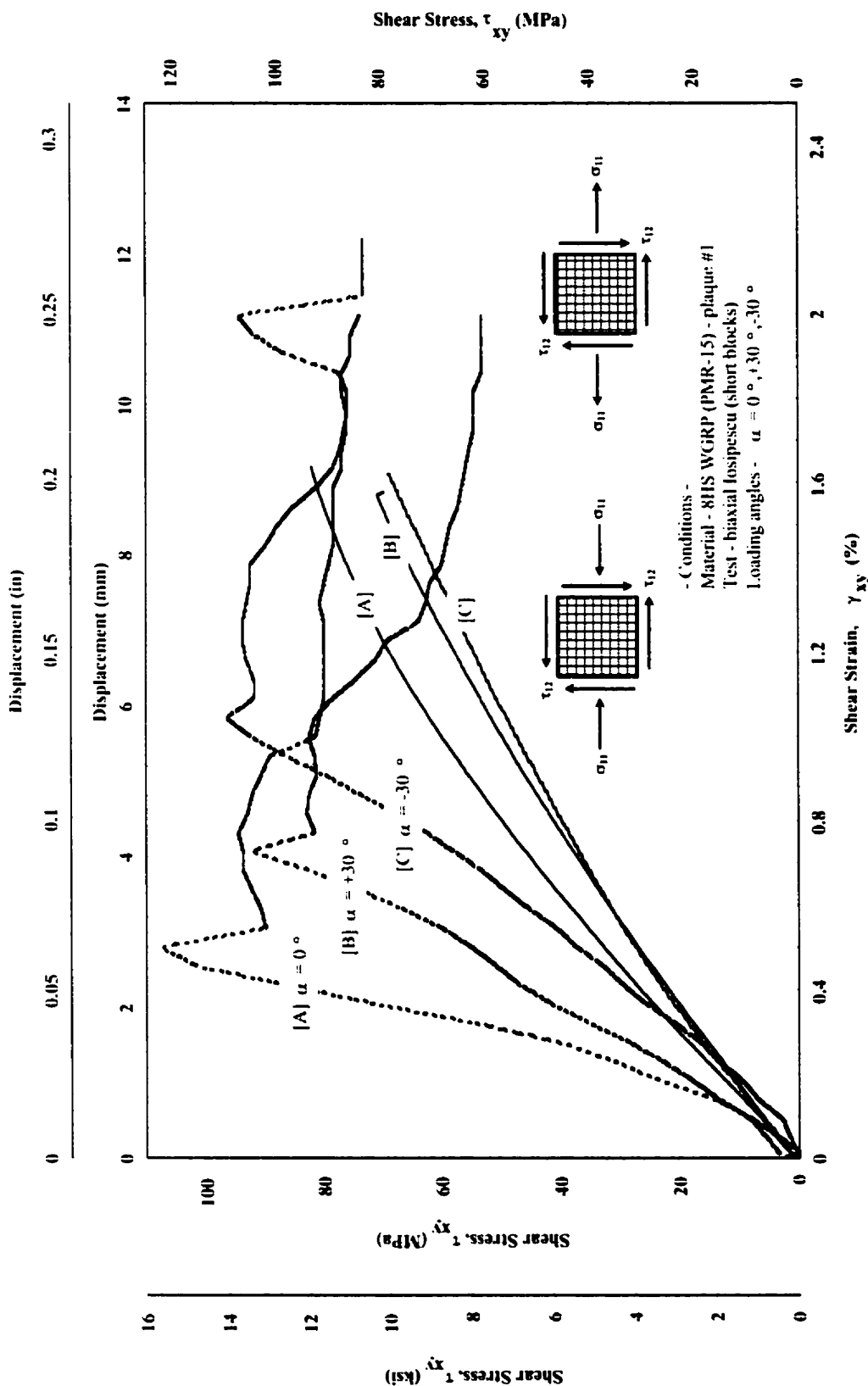


Figure 4.21. Superimposed shear stress-displacement and shear stress-strain curves for graphite-PMR15 specimens from the first plaque tested at $\alpha = 0^\circ, +30^\circ$ and -30° .

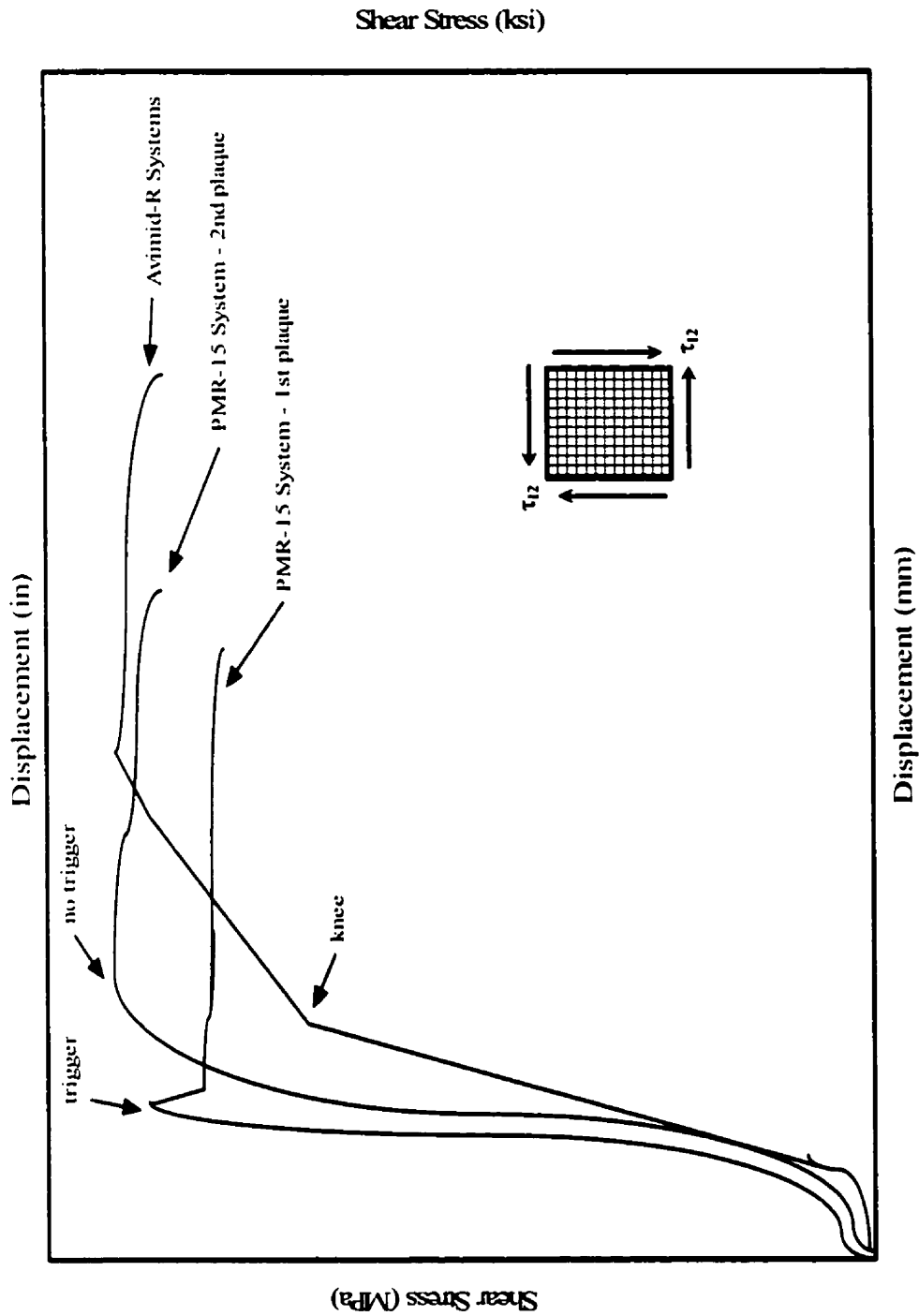


Figure 4.22. Comparative shear stress-displacement curves for Iosipescu specimens from the graphite-PMR15 and graphite-Avimid R composite plaques.

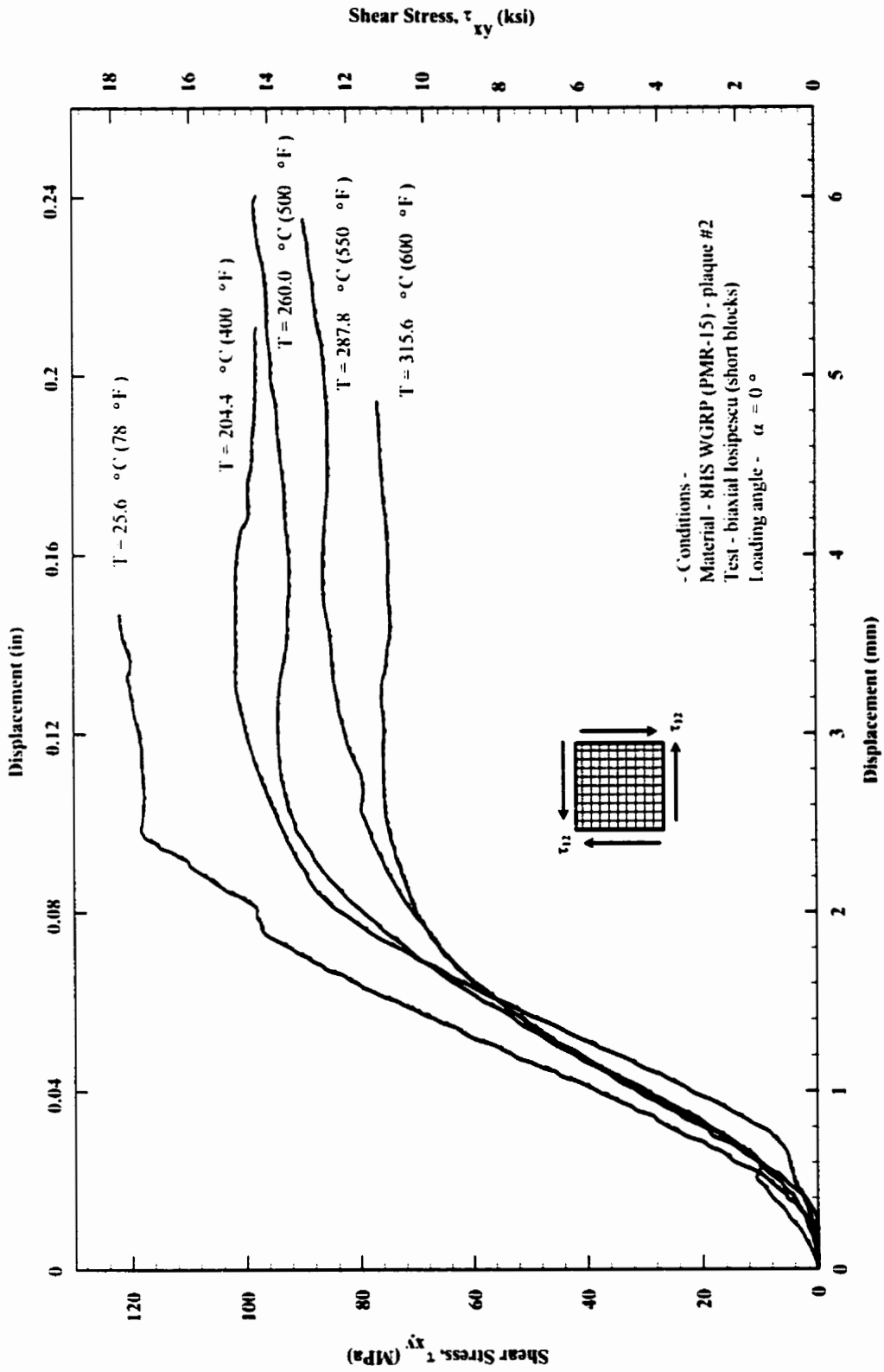


Figure 4.23. Shear stress-displacement curves for graphite-PMR15 specimens (plaque #2) at various temperatures.

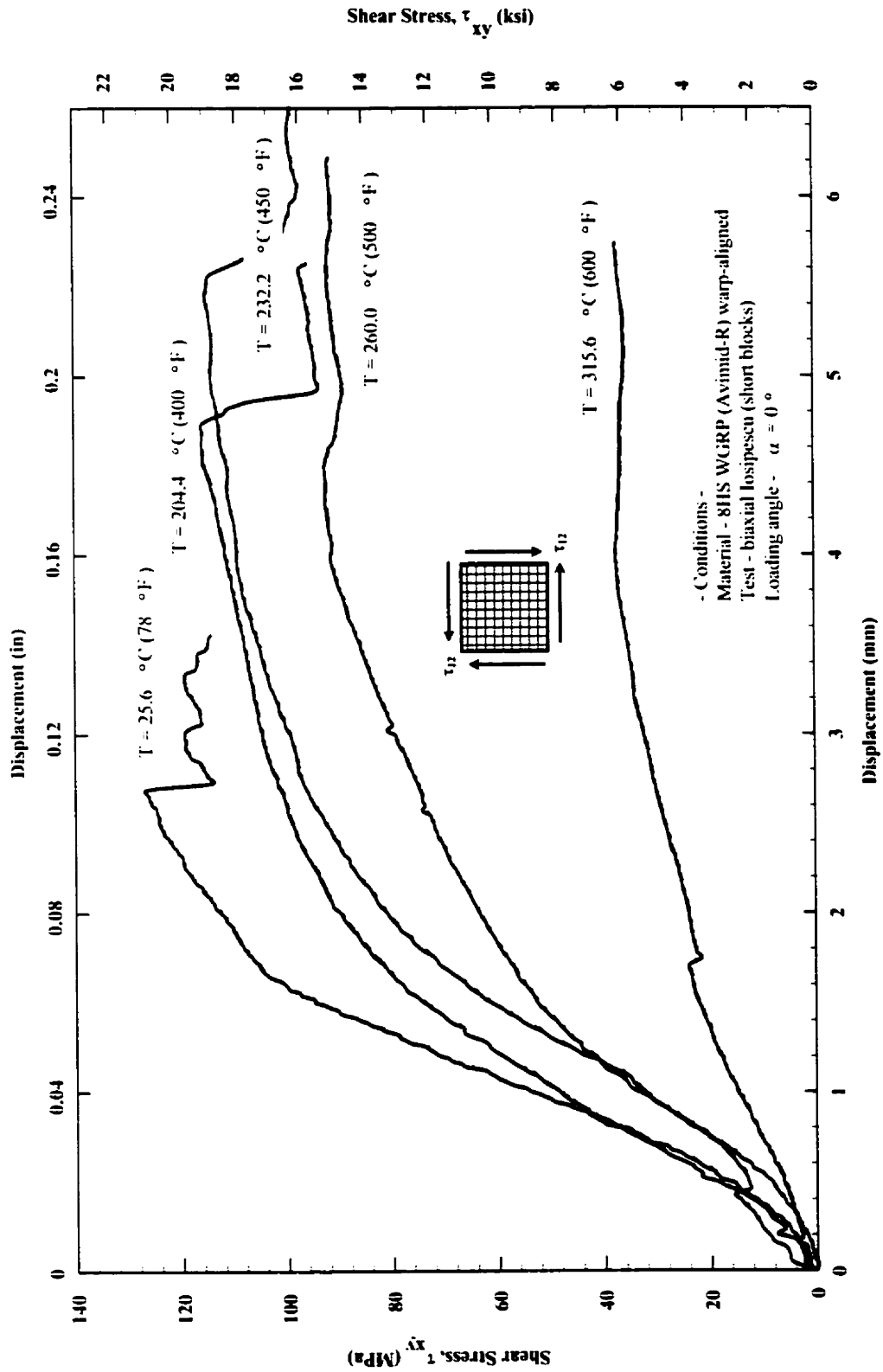


Figure 4.24. Shear stress-displacement curves for graphite-Aramid R specimens (warp-aligned) at various temperatures.

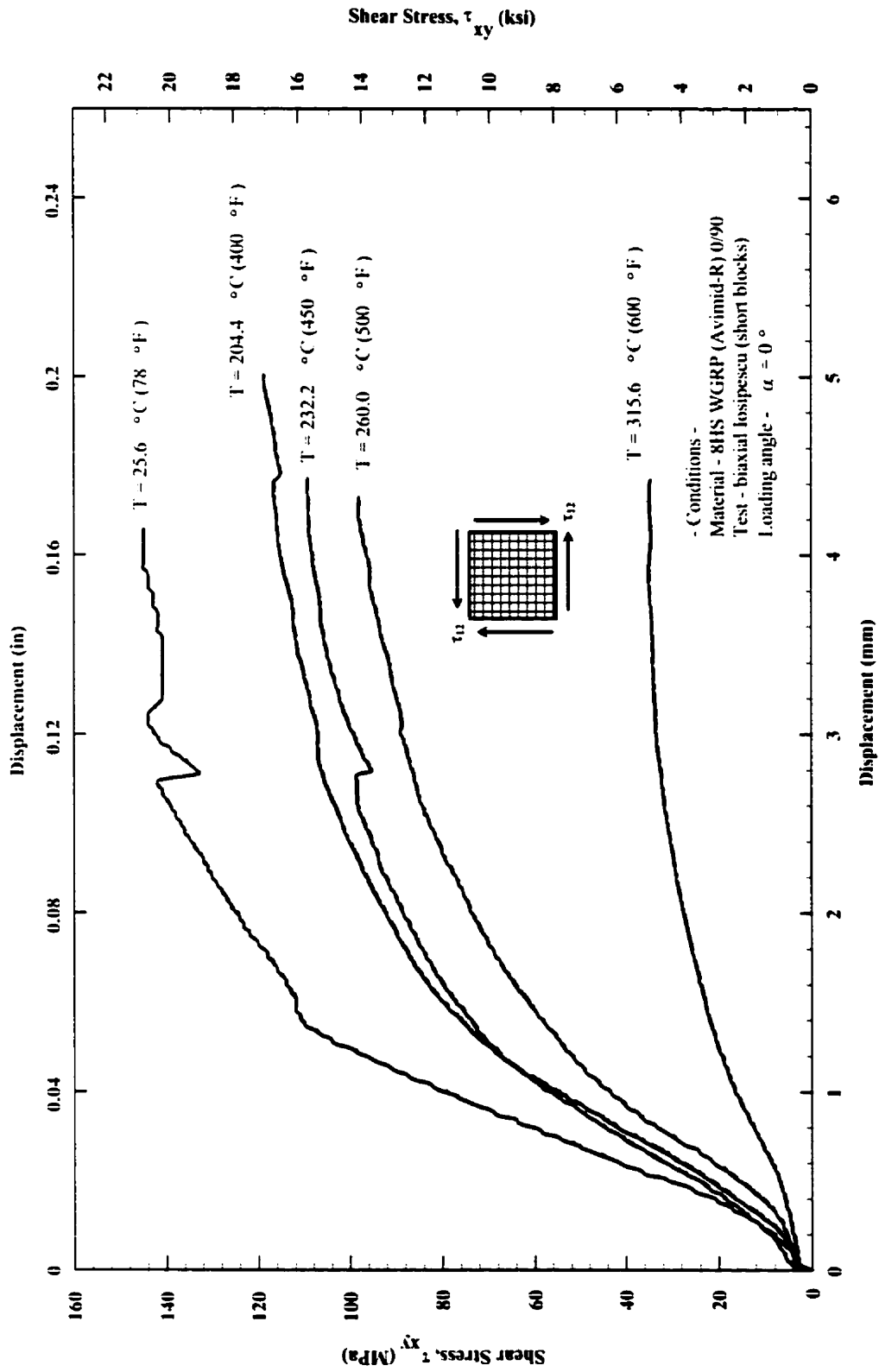


Figure 4.25. Shear stress-displacement curves for graphite-Aramid R specimens ($0^\circ/90^\circ$) at various temperatures.

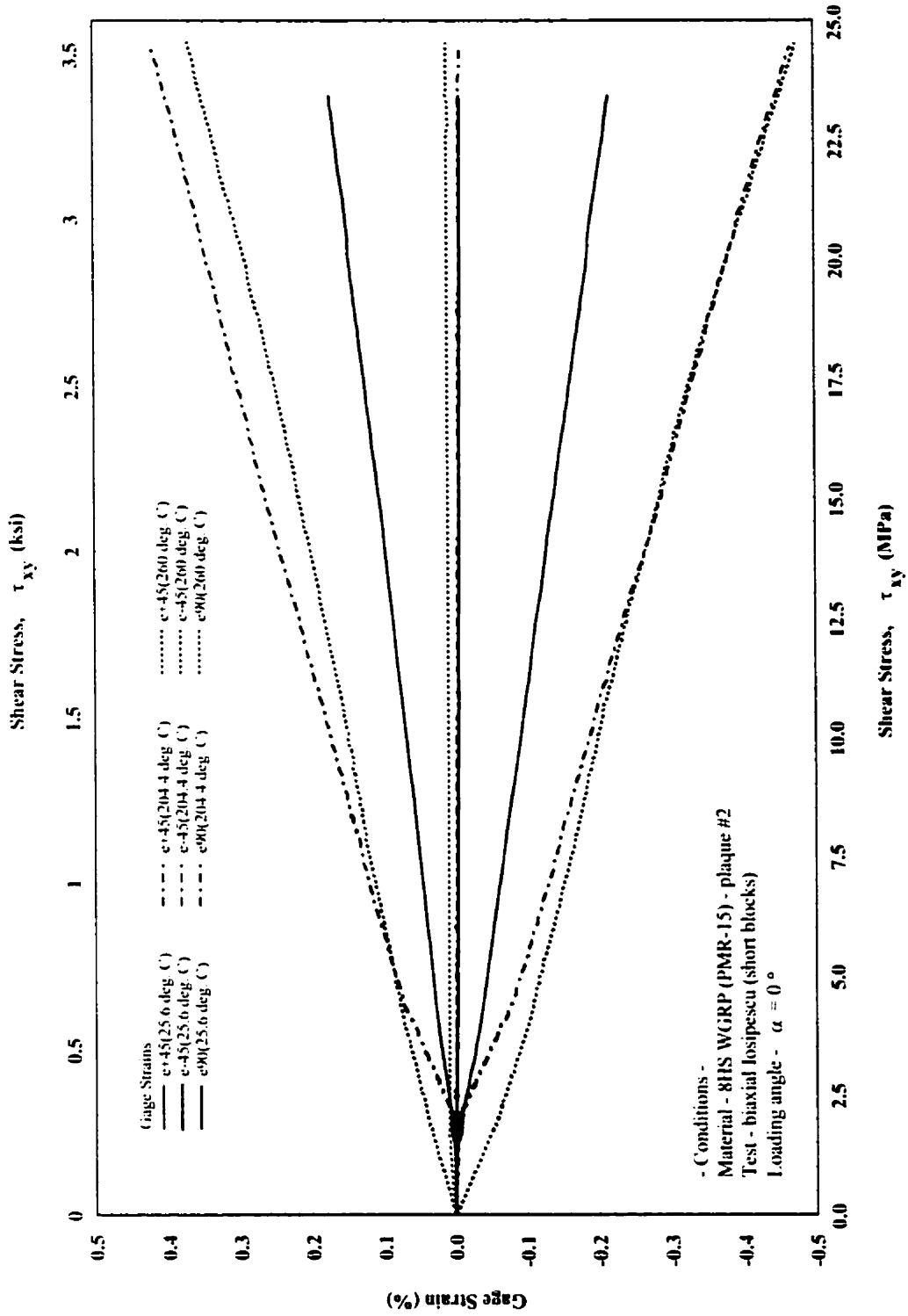


Figure 4.26. Representation of strain-shear stress relationships as a function of temperature for graphite-PMR15 Iosipescu specimens from plaque #2.

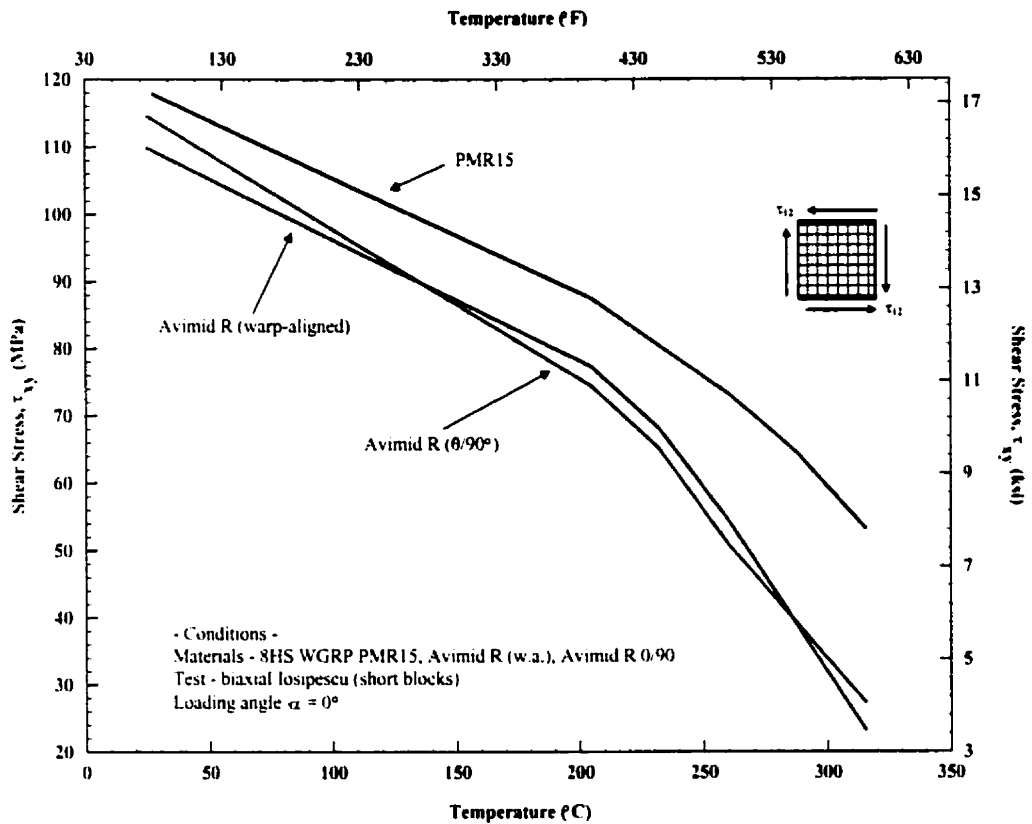


Figure 4.27(a). Trends in the average shear stresses at the onset of failure.

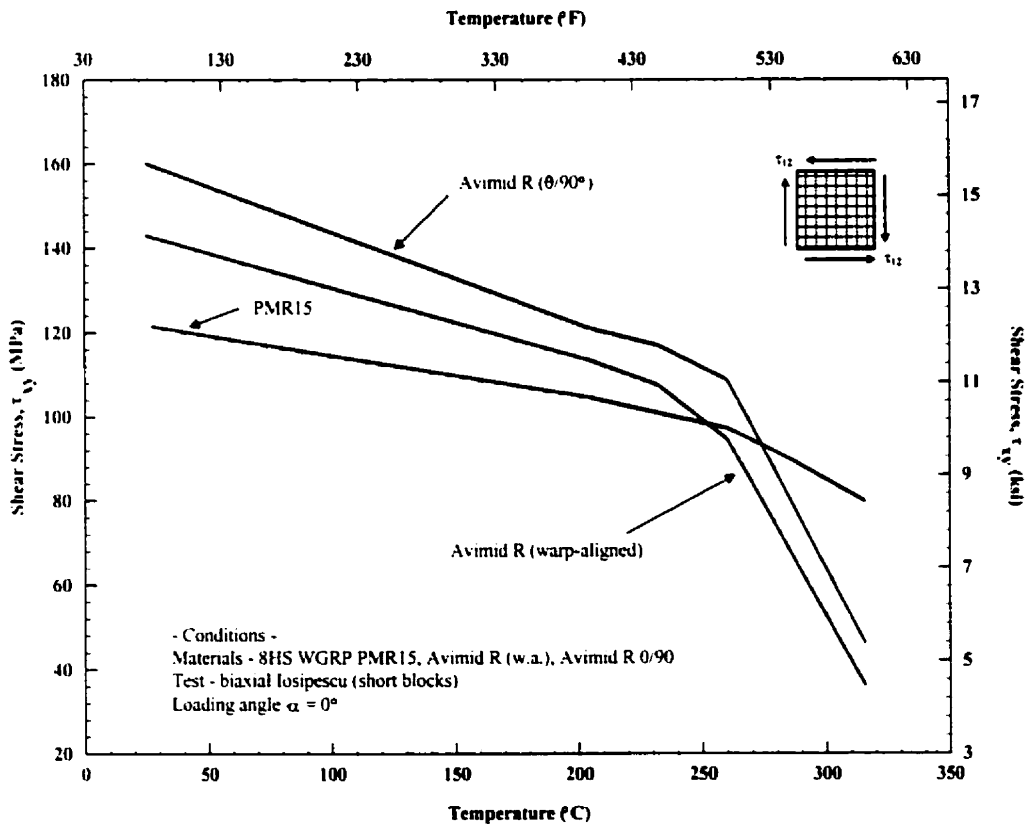


Figure 4.27(b). Trends in the average shear stresses at their maximums.

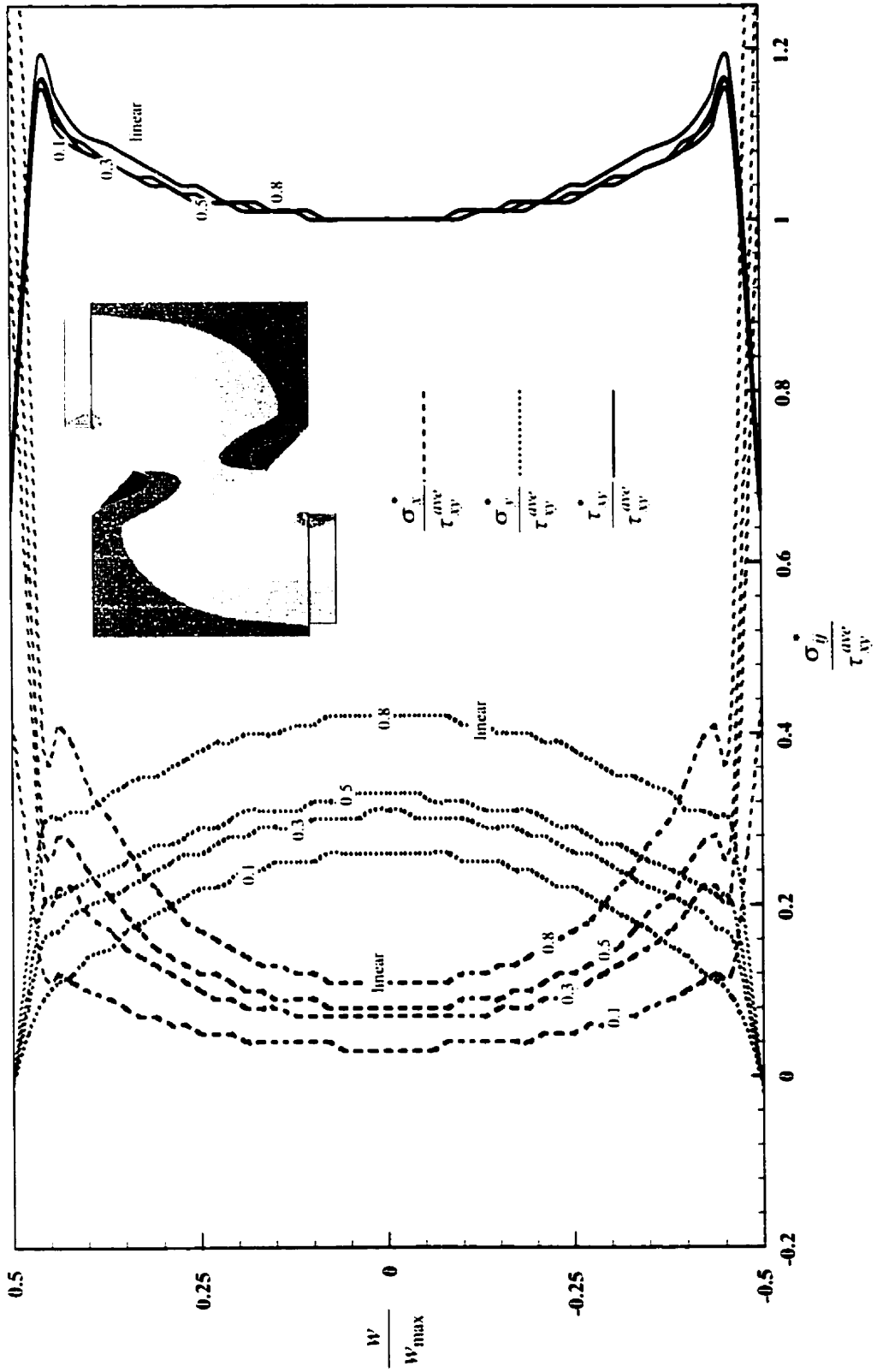


Figure 4.28. Shear and normal stress distributions along the notch root axis of the biaxial Iosipescu model.

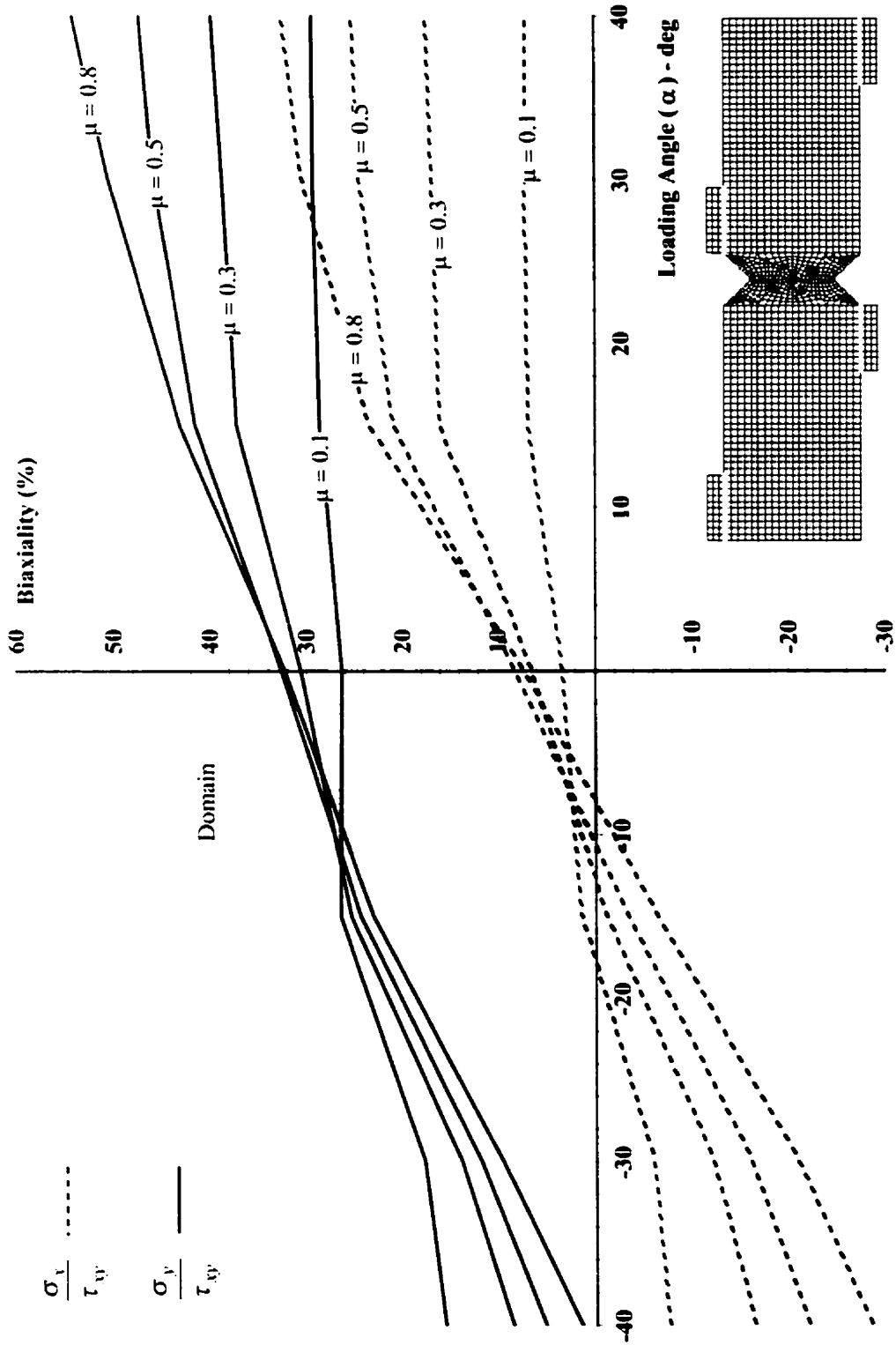


Figure 4.29. Biaxial stress ratios from the biaxial Iosipescu model for various loading angles.

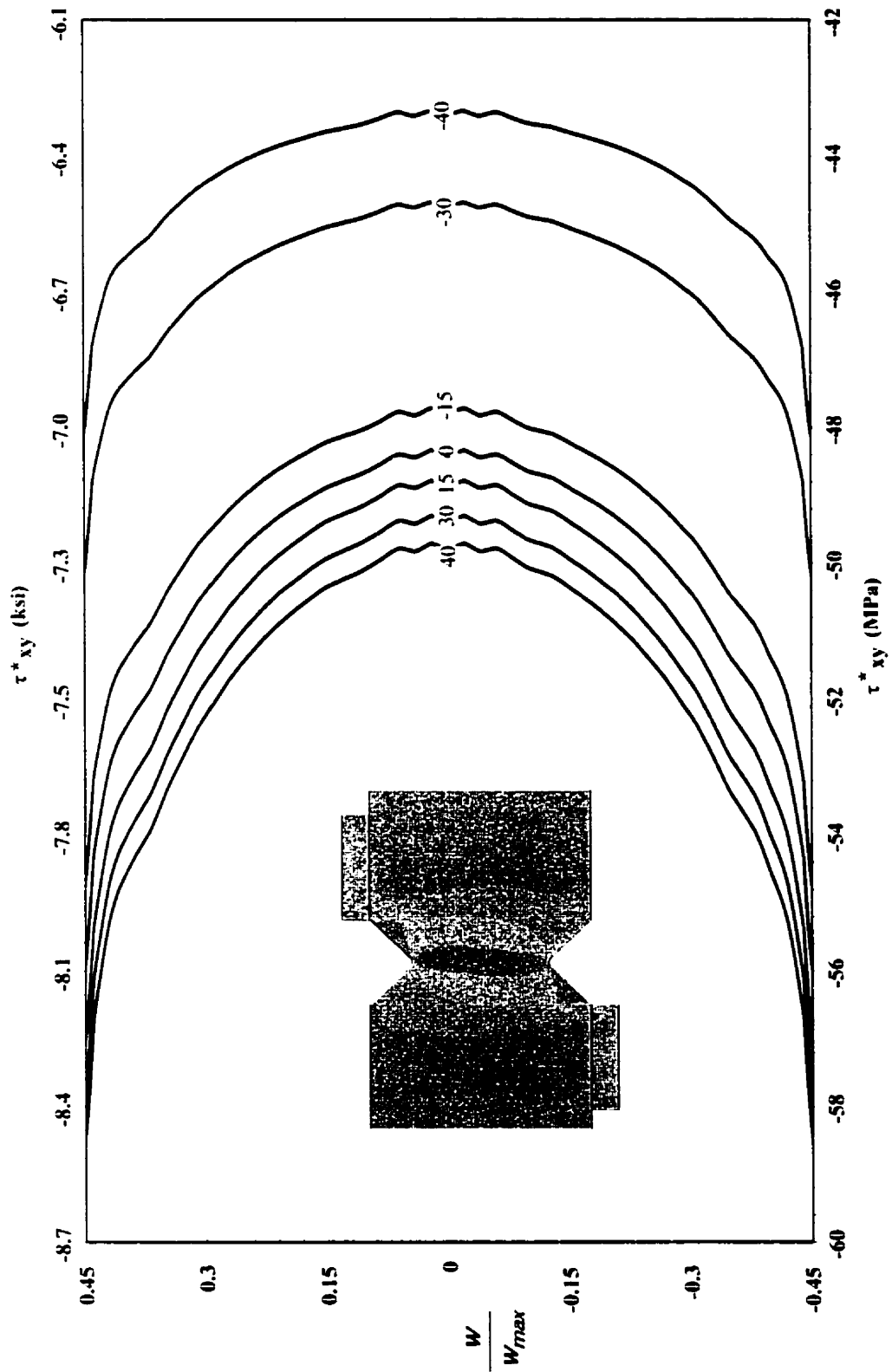


Figure 4.30. Shear stress distributions along the notch root axis of the biaxial Iosipescu model for ($\mu = 0.3$).

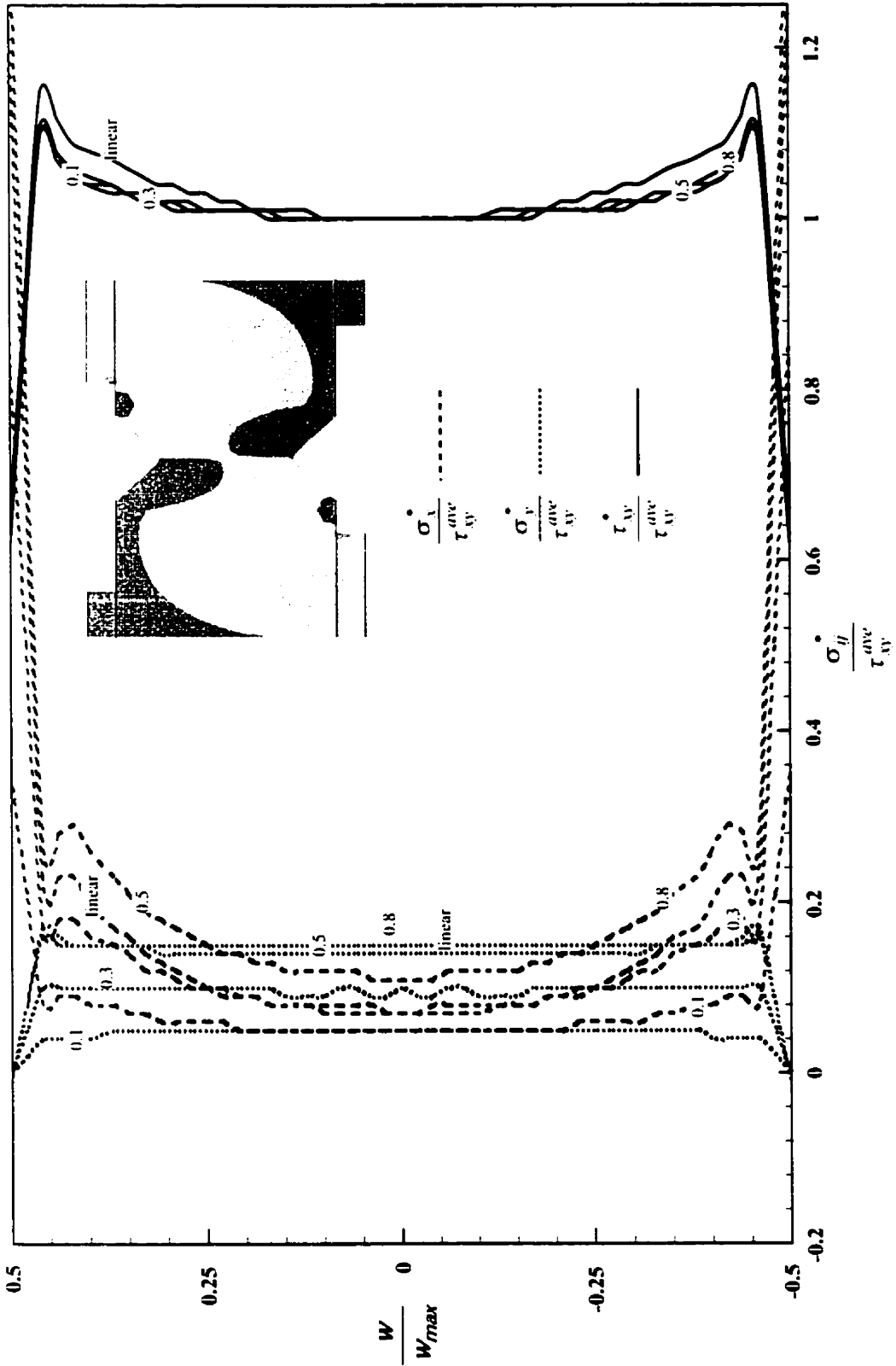


Figure 4.31. Shear and normal stress distributions along the notch root axis of the modified biaxial Iosipescu model.

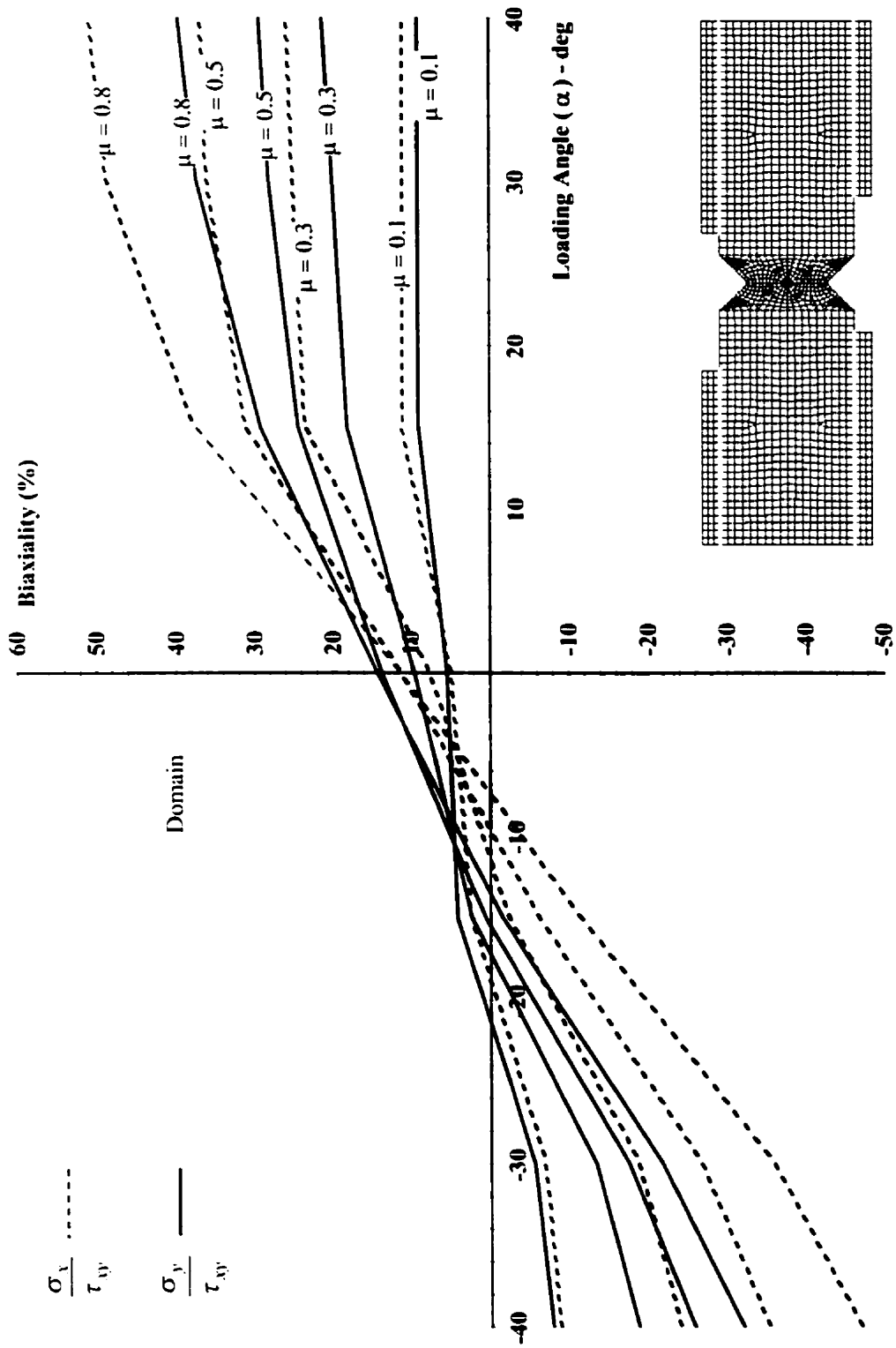


Figure 4.32. Biaxial stress ratios from the modified biaxial Iosipescu model for various loading angles.

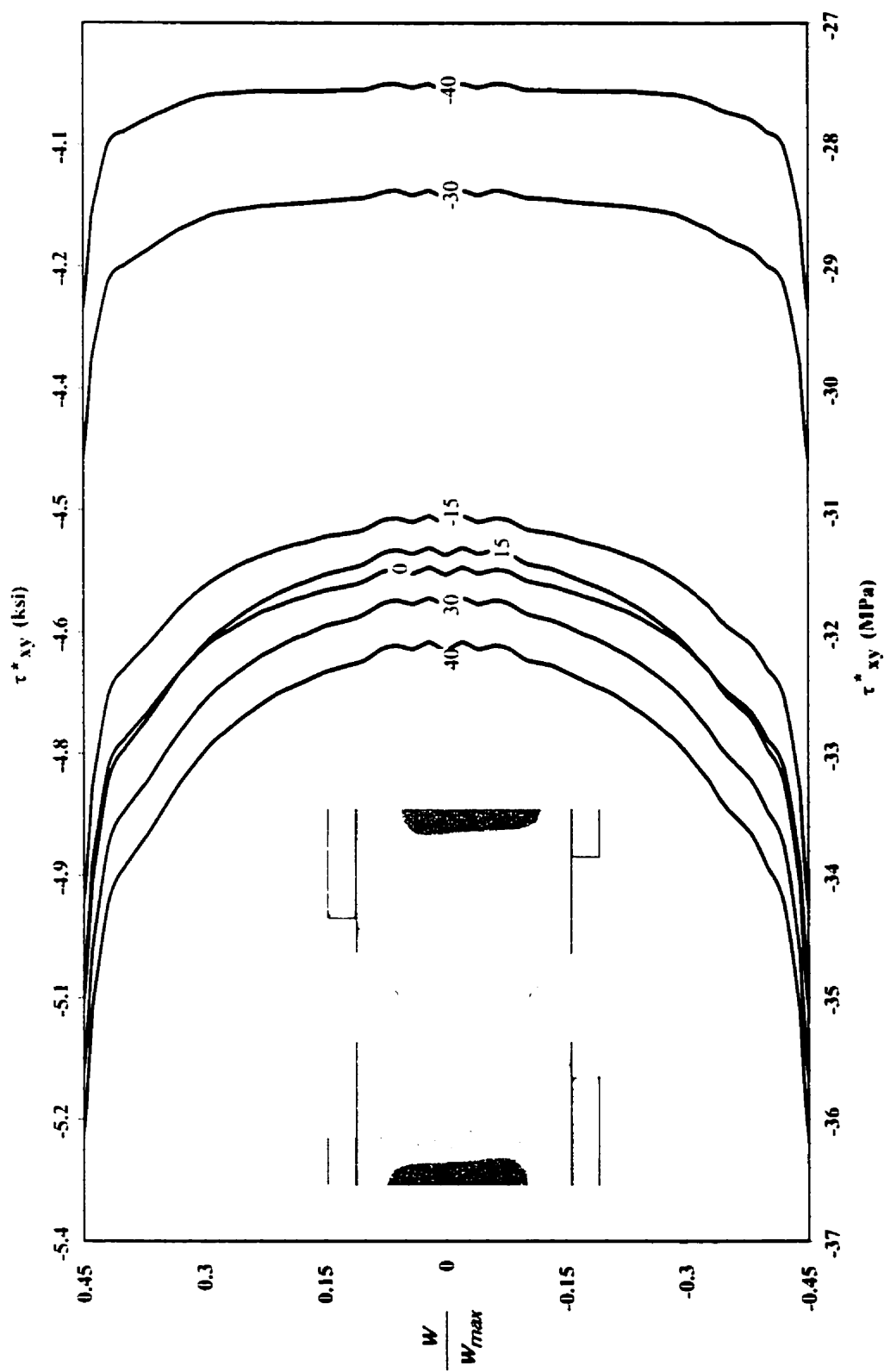


Figure 4.33. Shear stress distributions along the notch root axis of the modified Iosipescu model for ($\mu = 0.3$).

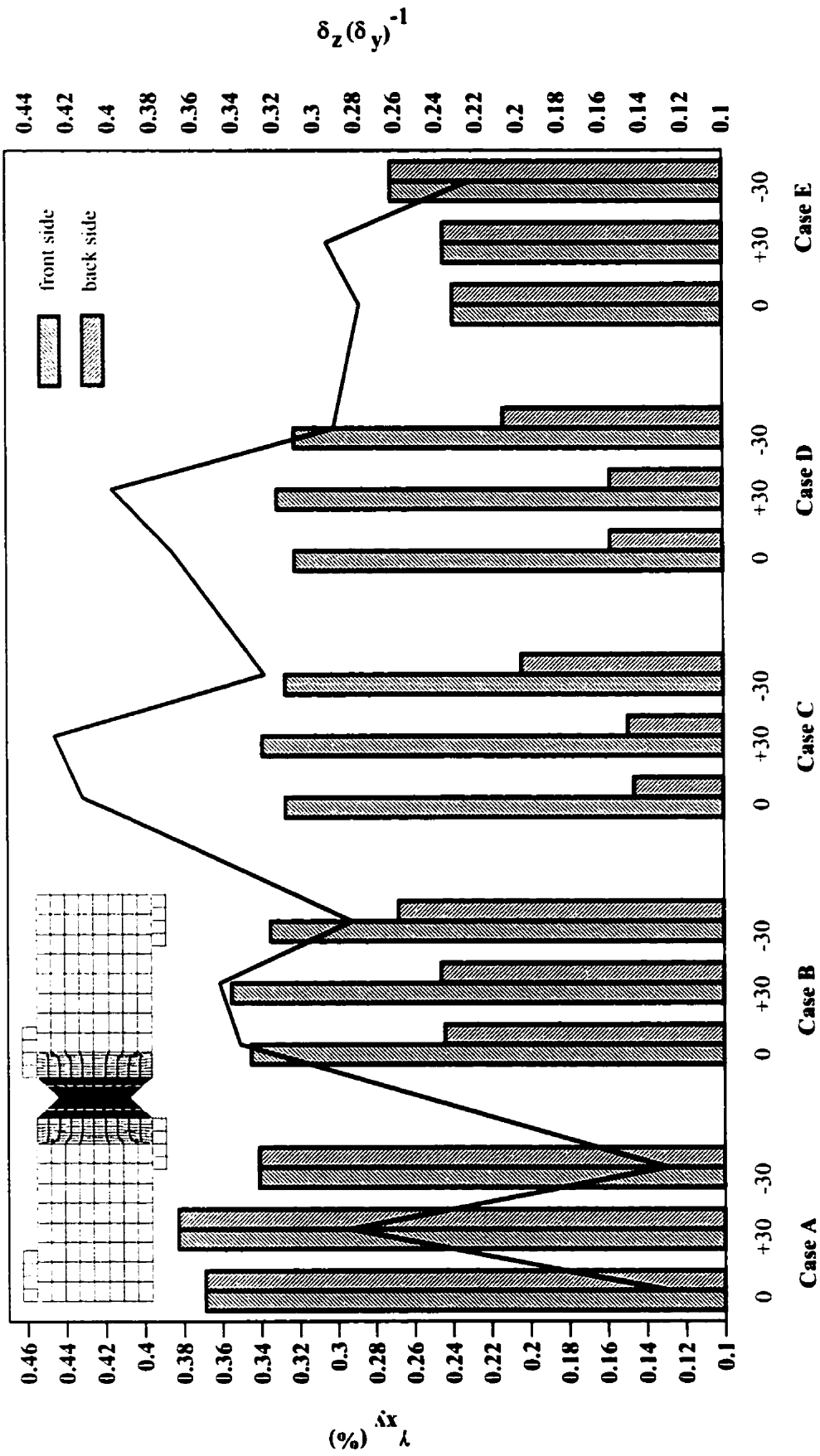


Figure 4.34. Integrated surface strains and lateral displacements of each load angle and eccentric case considered for the biaxial Iosipescu analyses.

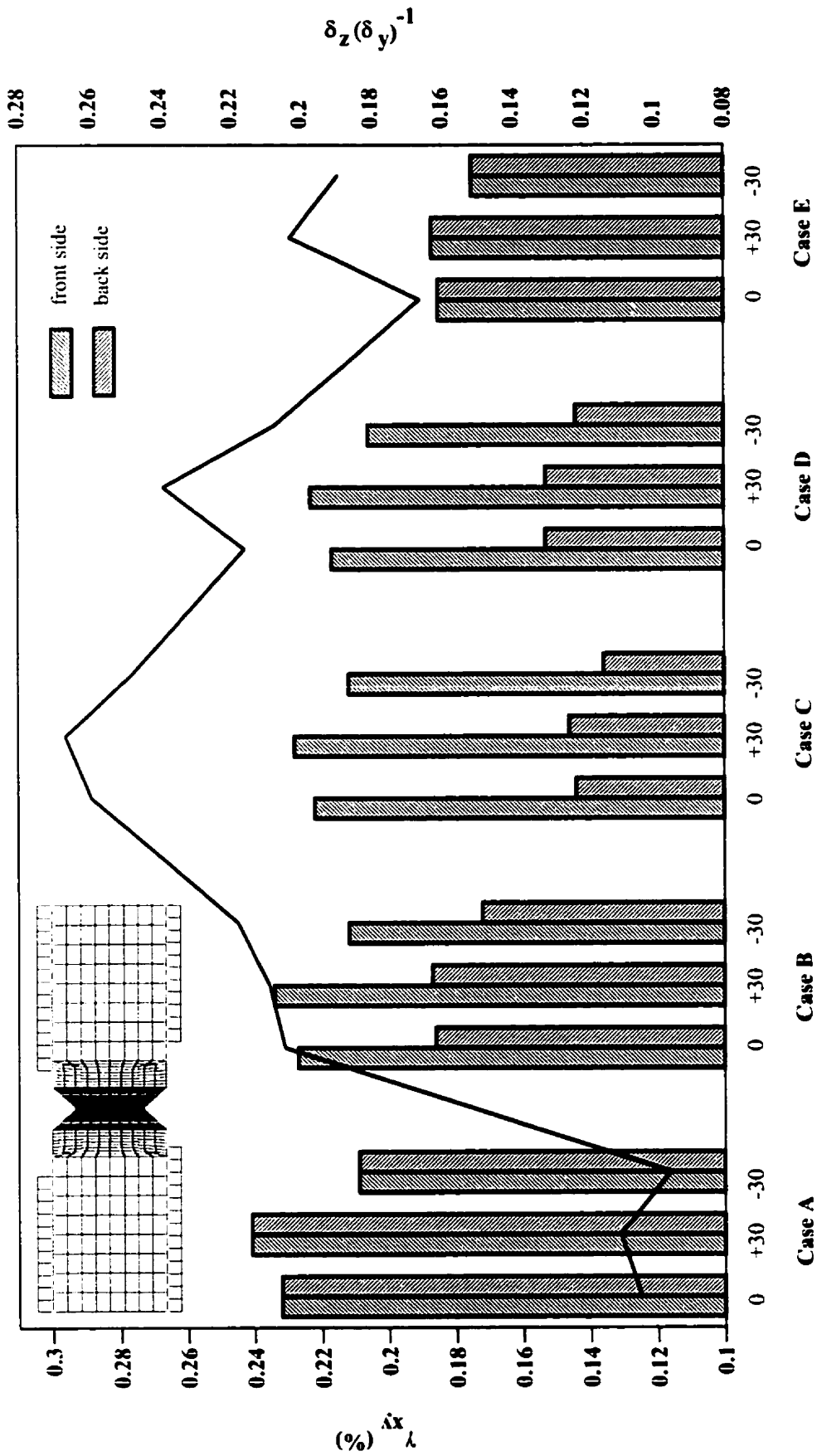


Figure 4.35. Integrated surface strains and lateral displacements of each load angle and eccentric case considered for the modified biaxial Iosipescu analyses.

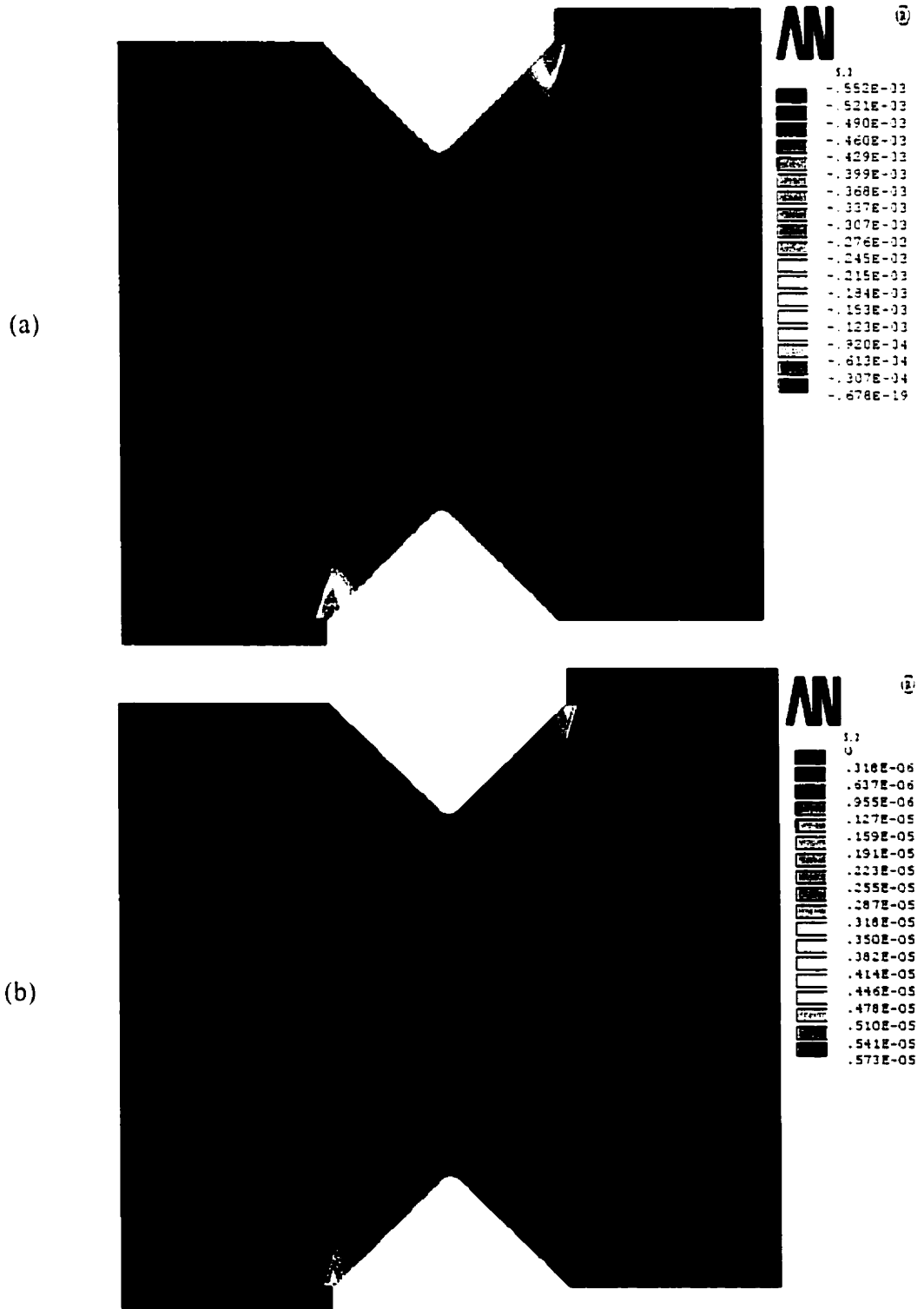


Figure 4.36. Plastic strain contours from biaxial Iosipescu analysis at an applied shear stress of 19.6 MPa (2.8 ksi), (a) γ_{xy}^{pl} , and (b) ϵ_{zz}^{pl} .

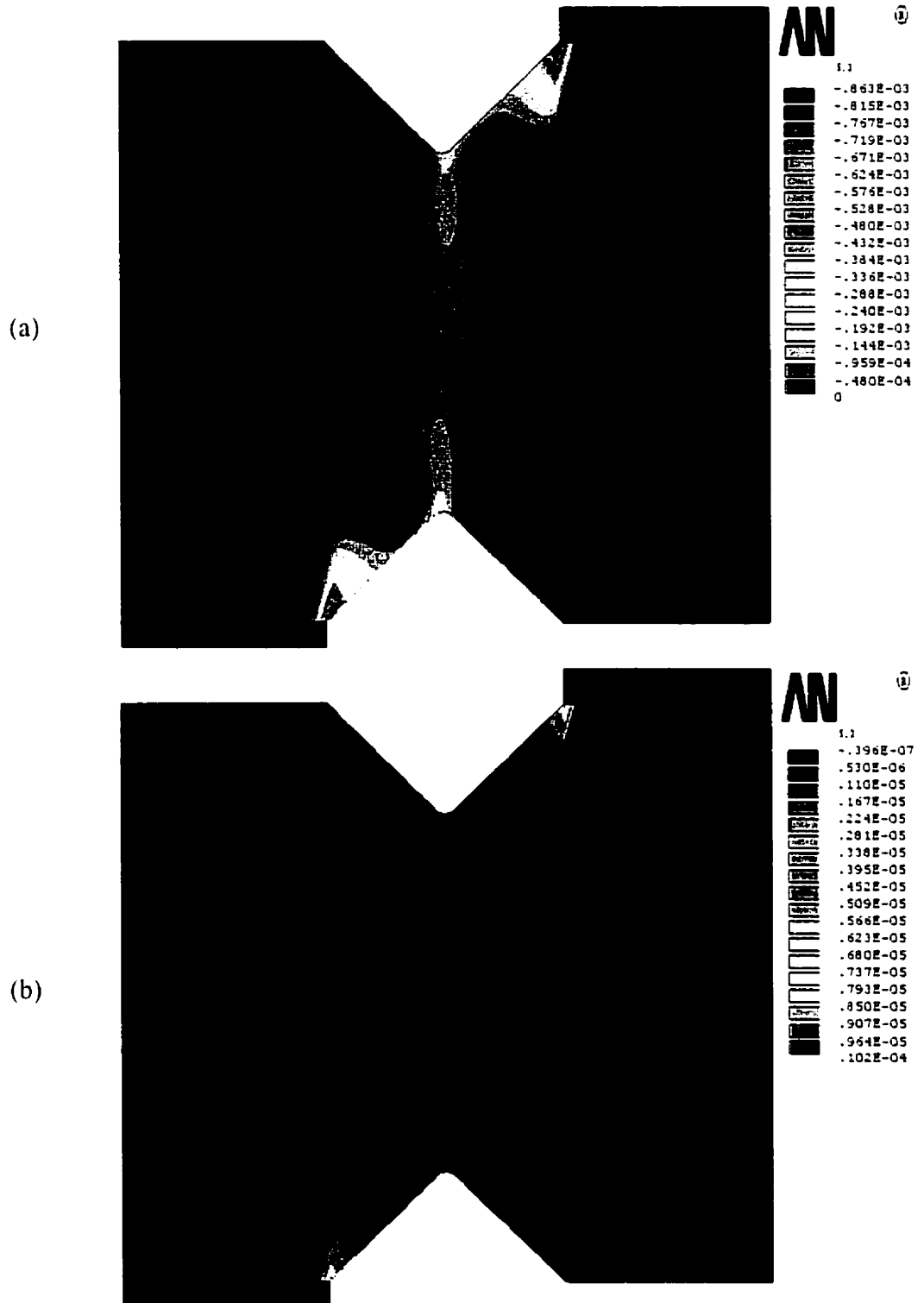


Figure 4.37. Plastic strain contours from biaxial Iosipescu analysis at an applied shear stress of 25.8 MPa (3.7 ksi), (a) γ_{xy}^{pl} , and (b) ϵ_{zz}^{pl} .

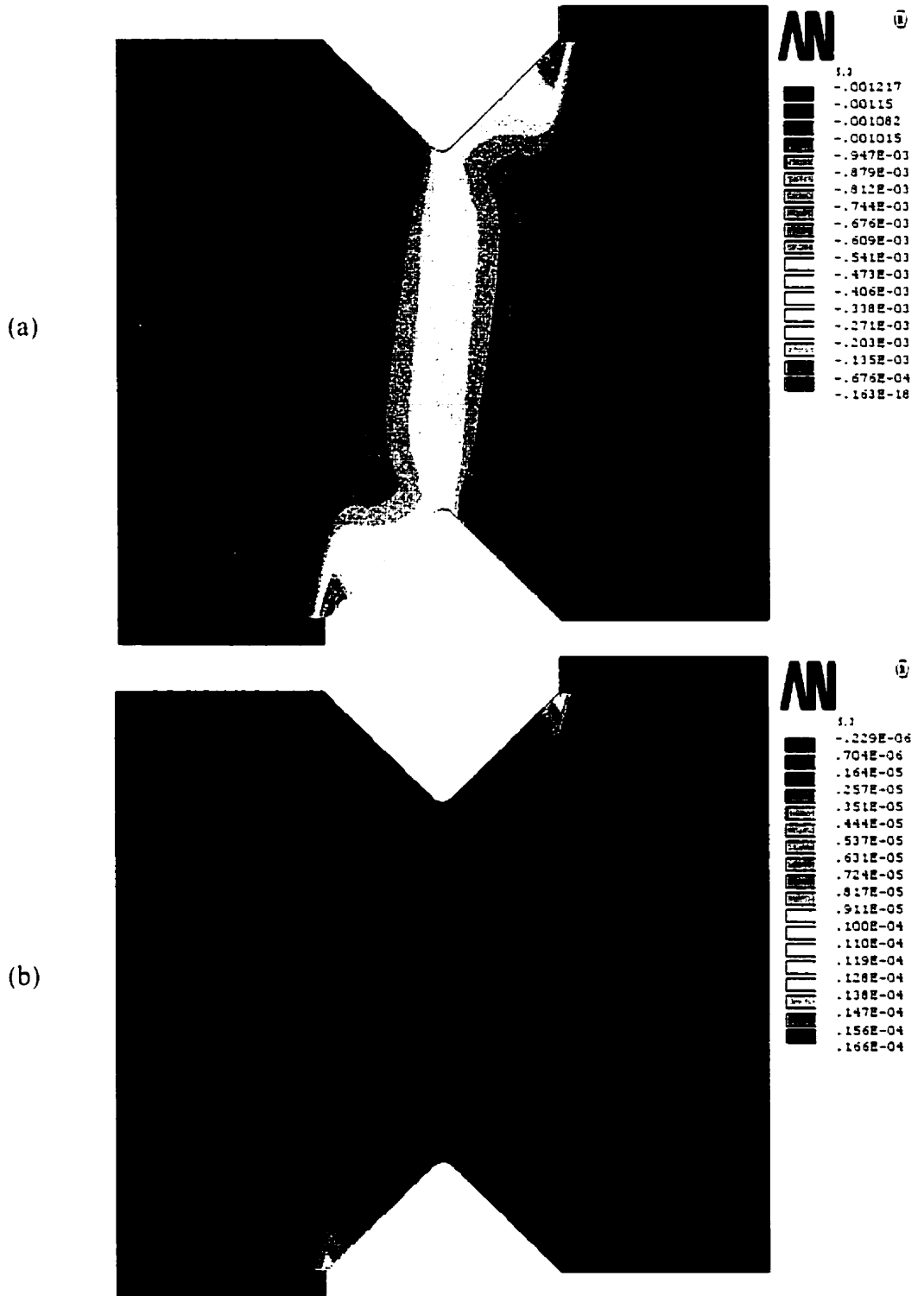


Figure 4.38. Plastic strain contours from biaxial Iosipescu analysis at an applied shear stress of 31.9 MPa (4.6 ksi), (a) γ_{xy}^{pl} , and (b) ϵ_{zz}^{pl} .



Figure 4.39. Plastic strain contours from biaxial Iosipescu analysis at an applied shear stress of 61.4 MPa (8.9 ksi), (a) γ_{xy}^{pl} , and (b) ϵ_{zz}^{pl} .



Figure 4.40. Plastic strain contours from biaxial Iosipescu analysis at an applied shear stress of 90.7 MPa (13.2 ksi), (a) γ_{xy}^{pl} , and (b) ϵ_{zz}^{pl} .

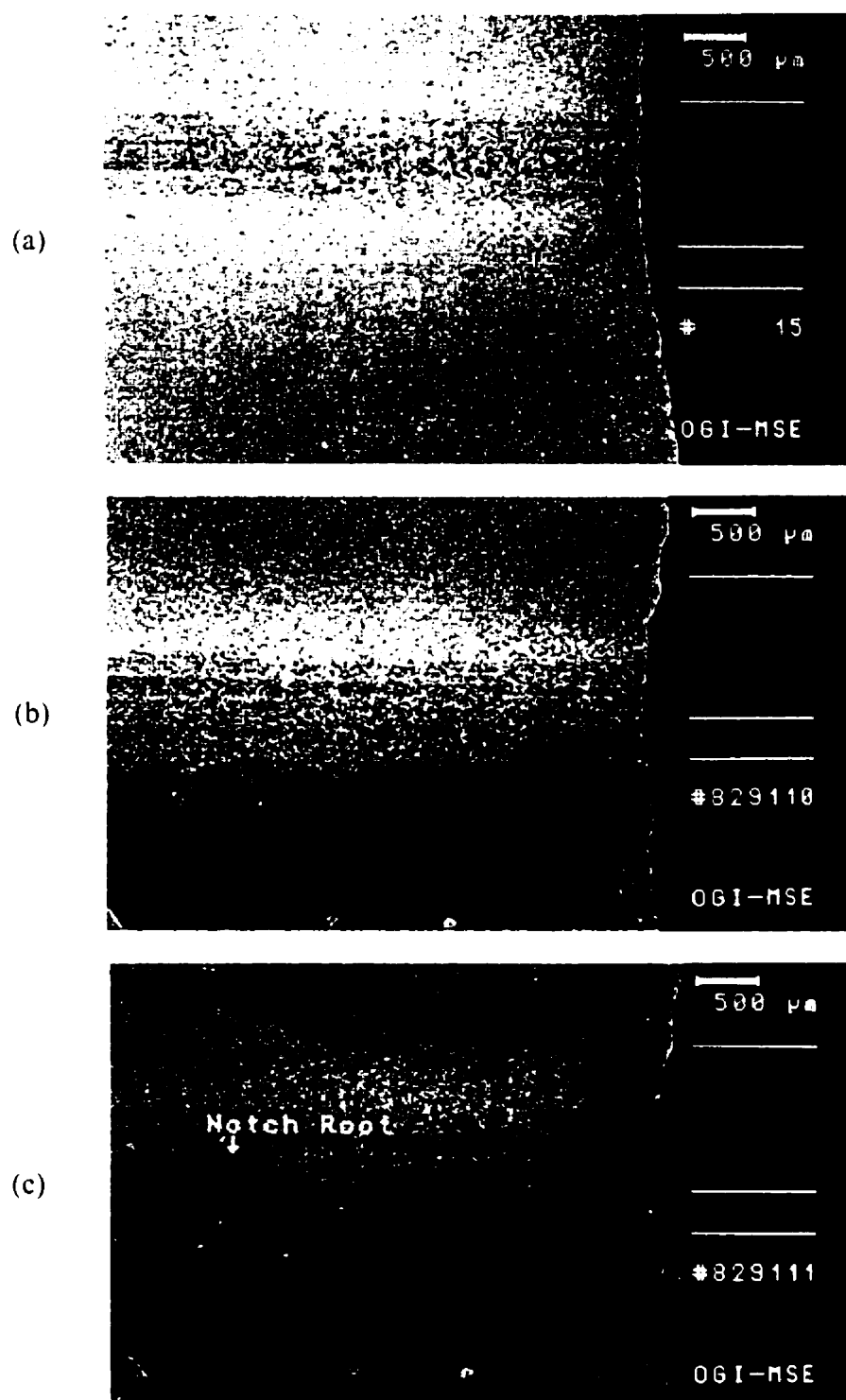


Figure 4.41. Progression of failure along notch root of Iosipescu specimens subjected to applied shear stresses of (a) 23.1 MPa (3.4 ksi), (b) 46.1 MPa (6.7 ksi) and (c) 69.2 MPa (10.1 ksi).

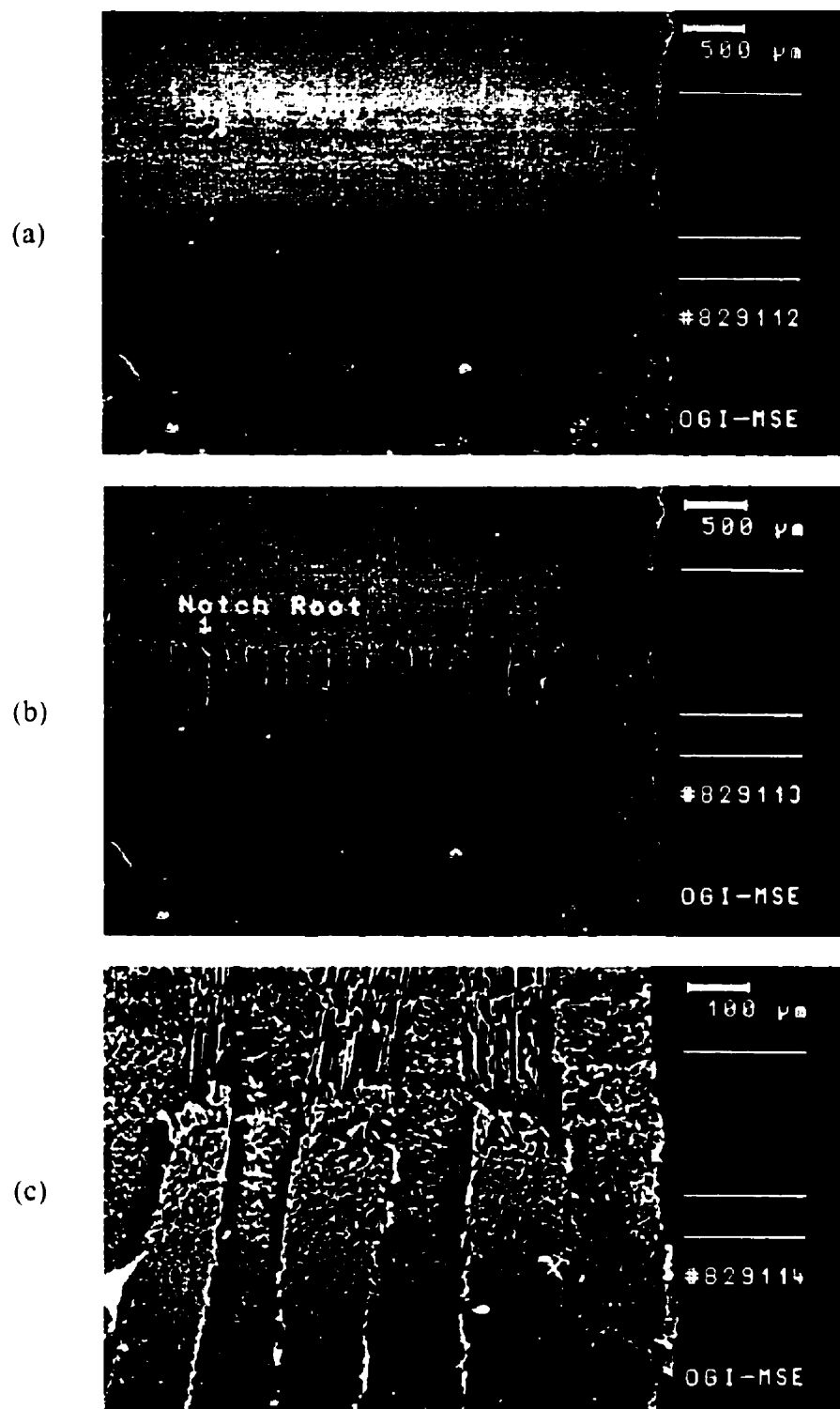
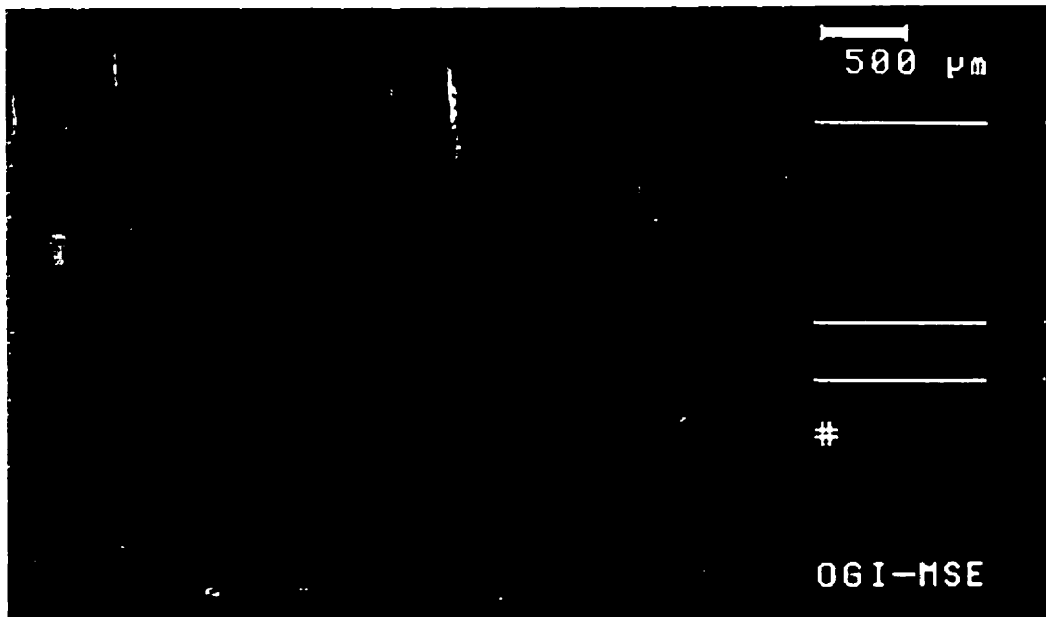
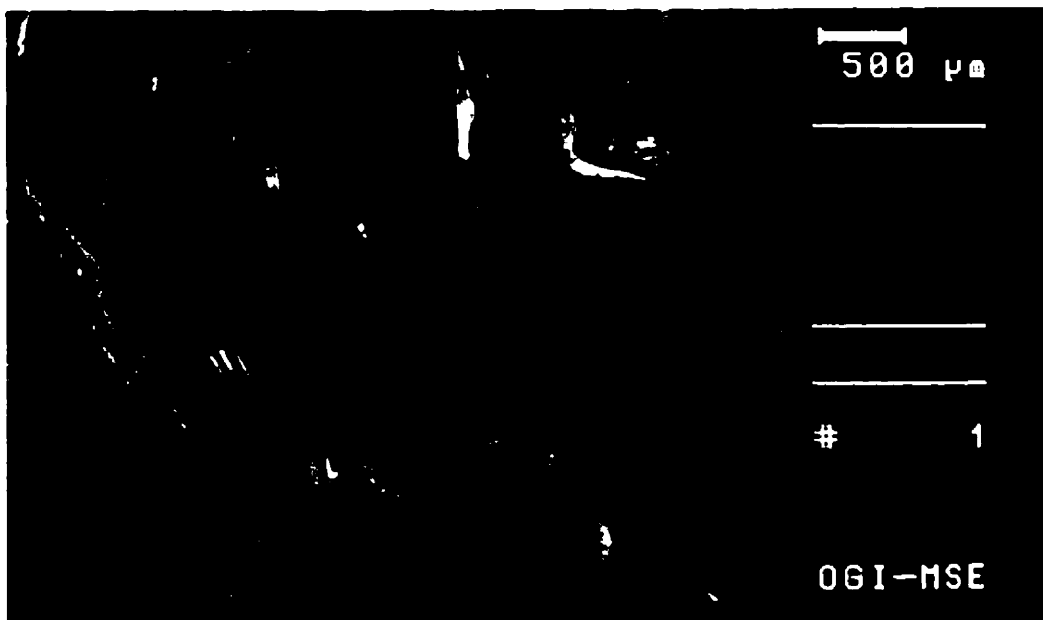


Figure 4.42. Progression of failure along notch root of Iosipescu specimens subjected to applied shear stresses of (a) 92.3 MPa (13.4 ksi), (b) 111.5 MPa (16.2 ksi) and (c) 111.5 MPa (16.2 ksi) at higher magnification.



(a)



(b)

Figure 4.43. Onset of failure (a) and catastrophic failure (b) with out-of-plane deformation (bulging) along the notch root of Iosipescu specimens subjected to shear at a loading angle $\alpha = 0^\circ$.

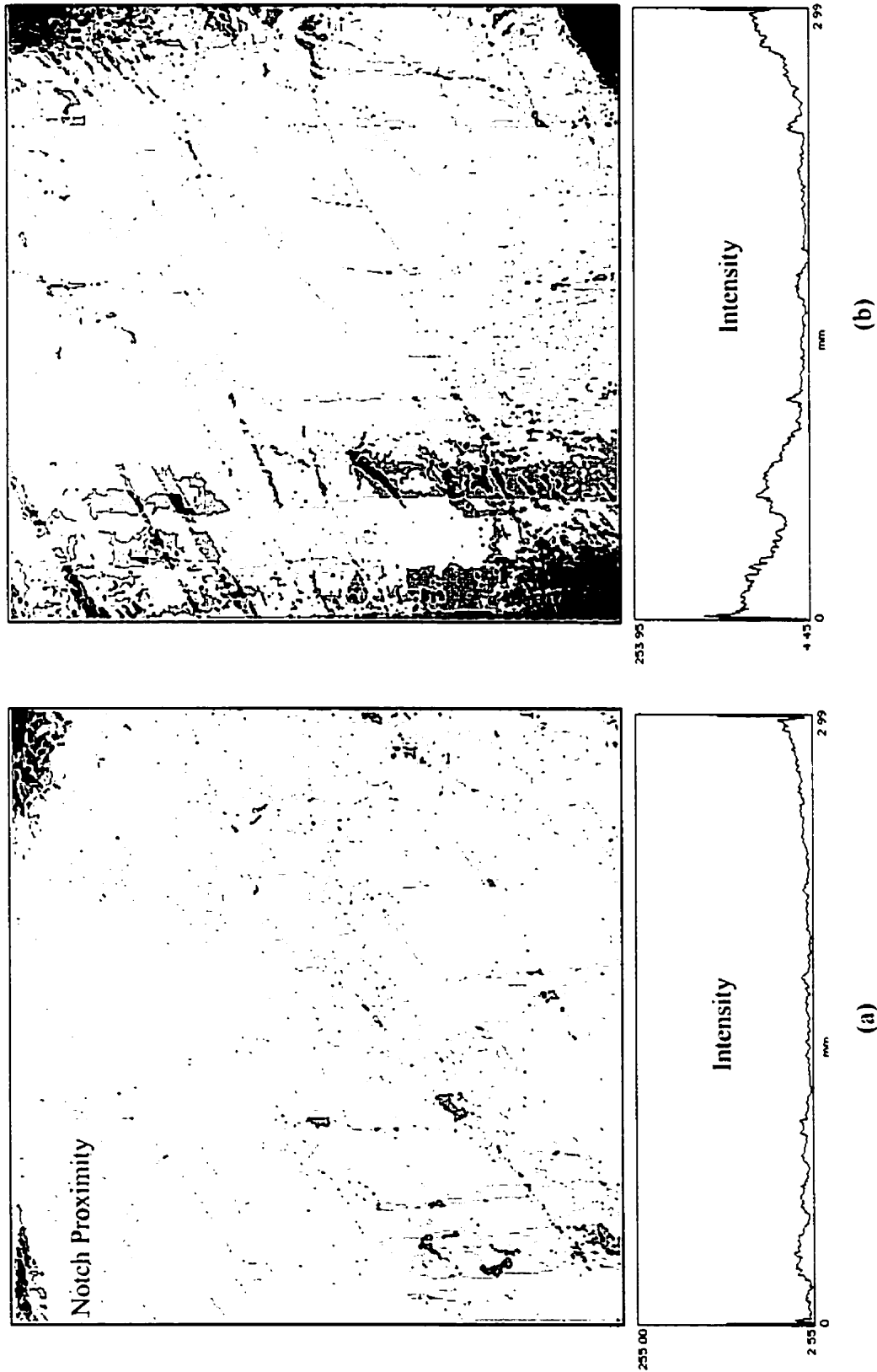


Figure 4.44. Two-dimensional damage serial reconstruction of shear tested (a) notch and (b) center sample targets.

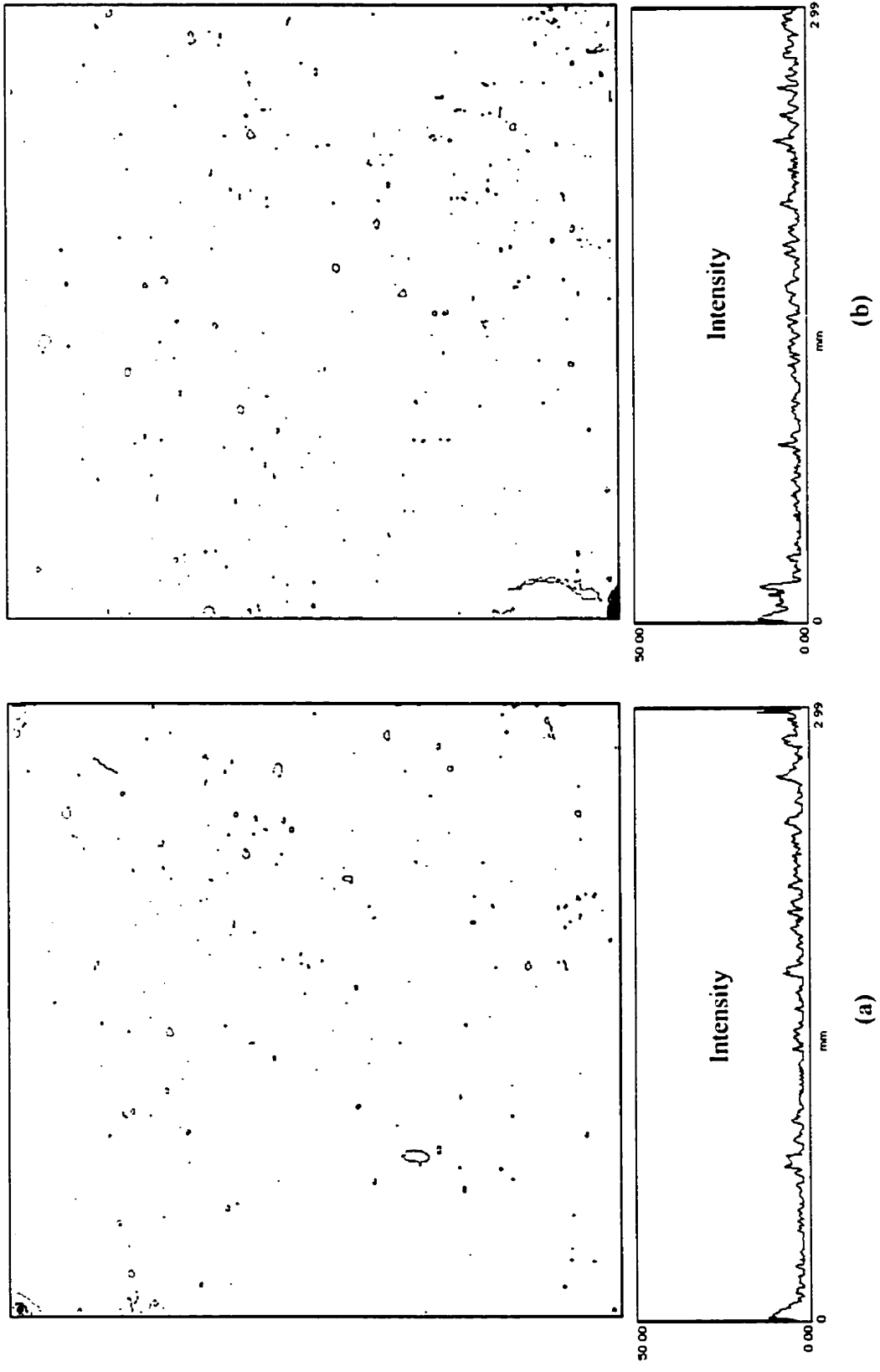


Figure 4.45. Two-dimensional damage serial reconstruction of untested (a) notch and (b) center sample targets.

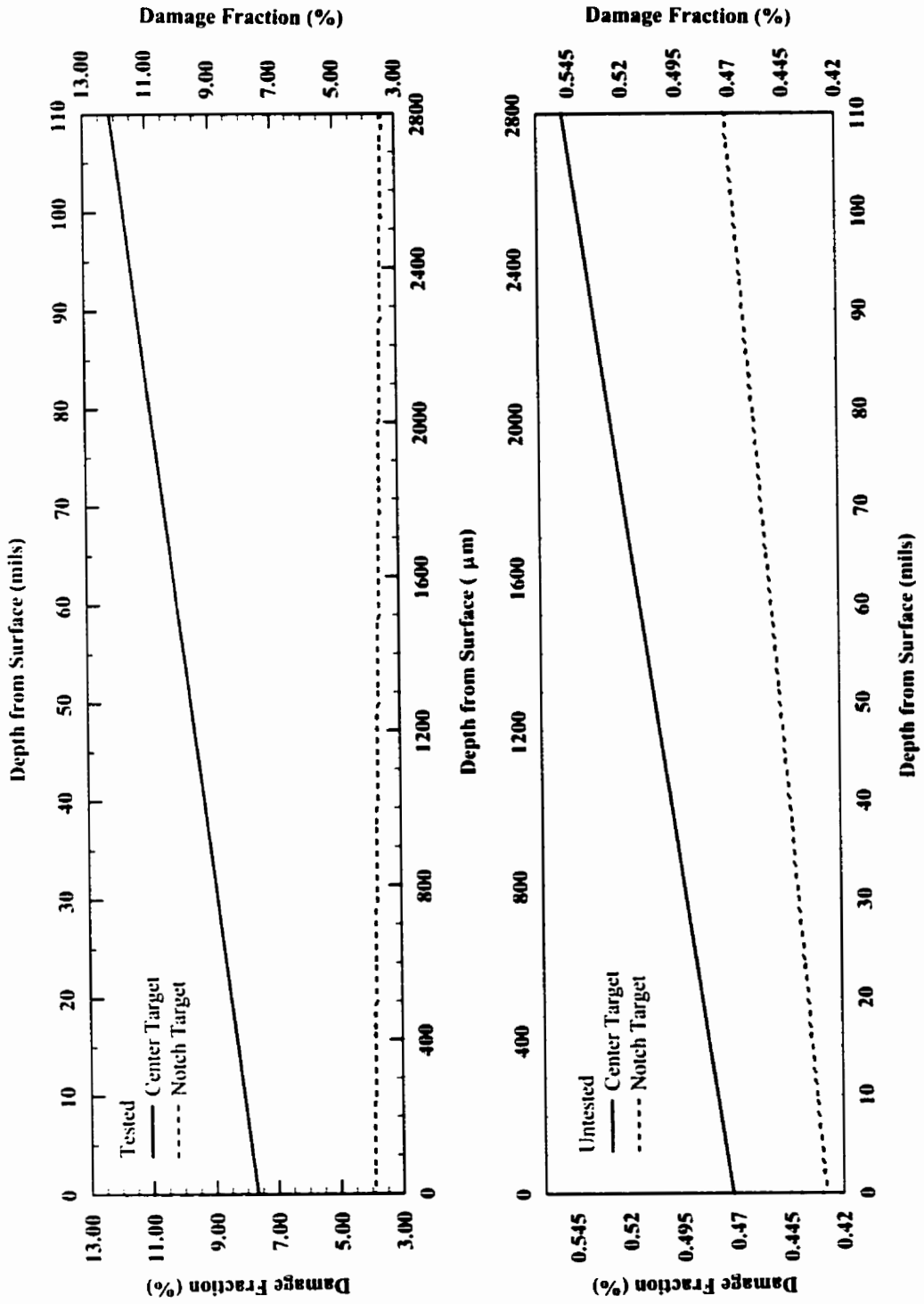


Figure 4.46. Sample center and notch target damage fractions from tested and untested Iosipescu specimens.

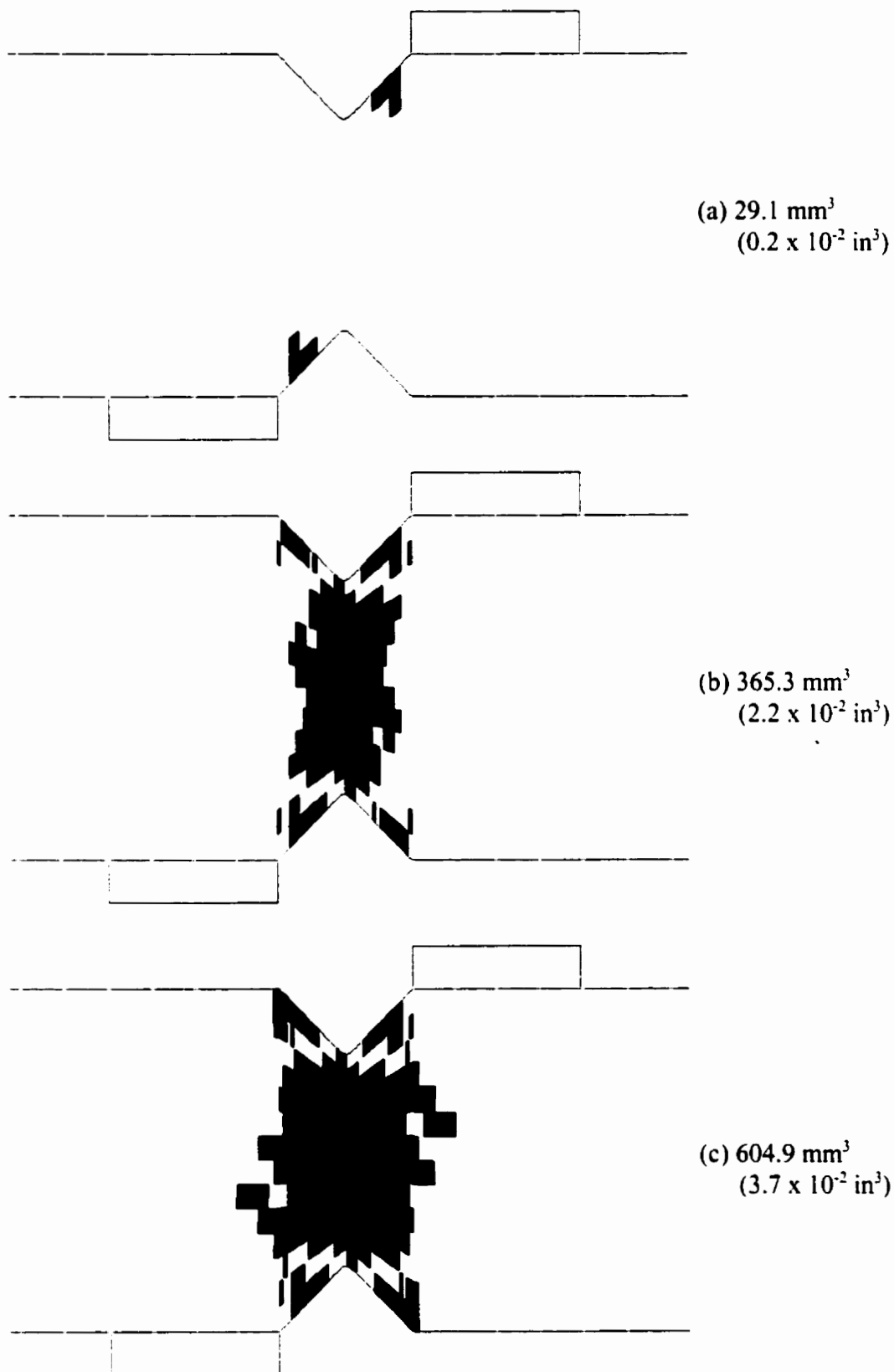


Figure 4.47. Prediction of the progression of damage in woven fabric composite biaxial Iosipescu specimens at shear strains γ_{xy} of (a) 0.38%, (b) 0.75%, and (c) 1.13%.

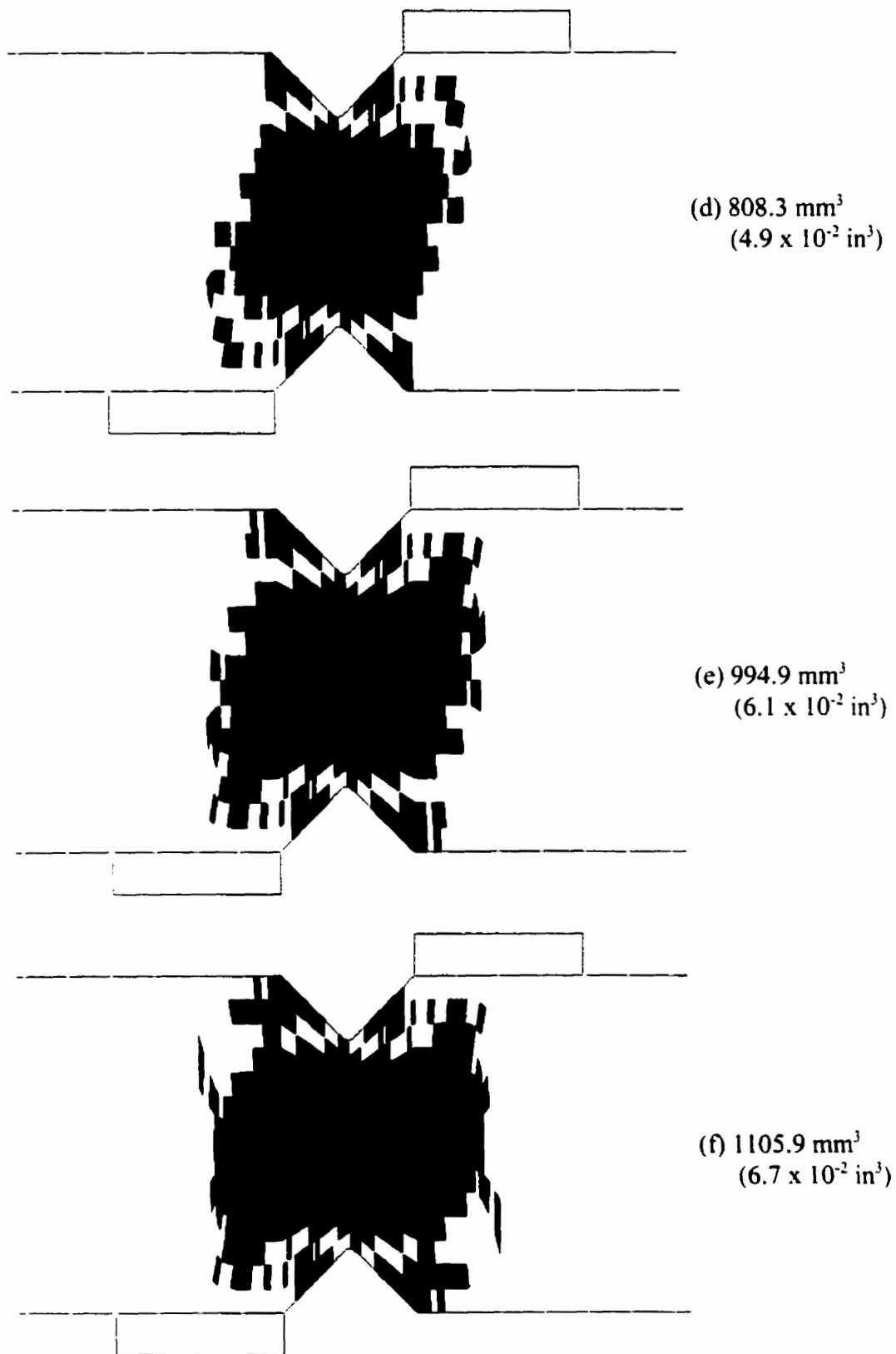


Figure 4.48. Prediction of the progression of damage in woven fabric composite biaxial Iosipescu specimens at shear strains γ_{xy} of (d) 1.50%, (e) 1.88%, and (f) 2.25%.

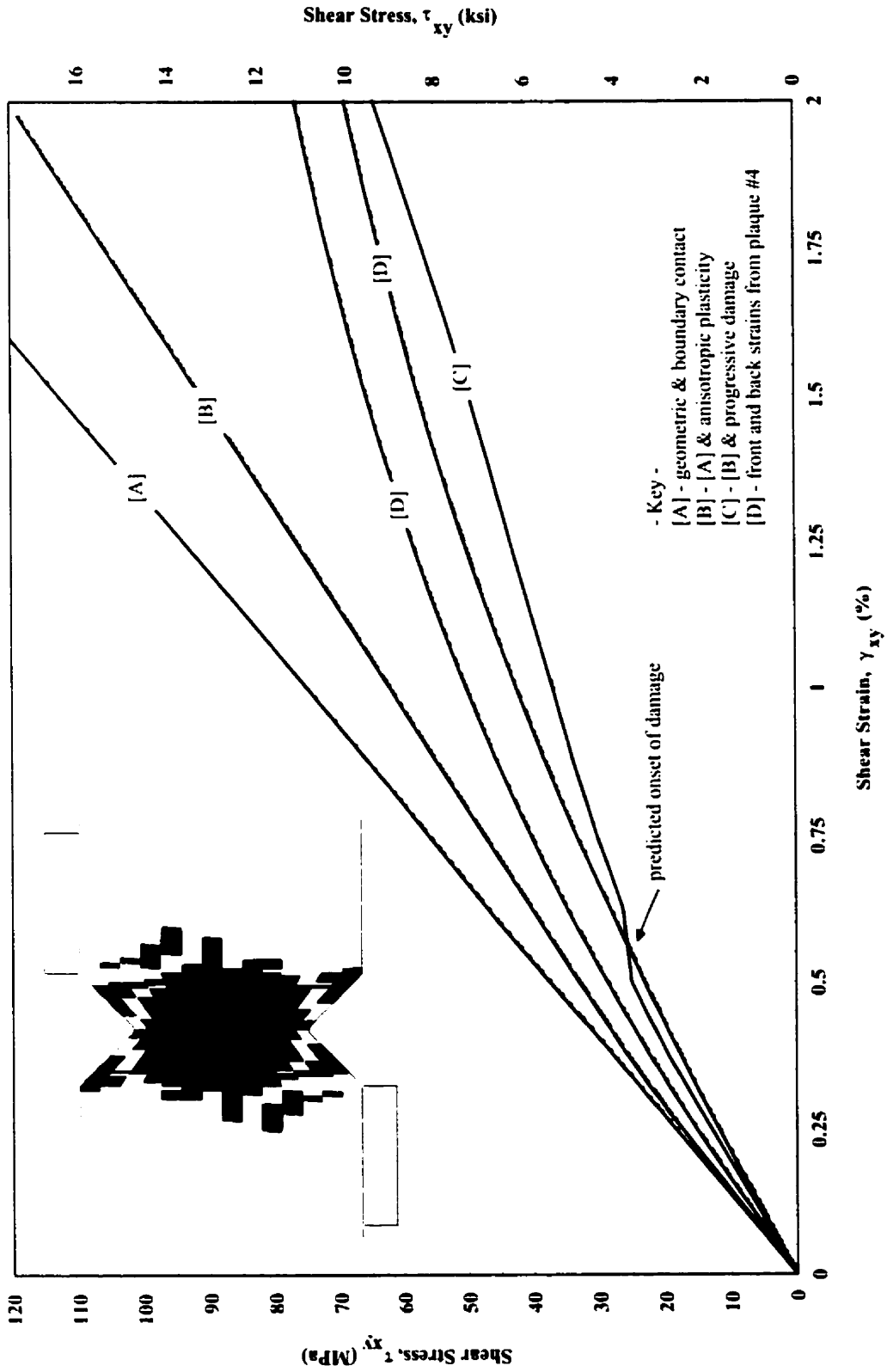


Figure 4.49. Influence of structural nonlinearities, anisotropic plasticity and progressive damage on the shear stress-strain response of the biaxial Iosipescu model as compared to experiments (plaque #4).

5

CONCLUSIONS

In Section 3 of this thesis, a simplified mechanics model was proposed to predict the elastic constants of 8HS woven fabric composites. The model was based on the use of cubic spline and polynomial functions obtained from the fitting of data points which represented the centerline and perimeter of woven tows. The constants predicted by the model were checked against experimental data and numerical strain energy methods. Also in Section 3, the in-plane and transverse normal stress distributions, within three arbitrary cutting planes of the woven 8HS IVE, were found by interpolation of sparse data using punctual kriging. The stress distributions were compared for uniaxial tension, uniaxial compression and in-plane shear loading conditions.

In Section 4 of this thesis, the apparent elastic properties of woven graphite-PMR15 and woven graphite-Avimid R composites were determined using the Iosipescu shear, standard tension and off-axis tension test methods. The apparent biaxial shear strength properties were also evaluated at room and elevated temperature conditions. Influence of specimen-to-fixture interactions on stress and strain distributions in the Iosipescu specimens were studied numerically in terms of load eccentricities and structural nonlinearities. Also in Section 4, anisotropic plasticity and progressive damage were considered in evaluating the nonlinear shear stress-strain behavior. An effort was made to compare the numerical plasticity and progressive damage results with actual damage in the Iosipescu specimens obtained by reconstruction of cross-sections assembled in series. Based on the results presented in Section 3 and in Section 4, several conclusions may be drawn:

1. A simplified micro-to-mesoscale analytical model has been presented for evaluating the elastic behavior of 8HS woven fabric composites. The model assumes that

random variation in geometries of the tow cross-sections and undulations can be adequately described by cubic splines and fitted m^{th} -order polynomials. The model also assumes that warp/fill tows can be considered UD composite materials and the 8HS woven lamina considered as a 2-layered laminate. Results for n -layered composite laminate properties show good agreement with experimentally obtained apparent elastic properties for the range of constituent properties studied. In comparison, the model suggests that the composite plaque constituent properties lie between those given for the F-b^(H) and F-c^(H) systems.

2. Evaluation of lamina compliances using the SMM model suggests a range of extension and extension-bending coupling constants for the composites considered. According to the model results, the limiting cases are shown to exist at local, off-axis undulation angles of 0° and 16° approximately. It seems that these angles are practical lower and upper bounds for UD and plain weave composite materials, respectively.
3. A 3-D finite element model was also presented to verify the predictions from the mechanics model. The idealized volume element simplified the 8HS representative volume element to facilitate appropriate use of prescribed displacement boundary conditions. The model used the measured tow aspect ratio and volume fraction arrived at through numerical iteration. Elastic properties were calculated from force equivalence and strain energy methods. The results compare favorably with both the analytical model and the experiments. It is suggested that the tow fiber volume fraction is more appropriate when the 8HS woven fabric lamina is evaluated in the manner presented and compared with apparent elastic properties.
4. Off-axis composite elastic behavior was evaluated through the use of the familiar equations of transformation. Structure-performance maps were introduced for several of the composite systems considered to show relationships between off-axis behavior and constituent properties. Comparison between the predicted and experimental off-

axis properties was favorable, but more importantly, the maps appear to serve as a possible guide for constituent composite material selection.

5. A method has been proposed to model the through-thickness stress distributions in woven fabric composites subjected to uniaxial tension, compression and in-plane shear. Three reference cutting planes were arbitrarily chosen within a 3-D finite element model of an 8HS woven idealized volume element (IVE) and stresses were extrapolated from the nodes to a sparse grid. The stress data from the sparse grid was interpolated to a very fine grid using punctual kriging. From the interpolated grid, the stress distributions of interest were determined to identify where the largest stress concentrations would be found within the 8HS IVE.
6. In uniaxial tension and compression, the largest concentrations of in-plane tensile and compressive stresses were found to occur in transverse tows of the bridging regions. In shear, the largest concentrations of in-plane shear and transverse normal stresses were found to occur in the undulated transverse tow. The normal stress from in-plane shear loading was far more significant than the normal stresses from the other load cases.
7. The finite element model proposed for the 8HS IVE cannot be used with absolute certainty to predict failure initiation, because it does not realistically consider structural and material nonlinearities. Also, the lenticular tow cross-sectional shapes terminate as edges with sharp corners which inevitably causes some stress magnification. If reasonable failure stresses are assumed for the constituent materials, then failures can be roughly approximated using the stress distributions in combination with a maximum stress failure approach.
8. The application of the biaxial Iosipescu technique has been successful in determining the biaxial shear dominated failure properties of woven graphite-polyimide composites at room and elevated temperatures. The biaxial strength properties of the graphite-PMR15 and graphite-Avimid R composites defined by the maximum load are different at room and elevated temperatures.

9. The apparent failure stress of the Avimid R system at room temperature determined from the maximum load is higher than the apparent failure stress of the PMR15 composite. However, the shear strength properties of the graphite-PMR15 composite at elevated temperatures are better than the properties of the Avimid R system.
10. It has been observed in this research that the onset of significant interlaminar damage can be associated with the formation of a knee on the shear stress-displacement diagrams for the Avimid R system. In the case of the PMR15 system, intralaminar damage can be defined by the onset of nonlinearity on the shear stress-strain curves, which typically occurs in the applied stress range of 20.0-40.0 MPa (2.9-5.8 ksi). It appears that development of substantial interlaminar damage in the PMR-15 system tested under biaxial conditions at room temperature occurs at lower shear stresses in comparison with the Avimid R-based composite. At elevated temperatures, the interlaminar damage in the PMR15 composite develops at a much higher level of applied shear stress than in the Avimid R composite.
11. The mechanical properties and failure modes of the PMR15 composite system tested at room temperature are dependent on the manufacturing process. The Iosipescu specimens machined from the thinner plate exhibit lower loads at failure in comparison with the specimens from the slightly thicker plate. It appears that the out-of-plane bulging in the thinner specimens is greater than in the thicker ones. Since the final failure of the specimens is associated with the formation of multiple interlaminar cracks, this might mean that the interlaminar strength properties of the composites also strongly depend on the manufacturing process.
12. The effect of eccentric loads on the mechanical response of woven graphite-polyimide Iosipescu specimens has been studied considering several possible eccentricities with shear dominated loading conditions. The influence of the eccentric loads on the shear strain and stress distributions in the gage section of the specimen has been found to be particularly strong if short loading blocks are used. The largest bending moment, which is responsible for the largest difference in the front to back

shear strains, is observed when the eccentric loading conditions simulate the effect of anti-symmetric specimen twisting. This bending moment can be reduced, but not entirely eliminated, if longer loading blocks are employed.

13. The presence of eccentric loads will also affect the distribution of shear stresses through the specimen thickness within the gage section. Similar to the effect of the eccentric loads on the surface shear strains, their influence on the shear stress gradients has been found to be the most substantial when the specimens were subjected to shear in combination with eccentric twisting.
14. The 2-D finite element computations of the Iosipescu specimens have shown that the specimens loaded in the biaxial Iosipescu fixture in shear develop large compressive stresses at the specimen center. This compression cannot be eliminated by rotating the specimens. For any biaxial loading conditions, the state of stress in the gage section of the specimens is always biaxial with large compressive stresses present along the notch root axis. It has been shown, however, that the compressive stresses generated by the loading blocks can be entirely eliminated if the longer loading block geometry is used in conjunction with specimen rotation toward the shear/tension loading condition.
15. The PMR15 and Avimid R composites have been tested using the biaxial and modified biaxial Iosipescu fixtures. Various biaxial shear-compression stress states in the specimens have been generated, based on the finite element computations, ranging from almost pure in-plane shear to shear-compression. It has been found that the effect of the large in-plane compressive stress generated by the loading blocks in the biaxial fixture do not affect the failure modes of the composites investigated under shear and shear-tension loading conditions. However, when the compressive stresses in specimen gage section are increased due to rotation towards larger shear-compression loading angles, the room temperature strength properties of the composites decrease.

16. A technique has been proposed to reconstruct the damage attributable to shear deformation within the gage section of woven fabric composite Iosipescu specimens. Two-dimensional damage maps have successfully been generated to measure the volume of damage through the specimen thickness. It has been shown that the reconstruction process does not contribute to any additional damage.
17. From the reconstruction results, it appears that the presence of relatively sharp notches does not influence the failure process in the 8HS woven fabric composite Iosipescu specimens. It has been found that at least 50% of the damage occurs central to the gage section. No significant damage was detected at the roots of the notches which suggests that the test produces a fairly uniform stress field in these materials.
18. The amount of damage increases as a function of the sub-surface depth and it is believed that this behavior is sigmoidal in nature with the maximum coincident to the specimen midline. This seems to fit the explanation for the symmetrical out-of-plane deformation (bulging) that is observed during mechanical shear testing.
19. The woven fabric composite Iosipescu specimen (biaxial) has been successfully modeled (3-D) numerically to include the effects of structural and material nonlinearities. To the author's knowledge, this in-depth of an analysis was the first such case. Boundary contact and geometric nonlinearities were included in conjunction with anisotropic plasticity and progressive damage. A failure criterion was proposed on the basis of the average to critical strain energy density ratios. It was found that simulation of progressive damage provided the best agreement between the experimental shear stress-strain behavior and the numerical model. Plastic deformation and structural nonlinearities had little influence on the shear response.
20. The progressive damage scheme predicted the onset of damage to be 25.0 MPa (3.6 ksi) whereas it was found experimentally to first occur at 23.0 MPa (3.3 ksi). The numerically generated damage could not be compared quantitatively with the damage determined from reconstruction. Qualitatively though, the shape of the accumulated numerical damage was nearly identical to the permanent deformation within the

specimen gage section. At this point, it can only be viewed as coincidence that the volume fraction of damage predicted numerically and experimentally differed by less than 10%.

21. The function which best described the numerically generated damage in terms of shear strain was a sigmoidal growth function. The function given by Eq. 4.43 resulted in a r^2 -value of 0.9996. This sigmoidal growth function still requires testing with experimental data to verify its uniqueness to the solution.

SUGGESTIONS FOR FUTURE WORK

Based on this research, there are numerous and interesting questions which can be raised in regard to the elastic and inelastic behavior of woven composites. Some of the subject areas which might be explored in future research endeavors are as follows:

1. In this research, the biaxial and modified biaxial Iosipescu shear test fixtures were employed to determine the mechanical shear and biaxial responses of 8HS woven fabric composite materials. Clearly, some uncertainty still exists regarding the interpretation of apparent strength properties for the composites using these tests. In a future study, it would be quite worthwhile to compare results for woven fabric composites obtained using the Iosipescu method with results obtained using the most desirable of biaxial shear test methods, i.e. the combined torsion test on hoop-wound tubes.
2. A 3-D linear elastic finite element model of the idealized volume from an 8HS RUC was developed in this research to verify elastic constants predicted by the SMM model and to study the distribution of stresses within a single lamina. It is not clear what influence mesh density would have on the accuracy of properties predicted or the distribution of stresses. Provided that computational facilities are less limited, it would be beneficial to perform mesh optimization and correlate error to mesh size.
3. The mesoscale linear elastic finite element model of the woven IVE is not sufficient to predict failure or completely understand the initiation of failure. For any failure model at this scale to be accurate in predicting the initiation of failure and “strength”, several issues must be considered. Firstly, plastic deformation effects between woven tows and within the resin-rich pockets must be included. Secondly, the influence of

sharp corners which define the lenticular cross-sections must be evaluated and lastly, boundary contact (sliding) must be permitted between the mutual tows once the matrix fails.

4. For complete knowledge of woven fabric failure behavior (particularly in shear), it is absolutely necessary to establish the relationships between the micro-, meso- and macroscales. These scales were treated somewhat independently of each other in this research in terms of stresses, progressive damage and catastrophic failure even though results at all scales were in fairly good agreement. On the basis of identifying specific failure mechanisms, the sensitivity of constituent properties and fabric architecture needs to be established.
5. The plasticity analysis was constrained by the conditions of the consistency equation and closed, elliptical yield surface. This formulation would have been better suited for macroscale studies of unidirectional composites, rather than quasi-isotropic composites. As it was, the {11} and {22} compressive properties needed to be somewhat overestimated in order for the conditions to be met. Although it seems that there was little influence on the results due to the overestimates, it might be worthwhile to establish other user-defined plasticity functions to be used with ANSYS which are less restrictive.
6. The progressive damage criterion proposed in this research generates numerically “damaged” element volumes whose accumulation only compares geometrically to actual damage in Iosipescu specimens reconstructed from serial sections. It would be helpful to study the application of other failure criteria to 3-D analyses of the Iosipescu specimen. Of particular use would be criteria based on progressive interply delaminations, since it is presumed that actual damage under shear dominated, biaxial loading conditions is predominantly interlaminar.
7. The attempts made herein to correlate actual damage with failed elements in the 3-D Iosipescu model are not inherently correct. A correlation between numerical and actual damage would be more correct if layers were considered or if, at least, a

greater number of elements was considered through-thickness. It would be of interest also to determine how the numerical growth function (Eq. 4.43) would fit or vary as a greater number of elements were considered through-thickness. Notwithstanding, more “fine” tuning of the reconstruction technique (particularly image registration methods) is required to validate the currently proposed macroscale cumulative growth function.

8. From the experimental shear testing, it is clear that viscoelastic and (or) viscoplastic effects are manifested in woven graphite-polyimide composites as a function of increasing temperature. At a minimum, the macroscale numerical studies need to be repeated while including time and temperature dependent material nonlinearities. Additionally, these studies would need to be carried out at the meso- and microscales to be of benefit in understanding how and if damage develops and progresses with changes in temperature. For these results to be of further use in applications for extreme environments, a logical progression of the time and temperature dependent material studies would be to additionally include hygroscopic effects.

References

1. Cox, B. N., and G. Flanagan. "Overview of Textiles." *Handbook of Analytical Methods for Textile Composites*, NASA Contractor Report 4750 (1-33). NASA Langley Research Center, Hampton, VA. (1997).
2. Chou, T. W. *Microstructural Design of Fiber Composites*. Cambridge University Press, G. B. (1992).
3. Meador, M. A., P. J. Cavano, and D. C. Malarik. "High temperature polymer matrix composites for extreme environments." *HITEMP Review* (1992): 529-39.
4. Vannucci, R. D. "PMR polyimide compositions for improved performance at 371 °C." NASA TM-88942. NASA Lewis Research Center, Cleveland OH. (1987).
5. Krishnamachari, S. I. *Applied Stress Analysis of Plastics: A Mechanical Engineering Approach*. Van Nostrand Reinhold, New York, NY. (1992).
6. Hull, D. *An Introduction to Composite Materials*. Cambridge University Press, G. B. (1981).
7. Easley, J. G. *Mechanics of Elastic Structures: Classical and Finite Element Methods*. Prentice Hall, Englewood Cliffs, NJ. (1989).
8. Ishikawa, T., and T. W. Chou. "Stiffness and strength behavior of woven fabric composites." *Journal of Materials Science* 17 (1982): 3211-20.
9. Ishikawa, T., and T. W. Chou. "Nonlinear behavior of woven fabric composites." *Journal of Composite Materials* 19 (1983): 399-412.
10. Ishikawa, T., M. Matsushima, and Y. Hayashi. "Experimental confirmation of the theory of elastic moduli of fabric composites." *Journal of Composite Materials* 19 (1985): 443-58.
11. Naik, N. K., and P. S. Shembekar. "Elastic behavior of woven fabric composites: I - lamina analysis." *Journal of Composite Materials* 26 (1992): 2196-2225.
12. Shembekar, P. S., and N. K. Naik. "Elastic behavior of woven fabric composites: II - laminate analysis." *Journal of Composite Materials* 26 (1992): 2226-46.

13. Naik, N. K., and P. S. Shembekar. "Elastic behavior of woven fabric composites: III - laminate design." *Journal of Composite Materials* 26 (1992): 2522-41.
14. Walsh, T. J., and O. O. Ochoa. "Analytical and experimental mechanics of woven fabric composites." *Mechanics of Composite Materials and Structures* 3 (1996): 133-52.
15. Sperling, L. H. *Introduction to Physical Polymer Science*. Second Edition, John Wiley & Sons, Inc., New York, NY. (1992).
16. Talreja, R. *Fatigue of Composite Materials*. Technomic Publishing Company, Inc., Lancaster, PA. (1987).
17. Anderson, T. L. *Fracture Mechanics: Fundamentals and Applications*. Second Edition, CRC Press, Inc., Boca Raton, FL. (1995).
18. Naik, N. K., P. S. Shembekar, and M. V. Hosur. "Failure behavior of woven fabric composites." *Journal of Composites Technology & Research* 13 (1991): 107-16.
19. Farouk, A., and A. Langrana. "Fracture properties of PMR-15/graphite-fiber composites." *Composites Science and Technology* 45 (1992): 265-77.
20. Mirzadeh, F., and K. L. Reifsnider. "Micro-deformations in C3000/PMR15 woven composite." *Journal of Composite Materials* 26 (1992): 185-205.
21. Grape, J. A., and V. Gupta. "Failure in carbon/polyimide laminates under biaxial compression." *Journal of Composite Materials* 29 (1995): 1850-72.
22. Naik, R. A. "Failure analysis of woven and braided fabric reinforced composites." *Journal of Composite Materials* 29 (1995): 2334-63.
23. Gyekenyesi, A. L., M. G. Castelli, J. R. Ellis, and C. S. Burke. "A study of elevated temperature testing techniques for the fatigue behavior of PMCs: Application to T650-35/AMB21." NASA TM-106927 (1995).
24. Alif, N., L. A. Carlsson, and J. W. Gillespie, Jr. "Mode I, mode II, and mixed mode interlaminar fracture of woven fabric carbon/epoxy." *Composite Materials Testing and Design, Thirteenth Volume*. ASTM special technical publication, West Conshohocken, PA. (1997), 82-106.
25. Zhang, Y. C., and J. Harding. "A numerical micromechanics analysis of the

- mechanical properties of a plain weave composite." *Computers and Structures* 36 (1990): 839-44.
26. Blacketter, D. M., D. E. Walrath, and A. C. Hansen. "Modeling damage in a plain weave fabric-reinforced composite material." *Journal of Composites Technology & Research* 15 (1993): 136-42.
 27. Woo, K., and J. D. Whitcomb. "Global/local finite element analysis for textile composites." *Journal of Composite Materials* 28 (1994): 1305-20.
 28. Whitcomb, J. D., K. Woo, and S. Gundapaneni. "Macro finite element for analysis of textile composites." *Journal of Composite Materials* 28 (1994): 607-17.
 29. Woo, K., and J. D. Whitcomb. "Three-dimensional failure analysis of plain weave textile composites using a global/local finite element method." *Journal of Composite Materials* 30 (1996): 984-1003.
 30. Hashin, Z., and B. W. Rosen. "The elastic moduli of fiber reinforced materials." *Journal of Applied Mechanics* 31 (1964): 223-32.
 31. Hashin, Z. "Analysis of properties of fiber composites with anisotropic constituents." *Journal of Applied Mechanics* 46 (1979): 543-50.
 32. Hashin, Z. "Analysis of composite materials - A survey." *Journal of Applied Mechanics* 50 (1983): 481-505.
 33. Sun, C. T., and R. S. Vaidya. "Prediction of composite properties from a representative volume element." *Composites Science and Technology* 56 (1996): 171-9.
 34. Raju, I. S., and J. T. Wang. "Classical laminate theory models for woven fabric composites." *Journal of Composites Technology & Research* 16 (1994): 289-303.
 35. Naik, N. K., and V. K. Ganesh. "Prediction of on-axis elastic properties of plain weave fabric composites." *Composites Science and Technology* 45 (1992): 135-52.
 36. Lekhnitskii, S. G. *Theory of Elasticity of an Anisotropic Body*. Holden-Day, San Francisco, CA. (1963).
 37. ANSYS Inc. "Analysis Tools: 15.12 Solving for Unknowns and Reactions." *ANSYS Theory Reference, Release 5.3.*, Ed.: P. Kohnke, Swanson Analysis Systems Inc.,

- Houston, P. A. (1994).
38. Foye, R. L. "Approximating the stress field within the unit-cell of a fabric reinforced composite using replacement elements." NASA CR-191422. Lockheed Engineering and Sciences Co., Hampton, VA. (1993).
 39. Marrey, R. V., and B. V. Sankar. "A micromechanical model for textile composite plates." *Journal of Composite Materials* 31 (1997): 1187-1213.
 40. Davis, J. C. *Statistics and Data Analysis in Geology*. Second Edition, John Wiley & Sons, New York, N. Y. (1986).
 41. Stein, M. L. *Interpolation of Spatial Data: Some Theory for Kriging*. Springer-Verlag, New York, N. Y. (1999).
 42. Halpin, J. C., and S. W. Tsai. "Environmental factors in composite materials design." Air Force Materials Laboratory Technical Report AFML-TR-67-423 (1967): 67-423.
 43. Chamis, C. C. "Simplified composite micromechanics equations for hygral, thermal and mechanical properties." NASA TM-83320. NASA Lewis Research Center, Cleveland OH. (1983).
 44. Standard Test Method for Tensile Properties of Polymer Matrix Composite Materials, West Conshohocken, PA., ASTM (1976). ASTM Standard D3039/D3039-76.
 45. Standard Test Method for Shear Properties of Composite Materials by the V-Notched Beam Method, West Conshohocken, PA., ASTM (1993). ASTM Standard D5379/D5379-93.
 46. Iosipescu, N. "New accurate procedure for single shear testing of metals." *Journal of Materials* 2 (1967): 537-66.
 47. Adams, D. F., and D. E. Walrath. "Iosipescu shear properties of SMC composite materials." *Composite Materials Testing and Design, Sixth Conference*. ASTM special technical publication, Philadelphia, PA. (1982), 19-33.
 48. Walrath, D. E., and D. F. Adams. "Current status of the Iosipescu shear test method." *Journal of Composite Materials* 21 (1987): 494-507.
 49. Walrath, D. E., and D. F. Adams. "Further developments of the Iosipescu shear test

- method." *Experimental Mechanics* 27 (1987): 113-19.
50. Slepetz, J. M., T. F. Zagaeski, and R. F. Novello. "In-plane shear test for composite materials." Army Materials and Mechanics Research Center, AMMRC TR 78-30 (1978).
 51. Walrath, D. E., and D. F. Adams. "Analysis of the stress state in an Iosipescu shear test specimen." Report UWME-DR-301-102-1, Department of Mechanical Engineering, University of Wyoming (1983).
 52. Barnes, J. A., M. Kumosa, and D. Hull. "Theoretical and experimental evaluation of the Iosipescu shear test." *Composites Science and Technology* 28 (1987): 251-68.
 53. Kumosa, M., and D. Hull. "Mixed-mode fracture of composites using the Iosipescu shear test." *Composites Science and Technology* 35 (1987): 83-102.
 54. Broughton, W. R., M. Kumosa, and D. Hull. "Analysis of the Iosipescu shear test as applied to unidirectional carbon-fiber reinforced composites." *Composites Science and Technology* 38 (1990): 299-325.
 55. Ifju, P. G. "Shear testing of textile composite materials." *Journal of Composites Technology & Research* 17 (1995): 199-204.
 56. Ifju, P. G., P. G. Masters, and W. C. Jackson. "The use of moiré interferometry as an aid to standard test-method development for textile composite materials." *Composites Science and Technology* 53 (1995): 155-63.
 57. Ifju, P. G. "The shear gage: For reliable shear modulus measurements of composite materials." *Experimental Mechanics* 34 (1994): 369-78.
 58. Broughton, W. R. "*Shear Properties of Unidirectional Carbon Fibre Composites.*" Ph.D. Thesis, University of Cambridge, G. B. (1989).
 59. Arcan, M., Z. Hashin, and A. Voloshin. "A method to produce uniform plane-stress states with application to fiber reinforced materials." *Experimental Mechanics* 18 (1978): 141-46.
 60. Bansal, A., and M. Kumosa. "Experimental and analytical studies of failure modes in Iosipescu specimens under biaxial loadings." *Journal of Composite Materials* 29 (1995): 334-58.

61. Sukumar, N., and M. Kumosa. "Finite element analysis of mixed mode fracture and failure in Iosipescu specimens." *International Journal of Fracture* 58 (1992): 177-92.
62. Bansal, A., and M. Kumosa. "Application of the biaxial Iosipescu method to mixed-mode fracture of unidirectional composites." *International Journal of Fracture* 71 (1995): 131-50.
63. Searles, K., G. Odegard, M. Castelli, and M. Kumosa. "Failure investigation of graphite polyimide fabric composites at room and elevated temperatures using the biaxial Iosipescu test." *Journal of Composite Materials* 33 (1999): 2038-79.
64. Kumosa, M., K. Searles, and G. Odegard. "Biaxial failure analysis of graphite reinforced polyimide composites." *Proceedings of the HITEMP Review 1997*, Advanced High Temperature Engine Materials Technology Program, NASA Lewis Research Center, Cleveland, OH., April 29-30, 1997.
65. Kumosa, M., K. Searles, G. Odegard, and M. Castelli. "Biaxial in-plane testing of high temperature graphite-polyimide fabric composites." *Proceedings of the High Temple Workshop XVIII*, Hilton Resort, Hilton Head Island, SC., January 20-22, 1998.
66. Odegard, G., K. Searles, and M. Kumosa. "A critical examination of the Iosipescu shear test as applied to 0° unidirectional composite materials." *Mechanics of Composite Materials and Structures* 6 (1999): 229-56.
67. Searles, K. and M. Kumosa. "Analysis of nonlinear behavior in 8-harness satin woven fabric composites subjected to in-plane biaxial shear deformation." *Proceedings of the High Temple Workshop XIX*, Downtown Hilton, Denver, CO., January 20-22, 1999.
68. Odegard, G., K. Searles, and M. Kumosa. "Non-linear analysis of woven fabric-reinforced graphite/PMR-15 composites under shear-dominated biaxial loads." *Mechanics of Composite Materials and Structures* 7 (1999): 129-52.
69. Pagano, N. J., and J. C. Halpin. "Influence of end constraints in the testing of anisotropic bodies." *Journal of Composite Materials* 2 (1968): 18.
70. Chamis, C. C., and J. H. Sinclair. "Ten-deg off-axis test for shear properties in fiber composites." *Experimental Mechanics* 17 (1977): 339-46.
71. Sun, C. T., and I. Chung. "An oblique end-tab design for testing off-axis composite

- specimens." *Composites* 24 (1993): 619-23.
72. Ifju, P. G. "Evaluation of a new electrical resistance shear gage using moiré interferometry." *Proceedings of the Second International Conference on Photomechanics and Speckle Metrology: Moiré Techniques, Holographic Interferometry, Optical NDT and Applications to Fluid Mechanics*, SPIE Vol. 1554B, San Diego, CA., August 1991, 420-8.
 73. Ifju, P. G., and D. Post. "A special strain gage for shear testing of composite materials." *Proceedings of SEM Spring Conference on Experimental Mechanics*, Milwaukee, WI., June 9-12, 1991.
 74. Pierron, F., and A. Vautrin. "Accurate comparative determination of the in-plane shear modulus of T300/914 by the Iosipescu and 45° off-axis tests." *Composites Science and Technology* 52 (1994): 61-72.
 75. Adams, D. F., and E. Q. Lewis. "Experimental strain analysis of the Iosipescu shear test specimen." *Experimental Mechanics* 35 (1995): 352-60.
 76. Pierron, F. "Discussion of the article: biaxial testing of unidirectional carbon-epoxy composite using biaxial Iosipescu test fixture." *Journal of Composite Materials* 33 (1999): 682-7.
 77. Kumosa, M. "Response to discussion of the article: biaxial testing of unidirectional carbon-epoxy composite using biaxial Iosipescu test fixture." *Journal of Composite Materials* 33 (1999): 688-94.
 78. Ho, H., J. Morton, and G. L. Farley. "Non-linear numerical analysis of the Iosipescu specimen for composite materials." *Composites Science and Technology* 50 (1994): 355-65.
 79. ANSYS, Inc. "Structures with Geometric Nonlinearities: 3.0 Introduction to Geometric Nonlinearities." *ANSYS Theory Reference, Release 5.3.*, Ed: P. Kohnke, Swanson Analysis Systems Inc., Houston, PA (1994): 1-27.
 80. Chen, W. H., and J. T. Yeh. "Three-dimensional finite element analysis of static and dynamic contact problems with friction." *Computers and Structures* 35 (1990): 541-52.
 81. Xiaoyu, J. "Frictional contact analysis of composite materials." *Composites Science and Technology* 54 (1995): 341-8.

82. ANSYS, Inc. "Analysis Tools: 15.9 Newton-Raphson Procedure." *ANSYS Theory Reference, Release 5.3.*, Ed: P. Kohnke, Swanson Analysis Systems Inc., Houston, PA (1994): 28-40.
83. ANSYS, Inc. "Element Library: 14.48 CONTAC48 - 2-D Point to Surface Contact." *ANSYS Theory Reference, Release 5.3.*, Ed: P. Kohnke, Swanson Analysis Systems Inc., Houston, P. A. (1994): 196-205.
84. Pindera, M. J., P. Ifju, and D. Post. "Iosipescu shear characterization of polymeric and metal matrix composites." *Experimental Mechanics* 30 (1990): 101-8.
85. Xing, Y. M., C. Y. Poon, and C. Ruiz. "A whole-field strain analysis of the Iosipescu specimen and evaluation of experimental errors." *Composites Science and Technology* 47 (1993): 251-9.
86. Ho, H., M. Y. Tsai, J. Morton, and G. L. Farley. "Numerical analysis of the Iosipescu specimen for composite materials." *Composites Science and Technology* 46 (1993): 115-28.
87. Odom, E. M., D. M. Blacketter, and B. R. Suratno. "Experimental and analytical investigation of the modified Wyoming shear-test fixture." *Experimental Mechanics* 34 (1994): 10-5.
88. Pierron, F., A. Vautrin, and B. Harris. "The Iosipescu in-plane shear test: validation on an isotropic material." *Experimental Mechanics* 35 (1995): 130-6.
89. Conant, N. R., and E. M. Odom. "An improved Iosipescu shear test fixture." *Journal of Composites Technology & Research* 17 (1995): 50-5.
90. ANSYS, Inc. "Element Library: 4.46 SOLID46 - 3-D Layered Structural Solid." *ANSYS Theory Reference, Release 5.3.*, Ed: P. Kohnke, Swanson Analysis Systems Inc., Houston, P. A. (1994): 181-8.
91. Hahn, H. T., and S. W. Tsai. "Nonlinear elastic behavior of unidirectional composite laminae." *Journal of Composite Materials* 7 (1973): 102-18.
92. Kenaga, D., J. F. Doyle, and C. T. Sun. "The characterization of boron/aluminum composite in the nonlinear range as an orthotropic elastic-plastic material." *Journal of Composite Materials* 21 (1987): 516-31.
93. Hansen, A. C., D. M. Blacketter, and D. E. Walrath. "An invariant-based flow rule

- for anisotropic plasticity applied to composite materials." *Journal of Applied Mechanics* 58 (1991): 881-8.
94. Xie, M., and D. F. Adams. "A plasticity model for unidirectional composite materials and its applications in modeling composites testing." *Composites Science and Technology* 54 (1995): 11-21.
 95. Owens, G. A., and S. E. Schofield. "Thermal cycling and mechanical property assessment of carbon fiber fabric reinforced PMR-15 polyimide laminates." *Composites Science and Technology* 33 (1988): 177-90.
 96. Vaziri, R., M. D. Olson, and D. L. Anderson. "A plasticity-based constitutive model for fibre-reinforced composite laminates." *Journal of Composite Materials* 25 (1991): 512-35.
 97. ANSYS, Inc. "Element Library: 14.95 SOLID95 - 20-Node Structural Solid." *ANSYS Theory Reference, Release 5.3.*, Ed: P. Kohnke, Swanson Analysis Systems Inc., Houston, P. A. (1994): 356-7.
 98. Hill, R. "*The Mathematical Theory of Plasticity.*" Oxford Classic Texts in the Physical Sciences, Oxford University Press, G. B. (1950).
 99. ANSYS, Inc. "Structures with Material Nonlinearities: 4.1 Rate-Independent Plasticity." *ANSYS Theory Reference, Release 5.3.*, Ed: P. Kohnke, Swanson Analysis Systems Inc., Houston, PA (1994): 4-24.
 100. Azzi, V. D., and S. W. Tsai. "Anisotropic strength of composites." *Experimental Mechanics* 5 (1965): 283-8.
 101. Tsai, S. W., and E. M. Wu. "A general theory of strength for anisotropic materials." *Journal of Composite Materials* 5 (1971): 58-80.
 102. Hashin, Z. "Failure criteria for unidirectional fiber composites." *Journal of Applied Mechanics* 47 (1980): 329-34.
 103. Bovik, A., Huang, T., and D. Munson Jr. "The effect of median filtering on edge estimation and detection." *IEEE Transactions on Pattern Analysis and Machine Intelligence* 9 (1987): 181-93.

APPENDIX A

A.1. FORTRAN 77 Code: Prediction of Laminate Elastic Constants

In A.1. of this appendix, compiler-ready example code, in Fortran 77 format, is given for predicting woven fabric elastic constants based on the simplified, two-dimensional mechanics model presented in Section 3. In A.1.1. sample input data files used in this investigation are also included for purposes of demonstrating file format. The example code provides an acceptable solution for lower bounds approximations. Elastic constants for other classes of composite laminates, such as cross-ply, may be predicted using this code by assuming 1st order polynomial approximations to woven tow centerline data, i.e. centerline coordinates for a line segment.

PROGRAM WEAVE

c
c

c

c This Fortran 77 program calculates the elastic constants of a woven 8-H satin fabric
c composite lamina by treating the lamina as a 2-layer laminate. Individual laminae are
c treated as unidirectional and transversely isotropic; laminae properties are determined
c using CCA.

c

c The laminae properties are evaluated at the woven tow volume fraction vs. the laminate
c volume fraction. Knowing the effective elastic properties of the equivalent warp and fill
c laminae (obtained by inverting the mean compliances), the stiffness of the woven fabric
c lamina and the apparent laminate elastic properties can be evaluated using the Kirchhoff
c hypothesis for analysis of thin plates i.e., Classical Lamination Theory.

c

c

```

PARAMETER(MaxN=15,MaxM=500)
INTEGER M,N
REAL A,B,C,P,X,Y
DIMENSION A(1:MaxN,1:MaxN),B(1:MaxN),C(1:MaxN),X(1:MaxM),Y(1:MaxM)
EXTERNAL P
OPEN (UNIT=10, FILE='CENTER.DAT', STATUS='OLD')
OPEN (UNIT=20, FILE='EPROPS.DAT', STATUS='OLD')
OPEN (UNIT=30, FILE='CPOLYFIT.DAT', STATUS='NEW')
OPEN (UNIT=40, FILE='LOCAL.DAT', STATUS='NEW')
OPEN (UNIT=50, FILE='CCA.DAT', STATUS='NEW')
OPEN (UNIT=60, FILE='LECONST.DAT', STATUS='NEW')
OPEN (UNIT=70, FILE='UPPER.DAT', STATUS='OLD')
OPEN (UNIT=80, FILE='LOWER.DAT', STATUS='OLD')
OPEN (UNIT=90, FILE='invABD.DAT', STATUS='NEW')
OPEN (UNIT=100, FILE='WFLAMINA.DAT', STATUS='NEW')
OPEN (UNIT=110, FILE='LAMINATE.DAT', STATUS='NEW')

```

c

c Least-Squares Polynomial Fit Subroutine Calls for Upper B-Spline

c

```

CALL CNTRLIN(X,Y,M,N)
IF (M.GT.MaxM) THEN
  PRINT*, 'ERROR: (M>500) TOW CENTERLINE B-SPLINE DATA EXCEEDS
& PROGRAM CAPABILITIES. PLEASE CREATE DATA FILE WITH FEWER
POINTS.'
ENDIF
CALL MATRIX(X,Y,M,A,B,N)
CALL POLYSLV(A,B,N,C)
CALL CENTROUT(C,N)

```

c

c Subroutine Calls for Determining Local Angle of Tow Undulation

c

```

CALL POLY(PCOEFF,N)
IF ((N-1).EQ.1) THEN
  CALL DP1(PCOEFF,N,ANG)
ELSEIF ((N-1).EQ.2) THEN
  CALL DP2(PCOEFF,N,ANG)
ELSEIF ((N-1).EQ.3) THEN
  CALL DP3(PCOEFF,N,ANG)
ELSEIF ((N-1).EQ.4) THEN

```

```
      CALL DP4(PCOEFF,N,ANG)
    ELSEIF ((N-1).EQ.5) THEN
      CALL DP5(PCOEFF,N,ANG)
    ELSEIF ((N-1).EQ.6) THEN
      PRINT*, 'ERROR: (N=6) EXCEEDS PROGRAM CAPABILITIES. PLEASE DE
& LETE DATA FILES CREATED WITH PROGRAM AND RERUN WITH A
      LOWER ORDER POLYNOMIAL APPROXIMATION.'
    ENDIF
```

c

c Subroutine Call for Sorting and Selecting Maximum Tow Centerline Angle

c

```
CALL SORT(MAXANG)
```

c

c Subroutine Call for Tow Property Analysis by CCA

c

```
CALL CCA(E11,E22HIGH,E22LOW,G12,G23HIGH,G23LOW,NU12)
```

c

c Subroutine Call for Compliance Reduction (Off-Axis Transformation) and
c Calculation of Laminae Engineering Constants

c

```
CALL TRANSFORM(EXXH,EXXL,EYYH,EYYL,GXYH,GXYL,NXYH,NXYL)
```

c

c Subroutine Call for Mean Thickness of Upper Cross-Sectional Area by
c Mean Value of Integration

c

```
CALL THICK1(AVEZ1)
```

c

c Subroutine Call for Mean Thickness of Lower Cross-Sectional Area by
c Mean Value of Integration

c

```
CALL THICK2(AVEZ2)
```

c

c Subroutine Call for "2-Ply" Laminate Engineering Constants From the
c [ABD]⁻¹ Matrices

c

```

CALL ABD1(AVEZ1,AVEZ2)
c

```

```

c Subroutine Call for "10-Ply" or "16-Ply" Laminate Engineering Constants
c From the [ABD]-1 Matrices
c
CALL ABD2(ExxH,ExxL,EyyH,EyyL,GxyH,GxyL,NxyH,NxyL)
c
c
STOP
END
c
c

```

```

c Least-Squares Polynomial Fit Subroutines for Tow Centerline B-Spline
c
SUBROUTINE CNTRLIN(X,Y,M,N)
PARAMETER (MaxM=500)
INTEGER K,M,N
REAL X,Y
DIMENSION X(1:MaxM),Y(1:MaxM)
DATA K,XDATA,YDATA /0,0.0,0.0/
M = 0
10 READ (10,*,END=20) XDATA, YDATA
M = M+1
GO TO 10
20 PRINT*, 'ENTER ORDER OF POLYNOMIAL TO FIT TOW CENTERLINE DATA:'
READ*, N
PRINT*,
IF (M.LT.(N+1)) THEN
PRINT*, 'ERROR, DATA POINTS MUST BE AT LEAST (N+1) OF ORDER'
PRINT*,
PRINT 25, M
25 FORMAT (1X,'THERE WERE ',I3,' DATA POINTS READ FROM A FILE')
GO TO 20
ENDIF
REWIND (UNIT=10)
DO 30 K=1,M
READ (10,*) XDATA, YDATA

```

```

        X(K) = XDATA
        Y(K) = YDATA
30 CONTINUE
    RETURN
    END
c
c
SUBROUTINE MATRIX(X,Y,M,A,B,N)
PARAMETER(MaxN=15,MaxM=500)
INTEGER Col,J,K,M,N,R
REAL A,B,Pow,Prod,X,XK,Y,YK
DIMENSION A(1:MaxN,1:MaxN),B(1:MaxN),X(1:MaxM),Y(1:MaxM)
DIMENSION Pow(0:MaxN)
DATA Col,J,K,R,Prod /0,0,0,0,0.0/
DO 10 R=1,(N+1)
    B(R) = 0
10 CONTINUE
    DO 30 K=1,M
        YK = Y(K)
        XK = X(K)
        Prod = 1
        DO 20 R=1,(N+1)
            B(R) = B(R)+YK*Prod
            Prod = Prod*XK
20 CONTINUE
30 CONTINUE
    DO 40 J=1,(2*N)
        Pow(J) = 0
40 CONTINUE
    Pow(0) = M
    DO 60 K=1,M
        XK = X(K)
        Prod = X(K)
        DO 50 J=1,(2*N)
            Pow(J) = Pow(J)+Prod
            Prod = Prod*XK
50 CONTINUE
60 CONTINUE
    DO 80 R=1,(N+1)
        DO 70 Col=1,(N+1)
            A(R,Col) = Pow(R+Col-2)

```

```

70 CONTINUE
80 CONTINUE
  RETURN
  END
c
c
  SUBROUTINE POLYSLV(A,B,N,C)
  PARAMETER(MaxN=15)
  INTEGER Col,J,K,N,P,Row,T
  REAL A,B,C,Sum
  DIMENSION A(1:MaxN,1:MaxN),B(1:MaxN),C(1:MaxN)
  DIMENSION Row(1:MaxN),Z(1:MaxN)
  DATA Col,J,K,Sum /0,0,0,0.0/
  DO 10 J=1,(N+1)
    Row(J) = J
10 CONTINUE
    DO 50 P=1,N
      DO 20 K=(P+1),(N+1)
        IF (ABS(A(Row(K),P)).GT.ABS(A(Row(P),P))) THEN
          T = Row(P)
          Row(P) = Row(K)
          Row(K) = T
        ENDIF
20 CONTINUE
      DO 40 K=(P+1),(N+1)
        A(Row(K),P) = A(Row(K),P)/A(Row(P),P)
        DO 30 Col=(P+1),(N+1)
          A(Row(K),Col)=A(Row(K),Col)-A(Row(K),P)*A(Row(P),Col)
30 CONTINUE
40 CONTINUE
50 CONTINUE
    Z(1) = B(Row(1))
    DO 70 K=2,(N+1)
      Sum = 0
      DO 60 Col=1,(K-1)
        Sum = Sum+A(Row(K),Col)*Z(Col)
60 CONTINUE
      Z(K) = B(Row(K))-Sum
70 CONTINUE
    C(N+1) = Z(N+1)/A(Row(N+1),N+1)
    DO 90 K=N,1,-1

```

```

      Sum = 0
      DO 80 Col=(K+1),(N+1)
        Sum = Sum+A(Row(K),Col)*C(Col)
80    CONTINUE
      C(K) = (Z(K)-Sum)/A(Row(K),K)
90  CONTINUE
      RETURN
      END

```

c

c

```

      REAL FUNCTION P(C,N,T)
      PARAMETER(MaxN=15)
      INTEGER K,N
      REAL C,Sum,T
      DIMENSION C(1:MaxN)
      DATA Sum /0.0/
      Sum = C(N+1)
      DO 10 K=N,1,-1
        Sum = C(K)+Sum*T
10  CONTINUE
      P = Sum
      RETURN
      END

```

c

c

```

      SUBROUTINE CENTROUT(C,N)
      PARAMETER (MaxN=125)
      INTEGER K,N
      REAL C
      DIMENSION C(1:MaxN)
      EXTERNAL P
      DO 10 K=1,N+1
        WRITE (30,*) C(K)
10  CONTINUE
      ENDFILE (UNIT=30)
      RETURN
      END

```

c

c

c

 c Subroutines for Local Angle of Tow Undulation

c

```

SUBROUTINE POLY(PCOEFF,N)
PARAMETER (MaxN=15)
INTEGER A,N
REAL PCOEFF
DIMENSION PCOEFF(1:MaxN)
DATA A /0/
REWIND (UNIT=30)
PRINT*, 'PLEASE VERIFY TOW CENTERLINE POLYNOMIAL ORDER: N = '
READ*, N
N = N+1
READ (30,*) (PCOEFF(A), A=1,N)
RETURN
END

```

c

c

```

SUBROUTINE DPI(PCOEFF,N,ANG)
PARAMETER (MaxN=15,Inc=1.0,PI=3.14159)
INTEGER N,H
REAL PCOEFF,MinY,MaxY,dY,dY1,dY2,ANG
DIMENSION PCOEFF(1:MaxN)
PRINT*,
PRINT*, 'ENTER LOWER LIMIT OF TOW CENTERLINE: '
READ*, MinY
PRINT*,
PRINT*, 'ENTER UPPER LIMIT OF TOW CENTERLINE: '
READ*, MaxY
DO 10 dY=MinY,MaxY,Inc
H =1
dY1 = dY+H
dY2 = dY-H
  dP = (((PCOEFF(N)*dY1**(N-1))+(PCOEFF(N-1)))-
&      ((PCOEFF(N)*dY2**(N-1))+(PCOEFF(N-1))))/2*H
  ANG = ABS((ATAN(dP))*(180/PI))
  WRITE (40,*) ANG
10 CONTINUE
RETURN
END

```

c

c

```

SUBROUTINE DP2(PCOEFF,N,ANG)
PARAMETER (MaxN=15,Inc=1.0,PI=3.14159)
INTEGER N,H
REAL PCOEFF,MinY,MaxY,dY,dY1,dY2,ANG
DIMENSION PCOEFF(1:MaxN)
PRINT*,
PRINT*, 'ENTER LOWER LIMIT OF TOW CENTERLINE: '
READ*, MinY
PRINT*,
PRINT*, 'ENTER UPPER LIMIT OF TOW CENTERLINE: '
READ*, MaxY
DO 10 dY=MinY,MaxY,Inc
H =1
dY1 = dY+H
dY2 = dY-H
  dP = (((PCOEFF(N)*dY1**(N-1))+(PCOEFF(N-1)*dY1**(N-2))+
&      (PCOEFF(N-2)))-((PCOEFF(N)*dY2**(N-1))+(PCOEFF(N-1)*
&      dY2**(N-2))+(PCOEFF(N-2))))/2*H
  ANG = ABS((ATAN(dP))*(180/PI))
  WRITE (40,*) ANG
10 CONTINUE
RETURN
END

```

c

c

```

SUBROUTINE DP3(PCOEFF,N,ANG)
PARAMETER (MaxN=15,Inc=1.0,PI=3.14159)
INTEGER N,H
REAL PCOEFF,MinY,MaxY,dY,dY1,dY2,ANG
DIMENSION PCOEFF(1:MaxN)
PRINT*,
PRINT*, 'ENTER LOWER LIMIT OF TOW CENTERLINE: '
READ*, MinY
PRINT*,
PRINT*, 'ENTER UPPER LIMIT OF TOW CENTERLINE: '
READ*, MaxY
DO 10 dY=MinY,MaxY,Inc
H =1
dY1 = dY+H
dY2 = dY-H

```

```

      dP = (((PCOEFF(N)*dY1**(N-1))+PCOEFF(N-1)*dY1**(N-2))+
&      (PCOEFF(N-2)*dY1**(N-3))+PCOEFF(N-3)))-((PCOEFF(N)*
&      dY2**(N-1))+PCOEFF(N-1)*dY2**(N-2))+PCOEFF(N-2)*
&      dY2**(N-3))+PCOEFF(N-3)))/2*H
      ANG = ABS((ATAN(dP))*(180/PI))
      WRITE (40,*) ANG
10 CONTINUE
   RETURN
   END
c
c
SUBROUTINE DP4(PCOEFF,N,ANG)
PARAMETER (MaxN=15,Inc=1.0,PI=3.14159)
INTEGER N,H
REAL PCOEFF,MinY,MaxY,dY,dY1,dY2,ANG
DIMENSION PCOEFF(1:MaxN)
PRINT*,
PRINT*, 'ENTER LOWER LIMIT OF TOW CENTERLINE: '
READ*, MinY
PRINT*,
PRINT*, 'ENTER UPPER LIMIT OF TOW CENTERLINE: '
READ*, MaxY
DO 10 dY=MinY,MaxY,Inc
  H = i
  dY1 = (dY+H)
  dY2 = (dY-H)
  dP = (((PCOEFF(N)*dY1**(N-1))+PCOEFF(N-1)*dY1**(N-2))+
&      (PCOEFF(N-2)*dY1**(N-3))+PCOEFF(N-3)*dY1**(N-4))+
&      (PCOEFF(N-4)))-((PCOEFF(N)*dY2**(N-1))+PCOEFF(N-1)*
&      dY2**(N-2))+PCOEFF(N-2)*dY2**(N-3))+PCOEFF(N-3)*
&      dY2**(N-4))+PCOEFF(N-4)))/2*H
  ANG = ABS((ATAN(dP))*(180/PI))
  WRITE (40,*) ANG
10 CONTINUE
   RETURN
   END
c
c
SUBROUTINE DP5(PCOEFF,N,ANG)
PARAMETER (MaxN=15,Inc=1.0,PI=3.14159)
INTEGER N,H

```

```

REAL PCOEFF,MinY,MaxY,dY,dY1,dY2,ANG
DIMENSION PCOEFF(1:MaxN)
PRINT*,
PRINT*, 'ENTER LOWER LIMIT OF TOW CENTERLINE: '
READ*, MinY
PRINT*,
PRINT*, 'ENTER UPPER LIMIT OF TOW CENTERLINE: '
READ*, MaxY
DO 10 dY=MinY,MaxY,Inc
H =1
dY1 = (dY+H)
dY2 = (dY-H)
  dP = (((PCOEFF(N)*dY1**(N-1))+(PCOEFF(N-1)*dY1**(N-2))+
&      (PCOEFF(N-2)*dY1**(N-3))+(PCOEFF(N-3)*dY1**(N-4))+
&      (PCOEFF(N-4)*dY1**(N-5))+(PCOEFF(N-5)))-((PCOEFF(N)*
&      dY2**(N-1))+(PCOEFF(N-1)*dY2**(N-2))+(PCOEFF(N-2)*
&      dY2**(N-3))+(PCOEFF(N-3)*dY2**(N-4))+(PCOEFF(N-4)*
&      dY2**(N-5))+(PCOEFF(N-5))))/2*H
  ANG = ABS((ATAN(dP))*(180/PI))
  WRITE (40,*) ANG
10 CONTINUE
  RETURN
  END
c
c


---


c


---


c  Subroutine for Sorting Tow Centerline Off-Axis Angles in Ascending Order
c
SUBROUTINE SORT(MAXANG)
PARAMETER (MaxM=5000)
INTEGER I,N,J,PTR,LAST,FIRST,K
REAL SLOPE,HOLD,MAXANG
DIMENSION SLOPE(1:MaxM)
I = 1
REWIND (UNIT=40)
10 READ (40,*,END=20) SLOPE(I)
  I = I+1
  GO TO 10
20 N = I-1

```

```

LAST = N
DO 40 J=1,N-1
  PTR = J
  FIRST = J+1
  DO 30 K=FIRST, LAST
    IF (SLOPE(K).LT.SLOPE(PTR)) THEN
      PTR = K
    ENDIF
30  CONTINUE
    HOLD = SLOPE(J)
    SLOPE(J) = SLOPE(PTR)
    SLOPE(PTR) = HOLD
40  CONTINUE
    MAXANG = SLOPE(N)
    RETURN
    END

```

c

c

c

c Adopted Method of Hashin for CCA Elastic Property Analysis

c

```

SUBROUTINE CCA(E11,E22HIGH,E22LOW,G12,G23HIGH,G23LOW,NU12)
  REAL E11,E22HIGH,E22LOW,G12,G23HIGH,G23LOW,NU12,EF,EFT,EM,GF,GFT,
& GM,NUF,NUM,VF,VM,GAMMA,RHO,BETAF,BETAM,ALPHA,GTHIGH,GTLOW,
& GM1,GM2,GM3,GM4,KT,KF,KM
  DATA EF,EFT,EM,GF,GFT,GM,NUF,VF /0.0,0.0,0.0,0.0,0.0,0.0,0.0,0.0/
  DATA VM,GAMMA,RHO,BETAF,BETAM,ALPHA /0.0,0.0,0.0,0.0,0.0,0.0/
  DATA GTHIGH,GTLOW,GM1,GM2,GM3,GM4 /0.0,0.0,0.0,0.0,0.0,0.0/
  DATA KT,KF,KM /0.0,0.0,0.0/
  READ (20,*) EF,EFT,GF,GFT,NUF,VF,EM,GM,NUM
  VM = 1-VF
  GAMMA = GFT/GM
  KF = ((4/EFT)-(4*NUF**2/EF)-(1/GFT))**(-1)
  KM = ((4/EM)-(4*NUM**2/EM)-(1/GM))**(-1)
  BETAF = KF/(KF+2*GFT)
  BETAM = KM/(KM+2*GM)
  RHO = (GAMMA+BETAM)/(GAMMA-1)
  ALPHA = (BETAM-(GAMMA*BETAF))/(1+(GAMMA*BETAF))
  KT1 = (KM*(KF+GM)*(1-VF))+(KF*VF*(KM+GM))

```

```

KT2 = ((KF+GM)*(1-VF))+(VF*(KM+GM))
KT = KT1/KT2
IF (GFT.GT.GM) THEN
  GM1 = (1+BETAM)*VF
  GM2 = RHO-(VF*(1+((3*BETAM**2*VM**2)/(ALPHA*VF**3+1))))
  GM3 = 1/(GFT-GM)
  GM4 = ((KM+2*GM)*VM)/(2*GM*(KM+GM))
  GTHIGH = GM*(1+(GM1/GM2))
  GTLOW = GM+(VF/(GM3+GM4))
ELSEIF (GFT.LT.GM) THEN
  GM1 = 1/(GFT-GM)
  GM2 = ((KM+2*GM)*VM)/(2*GM*(KM+GM))
  GM3 = (1+BETAM)*VF
  GM4 = RHO-(VF*(1+((3*BETAM**2*VM**2)/(ALPHA*VF**3-BETAM))))
  GTHIGH = GM+(VF/(GM1+GM2))
  GTLOW = GM*(1+(GM3/GM4))
ENDIF
E11 = EF*VF+EM*VM+((4*VF*VM*(NUF-NUM)**2)/(VM/KF+VF/KM+1/GM))
NU12 = NUF*VF+NUM*VM+((VF*VM*(NUF-NUM)*(1/KM-1/KF))
& /(VM/KF+VF/KM+1/GM))
E22HIGH = (4*KT*GTHIGH)/(KT+(1+(4*KT*NU12**2/E11))*GTHIGH)
E22LOW = (4*KT*GTLOW)/(KT+(1+(4*KT*NU12**2/E11))*GTLOW)
G12 = GM*((VM*GM+(1+VF)*GF)/((1+VF)*GM+VM*GF))
G23HIGH = GTHIGH
G23LOW = GTLOW
WRITE (50,*) E11
WRITE (50,*) E22HIGH
WRITE (50,*) E22LOW
WRITE (50,*) G12
WRITE (50,*) NU12
WRITE (50,*) G23HIGH
WRITE (50,*) G23LOW
RETURN
END

```

c

c

c

c Compliance Reduction by Local Off-Axis Angle of Transformation and

c Calculation of Laminae Engineering Constants

c

```

SUBROUTINE TRANSFORM(EXXH,EXXL,EYYH,EYYL,GXYH,GXYL,NXYH,NXYL)
  PARAMETER (MaxM=5000,PI=3.14159)
  INTEGER I
  REAL E11,E22HIGH,E22LOW,G12,NU12,G23HIGH,G23LOW,m,n,NU21H,NU21L,
    & NU23H,NU23L,S11H,S11L,S22H,S22L,S12H,S12L,S66H,S66L,SUM1A,
    & SUM1B,SUM2A,SUM2B,SUM12A,SUM12B,SUM6A,SUM6B,EXXH,EXXL,
    & EYYH,EYYL,GXYH,GXYL,NXYH,NXYL
  DIMENSION ANG(1:MaxM)
  DATA I,m,n,NU21H,NU21L,NU23H,NU23L /0,0,0,0,0,0,0,0,0,0,0,0,0,0,0,0/
  DATA S11H,S11L,S22H,S22L,S12H,S12L /0.0,0.0,0.0,0.0,0.0,0.0,0.0/
  DATA S66H,S66L,SUM1A,SUM1B,SUM2A,SUM2B /0.0,0.0,0.0,0.0,0.0,0.0,0.0/
  DATA SUM12A,SUM12B,SUM6A,SUM6B /0.0,0.0,0.0,0.0,0.0/
  I = 1
  REWIND (UNIT=40)
  REWIND (UNIT=50)
  READ (50,*) E11
  READ (50,*) E22HIGH
  READ (50,*) E22LOW
  READ (50,*) G12
  READ (50,*) NU12
  READ (50,*) G23HIGH
  READ (50,*) G23LOW
10 READ (40,*,END=20) ANG(I)
  m = COS(ANG(I)*(PI/180))
  n = SIN(ANG(I)*(PI/180))
  NU21H = (E22HIGH/E11)*NU12
  NU21L = (E22LOW/E11)*NU12
  NU23H = (E22HIGH/(2*G23HIGH))-1
  NU23L = (E22LOW/(2*G23LOW))-1
  S11H = (m**4/E11)+(((1/G12)-(2*NU12/E11))*m**2*n**2)+
    & (n**4/E22HIGH)
  S11L = (m**4/E11)+(((1/G12)-(2*NU12/E11))*m**2*n**2)+
    & (n**4/E22LOW)
  S22H = 1/E22HIGH
  S22L = 1/E22LOW
  S12H = ((NU21H*m**2)/E22HIGH)+((NU23H*n**2)/E22HIGH)
  S12L = ((NU21L*m**2)/E22LOW)+((NU23L*n**2)/E22LOW)
  S66H = (m**2/G12)+(n**2/G23HIGH)
  S66L = (m**2/G12)+(n**2/G23LOW)
  SUM1A = SUM1A+S11H

```

```

SUM1B = SUM1B+S11L
SUM2A = SUM2A+S22H
SUM2B = SUM2B+S22L
SUM12A = SUM12A+S12H
SUM12B = SUM12B+S12L
SUM6A = SUM6A+S66H
SUM6B = SUM6B+S66L
I = I+1
GO TO 10
20 EXXH = 1/(SUM1A/(I-1))
EXXL = 1/(SUM1B/(I-1))
EYYH = 1/(SUM2A/(I-1))
EYYL = 1/(SUM2B/(I-1))
GXYH = 1/(SUM6A/(I-1))
GXYL = 1/(SUM6B/(I-1))
NXYL = (SUM12A/(I-1))*EXXL
NXYH = (SUM12B/(I-1))*EXXH
WRITE (60,*) EXXH
WRITE (60,*) EXXL
WRITE (60,*) EYYH
WRITE (60,*) EYYL
WRITE (60,*) GXYH
WRITE (60,*) GXYL
WRITE (60,*) NXYH
WRITE (60,*) NXYL
RETURN
END

```

c

c

c

```

c Subroutine for Calculation of Mean Upper 1/2 Thickness of Tow Cross-
c Section by Mean Value of Integration
c

```

```

SUBROUTINE THICK1(AVEZ1)
PARAMETER (MaxM=500)
INTEGER I
REAL X,Z1
DIMENSION X(1:MaxM),Z1(1:MaxM)
DATA I,SUMX,SUMZ1 /1,0.0,0.0/

```



```

10 READ (70,*,END=20) X(I),Z1(I)
   SUMX = SUMX+ABS(X(I))
   SUMZ1 = SUMZ1+ABS(Z1(I))
   I = I+1
   GO TO 10
20 AVEZ1 = SUMZ1/I
   RETURN
   END

```

```

c
c

```

```

c

```

```

c Subroutine for Calculation of Mean Lower 1/2 Thickness of Tow Cross-
c Section by Mean Value of Integration

```

```

c

```

```

SUBROUTINE THICK2(AVEZ2)
PARAMETER (MaxM=500)
INTEGER I
REAL X,Z2
DIMENSION X(1:MaxM),Z2(1:MaxM)
DATA I,SUMX,SUMZ2 /1,0.0,0.0/
10 READ (80,*,END=20) X(I),Z2(I)
   SUMX = SUMX+ABS(X(I))
   SUMZ2 = SUMZ2+ABS(Z2(I))
   I = I+1
   GO TO 10
20 AVEZ2 = SUMZ2/I
   RETURN
   END

```

```

c
c

```

```

c

```

```

c Subroutine for Calculation of "2-Ply" Laminate Engineering Constants
c From the [ABD]-1 Matrices

```

```

c

```

```

SUBROUTINE ABD1(AVEZ1,AVEZ2)
REAL EXXH,EXXL,EYYH,EYYL,GXYH,GXYL,NXYH,NXYL,NYXH,NYXL,
& DnuH,DnuL,

```

```

& a11h,a11l,a22h,a22l,a66h,a66l,a12h,a12l,b11h,b11l,b22h,b22l,
& d11h,d11l,d22h,d22l,d66h,d66l,d12h,d12l,ht,UCEXXH,UCEXXL,
& UCEYYH,UCEYYL,UCGXYH,UCGXYL,UCNXYH,UCNXYL
DATA NYXH,NYXL,DnuH,DnuL,a11h,a11l /0.0,0.0,0.0,0.0,0.0,0.0/
DATA a22h,a22l,a66h,a66l,a12h,a12l /0.0,0.0,0.0,0.0,0.0,0.0/
DATA b11h,b11l,b22h,b22l,d11h,d11l /0.0,0.0,0.0,0.0,0.0,0.0/
DATA d22h,d22l,d66l,d66l,d12h,d12l /0.0,0.0,0.0,0.0,0.0,0.0/
DATA ht,UCEXXH,UCEXXL,UCEYYH,UCEYYL /0.0,0.0,0.0,0.0,0.0/
DATA UCGXYH,UCGXYL,UCNXYH,UCNXYL /0.0,0.0,0.0,0.0/
REWIND (UNIT=60)
READ (60,*) EXXH
READ (60,*) EXXL
READ (60,*) EYYH
READ (60,*) EYYL
READ (60,*) GXYH
READ (60,*) GXYL
READ (60,*) NXYH
READ (60,*) NXYL
NYXH = (EYYH/EXXH)*NXYH
NYXL = (EYYL/EXXL)*NXYL
DnuH = 1-(NXYH*NYXH)
DnuL = 1-(NXYL*NYXL)
ht = ((AVEZ1+AVEZ2)*2)
a11h = 1/(((EXXH+EYYH)*ht)/(2*DnuH))
a11l = 1/(((EXXL+EYYL)*ht)/(2*DnuL))
a22h = a11h
a22l = a11l
a66h = 1/(GXYH*ht)
a66l = 1/(GXYL*ht)
a12h = 1/((NXYH*EYYH*ht)/(DnuH))
a12l = 1/((NXYL*EYYL*ht)/(DnuL))
b11h = 1/(((EXXH-EYYH)*ht**2)/(8*DnuH))
b11l = 1/(((EXXL-EYYL)*ht**2)/(8*DnuL))
b22h = -b11h
b22l = -b11l
d11h = 1/(((EXXH+EYYH)*ht**3)/(24*DnuH))
d11l = 1/(((EXXL+EYYL)*ht**3)/(24*DnuL))
d22h = d11h
d22l = d11l
d66h = 1/((GXYH*ht**3)/12)
d66l = 1/((GXYL*ht**3)/12)

```

```

d12h = 1/((NXYH*EYYH*ht**3)/(12*DnuH))
d12l = 1/((NXYH*EYYH*ht**3)/(12*DnuH))
UCEXXH = 1/(a11h*ht)
UCEXXL = 1/(a11l*ht)
UCEYYH = 1/(a22h*ht)
UCEYYL = 1/(a22l*ht)
UCGXYH = 1/(a66h*ht)
UCGXYL = 1/(a66l*ht)
UCNXYH = (1/a12h)/(1/a22h)
UCNXYL = (1/a12l)/(1/a22l)
WRITE (90,*) a11h,a11l
WRITE (90,*) a22h,a22l
WRITE (90,*) a66h,a66l
WRITE (90,*) a12h,a12l
WRITE (90,*) b11h,b11l
WRITE (90,*) b22h,b22l
WRITE (90,*) d11h,d11l
WRITE (90,*) d22h,d22l
WRITE (90,*) d66h,d66l
WRITE (90,*) d12h,d12l
WRITE (100,*) UCEXXH,UCEXXL
WRITE (100,*) UCEYYH,UCEYYL
WRITE (100,*) UCGXYH,UCGXYL
WRITE (100,*) UCNXYH,UCNXYL
RETURN
END

```

c

c

c

c Subroutine for Calculation of "10-Ply" or "16-Ply" Laminate Engineering

c Constants From the [ABD]-1 Matrices

c

```

SUBROUTINE ABD2(ExxH,ExxL,EyyH,EyyL,GxyH,GxyL,NxyH,NxyL)
INTEGER N,I,J,K,L
REAL T,H,UCEXXH,UCEXXL,UCEYYH,UCEYYL,UCGXYH,UCGXYL,
& UCNXYH,UCNXYL,UCNYXH,UCNYXL,Q11H,Q11L,SUMQ11H,SUMQ11L,
& Q22H,Q22L,SUMQ22H,SUMQ22L,Q66H,Q66L,SUMQ66H,SUMQ66L,Q12H,
& Q12L,SUMQ12H,SUMQ12L,ExxH,ExxL,EyyH,EyyL,GxyH,GxyL,NxyH,NxyL
DATA H,UCNYXH,UCNYXL,Q11H,Q11L,SUMQ11H /0.0,0.0,0.0,0.0,0.0/

```

```

DATA SUMQ11L,Q22H,Q22L,SUMQ22H,SUMQ22L /0.0,0.0,0.0,0.0,0.0/
DATA Q66H,Q66L,SUMQ66H,SUMQ66L,Q12H,Q12L /0.0,0.0,0.0,0.0,0.0,0.0/
DATA SUMQ12H,SUMQ12L /0.0,0.0/
PRINT*,
PRINT*, 'ENTER NUMBER OF PLIES WITHIN THE COMPOSITE LAMINATE: '
READ*, N
PRINT*,
PRINT*, 'ENTER LAMINATE THICKNESS IN (MM): '
READ*, T
H = T/N
REWIND (UNIT=100)
READ (100,*) UCEXXH,UCEXXL
READ (100,*) UCEYYH,UCEYYL
READ (100,*) UCGXYH,UCGXYL
READ (100,*) UCNXYH,UCNXYL
UCNYXH = (UCEYYH/UCEXXH)*UCNXYH
UCNYXL = (UCEYYL/UCEXXL)*UCNXYL
DO 10 I=1,N
    Q11H = UCEXXH/(1-UCNXYH*UCNYXH)
    Q11L = UCEXXL/(1-UCNXYL*UCNYXL)
    SUMQ11H = SUMQ11H+(Q11H*H)
    SUMQ11L = SUMQ11L+(Q11L*H)
10 CONTINUE
    DO 20 J=1,N
        Q22H = UCEYYH/(1-UCNXYH*UCNYXH)
        Q22L = UCEYYL/(1-UCNXYL*UCNYXL)
        SUMQ22H = SUMQ22H+(Q22H*H)
        SUMQ22L = SUMQ22L+(Q22L*H)
20 CONTINUE
        DO 30 K=1,N
            Q66H = UCGXYH
            Q66L = UCGXYL
            SUMQ66H = SUMQ66H+(Q66H*H)
            SUMQ66L = SUMQ66L+(Q66L*H)
30 CONTINUE
            DO 40 L=1,N
                Q12H = (UCNXYH*UCEYYH)/(1-UCNXYH*UCNYXH)
                Q12L = (UCNXYL*UCEYYL)/(1-UCNXYL*UCNYXL)
                SUMQ12H = SUMQ12H+(Q12H*H)
                SUMQ12L = SUMQ12L+(Q12L*H)
40 CONTINUE

```

```

ExxH = 1/((1/SUMQ11H)*T)
ExxL = 1/((1/SUMQ11L)*T)
EyyH = 1/((1/SUMQ22H)*T)
EyyL = 1/((1/SUMQ22L)*T)
GxyH = 1/((1/SUMQ66H)*T)
GxyL = 1/((1/SUMQ66L)*T)
NxyH = (1/((1/SUMQ12H)*T))/(1/((1/SUMQ22H)*T))
NxyL = (1/((1/SUMQ12L)*T))/(1/((1/SUMQ22L)*T))
WRITE (110,*) ExxH,ExxL
WRITE (110,*) EyyH,EyyL
WRITE (110,*) GxyH,GxyL
WRITE (110,*) NxyH,NxyL
RETURN
END

```

A.1.1. Sample User Input Data

Constituent Fiber and Matrix Data File

```

258.6 ..... (E11 of T650-35 (3k) fibers)
40.0 ..... (E22 of T650-35 (3k) fibers)
24.0 ..... (G12 of T650-35 (3k) fibers)
14.3 ..... (G23 of T650-35 (3k) fibers)
0.26 ..... (ν12 of T650-35 (3k) fibers)
0.72 ..... (Vf of woven tow from image analysis)
4.5 ..... (E11 = E22 of PMR-15 matrix)
1.70 ..... (G12 of PMR-15 matrix)
0.34 ..... (ν12 of PMR-15 matrix)

```

Digitized Coordinates of Upper Tow Perimeter

```

(X) (Z)
-646 18 ..... (X-Z coordinate pairs referenced from tow centroid)
-635 25
-623 30
-610 32

```

-597	34
-585	37
-572	40
-559	42
-546	44
-533	47
-521	50
-508	53
-495	54
-482	55
-469	56
-456	59
-443	62
-430	62
-417	62
-404	65
-392	68
-379	70
-366	70
-353	71
-340	71
-327	71
-314	70
-300	71
-288	73
-275	75
-262	78
-249	80
-236	82
-223	83
-210	84
-197	85
-184	85
-171	85
-158	85
-145	85
-132	86
-119	86
-105	86
-92	86
-79	86

-66	86
-53	86
-40	86
-27	86
-14	86
-1	86
12	86
25	86
38	86
51	85
65	85
78	85
91	86
104	86
117	86
130	86
143	86
156	86
169	86
182	85
195	85
208	84
221	83
234	82
247	81
261	81
274	80
287	79
300	79
313	78
326	77
339	75
352	73
365	73
378	72
391	71
404	69
417	66
429	63
442	61
455	60

468	58
481	55
494	52
506	50
519	47
532	45
545	42
558	39
570	36
583	32
595	29
608	26
619	19
628	10
628	-3

Digitized Coordinates of Lower Tow Perimeter

(Y)	(Z)	
628	-3 (Y-Z coordinate pairs referenced from tow centroid)
624	-15	
614	-25	
604	-32	
592	-38	
579	-41	
567	-46	
554	-51	
541	-54	
528	-55	
516	-59	
503	-62	
490	-62	
477	-65	
464	-68	
451	-70	
438	-71	
424	-71	
411	-72	
398	-73	
385	-74	

372	-75
358	-76
345	-76
332	-77
319	-78
305	-79
292	-80
279	-81
266	-82
253	-83
239	-84
226	-85
213	-85
200	-86
187	-86
173	-87
160	-87
147	-87
134	-88
120	-88
107	-88
94	-89
81	-89
67	-89
54	-89
41	-89
28	-89
14	-88
1	-88
-12	-88
-25	-87
-39	-87
-52	-87
-65	-86
-78	-86
-92	-86
-105	-85
-118	-85
-131	-85
-145	-85
-158	-85

-171	-85
-184	-85
-197	-86
-211	-86
-224	-86
-237	-86
-250	-86
-264	-86
-277	-85
-290	-84
-303	-83
-317	-82
-330	-81
-343	-80
-356	-78
-369	-76
-382	-74
-396	-74
-409	-74
-422	-72
-434	-68
-447	-63
-460	-61
-473	-60
-486	-58
-499	-54
-511	-49
-523	-44
-536	-40
-549	-37
-561	-33
-574	-28
-586	-23
-598	-19
-611	-15
-623	-10
-635	-4
-644	5
-646	18

Digitized Coordinates of Tow Centerline

(X)	(Y)	
31	0 (X-Y coordinate pairs referenced from tow centroid)
61	0	
92	0	
123	0	
154	0	
184	0	
215	-1	
246	0	
276	2	
307	2	
337	-3	
367	-11	
398	-12	
428	-13	
458	-21	
487	-30	
517	-36	
548	-36	
579	-36	
609	-41	
639	-49	
669	-56	
698	-65	
727	-74	
757	-81	
787	-90	
817	-96	
847	-96	
878	-96	
907	-106	
934	-120	
964	-129	
992	-140	
1023	-144	
1053	-144	
1083	-150	

1113	-159
1143	-166
1172	-174
1202	-180
1233	-179
1263	-184
1293	-192
1324	-192
1354	-193
1384	-200
1414	-205
1445	-204
1476	-203
1506	-204
1537	-204
1568	-204
1599	-204
1629	-204
1660	-204
1691	-204
1722	-204
1752	-203
1783	-204
1814	-205
1844	-202
1874	-196
1905	-192
1935	-192
1966	-189
1996	-181
2025	-174
2055	-166
2084	-156
2114	-148
2144	-141
2174	-134
2203	-124
2232	-115
2261	-104
2290	-96
2321	-96

2352	-96
2381	-89
2410	-79
2440	-72
2471	-72
2502	-73
2532	-68
2562	-60
2592	-59
2623	-60
2653	-54
2682	-44
2711	-35
2742	-36
2773	-36
2804	-36
2834	-36
2865	-36
2896	-36
2926	-36
2957	-36
2988	-36
3019	-36

A.2. FORTRAN 77 Code: The Methods of Hashin, Halpin-Tsai and Chamis

In A.2. of this Appendix, compiler-ready example code, in Fortran 77 format, is given for predicting woven fabric elastic constants based on the established methods of Hashin, Halpin-Tsai and Chamis as referenced in Section 3. These methods are used as a basis of evaluating the finite element analysis results for prediction of constituent properties.

A.2.1. The Method of Hashin

PROGRAM HASHIN

c

c This Fortran 77 program calculates the elastic constants of a unidirectional composite

c lamina from constituent elastic properties according to the micromechanical relations
 c proposed by Hashin and Rosen: Composite Cylinder Assemblage (CCA)

c

c

c Output Variables:

c E11: longitudinal elastic modulus (GPa)
 c E22high: upper bound transverse elastic modulus (GPa)
 c E22low: lower bound transverse elastic modulus (GPa)
 c G12: shear modulus (GPa)
 c G23high: upper bound transverse shear modulus (GPa)
 c G23low: lower bound transverse shear modulus (GPa)
 c nu12: major Poisson's ratio

c Input Variables:

c Ef: longitudinal fiber elastic modulus (GPa)
 c Eft: transverse fiber elastic modulus (GPa)
 c Em: longitudinal matrix elastic modulus (GPa)
 c Gf: fiber shear modulus (GPa)
 c Gft: fiber transverse shear modulus (GPa)
 c Gm: matrix shear modulus (GPa)
 c nuf: fiber Poisson's ratio
 c num: matrix Poisson's ratio
 c vf: fiber volume fraction

c

c Inter-calculated Variables:

c gamma
 c rho
 c betaf
 c betam
 c alpha
 c Gthigh: bounded transverse shear modulus
 c Gtlow: bounded transverse shear modulus
 c Gm1
 c Gm2
 c Gm3
 c Gm4
 c kt: transverse bulk modulus
 c kf: fiber bulk modulus
 c km: matrix bulk modulus

c

c

REAL E11,E22high,E22low,G12,G23high,G23low,nu12,Ef,Eft,Em,Gf,Gft,

```
& Gm,nuf,num,vf,vm,gamma,rho,betaf,betam,alpha,Gthigh,Gtlow,  
& Gm1,Gm2,Gm3,Gm4,kt,kf,km  
c  
c All variables initially set to zero  
c  
E11 = 0.0  
E22high = 0.0  
E22low = 0.0  
G12 = 0.0  
G23high = 0.0  
G23low = 0.0  
nu12 = 0.0  
Ef = 0.0  
Eft = 0.0  
Em = 0.0  
Gf = 0.0  
Gft = 0.0  
Gm = 0.0  
nuf = 0.0  
num = 0.0  
vf = 0.0  
vm = 0.0  
gamma = 0.0  
rho = 0.0  
betaf = 0.0  
betam = 0.0  
alpha = 0.0  
Gthigh = 0.0  
Gtlow = 0.0  
Gm1 = 0.0  
Gm2 = 0.0  
Gm3 = 0.0  
Gm4 = 0.0  
kt = 0.0  
kf = 0.0  
km = 0.0  
c  
c Constituent properties input from user screen  
c  
PRINT*, 'Enter fiber longitudinal tensile modulus in (GPa) '  
READ*, Ef
```

```

PRINT*, 'Enter fiber transverse tensile modulus in (GPa) '
READ*, Eft
PRINT*, 'Enter fiber shear modulus in (GPa) '
READ*, Gf
PRINT*, 'Enter fiber transverse shear modulus in (GPa) '
READ*, Gft
PRINT*, 'Enter fiber Poissons ratio '
READ*, nuf
PRINT*, 'Enter fiber volume fraction '
READ*, vf
PRINT*, 'Enter matrix tensile modulus in (GPa) '
READ*, Em
PRINT*, 'Enter matrix shear modulus in (GPa) '
READ*, Gm
PRINT*, 'Enter matrix Poissons ratio '
READ*, num

c
c Begin inter-calculations
c
vm = 1-vf
gamma = Gft/Gm
kf = ((4/Eft)-(4*nuf**2/Eft)-(1/Gft))**(-1)
km = ((4/Em)-(4*num**2/Em)-(1/Gm))**(-1)
betaf = kf/(kf+2*Gft)
betam = km/(km+2*Gm)
rho = (gamma+betam)/(gamma-1)
alpha = (betam-(gamma*betaf))/(1+(gamma*betaf))
kt1 = (km*(kf+Gm)*(1-vf)+(kf*vf*(km+Gm))
kt2 = ((kf+Gm)*(1-vf)+(vf*(km+Gm))
kt = kt1/kt2

c
c Upper bounds calculations for Gft > Gm
c
If (Gft.GT.Gm) then
  Gm1 = (1+betam)*vf
  Gm2 = rho-(vf*(1+((3*betam**2*vm**2)/(alpha*vf**3+1))))
  Gm3 = 1/(Gft-Gm)
  Gm4 = ((km+2*Gm)*vm)/(2*Gm*(km+Gm))
  Gthigh = Gm*(1+(Gm1/Gm2))
  Gtlow = Gm+(vf/(Gm3+Gm4))

```



```

c Lower bounds calculations for  $G_{ft} < G_m$ 
c
  Elseif ( $G_{ft} < G_m$ ) then
     $G_{m1} = 1/(G_{ft} - G_m)$ 
     $G_{m2} = ((k_m + 2 * G_m) * v_m) / (2 * G_m * (k_m + G_m))$ 
     $G_{m3} = (1 + \beta_{em}) * v_f$ 
     $G_{m4} = \rho - (v_f * (1 + ((3 * \beta_{em} ** 2 * v_m ** 2) / (\alpha * v_f ** 3 - \beta_{em}))))$ 
     $G_{thigh} = G_m + (v_f / (G_{m1} + G_{m2}))$ 
     $G_{tlow} = G_m * (1 + (G_{m3} / G_{m4}))$ 
  Endif
c
c Begin lamina elastic constant calculations
c
   $E_{11} = E_f * v_f + E_m * v_m + ((4 * v_f * v_m * (\nu_f - \nu_m) ** 2) / (v_m / k_f + v_f / k_m + 1 / G_m))$ 
   $\nu_{12} = \nu_f * v_f + \nu_m * v_m + ((v_f * v_m * (\nu_f - \nu_m) * (1 / k_m - 1 / k_f))$ 
  &  $/ (v_m / k_f + v_f / k_m + 1 / G_m))$ 
   $E_{22high} = (4 * k_t * G_{thigh}) / (k_t + (1 + (4 * k_t * \nu_{12} ** 2 / E_{11})) * G_{thigh})$ 
   $E_{22low} = (4 * k_t * G_{tlow}) / (k_t + (1 + (4 * k_t * \nu_{12} ** 2 / E_{11})) * G_{tlow})$ 
   $G_{12} = G_m * ((v_m * G_m + (1 + v_f) * G_f) / ((1 + v_f) * G_m + v_m * G_f))$ 
   $G_{23high} = G_{thigh}$ 
   $G_{23low} = G_{tlow}$ 
c
c Output results
c
  PRINT *,
  PRINT *,
  PRINT 10, E11
10 FORMAT (1X,'Longitudinal Tensile Modulus of Lamina (E11) = ',F6.1)
  PRINT *,
  PRINT 20, E22high
20 FORMAT (1X,'Upper Bound Transverse Tensile Modulus of Lamina'
  & ' (E22high) = ',F5.1)
  PRINT *,
  PRINT 30, E22low
30 FORMAT (1X,'Lower Bound Transverse Tensile Modulus of Lamina'
  & ' (E22low) = ',F5.1)
  PRINT *,
  PRINT 40, G12
40 FORMAT (1X,'In-Plane Shear Modulus of Lamina (G12) = ',F5.1)
  PRINT *,
  PRINT 50, G23high

```

```

50 FORMAT (1X,'Upper Bound Transverse Shear Modulus of Lamina'
&      '(G23high) =',F5.1)
PRINT *,
PRINT 60, G23low
60 FORMAT (1X,'Lower Bound Transverse Shear Modulus of Lamina'
&      '(G23low) =',F5.1)
PRINT *,
PRINT 70, nu12
70 FORMAT (1X,'Poissons Ratio of Lamina (nu12) =',F5.2)
c
END

```

A.2.2. The Method of Halpin-Tsai

```

PROGRAM HLPTSAI
c
c This Fortran program calculates the elastic constants of a unidirectional composite
c lamina from constituent elastic properties according to the micromechanical relations
c proposed by Halpin and Tsai.
c
c
c Output Variables:
c      E11: longitudinal elastic modulus (GPa)
c      E22: transverse elastic modulus (GPa)
c      G12: shear modulus (GPa)
c      nu12: major Poisson's ratio
c      nu23: minor Poisson's ratio
c Input Variables:
c      Ef: longitudinal fiber elastic modulus (GPa)
c      Em: longitudinal matrix elastic modulus (GPa)
c      Gf: fiber shear modulus (GPa)
c      Gm: matrix shear modulus (GPa)
c      nuf: fiber Poisson's ratio
c      num: matrix Poisson's ratio
c      vf: fiber volume fraction
c
c
c REAL E11,E22,G12,nu12,nu23,Ef,Em,Gf,Gm,nuf,num,vf,zetaE,zetaG,
&      zetaNu,nE,nG,nNu
c

```

c All variables initially set to zero

c

```

E11 = 0.0
E22 = 0.0
G12 = 0.0
nu12 = 0.0
nu23 = 0.0
Ef = 0.0
Em = 0.0
Gf = 0.0
Gm = 0.0
nuf = 0.0
num = 0.0
vf = 0.0
zetaE = 0.0
zetaG = 0.0
zetaNu = 0.0
nE = 0.0
nG = 0.0
nNu = 0.0

```

c

c Constituent properties input from user screen

c

```

PRINT*, 'Enter fiber longitudinal tensile modulus in (GPa) '
READ*, Ef
PRINT*, 'Enter fiber shear modulus in (GPa) '
READ*, Gf
PRINT*, 'Enter fiber Poissons ratio '
READ*, nuf
PRINT*, 'Enter fiber volume fraction '
READ*, vf
PRINT*, 'Enter matrix tensile modulus in (GPa) '
READ*, Em
PRINT*, 'Enter matrix shear modulus in (GPa) '
READ*, Gm
PRINT*, 'Enter matrix Poissons ratio '
READ*, num

```

c

c

c Begin lamina elastic constant calculations

c

```

zetaE = 0.75
zetaG = 0.75
zetaNu = 0.10
E11 = Ef*vf+Em*(1-vf)
nE = ((Ef/Em)-1)/((Ef/Em)+zetaE)
nG = ((Gf/Gm)-1)/((Gf/Gm)+zetaG)
nNu = ((nuf/num)-1)/((nuf/num)+zetaNu)
E22 = Em*((1+zetaE*nE*vf)/(1-zetaE*vf))
G12 = Gm*((1+zetaG*nG*vf)/(1-zetaG*vf))
nu12 = nuf*vf+num*(1-vf)
nu23 = num*((1+zetaNu*nNu*vf)/(1-zetaNu*vf))
c
c  Output results
c
  PRINT *,
  PRINT *,
  PRINT 10, E11
10 FORMAT (1X,'Longitudinal Tensile Modulus of Lamina (E11) = ',F6.1)
  PRINT *,
  PRINT 20, E22
20 FORMAT (1X,'Transverse Tensile Modulus of Lamina (E22) = ',F6.1)
  PRINT *,
  PRINT 30, G12
30 FORMAT (1X,'In-Plane Shear Modulus of Lamina (G12) = ',F6.1)
  PRINT *,
  PRINT 40, nu12
40 FORMAT (1X,'Poissons Ratio of Lamina (nu12) = ',F4.2)
  PRINT *,
  PRINT 50, nu23
50 FORMAT (1X,'Poissons Ratio of Lamina (nu23) = ',F4.2)
c
  END

```

A.2.3. The Method of Chamis

```

PROGRAM CHAMIS
c
c  This Fortran program calculates the elastic constants of a unidirectional composite

```

c lamina from constituent elastic properties according to the micromechanical relations
 c proposed by Chamis.

c

c

c Output Variables:

c E11: longitudinal elastic modulus (GPa)

c E22: transverse elastic modulus (GPa)

c G12: shear modulus (GPa)

c G23: transverse shear modulus (GPa)

c nu12: major Poisson's ratio

c nu23: transverse Poisson's ratio

c Input Variables:

c Ef: longitudinal fiber elastic modulus (GPa)

c Eft: transverse fiber elastic modulus (GPa)

c Em: longitudinal matrix elastic modulus (GPa)

c Gf: fiber shear modulus (GPa)

c Gft: fiber transverse shear modulus (GPa)

c Gm: matrix shear modulus (GPa)

c nuf: fiber Poisson's ratio

c num: matrix Poisson's ratio

c vf: fiber volume fraction

c

c

REAL E11,E22,G12,G23,nu12,nu23,Ef,Eft,Em,Gf,Gft,Gm,nuf,num,vf,vm

c

c All variables initially set to zero

c

E11 = 0.0

E22 = 0.0

G12 = 0.0

G23 = 0.0

nu12 = 0.0

nu23 = 0.0

Ef = 0.0

Eft = 0.0

Em = 0.0

Gf = 0.0

Gft = 0.0

Gm = 0.0

nuf = 0.0

num = 0.0

```

vf = 0.0
vm = 0.0
c
c  Constituent properties input from user screen
c
PRINT*, 'Enter fiber longitudinal tensile modulus in (GPa) '
READ*, Ef
PRINT*, 'Enter fiber transverse tensile modulus in (GPa) '
READ*, Eft
PRINT*, 'Enter fiber shear modulus in (GPa) '
READ*, Gf
PRINT*, 'Enter fiber transverse shear modulus in (GPa) '
READ*, Gft
PRINT*, 'Enter fiber Poissons ratio '
READ*, nuf
PRINT*, 'Enter fiber volume fraction '
READ*, vf
PRINT*, 'Enter matrix tensile modulus in (GPa) '
READ*, Em
PRINT*, 'Enter matrix shear modulus in (GPa) '
READ*, Gm
PRINT*, 'Enter matrix Poissons ratio '
READ*, num
c
c
c  Begin lamina elastic constant calculations
c
vm = 1-vf
E11 = (Ef*vf)+(Em*vm)
E22 = Em/(1-vf*(1-(Em/Eft)))
G12 = Gm/(1-vf*(1-(Gm/Gf)))
G23 = Gm/(1-vf*(1-(Gm/Gft)))
nu12 = (nuf*vf)+(num*vm)
nu23 = (E22/(2*G23))-1
c
c  Output results
c
PRINT *,
PRINT *,
PRINT 10, E11
10 FORMAT (1X,'Longitudinal Tensile Modulus of Lamina (E11) = ',F6.1)

```

```
PRINT *,
PRINT 20, E22
20 FORMAT (1X,'Transverse Tensile Modulus of Lamina (E22) = ',F6.1)
PRINT *,
PRINT 30, G12
30 FORMAT (1X,'In-Plane Shear Modulus of Lamina (G12) = ',F6.1)
PRINT *,
PRINT 40, G23
40 FORMAT (1X,'Transverse Shear Modulus of Lamina (G23) = ',F6.1)
PRINT *,
PRINT 50, nu12
50 FORMAT (1X,'Poissons Ratio of Lamina (nu12) = ',F4.2)
PRINT *,
PRINT 60, nu23
60 FORMAT (1X,'Poissons Ratio of Lamina (nu23) = ',F4.2)
c
END
```

APPENDIX B

B.1. ANSYS User Files - 8HS Woven Lamina Stress Analysis

In B.1.1. of this appendix, a user input file is presented in ANSYS 5.3 format for evaluating the elastic properties of woven tows from constituent fiber and matrix properties. The tows are treated as UD composites which are represented by a single fiber embedded in a continuous matrix. The model is a square array and takes advantage of symmetry where possible. Elastic properties are evaluated from both volume averaging and reaction force summation methods using linearly independent boundary conditions. In B.1.2. of this appendix, results from the single fiber model are transferred to a 3-D model of a 8HS woven IVE. From this model, lamina elastic properties are evaluated using the same techniques as for the single fiber case. Stresses are also studied for three fundamental loading conditions, namely uniaxial tension, compression and in-plane shear. Stresses in the direction of loading and out-of-plane are compared on the basis of three parallel planes which cut through the thickness at specific locations within the IVE.

B.1.1. 1/4 Symmetry 3-D Square Array RVE

```
/FILNAM,QTRAXIAL_3D
/TITLE,Prediction of Woven Tow Elastic Constants Based on Constituent Properties
/STITLE,2,Square Array RVE Analysis
/UNITS,SI
/GRAPHICS,POWER
/PREP7
LOCAL,11,0,0,0,0,0,0,-90
CSYS,11
WPCSYS,,11
```



```

MOPT,LSMO,ON
BOPT,NUMB,OFF
ET,1,SOLID92          ! 10-node isoparametric tetrahedral element
ET,2,SOLID92
MP,EX,1,234.5e9      ! Graphite fiber elastic properties
MP,EY,1,13.8e9
MP,GXY,1,11.4e9
MP,GYZ,1,4.8e9
MP,NUXY,1,0.2
MP,NUXZ,1,0.25
MP,NUYZ,1,0.25
MP,EX,2,3.3e9       ! PMR-15 matrix elastic properties
MP,EY,2,3.3e9
MP,GXY,2,1.2e9
MP,NUXY,2,0.35
R,1
R,2
!
! This model treats the lenticular woven tow as a unidirectional composite material from
! which the fiber and matrix are idealized as a square array representative volume
! element (RVE). Based on the elastic properties of the constituents, the tow properties
! are predicted according to work and strain energy equivalence principles. The results
! are used as input for constituent properties in the 8-H Woven RVE analysis.
!
! All scalar values are in microns unless otherwise noted.
!
! Definition of the cross-sectional fiber geometry
f_diam=7.37          ! sized filament diameter of 7.37 microns
a=7.75              ! RVE dimensions for equivalent Vf = 0.71
b=a
c=b
CYL4,0,0,(f_diam/2),0,(f_diam/2),360,-(a/2)
/VIEW,1,1,1,1      ! switching to isometric view
/VUP,1,Z
!
! Definition of cutting planes for 1/4 symmetry
WPROTA,0,0,90
VSBW,ALL,SEPO
VDELE,3,,1
WPROTA,0,-90,0
VSBW,ALL,SEPO

```

```

VDELE,3,,1
!
! Definition of surrounding matrix geometry
WPROTA,0,90,0
WPROTA,0,0,-90
BLC5,0,0,b,c,-(a/2)
!
! Definition of cutting planes for 1/4 symmetry
WPROTA,0,0,90
VSBW,2,SEPO
VDELE,4,,1
WPROTA,0,-90,0
VSBW,3,SEPO
VDELE,4,,1
WPROTA,0,90,0
WPROTA,0,0,-90
NUMCMP,ALL
!
! Performing Boolean subtraction of fiber from matrix
VSBV,2,1,,KEEP
NUMCMP,ALL
!
! Meshing fiber 1/4 volume
VATT,1,1,1,0
ESHAPE,1,0
ESIZE,(f_diam)/5
MAT,1
REAL,1
TYPE,1
ESYS,0
VMESH,1
!
! Meshing matrix 1/4 volume
VATT,2,2,2,0
ESHAPE,1,0
ESIZE,a/5
MAT,2
REAL,2
TYPE,2
ESYS,0
VMESH,2

```

```
!  
! Defining fiber color separation  
VSEL,S,VOLU,,1  
ESLV,S,1  
/COLOR,ELEM,BLUE  
/COLOR,VOLU,BLUE  
/COLOR,OUTL,BLAC  
ESEL,ALL  
VSEL,ALL  
!  
! Defining matrix color separation  
VSEL,S,VOLU,,2  
ESLV,S,1  
/COLOR,ELEM,YELL  
/COLOR,VOLU,YELL  
/COLOR,OUTL,BLAC  
ESEL,ALL  
VSEL,ALL  
EPLOT  
FINISH  
/SOLU  
DISP=1  
!  
!Definition of the analysis type and analysis options  
ANTYP,STAT,NEW  
NROPT,1,,ON  
EQSLV,FRONT  
!  
! Definition of boundary conditions  
ASEL,S,AREA,,2  
ASEL,A,AREA,,11  
NSLA,S,1  
D,ALL,ALL,0  
NSEL,ALL  
ASEL,ALL  
ASEL,S,AREA,,1  
ASEL,A,AREA,,10  
NSLA,S,1  
D,ALL,UX,DISP  
NSEL,ALL  
ASEL,ALL
```

```

SAVE
SOLVE
SAVE
/POST1
SET, LAST
!
! Determination of surface tractions (P) normal to X-Y PLANE
ASEL, S, AREA, , 1
ASEL, A, AREA, , 10
NSLA, S, 1
NFOR
ALLSEL
!
! Determination of NU12
PRNSOL, EPEL, COMP
FINISH
SAVE
/EXIT, ALL

```

B.1.2. 8HS Woven 3-D IVE

```

/FILNAM, WEAVE_3D
/TITLE, Idealized Three-Dimensional Hybrid Analysis of 8-H Woven RVE
/STITLE, 2, Prediction of Composite Elastic Constants
/UNITS, SI
/GRAPHICS, POWER
/PREP7
MOPT, LSMO, ON
BOPT, NUMB, OFF
SHPP, OFF
ET, 1, SOLID92 ! 10-node isoparametric tetrahedral element
ET, 2, SOLID92
ET, 3, SOLID92
MP, EX, 1, 9.2e9 ! Graphite fiber warp/fill tow elastic properties
MP, EY, 1, 9.2e9
MP, EZ, 1, 169.8e9
MP, GXZ, 1, 4.6e9
MP, GXY, 1, 3.1e9
MP, GYZ, 1, 3.1e9

```

```

MP,NUXZ,1,0.24
MP,NUXY,1,0.38
MP,NUYZ,1,0.38
MP,EX,2,51.7e9           ! Tow undulation elastic properties
MP,EY,2,9.2e9
MP,EZ,2,51.7e9
MP,GXZ,2,4.5e9
MP,NUXZ,2,0.05
MP,EX,3,3.3e9           ! PMR-15 matrix elastic properties
MP,NUXY,3,0.35
R,1
R,2
R,3
! This model predicts the composite elastic properties based on input of the constituent
! elastic properties. The model is based on the periodicity of a representative volume
! element (RVE) for 8-H satin graphite-polyimide. The model assumes that the lenticular
! cross-section is ideal, however the exact aspect ratio and fiber volume fraction obtained
! from photomicrographs is intact.
!
! All scalar values are in microns unless otherwise noted.
!
! Definition of perimeter keypoints from lenticular tow shape
a_mod=(sqrt(8))/3.0
K,1,-((1393.6*a_mod)/2.0),0,0
K,2,((1393.6*a_mod)/2.0),0,0           ! 8.3:1 aspect ratio
K,3,0,(1393.6*a_mod)/(8.3*2.0),0
K,4,0,-((1393.6*a_mod)/(8.3*2.0)),0
!
! Definition of lenticular half B-splines
BSPLIN,1,3,2
BSPLIN,1,4,2
LDIV,2,0.5
!
! Definition of tow cross-sectional area
AL,ALL
APLOT
!
! Definition of representative volume element (RVE) dimensions
*GET,dim_1,KP,2,LOC,X
*GET,dim_2,KP,1,LOC,X
*GET,dim_3,KP,3,LOC,Y

```

```

*GET,dim_4,KP,4,LOC,Y
a=(dim_1)-(dim_2)
b=(dim_3)-(dim_4)
!
! Definition of matrix volume fraction multiplier
vf=1.175                                ! Vf = 0.62
!
! Copying x-sectional shape to other tow locations
AGEN,2,1,,,a,0,0,0,1,0                  ! defining top laminae plane
AGEN,2,1,,, -a,0,0,0,1,0
!
! Definition of outer tow top matrix cross-section
K,12,a/2.0,b*vf/2.0,0
K,13,3*a/2.0,b*vf/2.0,0
K,14,-a/2.0,b*vf/2.0,0
K,15,-3*a/2.0,b*vf/2.0,0
LSTR,6,12
LSTR,7,13
LSTR,12,13
LSTR,10,14
LSTR,9,15
LSTR,14,15
AL,7,14,15,13
AL,4,10,12,11
K,16,a/2.0,-b/2.0,0
K,17,3*a/2.0,-b/2.0,0
K,18,-a/2.0,-b/2.0,0
K,19,-3*a/2.0,-b/2.0,0
LSTR,6,16
LSTR,7,17
LSTR,8,16
LSTR,8,17
LSTR,10,18
LSTR,9,19
LSTR,11,19
LSTR,11,18
AL,18,16,6
AL,19,5,17
AL,21,9,22
AL,23,8,20
!

```

```

! Extrusion of boundary tow and matrix areas into volumes
/VIEW,1,1,1,1 ! switching to isometric view
VEXT,2,9,1,0,0,-3*a
VPLOT
!
! Defining warp tow undulation to "skin" fill tow surface
ASEL,S,AREA,,1
LSLA,S,1
KSLI,S,1
LGEN,2,1,,,a,0,0,0,1,0
LGEN,2,3,,,0,0,0,0,1,0
LDIV,58,0.5
NUMCMP,ALL
K,39,3*a/2.0,b/2.0,0
LSTR,38,39
LDELETE,60,,,1
NUMCMP,ALL
!
! Reflecting, rotating and translating undulation drag path
LSEL,S,LINE,,58,60,1
LSYMM,X,58,60,1,0,1,0
LOCAL,11,0,0,0,0,0,0,90
CSYS,0
LTRAN,11,58,63,1,0,1,1
LGEN,1,58,63,1,0,-b/2,-(3*a)/2.0,0,1,1
ALLSEL
NUMCMP,ALL
LPLOT
!
! Definition of center tow boundary matrix
LSTR,14,12
LSTR,18,5
LSTR,16,5
LGLUE,2,65,20
LGLUE,66,3,16
LGLUE,1,13,64,10
AL,1,69,64,70
AL,2,65,67
AL,3,66,68
NUMCMP,ALL
!

```

```

! Dragging tow/matrix x-sectional areas to form undulated volumes
LGLUE,63,61,62,59,58,60
NUMCMP,ALL
VDRAG,1,38,39,40,,,61
VGEN,2,9,12,1,0,0,-5*a/2.0,0,0,0
VDRAG,44,,,,,60,70,69,58
LDELE,58,61,1,1
LDELE,69,70,1,1
NUMCMP,ALL
L PLOT
!
! Definition of fill matrix at inner boundary
K,67,-a/2.0,b/2.0*vf,-2*a
K,68,a/2.0,b/2.0*vf,-2*a
AGEN,2,63,,,0,0,0,0,0,0
AGEN,2,85,,,0,0,0,0,0,0
LSTR,74,68
LSTR,73,67
LSTR,67,72
LSTR,68,71
LSTR,67,68
LGLUE,140,136,139,134,138
AL,142,143,136,146
AL,141,144,134,147
AL,137,141,145,142
AL,145,143,135,144
AGLUE,89,90,91,92,93,94
VA,89,91,92,93,94,95
LOCAL,12,0,0,0,-1.5*a
CSYS,12
VSYMM,Z,21,,,0,0,0
CSYS,0
!
! Modification of fill matrix at inner boundary
WPOFFS,-1.5*a,0,-a
VSBW,5,SEPO
VSBW,8,SEPO
WPOFFS,0,0,-a
VSBW,24,SEPO
VSBW,25,SEPO
VDELE,26,27,1,1

```


NUMCMP,ALL
 VPLOT
 AGEN,2,49,53,4,0,0,-a/2,0,0,0
 AINA,74,114
 L,101,96
 LCOMB,186,183,0
 LSTR,40,84
 LGLUE,154,183,68
 AL,185,186,68
 AL,68,79,81
 LGLUE,81,184,186
 AL,81,184,183
 LGLUE,79,185
 LGLUE,184,185
 AL,79,184,187
 AGLUE,115,117,114,116
 VA,118,119,114,120
 ADELE,113,..1
 VSYMM,X,25,..,0,0,0
 LOCAL,13,0,0,0,-1.5*a
 CSYS,13
 VSYMM,Z,25,..,0,1,0
 VOVLAP,ALL
 VDELE,28,30,1,1
 VSYMM,Z,37,..,0,1,0 ! non-overlapped volume
 CSYS,0
 NUMCMP,ALL
 !
 ! Manual repair of non-overlapped volume
 VDELE,1,..,0
 ADELE,1,..,0
 ADELE,11,13,1,0
 LSYMM,X,69,..,0,1,0
 LGLUE,167,75,78
 AL,75,71,78
 AL,1,2,3
 AL,29,3,27
 AGLUE,104,11,12,1
 VA,1,13,125,126
 BTOL,1E-03
 VGLUE,ALL

```

NUMCMP,ALL
!
! Definition of inner crimp boundary fill matrix
LOCAL,14,0,0,-b/2.0,0
VSYMM,Y,8,10,2,0,0,0
LOCAL,15,0,3*a/2.0,0,-3*a/2.0,0,0,90
CSYS,0
VTRAN,15,29,30,1,,1
AGEN,2,136,,1.5*a,0,0,0,1,0
ASBA,138,42
ADELE,140,,0
LDELE,190,191,1,1
LGEN,2,177,,a/2,0,0,0,1,0
LCOMB,195,193,0
LCOMB,195,194,0
LDELE,195,,1
LGLUE,104,189,191
AL,195,196,104
LGLUE,80,164,190,195
AL,189,197,191,80
AGLUE,138,139
AGLUE,142,141,124,48,140
VA,144,143,139,138,145
LOCAL,16,0,0,0,-1.5*a
CSYS,16
VSYMM,X,31,,0,1,0
BTOL,1E-04
VGLUE,31,32
NUMCMP,ALL
VSYMM,Z,31,32,1,0,1,0
CSYS,0
VDELE,29,30,1,1
NUMCMP,ALL
!
! Reflecting and rotating tow plane about axis
LOCAL,17,0,0,-b/2.0,0
VSYMM,Y,1,32,1,0,0,0
LOCAL,18,0,3*a/2.0,0,-3*a/2.0,0,0,90
CSYS,0
VTRAN,18,33,64,1,,1
!

```

```

! Definition of top crimp fill matrix
LGEN,2,213,215,2,-a/2,-b/2,0,0,1,0
LGEN,2,213,215,2,a/2,-b/2,0,0,1,0
LCOMB,383,384,0
LCOMB,385,386,0
LGLUE,2,115,383,385
AL,2,115,384,386
LSTR,58,158
LSTR,56,136
LSTR,56,58
LGLUE,158,383,384,385
AL,158,383,387,388
LSTR,59,168
LSTR,57,165
LSTR,57,59
LGLUE,159,385,386,389
AL,159,385,390,391
AL,90,91,158,159
AGLUE,92,123,287,288,289,290
VA,92,123,287,290,291,292
!
! Reflecting and rotating top crimp fill matrix to bottom side
LOCAL,18,0,0,-b/2,0,0
VSYMM,Y,65,0,0,0
LOCAL,19,0,3*a/2,0,0,-3*a/2,0,0,90
CSYS,0
VTRAN,19,66,,,0,1,1
!
! Repair of areas within undulation
VSEL,S,VOLU,,3
VSEL,A,VOLU,,20,21,1
VSEL,A,VOLU,,24,26,1
VSEL,A,VOLU,,35
VSEL,A,VOLU,,52,53,1
VSEL,A,VOLU,,56,58,1
VPLOT
VDELE,35,52,17,1
VDELE,3,20,17,1
AL,82,115,116
AL,337,340,341
AL,1,2,118

```

```
AL,207,211,214
LCOMB,82,116,0
LCOMB,340,341,0
LCOMB,1,118,0
LCOMB,211,214,0
LGLUE,115,86,2,84
LGLUE,3,337,85,207
AL,2,87,88,89
AL,3,84,85,86
AGLUE,29,39,42,107,108,155
VA,29,109,152,153,154,156
VGLUE,ALL
VSEL,A,VOLU,,11,12,1
VSEL,A,VOLU,,43,44,1
VGLUE,11,12,43,44
VPLOT
NUMCMP,ALL
!
! Meshing warp tows
VSEL,S,VOLU,,18
VSEL,A,VOLU,,49
VSEL,A,VOLU,,52,54,1
VSEL,A,VOLU,,63
VATT,1,1,1,0
ESHAPE,1,0
ESIZE,(3*a)/12
MAT,1
REAL,1
TYPE,1
ESYS,0
VMESH,ALL
ESLV,S,1
/COLOR,ELEM,RED           ! warp tow color separation
/COLOR,VOLU,RED
/COLOR,OUTL,BLAC
ALLSEL
!
! Meshing fill tows
LOCAL,11,0,0,0,0,0,-90
VSEL,S,VOLU,,19
VSEL,A,VOLU,,22,24,1
```

```

VSEL,A,VOLU,,33
VSEL,A,VOLU,,48
VATT,1,1,1,11
ESHAPE,1,0
ESIZE,(3*a)/12
MAT,1
REAL,1
TYPE,1
ESYS,11
VMESH,ALL
CSYS,0
ESLV,S,1
/COLOR,ELEM,DGRA           ! fill tow color separation
/COLOR,VOLU,DGRA
/COLOR,OUTL,BLAC
ALLSEL
!
! Meshing tow undulation
VSEL,S,VOLU,,3
VATT,2,2,2,0
ESHAPE,1,0
ESIZE,(3*a)/12
MAT,2
REAL,2
TYPE,2
ESYS,0
VMESH,ALL
ESLV,S,1
/COLOR,ELEM,RED
/COLOR,VOLU,RED
/COLOR,OUTL,BLAC
ALLSEL
EPlot
!
! Meshing matrix
VSEL,S,VOLU,,3
VSEL,A,VOLU,,18,19,1
VSEL,A,VOLU,,22,24,1
VSEL,A,VOLU,,33
VSEL,A,VOLU,,48,49,1
VSEL,A,VOLU,,52,54,1

```

```

VSEL,A,VOLU,,63
VSEL,INVE
VPLOT
VGLUE,6,11,61,26,7
VGLUE,37,56,62,41,36
VATT,3,3,3,0
ESHAPE,1,0
ESIZE,(3*a)/12
MAT,3
REAL,3
TYPE,3
ESYS,0
VMESH,ALL
ESLV,S,1
/COLOR,ELEM,YELL           ! matrix color separation
/COLOR,VOLU,YELL
/COLOR,OUTL,BLAC
ALLSEL
EPLOT
NUMCMP,ALL
NUMMRG,ALL
CPINTF,ALL
FINISH
/SOLU
DISP=5.0
!
! Definition of the analysis type and analysis options
ANTYP,STAT,NEW
NROPT,1,,ON
EQLV,FRONT
!
! Definition of boundary conditions
ASEL,S,AREA,,199,219,20     ! x = -(sqrt(8)*a)/2
ASEL,A,AREA,,178,251,73
ASEL,A,AREA,,203,213,10
ASEL,A,AREA,,158,192,34
ASEL,A,AREA,,237,249,12
ASEL,A,AREA,,163,258,95
ASEL,A,AREA,,14,22,8
NSLA,S,1
D,ALL,UX,0

```

```

!D,ALL,UY,0
!D,ALL,UZ,0
NSEL,ALL
ASEL,ALL
ASEL,S,AREA,,202,212,10      ! x = (sqrt(8)*a)/2
ASEL,A,AREA,,171,243,72
ASEL,A,AREA,,198,218,20
ASEL,A,AREA,,162,190,28
ASEL,A,AREA,,151,246,95
ASEL,A,AREA,,157,183,26
ASEL,A,AREA,,16,20,4
NSLA,S,1
D,ALL,UX,DISP
!D,ALL,UY,0
!D,ALL,UZ,0
NSEL,ALL
ASEL,ALL
ASEL,S,AREA,,1,8,1          ! z = 0
ASEL,A,AREA,,34,43,9
ASEL,A,AREA,,49,62,13
ASEL,A,AREA,,164,217,53
NSLA,S,1
!D,ALL,UX,0
!D,ALL,UY,0
!D,ALL,UZ,0
NSEL,ALL
ASEL,ALL
ASEL,S,AREA,,9,12,3        ! z = -(sqrt(8)*a)
ASEL,A,AREA,,13,21,2
ASEL,A,AREA,,37,83,46
ASEL,A,AREA,,52,55,3
ASEL,A,AREA,,66,160,94
ASEL,A,AREA,,220
NSLA,S,1
!D,ALL,UX,0
!D,ALL,UY,0
!D,ALL,UZ,0
NSEL,ALL
ASEL,ALL
SAVE
SOLVE

```

```

SAVE
FINISH
/POST1
SET, LAST
!
! Determination of equivalent force (P) normal to Y-Z PLANE
ASEL, S, AREA, , 202, 212, 10
ASEL, A, AREA, , 171, 243, 72
ASEL, A, AREA, , 198, 218, 20
ASEL, A, AREA, , 162, 190, 28
ASEL, A, AREA, , 151, 246, 95
ASEL, A, AREA, , 157, 183, 26
ASEL, A, AREA, , 16, 20, 4
NSLA, S, 1
/OUTPUT, FORCES, DAT
NFOR
/OUTPUT
ALLSEL
h=2*(((1393.6*a_mod)/(8.3*2.0))*vf)+2*(((1393.6*a_mod)/(8.3*2.0))
w=(3*a)*a_mod
/OUTPUT, AREA, DAT
area=h*w
/OUTPUT
!
! Determination of NU12
!PRNSOL, EPEL, COMP
!
FINISH
/PREP7
!
! Definition of through-thickness cutting planes
! PLANE #1
*GET, MAX_Y, NODE, , MXLOC, Y
*GET, MIN_Y, NODE, , MNLOC, Y
inc=((MAX_Y)-(MIN_Y))/9
*GET, MAX_Z, NODE, , MNLOC, Z
N, 10000, 0, MAX_Y, 0           ! sweep line #1
N, 10001, 0, MAX_Y, MAX_Z/2
N, 10002, 0, MAX_Y-inc, 0      ! sweep line #2
N, 10003, 0, MAX_Y-inc, MAX_Z/2
N, 10004, 0, MAX_Y-(inc*2), 0  ! sweep line #3

```



```

N,10005,0,MAX_Y-(inc*2),MAX_Z/2
N,10006,0,MAX_Y-(inc*3),0           ! sweep line #4
N,10007,0,MAX_Y-(inc*3),MAX_Z/2
N,10008,0,MAX_Y-(inc*4),0           ! sweep line #5
N,10009,0,MAX_Y-(inc*4),MAX_Z/2
N,10010,0,MAX_Y-(inc*5),0           ! sweep line #6
N,10011,0,MAX_Y-(inc*5),MAX_Z/2
N,10012,0,MAX_Y-(inc*6),0           ! sweep line #7
N,10013,0,MAX_Y-(inc*6),MAX_Z/2
N,10014,0,MAX_Y-(inc*7),0           ! sweep line #8
N,10015,0,MAX_Y-(inc*7),MAX_Z/2
N,10016,0,MAX_Y-(inc*8),0           ! sweep line #9
N,10017,0,MAX_Y-(inc*8),MAX_Z/2
N,10018,0,MAX_Y-(inc*9),0           ! sweep line #10
N,10019,0,MAX_Y-(inc*9),MAX_Z/2
FINISH
/POST1
LPATH,10000,10001
PDEF,SXZ,S,XZ
PDEF,SY,S,Y
/OUTPUT,PLANE1,DAT
PRPATH,SXZ,SY
/OUTPUT
LPATH,10002,10003
PDEF,SXZ,S,XZ
PDEF,SY,S,Y
/OUTPUT,PLANE1,DAT,,APPEND
PRPATH,SXZ,SY
/OUTPUT
LPATH,10004,10005
PDEF,SXZ,S,XZ
PDEF,SY,S,Y
/OUTPUT,PLANE1,DAT,,APPEND
PRPATH,SXZ,SY
/OUTPUT
LPATH,10006,10007
PDEF,SXZ,S,XZ
PDEF,SY,S,Y
/OUTPUT,PLANE1,DAT,,APPEND
PRPATH,SXZ,SY
/OUTPUT

```

```
LPATH,10008,10009
PDEF,SXZ,S,XZ
PDEF,SY,S,Y
/OUTPUT,PLANE1,DAT,,APPEND
PRPATH,SXZ,SY
/OUTPUT
LPATH,10010,10011
PDEF,SXZ,S,XZ
PDEF,SY,S,Y
/OUTPUT,PLANE1,DAT,,APPEND
PRPATH,SXZ,SY
/OUTPUT
LPATH,10012,10013
PDEF,SXZ,S,XZ
PDEF,SY,S,Y
/OUTPUT,PLANE1,DAT,,APPEND
PRPATH,SXZ,SY
/OUTPUT
LPATH,10014,10015
PDEF,SXZ,S,XZ
PDEF,SY,S,Y
/OUTPUT,PLANE1,DAT,,APPEND
PRPATH,SXZ,SY
/OUTPUT
LPATH,10016,10017
PDEF,SXZ,S,XZ
PDEF,SY,S,Y
/OUTPUT,PLANE1,DAT,,APPEND
PRPATH,SXZ,SY
/OUTPUT
LPATH,10018,10019
PDEF,SXZ,S,XZ
PDEF,SY,S,Y
/OUTPUT,PLANE1,DAT,,APPEND
PRPATH,SXZ,SY
/OUTPUT
FINISH
/PREP7
!
! PLANE #2
N,10000,a/2,MAX_Y,0
```

```
! sweep line #1
```

```

N,10001,a/2,MAX_Y,MAX_Z/2
N,10002,a/2,MAX_Y-inc,0           ! sweep line #2
N,10003,a/2,MAX_Y-inc,MAX_Z/2
N,10004,a/2,MAX_Y-(inc*2),0      ! sweep line #3
N,10005,a/2,MAX_Y-(inc*2),MAX_Z/2
N,10006,a/2,MAX_Y-(inc*3),0      ! sweep line #4
N,10007,a/2,MAX_Y-(inc*3),MAX_Z/2
N,10008,a/2,MAX_Y-(inc*4),0      ! sweep line #5
N,10009,a/2,MAX_Y-(inc*4),MAX_Z/2
N,10010,a/2,MAX_Y-(inc*5),0      ! sweep line #6
N,10011,a/2,MAX_Y-(inc*5),MAX_Z/2
N,10012,a/2,MAX_Y-(inc*6),0      ! sweep line #7
N,10013,a/2,MAX_Y-(inc*6),MAX_Z/2
N,10014,a/2,MAX_Y-(inc*7),0      ! sweep line #8
N,10015,a/2,MAX_Y-(inc*7),MAX_Z/2
N,10016,a/2,MAX_Y-(inc*8),0      ! sweep line #9
N,10017,a/2,MAX_Y-(inc*8),MAX_Z/2
N,10018,a/2,MAX_Y-(inc*9),0      ! sweep line #10
N,10019,a/2,MAX_Y-(inc*9),MAX_Z/2
FINISH
/POST1
LPATH,10000,10001
PDEF,SXZ,S,XZ
PDEF,SY,S,Y
/OUTPUT,PLANE2,DAT
PRPATH,SXZ,SY
/OUTPUT
LPATH,10002,10003
PDEF,SXZ,S,XZ
PDEF,SY,S,Y
/OUTPUT,PLANE2,DAT,.,APPEND
PRPATH,SXZ,SY
/OUTPUT
LPATH,10004,10005
PDEF,SXZ,S,XZ
PDEF,SY,S,Y
/OUTPUT,PLANE2,DAT,.,APPEND
PRPATH,SXZ,SY
/OUTPUT
LPATH,10006,10007
PDEF,SXZ,S,XZ

```

```
PDEF,SY,S,Y
/OUTPUT,PLANE2,DAT,,APPEND
PRPATH,SXZ,SY
/OUTPUT
LPATH,10008,10009
PDEF,SXZ,S,XZ
PDEF,SY,S,Y
/OUTPUT,PLANE2,DAT,,APPEND
PRPATH,SXZ,SY
/OUTPUT
LPATH,10010,10011
PDEF,SXZ,S,XZ
PDEF,SY,S,Y
/OUTPUT,PLANE2,DAT,,APPEND
PRPATH,SXZ,SY
/OUTPUT
LPATH,10012,10013
PDEF,SXZ,S,XZ
PDEF,SY,S,Y
/OUTPUT,PLANE2,DAT,,APPEND
PRPATH,SXZ,SY
/OUTPUT
LPATH,10014,10015
PDEF,SXZ,S,XZ
PDEF,SY,S,Y
/OUTPUT,PLANE2,DAT,,APPEND
PRPATH,SXZ,SY
/OUTPUT
LPATH,10016,10017
PDEF,SXZ,S,XZ
PDEF,SY,S,Y
/OUTPUT,PLANE2,DAT,,APPEND
PRPATH,SXZ,SY
/OUTPUT
LPATH,10018,10019
PDEF,SXZ,S,XZ
PDEF,SY,S,Y
/OUTPUT,PLANE2,DAT,,APPEND
PRPATH,SXZ,SY
/OUTPUT
FINISH
```

```

/PREP7
!
! PLANE #3
N,10000,a,MAX_Y,0 ! sweep line #1
N,10001,a,MAX_Y,MAX_Z/2
N,10002,a,MAX_Y-inc,0 ! sweep line #2
N,10003,a,MAX_Y-inc,MAX_Z/2
N,10004,a,MAX_Y-(inc*2),0 ! sweep line #3
N,10005,a,MAX_Y-(inc*2),MAX_Z/2
N,10006,a,MAX_Y-(inc*3),0 ! sweep line #4
N,10007,a,MAX_Y-(inc*3),MAX_Z/2
N,10008,a,MAX_Y-(inc*4),0 ! sweep line #5
N,10009,a,MAX_Y-(inc*4),MAX_Z/2
N,10010,a,MAX_Y-(inc*5),0 ! sweep line #6
N,10011,a,MAX_Y-(inc*5),MAX_Z/2
N,10012,a,MAX_Y-(inc*6),0 ! sweep line #7
N,10013,a,MAX_Y-(inc*6),MAX_Z/2
N,10014,a,MAX_Y-(inc*7),0 ! sweep line #8
N,10015,a,MAX_Y-(inc*7),MAX_Z/2
N,10016,a,MAX_Y-(inc*8),0 ! sweep line #9
N,10017,a,MAX_Y-(inc*8),MAX_Z/2
N,10018,a,MAX_Y-(inc*9),0 ! sweep line #10
N,10019,a,MAX_Y-(inc*9),MAX_Z/2
FINISH
/POST1
LPATH,10000,10001
PDEF,SXZ,S,XZ
PDEF,SY,S,Y
/OUTPUT,PLANE3,DAT
PRPATH,SXZ,SY
/OUTPUT
LPATH,10002,10003
PDEF,SXZ,S,XZ
PDEF,SY,S,Y
/OUTPUT,PLANE3,DAT,,APPEND
PRPATH,SXZ,SY
/OUTPUT
LPATH,10004,10005
PDEF,SXZ,S,XZ
PDEF,SY,S,Y
/OUTPUT,PLANE3,DAT,,APPEND

```

```
PRPATH,SXZ,SY
/OUTPUT
LPATH,10006,10007
PDEF,SXZ,S,XZ
PDEF,SY,S,Y
/OUTPUT,PLANE3,DAT,,APPEND
PRPATH,SXZ,SY
/OUTPUT
LPATH,10008,10009
PDEF,SXZ,S,XZ
PDEF,SY,S,Y
/OUTPUT,PLANE3,DAT,,APPEND
PRPATH,SXZ,SY
/OUTPUT
LPATH,10010,10011
PDEF,SXZ,S,XZ
PDEF,SY,S,Y
/OUTPUT,PLANE3,DAT,,APPEND
PRPATH,SXZ,SY
/OUTPUT
LPATH,10012,10013
PDEF,SXZ,S,XZ
PDEF,SY,S,Y
/OUTPUT,PLANE3,DAT,,APPEND
PRPATH,SXZ,SY
/OUTPUT
LPATH,10014,10015
PDEF,SXZ,S,XZ
PDEF,SY,S,Y
/OUTPUT,PLANE3,DAT,,APPEND
PRPATH,SXZ,SY
/OUTPUT
LPATH,10016,10017
PDEF,SXZ,S,XZ
PDEF,SY,S,Y
/OUTPUT,PLANE3,DAT,,APPEND
PRPATH,SXZ,SY
/OUTPUT
LPATH,10018,10019
PDEF,SXZ,S,XZ
PDEF,SY,S,Y
```

```
/OUTPUT,PLANE3,DAT,,APPEND  
PRPATH,SXZ,SY  
/OUTPUT  
FINISH  
SAVE  
/EXIT,ALL
```

APPENDIX C

C.1. ANSYS User Files - Validation of Experimental Biaxial Shear Tests

In C.1.1. of this appendix, a user input file is presented in ANSYS 5.3 format for evaluating the shear dominated, biaxial response of woven graphite fiber reinforced, polyimide composite materials, specifically graphite-PMR15. The fixtures assumed in these numerical analyses are the biaxial Iosipescu fixture, i.e. short loading blocks and the modified biaxial Iosipescu fixture, i.e. ASTM specified blocks. These analyses are nonlinear and include the capabilities to model geometric (large strain and rotation) and boundary contact (friction) nonlinearities. Fixture displacements are from 0.1 mm (3.9×10^{-3} in) to +3.0 mm ($+1.2 \times 10^{-1}$ in) and friction coefficients range from 0.1 to 0.8. The user file for the modified biaxial test is excluded, however the format is identical with the exception of lines specified for loading block geometry.

In C.1.2. of this appendix, a user input file is presented in ANSYS 5.3 format for evaluating the effects of eccentric load conditions on the biaxial shear behavior of the same composite as in C.1.1. The finite element analyses employ layered, 6 DOF elements which model the correct number of plies and interfaces within the composite material. These 3-D analyses are also nonlinear, including the capabilities to model geometric and boundary contact nonlinearities. As with the 2-D cases, the file for the modified biaxial test is excluded to avoid redundancy.

In C.1.3. of this appendix, capabilities of the 3-D Iosipescu models are extended to study the effects of anisotropic plasticity and progressive damage, separately and cumulatively. The key revision at this point is the change to an element type which supports plasticity and element birth and death scenarios of which the layered element does not

support. The focus with plasticity and progressive damage is twofold: 1) to determine which is more of a contribution towards the significant nonlinear behavior experimentally observed in the 8HS woven fabric composites, and 2) to evaluate which of the element death scenarios more closely represents the volume of damage generated by reconstruction of serial sections. Element death is controlled by any one of several well-known failure criteria to see which if any are applicable to the given stress/strain conditions in the Iosipescu specimens.

C.1.1. 2-D Biaxial Iosipescu Model (geometric and boundary contact)

```

*DO,h,0.3,0.3                                ! Definition of friction coefficients
FC=h*10
!
!
/FILNAM,CGP_M%FC%_YG
/TITLE,Nonlinear Analysis, M. Cambridge Research Model(PMR-15)-mu=%h%/YG
/STITLE,2,Loading angles (alpha) = -40 S/T to +40 S/T
/UNITS,SI
/PREP7
!
! This ANSYS 5.0a analysis pertains to biaxial loading of graphite polyimide Iosipescu
! specimens. The fixture used is the modified Cambridge design biaxial Iosipescu fixture.
!
!
! Test Conditions:
!         sliding (mu = 0.1 - 0.8)
!         prescribed displacements (d = 0.0 - +3.0)
!         with geometric nonlinearities
!
! Material Properties:
!         E11 = E22 = 79 GPa
!         G12 = 7.50 GPa
!         nu12 = 0.15
!
! Input units are consistently = MPa
!
MOPT,AMESH,RV51

```

```
ET,1,PLANE82
ET,2,PLANE82
ET,3,CONTAC48,,1,1,,,1
R,1,
R,2,
R,3,79e3,79e3/100,0.1,,1
MP,EX,1,79e3
MP,EY,1,79e3
MP,GXY,1,7.5e3
MP,NUXY,1,0.15
MP,EX,2,400e3
MP,GXY,2,400e3/2*(1+0.30)
MP,MU,3,h
!
! Definition of keypoints around specimen boundary
K,1,40,10,0
K,2,14,10,0
K,3,4,10,0
K,4,0,6,0
K,5,-4,10,0
K,6,-30,10,0
K,7,-40,10,0
K,8,-40,0,0
K,9,-40,-10,0
K,10,-14,-10,0
K,11,-4,-10,0
K,12,0,-6,0
K,13,4,-10,0
K,14,30,-10,0
K,15,40,-10,0
K,16,40,0,0
!
! Definition of keypoints within specimen interior
K,17,4,0,0
K,18,1.075,0,0
K,19,-1.075,0,0
K,20,-4,0,0
K,21,0,1.075,0
K,22,0,-1.075,0
!
! Definition of keypoints for loading blocks
```

```
K,23,-30,12.5,0
K,24,-40,12.5,0
K,25,-14,-12.5,0
K,26,-4,-12.5,0
K,27,30,-12.5,0
K,28,40,-12.5,0
K,29,14,12.5,0
K,30,4,12.5,0
!
! Definition of contact keypoints
K,31,-40,10+.0001,0
K,32,-30,10+.0001,0
K,33,-14,-10-.0001,0
K,34,-4,-10-.0001,0
K,35,4,10+.0001,0
K,36,14,10+.0001,0
K,37,30,-10-.0001,0
K,38,40,-10-.0001,0
KPLOT
!
! Definition of lines with respect to keypoints
L,32,23                ! line 1
L,23,24                ! line 2
L,24,31                ! line 3
L,31,32                ! line 4
L,26,34                ! line 5
L,34,33                ! line 6
L,33,25                ! line 7
L,25,26                ! line 8
L,36,29                ! line 9
L,29,30                ! line 10
L,30,35                ! line 11
L,35,36                ! line 12
L,28,38                ! line 13
L,38,37                ! line 14
L,37,27                ! line 15
L,27,28                ! line 16
L,20,5                 ! line 17
L,5,6                  ! line 18
L,6,7                  ! line 19
L,7,8                  ! line 20
```

```

L,8,20                ! line 21
L,11,20              ! line 22
L,8,9                ! line 23
L,9,10              ! line 24
L,10,11             ! line 25
L,16,1              ! line 26
L,1,2               ! line 27
L,2,3               ! line 28
L,3,17             ! line 29
L,17,16            ! line 30
L,15,16            ! line 31
L,17,13            ! line 32
L,13,14            ! line 33
L,14,15            ! line 34
L,4,5              ! line 35  top notch
L,3,4              ! line 36
!
! Definition of top notch root radius = 0.45 mm
LFILLT,35,36,0.45,100 ! line 37
L,21,100           ! line 38
LCSL,37,38        ! line 38 becomes line 39
!                 ! radius left is line 40
!                 ! radius right is line 41
!                 ! removed line is line 42
LDELE,42
KDELE,100
KDELE,4
L,20,19           ! line 37
L,19,21          ! line 38
L,17,18          ! line 42
L,18,21          ! line 43
L,12,11          ! line 44  bottom notch
L,12,13          ! line 45
!
! Definition of bottom notch root radius = 0.45 mm
LFILLT,44,45,0.45,100 ! line 46
L,22,100         ! line 47
LCSL,46,47      ! line 47 becomes line 48
!                 ! radius left is line 49
!                 ! radius right is line 50
!                 ! removed line is line 51

```

```

LDELE,51
KDELE,100
KDELE,12
L,19,22          ! line 46
L,18,22          ! line 47
!
! Definition of areas from existing lines
AL,1,2,3,4       ! area 1
AL,5,6,7,8       ! area 2  loading blocks
AL,9,10,11,12    ! area 3
AL,13,14,15,16   ! area 4
!
AL,17,18,19,20,21 ! area 5
AL,22,21,23,24,25 ! area 6  specimen body
AL,26,27,28,29,30 ! area 7
AL,31,30,32,33,34 ! area 8
!
AL,17,37,38,39,40,35 ! area 9
AL,29,42,43,39,41,36 ! area 10 upper notch region
!
AL,22,37,46,49,48,44 ! area 11
AL,32,42,47,49,50,45 ! area 12 lower notch region
!
AL,38,46,47,43     ! area 13 strain gage grid
!
APLOT
!
! Shaping and meshing areas
AATT,2,2,2,0
ESHAPE,3,0
ESIZE,1.0
MAT,2
REAL,2
TYPE,2
ESYS,0
AMESH,1,4
AATT,1,1,1,0
ESHAPE,3,0
ESIZE,1.0
MAT,1
REAL,1

```

```

TYPE,1
ESYS,0
AMESH,5,8
AATT,1,1,1,0
ESHAPE,3,0
ESIZE,0.5
MAT,1
REAL,1
TYPE,1
ESYS,0
AMESH,9,13
MAT,3
TYPE,3
LSEL,S,LINE,,19                ! Select logic for contact lines
NSLL,S,1
CM,TAR19,NODE
NSEL,ALL
LSEL,ALL
LSEL,S,LINE,,4
NSLL,S,1
CM,CON4,NODE
NSEL,ALL
LSEL,ALL
REAL,3
GCGEN,CON4,TAR19
LSEL,S,LINE,,25                ! Select logic for contact lines
NSLL,S,1
CM,TAR25,NODE
NSEL,ALL
LSEL,ALL
LSEL,S,LINE,,6
NSLL,S,1
CM,CON6,NODE
NSEL,ALL
LSEL,ALL
REAL,3
GCGEN,CON6,TAR25
LSEL,S,LINE,,28                ! Select logic for contact lines
NSLL,S,1
CM,TAR28,NODE
NSEL,ALL

```

```

LSEL,ALL
LSEL,S,LINE,,12
NSLL,S,1
CM,CON12,NODE
NSEL,ALL
LSEL,ALL
REAL,3
GCGEN,CON12,TAR28
LSEL,S,LINE,,34           ! Select logic for contact lines
NSLL,S,1
CM,TAR34,NODE
NSEL,ALL
LSEL,ALL
LSEL,S,LINE,,14
NSLL,S,1
CM,CON14,NODE
NSEL,ALL
LSEL,ALL
REAL,3
GCGEN,CON14,TAR34
/COLOR,ELEM,MAGE,1963,1978
EPLOT
FINISH
!
! Definition of loading angle options for biaxiality
!*DO,ALPHA,-40,40,10
ALPHA=0
/SOLU
!OUTPR,BASI,LAST
!OUTRES,BASI,LAST
!
! Definition of the analysis type and analysis options
ANTYP,STAT,NEW
NLGEOM,ON
SSTIF,ON
NROPT,1,,ON
EQSLV,FRONT
!
! Definition of the load step options
*DO,i,0.1,3.6,0.1
DDELE,ALL,ALL

```

```

FDELE,ALL,ALL
PI=ACOS(-1)
ALPH=ALPHA/10
ALPHA=ALPHA*(-1)
DISPY=i/2
DISPX=DISPY*TAN(ALPHA*PI/180)
!
! General options
AUTOTS,ON
NSUBST,100,1000,10
!
! Dynamic options
TIMINT,OFF
!
! Definition of nonlinear options
NEQIT,2500
PRED,ON,,ON           ! Auto time-stepping/prediction
CSYS,0                ! Default coordinate system
!
! Definition of file output variables
FRICTION=FC           ! Applied friction coefficient
D,6219,ALL,O          ! Center restraint
!
LSEL,S,LINE,,2        ! Block restraints
NSLL,S,1
D,ALL,UX,-DISPX
D,ALL,UY,DISPY
NSEL,ALL
LSEL,ALL
LSEL,S,LINE,,8
NSLL,S,1
D,ALL,UX,-DISPX
D,ALL,UY,DISPY
NSEL,ALL
LSEL,ALL
LSEL,S,LINE,,10
NSLL,S,1
D,ALL,UX,DISPX
D,ALL,UY,-DISPY
NSEL,ALL
LSEL,ALL

```



```

LSEL,S,LINE,,16
NSLL,S,1
D,ALL,UX,DISPX
D,ALL,UY,-DISPY
NSEL,ALL
LSEL,ALL
CS,15,0,6219,5348,5039
CSYS,15
SAVE
SOLVE
*ENDDO
SAVE
FINISH
/POST1
*DO,j,1,36,1
SET,j
LS=j
CSYS,0
!
! Definition of select path logic for integration along notch root axis
!
LPATH,5037,5629
PDEF,SX,S,X
PDEF,SY,S,Y
PDEF,SXY,S,XY
PDEF,EX,EPTO,X
PDEF,EY,EPTO,Y
PDEF,EXY,EPTO,XY
PCALC,INTG,INTA,SXY,S
PCALC,INTG,INTB,EXY,S
/OUTPUT,INTG%ALPH%%FRICTION%%LS%,DAT
PRPATH,INTA,INTB
/OUTPUT,NSTS%ALPH%%FRICTION%%LS%,DAT
PRPATH,SX,SY,SXY
/OUTPUT,NSTN%ALPH%%FRICTION%%LS%,DAT
PRPATH,EX,EY,EXY
/OUTPUT
!
! Definition of select path logic for stresses/strains along top notch
LPATH,470,5015,5038,5037,5353,5352,2815
PDEF,SX,S,X

```

```

PDEF,SY,S,Y
PDEF,SXY,S,XY
PDEF,EX,EPTO,X
PDEF,EY,EPTO,Y
PDEF,EXY,EPTO,XY
/OUTPUT,VSTS%ALPH%%FRICTION%%LS%,DAT
PRPATH,SX,SY,SXY
/OUTPUT,VSTN%ALPH%%FRICTION%%LS%,DAT
PRPATH,EX,EY,EXY
/OUTPUT
!
! Definition of select logic for moment summations
LSEL,S,LINE,,10
NSLL,S,1
/OUTPUT,M1%ALPH%%FRICTION%%LS%,DAT
NFOR
/OUTPUT
NSEL,ALL
LSEL,ALL
LSEL,S,LINE,,16
NSLL,S,1
/OUTPUT,M2%ALPH%%FRICTION%%LS%,DAT
NFOR
/OUTPUT
NSEL,ALL
LSEL,ALL
!
! Definition of select logic for strain gage grid
ASEL,S,,,13
ESLA,S
!
! Definition of element centroids
ETABLE,LOCX,CENT,X
ETABLE,LOCY,CENT,Y
/OUTPUT,LOC%ALPH%%FRICTION%%LS%,DAT
PRETAB,LOCX,LOCY
/OUTPUT
CSYS,15
RSYS,15
PLNSOL,EPTO,X
!

```

```

! Definition of element average strains
ETABLE,STRAINX,EPTO,X
ETABLE,STRAINY,EPTO,Y
/OUTPUT,STRN%ALPH%%FRICTION%%LS%,DAT
PRETAB,STRAINX,STRAINY
RSYS,0
/OUTPUT,STRS%ALPH%%FRICTION%%LS%,DAT
PRNSOL,S,COMP
/OUTPUT
ASEL,ALL
ESEL,ALL
*ENDDO
!
FINISH
!*ENDDO
SAVE
!/CLEAR,START
*ENDDO
SAVE
/EXIT,ALL

```

C.1.2. 3-D Biaxial Iosipescu Model (load eccentricities)

```

FC=0.3
/FILNAM,B_3D_%FC%
/TITLE,3D Nonlinear Analysis, Biaxial Research Model(PMR-15)-mu=%FC%
/STITLE,2.Loading angles (alpha) = -30 S/T to +30 S/T
/UNITS,SI
/PREP7
/PLOPTS,VERS,1
!
! This ANSYS 5.3 analysis pertains to biaxial loading of graphite polyimide Iosipescu
! specimens. The fixture used is the modified Cambridge design biaxial Iosipescu fixture
! with short blocks. The model uses layered solid elements (SOLID46) and incorporates the
! following failure criteria:
!
! Maximum Stress or Tsai-Wu Failure Criterion
!
!

```

! Test Conditions:
 ! sliding ($\mu = 0.3$)-boundary contact nonlinearities
 ! prescribed displacements ($d = 0.0 - 0.3$)
 ! with geometric nonlinearities

! Material Properties:
 ! $E_{11}(C) = E_{22}(C) = 70.0 \text{ GPa}$
 ! $E_{33}(C) = 11.3 \text{ GPa}$
 ! $G_{12}(C) = 7.0 \text{ GPa}$
 ! $G_{13}(C) = 4.9 \text{ GPa}$
 ! $G_{23}(C) = 5.1 \text{ GPa}$
 ! $\nu_{12}(C) = 0.10$
 ! $\nu_{13}(C) = 0.25$
 ! $\nu_{23}(C) = 0.27$

! $E_{11}(M) = E_{22}(M) = E_{33}(M) = 4.0 \text{ GPa}$
 ! $\nu_{12}(M) = 0.35$
 ! $G_{12}(M) = E_{11}(M)/2(1+\nu_{12}(M))$

! Composite Layer Characteristics:
 ! Laminae (0/90)_{8s} - $t = 289.0u = 0.289\text{mm}$
 ! Matrix Interfaces - $t = 25.0u = .025\text{mm}$
 ! Total Layers = 31

! Input units are consistently = MPa

! MOPT,AMESH,RV51
 ! ET,1,SOLID46,,,4,,2,1
 ! KEYOPT,1,8,1
 ! KEYOPT,1,9,1
 ! KEYOPT,1,10,0
 ! ET,2,SOLID45
 ! ET,3,CONTAC49,,1,1
 ! KEYOPT,3,7,1

! Definition of composite layer orientations and thicknesses

R,1,
 RMODIF,1,1,31
 RMODIF,1,7,0
 RMODIF,1,13,1,0,0.289,4,0,0.025,

```

R,3,79e3,79e3/100,0.1,1
R,4,
!
! Definition of material properties
MP,EX,1,70.0e3
MP,EY,1,70.0e3
MP,EZ,1,11.3e3
MP,GXY,1,7.0e3
MP,GXZ,1,4.9e3
MP,GYZ,1,5.1e3
MP,NUXY,1,0.10
MP,NUXZ,1,0.25
MP,NUYZ,1,0.27
!
MP,EX,2,400e3
MP,GXY,2,400e3/(2*(1+0.30))
!
MP,MU,3,0.3
!
MP,EX,4,4.0e3
MP,GXY,4,4.0e3/(2*(1+0.35))
!
! Definition of failure criterion - Maximum Stress
TB,FAIL,1,1
TBTEMP,CRIT

```

```

TBDATA,2,1
TBTEMP,78
TBDATA,10,1e3,-0.5e3,1e3,-0.5e3,.05e3,-0.2e3
TBDATA,16,0.1e3,0.03e3,0.03e3
TBLIST
!
! Definition of Iosipescu specimen volume
/VIEW,1,1,1,1
RECTNG,-40,40,-10,10
K,5,0,6
K,6,-4,10
K,7,4,10
LSTR,5,6
LSTR,5,7
LFILLT,5,6,0.45
LSEL,S,LINE,,5,7,1
LCOMB,ALL
ALLSEL
LSYMM,Y,5
ASBL,1,5,SEPO,DELETE,DELETE
ASBL,3,6,SEPO,DELETE,DELETE
ADELE,1,2,1,1
WPROTA,,,-90
WPOFFS,0,0,1
ASBW,4
WPOFFS,0,0,3
ASBW,1
WPOFFS,0,0,5
ASBW,4
WPOFFS,0,0,-10
ASBW,2
WPOFFS,0,0,-3
ASBW,6
WPOFFS,0,0,-5
ASBW,2
WPOFFS,0,0,9
WPROTA,,,-90
AGLUE,ALL
!
! Mapped meshing of Iosipescu volume
ET,4,PLANE82
! Dummy elements

```

```
AATT,4,4,4,0
ESHAPE,2,0
ESIZE,,10
AMESH,4
AMESH,3
AMESH,7
ESIZE,,8
AMESH,1
AMESH,6
ESIZE,,8
AMESH,5
AMESH,8
VATT,1,1,1,0
ESHAPE,2,0
ESIZE,,1
MAT,1
REAL,1
TYPE,1
ESYS,0
VEXT,ALL,,,0,0,-5
ACLEAR,1
ACLEAR,3,8,1
!
! Definition of short loading blocks
BLOCK,4,14,10,12.5,2.5,-7.5
BLOCK,30,40,-10,-12.5,2.5,-7.5
BLOCK,-4,-14,-10,-12.5,2.5,-7.5
BLOCK,-30,-40,10,12.5,2.5,-7.5
!
! Meshing of short loading blocks
VATT,2,2,2,0
ESHAPE,2,0
ESIZE,2.5
MAT,2
REAL,2
TYPE,2
ESYS,0
VMESH,8,11,1
!
! Definition of boundary contact between blocks and specimen
MAT,3
```

```
TYPE,3
ASEL,S,AREA,,39
NSLA,S,1
CM,CON1,NODE
ALLSEL
ASEL,S,AREA,,11
ASEL,A,AREA,,24
NSLA,S,1
CM,TAR1,NODE
ALLSEL
REAL,3
GCGEN,CON1,TAR1
REAL,3
GCGEN,TAR1,CON1
!
ASEL,S,AREA,,46
NSLA,S,1
CM,CON2,NODE
ALLSEL
ASEL,S,AREA,,9
NSLA,S,1
CM,TAR2,NODE
ALLSEL
REAL,3
GCGEN,CON2,TAR2
REAL,3
GCGEN,TAR2,CON2
!
ASEL,S,AREA,,52
NSLA,S,1
CM,CON3,NODE
ALLSEL
ASEL,S,AREA,,26
ASEL,A,AREA,,35
NSLA,S,1
CM,TAR3,NODE
ALLSEL
REAL,3
GCGEN,CON3,TAR3
REAL,3
GCGEN,TAR3,CON3
```



```

!
ASEL,S,AREA,,57
NSLA,S,1
CM,CON4,NODE
ALLSEL
ASEL,S,AREA,,28
NSLA,S,1
CM,TAR4,NODE
ALLSEL
REAL,3
GCGEN,CON4,TAR4
REAL,3
GCGEN,TAR4,CON4
/ESHAPE,1
NUMCMP,ALL
EPLT
FINISH
!
! Definition of loading angle for biaxiality
ALPHA=0
/SOLU
!OUTPR,BASI,LAST
!OUTRES,BASI,LAST
!
! Definition of the analysis type and analysis options
ANTYP,STAT,NEW
NLGEOM,ON
SSTIF,ON
NROPT,1,,ON
EQSLV,FRONT
!
! Definition of the load step options
*DO,i,0.05,0.05
DDELE,ALL,ALL
FDELE,ALL,ALL
PI=ACOS(-1)
ALPH=ALPHA/10
ALPHA=ALPHA*(-1)
DISPY=i/2
DISPX=DISPY*TAN(ALPHA*PI/180)
!

```

```

! General options
AUTOTS,ON
NSUBST,100,1000,10
!
! Dynamic options
TIMINT,OFF
!
! Definition of nonlinear options
NEQIT,500
PRED,ON,,ON
CSYS,0
!
! Definition of file output variables
FRICTION=FC*10
!
ASEL,S,AREA,,58
NSLA,S,1
D,ALL,UX,-DISPX
D,ALL,UY,DISPY
D,ALL,UZ,0
NSEL,ALL
ASEL,ALL
ASEL,S,AREA,,51
NSLA,S,1
D,ALL,UX,-DISPX
D,ALL,UY,DISPY
D,ALL,UZ,0
NSEL,ALL
ASEL,ALL
ASEL,S,AREA,,45
NSLA,S,1
D,ALL,UX,DISPX
D,ALL,UY,-DISPY
D,ALL,UZ,0
NSEL,ALL
ASEL,ALL
ASEL,S,AREA,,40
NSLA,S,1
D,ALL,UX,DISPX
D,ALL,UY,-DISPY
D,ALL,UZ,0
! Auto time-stepping/prediction
! Default coordinate system
! Applied friction coefficient
! Block restraints

```

```

NSEL,ALL
ASEL,ALL
SAVE
SOLVE
*ENDDO
SAVE
FINISH
/POST1
*DO,j,1,1
SET,j
LS=j
CSYS,0
!
! Definition of node selection along notch root axis for extraction
! of ply and interface properties
!
NSEL,S,NODE,,12
NSEL,A,NODE,,203,219,2
NSEL,A,NODE,,52
*DO,k,17,31,2           ! plies
LAYER,k
/OUTPUT,PLYR%k%,DAT
PRNSOL,S,COMP
/OUTPUT
*ENDDO
!
*DO,k,16,30,2           ! interfaces
LAYER,k
/OUTPUT,MLYR%k%,DAT
PRNSOL,S,COMP
/OUTPUT
*ENDDO
ALLSEL
LAYER,ALL
!
! Definition of select path logic for integration along front surface
!
LPATH,52,12
PDEF,SX,S,X
PDEF,SY,S,Y
PDEF,SZ,S,Z

```

```

PDEF,SXY,S,XY
PDEF,SXZ,S,XZ
PDEF,SYZ,S,YZ
PDEF,EX,EPTO,X
PDEF,EY,EPTO,Y
PDEF,EZ,EPTO,Z
PDEF,EXY,EPTO,XY
PDEF,EXZ,EPTO,XZ
PDEF,EYZ,EPTO,YZ
PCALC,INTG,INTA,SXY,S
PCALC,INTG,INTB,EXY,S
/OUTPUT,FITG%ALPH%%FRICITION%%LS%,DAT
PRPATH,INTA,INTB
/OUTPUT,FSTS%ALPH%%FRICITION%%LS%,DAT
PRPATH,SX,SY,SZ,SXY,SXZ,SYZ
/OUTPUT,FSTN%ALPH%%FRICITION%%LS%,DAT
PRPATH,EX,EY,EZ,EXY,EXZ,EYZ
/OUTPUT
!
! Definition of select path logic for integration along back surface
!
LPATH,2550,2530
PDEF,SX,S,X
PDEF,SY,S,Y
PDEF,SZ,S,Z
PDEF,SXY,S,XY
PDEF,SXZ,S,XZ
PDEF,SYZ,S,YZ
PDEF,EX,EPTO,X
PDEF,EY,EPTO,Y
PDEF,EZ,EPTO,Z
PDEF,EXY,EPTO,XY
PDEF,EXZ,EPTO,XZ
PDEF,EYZ,EPTO,YZ
PCALC,INTG,INTA,SXY,S
PCALC,INTG,INTB,EXY,S
/OUTPUT,BITG%ALPH%%FRICITION%%LS%,DAT
PRPATH,INTA,INTB
/OUTPUT,BSTS%ALPH%%FRICITION%%LS%,DAT
PRPATH,SX,SY,SZ,SXY,SXZ,SYZ
/OUTPUT,BSTN%ALPH%%FRICITION%%LS%,DAT

```

```

PRPATH,EX,EY,EZ,EXY,EXZ,EYZ
/OUTPUT
!
! Definition of output for moment summation
SPOINT,0,0,0,-2.5
ASEL,S,AREA,,51
ASEL,A,AREA,,58
NSLA,S,1
/OUTPUT,ML%ALPH%%FRICTION%%LS%,DAT
NFOR
/OUTPUT
ALLSEL
ASEL,S,AREA,,40
ASEL,A,AREA,,45
NSLA,S,1
/OUTPUT,MR%ALPH%%FRICTION%%LS%,DAT
NFOR
/OUTPUT
ALLSEL
!
! Definition of output for maximum lateral displacements
/OUTPUT,DISP%ALPH%%FRICTION%%LS%,DAT
PRNSOL,U,Z
/OUTPUT
*ENDDO
FINISH
/EXIT,ALL

```

C.1.3. 3-D Biaxial Iosipescu Model (anisotropic plasticity and progressive damage)

```

FC=0.3
/FILNAM,PDAMAGE_3D%FC%
/TITLE,3D Nonlinear Analysis, Biaxial Research Model(PMR-15)-mu=%FC%
/STITLE,2>Loading angle (alpha) = 0
/UNITS,SI
/PREP7
/PLOPTS,VERS,1
/NERR,1000,50000
!

```

! This ANSYS 5.3 analysis pertains to biaxial loading of graphite polyimide Iosipescu
! specimens. The fixture used is the modified Cambridge design biaxial Iosipescu fixture
! with short blocks. The model uses 20-node solid elements (SOLID95) and incorporates
! 3-D anisotropic plasticity (Hill's formulation). The model also incorporates progressive
! damage according to a criterion based on the ratios of elastic strain energy densities.

! Test Conditions:

! sliding ($\mu = 0.3$)-boundary contact nonlinearities
! prescribed displacements ($d = 0.0 - 1.0$)
! with geometric nonlinearities

! Material Properties:

! $E_{xx}(C) = E_{yy}(C) = 70.0 \text{ GPa}$
! $E_{zz}(C) = 11.3 \text{ GPa}$
! $G_{xy}(C) = 7.0 \text{ GPa}$
! $G_{xz}(C) = 4.9 \text{ GPa}$
! $G_{yz}(C) = 5.1 \text{ GPa}$
! $\nu_{xy}(C) = 0.10$
! $\nu_{xz}(C) = 0.25$
! $\nu_{yz}(C) = 0.27$

! Anisotropic Plasticity Data:

! Yield Stresses

! $X_t = 990 \text{ MPa}$! $Y_t = 990 \text{ MPa}$! $Z_t = 497 \text{ MPa}$
! $X_c = 990 \text{ MPa}$! $Y_c = 990 \text{ MPa}$! $Z_c = 497 \text{ MPa}$
! $XY = 95 \text{ MPa}$! $YZ = 53 \text{ MPa}$! $XZ = 53 \text{ MPa}$

! Tangent Moduli

! $E_{xx_tan}(t,c) = E_{yy_tan}(t,c) = 0.01 * E_{xx}(yy)$
! $E_{zz_tan}(t,c) = 0.0064 * E_{zz}$
! $G_{xy_tan} = G_{yz_tan} = G_{xz_tan} = 0$

! Critical Strain Energies

! $S_x E_{x_c} = 6.2618 \text{ MJ/mm}^3$! $S_y E_{y_c} = 6.2618 \text{ MJ/mm}^3$
! $S_z E_{z_c} = .0013 \text{ MJ/mm}^3$! $S_{xy} E_{xy_c} = .0345 \text{ MJ/mm}^3$
! $S_{xz} E_{xz_c} = .0400 \text{ MJ/mm}^3$! $S_{yz} E_{yz_c} = .0400 \text{ MJ/mm}^3$

```
!  
! Input units are consistently = MPa  
!  
!  
MOPT,AMESH,RV51  
ET,1,SOLID95  
KEYOPT,1,5,2  
ET,2,SOLID45  
ET,3,CONTAC49,,1,1  
KEYOPT,3,7,1  
!  
! Definition of composite layer orientations and thicknesses  
R,1,  
R,2,  
R,3,70e3,70e3/100,0.1,,1  
R,4  
!  
! Definition of material properties  
MP,EX,1,70.0e3  
MP,EY,1,70.0e3  
MP,EZ,1,11.3e3  
MP,GXY,1,7.0e3  
MP,GXZ,1,4.9e3  
MP,GYZ,1,5.1e3  
MP,NUXY,1,0.10  
MP,NUXZ,1,0.25  
MP,NUYZ,1,0.27  
!  
! Definition of damage properties  
MP,EX,4,70.0e3*0.50  
MP,EY,4,70.0e3*0.50  
MP,EZ,4,11.3e3*0.50  
MP,GXY,4,7.0e3*0.50  
MP,GXZ,4,4.9e3*0.50  
MP,GYZ,4,5.1e3*0.50  
MP,NUXY,4,0.10  
MP,NUXZ,4,0.25  
MP,NUYZ,4,0.27  
!  
MP,EX,2,400e3  
MP,GXY,2,400e3/(2*(1+0.30))
```

```
!  
MP,MU,3,0.3  
!  
! Definition of plasticity criteria - anisotropic  
TB,ANISO,1  
TBMODIF,1,1,0.990e3  
TBMODIF,1,2,0.990e3  
TBMODIF,1,3,0.497e3  
TBMODIF,2,1,70.0e3-(0.01*70.0e3)  
TBMODIF,2,2,70.0e3-(0.01*70.0e3)  
TBMODIF,2,3,11.3e3-(0.0064*11.3e3)  
TBMODIF,3,1,0.990e3  
TBMODIF,3,2,0.990e3  
TBMODIF,3,3,0.497e3  
TBMODIF,4,1,70.0e3-(0.01*70.0e3)  
TBMODIF,4,2,70.0e3-(0.01*70.0e3)  
TBMODIF,4,3,11.3e3-(0.0064*11.3e3)  
!TBMODIF,5,1,0.095e3  
!TBMODIF,5,2,0.053e3  
!TBMODIF,5,3,0.053e3  
TBMODIF,5,1,0.023e3  
TBMODIF,5,2,0.015e3  
TBMODIF,5,3,0.015e3  
TBMODIF,6,1,7.0e3-(0.17*7.0e3)  
TBMODIF,6,2,5.1e3-(0.25*5.1e3)  
TBMODIF,6,3,4.9e3-(0.25*4.9e3)  
!  
! Definition of Iosipescu specimen volume  
/VIEW,1,1,1,1  
RECTNG,-40,40,-10,10  
K,5,0,6  
K,6,-4,10  
K,7,4,10  
LSTR,5,6  
LSTR,5,7  
LFILLT,5,6,0.45  
LSEL,S,LINE,,5,7,1  
LCOMB,ALL  
ALLSEL  
LSYMM,Y,5  
ASBL,1,5,SEPO,DELETE,DELETE
```


ASBL,3,6,SEPO,DELETE,DELETE

ADELE,1,2,1,1

WPROTA,,,-90

WPOFFS,0,0,1

ASBW,4

WPOFFS,0,0,3

ASBW,1

WPOFFS,0,0,5

ASBW,4

WPOFFS,0,0,-10

ASBW,2

WPOFFS,0,0,-3

ASBW,6

WPOFFS,0,0,-5

ASBW,2

WPOFFS,0,0,9

WPROTA,,,-90

AGLUE,ALL

!

! Mapped meshing of Iosipescu volume

ET,4,PLANE82

! Dummy elements

AATT,4,4,4,0

ESHAPE,2,0

ESIZE,,14

AMESH,4

AMESH,3

AMESH,7

ESIZE,,6

AMESH,1

AMESH,6

ESIZE,,12

AMESH,5

AMESH,8

VATT,1,1,1,0

ESHAPE,2,0

ESIZE,,1

MAT,1

REAL,1

TYPE,1

ESYS,0

VEXT,ALL,,0,0,-5

```
ACLEAR,1
ACLEAR,3,8,1
!
! Definition of short loading blocks
BLOCK,4,14,10,12.5,2.5,-7.5
BLOCK,30,40,-10,-12.5,2.5,-7.5
BLOCK,-4,-14,-10,-12.5,2.5,-7.5
BLOCK,-30,-40,10,12.5,2.5,-7.5
!
! Meshing of short loading blocks
VATT,2,2,2,0
ESHAPE,2,0
ESIZE,2.5
MAT,2
REAL,2
TYPE,2
ESYS,0
VMESH,8,11,1
!
! Definition of boundary contact between blocks and specimen
MAT,3
TYPE,3
ASEL,S,AREA,,39
NSLA,S,1
CM,CON1,NODE
ALLSEL
ASEL,S,AREA,,11
ASEL,A,AREA,,24
NSLA,S,1
CM,TAR1,NODE
ALLSEL
REAL,3
GCGEN,CON1,TAR1
REAL,3
GCGEN,TAR1,CON1
!
ASEL,S,AREA,,46
NSLA,S,1
CM,CON2,NODE
ALLSEL
ASEL,S,AREA,,9
```

```
NSLA,S,1
CM,TAR2,NODE
ALLSEL
REAL,3
GCGEN,CON2,TAR2
REAL,3
GCGEN,TAR2,CON2
!
ASEL,S,AREA,,52
NSLA,S,1
CM,CON3,NODE
ALLSEL
ASEL,S,AREA,,26
ASEL,A,AREA,,35
NSLA,S,1
CM,TAR3,NODE
ALLSEL
REAL,3
GCGEN,CON3,TAR3
REAL,3
GCGEN,TAR3,CON3
!
ASEL,S,AREA,,57
NSLA,S,1
CM,CON4,NODE
ALLSEL
ASEL,S,AREA,,28
NSLA,S,1
CM,TAR4,NODE
ALLSEL
REAL,3
GCGEN,CON4,TAR4
REAL,3
GCGEN,TAR4,CON4
/ESHAPE,1
NUMCMP,ALL
EPLOT
FINISH
!
! Definition of loading angle for biaxiality
ALPHA=0
```

```

/SOLU
!OUTPR,BASIC,ALL
!OUTRES,BASIC,ALL
!
! Definition of the analysis type and analysis options
ANTYPE,STAT,NEW
NLGEOM,ON
SSTIF,ON
NROPT,1,,ON
EQLV,FRONT
!
! Definition of the load step options
*DO,i,0,0.0125,0.250,0.0125
/GO
DDELE,ALL,ALL
FDELE,ALL,ALL
PI=ACOS(-1)
ALPH=ALPHA/10
ALPHA=ALPHA*(-1)
DISPY=i/2
DISPX=DISPY*TAN(ALPHA*PI/180)
!
! General options
AUTOTS,ON
NSUBST,200,1000,10
!
! Dynamic options
TIMINT,OFF
!
! Definition of nonlinear options
NEQIT,500
PRED,ON,,ON           ! Auto time-stepping/prediction
CSYS,0                ! Default coordinate system
!
! Definition of file output variables
FRICTION=FC*10       ! Applied friction coefficient
!
CENTER=NODE(0,0,-2.5)
D,CENTER,ALL,0
ASEL,S,AREA,,58      ! Block restraints
NSLA,S,1

```

```
D,ALL,UX,-DISPX
D,ALL,UY,DISPY
D,ALL,UZ,0
NSEL,ALL
ASEL,ALL
ASEL,S,AREA,,51
NSLA,S,1
D,ALL,UX,-DISPX
D,ALL,UY,DISPY
D,ALL,UZ,0
NSEL,ALL
ASEL,ALL
ASEL,S,AREA,,45
NSLA,S,1
D,ALL,UX,DISPX
D,ALL,UY,-DISPY
D,ALL,UZ,0
NSEL,ALL
ASEL,ALL
ASEL,S,AREA,,40
NSLA,S,1
D,ALL,UX,DISPX
D,ALL,UY,-DISPY
D,ALL,UZ,0
NSEL,ALL
ASEL,ALL
SAVE
SOLVE
SAVE
FINISH
!
! Begin progressive element death scenario according to failure criterion
! of critical elastic strain energy density ratios
/POST1
SET,LAST
SXEX_C=6.2618
SYEY_C=6.2618
SZEZ_C=.0013
SXYEXY_C=.0345
SXZEXZ_C=.0400
SYZEYZ_C=.0400
```

```

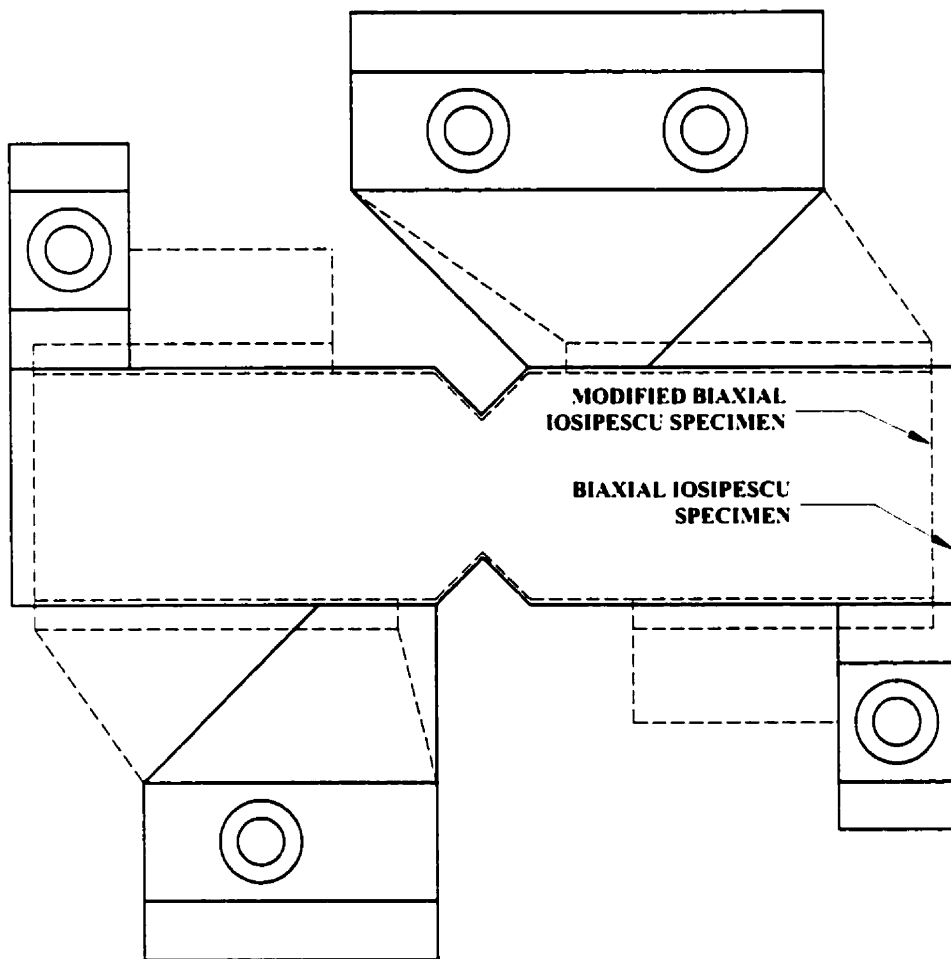
ETABLE,SX,S,X                               ! Strain Energy Ratio (x-component)
ETABLE,EX,EPEL,X
SMULT,SXEX,SX,EX,0.5,1/SXEX_C
!
ETABLE,SY,S,Y                               ! Strain Energy Ratio (y-component)
ETABLE,EY,EPEL,Y
SMULT,SYEY,SY,EY,0.5,1/SYEY_C
!
ETABLE,SZ,S,Z                               ! Strain Energy Ratio (z-component)
ETABLE,EZ,EPEL,Z
SMULT,SZEZ,SZ,EZ,0.5,1/SZEZ_C
!
ETABLE,SXY,S,XY                             ! Strain Energy Ratio (xy-component)
ETABLE,EXY,EPEL,XY
SMULT,SXYEXY,SXY,EXY,0.5,1/SXYEXY_C
!
ETABLE,SXZ,S,XZ                             ! Strain Energy Ratio (xz-component)
ETABLE,EXZ,EPEL,XZ
SMULT,SXZEXZ,SXZ,EXZ,0.5,1/SXZEXZ_C
!
ETABLE,SYZ,S,YZ                             ! Strain Energy Ratio (yz-component)
ETABLE,EYZ,EPEL,YZ
SMULT,SYZEYZ,SYZ,EYZ,0.5,1/SYZEYZ_C
!
! Begin calculation of failure criterion based on the ratios of the
! elastic strain energy density ratios
SADD,RATIO1,SXEX,SYEY,1,1
SADD,RATIO2,SZEZ,SXYEXY,1,1
SADD,RATIO3,SXZEXZ,SYZEYZ,1,1
SADD,RSUM1,RATIO1,RATIO2,1,1
SADD,RSUM2,RSUM1,RATIO3,1,1
ESEL,S,ETAB,RSUM2,1                         ! Select elements which satisfy
*GET,LS,ACTIVE,,SET,LSTP
CM,DV%LS%,ELEM                              ! Assemblies of damage volumes
SAVE
FINISH
/SOLU
ANTYPE,,REST
MPCHG,4,ALL                                 ! Change to damage properties
ESEL,ALL
*ENDDO

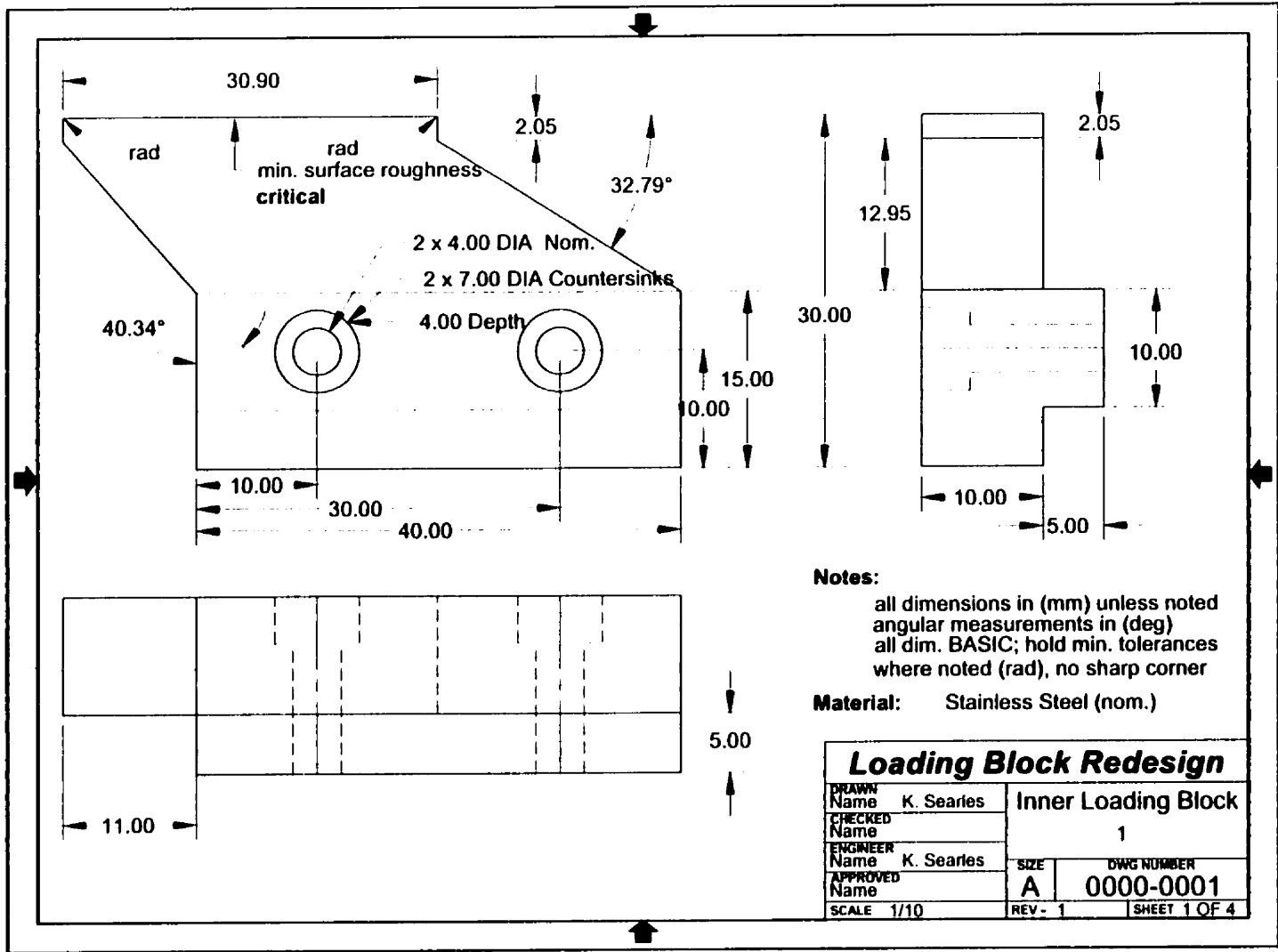
```

```
SAVE
FINISH
/POST1
*DO,j,1,20,1
SET,j
LS=j
CSYS,0
!
! Definition of select path logic for stress-strain data along specimen
! notch root axis
LPATH,4978,4991
PDEF,SX,S,X
PDEF,SY,S,Y
PDEF,SZ,S,Z
PDEF,SXY,S,XY
PDEF,SXZ,S,XZ
PDEF,SYZ,S,YZ
PDEF,EX,EPTO,X
PDEF,EY,EPTO,Y
PDEF,EZ,EPTO,Z
PDEF,EXY,EPTO,XY
PDEF,EXZ,EPTO,XZ
PDEF,EYZ,EPTO,YZ
/OUTPUT,STS%ALPH%%FRICTION%%LS%,DAT
PRPATH,SX,SY,SZ,SXY,SXZ,SYZ
/OUTPUT,STN%ALPH%%FRICTION%%LS%,DAT
PRPATH,EX,EY,EZ,EXY,EXZ,EYZ
/OUTPUT
*ENDDO
FINISH
/EXIT,ALL
```

APPENDIX D

D.1. Mechanical Design: Modified Loading Block Geometry



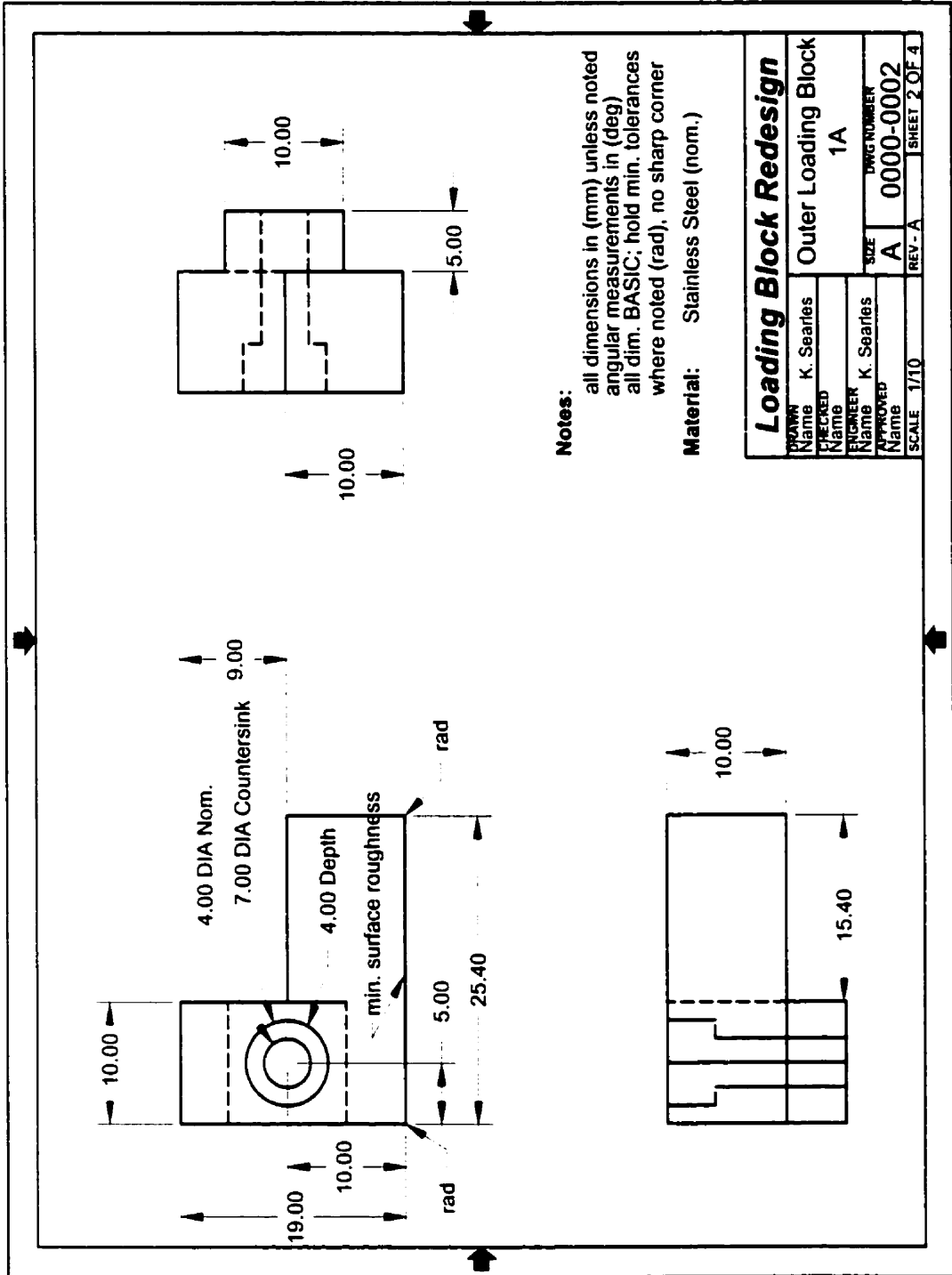


Notes:
 all dimensions in (mm) unless noted
 angular measurements in (deg)
 all dim. BASIC; hold min. tolerances
 where noted (rad), no sharp corner

Material: Stainless Steel (nom.)

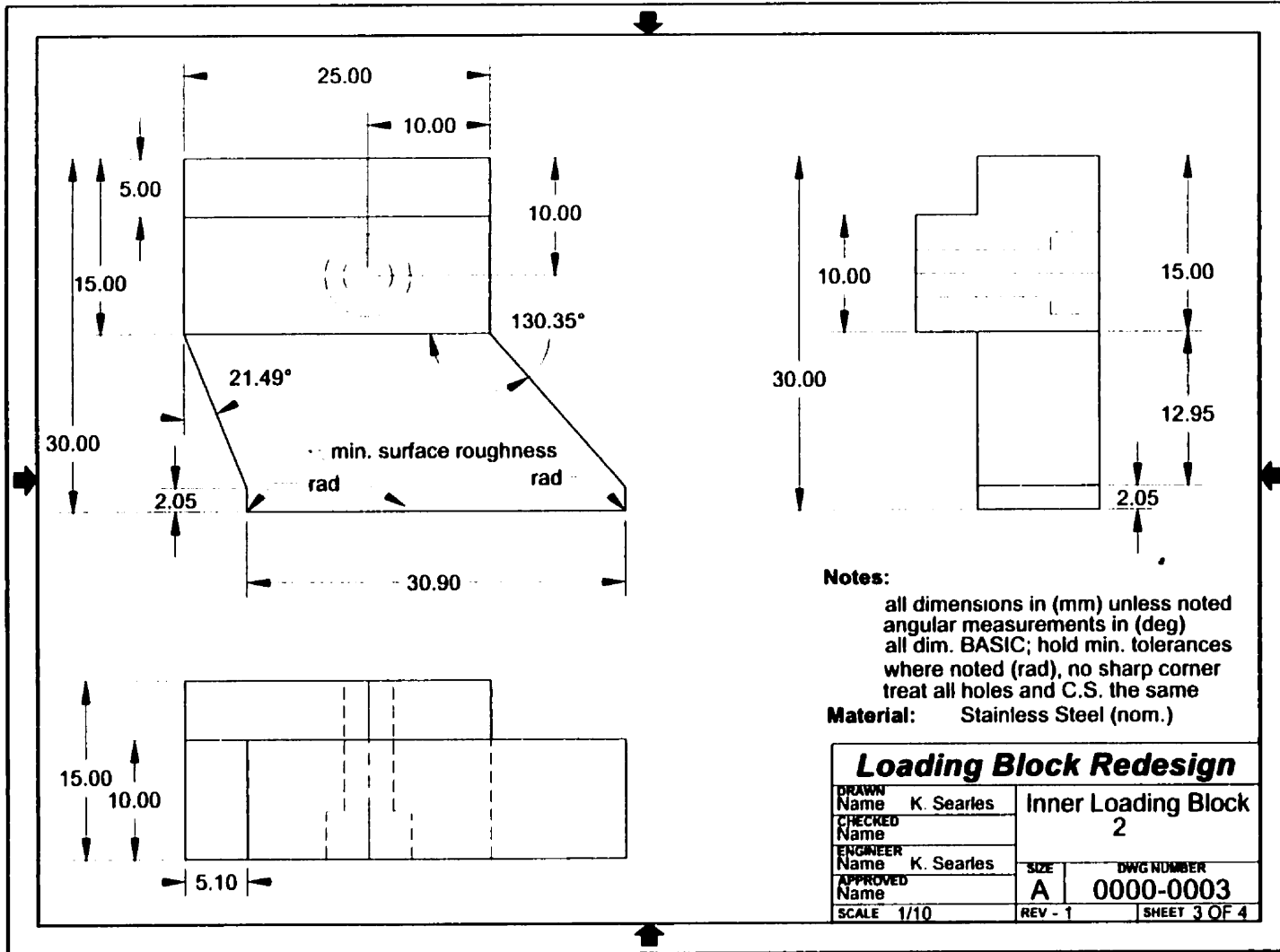
Loading Block Redesign

DRAWN Name K. Searies		Inner Loading Block	
CHECKED Name		1	
ENGINEER Name K. Searies		SIZE	DWG NUMBER
APPROVED Name		A	0000-0001
SCALE 1/10	REV - 1	SHEET 1 OF 4	



Notes:
 all dimensions in (mm) unless noted
 angular measurements in (deg)
 all dim. BASIC; hold min. tolerances
 where noted (rad), no sharp corner

Material: Stainless Steel (nom.)



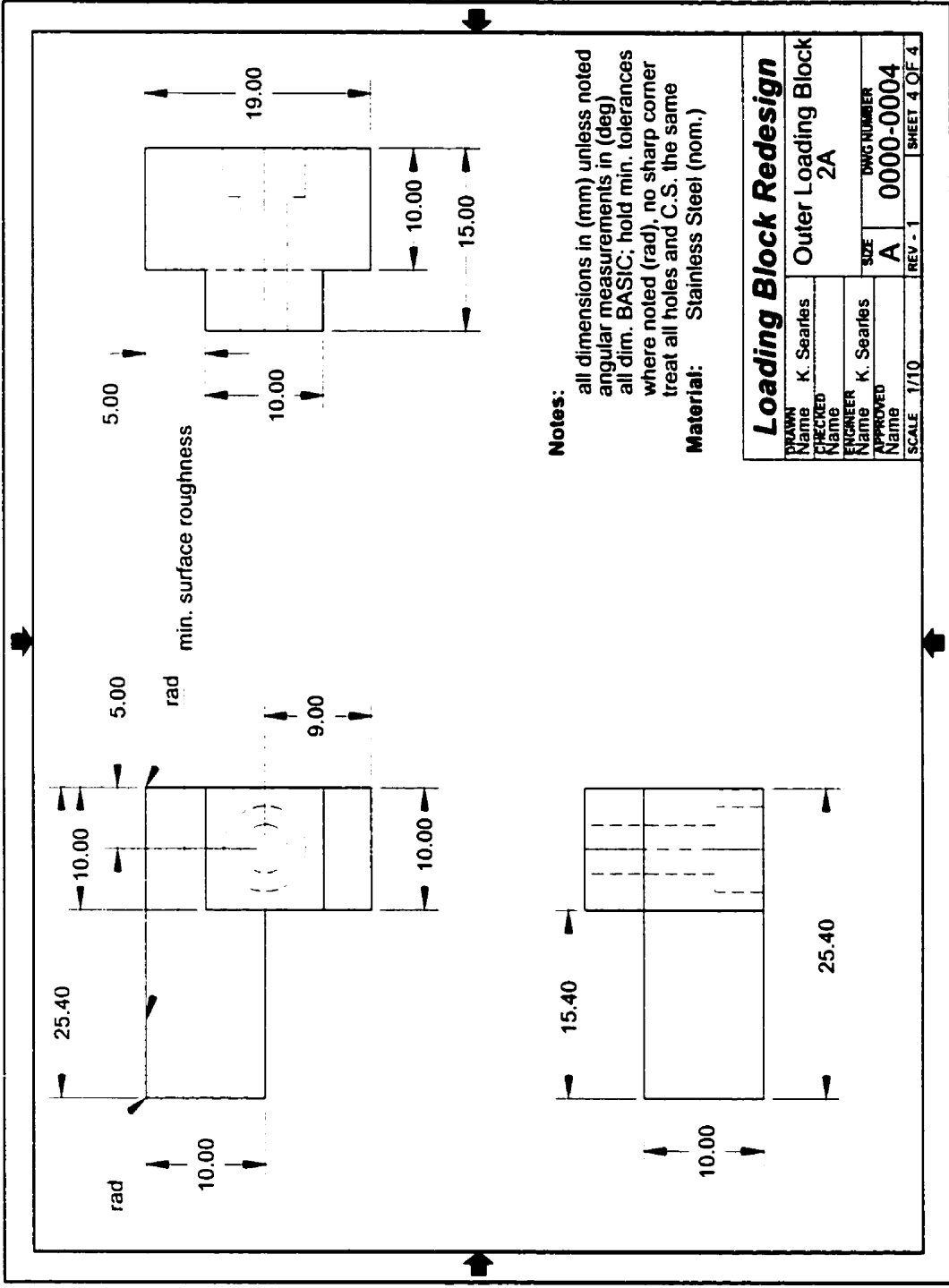
Notes:

all dimensions in (mm) unless noted
 angular measurements in (deg)
 all dim. BASIC; hold min. tolerances
 where noted (rad), no sharp corner
 treat all holes and C.S. the same

Material: Stainless Steel (nom.)

Loading Block Redesign

DRAWN Name K. Searles		Inner Loading Block 2	
CHECKED Name		2	
ENGINEER Name K. Searles		SIZE	DWG NUMBER
APPROVED Name		A	0000-0003
SCALE 1/10		REV - 1	SHEET 3 OF 4



Notes:
 all dimensions in (mm) unless noted
 angular measurements in (deg)
 all dim. BASIC; hold min. tolerances
 where noted (rad), no sharp corner
 treat all holes and C.S. the same
Material: Stainless Steel (nom.)

Loading Block Redesign			
DRAWN Name	K. Searfes	Outer Loading Block 2A	
CHECKED Name		SIZE	DWG NUMBER
ENGINEER Name	K. Searfes	A	0000-0004
APPROVED Name		REV - 1	SHEET 4 OF 4
SCALE	1/10		

BIOGRAPHICAL NOTE

The author was born on the 26th of June, 1966 in Klamath Falls, Oregon. He received his Bachelor of Science degree in Mechanical Engineering from Oregon Institute of Technology, Klamath Falls, Oregon in 1993. After completing his undergraduate studies, he joined Intel Corporation within the domain of sub-0.5 μ manufacturing and process of VLSI circuits. Here, he focused on manufacturing and process improvements to the Back-End-of-Line (BEOL) tungsten chemical mechanical planarization (W-CMP) process.

While remaining a full-time employee of Intel Corporation, the author joined the graduate program in the Materials Science and Engineering Department at Oregon Graduate Institute of Science and Technology (OGIST) in January 1995. During the course of his study at OGIST and while serving as a visiting scientist to the Center for Advanced Materials and Structures at the University of Denver, he has authored or co-authored the following technical papers:

1. Kumosa, M., K. Searles, and G. Odegard. "Biaxial failure analysis of graphite reinforced polyimide composites." *Proceedings of the HITEMP Review 1997*, Advanced High Temperature Engine Materials Technology Program, NASA Lewis Research Center, Cleveland, OH., April 29-30, vol. I paper 18.
2. Searles, K., J. McCarthy, and M. Kumosa. "An image analysis technique for evaluating internal damage in graphite-polyimide fabric composites." *Composites Science and Technology* 58 (1998): 1607-19.
3. Searles, K., G. Odegard, M. Castelli, and M. Kumosa. "Failure investigation of graphite polyimide fabric composites at room and elevated temperatures using the biaxial Iosipescu test." *Journal of Composite Materials* 33 (1998):2038-79.
4. Kumosa, M., K. Searles, G. Odegard, and M. Castelli. "Biaxial in-plane testing of high temperature graphite-polyimide fabric composites." *Proceedings of the High*

Temple Workshop XVIII, Hilton Resort, Hilton Head Island, SC., January 20-22, 1998.

5. Searles, K., G. Tewksbury, B. Tahmasebi, A. Huffstutter, and J. Harvey. "Evaluation of retained apparent shear strength properties in adhesives based on epoxy and cyanate ester chemistries." *Proceedings of the 43rd International SAMPE Symposium & Exhibition*, Anaheim, CA., June 1998.
6. Odegard, G., K. Searles, and M. Kumosa. "A critical examination of the Iosipescu shear test as applied to 0° unidirectional composite materials." *Mechanics of Composite Materials and Structures* 6 (1999): 229-56.
7. Searles, K. and M. Kumosa. "Analysis of nonlinear behavior in 8-harness satin woven fabric composites subjected to in-plane biaxial shear deformation." *Proceedings of the High Temple Workshop XIX*, Downtown Hilton, Denver, CO., January 20-22, 1999.
8. Odegard, G., K. Searles, and M. Kumosa. "Non-linear analysis of woven fabric-reinforced graphite/PMR-15 composites under shear-dominated biaxial loads." *Mechanics of Composite Materials and Structures* 7 (1999): 129-52.
9. Searles, K., G. Odegard, and M. Kumosa. "Micro- and mesomechanics of 8-harness satin woven fabric composites: I-Evaluation of elastic behavior." *Composites Part A: Applied Science and Manufacturing* (1999), accepted for publication.
10. K. H. Searles. "Composites-A general review on composite materials and structures." *Encyclopedia of Smart Materials* (1999), John Wiley & Sons, Inc., accepted for publication.
11. Searles, K., G. Odegard, and M. Kumosa. "The effect of eccentric loads on the macroscopic strain and stress distributions in woven fabric composite Iosipescu specimens." *Journal of Composite Materials* (2000), submitted for publication.
12. Odegard, G., D. Armentrout, K. Searles, and M. Kumosa. "Failure analysis of ± 45° off-axis woven fabric composite tensile specimens." *Journal of Composites Technology & Research* (2000), accepted for publication.
13. Odegard, G., K. Searles, and M. Kumosa. "Non-linear stress analysis of unidirectional and woven graphite/polyimide biaxial Iosipescu specimens." *Experimental Mechanics* (2000), submitted for publication.

14. Searles, K., G. Odegard, and M. Kumosa. "Micro- and mesomechanics of 8-harness satin woven fabric composites: II-Modeling fundamental lamina stress distributions." *Composites Part A: Applied Science and Manufacturing* (2000), accepted for publication.
15. Kumosa, M., K. Searles, V. Thirumalai, and M. V. Balakrishnan. *Biaxial Failure Analysis of Graphite Reinforced Polyimide Composites*. Annual progress report (August 31, 1996) to the Air Force Office of Scientific Research (AFOSR) under grant F49620-95-1-0250.
16. Kumosa, M., K. Searles, and V. Thirumalai. *Biaxial Failure Analysis of Graphite Reinforced Polyimide Composites*. Annual progress report (August 31, 1997) to the Air Force Office of Scientific Research (AFOSR) under grant F49620-95-1-0250.
17. Kumosa, M., K. Searles, G. Odegard and S. H. Carpenter. *Biaxial Failure Analysis of Graphite Reinforced Polyimide Composites*. Annual progress report (August 31, 1998) to the Air Force Office of Scientific Research (AFOSR) under grant F49620-96-1-0314.
18. Kumosa, M., K. Searles and G. Odegard. *Biaxial Failure Analysis of Graphite Reinforced Polyimide Composites*. Final annual progress report (August 31, 1999) to the Air Force Office of Scientific Research (AFOSR) under grant F49620-96-1-0314.